BERGISCHE UNIVERSITÄT WUPPERTAL

Fakultät für Mathematik und Naturwissenschaften
Fachgruppe Physik
Fachrichtung Theoretische Chemische Physik

Modeling Filler Flocculation in Elastomers – an Approach Based on Surface Free Energies and Monte Carlo Simulation

Dissertation zur Erlangung des akademischen Grades eines
Doktors der Naturwissenschaften (Dr. rer. nat.)
vorgelegt von

Norman Gundlach

Wuppertal, 2019

The PhD thesis can be quoted as follows:

urn:nbn:de:hbz:468-20191104-092844-4
[http://nbn-resolving.de/urn/resolver.pl?urn=urn%3Anbn%3Ade%3Ahbz%3A468-20191104-092844-4]

DOI: 10.25926/pq5r-qx14
[https://doi.org/10.25926/pq5r-qx14]

Danksagung

An dieser Stelle möchte ich die Gelegenheit nutzen, um mich bei allen an dieser Arbeit beteiligten Personen zu bedanken.

An erster Stelle gilt mein Dank Herrn Prof. Dr. Reinhard Hentschke, der mich während meiner kompletten Arbeit betreut hat. Er stand mir zu jeder Zeit mit Ratschlägen beiseite und half mir mit seinen vielfältigen Erklärungen und Anregungen auch in Phasen weiter, in welchen ich nicht mehr weiter wusste. Vielen Dank für das außerordentlich gute Betreuungsverhätlnis und die stets offene Tür.

Für die Übernahme der Zweitkorrektur und die produktive Zusammenarbeit über die Dauer des Projekts danke ich Herrn Prof. Dr. Nils W. Hojdis ganz besonders.

Desweiteren möchte ich mich für die produktive und angenehme Zusammenarbeit bei den Unterstützern der Contintental AG bedanken. Dies sind die Damen Dr. Darja Klat, Dr. Carla Recker und Dr. Julia Schöffel, sowie die Herren Frank Fleck, Dr. Jorge Lacayo-Pineda, Dr. Hossein Ali Karimi-Varzaneh und Dr. Thomas Müller-Wilke. In diversen Treffen sind durch das ergiebige Feedback erst viele Fragestellungen ersichtlich geworden, welche den Verlauf dieser Arbeit wesentlich beeinflussten.

Für die Schaffung einer freundschaftlichen als auch wissenschaftlich fundierten Arbeitsatmosphäre in der Arbeitsgruppe der Theoretischen Chemischen Physik möchte ich mich bei Frau Mariia Viktorova und den Herren Dr. Jonathan Hager, Dr. Jan Meyer, Sven Engelmann und Sergej Berdnikow bedanken.

Außerdem möchte ich mich bei Prof. Dr. Michael Karbach bedanken, der mich während meines ganzen Studiums begleitet hat und sowohl bei privaten als auch fachlichen Problemen immer ein offenes Ohr hatte. Seine Teilnahme als Mitglied der Prüfungskomission freut mich sehr.

Für die weitere Teilnahme als Mitglied der Prüfungskomission möchte ich mich bei Herrn Prof. Dr. Dirk Lutzenkirchen-Hecht bedanken.

Des Weiteren geht ein besonderer Dank an Tim Heger, Christoph Bernauer und Jan Kühn, welche mich bei der sprachlichen und inhaltlichen Korrektur unterstüzt haben.

Schließlich möchte ich meiner Familie danken. Ihr standet stets an meiner Seite und habt mich auch in den beschwerlichen Phasen der Promotion, des Studiums und des Lebens unterstützt und immer an mich geglaubt. Danke!

Abstract

Elastomer materials, such as tires, damping elements, and rubber soles of shoes require the addition of filler particles for reinforcement and durability as well as the enhancement of other properties of the final product. During the post-mixing stages the previously dispersed filler undergoes (re-)agglomeration in a process called flocculation. The resulting filler network morphology strongly influences the mechanical properties of the rubber material. This means that the structure itself, its dependence on the physicochemical properties of the underlying components, and its attendant influence on, for instance, the dynamic rubber moduli are of significant interest. In this work, a coarse-grained simulation approach for the investigation of filler structures within elastomers created due to flocculation is presented: the morphology generator. It utilizes a lattice model of the components, whose thermodynamic development is governed by (measured) surface and interface free energies. The flocculation process is mimicked via a nearest-neighbor site-exchange Metropolis Monte Carlo algorithm. It minimizes the free enthalpy and the number of Monte Carlo moves provides a rough measure of time due to the local nature of the moves. The elastomer materials investigated in this work consist of different rubbers plus filler of variable type. The focus is hereby on natural and styrene-butadiene rubber – either individually or as a blend – containing carbon black or silica of different grades. For the filler particles, the model allows to assign the property of surface treatment individually to each side of the particle. A specific example of surface treatment in the case of silica particles is silanization. The resulting morphologies are investigated with simulated transmission electron microscopy and small angle scattering. Quantities of interest include the size of the aggregates and their mass fractal dimension, the fractional interface lengths between the components, and the categorization of filler networks in mass, size, and, if feasible, their mass fractal dimension.

Contents

1. Introduction

Elastomer materials for use in mechanically demanding products, e.g., car or truck tires, damping elements, and rubber soles on shoes require reinforcement by filler particles. During the initial mixing stage in the materials production, these fillers, consisting of agglomerates of nano-particles, i.e., particles with a diameter on the order of 10 nm, are finely dispersed in the elastomer matrix. The prevailing particle structures during this process are aggregates, broken down from the agglomerates, which are themselves not further broken down into the primary particles they are composed of. However, in the post mixing stages, like storage, extrusion or vulcanization, before the polymer network is fully established, these finely dispersed aggregates tend to re-agglomerate in a process called flocculation [1–5]. Flocculation leads to the formation of filler networks, which determine the dynamic mechanical properties of the elastomer material to a large extend. Notably, the filler network is a major contributor to the non-linear amplitude dependence of the dynamic moduli, i.e., the Payne effect [6, 7]. This effect is the overwhelming contributor to fuel consumption due to rolling resistance of vehicle tires. The Payne effect cannot be avoided, but it may be controlled and even usefully employed to enhance desirable properties, e.g., a tire's grip. Control became more versatile when the tire industry introduced the so-called 'green tire technology' roughly two decades ago, which meant that the filler system in the tread compounds for high-performance passenger car tires was changed from carbon black to silica [8]. Compatibilization of rubber with silica, using sulfur containing silanes, led to a better filler dispersion during the mixing process, governed by the silane chemistry and its attendant influence on the interface tensions between the components.

So far no unified approach encompassing both flocculation as well as the analytical calculation or the simulation of the dynamic moduli appears to exist. On the other hand, the theory of the dynamical moduli has received considerable attention. The reinforcement induced by fillers has been known for a long time, which is well documented in older standard texts (e.g., G. Kraus [9]). It was also Kraus who developed a model, describing both the storage modulus and the loss modulus as a function of amplitude in filled elastomers, which is still used today [10]. Other models, essentially models of the Payne effect, were developed subsequently. A critical discussion of the models up to 2009 is given in chapter 10 in [7]. An important conceptual step was the application of ideas developed in the early 1980s in the context of the physics of fractals by Mandelbrot [11], or self-similarity in general [12], to the reinforcement of elastomers by filler particles [13–16]. A recently developed model of the Payne effect, which is based on self-similarity in filled elastomers is described in [17, 18]. Complementary to these analytical models, numerical models, mostly based on the finite element method (cf. the introduction in [18]), and particle simulation approaches were developed [19–22]. These particle simulation approaches to non-linearity in filled elastomers utilize the dissipative particle dynamics (DPD) method or methods close to DPD. The smallest unit is the primary filler particle from which aggregates and agglomerates may be build via diffusion limited aggregation and cluster-cluster aggregation methods. Nevertheless, these approaches do not take into consideration the different surface free energies present in real systems. Including more detail of the filler-polymer and filler-filler interfaces comes at the expense of much smaller systems, which do not capture the filler network structure [23–31]. Modeling flocculation, aside

from the mathematical models developed in the context of the physics of fractals (e.g., [12, 32]), has received much less attention in the past. Recently, an approach to the flocculation of fillers inside polymer matrices based on a combination of thermodynamics with game theory was developed [33]. Therein, thermodynamics refer to the utilization of measured surface free energies between different polymers and different fillers. Literature sources on surface free energy measurements for rubber compound ingredients are rare. An extensive measurement was, however, performed in [34]. Additional values are also found, but to a much lesser extend, in [35–38].

From the viewpoint of experiments, the combination of structural information obtained by transmission electron microscopy (TEM) and/or small angle (X-ray) scattering (SAXS) and dynamic mechanical analysis (DMA) has become a standard method [35, 39–43]. These studies focused on the structural development of the filler particles within the elastomer matrix. This includes the development of aggregates and agglomerates as well as percolating filler networks. More recent works such as [35, 41] include the contribution of surface free energies to the formation of structures and the subsequent impact on the dynamic moduli. Other studies, focusing on systems containing polymer blends, investigated the connection between the mechanical properties and the distribution of filler particles [44–47] – without taking the surface free energies of the constituents into account.

The objective of this thesis is to develop a model, which mimics the flocculation process of filler particles inside elastomer matrices on the basis of surface free energies. This model is the morphology generator – a coarse-grained simulation approach utilizing a nearest-neighbor site-exchange Metropolis Monte Carlo (MC) algorithm. Its transition probabilities rely on surface free energies and the resulting interfacial free energies between different components such as polymers, fillers, and surface modified fillers. Those energies are either taken from the experiment or, due to their limited availability, mimicked in close proximity to them. The mimicked size region is in the range of $1\,\mu$m to $2\,\mu$m. The purpose of this work is to find a suitable simulation approach to generate morphologies, which can be described in simple quantities and are comparable to experimental works. Quantities are, for instance, the size of the aggregates and their mass fractal dimension, size and structure of filler networks, including their mass fractal dimension, or the affinity of a certain filler particle towards a distinct polymer. All of them are obtained in the same way as in the experiment, i.e., by utilizing TEM and SAXS. Within this work both methods are performed by utilizing a simulation. Additionally, the wetting-envelope - work of adhesion plot introduced in [35] is used as a predictor for the compatibility between the ingredients. It allows to analyze the polymer-filler compatibility based on the dispersive and polar parts of the surface free energies. A match between the predicted and actual behavior of the simulated morphologies consequently yields a consensus between theory and simulation. In a later stage, i.e., a succeeding project, those morphologies are then subject to DMA, in order to obtain their mechanical properties. A certainly important quantity in this context is the filler network. Hence, they are focused on throughout the entire work.

The approach is computationally cheap and capable of creating morphologies comparable to the experiment. This makes it suitable for screening studies like testing different combinations of polymers, fillers, and surface modified fillers. Throughout this work, more than five hundred rubber recipes were tested and questions like the compatibility between certain combinations or the building of filler networks inside distinct polymers were answered. Mainly, those poly-

mers are natural rubber (NR) and styrene-butadiene rubber (SBR), because they are both individually and as a compound commonly used in tire applications [48, 49] and for rubber soles in shoes [50]. The filler particles used throughout, were mostly mimicked in a broad spectrum of their surface free energies and, hence, resemble various grades of carbon black and different types of silica, such as methylated, fumed or precipitated. The surface modified fillers were either silica coated with monofunctional silanes, such as octeo (octyltriethoxysilane) or APDMES (aminopropyldimethylethoxysilane), or with bifunctional silanes, such as TESPT (Bis[3-(triethoxysilyl)propyl] Tetrasulfide). Furthermore, surface modified fillers was also mimicked in close proximity to those just listed in the last main chapter of this thesis.

1.1. Outline of the Thesis

The thesis is split into two main parts. The first one consists of the three main chapters and the second one of the four appendices. The three main chapters contain all necessary information about the methodology, basic theory, and the results. For readers familiar with the concepts of SAXS, TEM, surface free energies, and MC simulations it is therefore sufficient to consider only this main part. Therein, each chapter is consistent on its own. Following chapters extend the model individually. This is feasible due to the modular conceptualization of the morphology generator. In the appendices, the reader finds additional information on the theory behind the methods. This includes surface free energies and scattering, but also the nomenclature as well as the simulation methodology used within this work.

The introduction of the morphology generator is dealt with in chapter 2. Therein, the necessary theoretical concepts are stated and motivated. Simple examples are chosen to introduce the reader to the concepts behind the morphology generator and the screening methods used to analyze its results. The first three subsections in this chapter build the foundation in order to understand all upcoming results. Thereafter, some example systems are investigated using the derived method, showing the potential of the morphology generator. Finally, the governing parameters of the morphology generator are tested. They include the number of MC steps, the filler volume content, and the temperature. Continuously, single polymers with heterogeneously surface modified filler particles are considered.

An extension of the morphology generator by introducing an additional polymer type is discussed in chapter 3. Furthermore, the heterogeneous surface modification of the filler particles used in the former chapter is abolished and homogeneous filler particles are considered. This leads to certain changes in the basic concepts stated in chapter 2. After those changes are stated, the information drawn from the variation of parameters in chapter 2 are used to apply them to two polymer blends, i.e., 50/50-NR/SBR and 70/30-NR/SBR. Additionally, the impact of longer simulation times is considered.

In chapter 4, the concepts of chapters 2 and 3 are combined, i.e., heterogeneously surface modified filler particles inside polymer blends are considered. This again leads to certain changes of the morphology generator and to adjustments regarding some screening methods. The filler particles mimicked within this chapter are closest to those used by the industry.

In order to find common ground in the terms used throughout this work, Appendix A builds the foundation for the nomenclature. Beside the definition of the terms their chemical, phys-

ical, and technical aspects are elucidated. In addition, the link between the morphology of a compound and its mechanical properties is explained.

Appendix B explains the molecular interactions, which lead to the concept of surface free energies – a basic constituent of the morphology generator. This is done theoretically, by considering the thermodynamic and statistical mechanic derivation as well as experimentally, by considering some state-of-the-art experiments.

A major part of the results obtained by the morphology generator are analyzed by means of scattering, either light for TEM pictures or X-ray for scattering (SAXS) intensities. Appendix C contains the derivations of the equations stated in chapter 2 and elucidates their origin. It also contains a brief description of mass fractals and how the corresponding dimension is connected to small angle scattering in general.

In Appendix D, the simulation methodology of the morphology generator is explained. This includes a discussion of random numbers and MC simulations in general, the derivation of the Metropolis criterion, periodic boundary conditions and minimum image convention, and the program sequence itself. A discussion of the runtime of the program concludes this appendix.

1.2. References

[1] Böhm, G. G., Nguyen, M. N., Flocculation of carbon black in filled rubber compounds. I. Flocculation occurring in unvulcanized compounds during annealing at elevated temperatures. *J. Appl. Polym. Sci.* **1995**, 55 (7), 1041–1050, DOI: 10.1002/app.1995.070550707.

[2] Lin, C. J. et al., On the Filler Flocculation in Silica-Filled Rubbers Part I. Quantifying and Tracking the Filler Flocculation and Polymer-Filler Interactions in the Unvulcanized Rubber Compounds. *Rubber Chem. Technol.* **2002**, 75 (5), 865–890, DOI: 10.5254/1.3547689.

[3] Mihara, S., Datta, R. N., Noordermeer, J. W. M., Flocculation in Silica Reinforced Rubber Compounds. *Rubber Chem. Technol.* **2009**, 82 (5), 524–540, DOI: 10.5254/1.3548262.

[4] Mihara, S. et al., Ultra Small-Angle X-Ray Scattering Study of Flocculation in Silica-Filled Rubber. *Rubber Chem. Technol.* **2014**, 87 (2), 348–359, DOI: 10.5254/rct.13.88958.

[5] Robertson, C. G., Flocculation in Elastomeric Polymers Containing Nanoparticles: Jamming and the New Concept of Fictive Dynamic Strain. *Rubber Chem. Technol.* **2015**, 88 (3), 463–474, DOI: 10.5254/rct.15.85950.

[6] Payne, A. R., Dynamic properties of filler-loaded rubbers. *Reinf. Elastomers*, edited by Kraus, G., New York: Interscience, **1965**, 69–123.

[7] Vilgis, T. A., Heinrich, G., Klüppel, M., Reinforcement of Polymer Nano-Composites: Theory, Experiments and Applications. New York: Cambridge University Press, **2009**, ISBN: 9780521874809, DOI: 10.1017/CBO9780511605314.

[8] Luginsland, H.-D., A Review on the Chemistry and the Reinforcement of the Silica Silane Filler System for Rubber Applications. Aachen: Shaker Verlag GmbH, **2002**, ISBN: 978-3832209506.

[9] Kraus, G., Reinforcement of Elastomers. Edited by Kraus, G., New York: Interscience, **1965**.

[10] Kraus, G., Mechanical Losses in Carbon-Black-Filled Rubbers. *J. Appl. Polym. Sci. Appl. Polym. Symp.* **1984**, 39, 75–92, URL: https://www.researchgate.net/publication/285109095.

[11] Mandelbrot, B. B., The fractal geometry of nature. Edited by Freeman, W., Third, San Francisco: Henry Holt and Company, **1982**, ISBN: 9780716711865.

[12] Stanley, H. E., Ostrowsky, N., On Growth and Form - Fractal and Non-Fractal Patterns in Physics. Edited by Stanley, H. E., Ostrowsky, N., Springer, Dordrecht, **1986**, ISBN: 978-94-009-5165-5, DOI: 10.1007/978-94-009-5165-5.

[13] Brown, W. D., The structure and physical properties of flocculating colloids. PhD Thesis, University of Cambridge, **1986**.

[14] Buscall, R. et al., Scaling Behaviour of the Rheology of Aggregate Networks forme from Colloidal Particles. *J. Chem. Soc., Faraday Trans. I* **1988**, 84 (12), 4249–4260, DOI: 10.1039/F19888404249.

[15] Witten, T., Rubinstein, M., Colby, R., Reinforcement of rubber by fractal aggregates. *J. Phys. II* **1993**, 3 (3), 367–383, DOI: https://doi.org/10.1051/jp2:1993138.

[16] Klüppel, M., Heinrich, G., Fractal Structures in Carbon Black Reinforced Rubbers. *Rubber Chem. Technol.* **1995**, 68 (4), 623–651, DOI: 10.5254/1.3538763.

[17] Hentschke, R., The Payne effect revisited. *Express Polym. Lett.* **2017**, 11 (4), 278–292, DOI: 10.3144/expresspolymlett.2017.28.

[18] Hentschke, R., Macroscopic mechanical properties of elastomer nano-composites via molecular and analytical modelling. *Soft Mater.* **2018**, 16 (4), 315–326, DOI: https://doi.org/10.1080/1539445X.2018.1518243.

[19] Long, D. R., Sotta, P., Nonlinear and plastic behavior of soft thermoplastic and filled elastomers studied by dissipative particle dynamics. *Macromolecules* **2006**, 39 (18), 6282–6297, DOI: 10.1021/ma061306e.

[20] Merabia, S., Sotta, P., Long, D. R., A microscopic model for the reinforcement and the nonlinear behavior of filled elastomers and thermoplastic elastomers (Payne and Mullins Effects). *Macromolecules* **2008**, 41 (21), 8252–8266, DOI: 10.1021/ma8014728.

[21] Raos, G., Casalegno, M., Nonequilibrium simulations of filled polymer networks: Searching for the origins of reinforcement and nonlinearity. *J. Chem. Phys.* **2011**, 134 (5), DOI: 10.1063/1.3537971.

[22] Xi, H., Hentschke, R., The influence of structure on mechanical properties of filler networks via coarse-grained modeling. *Macromol. Theory Simulations* **2014**, 23 (6), 373–382, DOI: 10.1002/mats.201400009.

[23] Brown, D. et al., Effect of filler particle size on the properties of model nanocomposites. *Macromolecules* **2008**, 41 (4), 1499–1511, DOI: 10.1021/ma701940j.

[24] Riggleman, R. A. et al., Entanglement network in nanoparticle reinforced polymers. *J. Chem. Phys.* **2009**, 130 (24), DOI: 10.1063/1.3148026.

[25] Jaber, E. et al., Network formation in polymer nanocomposites under shear. *Soft Matter* **2011**, 7 (8), 3852–3860, DOI: 10.1039/c0sm00990c.

[26] Kalathi, J. T., Grest, G. S., Kumar, S. K., Universal viscosity behavior of polymer nanocomposites. *Phys. Rev. Lett.* **2012**, 109 (19), 1–5, DOI: 10.1103/PhysRevLett.109.198301.

[27] Ndoro, T. V., Böhm, M. C., Müller-Plathe, F., Interface and interphase dynamics of polystyrene chains near grafted and ungrafted silica nanoparticles. *Macromolecules* **2012**, 45 (1), 171–179, DOI: 10.1021/ma2020613.

[28] Chen, Y. et al., Computational study of nanoparticle dispersion and spatial distribution in polymer matrix under oscillatory shear flow. *Langmuir* **2013**, 29 (45), 13932–13942, DOI: 10.1021/la4028496.

[29] Guseva, D. V., Komarov, P. V., Lyulin, A. V., Molecular-dynamics simulations of thin polyisoprene films confined between amorphous silica substrates. *J. Chem. Phys.* **2014**, 140 (11), DOI: 10.1063/1.4868231.

[30] Meyer, J. et al., A nano-mechanical instability as primary contribution to rolling resistance. *Sci. Rep.* **2017**, 7 (1), 11275, DOI: 10.1038/s41598-017-11728-6.

[31] Meyer, J. et al., Molecular Simulation of Viscous Dissipation due to Cyclic Deformation of a Silica-Silica Contact in Filled Rubber. *Macromolecules* **2017**, 50 (17), 6679–6689, DOI: 10.1021/acs.macromol.7b00947.

[32] Bak, P., Chen, K., The physics of fractals. *Phys. D Nonlinear Phenom.* **1989**, 38 (1-3), 5–12, DOI: 10.1016/0167-2789(89)90166-8.

[33] Stöckelhuber, K. W. et al., Filler flocculation in polymers-a simplified model derived from thermodynamics and game theory. *Soft Matter* **2017**, 13 (20), 3701–3709, DOI: 10.1039/c6sm02694j.

[34] Stöckelhuber, K. W. et al., Contribution of physico-chemical properties of interfaces on dispersibility, adhesion and flocculation of filler particles in rubber. *Polymer (Guildf).* **2010**, 51 (9), 1954–1963, DOI: 10.1016/j.polymer.2010.03.013.

[35] Stöckelhuber, K. W. et al., Impact of filler surface modification on large scale mechanics of styrene butadiene/silica rubber composites. *Macromolecules* **2011**, 44 (11), 4366–4381, DOI: 10.1021/ma1026077.

[36] Natarajan, B. et al., Effect of interfacial energetics on dispersion and glass transition temperature in polymer nanocomposites. *Macromolecules* **2013**, 46 (7), 2833–2841, DOI: 10.1021/ma302281b.

[37] Qu, L. et al., Contribution of silica-rubber interactions on the viscoelastic behaviors of modified solution polymerized styrene butadiene rubbers (M-S-SBRs) filled with silica. *RSC Adv.* **2014**, 4 (109), 64354–64363, DOI: 10.1039/c4ra09492a.

[38] Klat, D., Karimi-Varzaneh, H. A., Lacayo-Pineda, J., Phase morphology of NR/SBR blends: Effect of curing temperature and curing time. *Polymers (Basel).* **2018**, 10 (5), 1–15, DOI: 10.3390/polym10050510.

[39] Bergström, J. S., Boyce, M. C., Mechanical Behavior of Particle Filled Elastomers. *Rubber Chem. Technol.* **1999**, 72 (4), 633–656, DOI: https://doi.org/10.5254/1.3538823.

[40] Jouault, N. et al., Well-dispersed fractal aggregates as filler in polymer-silica nanocomposites: Long-range effects in rheology. *Macromolecules* **2009**, 42 (6), 2031–2040, DOI: 10.1021/ma801908u.

[41] Baeza, G. P. et al., Multiscale filler structure in simplified industrial nanocomposite silica/SBR systems studied by SAXS and TEM. *Macromolecules* **2013**, 46 (1), 317–329, DOI: 10.1021/ma302248p.

[42] Bouty, A. et al., Nanofiller structure and reinforcement in model silica/rubber composites: A quantitative correlation driven by interfacial agents. *Macromolecules* **2014**, 47 (15), 5365–5378, DOI: 10.1021/ma500582p.

[43] Tunnicliffe, L. B. et al., Flocculation and viscoelastic behaviour in carbon black-filled natural rubber. *Macromol. Mater. Eng.* **2014**, 299 (12), 1474–1483, DOI: 10.1002/mame.201400117.

[44] Cotten, G. R., Murphy, L. J., Mixing of Carbon Black with Rubber. VI. Analysis of NR/SBR Blends. *Rubber Chem. Technol.* **1988**, 61 (4), 609–618, DOI: 10.5254/1.3536207.

[45] Meier, J. G. et al., Kieselsäuregefüllte Elastomerblends durch Masterbatchtechnologie - Steuerung des Mischungszustandes und der Materialeigenschaften. *Kautschuk Gummi Kunststoffe* **2005**, 58, 587–594, URL: https://www.researchgate.net/publication/235673707.

[46] Lorenz, H., Steinhauser, D., Klüppel, M., Morphology and Micro-mechanics of Filled Elastomer Blends: Impact on Dynamic Crack Propagation. *Lect. Notes Appl. Comput. Mech.* Edited by Grellmann, W. et al., Berlin, Heidelberg: Springer-Verlag Berlin Heidelberg, **2013**, chapter 3, 81–128, DOI: 10.1007/978-3-642-37910-9_3.

[47] Wunde, M., Klüppel, M., Impact of mixing procedure on phase morphology and fracture mechanical properties of carbon black-filled NR/SBR blends. *Contin. Mech. Thermodyn.* **2017**, 29 (5), 1135–1148, DOI: 10.1007/s00161-017-0562-1.

[48] Hess, W. M., Herd, C. R., Vegvari, P. C., Characterization of Immiscible Elastomer Blends. *Rubber Chem. Technol.* **1992**, 66 (4), 330–375, DOI: 10.5254/1.3538316.

[49] Röthemeyer, F., Sommer, F., Kautschuk Technologie: Werkstoffe - Verarbeitung - Produkte. München: Carl Hanser Verlag, **2001**, ISBN: 978-3-446-43760-9.

[50] Lin, H., Jiang, Z., Study on the effect of rubber sole on pressure change of foot movement. *Leather Footwear J.* **2018**, 18 (1), 33–38, DOI: 10.24264/lfj.18.1.4.

2. The Morphology Generator – Introduction and Impact of Heterogeneity in Single Polymers

In this chapter, we introduce the Monte Carlo-based morphology generator. The basic elements are cubic cells on a cubic lattice which, for now, can be either filler particles or rubber volume elements in adjustable proportion. The faces of the filler particles can be altered, i.e., mimic a modified surface. A specific example are silanized silica filler particles. The number of modified faces is variable. The model allows the assignment of surface free energies to the individual faces, which are either taken from different experimental works [1–5] or artificially chosen in close proximity. In this way, a variety of different rubbers and fillers are mimicked. We use a nearest-neighbor site-exchange Metropolis Monte Carlo (MC) algorithm to generate filler morphologies, mimicking flocculation. The transition probabilities of the MC are based on the interfacial free energies between the three components (polymer, filler, and surface modified filler), which in turn are dependent on the surface free energies of the different components, the temperature where the flocculation takes place, and the effective contact area between the particles. Along the MC trajectory, we calculate transmission electron microscopy (TEM) images as well as small angle X-ray scattering (SAXS) intensities. Additionally, another tool, the so-called wetting-envelope - work of adhesion plot, is introduced. It allows to examine the compatibility between a solid, for instance the filler particle, and a liquid, for instance the polymer, in the pure context of surface free energies. To illustrate the potential of the morphology generator, various example systems with different system parameters are investigated.

Introductory, we describe the structure of our model with its most basic parameters such as size of the system, filler content, and amount of modified surfaces. Here, we already show the connection to experimental data or rather how to identify the simulation parameters with those from the experiment. The function of the model as a morphology generator by using a MC simulation follows together with the introduction of the surface free energies. After the model and its function as a morphology generator is fully described, we state the theoretical foundations for the screening techniques like TEM, SAXS, and the wetting-envelope - work of adhesion plot. Finally, results for systems containing different rubbers, fillers, and surface modified fillers are discussed and evaluated. Furthermore, the impact on the variation of different system parameters is discussed explicitly. The explanation of the model, derivation of the screening methods, and parts of the results on systems with experimental surface free energies in section 2.4 are published in [6].

2.1. The Morphology Generator

The model consists of cubic cells implemented on an attendant lattice of size L^3, which we call particles. A typical value of L is 128, resulting in roughly two million particles. For all particles, periodic boundary conditions apply. The property 'filler' is initially assigned to each

particle on the lattice with probability ϕ, which is later on referred to as the filler volume content. The remaining particles subsequently possess the property 'rubber'. The introduction of more particle types is straightforward and is used in the next chapters by creating systems with rubber blends, i.e., using two different rubber types. In this chapter, we want to demonstrate the potential of the morphology generator and the impact of the different system parameters. We thus limit ourselves to just one type of rubber. All particles are monodisperse and their size is set by experimental values of the filler particles. Each of the six faces of a filler particle obtains the state 'treated' – or 'modified' – independently with probability θ. In the case of silica filler particles the surface treatment – or modification – is equal to silanization. The remaining faces possess the property 'untreated' – or 'unmodified'. In the case of silica filler particles the term 'bare' silica also applies. For a deeper understanding on the properties of the particles, the reader is encouraged to look into Appendix A. The left panel of Figure 2.1 depicts a portion of such a system showing the filler particles only. Here, blue indicates an untreated surface, whereas red means that the surface is treated. The right panel shows a close-up of the filler particles with treated and untreated surfaces.

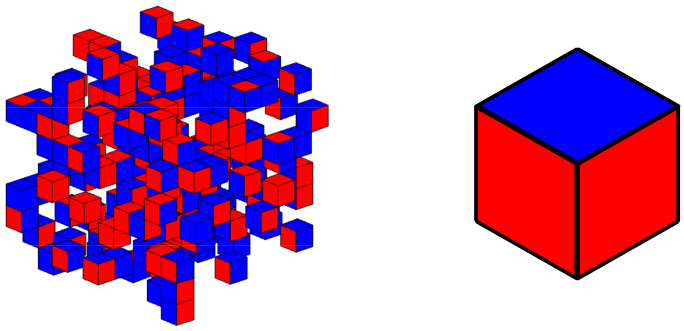

Figure 2.1.: Left: An example system of the model with size $L = 10$. Only the filler particles are shown. Right: An example of a heterogeneously treated particle. The different colored faces either represent untreated (**blue**) or treated particle surfaces (**red**).

2.1.1. Determining the Filler Volume Content

Table 2.1.: Simplified example recipe for a rubber compound used by the tire industry. Note that a real rubber recipe contains additional ingredients like sulfur, zinc oxide etc.

type	example	amount in *phr*	ρ [g/cm^3]
polymer	Styrene-butadiene rubber (SBR)	100	0.94[7]
filler	Ultrasil VN3 granulated (HD silica)	40	$\approx$ 2.00[8]
silane	TESPT	5	$\approx$ 1.10[9]

In our simulation we can set the amount of filler particles by simply altering the value of ϕ. But what is a reasonable value for ϕ, if we want to conduct experimentally comparable

simulations? In order to answer this question, we can, for instance, look at a typical recipe used by the tire industry like the one shown in Table 2.1.

The ingredients in such recipes are not given in total amounts. They are always given in parts per hundred rubber (*phr*). Although this may seem odd at first glance, it is beneficial in practice. With this recipe the amount of polymer simply needs to be fixed in order to find the right amounts for the other ingredients. For instance, starting with 100 g of polymer we need to add 40 g of filler and 5 g of silane. Their densities are not important. Although this procedure is handy for the manufacturer, issues arise for the simulation. To determine the right volume content for a given recipe in *phr* we need to know the densities of the ingredients. Then we can find the volume content of each ingredient i via

$$\phi_i = \frac{V_i}{V_{total}} = \frac{\frac{phr_i}{\rho_i}}{\sum_i \frac{phr_i}{\rho_i}}. \tag{2.1}$$

Here, V_i are the volumes of the individual particles and ρ_i are their densities as given in Table 2.1. With those values, we get a filler volume content of $\phi \approx 15\%$.

It should be noted that finding exact values for the densities is quite difficult. Generally, other quantities such as BET or the tapped density are far more important for the industry. Thus, the calculated value of ϕ gives us more of an initial idea instead of an exact value. With the given densities, any ϕ value encountered in this work can be calculated to *phr* using Equation (2.1).

2.1.2. Homogeneous and Heterogeneous Silanization

When a rubber compound is prepared, the ingredients are not mixed together in a single step. They are always added one at a time [10–12]. In general, we find that adding silica particles is mostly accompanied by the addition of silanes. This procedure is called in-situ silanization. Another possibility is the prereaction of silanes. In both cases, the silanes adhere to the surface of the filler particles by reacting with the silanol groups on the surface. This enhances the reinforcing properties of silica manifold by enhancing the dispersion of the silica inside the elastomer matrix and its interaction with the elastomer matrix[1]. Whether it is done in-situ or as a prereaction, the result may not necessarily yield a homogeneous distribution. Due to the shape of the surface, some areas, such as pores, are more favored than others, because of the higher available surface. Silanes might also adhere more favorably to areas where other silanes already adhered to. Additionally, during the mixing process agglomerates and, in special cases, aggregates are broken down by shear forces (cf. Appendix A). This results in non-silanized areas, where formerly connections between those structures existed. Therefore, a heterogeneous silanization is very likely.

In order to mimic heterogeneity, we introduce the factor θ. Looking at Figure 2.1, we see that it determines the percentage of faces to be silanized (or more generally to be treated). In a physical and chemical context this can be interpreted in two ways. Our reference is a completely homogeneously coated particle as illustrated in the middle of Figure 2.2, i.e.,

[1] A more detailed description can be found in Appendix A.3.

$\theta = 1.0$. Note that the particles are depicted as spherical. This is for better resemblance with realistic silica particles and not too far away from the experiment as described in Appendix A. In the style of our cubic cells, this case would be represented by a completely red cube.

As an example, we now change θ to a value of 0.5. The first thing that might come to our mind is now that we can still maintain homogeneity. This is certainly true, because we only need to erase every second silane from the surface. This alters the necessary amount of silane and the local density on the surface (the number of silanes per $n\text{m}^2$) simultaneously. However, we want θ to mimic heterogeneity. Therefore, this is no possibility in our case. We are consequently left with the two other cases depicted in Figure 2.2.

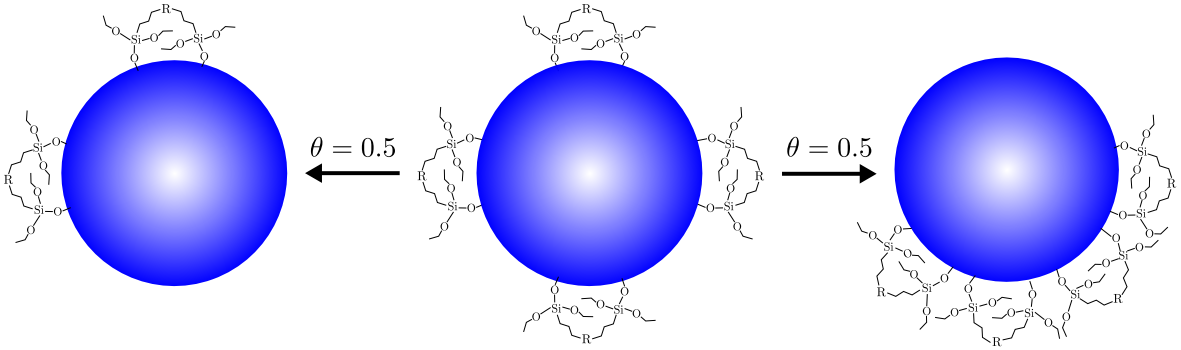

Figure 2.2.: Possible interpretations of θ. The middle particle represents $\theta = 1.0$, i.e., homogeneous silanization. On the left, we have the same silane density but only on one half of the particle. On the right, the silane density is doubled and still one half of the surface is covered. In both cases we have $\theta = 0.5$. θ alone is not capable to characterize the silane distribution and the local density.

Let us assume we have a fixed amount of silane like in the example recipe in Table 2.1 and we distribute this entire amount on the silica surface, but only cover half of it. Then we end up with the picture on the right of Figure 2.2. The silane density on the silica surface is doubled locally. As a consequence, the surface free energy is also affected. This is because in the experiment, when surface free energies are measured for silanized particles, it is assumed that their distribution is homogeneous. However, the extent by which the value is altered is not clear.

The last possibility is given on the left of Figure 2.2. One half of the silica particle is covered with silanes, but the local density is unaltered. As a consequence, the surface free energy is not affected. In this case, the amount of silane needed is only half of that in the original recipe in Table 2.1.

Therefore, when we keep all parameters except θ fixed, it gives us information about the amount of silane rather than the surface density. In chapter 4, additional changes to the surface free energy are also performed. Therein, the other interpretation of θ, i.e., the increasing surface density can be applied.

We can derive formulae to calculate the amount as well as the surface density of the silanes. Depending on the value we want to obtain, we just need to fix the other one. Due to their

dependency it is sufficient to find a formula for only one of the quantities, because its rearrangement always yields the other one.

Let us assume that we are given a recipe like the one in Table 2.1 and we want to calculate the silane surface density σ_{silane}. Because it does not only depend on the amount of silanes, but also on the amount of silica, it is convenient to introduce the ratio of silane to silica, i.e., $\Gamma_{silane/silica}$. It describes a mass ratio, is dimensionless, and is clearly defined in each recipe that we are given. If we assume that the silanes are distributed in the same way for each silica particle, then the mass ratio in the recipe will be equal to the mass ratio of silane to silica for each individual particle. Because the silica particles are spherical, their mass follows directly from experimental data via

$$m_{silica} = \frac{4\pi}{3} \cdot \rho_{silica} \cdot R_{silica}^3, \tag{2.2}$$

where ρ_{silica} is the mass density and R_{silica} is the radius of the (primary) silica particle. For the mass of the silanes we need to know the mass of a single silane molecule. We are using TESPT here and can determine its mass by dividing its molecular weight, which is constituted by its chemical formula $C_{18}H_{42}O_6S_4Si_2$, by Avogadro's constant, i.e., $m_{TESPT} = M_{TESPT}/N_A$. Now we can calculate the mass of silanes adhered to a single silica particle with surface area S_{silica} as a function of θ via

$$m_{silane}(\theta) = m_{TESPT} \cdot \sigma_{silane} \cdot S_{silica} \cdot \theta, \tag{2.3}$$

Dividing (2.3) by (2.2) we find our mass ratio, $\Gamma_{silane/silica}$. After rearranging and performing some simplifications, we find that our silane surface density as a function of θ is given by

$$\sigma_{silane}(\theta) = \frac{\Gamma_{silane/silica} \cdot \rho_{silica} \cdot R_{silica}}{3 \cdot m_{TESPT} \cdot \theta}. \tag{2.4}$$

Using the values for the mass density and primary particle radius of Ultrasil VN3[2], mass of the TESPT molecule, and the silane to silica ratio given in the recipe in Table 2.1 together with $\theta = 0.5$, we get a silane surface density of $\sigma_{silane} \approx 1.5\,n\mathrm{m}^{-2}$. This value is quite high compared to those found in experiments with $\sigma_{silane} = 0.5\,n\mathrm{m}^{-2}$ [13]. When compared to the possible values due to the number of silanol groups on the surface, i.e., 1 to 3 per $n\mathrm{m}^2$ as explained in Appendix A.3, and especially to the values found using molecular dynamic simulations, i.e., 1 to 1.5 per $n\mathrm{m}^2$ [14], then this value is in good agreement. When we choose lower values of θ, for instance $0 < \theta < 0.25$, then the silane surface densities are greater than the theoretical possible values. Thus, $\theta = 0.25$ is the lowest threshold used throughout this work.

It should be noted that when we identify θ for the amount of silane, then we need to keep in mind that a change in θ also changes the value of ϕ. This can be directly seen when looking at (2.1). Let us say we simply set the silane surface density to the value of the simulation, $\sigma_{silane} = 1.5\,n\mathrm{m}^{-2}$, and $\theta = 0.5$. Then we get an amount of silane of $2.5\,phr$. Calculating ϕ

[2] $R_{silica} = 8\,n\mathrm{m}$

again now yields $\phi \approx 15.6\%$ compared to the 15.3% we had before. Since the effect is rather minor, namely less than 1%, it is still reasonable to use the same value of ϕ.

2.2. Monte Carlo Simulation of Flocculation

In this part we explain our flocculation process, which is mimicked by a Monte Carlo (MC) simulation. The moves are introduced, the Metropolis criterion is stated, and its attendant quantities are explained. A derivation and discussion of the Metropolis criterion as well as a description of MC in general are found together with the explanation of the simulation methodology in Appendix D. Subsequently, we introduce the theory of surface free energies used in this work. They are part of the Metropolis criterion and thus necessary to evaluate it. Again, the formulae are motivated and not derived as insight on how to measure surface energies experimentally and their theoretical consideration is found in detail in Appendix B. A simple example follows in order to understand the mechanisms of the MC simulation. Finally, we state the basic quantities of the system which can be directly obtained.

2.2.1. The Metropolis Criterion

The flocculation process is modeled by employing two local MC moves as depicted in Figure 2.3, which are together considered one MC step .

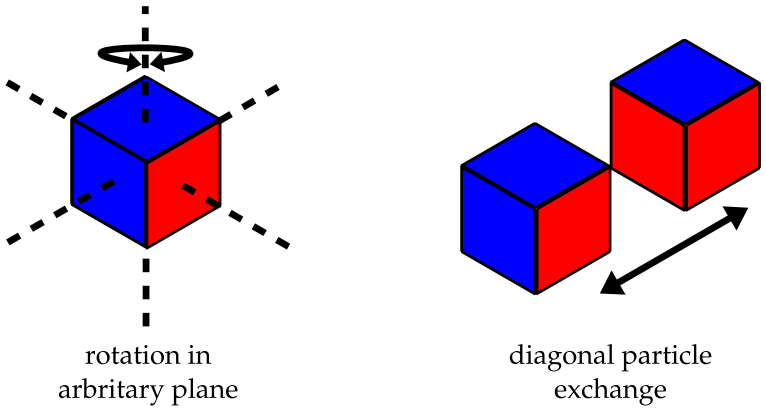

Figure 2.3.: Illustration of MC moves. Left side: particle (cube) rotation; Right side: neighboring particle exchange.

The first move consists of the random selection of a particle and its subsequent rotation by a random multiple of $\pi/2$ with respect to a likewise random axis of the cubic lattice. Subsequently, a nearest-neighbor site exchange move interchanges two diagonal neighbor particles. Again, the pair to be exchanged is picked randomly. Although the particle exchange limits the movement onto a diagonal sub-lattice, the huge number of particles and MC steps (roughly 1000 per particle on average) make up for this. Additionally, the moves are chosen because they can be implemented quite efficiently. Each move is separately followed by a Metropolis criterion, i.e.,

$$\exp[\beta \Delta W(\gamma)] \geq \xi \ . \tag{2.5}$$

Here, $\beta^{-1} = k_B T$, where k_B is Boltzmann's constant and T is the temperature where the flocculation takes place. It is chosen to be in the same region where the experimental flocculation experiments take place, i.e., well above 100 °C [15]. Thus, mostly values of 140 °C or 160 °C are chosen. This is in close proximity to values in [1], where a large portion of the experimentally available surface energies are taken from. The quantity $\Delta W(\gamma)$ is a function of surface free energies γ. It describes the difference in work of adhesion, which is the driving force for flocculation/reagglomeration [16]. It is given by

$$\Delta W(\gamma) = -\gamma_j \Delta A_j = -\gamma_j a \Delta n_j, \tag{2.6}$$

where γ_j denotes the interfacial free energy of a face-to-face pairing of type j and $A_j = n_j a$ denotes the attendant total area of j-type interfaces in the system. Note, that the summation convention applies. When performing an MC step the changes in the number of surfaces Δn_j is simply counted in order to calculate (2.6). The constant a is the effective contact area per face, which we assume to be the same for all j. It is calculated under the following assumptions: The reactive groups on the surfaces of our (spherical) particles, i.e., the silanol groups for our silica particles, the bonds of the elastomer coils for our rubber particles, and the functional ends of our silanized particles, have a limited physical length. Thus, the particles need to get into close proximity in order to interact with each other via van der Waals forces, chemical bonds, permanent dipol-dipol-interactions or other types of interactions. Using the chord theorem we calculate the effective contact area to be $a(h) \approx 2\pi R h$ for small values of h as depicted in Figure 2.4. It should be noted that a is independent of the lattice constant d.

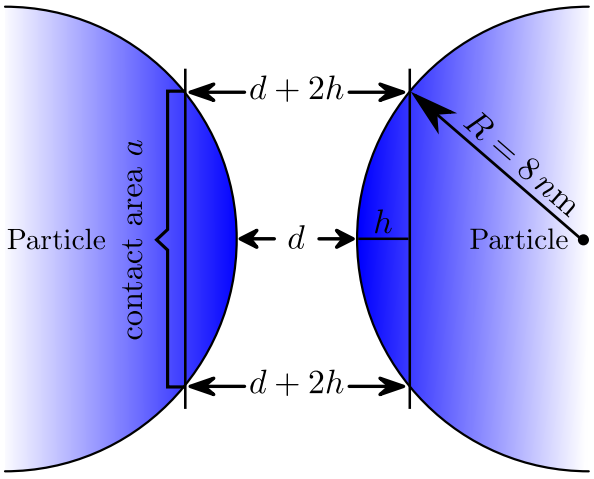

Figure 2.4.: Graphical representation for the effective contact area a. For a given distance d between two spherical particles, the effective contact area at the distance $d + 2h$ can be calculated using the chord theorem to $a(h) = \pi(2Rh - h^2) \approx 2\pi Rh$.

Here, $R = 8\,n\text{m}$ is the radius of the particle and $h \approx 0.1\,n\text{m}$. The value for the radius was fixated in the beginning of the project. It was chosen on the basis of the mean value for Ultrasil VN3 from the original patent [17] and a source of the same company several years later [18]. Ultrasil VN3 was chosen, because its surface free energy is listed in [1] and used quite frequently throughout the literature [4, 11, 19–21]. Unfortunately, most of the primary particle size values are – if mentioned at all – highly variable. The range of sizes, however, is still comparable[3], i.e, below $10\,n\text{m}$. Thus, this value was used for all particles throughout this work in order to maintain monodispersability and comparability. This also matches with carbon blacks in the N1xx size category, which are accounted for high reinforcement (cf. Appendix A. Those values lead to a contact area of $a \approx 4.8\,n\text{m}^2$. In addition, ξ is a random number between zero and unity. If this inequality is satisfied, then the respective move will be accepted.

2.2.2. Introduction of Surface Free Energies

In order to evaluate the Metropolis criterion (2.5), we need to introduce the surface free energies. Therefore, we approximate the interfacial tensions between the different face-to-face pairings using the approach of Owens and Wendt. It is also known as the OWRK theory after Owens, Wendt, Rabel, and Kaelble [22] and is given by

$$\gamma_j \equiv \gamma_{\alpha\beta} = \gamma_\alpha + \gamma_\beta - 2\left(\sqrt{\gamma_\alpha^d \gamma_\beta^d} + \sqrt{\gamma_\alpha^p \gamma_\beta^p}\right), \tag{2.7}$$

where $\gamma_\alpha = \gamma_\alpha^d + \gamma_\alpha^p$, which holds for β as well of course. The superscripts d and p indicate the dispersive and polar part of the surface free energies of α or β. This approach is commonly used when surface free energies are considered in either context, experimentally (e.g., [2, 5, 19, 23]) as well as in simulations and theory (e.g., [16, 24, 25]). Owens and Wendt developed it drawing on earlier works of Fowkes [26] and Girifalco and Good [27–29]. Girifalco and Good were the first to calculate the interfacial tensions between different phases based on the Lennard-Jones potential. Fowkes was the first to introduce the separation of the surface tension into two parts, a dispersive one, on which he focused, and because he looked at mercury, a part due to metallic bonds. Owens and Wendt then extended Fowkes approach splitting the surface tensions into two parts, a dispersive one and a polar one, for all molecules.

To obtain the surface free energies of different materials various techniques are common (e.g., [30]). Most prominently known are the sessile drop technique, the pendant drop method, and the Wilhelmy plate method. The sessile drop technique is used to obtain the surface free energy of a solid, whereas the pendant drop and Wilhelmy plate methods are used for liquids. However, all methods measure the contact angle θ, which relates to the surface free energy via the Young equation

$$\gamma_s - \gamma_{sl} = \gamma_l \cos\theta. \tag{2.8}$$

[3] For instance, in [18] several other high dispersion silica grades, i.e., those with high BET surface area, are named: Ultrasil VN2 ($R = 8.25\,n\text{m}$) and Ultrasil 7000 ($R = 7\,n\text{m}$).

Here, the subscripts s and l denote the solid substrate and the probe liquid. If $\theta < 90°$, then the liquids wets the solid surface. A value of $\theta = 0°$ is considered as perfect wetting of the liquid on the solid. In the context of filler and polymer, wetting can give a hint on dispersibility. Combining (2.7) with (2.8) and using $\alpha = s$ together with $\beta = l$, we find

$$(\gamma_l^d + \gamma_l^p)\frac{\cos\theta + 1}{2} = \sqrt{\gamma_s^d \gamma_l^d} + \sqrt{\gamma_s^p \gamma_l^p}\ . \tag{2.9}$$

This is the so-called wetting - envelope equation. By measuring the contact angle of different probe liquids, for which γ_l^d and γ_l^p are known, on a solid substrate it allows to obtain γ_s^d and γ_s^p. Subsequently, the values for the interfacial tensions immediately follow using (2.7).

2.2.3. Example Mixing of Water and Oil

It is useful to consider an example like the one shown in Figure 2.5. The four cells, two corresponding to water and two corresponding to oil, initially possess two mixed interfaces for which $j = wo$. Subsequently, the cells are rearranged so that the water(w)-oil(o) interfaces are replaced by water-water (j = ww) and oil-oil (j = oo) interfaces.

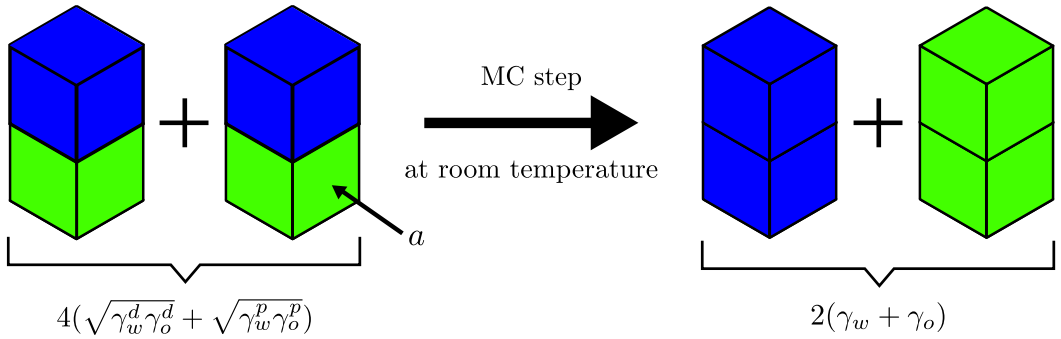

Figure 2.5.: Example MC step in a water-oil mixture as explained in the text. The neighboring particle exchange step is performed at room temperature, i.e., $k_B T = 2.48\,\mathrm{kJ/mol}$. The interfacial area for each type of interface is a.

Since we create two new surfaces and destroy two old surfaces, the attendant $\Delta W(\gamma)$ is given by

$$\Delta W(\gamma) = -\gamma_j\, a\, \Delta n_j = -\gamma_{ww} a - \gamma_{oo} a + 2\gamma_{wo} a. \tag{2.10}$$

Inserting (2.7) together with $\alpha = w$ and $\beta = o$, we find

$$\Delta W(\gamma) = 2a\left(\gamma_w + \gamma_o - 2(\sqrt{\gamma_w^d \gamma_o^d} + \sqrt{\gamma_w^p \gamma_o^p})\right). \tag{2.11}$$

We can now use values from the literature for the surface free energies of water $\gamma_w^d = 13.1\,k\mathrm{J}/(\mathrm{mol}\cdot n\mathrm{m}^2)$, $\gamma_w^p = 30.7\,k\mathrm{J}/(\mathrm{mol}\cdot n\mathrm{m}^2)$ and olive oil $\gamma_o^d = 18.9\,k\mathrm{J}/(\mathrm{mol}\cdot n\mathrm{m}^2)$, $\gamma_o^p = 0.96\,k\mathrm{J}/(\mathrm{mol}\cdot n\mathrm{m}^2)$ [31]. Performing our example mixing at room temperature, i.e., $k_BT = 2.48$ kJ/mol, the exponent of our Metropolis criterion yields

$$\beta\Delta W(\gamma) \approx 17\,a\,n\mathrm{m}^{-2}. \tag{2.12}$$

This means that this particular MC step is accepted, regardless of what the specific size of a is. This is reasonable, because from our daily experience we know that water and oil, once mixed due to shaking for instance, will separate after some time.

2.2.4. Basic Quantities of the System

After a typical run of the simulation, information of the system can be directly obtained without the help of other methods. Those quantities are called basic. Most of them rely on clusters. With clusters we mean all structures in our system that develop during the MC and we identify with a certain rule. Because the formation of filler structures is of utmost importance, clusters are only formed by them. The definition to identify which filler combinations are considered a cluster is:

Definition: Two filler particles belong the same Cluster C, if they do share an untreated surface.

It is chosen based on the hierarchical process in real systems (cf. Appendix A.2.2). Clusters are identified after the MC, i.e., after the flocculation process. They are assigned a mass, which is simply just the number of particles, N, within a cluster

$$m_C = N, \tag{2.13}$$

and a size, which is given by the squared radius of gyration

$$R_G^2 = \frac{\sum_{i\in C} |(\vec{r}_i - \vec{r}_s)|^2}{m_C}. \tag{2.14}$$

It is the averaged squared distance of any point $\vec{r}_i$ inside a cluster C from its center of mass $\vec{r}_s$. In our model we use the center of a cubic cell, representing a particle, as its coordinate. Also, the minimum image convention applies[4]. Both quantities allow us to get an idea of the dimension of the structures developed during the MC. For instance, a cluster of high mass and size is very likely to be considered a filler network. Smaller clusters, on the other hand, may be in the region of agglomerates or aggregates.

Another important quantity, which is straightforwardly obtained, is the interfacial length. It is the number of contacts n_{ij} for any given surface pair ij in the system. Here, i and j

[4]For more detail cf. to Appendix D.

can take the values of filler (f), surface modified filler (s), and rubber, which is abbreviated depending on its name. The three distinct sides lead to six possible combinations. In this manner, n_{fr} gives us the number of all filler-rubber contacts in the system, if we abbreviate rubber with r for the moment. The total number of all contacts is given by

$$n_{total} = \sum_{i,j} n_{ij} = \frac{6 \cdot L^3}{2}, \tag{2.15}$$

where L again is the linear dimension of the lattice and i and j run over the particle types f, s, and r. It is now straightforward to calculate the percentage or fraction of specific contacts compared to n_{total}. However, if we are, for example, interested in contacts involving filler, then it is more informative to look at the 'wetted surface fraction', for which the normalization includes only the number of contacts involving filler. The following formula illustrates the wetted surface fraction, l_{fr}, in the case of the f-r-contact:

$$l_{fr} = \frac{n_{fr}}{\sum_j n_{fj}} = \frac{n_{fr}}{n_{fr} + n_{ff} + n_{fs}}. \tag{2.16}$$

A large value of l_{fr} gives us the information that the filler particles are dispersed well inside the elastomer matrix. Analogously, other combinations can be computed, which yield other information. It should be noted that changing the order of i and j also alters the normalization. This means that $l_{fr} \neq l_{rf}$. The wetting of a surface is always out of the perspective of the surface type i.

2.3. Screening Methods

Beside the basic quantities, we need to derive other methods in order to analyze our systems in more detail. Those 'screening methods' consist of transmission electron microscopy (TEM), small angle X-ray scattering (SAXS), and the so-called wetting-envelope - work of adhesion plots. We start with the latter, as they are a helpful tool to demonstrate the compatibility between filler and polymer on the pure relation of surface free energies. This means that they are independent of the simulation itself. Then we introduce the TEM pictures. They give us visual feedback of filler dispersion inside the elastomer matrix. Both methods are evaluated together with the wetted surface fractions derived prior. For instance, if a specific filler aggregates inside a polymer and this is shown in a TEM picture, then it is of interest whether this aggregation yields structures according to our cluster definition or if the particles aggregate through silane interfaces. Finally, we introduce the calculation of SAXS intensities. They are the primary source to obtain structural information of our system, such as the mean size of the aggregates inside the clusters, as well as their mass fractal dimension or that of the filler networks. A combined analysis of TEM and SAXS is essential to obtain a conclusive picture of the system. This combination is also recommended for experiments [32].

2.3.1. Wetting-Envelope - Work of Adhesion Plots

The concept of wetting is a helpful tool to analyze the compatibility between filler and polymer, as well as filler and silane, which is discussed in more detail in Appendix B. Wetting-envelopes allow for representing this by plotting regions of compatibility in the plane. They are obtained by solving the wetting-envelope Equation (2.9) for a fixed contact angle θ[5] and a fixed pair of surface free energies of the liquid or the solid[6]. In order to solve the equation, it is useful to define coordinates for the dispersive and polar part of the surface free energies of the liquid

$$\gamma_l^d = R\cos\psi \qquad \text{and} \qquad \gamma_l^p = R\sin\psi \tag{2.17}$$

or the solid

$$\gamma_s^d = R'\cos\psi' \qquad \text{and} \qquad \gamma_s^p = R'\sin\psi'. \tag{2.18}$$

We can now solve for R and R' respectively

$$R(\psi,\theta) = \left(\frac{\sqrt{\gamma_s^d\cos\psi} + \sqrt{\gamma_s^p\sin\psi}}{\cos\psi+\sin\psi}\right)^2 \frac{4}{(\cos\theta+1)^2}, \tag{2.19}$$

$$R'(\psi',\theta) = \left(\frac{\gamma_l^d+\gamma_l^p}{\sqrt{\gamma_l^d\cos\psi'} + \sqrt{\gamma_l^p\sin\psi'}}\right)^2 \frac{(\cos\theta+1)^2}{4}. \tag{2.20}$$

Thus, we get for the liquid $\gamma_l^d = R(\psi,\theta)\cos\psi$, $\gamma_l^p = R(\psi,\theta)\sin\psi$ and for the solid $\gamma_s^d = R'(\psi',\theta)\cos\psi'$, $\gamma_s^p = R'(\psi',\theta)\sin\psi'$. For every fixed value of θ we can now obtain the respective dispersive and polar part of the surface free energy by varying the according ψ (ψ') from 0 to $\pi/2$, i.e., both parts of the surface free energy are positive, for the solid as well as for the liquid. The solution of both equations is exemplarily shown in Figure 2.6.

The solid lines are called iso contact angle lines, i.e., lines with a fixed value of θ. Higher values of θ correspond to decreasing wettability (or compatibility). Both plots show the same fixed values of either the liquid (left picture) or the solid (right picture). The information content is the same in both cases, because it is always the wetting-envelope Equation (2.9) which is solved. We can even map back and forth between both plots. Consider the dark red dot at $\gamma_l = 22.0\,m\mathrm{J/m^2}$, $\gamma_l^p = 6.1\,m\mathrm{J/m^2}$ in the left portion of Figure 2.6. For the right portion of Figure 2.6, the wetting-envelope plot is created with those 'coordinates' fixed, i.e., we insert both values into Equation (2.20). We then find the dark red dot, now with $\gamma_s = 22.0\,m\mathrm{J/m^2}$, $\gamma_s^p = 6.1\,m\mathrm{J/m^2}$, at the same position.

[5] This θ should not be confused with the value of θ used for silanization.
[6] This kind of representation was first used in [2]

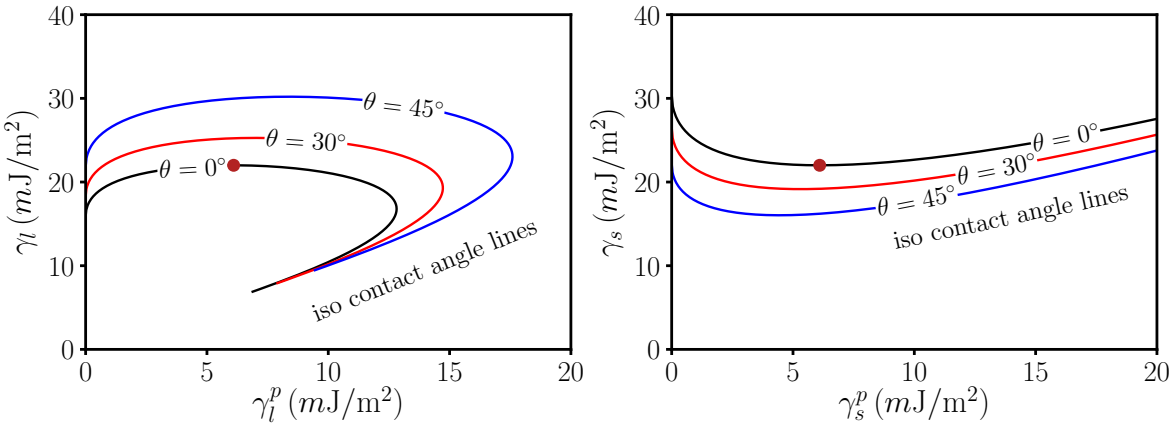

Figure 2.6.: Examples for wetting-envelope plots for three fixed values of θ (iso contact angle lines). In both cases, $i = l, s$, the fixed values are identical ($\gamma_i^d = 15.9\,mJ/m^2$ and $\gamma_i^p = 6.1\,mJ/m^2$). Left: Plot of equations (2.18) and (2.20) with fixed surface free energy of the solid. All liquids inside the $\theta = 0°$ envelope are considered to be completely wetted by the solid. Right: Plot of equations (2.17) and (2.19) with fixed surface free energy of the liquid. All solids above the $\theta = 0°$ line are considered to be completely wetted by the liquid. The dark red dot in both plots shows that the information content is independent of the representation, because it is always Equation (2.9) which is solved.

In this work, we equate the solid with the filler (f) and the liquid with the polymer (p) or the surface modified filler (s). This choice is most natural, as the polymer still flows, albeit slowly, before vulcanization and surface modifications are simply liquids. In the original paper, [2], the authors also equate the filler with the solid and the polymer with the liquid. Their wetting-envelope plots, however, are in the style of the left plot of Figure 2.6, i.e., they interchanged solid, s, and liquid, l. Generally, this is not possible, because the wetting-envelope Equation (2.9) is not symmetric under this interchange for fixed values of θ. In [3] they equate the filler with the liquid and the polymer with the solid and produce the same plots as the authors in [2]. Although this is now correct, the correspondence between a solid material and a liquid drop is difficult to rationalize in the context of wetting (cf. Appendix B). Thus, for the remainder of this work, the wetting-envelopes between filler and polymer or silane are plots in style of the right part of Figure 2.6.

The work of adhesion part inside the plots is obtained by solving Equation (2.6), i.e., the function inside the Metropolis criterion, with a unit contact area a. For a better distinction, we name the (change in) work of adhesion ΔW_a. Note that work of adhesion, W_a, is defined as the free energy change, or reversible work done, to separate a unit p-f-interface from contact to infinity (e.g., [30]), i.e., $W_a = \gamma_p + \gamma_f - \gamma_{pf}$. For the plots, we are interested in the change of the work of adhesion, ΔW_a, which is given by $\Delta W_a = W_{a,pp} + W_{a,ff} - 2W_{a,pf}$. This really is a difference of (reversible) works of adhesion, because the intermediate states, corresponding to the separated interfaces, cancel. ΔW_a is the driving force for flocculation/reagglomeration [16] and allows us to compare system configurations obtained using our morphology generator in the context of this method.

A complete example of a wetting-envelope - work of adhesion plot for natural rubber is given in Figure 2.7. The detailed surface free energies for the polymer are given inside the caption of

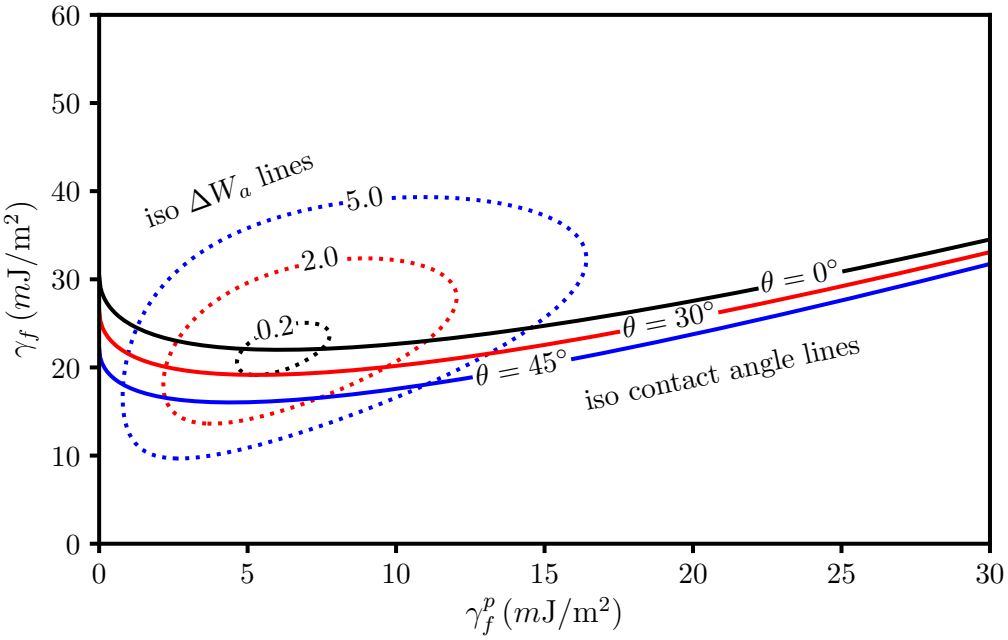

Figure 2.7.: Example of a wetting-envelope - work of adhesion plot for natural rubber (NR, TMR – Standard Malaysian Rubber SMR 20, $\gamma_p^d = 15.9\,m\mathrm{J/m^2}$ and $\gamma_p^p = 6.1\,m\mathrm{J/m^2}$). Surface free energy values taken from [1] and obtained therein by sessile drop contact angle measurements. The solid lines are iso contact angle lines and the dashed closed loops are lines of constant work of adhesion between filler and polymer. Every filler particle whose surface free energy is above the black solid line is considered to be perfectly wetted by the polymer. Fillers inside the inner black dashed loop have the lowest tendency to flocculate.

the figure. The closed dashed loops are the lines of constant work of adhesion – iso ΔW_a lines – and the solid lines are, as before, the lines of constant contact angles – iso contact angle lines. Moving away from the central loop means larger values of ΔW_a and a correspondingly stronger tendency for the filler to flocculate.

2.3.2. TEM – Transmission Electron Microscopy

Light microscopes are limited in their resolution by the wavelength of the photons used to probe the sample, i.e., the Abbe diffraction limit[7]. Using electrons, this resolution is increased by several orders of magnitude. This yields a resolution in the range of nanometers. Because the electron mean free path in the samples is short, they must be cut into slices whose thickness is less than $100\,n\mathrm{m}$ [20]. Experimentally, the preparation of samples is a complex procedure and very time consuming [5]. For our model, producing simulated TEM pictures in order to have a visual representation of the structures inside the system is very simple. Our sample preparation process consists of the same steps as in the experiment. We perform a cut

[7]Ernst Karl Abbe found in 1873 that the minimum resolveable distance for light microscopes is given by $d = \lambda/2\mathrm{NA}$, where λ is the wavelength of the light and NA is the numerical aperture, which is $1.4 - 1.6$ in modern optics.

through our system after a fixed number of MC steps with a fixed thickness and size. This shows the system after different flocculation times and consequently gives information on the structural development during the MC simulation. The coordinates of the filler particles are then extracted and plotted as grey circles onto the plane, as shown in Figure 2.8.

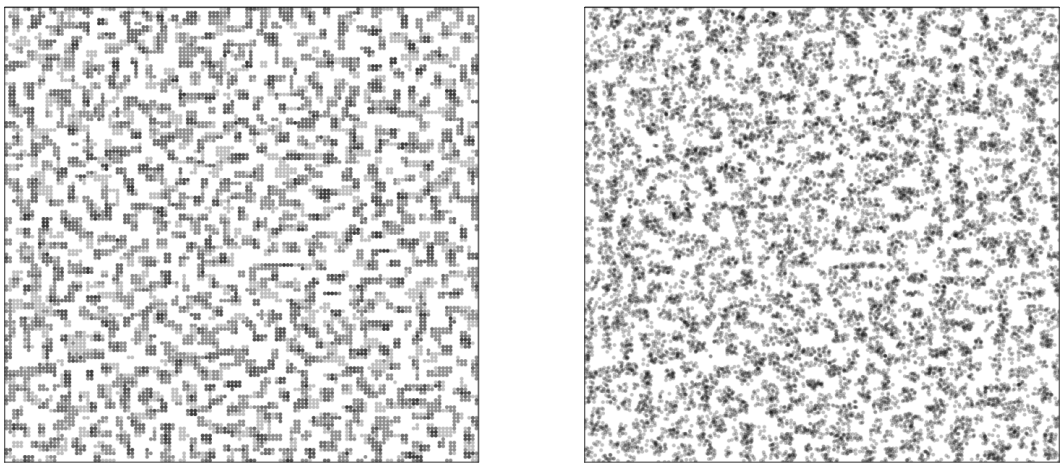

Figure 2.8.: Mock TEM picture generation of a system containing polymer, silica, and silane. Left: A slice with a thickness of five particle diameters is extracted from the simulation after $L^3 \cdot 10^3$ MC steps; Right: small random displacements, as described in the text, are applied to every particle. Darker spots are due to two or more particles superimposed along the line of sight. The polymer is polybutadiene rubber (BR, Lanxess Buna CB25, $\gamma_p^d = 18.4\,m\mathrm{J/m^2}$ and $\gamma_p^p = 3.7\,m\mathrm{J/m^2}$), the filler precipitated silica (Ultrasil VN3, granulated form, $\gamma_f^d = 18.7\,m\mathrm{J/m^2}$ and $\gamma_f^p = 22.7\,m\mathrm{J/m^2}$), and the silane (Coupsil 8113, powdered form, $\gamma_s^d = 22.2\,m\mathrm{J/m^2}$ and $\gamma_s^p = 10.8\,m\mathrm{J/m^2}$). All values are taken from [1]. The size of the system is $L = 128$. A filler volume content of $\phi = 20\%$, heterogeneously silanization with $\theta = 0.25$, and a temperature of $T = 160\ ^\circ\mathrm{C}$ are used.

The shading becomes darker when filler cells are stacked along the line of sight. The thickness of the probe, in particle layers on top of each other, is five, which is equivalent to $40\,n\mathrm{m}$ in our identification of primary particle radii of $R = 8\,n\mathrm{m}$. The size of this TEM picture is 128×128 particles, which is equivalent to approx. $1\,\mu\mathrm{m} \times 1\,\mu\mathrm{m}$. The line of sight, in this example, is along the z-axis. The cut was performed in the middle of the system, i.e., between layers 62 and 67. The left portion of Figure 2.8 is directly obtained from the simulation and clearly shows the underlying lattice structure of our model. A filler network was established inside the elastomer matrix during the simulation. As the resemblance to real TEM pictures is minor (e.g., [33, 34]), small random displacements are applied to all particles. The maximum displacement in any direction is 0.6 times the lattice spacing d. Applying this to the aforementioned slice in Figure 2.8, we obtain the right panel. The lattice structure of our model also leads to some difficulties when using small angle X-ray scattering. The displacement procedure helps to decrease these and is therefore used prior to it, as explained in more detail in the next part.

It is noted that the discussion between the different length scales of lattice, d, and radius of the particles, R, is done consistently within the next part and yields $d = R$. It is stressed

once more that TEM pictures are only used as a tool to *visualize* the system. This means that each individual cell is represented on the lattice as a grey circle. The 'overlap' between the particles, which results from $d = R$, is thus neglected in order to increase visibility.

2.3.3. SAXS – Small Angle X-ray Scattering

Scattering techniques in general, i.e., beside X-ray (SAXS), also neutron (SANS), and light are used throughout the scientific community to analyze the structures of nanocomposites in detail (e.g., [35, 36]). SAXS turned out to be useful to probe the dispersion of nanoparticles inside an elastomer matrix and has been used for this purpose over several decades [37–41]. The reason for this is that the scattering length density of silica, ρ, is very high compared to that of the elastomers. This results in a high scattering contrast, $\Delta\rho$, and subsequently allows to distinguish between filler and the surrounding elastomer matrix quite easily. In the case of our model system, we do not need a high scattering contrast, because we are using the positions of the filler particles directly. Due to the vast information related to this topic a detailed derivation and discussion is found in Appendix C. Here, we only motivate the procedure and equations in order to perform SAXS on our model system. Particularly, we explain the technical aspects necessary to obtain the final SAXS plots and elucidate how to obtain structural information about the system thereout. If not mentioned otherwise, all results shown here relate on the example system depicted in form of a TEM in Figure 2.8.

The scattering intensity of dilute systems, i.e., if no correlation between the single particles exists, can be calculated by the sum of single particle intensities [42]. In our case, we would just need the equation for a spherical scatterer, for example given in [43], and summarize over all filler particles. But here we deal with dense, colloidal particle systems consisting of spherical particles, which are similar to silica or very small carbon black particles (cf. Appendix A). This approach can therefore not be applied, because we need to take the development of structures due to the MC simulation into consideration. An approach, which follows this concept, is given in [44]. Therein, the total intensity is the product of two contributors, i.e., the structure factor, $S_{a/n}$, and the form factor, F_p. Each depends on the magnitude of the scattering vector, q, i.e., the scattering length

$$I(q) = S_{a/n}(q)F_p(q). \tag{2.21}$$

The form factor, $F_p(q)$, is contributed by the (primary) filler particles. As stated before, we could use several equations to model them explicitly, but instead we assume that the particles possess radial symmetry and a well defined surface. This means that, in the respective limits of large and small q, we have

$$F_p(q) \propto \begin{cases} S\,q^{-4}, & q \to \infty, \\ V^2, & q \to 0. \end{cases} \tag{2.22}$$

Here, $S = 4\pi R^2$ and $V = 4\pi R^3/3$ are the surface and the volume of the filler particles, respectively. The q^{-4}-behavior is known as Porod's law and the constant behavior for very small q as Guinier's regime [44]. For particles possessing a fractal surface structure, characterized by

a surface fractal exponent, d_s, one can show that Porod's law is replaced by q^{-6+d_s} [45]. The cross-over from one limit to another occurs in a narrow regime around $qR = \pi$. This means that the scattering intensity above the particular value of q is essentially constant and does not affect the q-dependence of the total intensity in this range. The latter is dominated by $S_{a/n}(q)$, which is due to aggregated particles and the filler network in general. We express $F_p(q)$ in terms of an approximation due to Beaucage [35], combining the laws of Guinier and Porod, which is approximately valid over the entire q-range via

$$F_p(q) = \Delta\rho^2 \left(V^2 \exp[-q^2 R^2/5] + 2\pi S(q^*)^{-4} \right). \tag{2.23}$$

Here, $q^* = q/(\mathrm{erf}(qR/\sqrt{10}))^3$ and $\Delta\rho$ is the aforementioned scattering difference between filler and the elastomer matrix. As argued in Appendix A, realistic filler particles are polydisperse. Therefore, the value of R is the mean particle size of the attendant distribution and $F_p(q)$ is the corresponding average intensity.

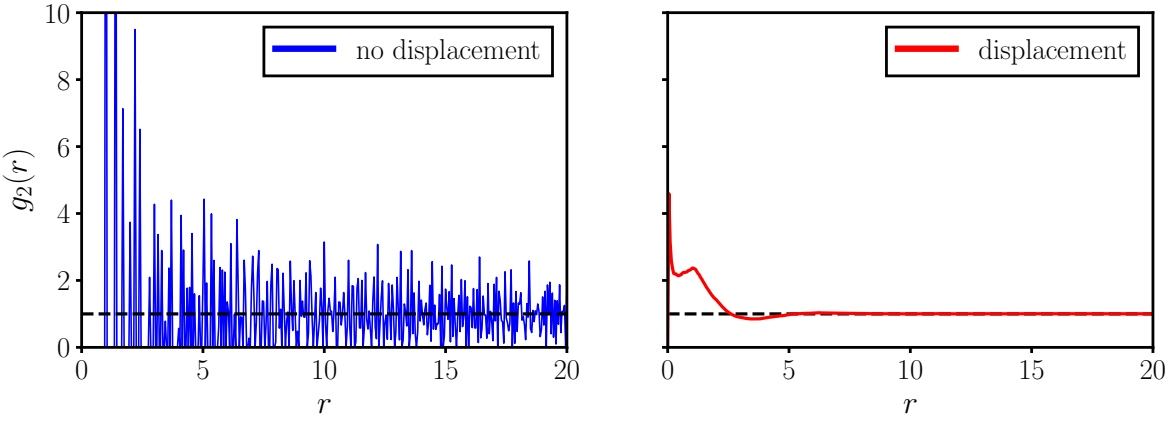

Figure 2.9.: Displacement of the particle positions. Left: Pair correlation function $g_2(r)$ obtained directly from a system without any displacements. The deviations around unity become smaller as the distance increases (cf. black dashed line). Right: The same function after applying displacements in the order of 0.6 times the lattice spacing, d. For greater r values the deviations around unity are very low. The distance, r, is given in units of the lattice spacing, d. The bin width is $\Delta r = 0.05\, d$ (cf. Appendix C).

The structure factor, $S_{a/n}(q)$, on the other hand, is given by

$$S_{a/n}(q) = \phi \left(1 + 4\pi D \int_0^\infty dr r^2 \frac{\sin(qr)}{qr} (g_2(r) - 1) \right). \tag{2.24}$$

The quantity ϕ is the filler volume fraction, D the filler particle number density and $g_2(r)$ is the radial filler particle pair correlation function. In our simulation, we limit the upper bound of the integral by half the size of the simulation box, $L/2$, due to the periodic boundary conditions. Looking at the left portion of Figure 2.9, we find the corresponding $g_2(r)$ function to the left portion of Figure 2.8. The lattice structure of the model system results in sharp,

distinct peaks for $g_2(r)$. The distance, r, is given in units of the lattice spacing, d, which is the underlying length scale to calculate the structure factor in Equation (2.24). The bin width is chosen as $\Delta r = 0.05\,d$. The empty bins are due to the lattice model itself: only distinct distances are possible. In the short-range order, the lowest possible distance is $r = d$. For higher distances, more possibilities arise. The structure factor, $S_{a/n}(q)$, in Equation (2.24) may yield negative values for this $g_2(r)$ for distinct q values, due to the difference in the integral. This in turn leads to negative "intensities", which is impossible, of course[8]. The right portion of Figure 2.9 corresponds analogously to the right portion of Figure 2.8. Here, akin to a liquid, the particles can penetrate each other, i.e., $r < d$ is now possible. This is justified when looking at real systems. The primary particles are merged together and can not be distinguished easily (cf. Appendix A). Nevertheless, generally a minimum distance is always given in real systems. Although this is accounted for after the displacement procedure, albeit very slightly as the first peak is around $r \approx 0.05\,d$, it is not the short-range order we want to look at in detail. We are looking at structures in the region of $r \gg d$. Additionally, it is the form factor in Equation (2.23) which controls the short-range area.

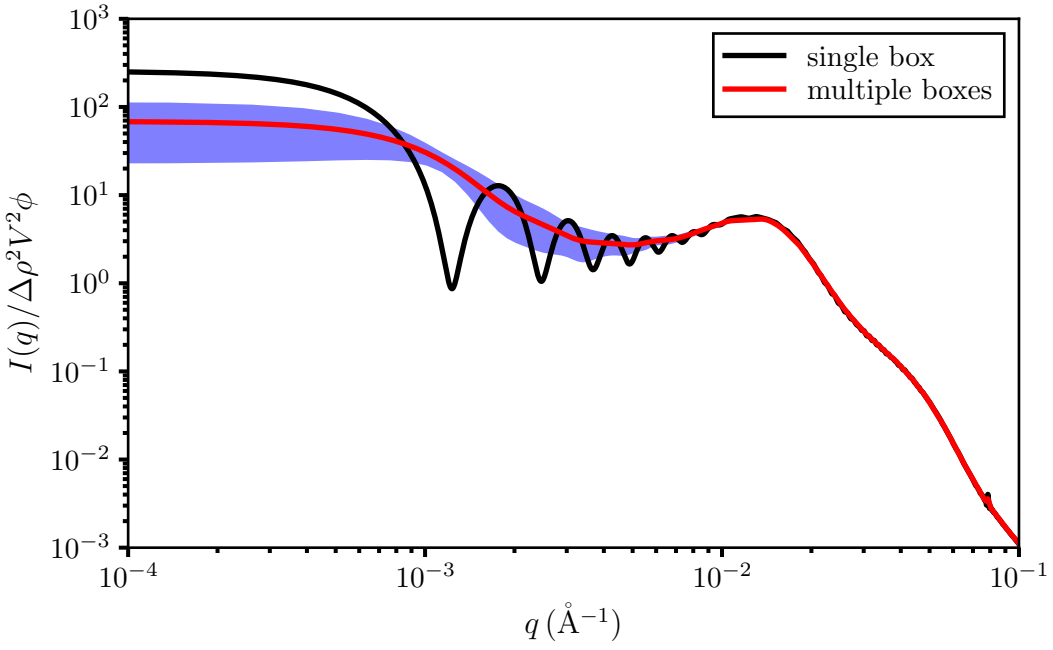

Figure 2.10.: Reduced scattered intensity vs. magnitude of the scattering vector, q. Black: Result obtained from a single MC configuration generated in a cubic box with periodic boundary conditions; Red: Result obtained after the averaging procedure explained in the text. Blue shaded area: Standard deviation due to the cutting procedure elucidated in the text.

When we now calculate the structure factor with particle displacement for a single system, we see significant oscillations over a wide range of q-values (unless of course for $g_2(r) = 1$, which almost never is exactly true) for the reduced scattering intensity. Figure 2.10 shows

[8]The reason for this is the Equation (2.24) itself. The simplifications we made to obtain it do not apply anymore (cf. Appendix C).

an example plot. Note that it is represented on a double logarithmic scale. The black curve is the reduced intensity obtained from a single finite box. The resulting oscillations may be reduced by averaging the intensities obtained for boxes of different size – akin to the primary particles themselves. Averaging over same systems sizes, i.e., producing multiple systems with the same set of parameters and then average over those, does not yield the same results, as the oscillations occur at the same positions for each system and do not cancel out. Obtaining boxes of different sizes can be achieved by repeatedly cutting smaller boxes from a single large simulation box at a given configuration. Generally, we use 50 boxes varying in size between 100% to 18% in L, where L^3 is the volume of the original box. The result is the red curve in Figure 2.10. The blue shaded area is the standard deviation due to the cutting procedure. Notice that the curve is now much smoother, but the intensity is reduced in the small q limit. Notice also that the standard deviation becomes zero when the form factor takes over. The lower limit for the size of the cut out boxes is chosen empirically. It ensures that the filler particle number density, D, is high enough inside each box to be representative for the structure of the whole system. Note that the double logarithmic representation of the data leads to an asymmetric behavior in the uncertainty.

The structural information we can obtain from the double logarithmic representation of the scattering intensity plots can be subdivided into different q-regimes as shown schematically in Figure 2.11. The boundaries of the respective regimes, as well as the data itself, should not be taken for granted. Both are heavily depending on the parameters of the system.

We see a typical plot of the reduced intensity, $I(q)/\Delta\rho V^2\phi$, vs. the magnitude of the scattering vector, q, obtained at different stages of the MC. In the limit of large q, i.e., the region before the first black dashed line from the right, the intensity is entirely governed by $F_p(q)$ and is thus not affected by the MC at all. Consequently, the slope in this regime is governed by Porod's law for surface smooth objects, i.e., $\propto q^{-6+d_s}$ with $d_s = 2$. A small kink is found at $2\pi/R$, where $R = 80\,\text{Å}$ is the average radius of the primary filler particles. The radius is an input parameter and allows us to express q in units of a specific inverse length. The kink is a result of the weighting function in the structure factor in Equation (2.24). Note that a deviation in the slope is found between $2\pi/R$ and π/R. This is a result of the approximation used to obtain the form factor [35] and is not observed experimentally. The first break in slope due to the formation of structures is found at $q_{si} = \pi/R$, i.e., the radius of the primary filler particles. The strongest effect is due to the formation of aggregates during the MC, leading to a broad peak that characterizes the mean size of the aggregates, $R_{agg} \approx \pi/q_{agg}$. Generally, this is the second break in slope in scattering intensity plots. Experimentally, this peak is not observed. A reason for this is the fact that we are using monodisperse particles. They build, for the same set of input parameters, aggregates, which can also be considered as monodisperse. In experiments polydisperse particles are used, which in turn also produce polydisperse aggregates. Due to the broad variance in aggregate sizes no peak is discernible. Instead a slight change in slope is noticeable at q_{agg}, representing the mean size of the aggregates. The next q-regime governs the agglomerates and the filler networks. The q-range labeled $\propto q^{-d_m}$ between the blue dotted line and the last black dashed line, reflects their mass fractal dimension, d_m. It should be dependent on the number of MC steps, as well as on the surface free energies, and the filler volume content ϕ. The problem is that the attendant q-range should be at least an order of magnitude wide for reliable results [47, 48]. This requires quite large system sizes of at least $L = 256$, resulting in the order of 10^8

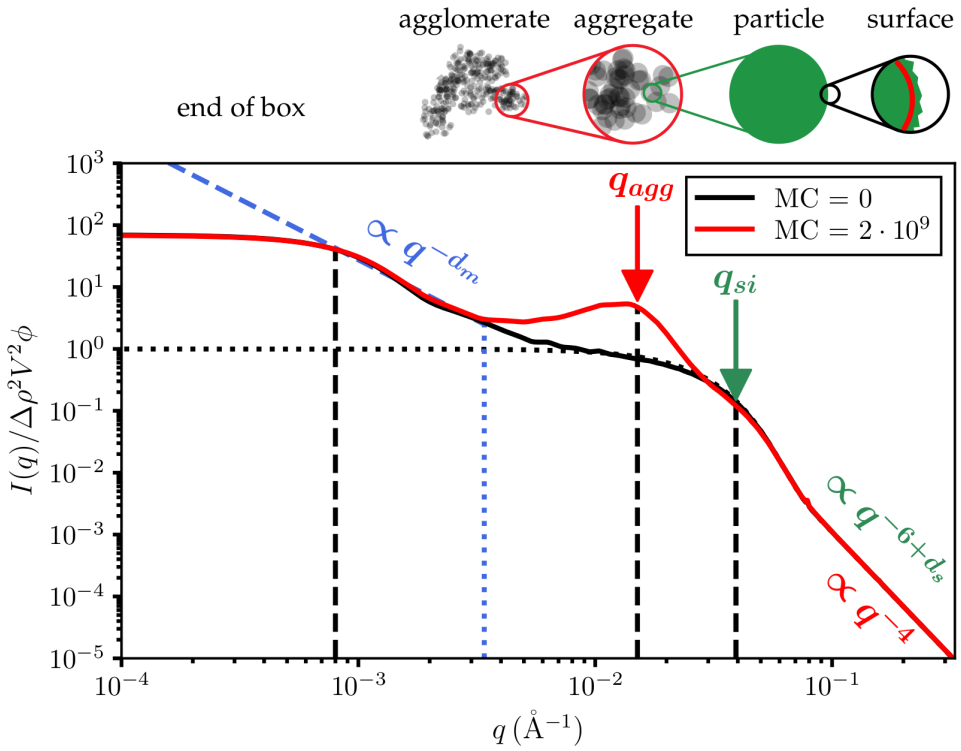

Figure 2.11.: Reduced scattered intensity, $I(q)/\Delta\rho V^2\phi$, vs. magnitude of the scattering vector, q. Depicted are the different q-regimes subdivided by black dashed lines. The limit of large q is governed by Porod's law or, in the case of surface fractal particles, by the attendant law exhibiting a surface fractal dimension, d_s. The first break in slope, indicated by q_{si}, gives information about the size of the primary particles. The subsequent region holds information about the aggregates, with their mean size, q_{agg}, given at the second break in slope. In our case, it is clearly discernible as a peak. The third region contains information about the higher order structures, such as agglomerates or filler networks. The blue dotted line marks the onset of the linear regime with slope $\propto q^{-d_m}$, containing information about the mass fractal dimension of the filler networks. The finite size of the simulated system induces a plateau, terminating useful information at small q. The observed structure depends on the surface free energies and other system parameters, such as the number of MC steps. The black dotted line shows the form factor of the primary particles, $F_p(q)$. This figure is made in style of [46].

particles. This leads to very long simulation times (cf. Appendix D). Due to the huge number of parameter combinations considered in this work, a consideration of such large systems is only done exemplarily in the following. If q becomes very small, i.e., smaller than $\pi/(RL)$, the box size, L, is exceeded and the scattering intensity levels off.

It should be noted that the boundaries of the q-range for the mass fractal dimension of the filler network and the agglomerates are not well defined. They are generally specified as the linear regime between the breaks in slope, which indicate the aggregates and the agglomerates [20, 38, 49, 50]. This is done akin to the case of the mass fractal dimension of the aggregates, where the boundaries are given as the second and first break in slope, i.e., q_{agg} and q_{si}, [51–53].

Most literature sources rather concentrate on the aggregates than the large scale behavior of agglomerates and the filler network. The reason for this is merely the limited q-range of SAXS. Lower q values are only reached by using the extended version of the scattering techniques, namely, USAXS and USANS.

Unfortunately, the monodispersability leading to the pronounced peak does not allow to determine the mass fractal dimension of the aggregates, d_m^{agg}, using the fit approach. Although this might be circumvented by creating artificial polydispersity, the size of the aggregates is relatively small, which limits the possible q-range similar to that of the filler networks. An alternative in the form of the box-counting algorithm is given later on. For the filler networks, however, creating larger systems is a possible solution to obtain d_m for the agglomerates or the filler network.

Before we consider an example, we need to know whether this linear region represents a filler network or an agglomerate. For this, it is useful to consider the basic quantities. A certain threshold in mass or size should distinguish the both. However, the cluster mass alone is not sufficient. Clusters containing lots of particles can simply form very dense, ball like structures. On the other hand, clusters with relatively small amounts of particles can already percolate through the elastomer matrix. For instance, a cluster with a mass of $m_C = L$, where L is the linear dimension of the cubic lattice, is theoretically capable to do so. This case is, however, statistically very unlikely and was never observed in the thousands of systems simulated for this work. Nevertheless, if about 50% of all particles are bound into one single cluster, it is reasonable to consider the corresponding TEM picture for visual feedback. Beside the mass, the size of the clusters should also be considered. A radius of gyration of at least half the lattice size, i.e., $R_G = L/2$, indicates a cluster which is reaching throughout the entire system – at least in one direction. With these thresholds, we can define:

Definition: We consider filler particles to built a filler network, if at least 50% of all available particles are bound into a single cluster *or* the radius of gyration is at least half the lattice size, i.e., $R_G = L/2$. Additionally, the corresponding TEM must support the impression of a filler network.

Let us now consider an example to obtain the mass fractal dimension using the fitting method. For this, we contemplate the system in Figure 2.8, but with increased system size, i.e., $L = 256$. Of the 20% filler particles, we find 84% inside a single large cluster with a size of $R_G = L/2 = 128$. Thus, both thresholds are fulfilled and we are dealing with a filler network. Figure 2.12 depicts the fitting procedure performed on the linear regime of the scattering curve together with the corresponding TEM picture. It also supports the impression of a fine, continuous filler network. Note that the TEM has a size of 50×50 particles, which is equivalent to $400\,n\mathrm{m} \times 400\,n\mathrm{m}$. The size is chosen to better visualize the fine network.

The black curve is the scattering intensity. Notice that compared to Figure 2.10, the linear regime is now approximately one decade in width. It is indicated as the red section, which is found for $5 \cdot 10^{-4} < q < 3 \cdot 10^{-3}$. The blue shaded area is the standard deviation of the scattered intensity due to the cutting procedure (cf. Figure 2.10). The black dashed line is the fit function, which is $\propto q^{-d_m}$. To account properly for the uncertainties on the intensity, the fit is performed three times. Once with the uncertainties added, once subtracted, and

once through the mean. Then the mean and the standard deviation of the three values are calculated. Consequently, for this system a mass fractal dimension of $d_m = 2.12 \pm 0.11$ is found for the filler network as indicated in the plot.

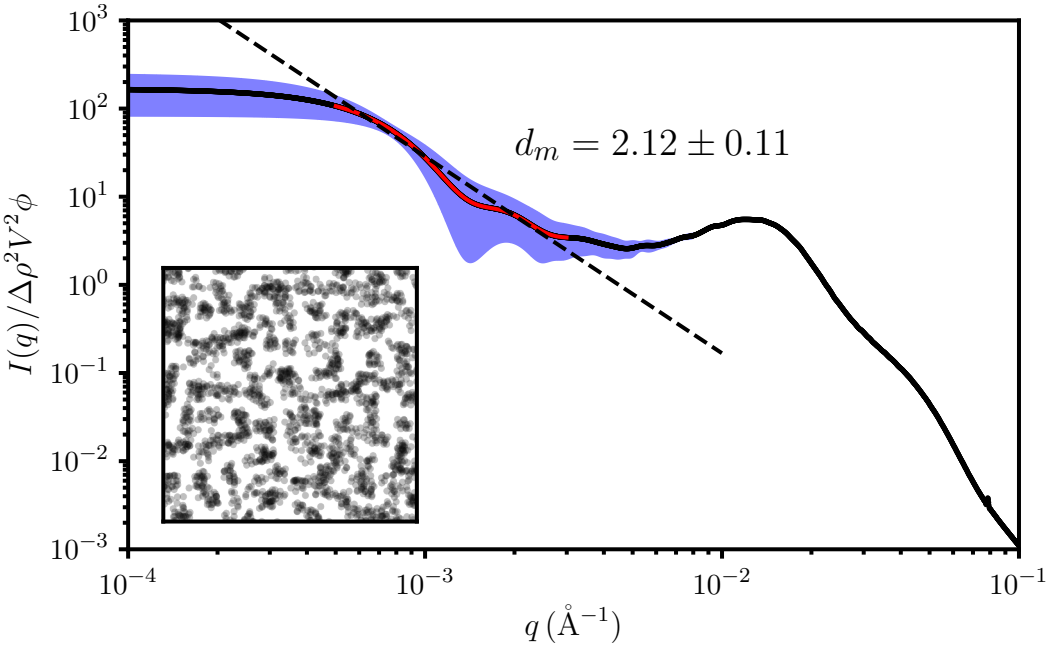

Figure 2.12.: Determining the mass fractal dimension out of a scattering intensity curve. The black continuous line is the reduced scattering intensity obtained after $10^3 \cdot L^3$ MC steps. The blue shaded area is the corresponding error, i.e., the standard deviation due to the cutting procedure. The red highlighted area is the fitting regime. The dashed line is the fit, which is $\propto q^{-d_m}$. Here, d_m is a mean value obtained from fitting with the uncertainty added, subtracted, and once without taking them into account, i.e., a fit through the red highlighted area. The error is the standard deviation of the mean. The TEM picture shows the example system considered so far but with $L = 256$. The size of the picture is 50×50 particles, which is equivalent to $400\,n\text{m} \times 400\,n\text{m}$.

The mass fractal dimension of the aggregates, d_m^{agg}, cannot be obtained in the same way, as discussed before. However, we can find it alternatively by using the box-counting algorithm. Generally, this means that the system is partitioned into n^3 boxes. Whenever a box contains at least one particle, it is considered occupied. n varies from 2 to L and is doubled in each step, i.e., $2, 4, 8, \ldots, L$. Plotting the logarithm of the number of occupied cells, $\ln A_n$, vs. $\ln n$, should yield a slope equal to d_m^{box} for sufficiently large n [54]. For $n = L$ we have the highest possible resolution. The number of boxes matches the number of cubic cells, i.e., we have resolution of one box. In the third and the second to last step, we find boxes consisting of $2^3 = 8$ and $4^3 = 64$ cubic cells. Those three box sizes are thus approximately mimicking the size region, which corresponds to the missing linear regime between q_{si} and q_{agg} in the scattering intensity plot in Figure 2.11. Consequently, a fit through those three values should yield a slope where $d_m^{box} = d_m^{agg}$. It should be noted, however, that this method is not sufficient

for higher filler volume fractions, ϕ, because the number of unoccupied boxes consequently decreases with increasing values of ϕ. At a fixed, fairly low filler volume content, however, the difference between systems with different surface free energies can be investigated.

This method can also be used experimentally on TEM pictures, with the drawback of neglecting the 3D information of the system[9]. For us, this method circumvents beside the missing linear regime a couple of other drawbacks. The box cutting procedure is no issue anymore. It is even independent of the displacement procedure and operates on the lattice itself. Theoretically, it is also suitable to obtain the mass fractal dimension of the filler networks as well. For this, however, we are still in need of bigger systems. For instance, with $L = 256$ we get only eight data points. In the first steps, it is almost certain to find a filler particle inside every box. This leads to an over representation of the euclidean dimension compared to a wanted mass fractal dimension.

To see the influence on the filler volume fraction, ϕ, Figure 2.13 shows the values of the different mass fractal dimensions, d_m and d_m^{agg}, for our example system with $L = 256$. Note that for $\phi < 20\%$ no filler networks developed[10] and the mass fractal dimensions therefore represent those of the agglomerates.

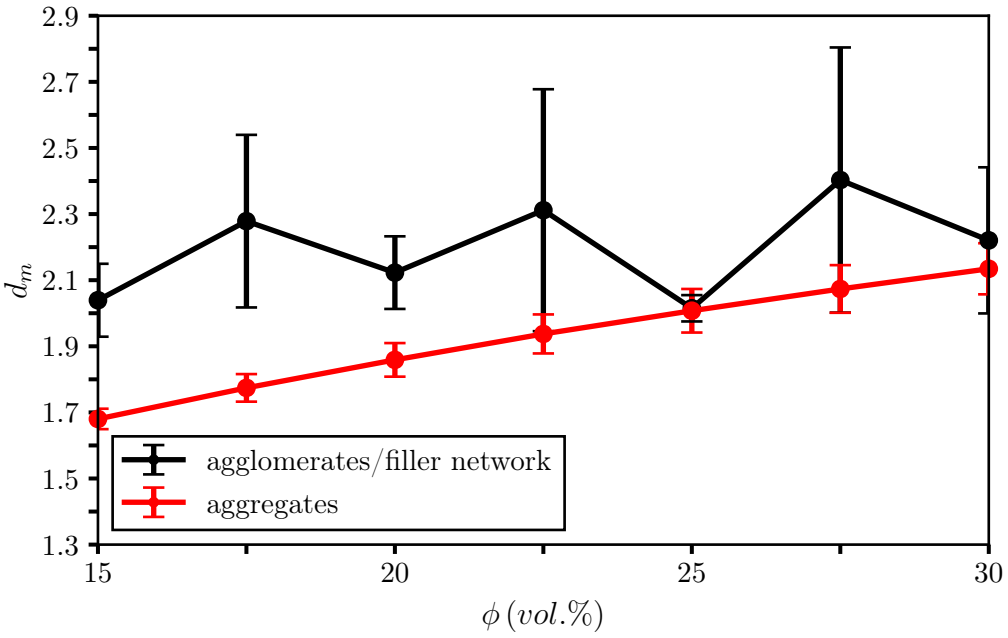

Figure 2.13.: Mass fractal dimensions of the large network structures and the aggregates vs. filler volume fraction, ϕ. Black: d_m of the agglomerates/filler network calculated from fits to the scattering intensity in the range $5 \cdot 10^{-4} < q < 3 \cdot 10^{-3}$; red: d_m^{agg} calculated via box-counting algorithm. Note that the system studied here for $\phi = 20\%$ is identical to that in Figure 2.12.

[9] Although methods for 3D TEM exist [55] and the procedure could therefore be adapted.
[10] Both thresholds of our definition were not surpassed.

The uncertainties for the fitting method are fairly high. This is due to the averaging over boxes of different size, as explained in the context of Figure 2.10. The standard deviation of the intensities is dependent on the size of the individual boxes. A more narrow distribution of the box sizes yields smaller deviations of the intensities. For the box-counting algorithm, we find increasing uncertainties for increasing filler volume content. This is simply a result of the higher variability in the number of occupied boxes.

The mass fractal dimension of the aggregates is mostly far lower than that of the agglomerates or the filler network. Only for $\phi = 25\%$ we find that they behave similarly. The increase in the value of the aggregates shows a trend to reach $d_m^{agg} = 3$ for $\phi = 100\%$. Note that the values are obtained after $L^3 \cdot 10^3$ MC steps and are different from those if no MC is performed. Higher mass fractal dimensions for higher filler volume fractions are also found in literature [51].

The values we obtained for the filler network are already comparable to those found in [38]. For a system composed of styrene-butadiene-rubber (SBR) loaded with various volume fractions, $\phi = 8\% - 21\%$, of simplified silica (Zeosil 1165 MP) mass fractal dimensions of $d_m = 2.4 \pm 0.3$ were found. It is explicitly argued that this value is for the fractal network. In our simulation we only obtain filler networks for volume contents equal to or greater than 20%. A reason might be the additional components of the compound or their mixing procedure. Also, the ingredients we used here are different. Butadiene rubber (BR) instead of SBR, Ultrasil VN3 gran. as the silica instead of Zeosil 1165 MP, and TESPT as the silane instead of octeo are used. But as argued before, literature sources on the fractal behavior of the large network structure are rare. The same is true for the surface free energy values. Nevertheless, we find the same trend. A mass fractal dimension of $d_m = 2.12 \pm 0.11$ using the fitting method is obtained for the filler network, which agrees fairly well.

The mass fractal dimensions of the aggregates are comparable to those obtained by kinetic growth processes with d_m^{agg} between 1.7 and 2.1 [32, 50, 56]. For the pure simplified silica Zeosil 1165 MP a value of $d_m^{agg} = 2.13$ was found [52]. For pure carbon blacks values between 1.5 and 1.9 are found. If incorporated inside ethylene-propylene rubber (EPR), a value of 1.5 is measured [53].

Altogether, the mass fractal dimension is a helpful additional parameter to characterize the systems. Simulating different kinds of filler particles should yield different mass fractal dimensions. The fitting method is the same procedure as used for experimental data. But for agglomerates or filler networks the boundaries are poorly defined and very large system sizes of at least $L = 256$ are necessary. For significant results, several systems with the same set of parameters are necessary. Unfortunately, the long simulation time is then a critical parameter (cf. Appendix D). Thus, the mass fractal dimension of the higher order structures is not considered in the following. For aggregates the procedure is not even applicable. The box-counting algorithm is then a promising alternative. It is quite easy and reliable to obtain and therefore used throughout the entire work.

Identifying the peaks for the primary particles, q_{si}, and those for the aggregates, q_{agg}, is, especially in experiments, a difficult task. Generally, both peaks are not very distinct. This may be due to interference with other ingredients of the probe, the probe itself, or the experimental setup. In the simulation, we deal with the filler particles alone. Identification of

the peak for the mean aggregate size is thus fairly simple. However, this can be even further improved by multiplying the intensity with q^2. This yields a so-called Kratky plot as shown in Figure 2.14.

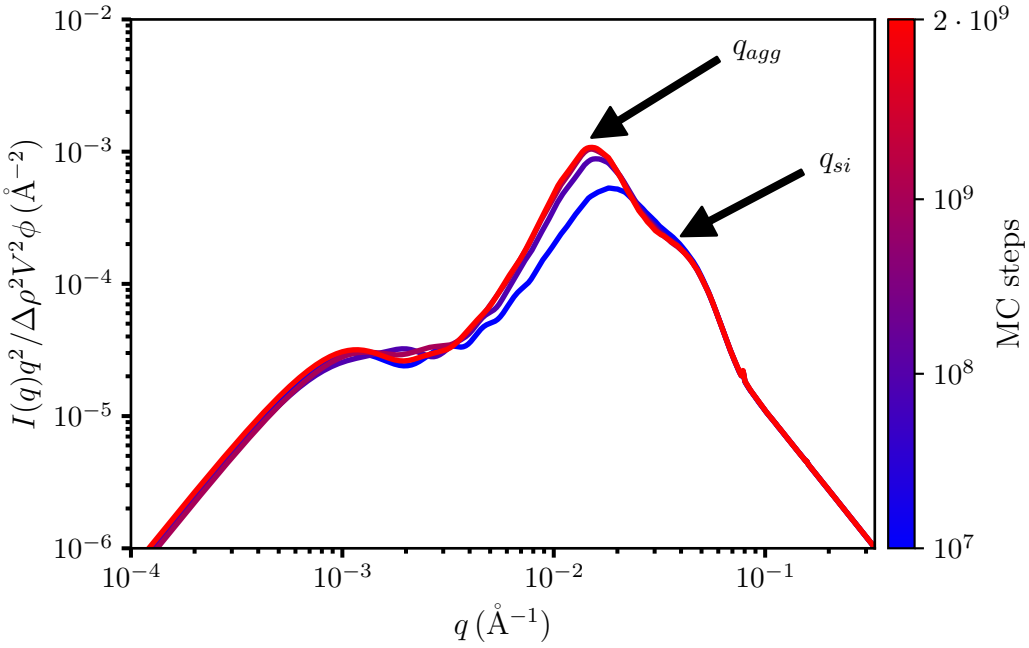

Figure 2.14.: Kratky representation of the scattering intensity vs. q for different number of MC steps. An increasing number of MC steps shifts the aggregate peak at q_{agg} to smaller q values resulting in growing aggregates. The particle peak at q_{si} remains at its position. The red line corresponds exactly to the system in Figure 2.8.

Here, the representation of the uncertainties is omitted to retain clarity. The different colors of the lines are identified with the corresponding MC steps as indicated by the color bar beside the figure. For this particular system, a higher number of MC steps clearly produces growing aggregates, because the respective peak is shifted to lower q values. The peak of the primary particles, on the other hand, is not affected by the MC and stays at its position. This behavior of MC dependency on aggregate growth is not necessarily true for all systems, because it is highly depending on the surface free energies as we will see later on.

Kratky style plots are a very useful tool in order to compare different systems, because we can identify a single scalar quantity, i.e., the mean aggregate size, q_{agg}, with ease. One possibility to obtain it, is to fit a (modified) log-normal probability density function to the scattering intensity (cf. [38]). It is given as

$$G_{agg}(q) = \frac{A_{agg}}{\sqrt{2\pi}\sigma_{agg}q}\exp\left(-\frac{\ln\left(\frac{q}{\tilde{q}_{agg}}\right)^2}{2\sigma_{agg}^2}\right). \tag{2.25}$$

Here, A_{agg} is the amplitude and σ_{agg} is the width of the log-normal function. The authors identified the mean as the corresponding mean size of the aggregate, i.e., $q_{agg} = \widetilde{q}_{agg}$. This leads to a shift to higher q values and does not match with the exact peak position. In the spirit of this approach it is also possible to use an unmodified log-normal probability density function, i.e.,

$$G_{agg}(q) = \frac{A_{agg}}{\sqrt{2\pi}\sigma_{agg}q} \exp\left(-\frac{\ln\left(q-\widetilde{q}_{agg}\right)^2}{2\sigma_{agg}^2}\right) \tag{2.26}$$

and calculate the peak position of the mean size of the aggregates via

$$q_{agg} = e^{\widetilde{q}_{agg}-\sigma_{agg}^2}. \tag{2.27}$$

This is the mode of the log-normal distribution. Although this procedure is reasonable and works quite well, it is more comfortable to use yet another approach. We simply extract the highest intensity value out of our data and determine the corresponding q value. However, in this approach we need to think about the uncertainties for q_{agg}.

In both of the former approaches numerical fitting methods are used. The first case yields a direct uncertainty on q_{agg}, because it is a fitting parameter. The second case also yields uncertainties in the fitting parameters, which are used for the calculation of the uncertainty of q_{agg} in the context of propagation of uncertainty. To find a reasonable estimator for the uncertainty in our approach, we obtain the mean aggregate size by identifying the peak position of the Kratky plot once with the uncertainty of the intensity added, once subtracted, and once through the mean. The maximum difference to the value obtained from the mean is then the uncertainty, σ_{agg}. This, fairly rough, approximation matches surprisingly well with the second approach.

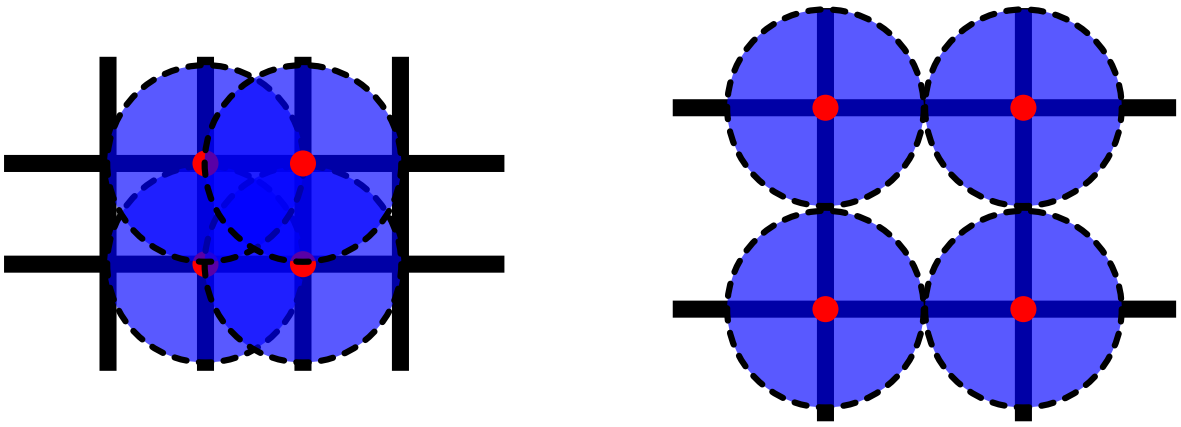

Figure 2.15.: Relation between the length scale of the form factor, R, and of the structure factor, d. The size of the primary particles is fixed by their attendant value of R. Left: The lower limit case $d = R$. The particles overlap in their centers. Right: The upper limit case $d = 2R$. The particles are in contact with each other. The structure formed on the left side is with $3R$ smaller than that on the right side with $4R$.

It is worth to mention that the reduced scattering intensity is a product of two functions with conceptually different length scales. The length scale for the form factor in Equation (2.23) is R, whereas for the structure factor in Equation (2.24) it is the lattice spacing, d. As mentioned before, we use the form factor – or to be more precise R – to set the scale in order to interpret the size of our aggregates. But what is the relation between R and d?

We know from experiments that the filler particles must overlap when they form higher order structures (cf. Appendix A.2.2). Consequently, we have an upper limit of $d = 2R$. In this case the particles are exactly in contact with each other. The lower limit is more difficult to define, because it is not possible to measure a value by how much the primary particles overlap. However, it is reasonable to say that the particles should not overlap completely. Thus, the most natural and easiest choice is $d = R$, which we set to be the lower limit. The sketch in Figure 2.15 depicts both cases. Other cases are certainly possible. For instance, as an intermediate case we can take $d^3 = 4\pi/3R^3$. This demands that a cubic lattice cell occupies the same volume as the corresponding sphere with the fixed value of R. This leads to a little less overlap than that depicted on the left portion of Figure 2.15.

If we now perform a Kratky style plot of the three example cases we get Figure 2.16. The different behavior of the three curves is due to the averaging procedure mentioned before. However, the value of the primary particles is fixed for all three cases at $R = 8\,n\mathrm{m}$.

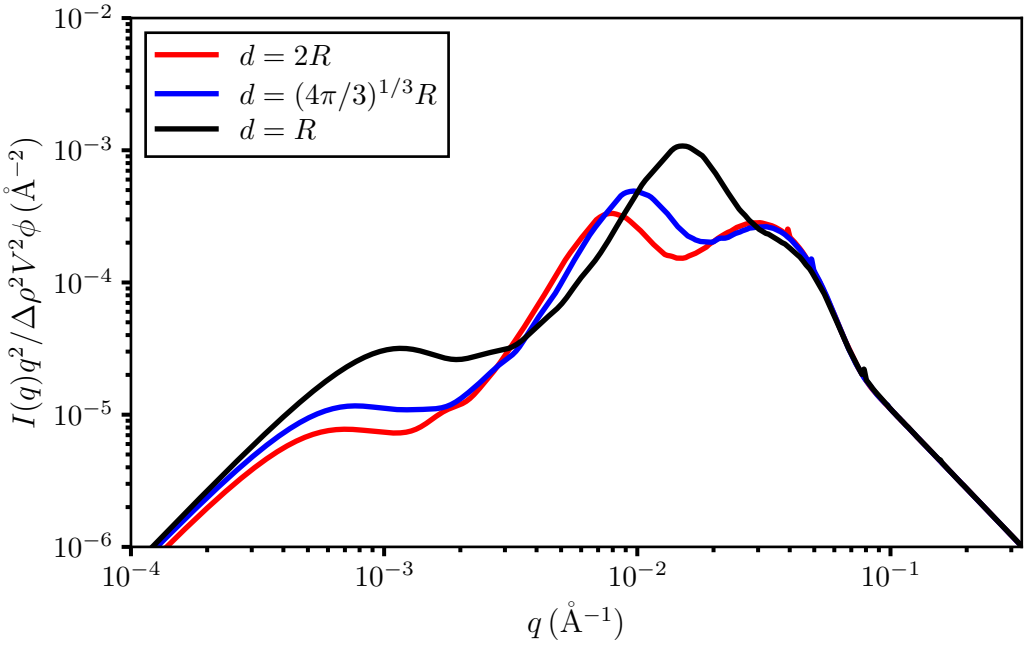

Figure 2.16.: Setting the scaling between the lattice, d, and the primary particles, R. The scattering intensities are normalized to the fixed value of $R = 80\,\mathrm{\AA}$. The different values of d thus result in bigger aggregates, i.e., the peaks move to smaller q values, as the centers of the primary particles are more apart from each other. This yields two distinct peaks. The kinks for high q values are always located at $q = 2\pi/d$.

The bigger lattice spacing, d, allows the particles to occupy more space. Thus, the respective aggregate peak moves to smaller q values. This leads to a separation of both peaks. Although the mean aggregate size in each case is reasonable, i.e., for the red curve $R_{agg} \approx 45\,n$m, blue curve $R_{agg} \approx 32\,n$m, and black curve $R_{agg} \approx 22\,n$m (neglecting the uncertainties for the moment), the shape of the red and blue curve is not. In experiments the primary particles are always merged together in aggregates and can not be distinguished to such an extent, as indicated by the according peak in Figure 2.16. Thus, we chose for the remainder of this work $d = R$, as it shows the biggest accordance towards experimental Kratky plots (e.g., [34, 38]).

2.4. Example Systems – the Potential of the Morphology Generator

In this part we consider different example systems, whose surface free energies are taken entirely from the literature [1, 3]. We are probing distinct combinations of polymer, modified and unmodified silica particles and thus show the capability of our morphology generator to mimic the flocculation process. To check whether the results are reasonable or not, we use the same methods for our simulation approach as the literature – where we are taking the surface free energy values from – does for experiments. We discuss the combinations of modified and unmodified silica and polymer in the context of wetting-envelope - work of adhesion plots. Here, we already use a quantity obtained from the simulation: the wetted surface fractions. We derive their ordering and consequently find insights on the morphologies of the systems. Furthermore, we produce simulated TEM pictures and SAXS intensities of our simulated systems and discuss the results in the same context. Additionally, we use the cluster mass distribution to obtain an even more detailed picture of our system. The ingredients shown in Table 2.2 are used to setup our example systems.

Table 2.2.: Surface free energies for the ingredients to obtain various example systems. The type 'mod. sil.' is the abbrevation for surface modified silica particles. The Ultrasil VN3 grades are precipitated silicas wheras Aerosil 200 is fumed. The values for the surface free energies are taken from [1, 3].

type	name	γ^d [mJ/m^2]	γ^p [mJ/m^2]	γ - total [mJ/m^2]
mod. sil.	Coupsil 8113 powd.	22.2	10.8	33.0
mod. sil.	amino-modified silica	37.8	5.8	43.6
filler	Ultrasil VN3 gran.	18.7	22.7	41.4
filler	Ultrasil VN3 powd.	19.4	18.9	38.3
filler	Aerosil 200	20.0	17.3	37.3
polymer	polychloroprene rubber (CR)	19.3	23.7	43.0

The values for the surface free energies for the silica particles are obtained via the mean contact angle of the Wilhelmy method. Those for the polymer, polychloroprene rubber (CR), were

obtained using the sessile drop technique. Both are taken from [1] and are explained in Appendix B. The values for the surface modified silica particles are taken from [1] (Coupsil 8113 powd.) and [3] (amino-mod-silica). If we are given the surface free energy of the respective unmodified silica particle, this is an ideal combination. Fortunately, this is the case for Coupsil 8113, which is the TESPT modified version of Ultrasil VN3. The values for the unmodified version of the amino-mod-silica particles were not available. In the corresponding source, they are stated as Nissan silica particles coated with the monofunctional silane APDMES (aminopropyldimethylethoxysilane: $NH_2-C_3H_6-Si-(CH_3)_2-O-C_2H_5$). Their primary particle radius is given therein as $R = 7 \pm 2\,n\mathrm{m}$, which is in good agreement with the $R = 8\,n\mathrm{m}$ we use throughout this work. When we compare the surface free energies of Coupsil and Ultrasil, we notice that silanization increases the dispersive and decreases the polar part of the surface free energy of the then modified silica particle. Because both modified silica particles have a higher dispersive and a lower polar part compared to all silica particles, it is at least reasonable to use both surface modifications for all three silica particles. This allows us to investigate the impact of different surface modifications on the flocculation process. We expect that the modification with a monofunctional silane yields systems, which are better dispersed than those with the bifunctional one. This is because the former is used to aid the dispersion process and the latter for coupling between filler and polymer (cf. Appendix A.3).

At this point it is stressed that we want to show the potential of our morphology generator and not the impact on variation of parameters. They are thus fixed to:

- system size L: 128
- filler volume fraction ϕ: 0.2
- heterogeneous silanization θ: 0.25
- temperature T: 433K
- maximum number of MC steps: $10^3 \cdot L^3$

Altogether, this results in six different systems for which we can look at the influence of different silica and silane combinations in a single polymer. Each of the six systems is simulated 10 times to improve the statistics regarding the wetted surface fractions and the mass distribution of the clusters. Thus, all of these values used in our discussion are mean values, attended with their respective standard deviations.

2.4.1. Wetting-Envelope - Work of Adhesion Plots

We start with the pure relation between the different surface free energies, i.e., we produce a wetting-envelope - work of adhesion plot for CR, as showed in Figure 2.17.

Both surface modified silica particles have a high tendency to flocculate inside the polymer as they are far outside the dotted iso work of adhesion loops. In comparison, the flocculation is higher for amino-mod-silica than for Coupsil 8113. For the wetting behavior towards the polymer it is the other way around. For the unmodified silica particles we find Aerosil 200 to have the worst wetting behavior, followed by the powdered version of Ultrasil VN3. The granulated form shows good wetting. The highest flocculation tendency is found for Aerosil

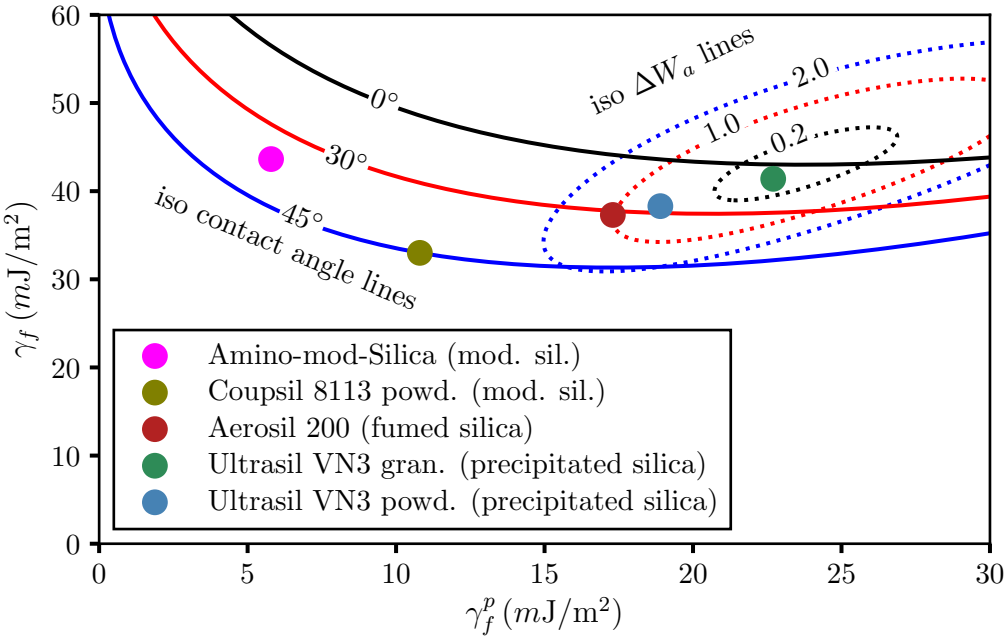

Figure 2.17.: Example of a wetting-envelope - work of adhesion plot for CR. The colored dots are described in the legend. They represent the different surface modified and unmodified silica types, as given in Table 2.2. The interpretation of the individual positions with respect to flocculation and wetting behavior is given in the text.

200 and a close to zero one for Ultrasil VN3 gran. The combination of both properties tells us something about the behavior of the respective filler particle inside the elastomer matrix. Low flocculation tendency and good wetting should result in a system, where the silica particles are well dispersed. This means that we should find zero aggregation, or at most some small aggregates, i.e., there should be no second peak in a Kratky plot and the corresponding TEM picture should not show any structures. Additionally, the wetted surface fraction between the silica particles, l_{ff}, should be low. The one between the silica and the elastomer matrix, l_{fr}, on the other hand, should be very high. Worse wetting behavior should yield lower values of l_{fr} and higher flocculation tendency should yield higher values for l_{ff}. The impact of surface modification is somewhat difficult to obtain from this plot alone. This is due to the restriction we impose in our model. After modification, the silanized surfaces make up 25% of all filler surfaces and are thus not able to move independently from them throughout the system. However, when we compare systems with the same modification we fix the interaction with the elastomer matrix. Then, the flocculation of silica particles inside it can be ordered as: Aerosil 200, Ultrasil VN3 powd., and Ultrasil VN3 gran., from high to low. The wetting behavior should yield the same, but reversed. This is because the bare silica surfaces still make up the majority of all filler surfaces. Thus, we should find for any fixed surface modification

$$l_{ff}^{A200} > l_{ff}^{VN3p} > l_{ff}^{VN3g} \quad \text{and} \quad l_{fr}^{VN3g} > l_{fr}^{VN3p} > l_{fr}^{A200}. \tag{2.28}$$

When we now want to investigate the impact of different surface modifications, we first need to look at the interaction between the unmodified and the surface modified silica, l_{fs}. The surface modification due to the silanes can be interpreted as a liquid coating on a solid substrate. Thus, we use again the wetting-envelope - work of adhesion plot, but with the surface modified silica as the liquid instead of the polymer. Figure 2.18 shows the two corresponding plots.

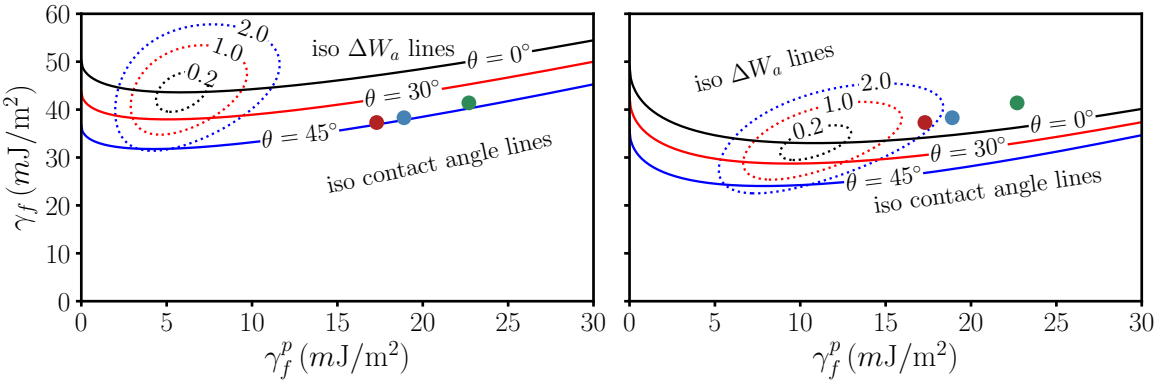

Figure 2.18.: Wetting-envelope - work of adhesion plots for different surface modified silica particles as the liquids. In both plots the colored dots are the silica filler particles with the same encoding as in Figure 2.17. Left: Amino-mod-silica. The wetting of all silica particles is bad and they all show high flocculation tendency. Ultrasil VN3 gran. shows the highest ΔW_a value. Right: Coupsil 8113 powd. All silica particles show perfect wetting. The flocculation tendency is less than for amino-mod-silica, but still high. Again, Ultrasil VN3 gran. shows the highest tendency.

On the left we see amino-mod-silica and on the right Coupsil 8113 powd. The dots have the same color encoding for silica as in Figure 2.17. The flocculation tendency of surface modified silica particles within the elastomer matrix as well as with the unmodified silica particles is high, independent of the modification itself. This should result in a high value of l_{ss} and thus

$$l_{ss}^{VN3g} > l_{ss}^{VN3p} > l_{ss}^{A200}, \tag{2.29}$$

because of the flocculation tendencies of the respective silica particles. The wetting behavior of every silica particle for amino-mod-silica as the surface modification is very low. This should result in a very low value of l_{fs}. To find the correct ordering, we just need to combine the information of Equations (2.28) and (2.29). For Ultrasil VN3 gran., we find the highest flocculation tendency towards surface modified silica particles. Towards the polymer, on the other hand, we find the lowest. As argued before, the wetting of this silica inside CR is the highest. Thus, we should also find the highest value of l_{sr}, i.e., wetting between polymer and surface modified silica. Finally, we can deduce that when we find the highest value of l_{ss} and l_{sr} for Ultrasil VN3 gran., then we will find the lowest value of l_{fs} for it. This argumentation can be applied to the other filler particles as well and thus we finally find

$$l_{sr}^{VN3g} > l_{sr}^{VN3p} > l_{sr}^{A200} \quad \text{and} \quad l_{fs}^{A200} > l_{fs}^{VN3p} > l_{fs}^{VN3g} \tag{2.30}$$

within systems, where we do not change the surface modification.

This gives us an overall ordering between the different ingredients of our system. Because we only look at the ordering and not at specific values, the ordering still holds for l_{sf}. The same argumentation applies for our other surface modified silica, Coupsil 8113, with the difference that the values of l_{fs} should be very high due to the perfect wetting. With that in mind we can conclude the impact of the different surface modifications on otherwise identical systems. The enhancement of l_{fs} and degradation of l_{ss} must lead to an increase of l_{ff} due to the spatial confinement of the silanized surfaces, which in turn decreases l_{fr}. The moderate flocculation behavior in comparison to amino-mod-silica in both, polymer and silica, should lead to a lower value of l_{ss}, which in turn increases l_{sr}. To check if our argumentation is reasonable, we now look at TEM pictures together with SAXS intensities.

2.4.2. TEM Pictures and SAXS Intensities

To get a better overview on the impact of the different modified surfaces, we use side by side plots where the silica part is the same and the surface modification differs. In order to investigate the change of silica by otherwise unaltered systems, the corresponding sides in the plots need to be compared. It is convenient to plot the TEM pictures inside the Kratky plots, because the visual feedback of the TEM pictures is directly compared to the size of the aggregates obtained from SAXS. The different scattering intensities give us an information about the structural development during flocculation. The colored border of the TEM matches with the according scattering intensity. They are in turn identified with the colorbar inside the plot, which indicates the number of MC steps. The TEM pictures are cut out in the middle of the system with a thickness of five layers. Their size is 128×128. Beside the mass distribution of the clusters, we use the wetted surface fractions to compare the change of surface modifications. Any values regarding both quantities are mean values of 10 independent simulations. Note that the value of the mean size of the aggregates corresponds to the displayed figure and is no average value. Its deviation is, however, very minor, i.e., below $1\,n$m and oftentimes even within the range of the given uncertainties. A complete overview between all systems in the context of wetted surface fractions will be given at the end.

On the left of Figure 2.19 we see Aerosil 200 with modified surfaces represented by APDMES (amino-mod-silica). The Kratky intensity shows barely any structural development at all. Small aggregates seem to form in the end of the flocculation process. The dashed line indicates the q_{agg} position, i.e., the size of the aggregates. It yields $R_{agg} \approx 18\,n$m. The corresponding TEM picture supports this impression. The system seems dispersed and no structures can be identified. We can analyze this further if we look at some basic quantities, such as the distribution of the cluster masses. It shows that only roughly 15% of all particles are bound into clusters, and those clusters are mostly very small, i.e., about 84% of the particles are found in clusters with a mass lower than ten. The standard deviations in both cases are negligible as they are far below 0.1%.

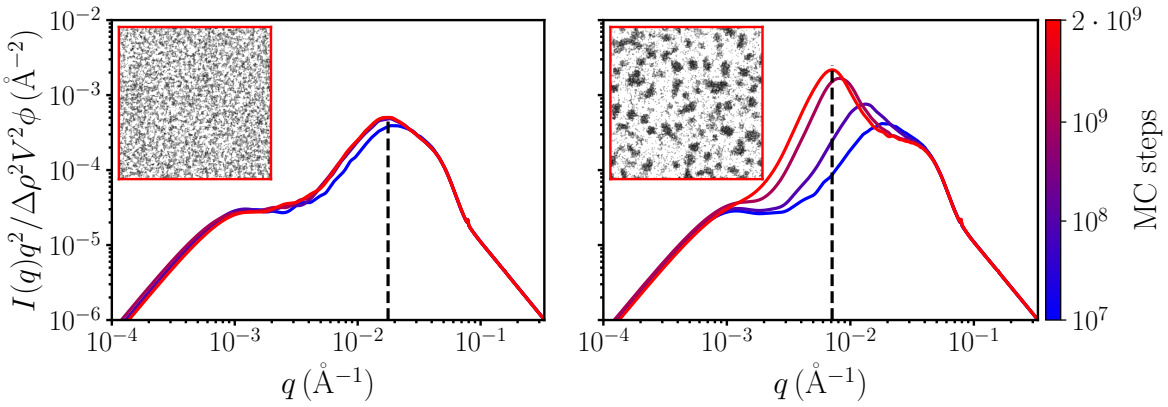

Figure 2.19.: Comparison of Kratky plots with TEM pictures of the silica Aerosil 200 with modified surfaces represented by APDMES (amino-mod-silica) and TESPT (Coupsil 8113 powd.). Left: APDMES. A structural development is barely given as indicated by the scattering intensities. Some minor aggregates are formed with sizes of $R_{agg} = 17.9 \pm 0.1\,n$m, indicated by the black dashed vertical line. The TEM picture supports this impression. No structures can be identified. Right: TESPT. Several distinct agglomerates develop during flocculation as indicated by the corresponding SAXS peak moving to lower q values. The mean size of the aggregates is $R_{agg} = 43.7 \pm 0.4\,n$m, indicated by the black dashed vertical line. The TEM again supports this, although we additionally find some primary particles still incorporated inside the elastomer matrix without aggregation.

When we now change the surface modification and use TESPT (Coupsil 8113 powd.), i.e., we look at the right portion of Figure 2.19, we see a change in structure. Several agglomerates formed during the MC. This is indicated by the corresponding peak of the Kratky plot moving to lower q values. The mean size of the aggregates, obtained from the position of the black dashed line, yields $R_{agg} \approx 44\,n$m. Again, the TEM picture supports this. We see distinct black areas, occupied by lots of primary particles. In between those 'lumps' we still find single primary particles, which are incorporated inside the elastomer matrix. Looking at the distribution of the cluster masses, we find that far more particles are now bound into clusters, i.e., about $62 \pm 2\%$. Moreover, very few particles, i.e., roughly 7% are found in clusters with a mass lower than ten. This value does not show any significant variation. Thus, the deviation in the mean results follows from the formation process of bigger clusters. If we look for instance at the mean size of the biggest cluster, we find a mass of 4250 ± 1000, which supports our argument. When we now compare the wetted surface fractions of both systems, we immediately see that l_{ff} is obviously increased and l_{fr} is decreased. In fact, l_{ff} is increased by a factor of two and l_{fr} is decreased by one third. The wetted surface fractions regarding the modified silica surfaces can not be concluded from TEM or Kratky plots. But the underlying data shows that we indeed have an increase in l_{fs} by roughly a factor of ten, an decrease of l_{ss} and an increase of l_{sr} each by a factor of three. Although not mentioned in our discussion before, it should be noted that l_{rr} is also increased as one would expect when looking at the corresponding TEM pictures. This change in structure is thus in accordance with our argumentation regarding the change of the surface modifications for otherwise identical systems.

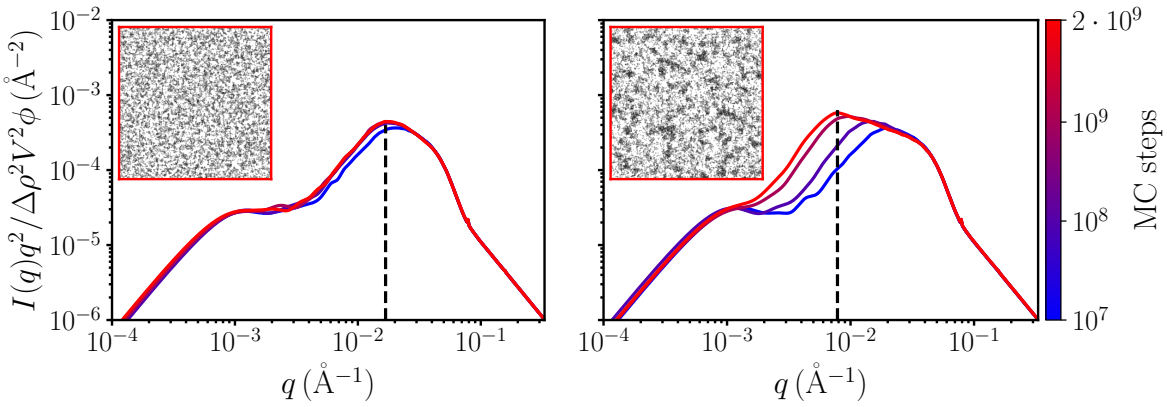

Figure 2.20.: Comparison of Kratky plots with TEM pictures of the silica Ultrasil VN3 in powdered form with modified surfaces represented by APDMES (amino-mod-silica) and TESPT (Coupsil 8113 powd.). Left: APDMES. A structural development is barely given as indicated by the scattering intensities. Some minor aggregates are formed with sizes of $R_{agg} = 16.30 \pm 0.02\,n$m, indicated by the black dashed vertical line. The TEM picture supports this impression. No structures can be identified. Right: TESPT. Several agglomerates develop during flocculation as indicated by the corresponding SAXS peak moving to lower q values. The mean size of the aggregates is $R_{agg} = 36.79 \pm 1.72\,n$m, indicated by the black dashed vertical line. In the TEM picture we see that structures are developed, but they look less dense compared to Figure 2.19. Additionally, lots of smaller clusters and single primary particles can be found in between the bigger structures, rendering the picture blurry.

The next comparison is for the silica Ultrasil VN3 in powdered form. On the left of Figure 2.20 we see that no distinct peaks developed during the flocculation process. The dashed black line indicates aggregates of mean size $R_{agg} \approx 16\,n$m. The corresponding TEM picture again supports this impression. The distribution of the cluster masses shows that slightly more particles are bound into clusters compared to Aerosil 200, i.e., now roughly 16%. But the individual masses of the clusters became less. Now, about 91% of the particles are found in clusters with a mass less than ten. The different simulated systems showed no significant deviation in the distribution of the cluster masses. Changing the modified surfaces of the silica particle, i.e., looking at the right portion of Figure 2.20, shows a structural difference. The filler particles aggregate according to the corresponding q_{agg} peak moving to lower q values during the MC. The mean size of the aggregates is $R_{agg} \approx 37\,n$m. The overall TEM picture seems more blurry. It shows several bigger agglomerates and lots of primary particles and smaller aggregates in between. The look into the cluster mass distribution reveals that only about 19% of all particles are bound into clusters and 63 ± 1% of them are found in clusters with a mass smaller than ten. Compared to Aerosil 200 this is a huge decrease, which is also reflected in the Kratky plot: the height of the aggregate peak is much lower. Looking at the wetted surface fractions we can draw the same conclusions as for the change of surface modifications for the systems containing Aerosil 200. Both filler related quantities l_{ff} and l_{fr} are increased and decreased respectively, although the extent is muss less pronounced. The former is increased by one third and the latter decreased by roughly 15%. The modified silica related surface fractions follow the same trend and thus encourage our argumentation within the context of wetting-envelope - work of adhesion plots. l_{fs} is increased by a factor

of nine, l_{ss} decreased by approximately half and f_{sr} by factor of four. Although we will draw a large conclusive picture at the end of the discussion of all six systems, we can already see a trend when changing the silica by otherwise same system parameters. The impact of surface modification becomes more pronounced for the interface between the polymer and the surface modified silica. This conveys the impression that silica particles that flocculate less inside the elastomer matrix and wet it better, allow the silanized surfaces to better connect with the surrounding elastomer matrix. This seems to be much more pronounced for silica surfaces modified with the bifunctional silane TESPT than for those with the monofunctional silane APDMES.

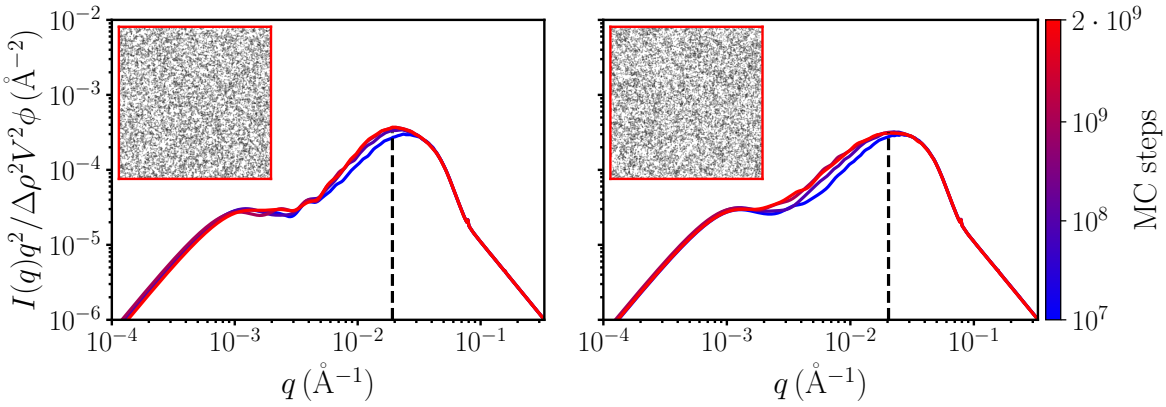

Figure 2.21.: Comparison of Kratky plots with TEM pictures of the silica Ultrasil VN3 in granulated form with modified surfaces represented by APDMES (amino-mod-silica) and TESPT (Coupsil 8113 powd.). Left: APDMES. A structural development is barely given as indicated by the scattering intensities. Some minor aggregates are formed with sizes of $R_{agg} = 14.9 \pm 0.2\,n$m, indicated by the black dashed vertical line. Right: TESPT. No aggregation is visible. The mean size of the aggregates is $R_{agg} = 14.2 \pm 0.3\,n$m, indicated by the black dashed vertical line. The TEM pictures for both plots do not allow to identify any structures.

The last systems contain the silica Ultrasil VN3 in granulated form. Both systems in Figure 2.21 show no structural development during the MC. Neither the Kratky plot nor the TEM pictures allow to identify structures. Nevertheless, very small aggregates of about $R_{agg} \approx 14\,n$m are found in both systems. The difference in between both mean aggregate sizes is negligible. The same is true for the cluster mass distributions. They yield that roughly 17% of all particles are bound into a cluster and almost every particle, i.e., 97%, is found in a cluster with mass less than ten. There is no distinct variation in the cluster mass distribution over the course of 10 simulated systems. The screening methods do not render it possible to make a comment about the wetted surface fractions, no matter in which context. We can just conclude that the silica type with the best dispersion and wetting behavior shows the lowest impact when using different surface modifications. Looking at the changes in the wetted surface fractions we still find the same ordering as argued before. l_{ff} slightly increases and l_{fr} decreases in the same manner. Those containing the surface modified silica surfaces, i.e., l_{fs}, l_{sr} and l_{ss} increase by a factor of ten and five and decrease by half, respectively. The trend mentioned before seems to be correct. The best dispersed silica type, allows both surface

modified silica surfaces to connect even more to the elastomer matrix. Again, the effect is stronger for the TESPT modified surfaces than for those with APDMES.

To discuss all systems in a more conclusive manner, and to get a better overview, we use the wetted surface fractions of all systems to compare them directly. We separate our discussion into a unmodified and modified silica based focus.

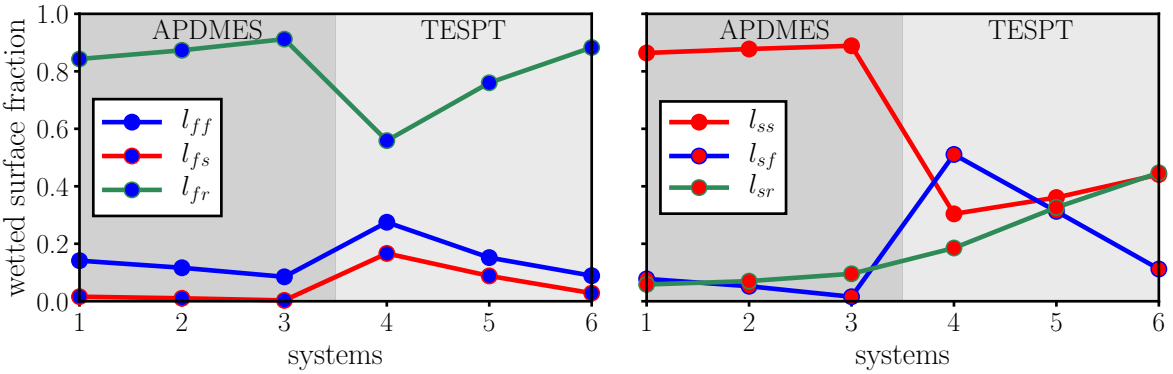

Figure 2.22.: Comparison of different wetted surface fractions in systems containing CR. Systems 1 to 3 (and 4 to 6) represent Aerosil 200, Ultrasil VN3 powd. and gran., respectively. The corresponding modified surfaces represented by APDMES (TESPT) are indicated in the plots. Left: The silica particles in focus. Better dispersed filler particles show decreased l_{ff}, l_{fs} and increased l_{fr} values, independent of the modification. Right: The modified silica surfaces in focus. Better dispersed filler particles show decreased l_{sf} and increased l_{sr}, l_{ss} values, independent of the modification. The modified silica surfaces represented by the monofunctional silane APDMES seem to have a lower impact than those with the bifunctional silane TESPT.

On the left of Figure 2.22 the unmodified silica surfaces are in focus and on the right, the modified surfaces. Systems 1 to 3 (and 4 to 6) represent systems containing APDMES (TESPT) as the modification, indicated by the different grey background shadings. In between the systems with the same surface modified silica, we keep the same ordering as in the discussion before, i.e., systems 1 to 3 correspond to the left and systems 4 to 6 to the right plots in Figures 2.19, 2.20, and 2.21. It should be noted that the standard deviation of all mean wetted surface fractions is far below 0.1% and is thus not shown in the respective plots. The ordering we concluded for fixed modified silica surfaces in the context of the wetting-envelope - work of adhesion plot in Figure 2.17 is as we expected. Better dispersion and wetting of unmodified silica particles lead to the corresponding increases of the wetted surface fractions. However, the impact of silica change when using APDMES is far less than for TESPT – regardless of the specific wetted surface fraction. In the case of l_{sr}, this seems to be contrary to our former identification of wetting, i.e., better wetting behavior towards the polymer should yield higher values of the corresponding wetted surface fraction. One would thus expect that APDMES has higher values of l_{sr} compared to TESPT. The reason why this is not the case is the flocculation behavior of the individual modified silica surfaces. That of APDMES is strikingly increased compared to TESPT and, as we can see from Figure 2.22, the values for

l_{ss} are correspondingly very high. Thus, less modified interfaces are left to connect to the polymer. From the chemical point of view this is reasonable. Silica particles modified with monofunctional silanes yield better dispersed systems. We indeed find that this is the case, as the corresponding wetted surface fraction l_{fr} is higher for APDMES than for TESPT. This impact is lower for silica particles that already show good dispersion, like Ultrasil VN3 gran. in our case. This is also reasonable due to the spatial confinement we impose in our model. The silica surface makes up a majority of our filler particles and thus their tendency to wet or to disperse is more dominant.

Table 2.3.: Comparison of the mass fractal dimension of the aggregates for different filler and silane combinations inside CR with $\phi = 0.20$ at $T = 433$ K. Note that the box-counting algorithm was used and four digit precision was chosen to better show the differences between the systems. All values are taken after the final number of MC steps. Those containing APDMES are very much the same. Only their uncertainty increases with increasing silica dispersibility. The same trend is observable for systems containing TESPT. The one with Aerosil 200 has the highest value and lowest uncertainty. Ultrasil VN3 powd. with TESPT has a slightly higher value and lower uncertainty than that with APDMES. Ultrasil VN3 gran. shows to be rather the same for both modified silica surfaces – except of the higher uncertainty for TESPT.

system	silica	silane	$\bar{d}_m^{agg}$
1	Aerosil 200	APDMES	1.841 ± 0.171
2	Ultrasil VN3 powd.	APDMES	1.840 ± 0.192
3	Ultrasil VN3 gran.	APDMES	1.839 ± 0.219
4	Aerosil 200	TESPT	1.870 ± 0.054
5	Ultrasil VN3 powd.	TESPT	1.843 ± 0.171
6	Ultrasil VN3 gran.	TESPT	1.840 ± 0.243

Table 2.3 lists the averaged mass fractal dimension of the aggregates, $\bar{d}_m^{agg}$, for every system with the averaged uncertainty $\bar{\sigma}_m^{agg}$. It is chosen, because the values of individual systems did not alter much and consequently an uncertainty of the mean neglects the information of the individual uncertainty for each system. Note that four digit precision is chosen to better show the slight differences in the APDMES cases (without taking the uncertainties into account). All systems, which showed good dispersion in the TEM pictures and rather small aggregates have a similar mass fractal dimension of their aggregates. These systems contained APDMES modified silica surfaces. For TESPT modified silica surfaces, only Ultrasil VN3 gran. shows this behavior. The only difference is found for the uncertainties. Two systems showed to have recognizable aggregates via SAXS and TEM, i.e., 4 and 5 on the right of Figures 2.19 and 2.20, respectively. For them we find the lowest uncertainties and the highest mass fractal dimension of their aggregates. Additionally, they are the only two systems, whose values differ from those obtained right before the MC.

Altogether, we showed the capability to mimic the flocculation process with our morphology generator. The usage of TEM together with SAXS as a Kratky plot allowed us to analyze the produced systems. More detail was obtained when taking some basic quantities as well as the wetted surface fractions into account. In this context, the wetting-envelope - work of adhesion plots showed to be a powerful tool to predict the behavior of filler particles inside the elastomer matrix as well as the behavior between modified and unmodified silica. The deviations in the cluster mass distribution and mean aggregate size for systems with the same set of parameters is minor. Additionally, the mass fractal dimension of the aggregates has been obtained. It also behaves similar for systems with the same set of parameters.

2.4.3. Compatibility of Modified and Unmodified Silica with Polymers

Taking all literature sources we found on the topic of surface free energies, regarding modified and unmodified silica and polymer, into account we can generate an overview of the wetting and flocculation behavior. Deduced from the example systems we investigated before, we use the rating system given in Table 2.4. The according quantity for wetting is the contact angle θ. That for flocculation/dispersion is the difference in work of adhesion ΔW_a .

Table 2.4.: Rating system for wetting and dispersion behavior of filler particles for fixed polymers in the context of the position inside wetting-envelope - work of adhesion plot. Wetting behavior is depending on the position in relation to the iso contact angle lines for fixed values of θ. The dispersion behavior depends on the position inside the iso work of adhesion loops for fixed values of ΔW_a.

grade	symbol	wetting	dispersion
perfect	++	$\theta = 0°$	$\Delta W_a < 0.2$
good	+	$30° \gtrsim \theta \gtrsim 0°$	$0.2 < \Delta W_a < 2.0$
mediocre	*o*	$\theta \approx 30°$	$2.0 < \Delta W_a < 5.0$
bad	−	$45° \gtrsim \theta \gtrsim 30°$	$\Delta W_a > 5.0$
poor	−−	$\theta \gtrsim 45°$	$\Delta W_a \gg 5.0$

We split our consideration into silica and silane and start with the former as given in Table 2.5. In each cell of the table we find two ratings. The first is with respect to wetting and the last to dispersion. For each polymer a wetting-envelope - work of adhesion plot was produced and the position of the silica particles inside the plot was rated according to Table 2.4. To obtain the plots we need the surface free energy values for all ingredients. Those for all silica particles are taken from [1]: precipitated silica (UVN3 powd./gran., Evonik Ultrasil VN3 in powder and granulated form), fumed silica (A200, Lanxess Aerosil 200) and methylated fumed silica (AR974, Lanxess Aerosil R974). A majority of the polymer values are also taken from this source, namely: natural rubber (NR1, TMR – Standard Malaysian Rubber SMR 20), polybutadiene rubber (BR, Lanxess Buna CB25), ethylene-propylene-diene rubber (EPDM, Lanxess Buna EP G6850), three different acrylonitrile-butadiene rubbers with different acrylonitrile content (P1846F, Lanxess Perbunan 1846F and P3446F, Lanxess Perbunan 3446F

and P4456F, Lanxess Perbunan 4456F), hydrogenated acrylonitrile-butadiene rubber (HNBR, Lanxess Therban TM A3407), polychloroprene rubber (CR, Lanxess Baypren) and carboxylated acrylonitrile-butadiene rubber (XNBR, Lanxess Krynac X740). Other polymers are also used: solution-polymerized styrene-butadiene rubber (S-SBR, Lanxess Buna VSL5025-0 HM, [2]), two different styrene-butadiene rubbers (Nipol SBR, 24 wt% styrene and 34.2 wt% vinyl and DSSK SBR, 24 wt% styrene and 67.2 wt% vinyl), and another natural rubber (NR2), all taken from [5]. All polymers have different surface free energies and are thus different in the context of wetting and dispersion. The individual values can be obtained from the respective sources.

Table 2.5.: Wetting and flocculation behavior of silica particles within various polymers. The rating is done according to Table 2.4. In each cell we find two values. The first corresponds to the wetting behavior and the latter to the dispersion. The ordering inside the table for the silica particles from left to right is, as well as for the polymers from top to bottom, from low to high polar surface energy. The wetting of the silica particles is, with exception of Aerosil R974, perfect for most of the polymers considered here. Their dispersion, however, is mostly poor.

	AR974	A200	UVN3 powd.	UVN3 gran.
SSBR	$--/o$	$+/--$	$+/--$	$+/--$
Nipol SBR	$--/--$	$-/+$	$-/o$	o/o
HNBR	$--/-$	$++/--$	$++/--$	$++/--$
EPDM	$--/-$	$++/--$	$++/--$	$++/--$
BR	$--/-$	$++/--$	$++/--$	$++/--$
DSSK SBR	$--/--$	$+/--$	$+/--$	$+/--$
NR2	$--/--$	$++/--$	$++/--$	$++/--$
P3446F	$--/-$	$++/-$	$++/--$	$++/--$
NR1	$--/-$	$++/-$	$++/--$	$++/--$
P1846F	$--/-$	$++/-$	$++/-$	$++/--$
P4456F	$--/--$	$++/o$	$++/o$	$++/--$
CR	$--/--$	$o/+$	$o/+$	$+/++$
XNBR	$--/--$	$-/-$	$-/o$	$-/o$

The methylated fumed silica AR974 shows very bad wetting behavior for all polymers and a high tendency to flocculate. For the other silica particles, we find a generally poor wetting behavior for polymers with low or very high polar surface free energy. This is inverted regarding dispersion: The silica particles show better dispersion in polymers with low and high polar parts of the surface free energy. However, a complete picture can not be drawn from the surface polarity alone as all silica particles and polymers are also different in their dispersive parts. Thus, Table 2.5 should not be taken as a predictor for the behavior of silica particles, due to the pure basis of surface polarity. For the surface modified silica particles

we repeat this process. The ratings are listed in Table 2.6. Surface modified with the bifunctional silane TESPT are the Ultrasil VN3 grades (C8113 powd./gran., Evonik Coupsil 8113 in powder and Coupsil 8113GR granulated form), which are taken from [1]. Surface modified with several monofunctional silanes are Nissan silica particles in methyl ethyl ketone (MEK-ST). These are octyldimethylmethoxysilane (ODMMS: $CH_3-(CH_2)_7-Si(CH_3)_2-O-CH_3$), chloropropyldimethylethoxysilane (CPDMES: $Cl-C_3H_6-Si(CH_3)_2-O-C_2H_5$)), and aminopropyldimethylethoxysilane (APDMES: $NH_2-C_3H_6-Si-(CH_3)_2-O-C_2H_5$). All values are taken from [3].

Table 2.6.: Wetting and flocculation behavior of silanized silica particles within various polymers. The rating is done according to Table 2.4. The ordering inside the table for the silanized silica particles from left to right is, as well as for the polymers from top to bottom, from low to high polar surface energy.

	ODMMS	CPDMES	APDMES	C8113 pulv.	C8113 gran.
SSBR	++/+	++/*o*	++/−	++/−−	++/−−
Nipol SBR	−−/−−	−/−	*o*/−	−/*o*	−/+
HNBR	++/+	++/*o*	++/−	++/−	++/−−
EPDM	++/++	++/+	++/*o*	++/−	++/−−
BR	++/+	++/*o*	++/−	++/*o*	++/−−
DSSK SBR	+/+	++/+	++/+	*o*/*o*	+/−−
NR Conti	++/+	++/+	++/−	++/+	++/−
P3446F	++/*o*	++/*o*	++/−	++/+	++/*o*
NR	++/*o*	++/*o*	++/−	++/*o*	++/−
P1846F	++/*o*	++/*o*	++/−	++/+	++/*o*
P4456F	+/*o*	++/+	++/*o*	++/+	++/*o*
CR	−−/−−	−−/−−	−/−−	−−/−	*o*/+
XNBR	−−/−−	−−/−−	−−/−−	−−/−−	−−/−−

The combination of good wetting and high flocculation tendency should produce network like structures within the elastomer matrix. The necessary coupling between silica and polymer is chemically achieved using bifunctional silanes such as TESPT (cf. Appendix A). Looking at Table 2.6 we see that Coupsil 8113 gran. indeed shows this kind of behavior. The powdered version of the otherwise identical silanized silica particle already shows less flocculation tendency and is more comparable to particles surface modified with the monofunctional silane APDMES. The other two silanized silica particles show, as we would expect from the modification with monofunctional silanes, good wetting and dispersion for a majority of polymers.

The next steps could now be to use both tables and perform the simulations for all possible combinations. However, this approach has a few drawbacks. Not every combination of sur-

face modified and unmodified silica inside every polymer is reasonable to look at from the perspective of the industry. A new approach is introduced in the next part.

2.5. Mimicking Filler Particles in Single Polymers – Impact of Parameters

Every elastomer producing company has their own recipes. Even slight variations in the compound can lead to a huge impact of essential macroscopic properties. The most commonly used rubbers in tire and rubber sole production are NR, SBR, and BR due to their wide application areas [10, 57, 58]. For the remainder of this work, we focus on the former two. The specific filler particles used in recipes, such as carbon black and silica, as well as surface treatments or coupling agents, like silanes, are generally known [10]. The most common silane is TESPT as mentioned in Appendix A.3. We thus mimic silanization by using the surface free energy of a TESPT modified silica particle, i.e., Coupsil 8113 powd. For the filler particles, on the other hand, many different types are used. Unfortunately, just a few, as in the case of silica only those listed in Table 2.5, are analyzed with respect to their surface free energy. Other physical and chemical properties are mostly more important for the elastomer industry, for instance the BET or CTAB surface (cf. Appendix A). Additionally, the measurement is difficult and yields highly variable results, depending on the method (cf. [1]). To overcome this drawback for our model, we simply mimic different filler particles by altering their dispersive and polar parts of the surface free energies. This allows us to create a variety of systems containing different types of silica, such as fumed, methylated fumed, precipitated, or even some grades of carbon black. For the latter we need to keep in mind that the treated surfaces are still represented by the values of Coupsil 8113 powd., i.e., a surface modified silica. Although some surface modifications of carbon black exist, such as graphitizing, it is not clear whether their surface free energies are altered to such an extent that they are correctly represented by those values. However, carbon blacks have very low surface polarity, which means that our mimicked filler particles are mainly identified as silica.

All systems produced this way are then analyzed using our screening methods and evaluated in the same way as the example systems. Because this produces a tremendous amount of data, we need to find a more compact way to compare different systems instead of comparing Kratky plots as done previously. One possibility is to obtain the mean aggregate size as a single quantity from those plots. It can be plotted against the polar part of the surface free energy and allows to analyze the corresponding impact on structural development. The result is a so-called 'aggregation phase diagrams', which is accompanied by TEM pictures for visual feedback. A detailed analysis of the systems is again achieved by using the wetted surface fractions and/or other basic quantities. The wetting-envelope - work of adhesion plots are a helpful tool to identify promising example systems for which to simulate TEM pictures. The mass fractal dimension of the aggregates is also discussed. Table 2.7 shows the surface free energies used for the different systems in this part.

Beside the right choice of the ingredients, we need to investigate the impact of our other simulation parameters. We therefore alter the filler volume content ϕ and the temperature T, to examine their impact on the development of structures. The system parameters for all simulations conducted in this section are chosen as follows:

Table 2.7.: Surface free energies of the ingredients for aggregation phase diagrams in single polymers. The values of the surface modified silica, abbrevated as 'mod. sil.', are taken for all treated surfaces. The values of the filler particles allow to mimic different filler particles, such as fumed, methylated, and precipitated silica as well as different grades of carbon black. The polymers are common constituents of rubber recipes in the tire industry [10, 57] and for rubber soles of shoes [58]. The values for SBR are taken from [5], therein named SBR-LV. All other values are taken from [1].

type	name	γ^d $[m\mathrm{J/m^2}]$	γ^p $[m\mathrm{J/m^2}]$	γ - total $[m\mathrm{J/m^2}]$
mod. sil.	Coupsil 8113 powd.	22.2	10.8	33.0
filler	-	20/30	$0, 5, \ldots, 30$	$20, \ldots, 60$
polymer	Natural Rubber (NR)	15.9	6.1	22.0
polymer	Styr.-Butad. Rubber (SBR)	29.9	1.6	31.5

- system size L: 128
- filler volume content ϕ (in vol. %): 10, 15, 20, 25
- heterogeneous silanization θ: 0.25
- temperature T in K: 413, 433, 453, 473
- maximum number of MC steps: $10^3 \cdot L^3$

The aggregation phase diagrams allow us to compare different systems with respect to the alternating parameters. The investigation of the flocculation time, which is in our case the number of MC steps, will also be taken into more consideration than for the example systems. Altogether, this leads to 448 recipes in total, not including the different flocculation times. Therefore, not every possible combination is considered here. Note that different to the example systems only one simulation per system is conducted. This is reasoned by the minor uncertainties we have seen before.

2.5.1. Wetting-Envelope - Work of Adhesion Plots

We begin identical to our example systems with the wetting-envelope - work of adhesion plots. They are independent of any system parameters as they only rely on the surface free energies. Therefore, we just need to vary the positions of our mimicked filler particles inside the corresponding plots. As we are striving to compare both polymers and need to take the interaction between the fillers and the surface modified silica into account, we use plots as shown in Figure 2.23 for different dispersive parts of the surface free energy of the filler particles, γ_f^d. Figure 2.23a depicts NR and Figure 2.23b SBR. The red dots inside both systems are artificial filler particles with $\gamma_f^d = 20\,m\mathrm{J/m^2}$. The numbers indicate systems we investigate in more detail for the remainder of this part. They are fixed by their polar part of the surface free energy and are not changed when their dispersive part is changed to $\gamma_f^d = 30\,m\mathrm{J/m^2}$. They are chosen to have a good mixture and variety in wetting and flocculation behavior in

both polymers. The olive colored dot in each of the plots represents the silane. It should be noted that the values for the dotted iso ΔW_a lines are chosen to match our rating system introduced in Table 2.5 and are thus bigger compared to our example systems. The solid iso contact angle lines are not altered. To find the ordering as we did for our example systems, we need to examine the interactions between the fillers and the surface modified silica. Thus, it is again useful to plot a wetting-envelope - work of adhesion plot in which the surface modified silica is identified as the liquid. The plot is basically the same as the right portion of Figure 2.18, just with the corresponding filler particles added and with the aforementioned difference in the iso ΔW_a. It is shown in Figure 2.23c.

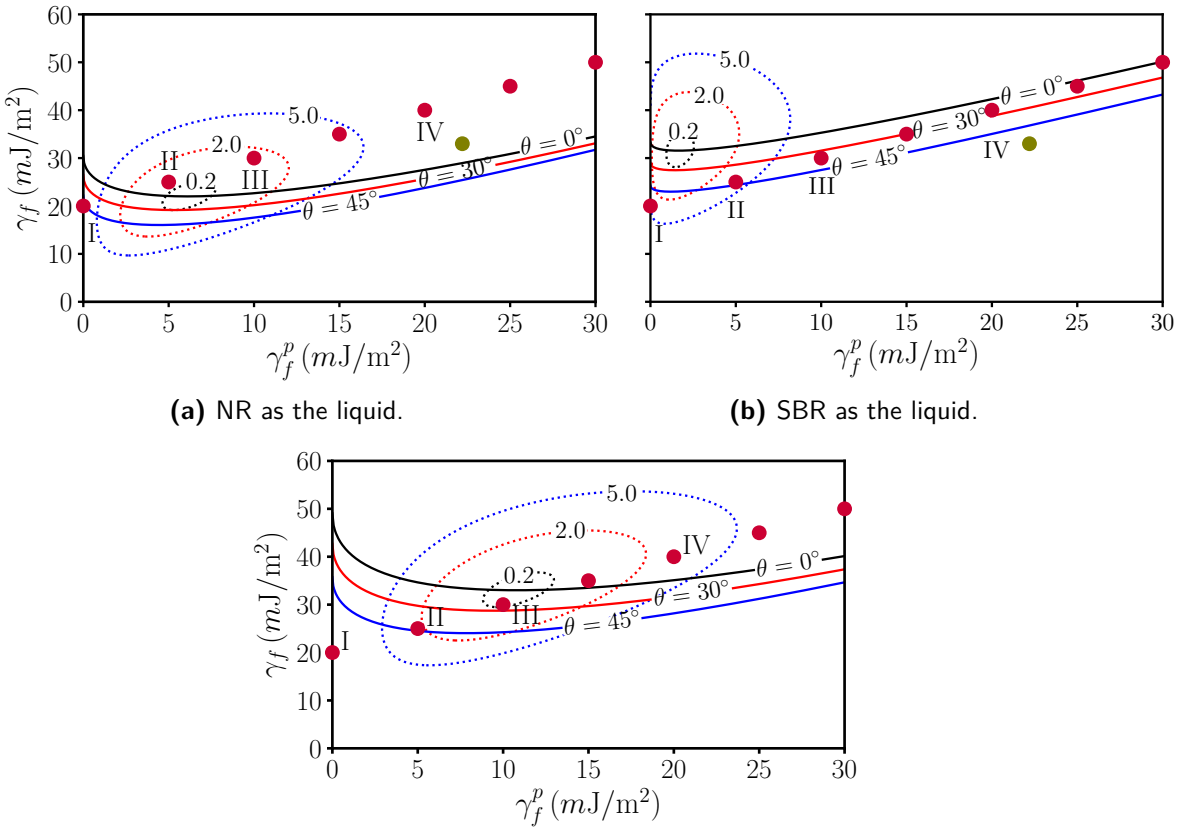

(a) NR as the liquid.

(b) SBR as the liquid.

(c) Surface modified silica as the liquid.

Figure 2.23.: Wetting-envelope - work of adhesion plots for NR, SBR, and surface modified silica containing artificial filler types with $\gamma_f^d = 20\,mJ/m^2$, marked as red dots. Those labeled by roman numerals I to IV are chosen to be investigated further. The olive colored dot in both of the top plots **(a)** and **(b)** marks the position of the surface modified silica Coupsil 8113 powd.

We are now able to deduce the ordering in the same way as for the example systems. Here, we concentrate only on the four filler particle types indicated by the roman numerals in Figure 2.23. A complete overview on the development of the wetted surface fractions is again given in the detailed analysis of the simulated TEM pictures.

We start with the case of filler types having $\gamma_f^d = 20\,m\mathrm{J/m^2}$ and being incorporated inside NR, i.e., Figure 2.23a. First of all, the surface modified silica (olive dot) has a high flocculation tendency and is perfectly wetted by the polymer. Thus, the wetting should yield strong impacts regarding every filler related interface. This is because the flocculation of the surface modified silica is always bound to filler flocculation, due to the spatial confinement imposed in our model.

With that in mind, we start with filler type I. It shows bad wetting and high flocculation tendency for the polymer as well as for the surface modified silica. Thus, we expect a high value of l_{ff} and subsequently a low value for l_{fr}. The positioning of the filler type in Figure 2.23c indicates that it flocculates, if it is surrounded by surface modified silica. It is not wetted by them. Thus, l_{fs} (l_{sf}) should be very low. From the viewpoint of the surface modified silica, the flocculation tendency is high for the polymer as well as for the filler, but at the same time, the wetting for the polymer is extensively higher. This should lead to l_{sr} being very high, meaning that in the aggregation process filler particles with many surface modified sides are pushed into the outer layers of the filler structures. Subsequently, this must lead to a fairly low value of l_{ss}, because of the spatial confinement of the modified surfaces.

Starting from filler type II, the wetting of all filler types with higher polar surface free energies is now perfect for the polymer and only the flocculation tendency differs. Filler type II shows the lowest tendency. The wetting between filler and surface modified silica can still not be considered good but the flocculation tendency gets less and is rated mediocre. Thus, the value of l_{ff} should be very low and that of l_{fr} very high. The tendency for the filler to flocculate around surface modified silica gets less and the wetting increases slightly, which in turn leads to an elevated value in l_{fs} (l_{sf}). Due to the low filler flocculation but still same tendency of the surface modified silica to flocculate, the value of l_{ss} should increase. Because both surface modified silica related interfaces increase, the value of l_{sr} must become lower.

The flocculation tendency of filler type III is now higher, which in turn must lead to an increase in l_{ff}, but it is still lower than I. This, together with the better wetting behavior, should give a higher value of l_{fr} compared to I. Because the filler particles are dispersed, if surrounded by surface modified silica and the wetting between both is also increasing, this should yield the highest value of l_{fs} (l_{sf}). In turn, the other surface modified silica related interfaces must decrease. Those regarding rubber more than those regarding surface modified silica, because all modified surfaces are turned towards the filler surfaces.

All filler types with polar surface free energy higher than those of type IV show a very high flocculation tendency beside their perfect wetting. Thus, l_{ff} must increase further, coming from III, which in turn decreases l_{fr}. Because of the higher flocculation tendency compared to I we should finally find

$$l_{ff}^{IV} > l_{ff}^{I} > l_{ff}^{III} > l_{ff}^{II} \quad \text{and} \quad l_{fr}^{II} > l_{fr}^{III} > l_{fr}^{I} > l_{fr}^{IV}\,. \tag{2.31}$$

Because the flocculation tendency of the filler types for surface modified silica increases from the perspective of III in every direction, the corresponding mixed interface l_{fs} must decrease. With the ordering of the filler types in Equation (2.31) in mind, we conclude for the ordering of filler and surface modified silica

$$l_{fs}^{III} > l_{fs}^{II} > l_{fs}^{IV} > l_{fs}^{I}. \tag{2.32}$$

This also gives us insight in the development of l_{ss}. It must decrease because l_{ff} increases and because both surface modified silica related surface fractions decrease, l_{sr} has to increase. Due to the ordering in Equation (2.31), this leads to

$$l_{ss}^{II} > l_{ss}^{III} > l_{ss}^{I} > l_{ss}^{IV} \quad \text{and} \quad l_{sr}^{I} > l_{sr}^{IV} > l_{sr}^{II} > l_{sr}^{III}, \tag{2.33}$$

giving us the final ordering in this case.

When we now change the polymer to SBR and look at Figure 2.23b, we find the surface modified silica to show an even higher flocculation tendency but a poor wetting behavior towards the polymer. Because the flocculation tendency of all filler types towards the surface modified silica is obviously unaltered (Figure 2.24c is still used for the behavior between filler and surface modified silica), we expect the same ordering of l_{fs} (l_{sf}) like before, albeit the absolute values will be different due to the other surface modified silica related interface changes.

The surface modified silica flocculation inside the elastomer matrix, l_{ss} should be the highest for filler type I and then decrease continuously. This can be justified by Equation (2.32) together with the increasing flocculation tendency of the filler particles inside the elastomer matrix, i.e., the lowest is found for I. Thus,

$$l_{fs}^{III} > l_{fs}^{II} > l_{fs}^{IV} > l_{fs}^{I} \quad \text{and} \quad l_{ss}^{I} > l_{ss}^{II} > l_{ss}^{III} > l_{ss}^{IV}. \tag{2.34}$$

To find the ordering regarding the filler-polymer surface fractions l_{fr}, we just need to take a look at the ordering of flocculation tendency of the filler types inside the elastomer matrix, regardless of the surface modified silica, which yields

$$l_{fr}^{I} > l_{fr}^{II} > l_{fr}^{III} > l_{fr}^{IV}. \tag{2.35}$$

The filler-filler wetted surface fraction, l_{ff}, is affected due to the flocculation tendency for both elastomer matrix and surface modified silica. As the systems want to minimize their free enthalpy, combinations which yield a low difference in work of adhesion are favored. Filler type III shows the lowest flocculation tendency towards the surface modified silica, i.e., the highest value of l_{fs}. At the same time, it is high inside the elastomer matrix. Due to the possibility to minimize the free enthalpy, the filler-filler flocculation is avoided as much as possible. Filler type II comes next, followed by I and IV.

Finally, the wetted surface fraction between surface modified silica and the elastomer matrix is discussed. It can be most effectively deduced by using the orderings we found so far. Filler types with the highest value of l_{sr} should be found where we have the highest l_{ff} value combined with lowest possible values for l_{fs} and l_{ss}. This is given for filler type IV. Following this procedure we find I next, followed by III and II. This gives as the last orderings

$$l_{ff}^{IV} > l_{ff}^{I} > l_{ff}^{II} > l_{ff}^{III} \quad \text{and} \quad l_{sr}^{IV} > l_{sr}^{I} > l_{sr}^{III} > l_{sr}^{II}. \tag{2.36}$$

The orderings in the wetted surface fractions between NR and SBR are different. For instance, no filler incorporated in SBR will show complete dispersion – at least not with the surface modified silica we used. For NR, however, filler type II looks promising. These simple conclusions are drawn from the orderings of l_{ff} and l_{fr}. But the possibilities to draw conclusions on aggregation or dispersion are very limited. For a more conclusive picture, we need take the simulated scattering intensities and TEM pictures as well as the values of the wetted surface fractions into account. The ordering of the latter, however, should at least give us a consistency check, whether the development of the structures is reasonable or not in the pure terms of surface free energies.

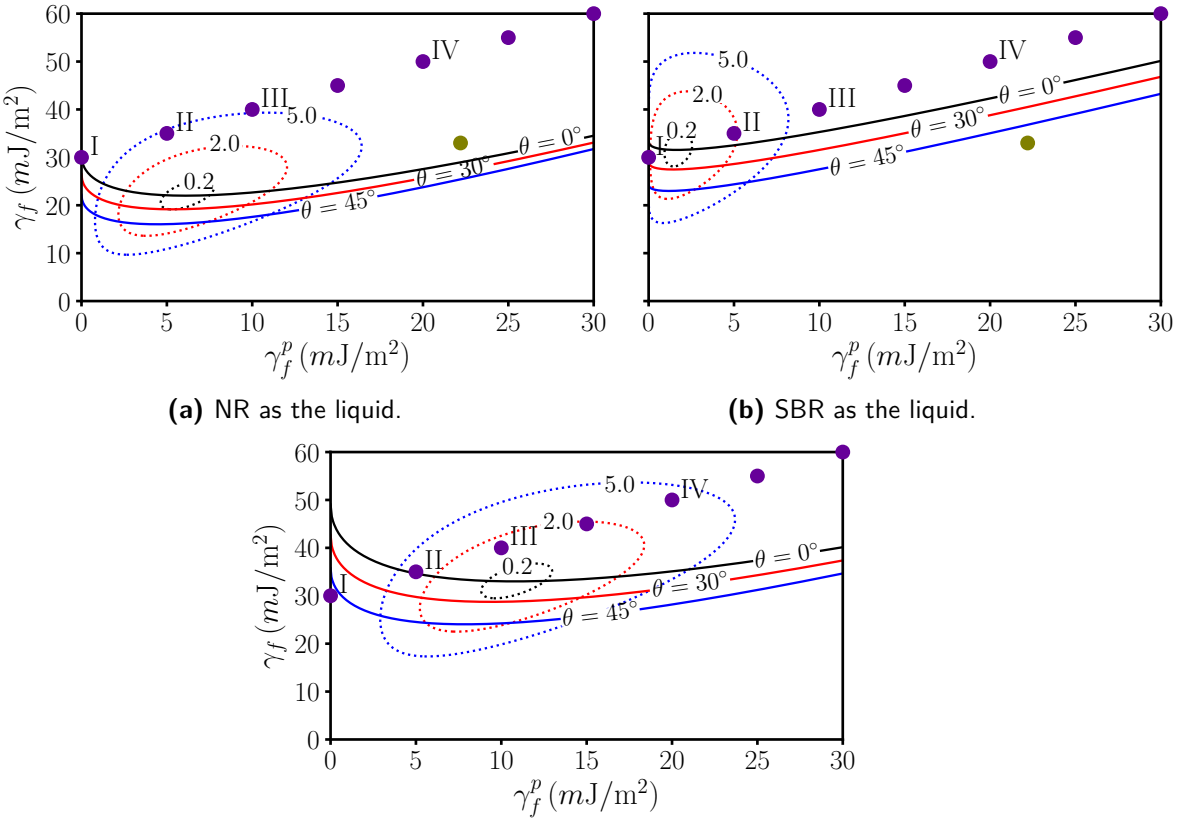

(a) NR as the liquid.

(b) SBR as the liquid.

(c) Surface modified silica as the liquid.

Figure 2.24.: Wetting-envelope - work of adhesion plots for NR, SBR, and surface modified silica containing artificial filler types with $\gamma_f^d = 30\,mJ/m^2$, marked as purple dots. Those labeled by roman numerals I to IV are chosen to be investigated further. The olive colored dot in both of the top plots **(a)** and **(b)** marks the position of the surface modified silica Coupsil 8113 powd.

We can now repeat this procedure for the filler types with $\gamma_f^d = 30\,mJ/m^2$, as depicted in Figure 2.24. The style of the plot is equal to Figure 2.23.

First of all, increasing the dispersive part leads to a vertical shift for all filler particle types. Subsequently, the wetting behavior gets better, despite of the liquid. In the case of NR, i.e., Figure 2.24a, the shift additionally leads to higher flocculation tendencies, except for I. It is unaffected in this aspect. Its wetting behavior, however, is way better. Beside the fact that the absolute values of all wetted surface fractions will be different, we only see minor changes in ordering. Filler types II and III are now basically identical with respect to NR. However, III still shows better dispersion for the surface modified silica. Thus, the ordering regarding the filler-filler wetted surface fraction l_{ff} is changed in the positioning of II and III, compared to the left part of Equation (2.31). Because the overall values of l_{ff} are increased for those two filler particles, their l_{fr} values must decrease. Their ordering, however, should not be affected. The values for l_{fr} of types II and III should be nearly equal. For SBR, i.e., Figure 2.24b, the flocculation tendency is decreased for I and II, whereas the other particles are more or less unaltered. This should result in higher values of l_{fr} and lower values in l_{ff}. The impact on the interaction between filler and surface modified silica is also affected, as can be seen in Figure 2.24c. The flocculation tendency of all filler types is increased. The ordering, however, should not be affected at all.

In the next parts, we use our morphology generator to produce all of the above systems and check, whether the ordering deduced here is in agreement with our results. This check is performed by combining the results of the different screening methods. The focus is on the change of the different system parameters. These are the flocculation time, filler volume content, ϕ, and the temperature, T. We start with the former, i.e., taking a look at the systems after different number of MC steps.

2.5.2. Impact of Flocculation Time

A variable number of MC steps for a given system allows to analyze the structural development over time[11]. We already saw in the introductory part of the screening methods that a certain number of MC steps needs to pass before any development can be observed. Generally, the mean is ten steps per particle. This results in the order of 10^7 MC steps in total for our systems. Therefore, we do not consider systems below this threshold. In order to limit the variations of the parameter space and focus on the impact of flocculation time, we need to fix the filler volume content and the temperature. Akin to our example systems, we use $\phi = 20\%$ in vol. and $T = 433$ K. Again, we briefly summarize the procedure: Kratky plots for each system are produced and evaluated with respect to their mean aggregate size, q_{agg}. Those values are plotted against the polar part of the surface free energy and compared for different number of MC steps. TEM pictures are embedded inside these aggregation phase diagrams. Plots of the wetted surface fractions are used to analyze them in more detail. Additionally, the distribution of the cluster masses is considered.

We start with filler types having a dispersive part of the surface free energy of $\gamma_f^d = 20\,m\mathrm{J/m}^2$ incorporated inside NR, i.e., Figure 2.25.

The plot in the top, Figure 2.25a, shows the aforementioned corresponding aggregation phase diagram. The left axis shows the magnitude of the scattering vector for the aggregate, i.e.,

[11] MC simulations do not have any time scale per se. The identification of MC steps as a time is discussed in Appendix D.

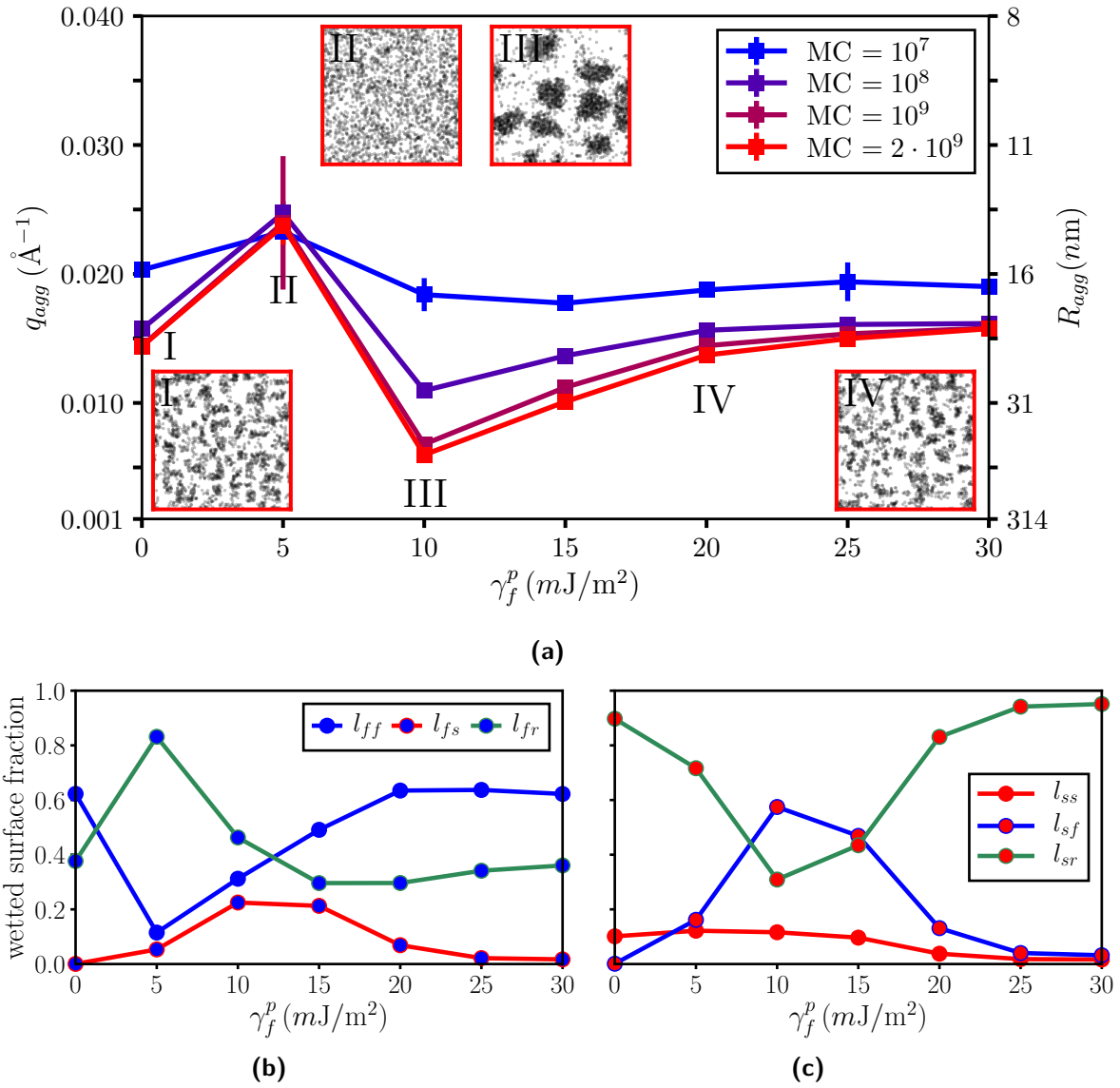

Figure 2.25.: (a): Aggregation phase diagram for filler types with $\gamma_f^d = 20\,mJ/m^2$ incorporated in NR with $\phi = 0.20$ at $T = 433$ K including embedded TEM pictures for systems indicated by roman numerals. The colored border of each TEM corresponds to the according number of MC steps given in the legend. **(b)**: Wetted surface fractions with the unmodified filler in focus. **(c)**: Wetted surface fractions with the modified silica sides in focus. Both wetted surface fractions are corresponding to the TEM pictures embedded in **(a)**.

the second peak in the Kratky style plot, q_{agg}. On the right axis we find the radius of the aggregates. It is calculated via $R_{agg} = \pi/q_{agg}$. Note that this axis does not scale linearly. The embedded TEM pictures for the filler particles indicated by roman numerals, show a 50×50 portion of each system to render the differences more clearly. This is equal to $0.4\mu m \times 0.4\mu m$. The colored border of the TEM pictures is corresponding to the number of MC steps indicated in the legend. The error on each data point arises due to the procedure

elucidated in the screening methods section and is given for the q_{agg} values. Note that all the information given for this plot also applies for all other upcoming plots of the same type. The two plots at the bottom, Figures 2.25b and 2.25c, show the corresponding wetted surface fractions for the bare filler and the silanized surfaces respectively. They need to be compared with the TEM pictures and thus, with the red data points in Figure 2.25a.

The blue data points in Figure 2.25a are corresponding to our lowest value of MC steps where we expect any structural development. Here, the size of the aggregates is not significantly depending on the polar part of the surface free energy and the aggregates show sizes of roughly $16\,n$m. Increasing the mean number of MC steps per particle by a factor of ten, which are the dark purple data points obtained after 10^8 MC steps, we start to see differences between the filler particles. This trend becomes more clear for even higher number of MC steps. Individually, the impact of flocculation time differs. The mean size of the aggregates of filler type I increases, but the trend shows that longer flocculation times do not change their size drastically. Filler type II is completely unaffected by the number of MC steps. The particles are dispersed throughout the elastomer matrix and no structures develop. The opposite is found for filler type III. The ongoing flocculation time produces growing aggregates with mean aggregate sizes of $R_{agg} \approx 53\,n$m. This effect diminishes for higher polar parts of the surface free energy such as for filler type IV, whose aggregates have an equal size compared to I, i.e., $R_{agg} \approx 23\,n$m.

The mean size of the aggregates for TESPT silanized silica particles inside NR with the same filler volume fraction of $\phi = 0.2$ is found to be $R_{agg} \approx 22.5 \pm 10\,n$m [51] (cf. Figure 7.9 therein). The silica particles used in this work are Ultrasil 7000. Experimental surface free energies for this silica particle were not obtainable. Although it is different from Ultrasil VN3, at least the production process is similar, i.e., both are precipitated silica. Therefore, we use the results for the filler particle which matches most with Ultrasil VN3. This is filler type IV. For that we find a value of $R_{agg} \approx 23\,n$m. The size of the primary particles is $7\,n$m and thus comparable to ours. We therefore find aggregates, which are comparable in size.

For the wetted surface fractions in Figures 2.25b and 2.25c, we find that the ordering we deduced in the context of the wetting-envelope - work of adhesion plots is correct, although the differences in l_{ss} for the first three particles is rather minor. Nevertheless, a closer look reveals that this ordering is also correct.

The wetted surface fractions of filler type I, which correspond to $\gamma_f^p = 0\,m\mathrm{J/m}^2$, show that those regarding the filler surface, i.e., Figure 2.25b, are completely divided into rubber and filler. If we look at the TEM picture I and the value for mean size of the aggregate, this is fairly reasonable. A network like structure developed inside the elastomer matrix with relatively small aggregates inside the branches. Single primary filler particles are not found in between the branches. This is supported by the cluster mass distribution, which shows a single large cluster containing roughly 90% of all filler particles. Clusters with a mass less than ten are far below 1%.

The significant boost in l_{fr} and loss in l_{ff} when changing the polar part of the surface free energy, i.e., now considering filler type II, is an agreement with the corresponding TEM picture. Almost no structural development is found and the primary particles are dispersed inside the elastomer matrix. The cluster mass distribution supports this reasoning, as only

63% of all particles are found in clusters and of those 83% have a mass less than ten. The biggest clusters found have a mass lower than one hundred. The decrement in the silane related surfaces in Figure 2.25c for rubber as well as the increment for the wetted surface fraction of filler and silane, l_{fs} (l_{sf}), is not represented by the TEM picture. This shows again that the combination of all screening techniques is mandatory to render a complete picture of the simulated systems.

Further increase of the polar part of the surface free energy leads to a strikingly decreased value of l_{fr} and further increase of both other filler related surface fractions. The TEM picture shows distinct structures and the mean size of the aggregates is considerably large. It has a value of $52.6 \pm 2.4\,n$m. Here, the value for the purely filler-filler related surface fraction, l_{ff}, does not indicate structures of this size. But if we take those regarding filler and surface modified silica into account, i.e., l_{fs} (l_{sf}), we can see that the distribution of the contacts between particles inside those structures has a relatively large share coming from this specific combination. Still, the majority comes from filler-filler contacts. The distribution of the cluster masses shows that 86% of all particles are bound into clusters. Only 11% of the particles are in clusters with a mass less than ten. More than half are found in clusters with a mass higher than one thousand. Higher values of γ_f^p lead to higher values of l_{ff} and lower values of l_{fr} and l_{fs} (l_{sf}). The mean size of the aggregates becomes smaller.

For filler type IV the TEM picture again indicates a filler network, but it is less continuous than that in I. More single large structures can be identified and the distances between individual branches seem to be higher. The distribution of the cluster masses supports this impression. Although there is a single large cluster again, it just includes around 60% of all particles inside it. The clusters with mass smaller than ten are again below 1%. Thus, we find several bigger single clusters with mass up to several thousands of primary filler particles. Those bigger aggregates start to merge with the cluster network, if the polar part of the surface free energy is increased further. It seems that the wetted surface fractions indicate a filler network, if the values for l_{ff} and l_{fr} are fairly high, while that of l_{fs} (l_{sf}) is low. Additionally, it is more continuous if the value of l_{sr} is high. The impact of l_{ss} on any structural behavior can not be established. In the context of the wetting-envelope - work of adhesion plots we find that high flocculation tendency of the filler particles inside the elastomer matrix and the surface modified silica environment results in filler networks. Key is the good wetting of the surface modified silica with respect to the elastomer. If the surface modified silica behave differently, this may lead to the development of other structures.

If we now change the polymer to SBR and look at the corresponding Figure 2.26, we see a major difference in every aspect. The impact of flocculation time is very limited and only significant for the first two filler types. Similar to NR, the lowest number of MC steps does not produce structures, regardless of the polar part of the surface free energy. Higher numbers start to produce structures, which do not seem to be very different with respect to the mean aggregate size. Filler type II, which showed very good dispersion inside NR, now produces with $R_{agg} \approx 27\,n$m the biggest aggregates. The large aggregates we saw for filler type III inside NR, on the other hand, are completely gone.

Experimentally, we find values of $R_{agg} \approx 34\,n$m [38]. They are obatined for compounds, which contain 21.1% HD silica Zeosil 1165 MP inside SBR, but modified with a different silane, i.e., octeo instead of TESPT. To compare our results, it is necessary to know the surface free

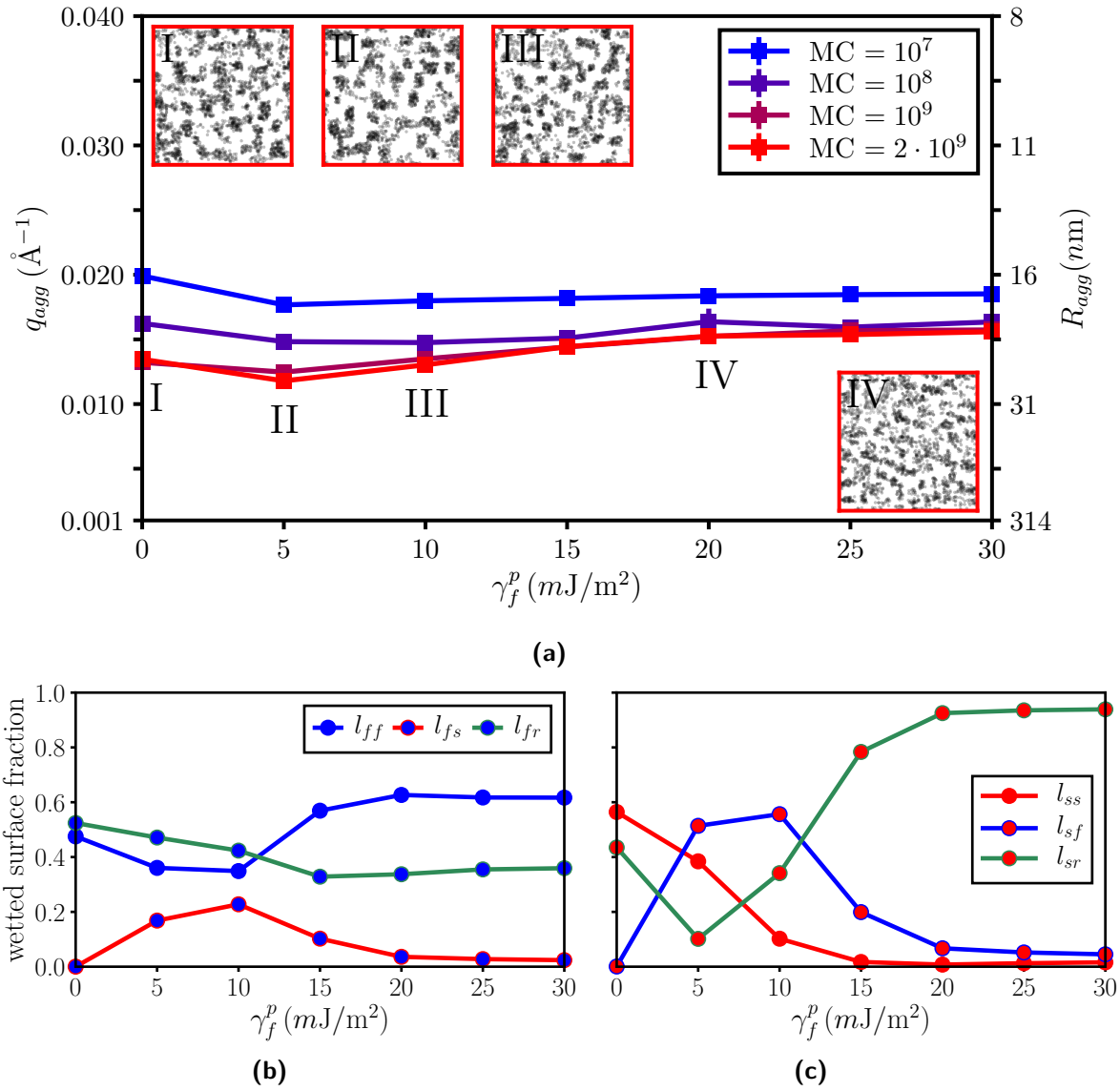

Figure 2.26.: (a): Aggregation phase diagram for filler types with $\gamma_f^d = 20\,mJ/m^2$ incorporated in SBR with $\phi = 0.20$ at $T = 433$ K including embedded TEM pictures for systems indicated by roman numerals. The colored border of each TEM corresponds to the according number of MC steps given in the legend. **(b)**: Wetted surface fractions with the unmodified filler in focus. **(c)**: Wetted surface fractions with the modified silica sides in focus. Both wetted surface fractions are corresponding to the TEM pictures embedded in **(a)**.

energy value of Zeosil 1165 MP. Unfortunately, it was not obtainable. By the manufacturer it is known, however, that Zeosil 1165 MP is identical to Ultrasil VN3 a precipitated silica [59]. Therefore, we again use filler type IV, for which we find a value of $R_{agg} \approx 21\,nm$. Although this value might be way less, we need to take the size of the primary particles into account. Here, we use $R_{si} = 8\,nm$ and consequently obtain a ratio between aggregate and primary

particle of $R_{agg}/R_{si} \approx 2.6$. If we take the mean size of the primary particles of Zeosil 1165 MP, i.e., $R_{si} = 13.85\,n$mm [38], we find a comparable ratio of $R_{agg}/R_{si} \approx 2.5$.

Looking at the wetted surface fractions in Figures 2.26b and 2.26c, we again find that the ordering we deduced in the context of the wetting-envelope - work of adhesion plots is correct.

For filler type I, the wetted surface fraction between filler and the surface modified silica, i.e., l_{fs} (l_{sf}), is close to zero, akin to NR. This is different for l_{ff} and l_{fr} that switch their positioning. The corresponding TEM picture in Figure 2.26a shows several massive structures not connected to one another. Looking at the cluster mass distribution, we find that this impression is indeed correct. Almost 98% of all primary filler particles are bound into clusters and of those, not even 2% are found in clusters with mass less than ten. In fact, almost half of all filler particles are bound into clusters with a mass greater than one thousand. This is a similar behavior compared to filler type III for NR in Figure 2.25. The strong difference in both TEM pictures is due to the difference in filler-surface modified silica contacts, i.e., l_{fs} (l_{sf}).

Increasing the polar part of the surface free energy, the structures inside the TEM pictures become well defined, more acute, and seem to be smaller. The amount of primary particles bound into clusters is similar to the system containing filler type I, i.e., 95%. Their distribution, however, is different. Primary particles inside small clusters with mass less than ten and in bigger ones with mass greater than one thousand combined only make up 15% of all cluster bound particles. It is again true that higher values of l_{fs} (l_{sf}) together with low values of l_{sr} yield more compact and smaller clusters.

The TEM picture for filler type III is more blurry compared to II and shows a higher quantity of smaller clusters. The trend we saw going from I to II is continued. Less particles are bound into clusters with mass greater than one thousand, i.e., 3%, and more particles are bound into smaller clusters with mass less than ten, i.e., 6%. Coming from I, we thus find that higher polar surface free energy breaks down the bigger structures. We saw this behavior also for NR, but more abrupt. The change from I to II completely destroyed the filler network. Aggregation into bigger single structures began in the change from II to III. Further increment then led to the formation of filler networks. This is also true for SBR.

The TEM for filler type IV shows a continuous filler network. The wetted surface fractions also fulfill all requirements, i.e., high values of l_{ff}, l_{fr}, and l_{sr} while at the same time having a low value of l_{fs} (l_{sf}). Indeed, the cluster mass distribution shows that this system contains a single large cluster, which comprises more than 80% of all primary filler particles. This is very similar to filler type I in NR, which is no surprise when we compare the corresponding wetted surface fractions in the bottom of Figures 2.25 and 2.26 and thus, the ordering we deduced in the context of the wetting-envelope - work of adhesion plots. The different wetting behavior of the surface modified silica with respect to the different polymers is a huge impact factor – at least for the system parameters we have chosen so far. Further increment of γ_f^p yields structures inside the elastomer matrix very similar to NR.

We now change the dispersive part of the surface free energy of all filler particles to $\gamma_f^d = 30\,m\mathrm{J/m}^2$ and investigate their behavior inside the different polymers again, i.e., we consider Figure 2.27.

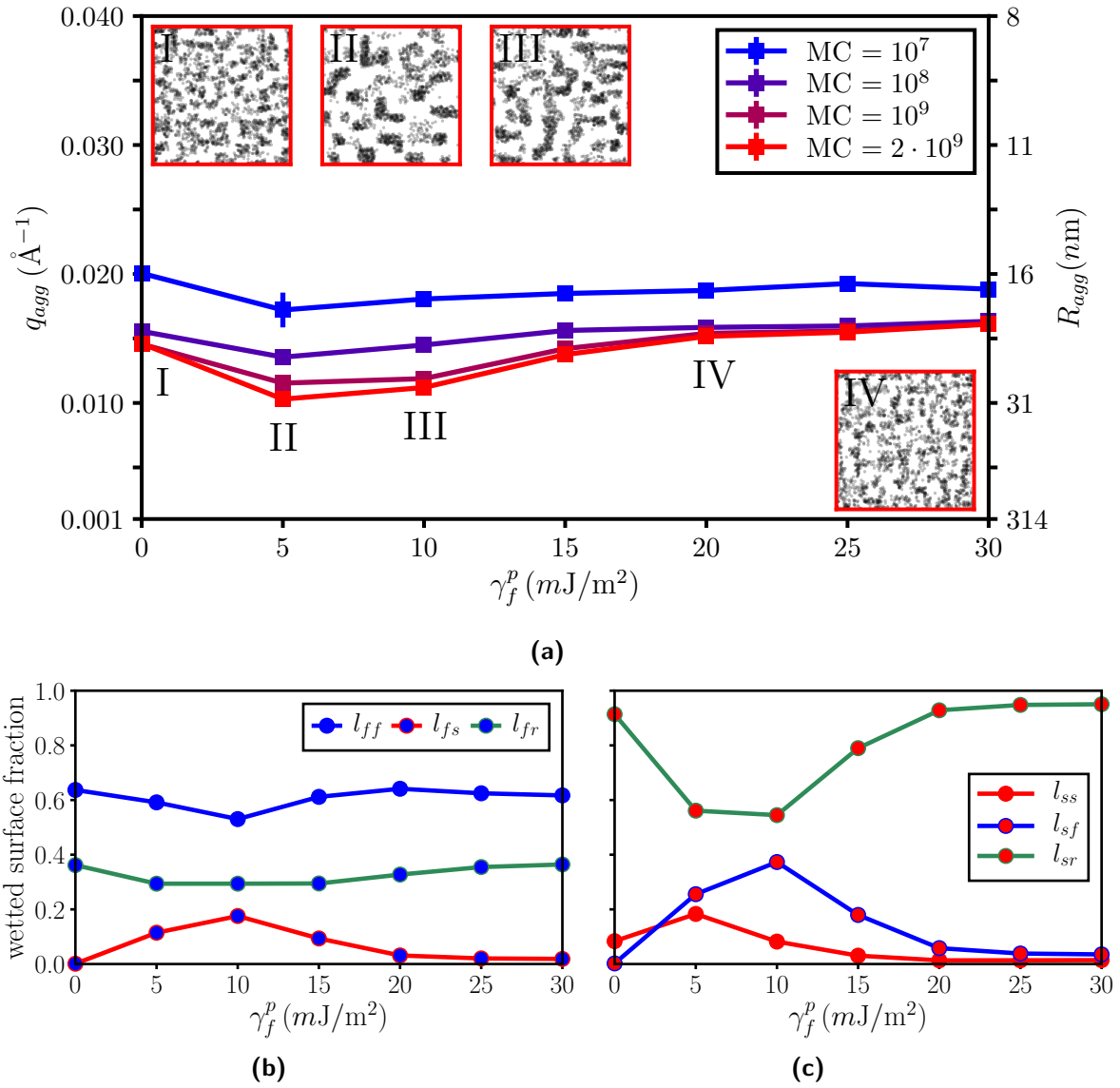

Figure 2.27.: (a): Aggregation phase diagram for filler types with $\gamma_f^d = 30\,mJ/m^2$ incorporated in NR with $\phi = 0.20$ at $T = 433$ K including embedded TEM pictures for systems indicated by roman numerals. The colored border of each TEM corresponds to the according number of MC steps given in the legend. **(b)**: Wetted surface fractions with the unmodified filler in focus. **(c)**: Wetted surface fractions with the modified silica sides in focus. Both wetted surface fractions are corresponding to the TEM pictures embedded in **(a)**.

Similar to the former case we start with NR. The impact of flocculation time is still comparable to the former case with $\gamma_f^d = 20\,mJ/m^2$, i.e., Figure 2.25a. A major change is, however, found for the system containing filler type II. It now shows a variation in the mean aggregate size, which was not seen before. Thus, the formerly well dispersed system containing filler type II now shows structural development. The big mean aggregates for type III are gone

and we instead find rather smaller ones. Both other systems containing types I and IV seem to be only affected minorly in this quantity.

The wetted surface fractions in both Figures 2.27b and 2.27c also show a very different behavior. In the context of the wetted-envelope - work of adhesion plots, we find that the ordering we deduced is correct. Even the equality between filler types II and III in l_{fr}, due to their very similar positioning regarding the flocculation inside NR and the silane, is found here.

Filler type I does not show any changes, compared to the $\gamma_f^d = 20\,m\mathrm{J/m^2}$ case. We find zero contact between filler and the surface modified silica, l_{fs} (l_{sf}), and a very high value of l_{sr} as well as l_{ff}. The TEM pictures are also very similar and show a network like structure inside the elastomer matrix. Due to those facts we expect no difference in the cluster mass distribution. This is indeed the case. A single large cluster permeates the elastomer matrix, containing roughly 90% of all primary filler particles again. Small clusters with mass less than ten are way below 1%.

Increasing the polar part of the surface free energy and moving to filler type II, we now find only very minor changes, which is completely different to the $\gamma_f^d = 20\,m\mathrm{J/m^2}$ case. Instead of a boost in l_{fr}, there is a slight decrease and the loss in l_{ff} is also considerably less. Regarding the modified silica surface fractions, we find a higher decrement in l_{sr} and slightly higher increment in l_{fs} (l_{sf}). This is in agreement with the rather compact and big aggregates we can see in the corresponding TEM picture. No continuous filler network is visible. The change in γ_f^p leads to a breakdown of the filler network into several big clusters. Almost half of all cluster bound particles, which are about 99% of all particles, are found in clusters with mass greater than one thousand. In the strict sense of filler network breakdown due to an increment in γ_f^p, the behavior in both cases is the same.

For filler type III, l_{fs} (l_{sf}) is increasing, but l_{ff} does decrease while l_{fr} shows no significant change. The high loss in l_{sr}, we saw before, has also a much lesser extent. The TEM picture indicates, similar to $\gamma_f^d = 20\,m\mathrm{J/m^2}$, bigger structures. Their mean aggregate size, however, is slightly smaller than for filler type II. Thus, the structures are slightly less dense, which is also supported by the TEM picture. Looking at the cluster mass distribution, we find that the number of primary filler particles inside clusters did not change. However, we now find less primary filler particles are bound into clusters with mass more than one thousand, i.e., only 40%. Although this might contradict our impression we got from our TEM picture, an even more detailed look reveals that the biggest clusters produced by filler type III are almost twice as big as those by filler type II. The distribution of the cluster sizes also gives a hint here. It is more narrow for filler type II than for III. The rearrangement of the structures into bigger ones is akin to the case with $\gamma_f^d = 20\,m\mathrm{J/m^2}$, albeit to a much lesser extent.

Further increasing the polar part of the surface free energy, i.e., filler type IV, decreases l_{fs} (l_{sf}) and slightly increases l_{ff} and l_{fr}. A large increase is found in l_{sr}. The combination of the last three mentioned wetted surface fractions indicates a filler network. This is supported by the TEM picture as well as the cluster mass distribution. The single large cluster, permeating the elastomer matrix, contains about 85% of all primary filler particles. Way below 0.1% of the filler particles are unbound. Different to the $\gamma_f^d = 20\,m\mathrm{J/m^2}$ case we thus find a more continuous network. If we compare the wetted surface fractions, we find for the less continuous

network lower values of l_{sr} and higher values of l_{fs} (l_{sf}). This is again an indication that our statement of network continuity is – at least for this parameter combination – correct.

So far we can state that in both cases we start with a filler network, which breaks up for increasing values of the polar part of the surface free energy. Further increment first leads to the formation of single big structures, which then form a filler network again. The extent is more pronounced for $\gamma_f^d = 20\,m\mathrm{J/m^2}$ than for $\gamma_f^d = 30\,m\mathrm{J/m^2}$, while the continuity of the filler networks behaves the other way around. At very large values of γ_f^p, i.e., greater than $20\,m\mathrm{J/m^2}$, the systems are not discernible. A reason for this behavior is the higher flocculation tendency we saw due to the change in the dispersive part of the surface free energy in the context of wetting-envelope - work of adhesion plots.

At last we are left with the behavior of the different filler types inside SBR. Figure 2.28 depicts these cases. The impact of flocculation time for filler types with different polar parts of the surface free energy is comparable to the case of $\gamma_f^d = 20\,m\mathrm{J/m^2}$. Again, only the first two types show any significant changes. For the lowest number of MC steps, we find the only significant difference for the system containing filler type I. This is comparable to the system containing filler type II with $\gamma_f^d = 20\,m\mathrm{J/m^2}$ in the case of NR (cf. Figure 2.25a). Increasing the number of MC steps leads to the formation of pronounced aggregates for every filler type. The size of the aggregates are representative for more complex structures. For filler type II we find a difference to the other case, as they are slightly bigger.

Filler type I is comparable to the carbon black N339, which has a dispersive part of $\gamma_f^d = 27\,m\mathrm{J/m^2}$ and a polar part of $\gamma_f^p = 0\,m\mathrm{J/m^2}$ [1]. In [49], the size of the corresponding aggregates has been determined using SAXS. They find values of $R_{agg} = 27\,n\mathrm{m}$. In the simulation we find $R_{agg} \approx 25\,n\mathrm{m}$. Before we compare both values, we need to calculate the ratio between aggregate and primary particle – akin to the consideration of the silica particles inside NR and SBR in the $\gamma_f^d = 20\,m\mathrm{J/m^2}$ case. For filler type I we consequently find $R_{agg}/R_{si} \approx 3.1$. Experimentally, we find, however, $R_{agg}/R_{si} \approx 2.1$, with $R_{si} = 13\,n\mathrm{m}$. The aggregates we obtain from the simulation are therefore bigger than those in the experiment. But we are considering the impact of flocculation time in this section. The mean size of the aggregates after the shorter simulation time, i.e., after 10^8 MC steps, yields a significantly lower value of $R_{agg} \approx 20\,n\mathrm{m}$. We consequently find a ratio of $R_{agg}/R_{si} \approx 2.5$. This matches with the experimental values quite well and gives a hint that shorter simulation times might be reasonable to consider.

The wetted surface fractions in Figures 2.28b and 2.28c are also more or less unaltered compared to those in Figures 2.26b and 2.26c, as we expected from the unaffected ordering in the context of the wetting-envelope - work of adhesion plots. We only see a change in the values, not in the individual courses itself.

Filler type I shows the predicted increment in l_{fr} and decrement in l_{ff}. Beside that, we find lower values of l_{sr} and higher values of l_{ss}. The corresponding TEM picture is more comparable to filler type II in the case of $\gamma_f^d = 20\,m\mathrm{J/m^2}$. It shows several big structures, albeit less acute. This renders the picture overall more blurry. The distribution of the cluster masses shows that we find about 95% of all primary filler particles bound into clusters. Of those, about 28% are found in clusters with mass greater than one thousand and only about 5% in clusters with mass less than ten. This is indeed similar to filler type II in the other

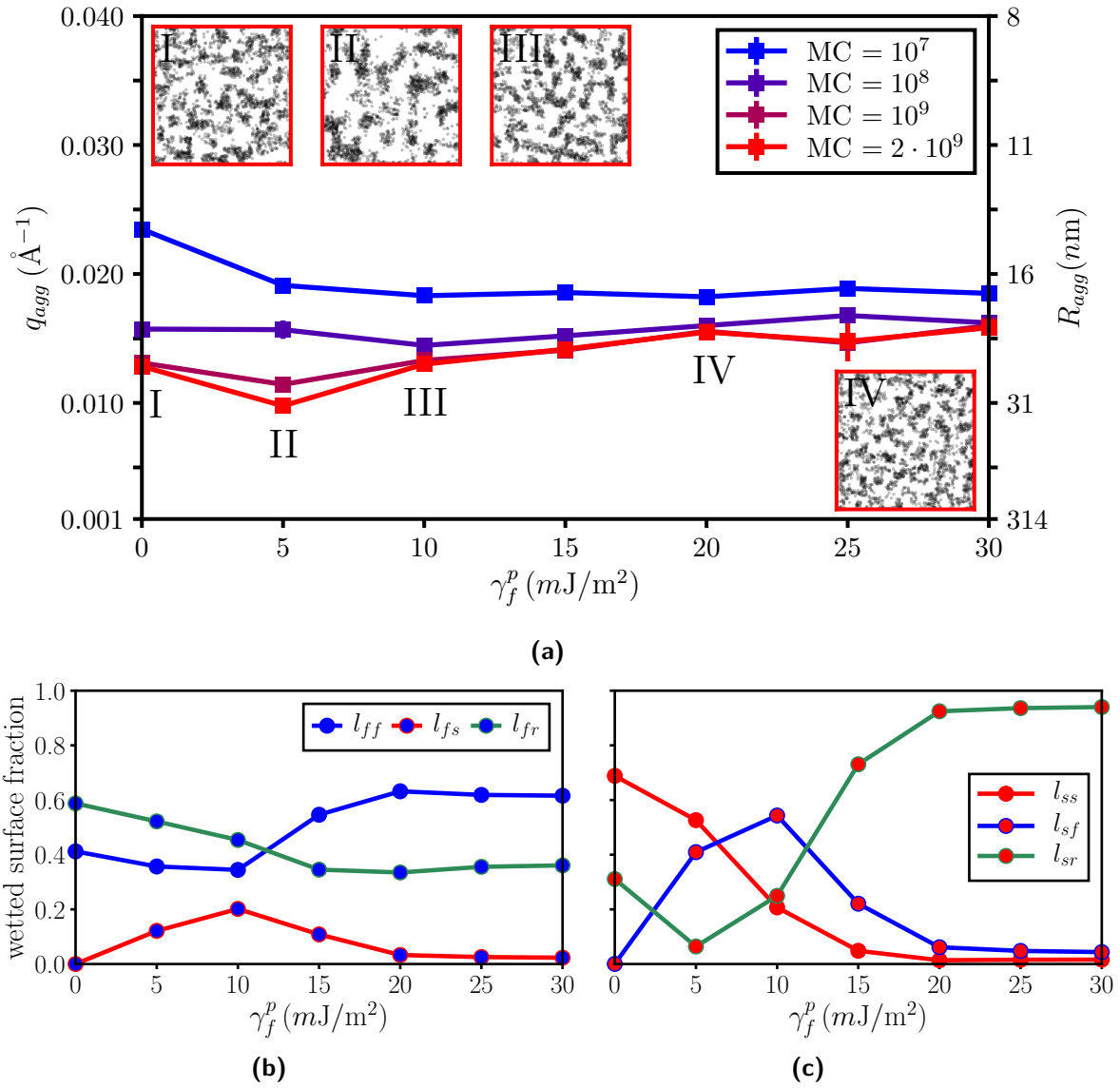

Figure 2.28.: (a): Aggregation phase diagram for filler types with $\gamma_f^d = 30\,mJ/m^2$ incorporated in SBR with $\phi = 0.20$ at $T = 433$ K including embedded TEM pictures for systems indicated by roman numerals. The colored border of each TEM corresponds to the according number of MC steps given in the legend. **(b)**: Wetted surface fractions with the unmodified filler in focus. **(c)**: Wetted surface fractions with the modified silica sides in focus. Both wetted surface fractions are corresponding to the TEM pictures embedded in **(a)**.

case, although there were more clusters with intermediate mass, i.e., between ten and one thousand. This is due to the higher number of l_{ss} contacts, which also accounts for the more blurry impression of the TEM picture.

For filler type II we see that l_{fs} (l_{sf}) is now lower than l_{ss} compared to the other case. The according TEM picture shows relatively large structures, which are far apart. In between

the bigger ones we find some smaller structures. If we look at the cluster mass distribution, we find a very similar distribution, identical to filler type I. The increasing value of l_{fs} (l_{sf}) indicates that the structures are now more compact, which is justified by the increasing mean aggregate size. The high value of l_{ss} separates the individual structures and drives them apart. Although the cluster mass distribution shows lots of similarities, the overall trend in reduction of bigger structures into smaller ones is still given, albeit to a way lesser extent. In fact, this combination of filler type and polymer shows the lowest impact of structural reduction of all systems investigated so far.

For filler type III this trend continues, similar to the other case. Now, the value for l_{fs} (l_{sf}) increases and that of l_{ss} is way lower. Additionally, the value of l_{sr} increases again, but to a much lesser extent compared to the other case. As observed for every other system, the structures become more compact, which renders the TEM picture more acute. The structures themselves are now closer together, because of the lower value of l_{ss}. The distribution of the cluster masses still shows the same amount of primary filler particles bound into clusters. The individual distribution, however, changed in accordance with the TEM picture. Of the primary filler particles bound into clusters, there are very few inside clusters with mass greater than one thousand, i.e., below 5%, and also inside clusters with mass lower then ten, i.e., about 5%.

Further increasing the values of the polar part of the surface free energy, leads to the development of bigger structures and manifests into the formation of filler networks. This is indistinguishable to the other case with $\gamma_f^d = 20\,m\mathrm{J/m^2}$. Here, however, the formation process is far less developed. It can not be observed for filler type IV, because it already produced the filler network. This is comparable to the other case to every extent. For instance, the cluster mass distribution of both filler types is very similar. But we are able to see it for the filler type in between III and IV. It shows smaller and lesser clusters with mass lower than ten thousand and more clusters in the regime between one thousand and ten thousand compared to the other case. Thus, it is reasonable to say that for $\gamma_f^d = 30\,m\mathrm{J/m^2}$ the structural reduction as well as the formation of filler networks is less pronounced than for $\gamma_f^d = 20\,m\mathrm{J/m^2}$ when changing the polar part of the surface free energy.

Altogether, we see that small variations in our parameters can lead to very distinct behavior. Some filler types behave similarly, independent of the dispersive part of the surface free energy or the polymer. This is the case for all types with a value of γ_f^p greater than $20\,m\mathrm{J/m^2}$. They form a filler network inside both polymers. We also see distinct trends when increasing γ_f^p. The impact of flocculation time is very dependent on the parameters of the filler types. Sometimes we see ongoing trends in structural development. For instance, filler type III with $\gamma_f^d = 20\,m\mathrm{J/m^2}$ inside NR (cf. Figure 2.25a). Other times, when a specific structure is formed in the early stages (or none at all), the impact of ongoing flocculation time seems to be minor. For instance, all filler types which develop a filler network inside the elastomer matrix and for the very dispersed case of filler type II with $\gamma_f^d = 20\,m\mathrm{J/m^2}$ inside NR (cf. Figure 2.25a).

Experimentally, the formation of filler networks is measured in different ways, depending on the type of filler. For carbon black filled compounds, resistivity measurements are conducted [60] or the change of the storage modulus at low strain amplitude over time is investigated [23]. For silica filled compounds, resistivity measurements are no option and thus, only the latter is used [15]. All sources, however, show that the flocculation process is a major contributor

to filler network formation. We can confirm this impact here. In none of the systems the formation of a filler network is observed without the initiation of the flocculation process.

The comparison with experimental values for silica inside NR [51] shows that the mean size of the aggregates matches quite well. The comparison to experimental results in the case of silica [20, 38] and carbon black [49] inside SBR show, that the sizes of the aggregates we obtain from the simulation are also reasonable. However, the latter showed that the number of MC steps can also be crucial. Sometimes systems obtained after less MC steps may already be in a state, which is experimentally more comparable.

For all systems we can determine the mass fractal dimension of the aggregates, d_m^{agg}, using the box-counting algorithm. Since we are considering the impact of flocculation time, it is reasonable to show their values for the last three values of MC steps we considered here, i.e., 10^8, 10^9, and $2 \cdot 10^9$. Figure 2.29 shows the corresponding results for both polymers NR and SBR and both dispersive parts of the surface free energy $\gamma_f^d = 20\,mJ/m^2$ and $\gamma_f^d = 30\,mJ/m^2$.

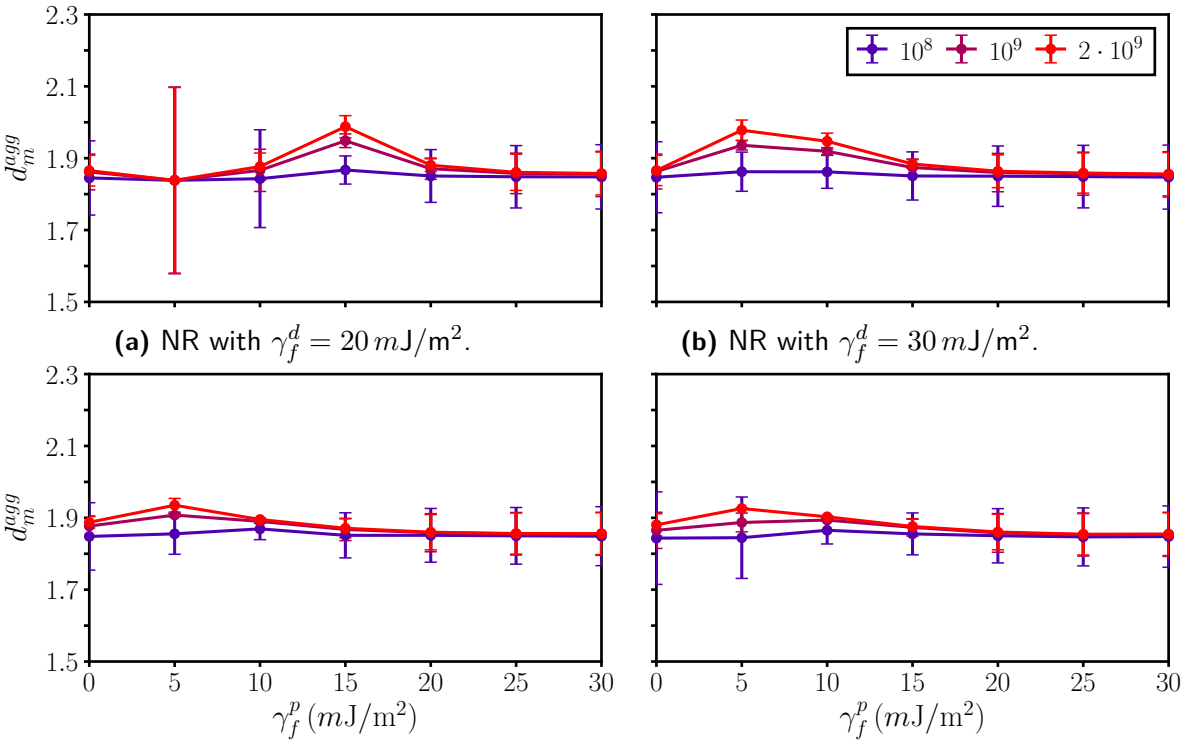

(a) NR with $\gamma_f^d = 20\,mJ/m^2$. **(b)** NR with $\gamma_f^d = 30\,mJ/m^2$.

(c) SBR with $\gamma_f^d = 20\,mJ/m^2$. **(d)** SBR with $\gamma_f^d = 30\,mJ/m^2$.

Figure 2.29.: Mass fractal dimension of the aggregates after different MC steps produced by different filler types inside NR and SBR with $\phi = 0.20$ for $\gamma_f^d = 20\,mJ/m^2$ and $\gamma_f^d = 30\,mJ/m^2$ at $T = 433$ K. Note that in **(a)** we had the very dispersed system for $\gamma_f^p = 5\,mJ/m^2$ which leads to a very high uncertainty. Generally, the mass fractal dimensions of the aggregates for the three highest surface polarities are identical, independent of the polymer or dispersive part. For shorter MC steps the impact of different surface polarities is rather minor.

In all plots the values obtained after 10^8 MC steps deviate only slightly, independent of the surface polarity. The values for the three highest surface polarities show also no deviation when compared with one another. This is in agreement with the very similar TEM pictures for filler type IV, for instance, and the overall very similar mean size of the aggregates, as discussed in the context of the respective aggregation phase diagrams. For filler types with $\gamma_f^d = 20\,m\mathrm{J/m^2}$ inside NR, i.e., Figure 2.29a, we find a filler type with a very large uncertainty, i.e., II. It showed no structural development at all and was dispersed, independent of the flocculation time. A similar observation was made in the section showing the potential of the morphology generator, i.e., cf. the values in Table 2.3. In this case, we also found the highest value of all systems with $d_m^{agg} = 1.99 \pm 0.03$ for $\gamma_f^p = 15\,m\mathrm{J/m^2}$. Increasing the dispersive part, i.e., considering Figure 2.29b, we find that the first two polar filler types, i.e., II and III, have rather high mass fractal dimensions. The corresponding TEM pictures in Figure 2.27 showed elongated and big aggregates. Changing the polymer to SBR, i.e., considering Figures 2.29c and 2.29d, we see that filler type II produces the aggregates with the highest mass fractal dimension. Compared to NR, filler type I has a higher value for both dispersive parts. Note that the highest mass fractal dimensions not necessarily correspond to the systems with the biggest aggregates, but in most cases this link seems to fit[12].

A comparison to experimental values is only possible to a very limited extent. However, in [39], the authors investigated different silica particles, i.e., LudoxLS colloidal silica and Zeosil 1165 MP, incorporated inside SBR, which are surface modified with different silanes, i.e., octeo and TESPT. For each combination they used two different amounts of silane. This resulted in 1 or 2 molecules per $n\mathrm{m}^2$ of silica. The surface free energies of both silica are unknown. The former one is rather special. It is a watery suspension of silica particles, which is used inside the compound via solvent casting systems. Thus, we focus on the compounds containing Zeosil 1165 MP coated with TESPT. For them, they found values of $d_m^{agg} = 2.1$ for compounds with $\phi = 21\%$ and 1 TESPT molecule per $n\mathrm{m}^2$ and $d_m^{agg} = 2.0$ for compounds with $\phi = 19.2\%$ and 2 TESPT molecules per $n\mathrm{m}^2$. They stated the uncertainties as 15%, i.e., approx. 0.3 which is quite large. Filler particles comparable to Zeosil 1165 MP should, as already stated, be those with $\gamma_f^p = 20\,m\mathrm{J/m^2}$, because it is close to the Ultrasil VN3 value and both are precipitated silica. For that we find $d_m^{agg} = 1.86 \pm 0.05$ for both dispersive parts. Although the mean value is considerably lower, the high uncertainty in the experiment results in the fact that the value matches quite well.

The following Table 2.8 lists all filler types, which were able to develop a filler network within the given polymer. For each network its mass and size are listed. Note that the size is calculated from the radius of gyration via $R_n = R_G \cdot R_{si}$ (cf. Equation (2.14)). It varies only slightly. The size of the aggregates is taken from the formerly considered aggregation phase diagrams and their mass fractal dimension from Figure 2.29. The networks are similar in almost every aspect. Only the filler type with $\gamma_f^d = 20\,m\mathrm{J/m^2}$ and $\gamma_f^p = 20\,m\mathrm{J/m^2}$ inside NR developed a filler network with considerably less mass. It contains the biggest aggregates with the highest mass fractal dimension. Generally, a trend of bigger cluster mass for higher surface polarity is discernible, neglecting the $\gamma_f^p = 0\,m\mathrm{J/m^2}$ cases in NR for the moment. The bigger the cluster mass gets, the smaller the aggregates become and, consequently, the more continuous the filler networks appear in the TEM pictures.

[12] An exception is Figure 2.29b, where filler type I has the same aggregate size as type III but a considerably lower mass fractal dimension

Table 2.8.: Filler networks developed by different filler types inside NR and SBR for $\phi = 0.20$, $T = 433$ K, and after $2 \cdot 10^9$ MC steps. Listed are their mass, size, and the size of their aggregates together with the corresponding mass fractal dimension. Note that the size of the filler networks is calculated from the radius of gyration via $R_n = R_G \cdot R_{si}$ (cf. Equation (2.14)).

polymer	γ_f^d $[m\mathrm{J/m^2}]$	γ_f^p $[m\mathrm{J/m^2}]$	m_n	R_n $[n\mathrm{m}]$	R_{agg} $[n\mathrm{m}]$	d_m^{agg}
NR	20	0	368867	509.6	21.8 ± 0.4	1.87 ± 0.04
		20	246547	508.0	23.0 ± 0.3	1.88 ± 0.02
		25	364628	512.8	21.0 ± 0.2	1.86 ± 0.05
		30	373663	512.0	19.9 ± 0.0	1.86 ± 0.06
	30	0	368861	510.4	21.5 ± 0.0	1.87 ± 0.04
		20	355218	511.2	20.7 ± 0.6	1.86 ± 0.05
		25	367449	509.6	20.3 ± 0.1	1.86 ± 0.06
		30	369448	512.0	19.5 ± 0.1	1.86 ± 0.06
SBR	20	20	342298	512.8	20.6 ± 0.4	1.86 ± 0.05
		25	352553	510.4	20.4 ± 0.4	1.86 ± 0.06
		30	359746	511.2	20.2 ± 0.1	1.86 ± 0.06
	30	20	337027	512.0	20.3 ± 0.0	1.86 ± 0.05
		25	347653	512.0	21.3 ± 2.2	1.85 ± 0.06
		30	365388	512.0	19.8 ± 0.3	1.86 ± 0.06

In the next section we vary the filler volume content, ϕ, and investigate its impact on filler network formation and the size of the aggregates, R_{agg}, as well as their mass fractal dimension, d_m^{agg}.

2.5.3. Varying the Filler Volume Content

To keep the impact on the variation of the filler volume content, ϕ, in focus, we again fix the other two system parameters. In the last part we saw that clear statements about systems, regarding their constitution and behavior, are only possible at the end of the flocculation process. Thus, we consider only systems after the maximum number of MC steps, i.e., $10^3 \cdot L^3$. The temperature is again set to $T = 433$ K. A variation of the filler volume content should yield a large impact on the formation of the filler networks, because a certain amount is likely to be needed in this process. This value is generally known as the critical volume fraction $\phi_c = f p_c$ [61]. Here, f is the filling factor , also called the atomic packing factor, and p_c is the percolation threshold. Both factors are dependent on the underlying lattice, the dimension, and the configuration of the individual particles. In the concept of percolation theory either sites or bonds of a given lattice are randomly occupied with a certain probability p. Here, we therefore deal with site percolation. At the critical threshold, p_c, continuous networks first appear. For simple cubic systems in three dimensions, the filling factor is $f = \pi/6$

and the site percolation threshold is $p_c = 0.31160768(15)$ [62]. From this follows the critical volume fraction of $\phi_c = 0.1631574$. This value is for spherical particles on a simple cubic lattice. However, this theory is not applicable to our model in the same way. During the MC simulation our particles are represented as cubic cells, which alters the filling factor to $f = 1$, and consequently $\phi_c = p_c$. The major difference is, however, that we investigate our systems after a certain number of MC steps. Hence, the lattice is not randomly occupied with a certain probability. The MC steps may lead to a lower threshold. We saw this in the last part. In some cases, the formation of large filler networks already took place at $\phi = 0.2$, which is way below the expected value of ϕ_c. Other times we saw no networks for this value at all. It is therefore reasonable to assume that mass fractal networks lower the percolation threshold. Still, we can learn from percolation theory that systems, which are dispersed, are likely to form a continuous network, if the amount of filler has at least the value ϕ_c.

Different from the approach for the flocculation time, we directly compare the impact of variation of the dispersive part of the surface free energy by using the aggregation phase diagrams with embedded TEM pictures and postpone the discussion of the wetted surface fractions to the end. We start again with NR, i.e, Figure 2.30. The top part shows filler types with $\gamma_f^d = 20\,m\mathrm{J/m^2}$ and the bottom those with $\gamma_f^d = 30\,m\mathrm{J/m^2}$. The borders of the embedded TEM pictures are color coded according to the legend in the top part. Additionally, they are ordered from low to high volume content from left to right.

The impact on the mean size of the aggregates is very minor for both dispersive parts. The overall behavior of the individual systems is not altered. Only the dispersed system at $\gamma_f^p = 5\,m\mathrm{J/m^2}$ in the top part of the plot shows slight aggregate growth. This can be explained due to the increased spatial confinement of the particles for growing ϕ values. Here, however, we concentrate on filler type IV, i.e., $\gamma_f^p = 20\,m\mathrm{J/m^2}$. In the part considering flocculation time, it showed the formation of a filler network, independent of the polymer and the dispersive part of the surface free energy. Therein, we chose a value of $\phi = 0.2$. Consequently, it is of interest to see how the system behaves at different filler volume contents, i.e., if the formation of filler networks at lower values of ϕ is possible.

Taking the TEM pictures into account, we directly recognize a very different behavior. In the top part for the lowest value of ϕ, i.e., the blue bordered, seemingly dilute TEM picture on the left, we see that indeed small aggregates have formed. But the formerly distinct network structure is not seen. This filler volume content is thus too low to create one. Considering the cluster mass distribution, we almost find no particle, which is not bound into a cluster. Those with a mass less than ten are also very limited, i.e., around 5%. Most primary filler particles are aggregating themselves in several higher order structures in the range of a couple of tens particles. The upper threshold of the structures consists of a few hundred particles, which is by far too low to build networks.

The purple bordered TEM picture, which is the second from the left, shows bigger structures, which are in more proximity to one another. It gives the impression that the filler particles are on the verge of forming a network, but are still not able to. This is supported by the cluster mass distribution. Similar to the filler volume content of $\phi = 0.10$, basically every particle is bound into a cluster. But now, less particles are found in clusters with a mass less than ten, i.e., only about 1%. A majority of the particles are found in clusters whose mass is

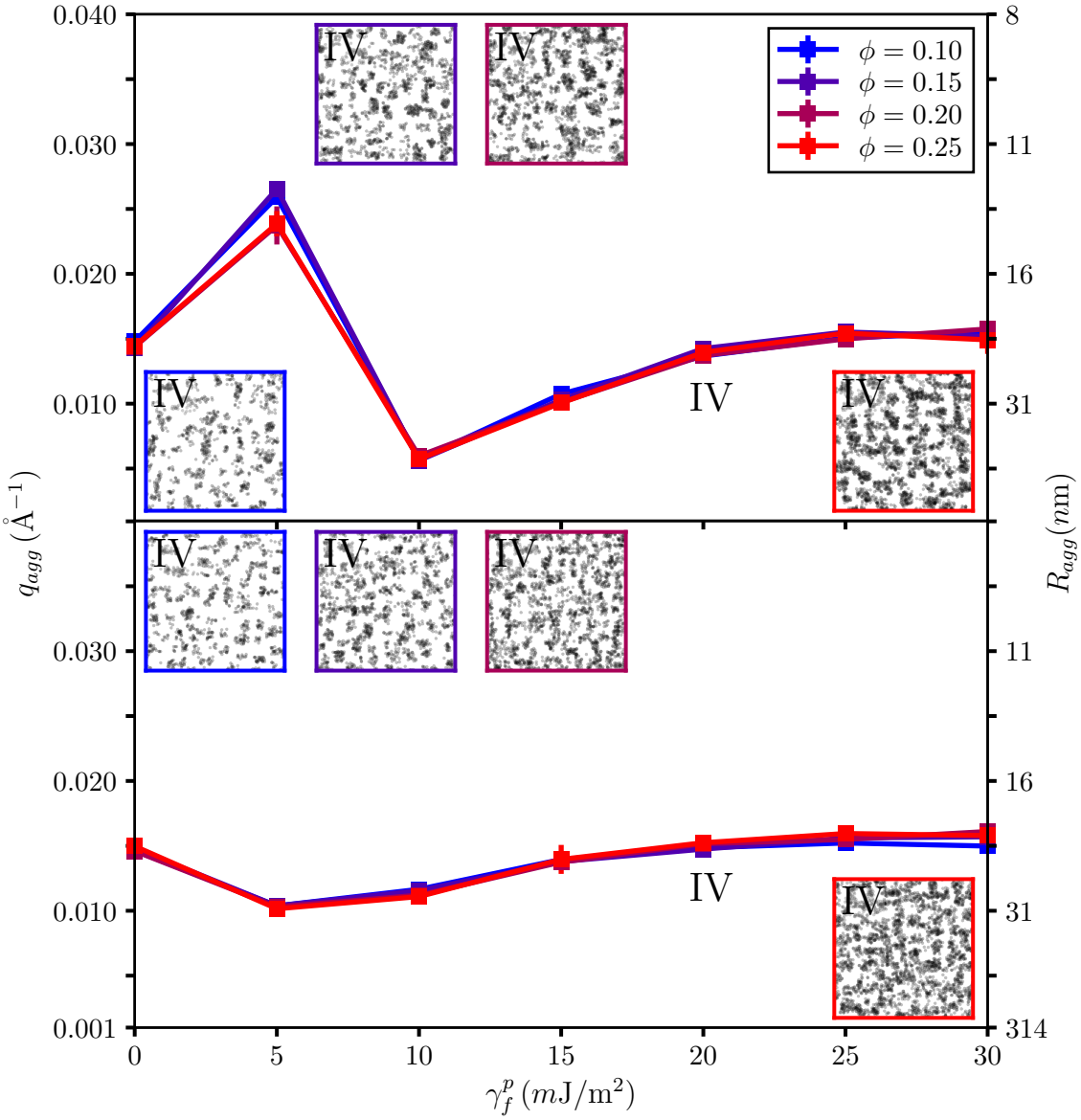

Figure 2.30.: Aggregation phase diagrams for filler types with $\gamma_f^d = 20\,m\mathrm{J/m}^2$ (top) and $\gamma_f^d = 30\,m\mathrm{J/m}^2$ (bottom) incorporated in NR for different filler volume contents at $T = 433$ K. The different embedded TEM pictures are taken for filler type IV. The different colored borders of the TEM pictures correspond to the values of the filler content ϕ given in the legend. Additionally, they are ordered from low to high ϕ values from left to right. The impact of the filler content ϕ on the mean size of the aggregates q_{agg} is very minor and only discernible for distinct filler types. In the top only for those with $\gamma_f^p = 5\,m\mathrm{J/m}^2$ and in the bottom very slightly for those with $\gamma_f^p = 30\,m\mathrm{J/m}^2$.

greater than one hundred. This shows that higher filler volume content drives the particles with this particular properties more and more into filler network formation.

The third TEM picture, which has a dark red border, is equivalent to that in Figure 2.25a marked as IV. The amount of filler particles is now sufficient to form a continuous filler network, percolating through the elastomer matrix.

The last TEM picture, on the right side in the top part of Figure 2.30, bordered red, depicts the case of $\phi = 0.25$. Therein, we can clearly identify the continuous filler network, which looks more connected than for $\phi = 0.20$. The cluster mass distribution shows that again every particle is bound into a cluster. The single large cluster representing the filler network now contains about 97% of all particles. This is indeed more than in the case of $\phi = 0.20$, where just 60% of the particles are bound into the single large cluster.

In the bottom of Figure 2.30, we find the filler types with $\gamma_f^d = 30\,m\mathrm{J/m^2}$. The TEM pictures overall look very similar compared to the $\gamma_f^d = 20\,m\mathrm{J/m^2}$ case. Only the last two TEM pictures to the right, bordered dark red and red, look overall less acute. The individual cluster mass distributions confirm the impressions we obtained from the analysis in the context of flocculation time for Figure 2.27. Filler types with $\gamma_f^d = 20\,m\mathrm{J/m^2}$ have a stronger tendency to develop filler networks inside NR than those with $\gamma_f^d = 30\,m\mathrm{J/m^2}$. While the amount of cluster bound primary filler particles is more or less unaltered, the distribution within shows more large clusters for $\gamma_f^d = 30\,m\mathrm{J/m^2}$ for every ϕ value. The most pronounced difference in this distribution is found for $\phi = 0.20$. For $\phi = 0.25$ the difference is minor.

Changing the polymer to SBR we get Figure 2.31. Here, the impact on the mean size of the aggregates is again very minor. Different from NR, we find slightly smaller aggregates for higher filler volume fractions of filler type IV. This is also seen in the experiment, albeit much more pronounced [38]. The aggregate values obtained therein are $R_{agg} = 39.2\,n\mathrm{m}$ for $\phi = 0.127$, $R_{agg} = 36.1\,n\mathrm{m}$ for $\phi = 0.168$, and $R_{agg} = 34.4\,n\mathrm{m}$ for $\phi = 0.211$. Their uncertainties are all approx. $1\,n\mathrm{m}$. Calculating the ratio to the mean size of the aggregates and the primary particles, i.e., R_{agg}/R_{si}, we find 2.83, 2.61, and 2.49 for $\phi = 0.127$, $\phi = 0.168$, and $\phi = 0.211$, respectively. The value for R_{si} is $13.85\,n\mathrm{m}$ and taken from the same source. The decrease in the ratio is higher in the first filler volume increase than for the second one. In our simulation, we find in the top of Figure 2.31 $R_{agg} = 21.2\,n\mathrm{m}$ for $\phi = 0.10$, $R_{agg} = 20.6\,n\mathrm{m}$ for $\phi = 0.15$, and $R_{agg} = 20.5\,n\mathrm{m}$ for $\phi = 0.20$. Although the filler volume fractions do not match perfectly, they are in good agreement. All uncertainties are less than $0.5\,n\mathrm{m}$. The respective ratios are, with $R_{si} = 8\,n\mathrm{m}$, 2.65, 2.58, and 2.56. This shows the same trend as in the experiment. Thus, we can conclude that higher filler volume content yields more compact aggregates.

Taking the TEM pictures in the top picture into account, we start again from the blue bordered, dilute system on the left. There, we see single small aggregates similar to NR. In neither of the polymers this amount of filler particles is sufficient to form a filler network. The mass distribution is slightly different for SBR. Although almost all filler particles are bound into clusters (similar to NR) more smaller clusters with mass less than ten, i.e., around 8% are found.

This is also true for the purple bordered TEM picture, second from the left, depicting $\phi = 0.15$. Here, however, we find more bigger clusters compared to NR, making it more comparable to the corresponding $\gamma_f^d = 30\,m\mathrm{J/m^2}$ case.

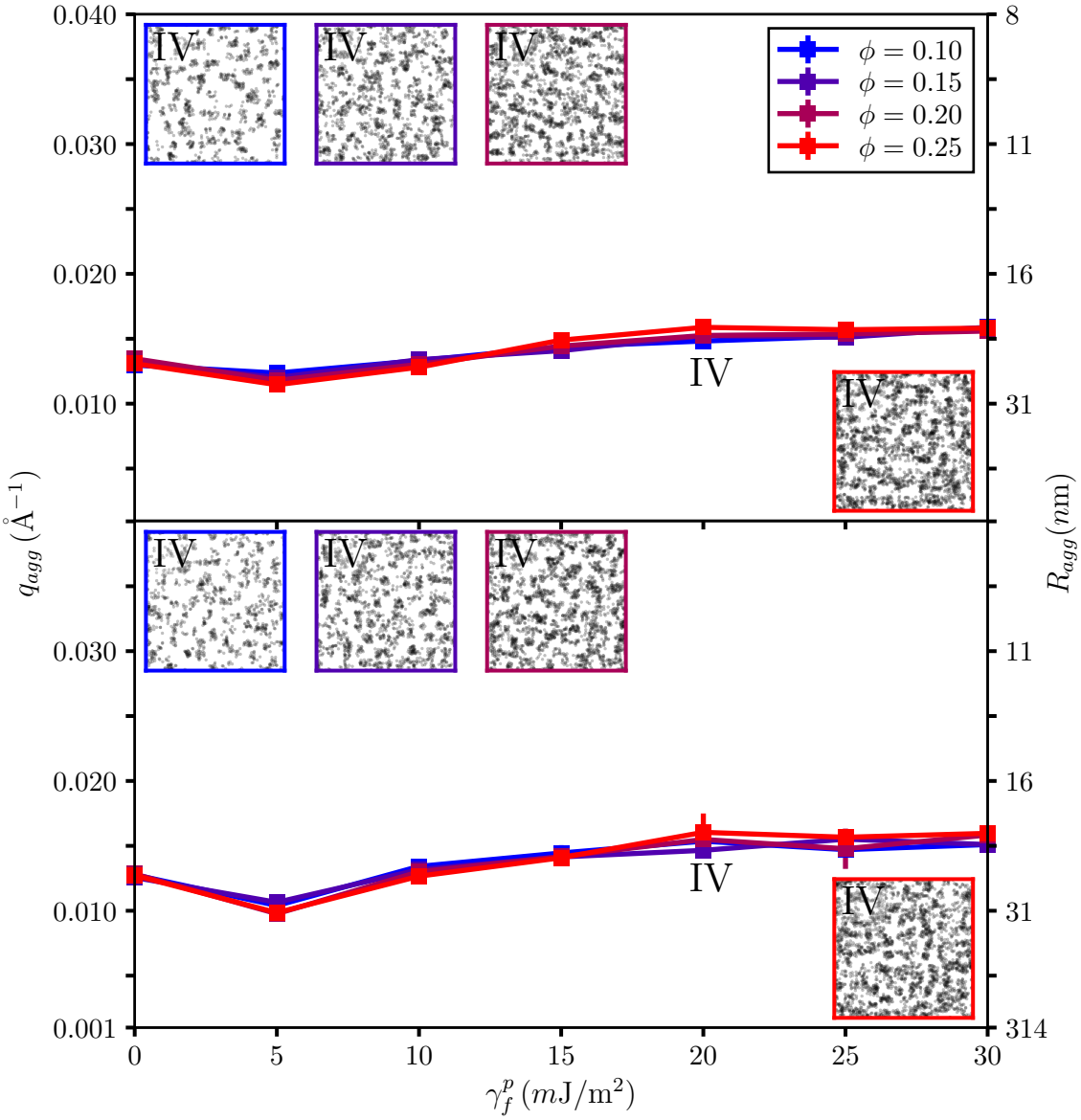

Figure 2.31.: Aggregation phase diagrams for filler types with $\gamma_f^d = 20\,m\mathrm{J/m}^2$ (top) and $\gamma_f^d = 30\,m\mathrm{J/m}^2$ (bottom) incorporated in SBR for different filler volume contents at $T = 433$ K. The different embedded TEM pictures are taken for filler type IV. The different colored borders of the TEM pictures correspond to the values of the filler content ϕ given in the legend. Additionally, they are ordered from low to high ϕ values from left to right. The impact of the filler content on the mean size of the aggregates q_{agg} is very minor.

Further increasing the filler volume content leads to the formation of a continuous filler network, where 80% of all filler particles are combined in one large cluster. This first major difference compared to NR was already discussed.

The TEM picture with the highest value of ϕ considered here, i.e., the red bordered one on the right, shows again a continuous filler network. Akin to the $\gamma_f^d = 30\,m\mathrm{J/m^2}$ case in NR, it does not look very acute. The cluster mass distribution is equal to that case. Changing the dispersive part of the surface free energy to $\gamma_f^d = 30\,m\mathrm{J/m^2}$, i.e., looking at the lower part of Figure 2.31, we see no structural differences for none of the TEM pictures. This is also true for the cluster mass distribution.

Finally, we can discuss the impact of filler volume content variation on the wetted surface fractions. It is depicted in Figure 2.32. The different ϕ values are given in the subcaptions **(a)** - **(d)**.

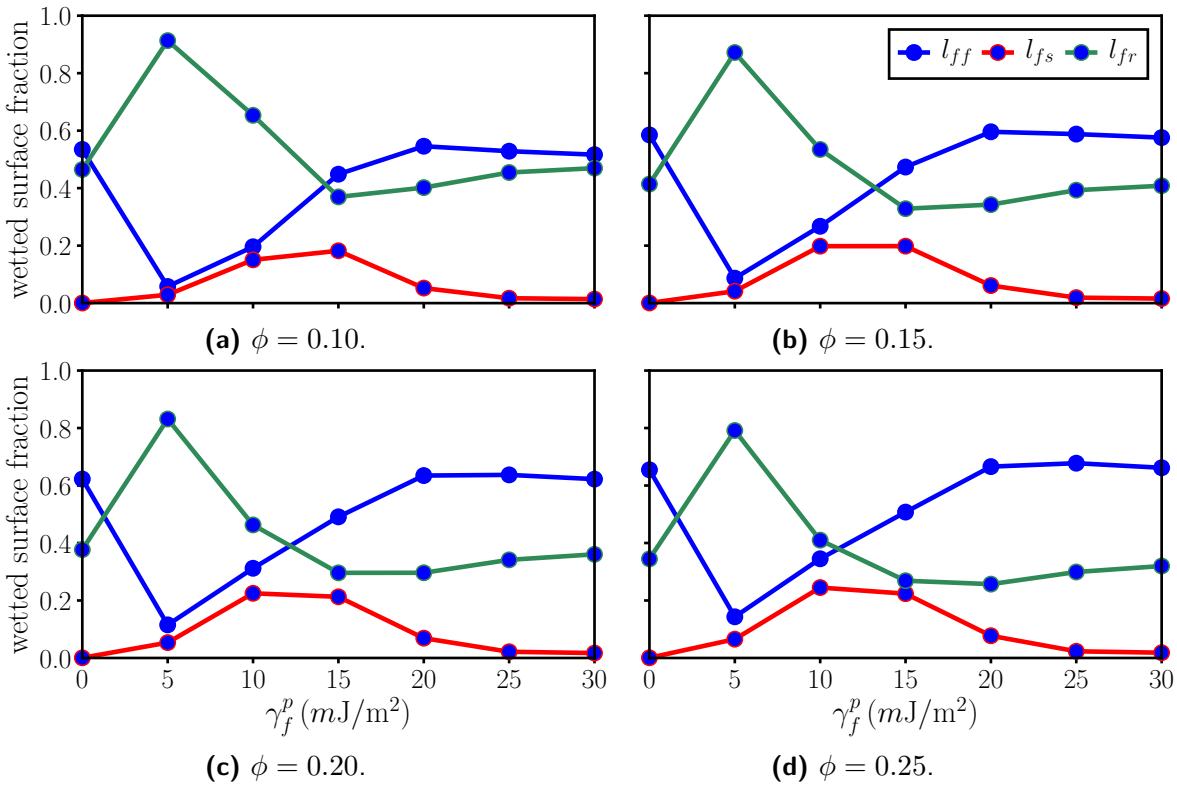

(a) $\phi = 0.10$. **(b)** $\phi = 0.15$.

(c) $\phi = 0.20$. **(d)** $\phi = 0.25$.

Figure 2.32.: Wetted surface fractions for bare silica surfaces for filler types with $\gamma_f^d = 20\,m\mathrm{J/m^2}$ incorporated inside NR for different values of ϕ at $T = 433$ K.

The overall impact is pretty minor, as one would expect from the discussion so far. The ordering, which we deduced in the context of the wetting-envelope - work of adhesion plots, is not affected by the system parameters we consider here. The impact on the absolute amounts of the individual surface fractions, however, is significant. The biggest impact is, unsurprisingly, found on any bare filler surface related fractions, on which we thus focus. As an example, we consider filler types with $\gamma_f^d = 20\,m\mathrm{J/m^2}$ incorporated inside NR. They showed at least for some γ_f^p values an impact on the variation of ϕ.

Increasing the filler content leads to higher l_{ff} and lower l_{fr} values. More primary filler particles increase the possibility for a bare filler surface to be wetted by the same surface

type, which consequently diminishes the wetted surface fraction towards the polymer. While this trend is also true for l_{fs}, it is far less developed. We also notice that for the lowest value of ϕ, i.e., Figure 2.32a, this value behaves differently. Although the ordering we derived between the four systems is still correct, the filler type formerly denoted as III, i.e., $\gamma_f^p = 10\,m\mathrm{J/m^2}$, does not show the highest of all l_{fs} values anymore. Now it is $\gamma_f^p = 15\,m\mathrm{J/m^2}$. This not surprising when we take the structural development into account and look at the positioning of this filler particle inside the wetting-envelope - work of adhesion plots in Figures 2.23a and 2.23c. The flocculation tendency is quite low, while the wetting behavior is perfect. Because the filler particles are not spatially confined into a large network structure, they are more free to arrange themselves. This favors the corresponding wetting.

While the impact of ϕ on the mean size of the aggregates and the wetted surface fractions is minor, it should be noted that for both values of γ_f^d the formation of a filler network for every value of γ_f^p is favored at the highest filler volume content considered here, i.e., $\phi = 0.25$. This is independent of the polymer. The only exception is the filler type with $\gamma_f^d = 20\,m\mathrm{J/m^2}$ and $\gamma_f^p = 5\,m\mathrm{J/m^2}$ inside NR. It does not develop any structures at all, regardless of the number of MC steps. Further increment of ϕ to near the percolation threshold, however, should show the formation of a continuous network. For all other filler types formerly not developing a network, we can explain this process by using the same argumentation as for our example filler type IV. At any value of ϕ, the aggregates developed by the individual filler particles have almost the same size. It is likely to assume that the structures we see in the TEM for $\phi = 0.10$ are the primary aggregates, i.e., the smallest building blocks for higher order structures. More filler content leads to the formation of more aggregates of the same size. They are, however, more and more spatially confined and start to connect with one other to form higher order structures. At a certain threshold, which is then the percolation threshold for this specific system configuration, those higher order structures are connected with one another and form the filler network. The connection in between the higher order structures must not necessarily be due to same structures. Aggregates or even smaller clusters may form 'bridges' in between them. This is supported by the individual number of clusters for each system. It generally decreases by roughly one third. Clusters who merge together are taken from any mass category, i.e., we find less smaller and bigger clusters. This shows that to form a filler network, several parameters are relevant. Those are the surface free energies, the filler volume content, and the number of MC steps.

It is now reasonable to consider the mass fractal dimensions of the aggregates within the filler networks. The case with $\phi = 0.20$ was already discussed in the former section regarding the impact of flocculation time. Here, we focus on $\phi = 0.25$. Note that only for the filler type with $\gamma_f^d = 20\,m\mathrm{J/m^2}$ and $\gamma_f^p = 5\,m\mathrm{J/m^2}$ inside NR no filler network developed. Table 2.9 lists all filler types with corresponding mass, size, and the size of the aggregates taken from the aggregation phase diagrams together with their mass fractal dimension.

The mass fractal dimension of the aggregates, d_m^{agg}, is generally higher compared to the $\phi = 0.2$ case. This can be simply explained by the higher amount of available filler particles. Thus, comparing the mass fractal dimensions for the same set of parameters, but with higher filler volume content, is not reasonable. Nevertheless, the values listed in Table 2.9 can be compared with one another, because all systems are identical with respect to the simulation parameters. Regardless of the polymer and the dispersive part of the polymer, the three

Table 2.9.: Filler networks developed by different filler types inside NR and SBR for $\phi = 0.25$, $T = 433$ K, and after $2 \cdot 10^9$ MC steps. Listed are their mass, size, and the size of their aggregates together with the corresponding mass fractal dimension. Note that the size of the filler networks is calculated from the radius of gyration via $R_n = R_G \cdot R_{si}$.

polymer	γ_f^d [mJ/m^2]	γ_f^p [mJ/m^2]	m_n	R_n [nm]	R_{agg} [nm]	d_m^{agg}
NR	20	0	518473	511.5	21.8 ± 0.6	2.01 ± 0.06
		10	338023	513.4	54.8 ± 2.2	2.03 ± 0.03
		15	468739	513.6	31.3 ± 0.2	2.10 ± 0.02
		20	508824	512.3	22.5 ± 0.1	2.02 ± 0.03
		25	516713	512.3	20.4 ± 0.2	2.01 ± 0.07
		30	518313	511.9	21.1 ± 1.5	2.01 ± 0.08
	30	0	516718	511.9	21.0 ± 0.3	2.01 ± 0.06
		5	490511	513.5	31.0 ± 0.3	2.09 ± 0.02
		10	484648	512.4	28.3 ± 0.1	2.07 ± 0.01
		15	503535	510.8	22.5 ± 1.8	2.02 ± 0.02
		20	515151	512.1	20.6 ± 0.1	2.01 ± 0.06
		25	519446	511.9	19.7 ± 0.0	2.01 ± 0.08
		30	517797	512.1	19.9 ± 0.2	2.01 ± 0.08
SBR	20	0	432578	511.9	24.6 ± 0.1	2.02 ± 0.03
		5	404535	511.7	27.4 ± 0.2	2.06 ± 0.01
		10	299729	511.8	24.5 ± 0.2	2.03 ± 0.01
		15	498934	511.8	21.1 ± 0.6	2.02 ± 0.04
		20	512981	512.2	19.8 ± 0.2	2.01 ± 0.07
		25	515172	512.3	20.0 ± 0.1	2.01 ± 0.07
		30	516008	511.9	19.9 ± 0.4	2.01 ± 0.08
	30	0	337027	509.9	24.7 ± 0.2	2.02 ± 0.05
		5	417175	514.0	31.9 ± 0.6	2.06 ± 0.00
		10	302798	510.9	24.8 ± 0.2	2.04 ± 0.01
		15	493665	512.6	22.3 ± 0.5	2.02 ± 0.03
		20	513341	512.3	19.6 ± 1.8	2.01 ± 0.06
		25	516232	512.2	20.1 ± 0.1	2.01 ± 0.07
		30	515176	512.2	19.7 ± 0.1	2.00 ± 0.08

highest polar filler types produce filler networks, which are similar in mass, size, size of the aggregates as well as their mass fractal dimension. The low polarity, carbon black filler types with $\gamma_f^p = 0\,m\mathrm{J/m^2}$ create more massive filler networks inside NR than in SBR. Therein, however, their aggregates are bigger and their mass fractal dimension is slightly higher. The intermediate filler types with polar surface free energies between $5\,m\mathrm{J/m^2}$ to $15\,m\mathrm{J/m^2}$ show

the biggest variances in all categories. Inside NR, they produce the biggest aggregates with the highest mass fractal dimension, while the mass of the respective filler networks is considerably lower than for other filler types. The same is true inside SBR, with the difference that the mass of the filler networks is even less and the size of the aggregates is smaller. This also applies to the mass fractal dimension.

In the context of the impact of flocculation time on filler network formation, we discussed that the flocculation time is a crucial contributor, which is also seen experimentally [15, 23, 60]. We now find that the flocculation time lowers the percolation threshold, ϕ_c, of a given system. For all filler particles listed in Table 2.8 ϕ_c is lowered to a value between 15% and 20% in volume, i.e., $0.15 < \phi_c \leq 0.20$. In this section we see that for every other filler type not listed therein, with the exception of $\gamma_f^d = 20\,m\mathrm{J/m^2}$ and $\gamma_f^p = 5\,m\mathrm{J/m^2}$ inside NR, we find $0.20 < \phi_c \leq 0.25$.

The last parameter we are able to control in our morphology generator is the temperature T, which is discussed in the next part.

2.5.4. Varying the Temperature

In the initial compounding process elevated temperatures of more than 100 °C are needed to initiate the vulcanization process, the silanization reaction, and to help the filler particles to better disperse inside the elastomer matrix. This temperature – called dump temperature – is directly accountable for the flocculation rate [21]. In our model, however, we have no temperature under which our initial dispersed state is produced. The temperature we use is thus only comparable to that used in the flocculation measurements . They are mostly performed at the same elevated temperatures, i.e., also well above 100 °C [15]. Oftentimes values between 140 °C to 160 °C are chosen [1, 23]. In order to investigate the impact of even higher temperatures, we choose four different values for T between 140 °C to 200 °C. We need to keep in mind that the temperature is only included in the denominator of our Metropolis criterion in Equation (2.5). It thus directly affects the probability whether a certain MC step is accepted or not. In order for the MC to deny a step with a certain probability, $\Delta W(\gamma) < 0$ must be fulfilled. If, on the other hand, $\Delta W(\gamma) \geq 0$, then it is always accepted. Independent of the temperature T. Because lower temperatures lead to higher absolute values of the exponent of the Metropolis criterion, they lead to lower acceptance rates. It is thus likely to assume that the lower temperature has a higher influence than the higher ones. Additionally, we need to keep in mind that the surface free energies are generally temperature dependent. We do not account for this dependency, because the extent is not clear. It is only certain that it is linearly decreasing with increasing temperature. This is discussed in more detail in Appendix B. The interpretation of temperature variation should thus be treated cautiously.

As for the other parameter variations investigated so far, we need to fix those on which we do not focus. We choose a filler volume content of $\phi = 0.25$, because at this value almost every filler particle is able to produce a filler network. The lower temperatures might retard the formation process, whereas the higher temperatures may lead to more continuity, because more MC steps are accepted. Additionally, for higher temperatures the formation process might be performed more quickly and thus influence the mass fractal dimension. For the

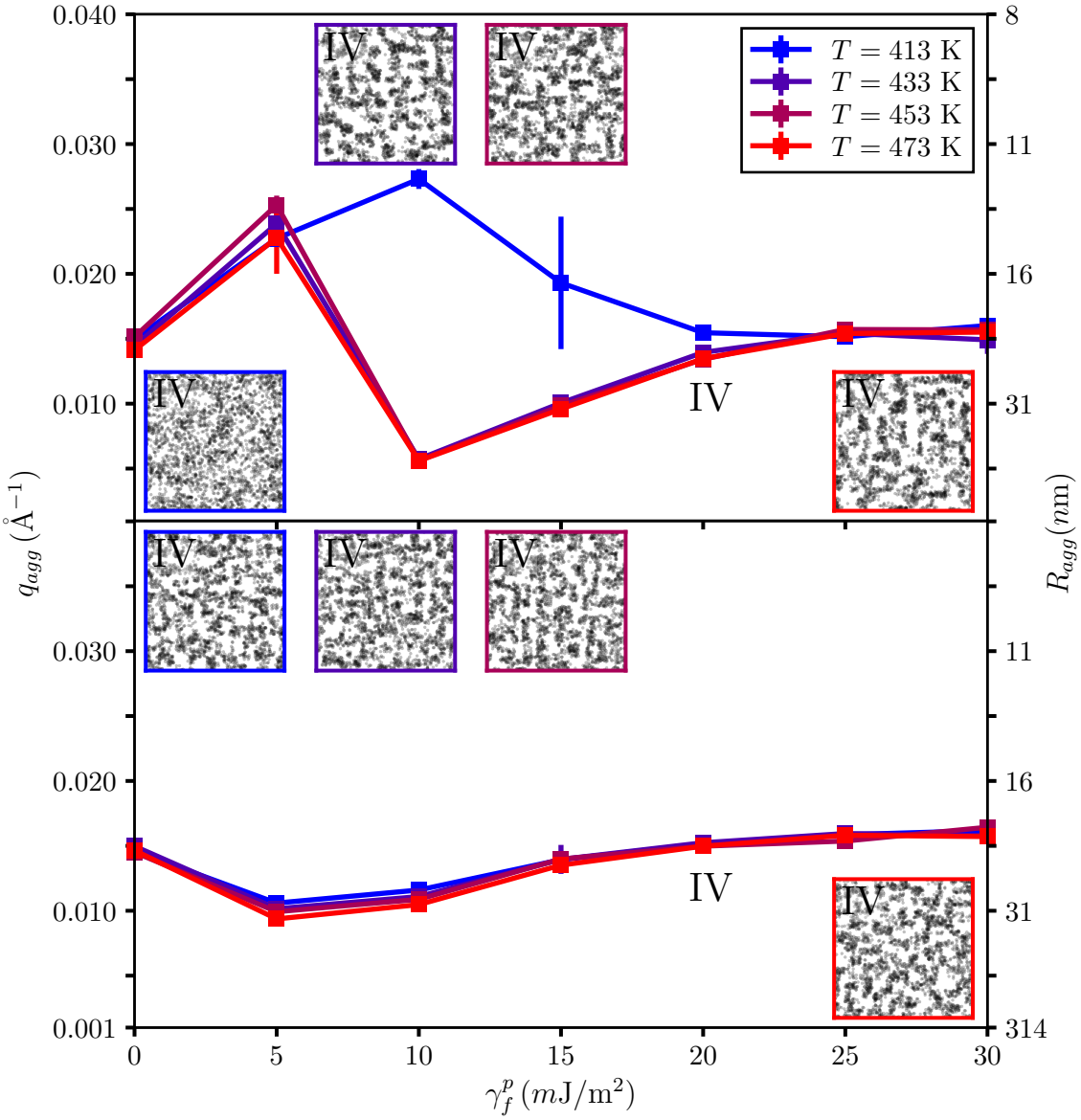

Figure 2.33.: Aggregation phase diagrams for filler types with $\gamma_f^d = 20\,mJ/m^2$ and $\gamma_f^d = 30\,mJ/m^2$ incorporated in NR with $\phi = 0.25$ for different temperatures. The different embedded TEM pictures are taken for the filler type IV. The different colored borders of the TEM pictures correspond to the values of the temperature T given in the legend. Additionally, they are ordered from low to high T from left to right. Top: The impact of temperature variation on the mean size of the aggregates as well as for the TEM pictures is significant only for $T = 413$ K. Bottom: No impact of temperature variation is observed.

flocculation time we use the maximum number of MC steps again. We start with filler particles incorporated inside NR with different values of γ_f^d, as depicted in Figure 2.33.

Looking at the top part of the respective figure, it is evident that our initial assumption on the higher influence of lower temperatures is so far correct. For filler types with low and high values of γ_f^p the temperature variation is not reflected by the mean size of the aggregates. For intermediate values, however, the blue curve shows that an additional filler type, apart from the one at $\gamma_f^p = 5\,m\mathrm{J/m^2}$ we already saw before, does not produce any structures at all. Apparently, the mean size of the aggregates is even lower, albeit slightly. The consequent formation of bigger aggregates we saw before is now shifted from $\gamma_f^p = 10\,m\mathrm{J/m^2}$ to $\gamma_f^p = 15\,m\mathrm{J/m^2}$. The extent, however, is much less pronounced.

Although not displayed by the TEM pictures, it is worth to briefly discuss the cluster mass distribution of all filler types and compare their values for different temperatures T. We start at $\gamma_f^p = 0\,m\mathrm{J/m^2}$ and find no difference between the temperatures. A single large cluster, comprising about 99% of all filler particles produces a filler network. By increasing γ_f^p, the filler network breaks down and the particles are dispersed inside the elastomer matrix. This happens again for all T values. At $\gamma_f^p = 10\,m\mathrm{J/m^2}$, we find almost no particles bound into clusters at all for $T = 413$ K. This is in accordance with the lower mean aggregate sizes. For other T values, we still find a filler network composed of big aggregates. The cluster mass distribution, however, is changing for higher T values. While we find that about 90% of all filler particles are bound into clusters for all T, the single large cluster representing the network contains less of those particles for higher T values. At $T = 433$ K it is about 75%, while at $T = 473$ K it is only about 45%. The network is split into more smaller clusters, i.e., the clusters with mass less than ten change from 8% to 13%, and more bigger clusters with mass more than one thousand, i.e., from 13% to 34%, for $T = 433$ K to $T = 473$ K. Elevating γ_f^p further, increases the mean aggregate size value for $T = 413$ K. The corresponding cluster mass distribution, however, shows no existing clusters at all. The same is true for all following γ_f^p values. The only possible explanation for this is given by the cluster definition itself. Because SAXS detects aggregates as spatially confined particles, they must have aggregated via their silanized sides and not their filler sides. Consequently, they are not detected as clusters. For other T values, no changes for all γ_f^p values higher than $15\,m\mathrm{J/m^2}$ are discernible.

For further investigation, we take the wetted surface fractions depicted in Figure 2.34 into account. We consider the lowest and the highest temperatures, i.e., Figures 2.34a and 2.34b depict the case with $T = 413$ K and Figures 2.34c and 2.34d that with $T = 473$ K.

We find, similar to the discussion of the cluster mass distributions, that the first two values of γ_f^p show no impact on temperature variation. Starting from $\gamma_f^p = 10\,m\mathrm{J/m^2}$, the differences are significant. l_{ff} drops to zero while l_{fs} increases continuously for higher γ_f^p values. Consequently, l_{fr} is very high and l_{sr} gets lower. l_{ss} is only slightly affected. For $T = 413$ K we thus find a different ordering, compared to that deduced in the context of the wetting-envelope - work of adhesion plots. The wetting is in this case stronger than the flocculation tendency. The wetting between surface modified silica and the polymer is discouraged for higher polar values of the surface free energy of the filler particles compared to that between filler and surface modified silica. However, the combination of wetted surface fractions which indicate the formation of a filler network is still accounted for. A high value of l_{sr} as well as a relatively low value of l_{fr} is indispensable for filler network formation. For the formation of structures

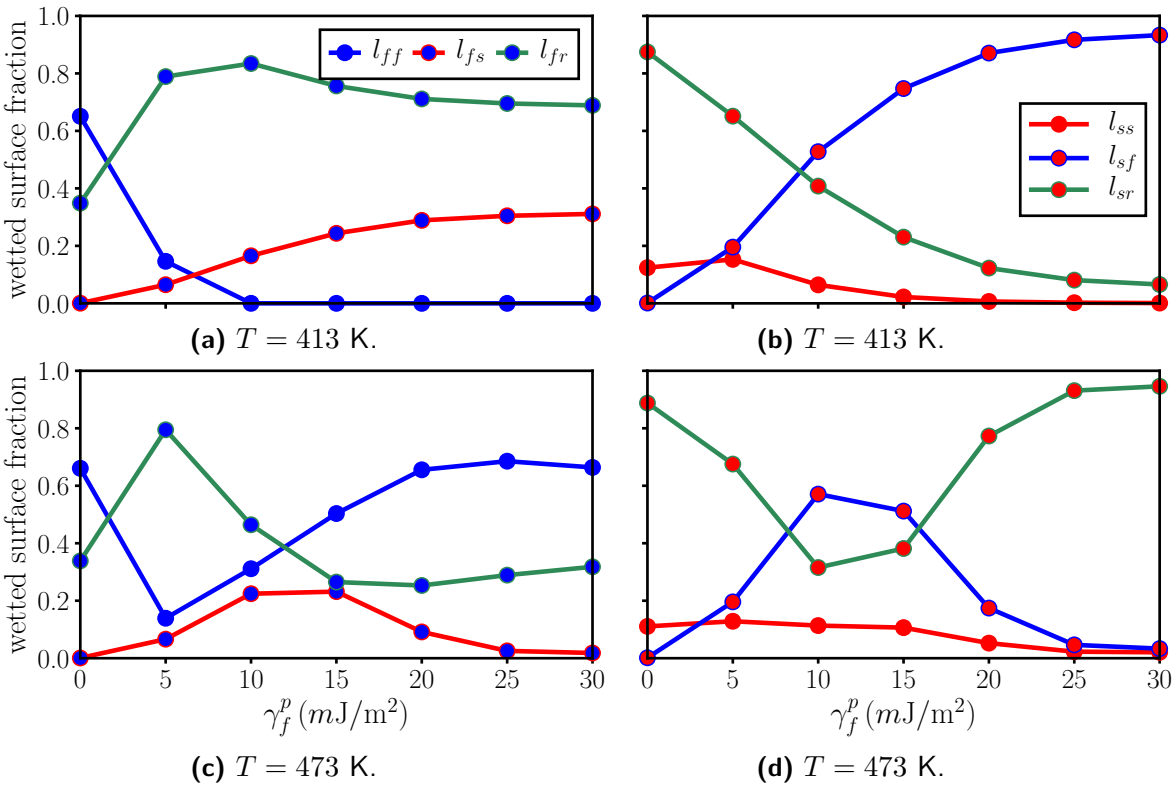

(a) $T = 413$ K. **(b)** $T = 413$ K.

(c) $T = 473$ K. **(d)** $T = 473$ K.

Figure 2.34.: Wetted surface fractions for filler types with $\gamma_f^d = 20\,mJ/m^2$ incorporated inside NR for $\phi = 0.25$ at different temperatures T. **(a)** and **(b)**: Temperature set to $T = 413$ K. **(c)** and **(d)**: Temperature set to $T = 473$ K.

in general, the combination of l_{sr} and l_{fs} seems to be crucial. The high l_{ff} value is, of course, necessary in both cases.

Considering the TEM pictures, we see a huge difference for $T = 413$ K in comparison to the other T values. The left, blue bordered, TEM picture represents $T = 413$ K. It looks more dispersed than the mean size of the aggregates indicates. No structural development can be identified at all, which fits the cluster mass distribution. The aggregation over silanized sides must produce lots of small filler 'clusters'. The other TEM pictures are very similar. This fits their cluster mass distributions as well.

The bottom part of Figure 2.33 shows no impact on the mean size of the aggregates due to temperature variation. Even the TEM pictures look similar as they all display a filler network. The according cluster mass distributions support both impressions. For the intermediate γ_f^p values, $5\,mJ/m^2$ to $15\,mJ/m^2$, however, we see slight trends for the filler networks. For $\gamma_f^p = 5\,mJ/m^2$, the network comprises more filler particles for increasing temperatures up to $T = 453$ K and generally more smaller clusters are produced. While the last trend even continues up to $T = 473$ K, the growth of the filler network stops at $T = 453$ K. For $\gamma_f^p = 10\,mJ/m^2$, we see that the filler network loses particles and gets slightly smaller. Again this trend stops at $T = 453$ K. For $\gamma_f^p = 15\,mJ/m^2$ it is similar, albeit to a minor extent.

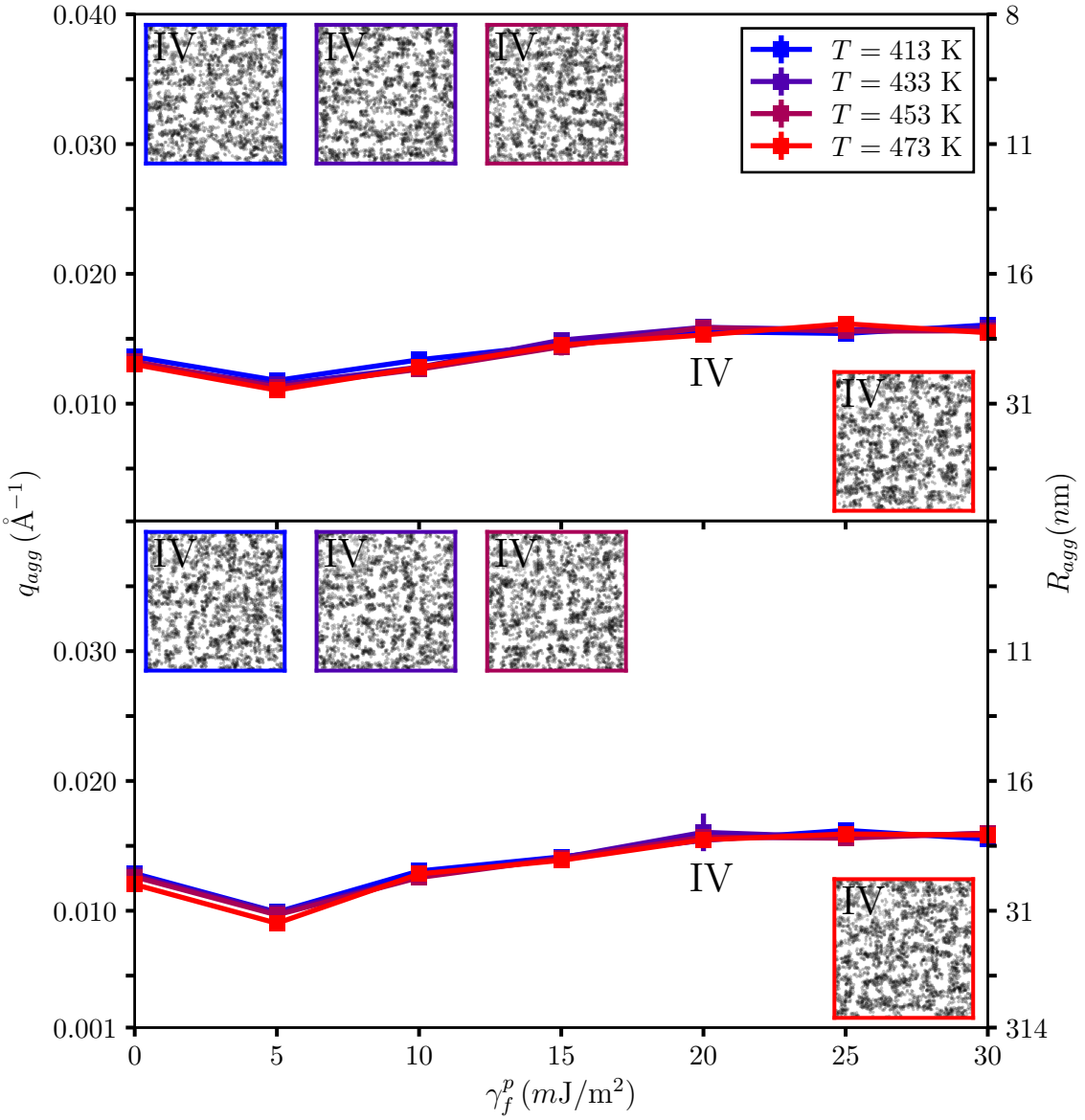

Figure 2.35.: Aggregation phase diagrams for filler types with $\gamma_f^d = 20\,m\mathrm{J/m^2}$ and $\gamma_f^d = 30\,m\mathrm{J/m^2}$ incorporated in SBR with $\phi = 0.25$ for different temperatures. The different embedded TEM pictures are taken for the filler type IV. The different colored borders of the TEM pictures correspond to the values of the temperature T given in the legend. Additionally, they are ordered from low to high T from left to right. In both cases the impact of temperature on the mean size of the aggregates as well as for the structural development displayed by the TEM pictures is very minor.

Changing the polymer to SBR, i.e., looking at Figure 2.35, we see again no impact of T. Regardless of the value of γ_f^d, the mean aggregate size as well as the TEM pictures are unaffected. The corresponding cluster mass distributions for the TEM pictures support this,

because they are all identical. For all γ_f^p values below $20\,mJ/m^2$, however, we see differences in the respective cluster mass distributions. Similar to the bottom part of Figure 2.33, we see an impact of T mostly for the intermediate values of γ_f^p. But here, it is limited on $5\,mJ/m^2$ to $10\,mJ/m^2$. For $\gamma_f^p = 5\,mJ/m^2$ and $\gamma_f^p = 10\,mJ/m^2$, the amount of clusters decreases for growing values of T. For the former we find an initial increase of the mass of the filler network when changing T from 413 K to 433 K, which does not continue for further increasing values of T. For the latter we find it the other way around. An initial decrease can be observed. Here, however, further increasing T leads to an increase of the mass of the filler network.

Taking the bottom part of Figure 2.35 into account, we find no discernible trends in the cluster mass distribution for temperature variation. Nevertheless, the largest variations are still found for $\gamma_f^p = 5\,mJ/m^2$ or $= 10\,mJ/m^2$. The wetted surface fractions behave similar to the mean aggregate sizes and the cluster mass distributions. No variances can be observed.

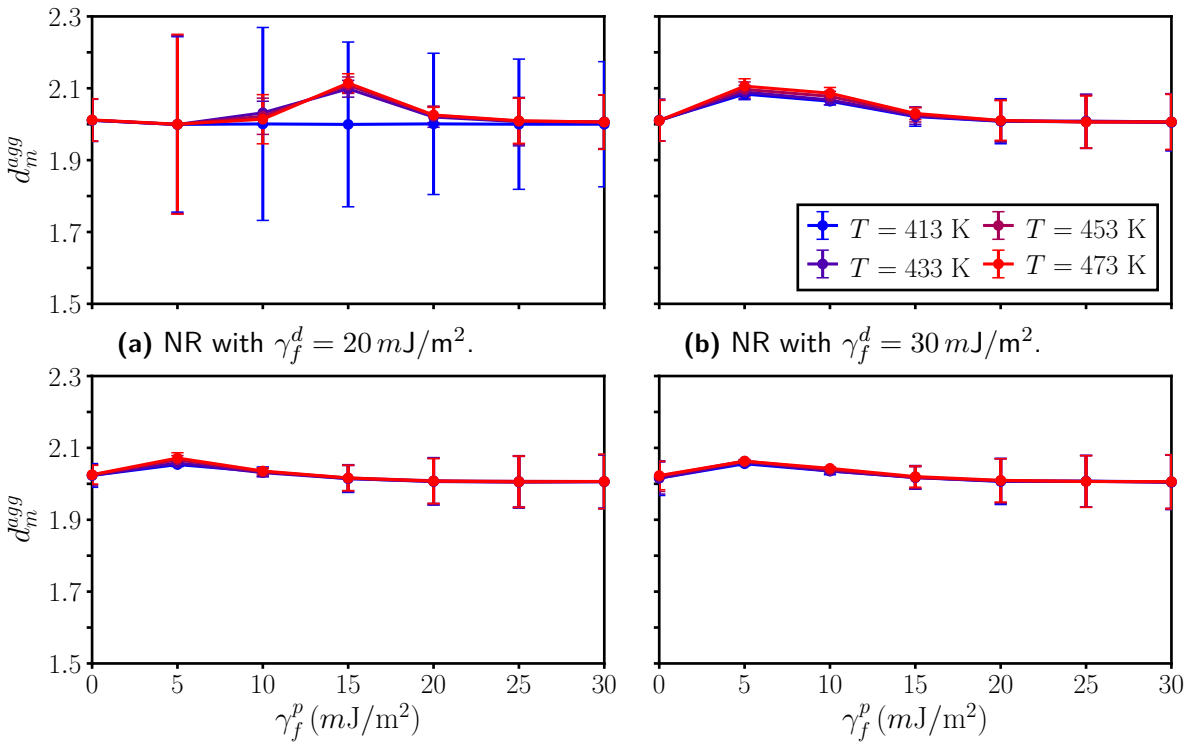

(a) NR with $\gamma_f^d = 20\,mJ/m^2$. **(b)** NR with $\gamma_f^d = 30\,mJ/m^2$.

(c) SBR with $\gamma_f^d = 20\,mJ/m^2$. **(d)** SBR with $\gamma_f^d = 30\,mJ/m^2$.

Figure 2.36.: Mass fractal dimension of the aggregates produced by different filler types inside NR and SBR with $\phi = 0.25$ for $\gamma_f^d = 20\,mJ/m^2$ and $\gamma_f^d = 30\,mJ/m^2$ at different temperatures T. Note that in **(a)** the lowest temperature led to the aggregation of filler particles via the modified silica sides. This leads to high uncertainties for the mass fractal dimension of the aggregates. For $\gamma_f^p = 5\,mJ/m^2$ the system is dispersed consequently leading to large uncertainties for each temperature.

Finally, we can consider the dependency of the mass fractal dimension on temperature variation. Figure 2.36 shows the different filler types inside NR and SBR for different γ_f^d values.

Note that in Figure 2.36a for the blue data, i.e., $T = 413$ K, aggregation of particles primarily takes place via the modified silica sides. This leads to high uncertainties for all filler types with $\gamma_f^p \geq 10\,m\mathrm{J/m^2}$. The filler type with $\gamma_f^p = 5\,m\mathrm{J/m^2}$ produced no structures at all. Consequently, the uncertainty for the mass fractal dimension is high regardless of the temperature.

Overall the impact of temperature variation on the mass fractal dimension of the aggregates, d_m^{agg}, is very minor. This matches with the impression we obtained from the TEM pictures and the mean size of the aggregates. The only noticeable aspect is that higher temperatures lead to slightly higher d_m^{agg} values. This effect is limited to filler types inside NR in the $\gamma_f^p = 30\,m\mathrm{J/m^2}$ case. Therein, it is only even observable for types with intermediate surface free energies.

The impact on the mean size of the aggregates is very minor, expect for one single case. For that, we observed a completely different behavior taking the cluster mass distribution into account. All filler particles aggregated through their modified silica sides, violating our definition of a cluster, and were thus not recognized as such. Additionally, the ordering of the wetted surface fractions, deduced in the context of wetting-envelope - work of adhesion plots, was violated. This may be accounted for the missing temperature dependency of the surface free energies. Because we are not able to take it into account and for this specific combination the ordering was violated, we consider this case as not plausible. In the structural development of other filler types we saw, if any, only slight trends in growth and reduction of filler networks.

2.6. Conclusion

In this chapter, we have introduced the morphology generator. A MC-based algorithm mimicking the flocculation process of filler particles inside an elastomer matrix. The respective governing quantities are the interfacial tensions. Variable parameters include the amount of filler, the temperature, the surface coverage with a compatibilizer, and the relevant surface free energies. The structural evolution of the filler distribution was investigated by numerous screening methods, which are also used in experiments. They include simulated TEM and SAXS. Both are calculated along the trajectory of the MC. Beside those methods, the cluster mass distribution, the size of the clusters, as well as the wetted surface fractions allowed for a more detailed analysis at the end of the MC. Information of the large scale behavior is represented by the mass fractal dimension of the filler networks or the agglomerates. It was obtained via the slope inside the linear regime of the SAXS plots. Unfortunately, this information relies on big systems, which could not be produced consistently. More insight on the substructures, i.e., the aggregates, inside the filler networks was obtained by the mass fractal dimension of the aggregates by utilizing a box-counting algorithm. Additionally, wetting-envelope - work of adhesion plots were analyzed to predict the behavior of the filler particles inside the elastomer matrix, which also provided a consistency check for obtained simulation results such as TEM pictures.

Various example systems, where the interfacial tensions were obtained from filler particles and surface modified silica particles from experiments, showed the potential of the morphology generator to mimic the flocculation process, as well as the behavior of the respective surface

modifications. A broad compatibility between numerous rubbers, fillers, and surface modified silica particles in the context of wetting-envelope - work of adhesion plots was investigated, as a potential aid for further flocculation experiments. Mimicking different filler types allowed to renounce from the need of their experimental surface free energies. The variation of system parameters and the investigation of the corresponding impact allowed to find reasonable working conditions of the morphology generator: Structural information is best obtained at the end of the MC, the filler volume content needs to surpass a certain threshold in order to create filler networks, and the temperature dependency is rather low, albeit it needs to be treated cautiously as unexpected behavior might appear and the temperature dependence of the surface free energies is not taken into account. Furthermore, the continuity of the filler networks seems to be linked to their mass and the size of the aggregates within. Networks with comparable mass appear more continuous, if the aggregates are smaller.

The entire approach is computationally cheap, unless the goal is the large scale network structure, here characterized in terms of a mass fractal dimension. If the initial aggregation behavior is sufficient, then the approach is particularly suited for screening studies.

Due to the local character of the MC steps, we can, albeit in a rough sense, relate the flocculation kinetics to the number of MC steps (cf. Appendix D). The present simulations are for systems containing three components, i.e., elastomer, filler, and a surface modification of the filler particles. Usually, the experimental studies focus on polymer blends. This and a lack of information regarding the relevant surface free energies in most of the experimental work listed in this chapter, i.e., [20, 32, 34, 38, 40, 49, 51–53, 63, 64], currently imposes severe limitations in terms of experimental results to compare to. Note that the authors in [38] also point out the need for more experimental work on simple model systems and in fact do mention this as part of their motivation. Nevertheless, several comparisons of the mean size of the aggregates and some mass fractal dimensions were performed. It was shown that the consensus with experimental data is reasonable in the context of the mean size of the aggregates and that for both NR and SBR. The same is true for the mass fractal dimension of the aggregates, although only very limited values were obtainable. Regarding the mass fractal dimension of the filler networks, reasonable values were also found using the fit method, which is also used experimentally.

The current restriction to a single rubber component is abolished in the next chapter. Therein, we use homogeneous filler particles inside a polymer blend, containing a combination of the two intensively investigated polymers, NR and SBR. This leads to several conceptual changes. The screening methods derived within this chapter, however, are generally not affected. We only alter the visualization method of the TEM picture and, of course, adjust the wetted surface fractions.

2.7. References

[1] Stöckelhuber, K. W. et al., Contribution of physico-chemical properties of interfaces on dispersibility, adhesion and flocculation of filler particles in rubber. *Polymer (Guildf).* **2010**, 51 (9), 1954–1963, DOI: 10.1016/j.polymer.2010.03.013.

[2] Stöckelhuber, K. W. et al., Impact of filler surface modification on large scale mechanics of styrene butadiene/silica rubber composites. *Macromolecules* **2011**, 44 (11), 4366–4381, DOI: 10.1021/ma1026077.

[3] Natarajan, B. et al., Effect of interfacial energetics on dispersion and glass transition temperature in polymer nanocomposites. *Macromolecules* **2013**, 46 (7), 2833–2841, DOI: 10.1021/ma302281b.

[4] Qu, L. et al., Contribution of silica-rubber interactions on the viscoelastic behaviors of modified solution polymerized styrene butadiene rubbers (M-S-SBRs) filled with silica. *RSC Adv.* **2014**, 4 (109), 64354–64363, DOI: 10.1039/c4ra09492a.

[5] Klat, D., Karimi-Varzaneh, H. A., Lacayo-Pineda, J., Phase morphology of NR/SBR blends: Effect of curing temperature and curing time. *Polymers (Basel).* **2018**, 10 (5), 1–15, DOI: 10.3390/polym10050510.

[6] Gundlach, N., Hentschke, R., Modelling filler dispersion in elastomers: Relating filler morphology to interface free energies via SAXS and TEM simulation studies. *Polymers (Basel).* **2018**, 10 (4), 1–15, DOI: 10.3390/polym10040446.

[7] Abraham, J. et al., Progress in Rubber Nanocomposites. Edited by Thomas, S., Maria, H. J., 1st ed., Duxford: Woodhead Publishing, **2017**, ISBN: 9780081004289.

[8] Evonik Industries AG, Safety Data Sheet Ultrasil VN3 GR. **2015**, URL: http://hbchemical.com/wp-content/uploads/2016/03/SDS-GHS-ULTRASIL-VN3-GR.pdf (visited on 08/30/2019).

[9] Evonik Industries AG, Product Information Si69. **2014**, URL: http://hbchemical.com/wp-content/uploads/2016/03/Si-69-Silane-Product-Information-Sheet.pdf (visited on 08/30/2019).

[10] Röthemeyer, F., Sommer, F., Kautschuk Technologie: Werkstoffe - Verarbeitung - Produkte. München: Carl Hanser Verlag, **2001**, ISBN: 978-3-446-43760-9.

[11] Meier, J. G. et al., Kieselsäuregefüllte Elastomerblends durch Masterbatchtechnologie - Steuerung des Mischungszustandes und der Materialeigenschaften. *Kautschuk Gummi Kunststoffe* **2005**, 58, 587–594, URL: https://www.researchgate.net/publication/235673707.

[12] Le, H. H. et al., Filler Wetting in Miscible ESBR/SSBR Blends and Its Effect on Mechanical Properties. *Macromol. Mater. Eng.* **2016**, 301 (4), 414–422, DOI: 10.1002/mame.201500325.

[13] Vilmin, F. et al., Reactivity of bis[3-(triethoxysilyl)propyl] tetrasulfide (TESPT) silane coupling agent over hydrated silica: Operando IR spectroscopy and chemometrics study. *J. Phys. Chem. C* **2014**, 118 (8), 4056–4071, DOI: 10.1021/jp408600h.

[14] Deetz, J. D., Ngo, Q., Faller, R., Reactive Molecular Dynamics Simulations of the Silanization of Silica Substrates by Methoxysilanes and Hydroxysilanes. *Langmuir* **2016**, 32 (28), 7045–7055, DOI: 10.1021/acs.langmuir.6b00934.

[15] Mihara, S., Datta, R. N., Noordermeer, J. W. M., Flocculation in Silica Reinforced Rubber Compounds. *Rubber Chem. Technol.* **2009**, 82 (5), 524–540, DOI: 10.5254/1.3548262.

[16] Wang, M.-J., Effect of Polymer-Filler and Filler-Filler Interactions on Dynamic Properties of Filled Vulcanizates. *Rubber Chem. Technol.* **1998**, 71 (3), 520–589, DOI: 10.5254/1.3538492.

[17] Friedrich Thurn, B. et al., Rubber Compositions Containing Silica and An Organosilane. US3873489A, GmbH, E. D., **1975**.

[18] Wehmeier, A., Fröhlich, J., Advanced Filler Systems for Rubber Reinforcement. (Essen), **2008**, URL: http://www.vkrt.org/lect.php?sel=admin/upload/20080214AW.pdf.

[19] Mihara, S., Reactive processing of silica-reinforced tire rubber: new insight into the time- and temperature-dependence of silica rubber interaction. Dissertation, University of Twente, **2009**, DOI: 10.3990/1.9789036528399.

[20] Mihara, S. et al., Ultra Small-Angle X-Ray Scattering Study of Flocculation in Silica-Filled Rubber. *Rubber Chem. Technol.* **2014**, 87 (2), 348–359, DOI: 10.5254/rct.13.88958.

[21] Kaewsakul, W. et al., Factors influencing the flocculation process in silica-reinforced natural rubber compounds. *J. Elastomers Plast.* **2016**, 48 (5), 426–441, DOI: 10.1177/0095244315580456.

[22] Owens, D. K., Wendt, R. C., Estimation of the surface free energy of polymers. *J. Appl. Polym. Sci.* **1969**, 13 (8), 1741–1747, DOI: 10.1002/app.1969.070130815.

[23] Tunnicliffe, L. B. et al., Flocculation and viscoelastic behaviour in carbon black-filled natural rubber. *Macromol. Mater. Eng.* **2014**, 299 (12), 1474–1483, DOI: 10.1002/mame.201400117.

[24] Landau, D. P., Binder, K., A Guide to Monte Carlo Simulations in Statistical Physics. 3rd ed., New York: Cambridge University Press, **2009**, ISBN: 9780511651762.

[25] Stöckelhuber, K. W. et al., Filler flocculation in polymers-a simplified model derived from thermodynamics and game theory. *Soft Matter* **2017**, 13 (20), 3701–3709, DOI: 10.1039/c6sm02694j.

[26] Fowkes, F. M., Attractive Forces At Interfaces. *Ind. Eng. Chem.* **1964**, 56 (12), 40–52, DOI: 10.1021/ie50660a008.

[27] Girifalco, L. A., Good, R. J., A theory for the estimation of surface and interfacial energies. I. Derivation and application to interfacial tension. *J. Phys. Chem.* **1957**, 61 (7), 904–909, DOI: 10.1021/j150553a013.

[28] Good, R. J., Girifalco, L. A., Kraus, G., A theory for estimation of interfacial energies. II. Application to surface thermodynamics of Teflon and graphite. *J. Phys. Chem.* **1958**, 62 (11), 1418–1421, DOI: 10.1021/j150569a016.

[29] Good, R. J., Girifalco, L. A., A theory for estimation of surface and interfacial energies. III. Estimation of surface energies of solids from contact angle data. *J. Phys. Chem.* **1960**, 64 (5), 561–565, DOI: 10.1021/j100834a012.

[30] Adamson, A. W., Gast, A. P., Physical Chemistry of Surfaces. Edited by Gast, A. P., 6th ed., New York: John Wiley & Sons, Inc., **1997**, ISBN: 0-471-14873-3.

[31] Michalski, M.-C. et al., Adhesion of edible oils to food contact surfaces. *J. Am. Oil Chem. Soc.* **1998**, 75 (4), 447–454, DOI: 10.1007/s11746-998-0247-9.

[32] Schaefer, D. W., Justice, R. S., How nano are nanocomposites?. *Macromolecules* **2007**, 40 (24), 8501–8517, DOI: 10.1021/ma070356w.

[33] Herd, C. R., McDonald, G. C., Hess, W. M., Morphology of Carbon-Black Aggregates: Fractal versus Euclidean Geometry. *Rubber Chem. Technol.* **1992**, 65 (1), 107–129, DOI: https://doi.org/10.5254/1.3538594.

[34] Jouault, N. et al., Well-dispersed fractal aggregates as filler in polymer-silica nanocomposites: Long-range effects in rheology. *Macromolecules* **2009**, 42 (6), 2031–2040, DOI: 10.1021/ma801908u.

[35] Beaucage, G., Approximations Leading to a Unified Exponential/Power-Law Approach to Small-Angle Scattering. *J. Appl. Crystallogr.* **1995**, 28 (6), 717–728, DOI: 10.1107/S0021889895005292.

[36] Martin, T. B., Entropic and Enthalpic Driving Forces on Morphology in Polymer Grafted Particle Filled Nanocomposites. **2016**, URL: https://scholar.colorado.edu/chbe_gradetds/95 (visited on 08/30/2019).

[37] Schaefer, D. W., Keefer, K. D., Structure of soluble silicates. *Mater. Res. Soc. Symp. Proc.* **1984**, 32, 1–14, DOI: 10.1557/PROC-32-1.

[38] Baeza, G. P. et al., Multiscale filler structure in simplified industrial nanocomposite silica/SBR systems studied by SAXS and TEM. *Macromolecules* **2013**, 46 (1), 317–329, DOI: 10.1021/ma302248p.

[39] Bouty, A. et al., Nanofiller structure and reinforcement in model silica/rubber composites: A quantitative correlation driven by interfacial agents. *Macromolecules* **2014**, 47 (15), 5365–5378, DOI: 10.1021/ma500582p.

[40] Odo, E. A. et al., SAXS Study of Silicon Nanocomposites. *Int. J. Compos. Mater.* **2015**, 5 (3), 65–70, DOI: 10.5923/j.cmaterials.20150503.03.

[41] Kim, S. et al., Structural Development of Nanoparticle Dispersion during Drying in Polymer Nanocomposite Films. *Macromolecules* **2016**, 49 (23), 9068–9079, DOI: 10.1021/acs.macromol.6b01939.

[42] Guinier, A., Fournet, G., Small-angle scattering of X-rays. Edited by Mayer, M. G., Michigan: John Wiley & Sons, Inc., **1955**, DOI: https://doi.org/10.1002/pol.1956.120199326.

[43] Pedersen, J. S., Modelling of Small-Angle Scattering Date from Colloids and Polymer Systems. *Neutrons, X-rays Light Scatt. Methods Appl. to Soft Condens. Matter*, edited by Lindner, P., Zemb, T., Aarhus: Elsevier Ltd, **2002**, chapter 16, 391–420, ISBN: 978-0-444-51122-5.

[44] Glatter, O., Kratky, O., Small Angle X-ray Scattering. Edited by Glatter, O., Kratky, O., New York: Academic Press, **1982**, DOI: 10.1007/978-3-642-03307-0.

[45] Bale, H. D., Schmidt, P. W., Small-Angle X-Ray-Scattering Investigation of Submicroscopic Porosity with Fractal Properties. *Phys. Rev. Lett.* **1984**, 53 (6), 596–599, DOI: 10.1103/PhysRevLett.53.596.

[46] Kohls, D. J., Beaucage, G., Rational design of reinforced rubber. *Curr. Opin. Solid State Mater. Sci.* **2002**, 6, 183–194, DOI: 10.1016/S1359-0286(02)00073-6.

[47] Teixeira, J., Small-angle scattering by fractal systems. *J. Appl. Crystallogr.* **1988**, 21 (6), 781–785, DOI: 10.1107/S0021889888000263.

[48] Besselink, R. et al., Not just fractal surfaces, but surface fractal aggregates: Derivation of the expression for the structure factor and its applications. *J. Chem. Phys.* **2016**, 145 (21), DOI: 10.1063/1.4960953.

[49] Koga, T. et al., New insight into hierarchical structures of carbon black dispersed in polymer matrices: A combined small-angle scattering study. *Macromolecules* **2008**, 41 (2), 453–464, DOI: 10.1021/ma0718671.

[50] Takenaka, M., Analysis of structures of rubber-filler systems with combined scattering methods. *Polym. J.* **2013**, 45 (1), 10–19, DOI: 10.1038/pj.2012.187.

[51] Schneider, G. J., Analyse der Struktur von aktiven Füllstoffen mittels Streumethoden. **2006**, URL: http://epub.uni-regensburg.de/10438/ (visited on 08/30/2019).

[52] Kohls, D. J. et al., Silica Fillers for Elastomer Reinforcement. *Curr. Top. Elastomers Res.* Edited by Bhowmick, A. K., Boca Raton: CRC Press, **2008**, 505–517, DOI: 10.1201/9781420007183.ch17.

[53] Oberdisse, J., Pyckhout-Hintzen, W., Straube, E., Structure Determination of Polymer Nanocomposites by Small Angle Scattering. **2009**, URL: https://hal.archives-ouvertes.fr/hal-00542764 (visited on 08/30/2019).

[54] Mandelbrot, B. B., The fractal geometry of nature. Edited by Freeman, W., Third, San Francisco: Henry Holt and Company, **1982**, ISBN: 9780716711865.

[55] Lacayo-Pineda, J., Filler Dispersion and Filler Networks. *Encycl. Polym. Nanomater.* Edited by Kobayashi, S., Müllen, K., Berlin, Heidelberg: Springer Berlin Heidelberg, **2015**, chapter F, 771–776, DOI: 10.1007/978-3-642-29648-2_291.

[56] Fry, D. et al., Structural crossover in dense irreversibly aggregating particulate systems. *Phys. Rev. E - Stat. Physics, Plasmas, Fluids, Relat. Interdiscip. Top.* **2004**, 69 (6), 10, DOI: 10.1103/PhysRevE.69.061401.

[57] Hess, W. M., Herd, C. R., Vegvari, P. C., Characterization of Immiscible Elastomer Blends. *Rubber Chem. Technol.* **1992**, 66 (4), 330–375, DOI: 10.5254/1.3538316.

[58] Lin, H., Jiang, Z., Study on the effect of rubber sole on pressure change of foot movement. *Leather Footwear J.* **2018**, 18 (1), 33–38, DOI: 10.24264/lfj.18.1.4.

[59] Solvay GmbH, Product Data Sheet - Zeosil 1165MP. **2018**, URL: https://www.solvay.com/en/product/zeosil-1165mp (visited on 08/30/2019).

[60] Gerspacher, M. et al., Flocculation in carbon black filled rubber compounds. **2002**, URL: http://www.all-electronics.de/ai/resources/72d8ab665f3.pdf (visited on 08/30/2019).

[61] Scher, H., Zallen, R., Critical Density in Percolation Processes. **1970**, URL: https://pdfs.semanticscholar.org/8e1b/a1249b603b3827e59808f8616a2605299bed.pdf (visited on 08/30/2019).

[62] Xu, X. et al., Simultaneous analysis of three-dimensional percolation models. *Front. Phys.* **2014**, 9 (1), 113–119, DOI: 10.1007/s11467-013-0403-z.

[63] Baeza, G. P. et al., Revealing nanocomposite filler structures by swelling and small-angle X-ray scattering. *Faraday Discuss.* **2016**, 186, 295–309, DOI: 10.1039/c5fd00117j.

[64] Wang, Y., Wu, J., Yin, Y., Small-Angle X-ray scattering study on nanostructures of MgO/LDPE nanocomposites. *ICEMPE 2017 - 1st Int. Conf. Electr. Mater. Power Equip.* Xi'an: International Conference on Electrical Materials and Power Equipment, **2017**, DOI: 10.1109/ICEMPE.2017.7982113.

3. Binary Polymer Blends – Impact of Homogeneity

In this chapter, we apply certain changes to our model. We introduce binary polymer blends, i.e., we create an additional cubic cell representing a second type of polymer. Major reasons for the usage of blends in the elastomer industry instead of individual elastomers are reduced compounding costs and enhanced properties of the final products [1, 2]. We focus on one of the most common blend compositions containing natural rubber (NR) and styrene-butadiene rubber (SBR) [3]. Both polymers were explicitly analyzed in the former chapter of this work, regarding the impact of different flocculation times, variable filler volume content, and temperature variation. Several benefits from both polymers are essential for the tire industry, as explained in more detail in Appendix A. NR, for instance, has the highest durability due to strain-induced crystallization. SBR compounds, on the other hand, show a good wet skid resistance. Using both polymers in a blend usually combines the properties of the individual polymers and even enhances them [4] (and references therein). For polymer blends, several possible ratios are used within the tire industry (e.g., [4–6]). Here, we focus on two of them, i.e., 50/50-NR/SBR and 70/30-NR/SBR. Additionally, we keep the filler particles homogeneous, i.e., use $\theta = 0$ or $\theta = 1$, depending on the perspective[1]. The former interpretation might be used for filler particles with low surface polarity, as they represent carbon blacks. As already mentioned, the surface treatment of carbon blacks is scarcely used (cf. Appendix A). The latter might be interpreted as silica particles, homogeneously coated by silane coupling agents of different types, i.e., different types of silanization . The homogeneity is chosen to focus on the impact of the second polymer type and to keep the parameter space low for the moment. Later on, i.e., in chapter 4, we again make use of the potential to mimic heterogeneously treated particles. Several studies revealed that low polarity fillers, such as carbon black, show a distinct affinity for SBR in the case of an NR/SBR blend [4, 7, 8] and that high polarity fillers, such as silica, show an affinity to NR in comparable blends [9]. Both affinities are investigated in detail in the course of this chapter.

As before, all particles are characterized by their respective surface free energies, which are the sums of dispersive, γ^d, and polar parts, γ^p. By choosing different values of γ_f^d and γ_f^p, different homogeneous surface treatments of the filler particles are mimicked. The values of other system parameters are, however, fixed. We use a temperature of $T = 413$ K throughout this chapter and only two different filler volume fractions, $\phi = 0.20$ and $\phi = 0.25$. In order to analyze the long term flocculation behavior, the number of MC steps is extended for a distinct blend ratio. The main results are again aggregation phase diagrams, wetted surface fractions, TEM pictures, mass fractal dimension of the aggregates, and wetting-envelope - work of adhesion plots.

We start with the changes regarding the morphology generator and several aspects of the screening methods. Thereafter, the results of the different systems are discussed, starting with the 50/50-NR/SBR and followed by the 70/30-NR/SBR blend ratio. These results are published in [10]. In addition to these results, the mass fractal dimension of the aggregates is

[1] θ was used to steer the surface modification of the filler particles.

considered here. Due to the limitation of the other system parameters, it is now reasonable to perform multiple simulations of a given system configuration. Subsequently, the long term flocculation behavior is discussed in the context of so-called wetting kinetics.

3.1. Changes due to Homogeneity

The incorporation of homogeneous filler particles inside an elastomer blend leads to several changes. Those changes are discussed here in detail. They are fairly small and only extend or reduce certain aspects of the model itself or the screening methods. We start with the changes regarding the model and the MC simulation followed by those of the screening methods.

3.1.1. The Morphology Generator

We still deal with a cubic lattice of size L^3, containing cubic cells, which we call primary particles. Any of those cells on the initial lattice are assigned the property filler with probability ϕ, i.e., the filler volume fraction. Different from the model constitution in chapter 2, the second probability θ, which assigns the attribute of surface treatment to each surface of the filler cube, i.e., the heterogeneous silanization, is now set to a value representing homogeneity. Depending on the interpretation of the filler particles itself, both possibilities, i.e., $\theta = 0$ or $\theta = 1$, arise. The former, representing no surface treatment at all, may be used in the context of low polarity filler particles such as carbon blacks. But also simply using different (non-silanized) silica particles is a reasonable interpretation. The latter is more suitable for silica particles, which are then interpreted to be homogeneously coated by a silane. This leads to a silane density[2] of $\sigma_{silane} \approx 0.75\,n\mathrm{m}^{-2}$, which is comparable to experimental results [11]. Note that this interpretation of homogeneity consequently changes the definition of a filler cluster made in chapter 2. Sharing an untreated surface is not possible anymore. Thus, they are considered a cluster, if they share a treated surface. The remaining cells are assigned the property rubber again. But now, according to the blend ratio, the rubber cells are either of type A or B. Thus, we find altogether three distinct particles (or cube types) in our model of homogeneous filler particles inside a binary polymer blend. However, it is worth noting that homogeneous surface treatments are experimentally unlikely and thus variable degrees of heterogeneity need to be considered. This is done in chapter 4.

The MC steps are also affected, because due to homogeneity the arbitrary rotation is now obsolete. Figure 3.1 shows the diagonal particle exchange on the left. This MC move is now solely considered a MC step. Followed by the arrow, indicating that the MC mimics the flocculation process, we find a representative illustration of the model and a close-up of a homogeneous filler particle. The color convention within this picture is kept throughout this chapter. Green cells represent NR, golden ones SBR, and blue cells filler particles.

All other aspects regarding the model are not altered. The Metropolis criterion is given as

$$\exp[\beta \Delta W] \geq \xi \; . \tag{3.1}$$

[2]Using the same values as in Equation (2.4), i.e., $\rho_{silica} = 2\,\mathrm{g/cm}^3$, $R_{silica} = 8\,n\mathrm{m}$, $\Gamma_{silane/silica} = 0.125$, and $m_{TESPT} = 8.95 \cdot 10^{-22}\,\mathrm{g}$

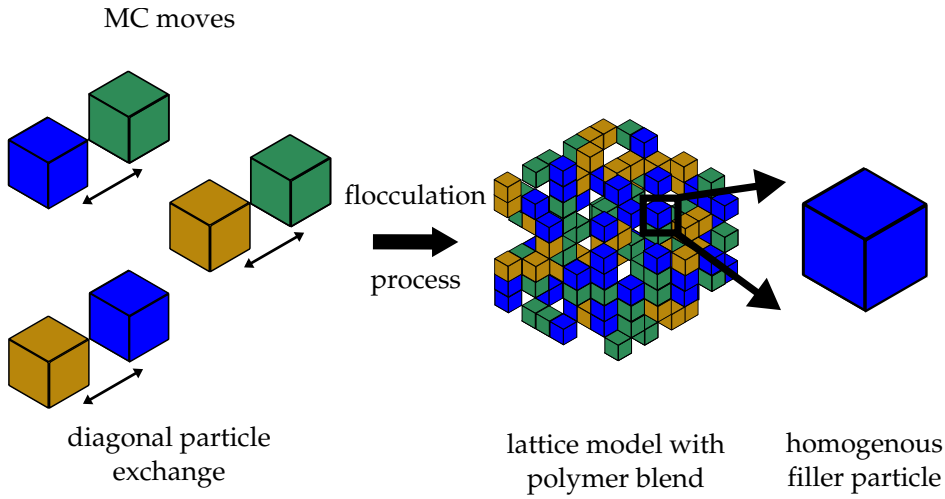

Figure 3.1.: Illustration of MC moves within binary polymer blends containing homogeneous filler particles. The MC step now consists only of a single MC move: the diagonal exchange of neighboring particles. **Green** and **golden** cells: polymer of NR and SBR respectively. **Blue** cells: filler particles.

It is, including the necessary quantities, just stated and briefly elucidated once more for the sake of completeness. The quantity ΔW is given by $\Delta W = -\gamma_j \Delta A_j = -\gamma_j a \Delta n_j$, where γ_j denotes the interface tension of a face-to-face pairing of type j, $A_j = n_j\, a$ denotes the attendant total area and n_j the number of j-type interfaces in the system. The constant a is the effective contact area per face, which we assume to be the same for all j. The interfacial free energy is dependent on the surface free energies of the attendant particles. Corresponding values are stated in the beginning of the results part. The theory behind MC in general is found in Appendix D, whereas that for the surface free energies in Appendix B.

3.1.2. Screening Methods

While most of the screening methods are unaffected by the additional particle type, TEM pictures need more attention. Generally, TEM pictures are black and white and can thus only show a difference between two components. Other visualization methods, such as atomic force microscopy (AFM), allow to differentiate between more components and are readily used for elastomer blends [1, 12]. From the viewpoint of the simulation, a visualization of all three components can be done in the same manner as the TEM pictures. This is crucial, as the flocculation of the filler particles may now lead to structural development in different regimes of the blend. Additionally, the blend morphology itself is of interest. In order to investigate this behavior, we visualize the filler particles in the style of a TEM picture just like before, but with the polymer particles added in the background, using the color coding in Figure 3.1. The stepwise procedure to obtain such pictures is depicted in Figure 3.2.

The TEM pictures of the simulated system are again obtained from slices with a thickness of five cells, extracted after a certain number of MC moves. Figure 3.2a shows an example of such a picture. The grey circles indicate the filler particles. The grey level corresponds

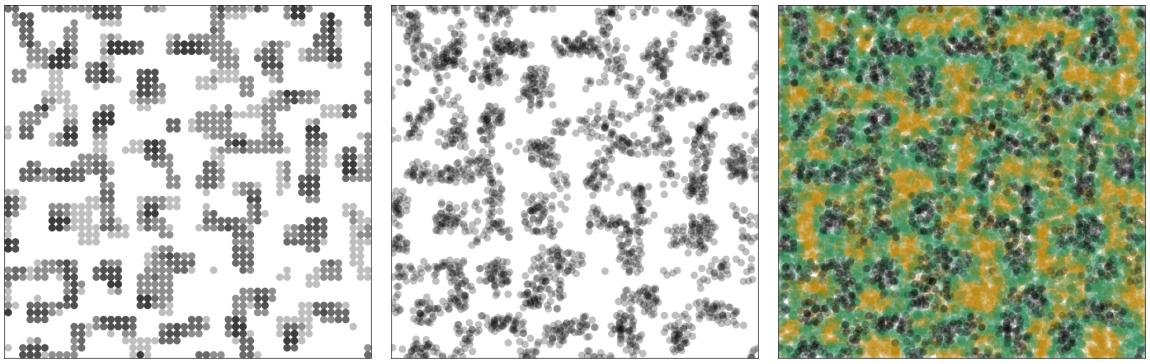

(a) model TEM. **(b)** mock TEM. **(c)** mock TEM with polymer blend.

Figure 3.2.: Mock TEM picture generation with polymer blend visualization. (**a**): A slice, five cells thick and showing the filler particles only, extracted from the simulation after $L^3 \cdot 10^3$ MC steps. Darker shades of grey result from two or more particles stacked on top of each other along the line of sight; (**b**): small random displacements are applied to every filler particle; (**c**): visualization of a polymer blend including the filler. Their affinity for the NR phase is discernible. Note that the polymer cells are subject to the same displacement procedure as the filler particles. The polymers are natural rubber (NR, NR2, $\gamma_p^d = 20.2$ mJ/m^2 and $\gamma_p^p = 5.5$ mJ/m^2) and styrene-butadiene rubber (SBR, SBR-LV, $\gamma_p^d = 29.9$ mJ/m^2 and $\gamma_p^p = 1.6$ mJ/m^2) both taken from [6]. The filler mimics a silica particle ($\gamma_f^d = 20.0$ mJ/m^2 and $\gamma_f^p = 20.0$ mJ/m^2). A filler volume content of $\phi = 20\%$, a blend ratio of $50/50$, and a temperature of $T = 140$ °C were chosen. The system's linear dimension is $L = 128$. However, the TEM only shows a portion of 50×50 lattice cells for better visibility.

to the number of filler particles stacked on top of each other along the line of sight. The displacement procedure, in order to increase the similarity with experimental TEM slices, is performed again to all particles, resulting in Figure 3.2b. The maximum displacement in any direction is, as before, 0.6 times the lattice spacing. Note that the polymer cells are also subject to the same procedure. Figure 3.2c shows the visualization of the polymer blend structure in the background of the filler network. Green particles indicate NR and golden particles indicate SBR. The size of the TEM pictures is 50×50 lattice cells for a clearer identification of the filler structures within the blend. The linear dimension of the system is $L = 128$. The cut is performed in the middle of the system, i.e., between layers 62 and 67 along the z-axis. Note that some white areas are still visible due to the displacement procedure and the visualization of particles as circles. Increasing the size of the circles diminishes this issue with the cost of less visibility of structural development inside different phases. Note also that the particles are plotted in layers, i.e., we start with SBR, followed by NR, and the filler particles at last. This is done, to get a better visualization of the filler structures. An interchange between NR and SBR is certainly important to better understand the polymer distribution. However, independent of the ordering of the layers, the impression obtained from the filler particles is not affected.

For this specific example, we see a filler network percolating through the NR phase of the blend, avoiding the SBR phase completely. Taking a closer look at the single layers, we find that SBR forms a continuous polymer phase, consisting of large, dense individual branches

embedded inside NR. A finer, more blurry phase can be found for NR, creating a continous polymer matrix. Thus, in the same way as [6], we can state that we find big domains of SBR embedded in a continuous NR matrix, which is in agreement with their results. It should, however, be noted that in the named source, the authors investigated a pure polymer blend without filler particles added. It is likely to assume that the flocculation process affects the development of structures for all three components and that they depend on each other. Thus, different filler particles may lead to different polymer blend morphologies.

It should also be noted that, since we are dealing with polymer blends, the morphology of the polymers themselves is also important. The difference in the work of adhesion, which determined the flocculation tendency of the filler particles, can also be used for the polymers. However, the term flocculation is then replaced by 'coagulation' [13].

The wetted surface fractions introduced as a basic quantity in chapter 2 need to be updated in their nomenclature. The procedure to obtain them is unaltered. We again need the number of corresponding contacts, n_{ij}, between cells of types i and j . Here, the cell types are abbreviated as f (filler), n (NR), and sb (SBR). The wetted surface fractions l_{ij} are now calculated in the same manner as before. The normalization depends on the first letter, i.e., the cell type i. For instance, the information to what extent the filler particles, f, are wetted by SBR, sb, is given by the corresponding wetted surface fraction, l_{fsb}, as

$$l_{fsb} = \frac{n_{fsb}}{\sum_j n_{fj}} = \frac{n_{fsb}}{n_{ff} + n_{fsb} + n_{fn}}. \tag{3.2}$$

Analogously, we compute the other surface fractions l_{ff}, l_{fn}, l_{nsb}, l_{sbsb}, and l_{nn}. Filler-polymer related wetted surface fractions allow to rate the dispersion of the filler particles within the respective polymer. Together with filler-filler related ones, it is possible to distinguish between different structure types, namely formation of filler networks, smaller or bigger clusters. Those related to polymer-polymer contacts allow to investigate the structural development of the different polymers. As no polymer clusters are considered, this method allows to investigate their development under the impact of different filler particles at least briefly. Note that as before changing the positioning of i and j leads to different wetted surface fractions due to the normalization, i.e., considering our example $l_{fsb} \neq l_{sbf}$. The information obtained from one combination, however, is sufficient. Thus, two plots of wetted surface fractions are needed to fully understand the behavior of a system. A purely filler related one, containing l_{ff}, l_{fn}, and l_{fsb}, and a polymer related one, containing l_{sbsb}, l_{nn}, and l_{nsb}.

3.2. Mimicking Homogeneous Filler Particles in Polymer Blends

In this part, we present the results for the simulated systems of the 50/50- and 70/30-NR/SBR blend. For their discussion, we keep the ordering used in chapter 2, i.e., after elucidating the recipe, we start with the wetting-envelope - work of adhesion plots, because they are only dependent on the surface free energies of the ingredients. From those we deduce an ordering for the wetted surface fractions, which gives us first insights on the behavior of the different filler particles. Subsequently, we show the results for the different blend ratios. For each of

them, the aggregation phase diagrams accompanied by TEM pictures, the wetted surface fractions, and the mass fractal dimension of the aggregates are discussed. The cluster mass distribution is again helpful for an in-depth analysis, on whether a filler formed a network or not. Finally, we discuss the impact of a higher filler volume content.

3.2.1. The Recipe

We use the recipe in Table 3.1. The attendant values of NR and SBR were obtained via the sessile drop technique in conjunction with the OWRK theory [6]. The background for this method is explained in detail in Appendix B. The dispersive and polar parts of the filler surface free energy, denoted with the subscript f in the following, are variable. Akin to the former chapter 2, this allows us to mimic different types of filler, e.g., fillers with low polarity such as carbon black as well as high polarity fillers such as the widely used Ultrasil VN3 [14–19].

Table 3.1.: Surface free energies of the components used in the binary polymer blend. Whereas the polymer values are fixed, filler values vary as indicated, mimicking different filler types. Note that the dispersive part is kept fixed while the polar part is varied in steps of $5\,m\mathrm{J/m^2}$. NR and SBR values were measured via the sessile drop technique and are taken from [6]. The SBR used here is called SBR-LV in the named reference.

type	name	γ^d $[m\mathrm{J/m^2}]$	γ^p $[m\mathrm{J/m^2}]$	γ - total $[m\mathrm{J/m^2}]$
filler	-	20/30	0,5,...,30	20,25,...,60
polymer	NR	20.2	5.5	25.7
polymer	SBR	29.9	1.6	31.5

Other system parameters are chosen as follows:

- system size L: 128
- filler volume content ϕ (in vol. %): 20, 25
- heterogeneous silanization θ: 0.0 resp. 1.0
- temperature T in K: 413
- maximum number of MC steps: $10^3 \cdot L^3$

The NR we investigated in chapter 2 is slightly different from the one we use here. At $T =$ 413K, we observed a different behavior of the former NR, which contradicts our expectation that we had deduced from the wetting-envelope - work of adhesion plots. Within this chapter, we argued that the missing temperature dependency of the surface free energies themselves leads to this 'nonphysical' behavior. The NR we consider here, however, does not show this extreme behavior and thus, the choice of the temperature shows, as for SBR, only a very minor impact. Additionally, very high temperatures, i.e., $T > 433$ K, are not used for flocculation experiments. The two filler volume contents we have chosen here displayed the formation of

filler networks in both polymers (cf. chapter 2). The number of MC steps is again chosen this high to investigate the structural development of filler networks. In total, 70 recipes are screened in this chapter not including the different flocculation times.

Note that for the systems discussed in this chapter, ten simulations for each set of parameters have been conducted – akin to the example systems in section 2.4. This is done to improve the statistics on the cluster mass distribution, the wetted surface lengths, the mean aggregate size, and the mass fractal dimension of the aggregates. It turns out that all quantities generally show only small uncertainties, which are summarized in the following.

For $\phi = 0.20$ in both blend ratios, we find that the amount of clusters deviates between 1% and 5% from the respective mean value of a given system. The amount of cluster bound particles deviates less than 0.5%. The distribution of the clusters in the respective mass categories does not deviate more than 1%. For systems developing a filler network, the deviation in the mass of the single large cluster is generally below 5%. The amount of particles they comprise consequently shows the same deviation. The corresponding size deviates less than 1%. There is, however, one exception for the 70/30 blend ratio for the filler particle with $\gamma_f^d = 30.00$ mJ/m^2 and $\gamma_f^p = 15.00$ mJ/m^2. It deviates around 8% in the mass. This sometimes leads to systems not containing a filler network, because the cluster definition, i.e., containing 50% of all particles or at least $R_G = L/2$, is not fulfilled. Additionally, we find for those systems fulfilling the definition that the sizes deviate with around 3% slightly more than for the other surface free energies. The wetted surface fractions, on the other hand, deviate less than 0.1% regardless of the specific type of length, blend ratio, or surface free energy.

For $\phi = 0.25$, we find higher deviations for the amount of clusters in cases where large filler networks are developed. This is due to the fact that sometimes smaller clusters are leftover in the filler network formation process. Because the networks comprise almost all filler particles, the distribution of the clusters in the respective mass categories is relatively unaffected. Other uncertainties are the same for the $\phi = 0.20$ case, but without the exception.

Consequently, we can state that regarding the basic quantities of the system, systems with a fixed combination of parameters behave very similar almost every time. Thus, numbers used in the discussion based on basic quantities and the presentation of the wetted surface fractions are mean values for the corresponding surface free energies with the uncertainties listed here.

A 'mean' TEM picture is rather meaningless. Thus, it is chosen as a representative example – in the same way as the example systems in section 2.4. For the mean aggregate size, however, we find that it has its own uncertainty due to the procedure elucidated in the screening methods section in chapter 2. Therefore, the calculation of a weighted mean with this uncertainty as the weight is reasonable to consider . Hence,

$$\bar{q}_{agg} = \frac{\sum_i g_i \cdot q^i_{agg}}{\sum_i g_i} \qquad \text{with} \qquad g_i = \frac{1}{(\sigma^i_{agg})^2}. \tag{3.3}$$

Here, i is running over the $N = 10$ simulations and q^i_{agg} with σ^i_{agg} are the mean size and uncertainty of the aggregates of simulation i. The corresponding standard deviation of the weighted mean is calculated via

$$\bar{\sigma}_{agg} = \frac{1}{\sqrt{\sum_i g_i}}. \tag{3.4}$$

It turns out that the deviations from the mean value are very small, i.e., mostly far less than $0.5\,n$m. The most pronounced deviations are found for a lower number of MC steps. Consequently, the aggregation phase diagrams in this chapter are representative for the corresponding combination of surface free energies, filler volume content, temperature, and number of MC steps. The values in the diagrams are thus chosen to match with the TEM pictures and are not the means over ten simulations.

The values for the mass fractal dimension of the aggregates obtained via the box-counting algorithm deviate rather minor, i.e., below 1%. This was also seen for the example systems in section 2.4. To better account for the individual uncertainty of the mass fractal dimensions, the mean uncertainty of the individual systems is stated instead of the weighted mean.

3.2.2. Wetting-Envelope - Work of Adhesion Plots

We start with the filler types having a dispersive part of the surface free energy of $\gamma_f^d = 20\,m\mathrm{J/m^2}$, as depicted in Figure 3.3. On the left, i.e., Figure 3.3a, we see NR and on the right, i.e., Figure 3.3b, we see SBR as the liquid. The red dots represent the filler types with variable polar surface free energies. Those marked with roman numerals are chosen to be investigated further. The golden dot in the NR plot and the green dot in the SBR plot, mark the positioning of the respective other polymer, following the color coding introduced in the context of Figure 3.1. The solid lines are the iso contact angle lines, which indicate the wetting behavior between the fixed polymer and the incorporated filler types (or with the other polymer). Everything above the black solid line is considered to be perfectly wetted by the corresponding polymer. The dotted loops represent the iso lines of the difference in work of adhesion. Filler types close to the inner, black dotted loop are considered to show the lowest flocculation tendency. Note that compared to the NR in chapter 2, i.e., Figure 2.23a, the dotted loops are slightly shifted vertically upwards and to the left. The overall shape is unaltered. This affects the flocculation tendency of all filler types.

Similar to the reflection on the example systems and the single polymers in chapter 2, we can deduce an ordering of the wetted surface fractions from the positioning of the filler types. We concentrate on those marked with roman numerals. A complete overview on the development of the wetted surface fractions is given in the detailed analysis in the context of the aggregate phase diagrams with embedded TEM pictures. The ordering of the wetted surface fractions of the polymers are always deduced after that of the fillers, as it is a direct consequence of their ordering.

Starting with filler type I, we see bad wetting behavior towards both polymers and for NR a high flocculation tendency. That for SBR is, according to our rating scheme introduced in chapter 2, considered mediocre. Thus, a high value of l_{ff} is very likely and that for l_{fn} should be considerably lower than that for l_{fsb}, because the filler particles aggregate in the phase with the lowest difference in work of adhesion.

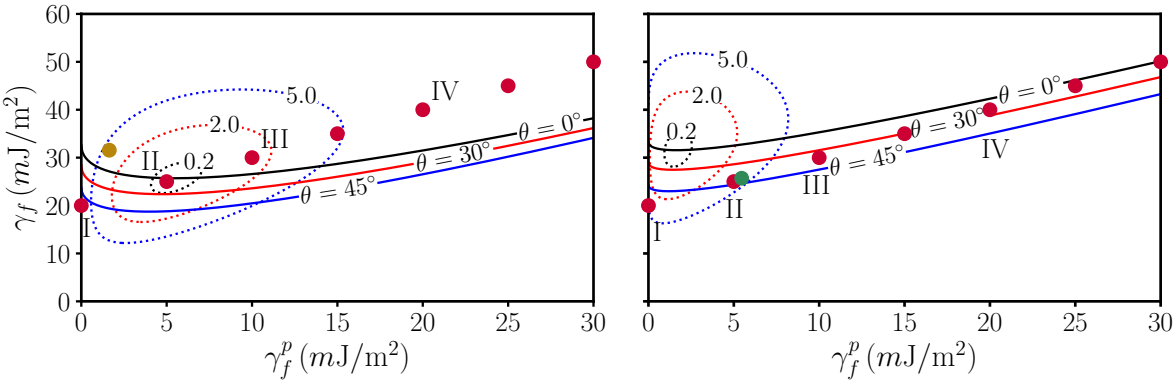

(a) NR as the liquid. **(b)** SBR as the liquid.

Figure 3.3.: Comparison of wetting-envelope - work of adhesion plots for NR **(a)** and SBR **(b)** containing artificial filler types with $\gamma_f^d = 20\,mJ/m^2$ in the case of binary polymer blends. Filler types are marked as red dots. Those labeled by roman numerals I to IV are chosen to be investigated further. The golden colored dot in **(a)** and the green dot in **(b)** marks the position of the respective other polymer, i.e., SBR inside NR and NR inside SBR.

Increasing the surface polarity, we see perfect dispersion for fillers of type II inside NR together with a good, close to perfect wetting behavior. At the same time, the flocculation tendency inside SBR is slightly elevated. The same is true for the wetting behavior. As we can see from the positioning of filler type II inside SBR, it is basically identical to NR. Because the system wants to minimize its free enthalpy, it is reasonable to assume that the filler particle is solely incorporated inside NR. Therein, it shows no aggregation at all. Consequently, l_{fn} has to be the highest value of all particles. Due to the increasing value of l_{fn}, the values of l_{fsb} and l_{ff} will drop considerably.

Filler type III is the first to show perfect wetting for NR and still has a good dispersion inside it. The flocculation tendency for SBR is high, while the wetting behavior is close to mediocre. Based on the same argumentation as for filler type II, it is reasonable to assume that those filler particles are now found solely inside NR. It is the best option for the system to minimize its free enthalpy. Because of the higher flocculation tendency, l_{ff} will be higher than in the case of filler type II, but lower than I. l_{fn} must therefore decrease and l_{fsb} will consequently be very low.

For the last filler type taken into consideration, i.e., IV, we find a high flocculation tendency for both polymers, albeit it is higher for SBR than for NR. Although the wetting behavior towards SBR is now considered good, for NR it is still perfect. l_{fsb} will consequently not differ from III and only the values of l_{ff} and l_{fn} are expected to change. Due to the higher flocculation tendency, l_{ff} must increase while l_{fn} has to decrease. Thus, we can state the ordering for the wetted surface fractions regarding filler-polymer as

$$l_{fn}^{II} > l_{fn}^{III} > l_{fn}^{IV} > l_{fn}^{I} \quad \text{and} \quad l_{fsb}^{I} > l_{fsb}^{II} > l_{fsb}^{III} > l_{fsb}^{IV}. \tag{3.5}$$

It should be noted that if the filler particles avoid a certain polymer, they are spatially confined. This results in a direct dependency of the wetted surface fractions of the polymers, where the filler particles are confined. If both polymers are equally good and the flocculation tendency is somewhat large, as for the case of filler type I, then those filler particles can and will aggregate inside them. Therefore, we attain for filler-filler related surface fractions

$$l_{ff}^{I} > l_{ff}^{IV} > l_{ff}^{III} > l_{ff}^{II}. \tag{3.6}$$

For the wetted surface fractions of the polymers, we can make use of the results obtained in Equations (3.5) and (3.6). It is reasonable to say that where we find the highest values of filler-polymer the respective value of the same polymer-polymer fraction will be the lowest. Thus, we find the lowest f_{nn} value for II and the lowest l_{sbsb} value of I. Because the flocculation tendency of the polymers within each other is fairly high, we cannot adopt the same argumentation for the lowest filler-polymer values, as the wetted surface fraction between both polymers, l_{nsb}, needs to be taken into account. To find its lowest value, we need to find a filler type, which has a very high value between filler and both polymers. This would be fulfilled by filler types I and II. For both, we already deduced that one of the polymer-polymer values will be the lowest. Because l_{fn} will presumably be much higher than l_{fsb} due to the positioning regarding the flocculation tendency, filler type II has to show the lowest value of l_{nsb}. Lots of NR surfaces are occupied by filler particles diminishing the options for SBR. This in turn can now flocculate. Thus, we find for II also the highest value of l_{sbsb}. Consequently, the highest value of l_{nn} is found for filler type I. l_{fsb} is the highest, while l_{fn} is the lowest. Filler type I aggregates heavily inside SBR. This allows NR to flocculate. The highest value for l_{nsb} is found, where the filler particles have their lowest wetted surface fractions towards each of the polymers. Taking Equations (3.5) and (3.6) into consideration, we find that filler type IV fulfills this the most. Where l_{nsb} is very high, the corresponding values of l_{nn} and l_{sbsb} must be fairly low. Thus, we find for the polymer-polymer related wetted surface fractions of identical polymers

$$l_{nn}^{I} > l_{nn}^{III} > l_{nn}^{IV} > l_{nn}^{II} \quad \text{and} \quad l_{sbsb}^{II} > l_{sbsb}^{III} > l_{fsb}^{IV} > l_{sbsb}^{I}. \tag{3.7}$$

Because filler type III was left and we knew the highest, lowest, and second lowest values of the polymer-polymer related wetted surface fractions of identical polymers, its positioning was obvious. We find that only the highest and the lowest value are interchanged. Due to both second highest values in Equation (3.7), we can turn the argumentation regarding the mixed polymer interface around. High values of identical polymer-polymer surface fractions must consequently lead to low values of the mixed interface. Therefore, we finally find

$$l_{nsb}^{IV} > l_{nsb}^{I} > l_{nsb}^{III} > l_{nsb}^{II}. \tag{3.8}$$

This final ordering leads to the expectation that filler type I is going to aggregate inside SBR, II to disperse inside NR, and III as well as IV to aggregate inside NR.

We now increase the dispersive part of the surface free energy to $\gamma_f^d = 30\,m\mathrm{J/m^2}$ and repeat the process. Generally, the flocculation tendency for all filler types inside NR is higher, al-

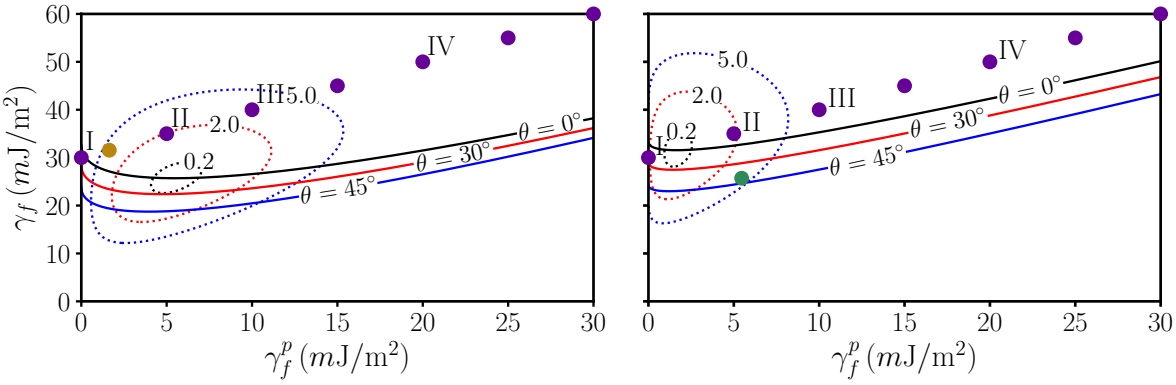

(a) NR as the liquid. **(b)** SBR as the liquid.

Figure 3.4.: Comparison of wetting-envelope - work of adhesion plots for NR **(a)** and SBR **(b)** containing artificial filler types with $\gamma_f^d = 30\,mJ/m^2$ in the case of binary polymer blends. Filler types are marked as red dots. Those labeled by roman numerals I to IV are chosen to be investigated further. The golden colored dot in **(a)** and the green dot in **(b)** marks the position of the respective other polymer, i.e., SBR inside NR and NR inside SBR.

though the change for I is only minor. For SBR we find better dispersion for filler types I and II, while the remaining types are unaltered. The wetting behavior of all filler types is increased due to the vertical shift. Only filler type I inside SBR shows non-perfect wetting.

Starting with this filler type, we find only a slight change compared to the $\gamma_f^d = 20\,mJ/m^2$ case. The better dispersion inside SBR and slightly higher flocculation inside NR will lead to an even lower value of l_{fn} and a higher value of l_{fsb}. Because the flocculation tendency is still relatively high, this filler type will aggregate inside SBR, leading to a fairly high value of l_{ff}.

Filler type II is equal for both polymers in every aspect. It shows the same flocculation tendency and is perfectly wetted by both polymers. It is thus reasonable to assume that all filler related wetted surface fractions will be similar. This must lead to a decrease of l_{fsb} and l_{ff} and to an increase of l_{fn}. Because the flocculation tendency of this filler type is the lowest for both polymers, we have already found the lowest value of l_{ff}. This case is somewhat special, because it is likely to assume that this filler type will aggregate along the interface of both polymers.

Further increasing the polar part of the surface free energy, i.e., looking at filler type III, we find a mediocre flocculation tendency inside NR and a high one inside SBR. Therefore, the filler particles of that type will aggregate inside NR. Subsequently, l_{fsb} and l_{fn} will decrease further and l_{ff} increases again. It will even have a higher value than for filler type I, and therefore the highest one for all filler types. This can be argued when looking at filler type I once more. It is the same situation but with the polymers exchanged. For filler type III we just have a slightly higher flocculation tendency for both polymers.

Filler type IV shows the same dependencies as in the case of $\gamma_f^d = 20\,mJ/m^2$, although the difference between the flocculation tendencies has become smaller. Thus the values of l_{fsb} should not be as low as before. Due to the higher flocculation tendency compared to III,

however, l_{fsb} must be lower. With that we find that the ordering of l_{fsb} is unchanged to the former case of $\gamma_f^d = 20\,m\mathrm{J/m^2}$. Because the difference in the flocculation tendencies between both polymers is now lower, but still the lowest is found in NR, we expect the filler type IV to aggregate mostly inside NR, albeit not as much as for filler type III. It is 'pulled' towards SBR, leading to less dense aggregates and therefore for a higher value of l_{fn} and a lower value of l_{ff}. Thus, we find changes in the ordering of both remaining filler related surface fractions given as

$$l_{fn}^{IV} > l_{fn}^{II} > l_{fn}^{III} > l_{fn}^{I} \quad \text{and} \quad l_{ff}^{III} > l_{ff}^{I} > l_{ff}^{IV} > l_{ff}^{II}. \tag{3.9}$$

We can adopt the same procedure for the polymers as in the case of $\gamma_f^d = 20\,m\mathrm{J/m^2}$ in the exact same manner. It should be noted, however, that filler type II, which is equal for both polymers, marks the lowest value of l_{nsb} and the highest values of l_{sbsb} and l_{nn}. Consequently, we find the following ordering

$$l_{nn}^{II} > l_{nn}^{I} > l_{nn}^{III} > l_{nn}^{IV} \quad \text{and} \quad l_{sbsb}^{II} > l_{sbsb}^{III} > l_{fsb}^{IV} > l_{sbsb}^{I}. \tag{3.10}$$

To find the highest value of l_{nsb} we stated before that we have to find the lowest value of both filler polymer related wetted surface fractions. For filler type I, we identify the lowest value of l_{fn} by far and for IV the lowest l_{fsb} value. Unfortunately, we find the highest value of l_{fn} at IV and for I the highest l_{fsb} value. Thus, we do not have the same case as before, where we could establish a filler type fulfilling our requirement. However, the overall flocculation tendency of filler type I is lower than for filler type IV. Especially, it is the lowest for I in SBR. Therefore, it is very likely that l_{fn} for filler type I is lower than l_{fsb} for filler type IV. Consequently, we find the highest l_{nsb} value for I and the second highest for IV. Because we already deduced what the lowest value is, we can finally state the last ordering as

$$l_{nsb}^{I} > l_{nsb}^{IV} > l_{nsb}^{III} > l_{nsb}^{II}. \tag{3.11}$$

In this case, we therefore expect filler type I to aggregate again inside SBR, but more centered within this phase. Filler type II will aggregate along the interphase of both polymers, and III and IV will again aggregate inside NR.

In the next sections we can check, whether this argumentation is sufficient and our predictions are correct. Additionally, it is of high interest, if the change in the blend ratio affects the ordering.

3.2.3. 50/50-NR/SBR Blend

The usage of polymer blends has several benefits regarding the properties of the final product, as introductory mentioned. Here, we focus on a 50/50 blend ratio. Different combinations of polymers are, for instance, used for different parts of the tire [1] or parts of a commercial shoe [2]. According to the first source, homogeneity of mixing and cure compatibility are of utmost importance when elastomer blends are considered. Therefore, not every polymer combination is worth to look at. We concentrate on the combination of NR and SBR. We start with a

completely dispersed state and investigate the flocculation behavior of the filler particles. As we are now considering elastomer blends, we contemplate the coagulation behavior of the elastomers themselves in addtion. As both structural developments contribute to several tire properties [6], it is reasonable to extend our former view of pure filler flocculation to the phase morphology of the different polymers. Because no polymer clusters are identified, we need to rely on the TEM pictures and the wetted surface fractions alone. The impact of temperature variation showed the same minor impact as for the single polymers considered in chapter 2 and the development of filler networks is nearly always found for filler volume contents only well above 15%. Therefore, we consider variable flocculation time but mainly concentrate on the variation of the polar part of the surface free energy.

We start with filler types having a dispersive part of the surface free energy of $\gamma_f^d = 20\,m\mathrm{J/m^2}$ incorporated inside the blend. The according aggregation phase diagram with embedded TEM pictures as well as the wetted surface fractions are depicted in Figure 3.5. The top plot, i.e., Figure 3.5a, shows the aggregation phase diagram. It is a plot of the mean size of the aggregates versus the polar part of the surface free energy of the filler particles. Smaller values of q_{agg} represent larger real space values R_{agg} as they are calculated via $R_{agg} = \pi/q_{agg}$. The uncertainties result from the procedure explained in detail in the screening methods section of chapter 2 and are given for the q_{agg} values. The embedded TEM pictures are taken according to the procedure mentioned before. The colored border of the TEM picture corresponds to the number of MC steps indicated by the legend. The two plots at the bottom, i.e., Figures 3.5b and 3.5c, show the corresponding wetted surface fractions for the filler and the polymers, respectively. They are to compared with the TEM pictures and thus, with the red data points in Figure 2.25a. Note that this basic description also applies for all other upcoming plots.

The blue data points show the development of the mean aggregate size after 10^7 MC steps, which is the lowest number we established in order to find any signs of structural development at all. The aggregates are generally in the size region of approx. $20\,n$m, with exception of filler type II, which is smaller. But it also shows a significant uncertainty. Increasing the number of MC steps we see increasing aggregate growth for every filler type, which becomes less pronounced for higher polar fillers. It is to be expected that this trend continues for even higher MC steps, which will be analyzed in more detail later on. The biggest mean aggregate size with approx. $31\,n$m is found for filler type III. The overall course is like a superposition of the individual courses of SBR and NR in the single polymer case (cf. Figures 2.25a and 2.26a), although the surface free energy values of NR are slightly different here. The overall size of the aggregates is generally bigger compared to the single polymer cases.

The wetted surface fractions in Figures 3.5b and 3.5c show that the ordering we deduced in the context of the wetting-envelope - work of adhesion plots is correct.

Before we start to discuss the filler types in their wetted surface fractions in detail, it should be noted that for low surface polarity fillers such as carbon blacks, i.e., in our case filler type I, experimental data is available. The authors in [4] investigated the phase morphology of NR/SBR blends of different ratios, also with a filler volume content of about $\phi = 20\%$. They used different mixing procedures and analyzed the distribution of carbon black within the blend. In the standard mixing procedure the polymers are mixed first. Other ingredients are added subsequently. In the batch mixing procedure the filler particles are first mixed with NR. Thereafter, in a second stage, SBR and other ingredients are added. Based on both

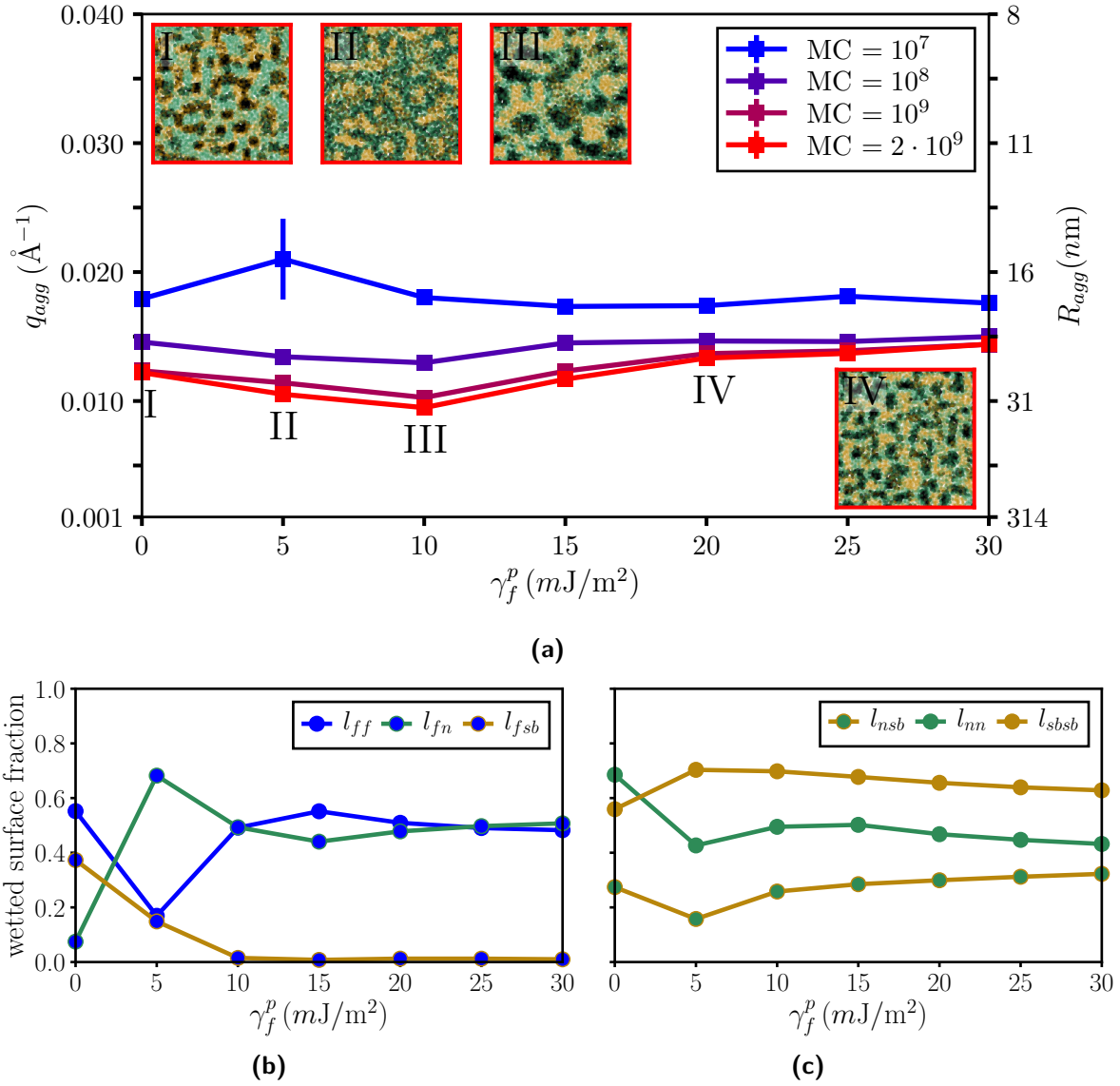

Figure 3.5.: **(a)**: Aggregation phase diagram for filler types with $\gamma_f^d = 20\,mJ/m^2$ incorporated inside a 50/50-NR/SBR blend with $\phi = 0.20$ at $T = 413$ K including embedded TEM pictures for systems indicated by roman numerals. The colored border of each TEM corresponds to the according number of MC steps given in the legend. **(b)**: Wetted surface fractions with the filler in focus. **(c)**: Wetted surface fractions with different polymers in focus. Both wetted surface fractions are corresponding to the TEM pictures in **(a)**.

procedures, it is reasonable to compare our results to theirs using the standard method. Using dynamic-mechanical analysis, they were able to calculate the filler volume fraction in the three phases, i.e., NR, SBR, and the interphase, whereas the latter is defined as the region where both polymers coexist. A blend ratio comparable to ours is 55/45-NR/SBR. More than half, i.e., 51%, of the carbon blacks were found in the SBR phase, more than one fourth, i.e., 26%, inside NR, and the rest, i.e., 24%, in the interphase. In our model, we do not calculate the

filler volume fraction within the different phases explicitly, but the wetted surface fractions contain the same degree of information. The only difference is for the interphase. For that, a discrete value is not available. Nevertheless, when taking the TEM pictures into account we can draw a reasonable conclusion based on the wetted surface fractions between filler and the single polymers.

Starting with the latter, we find that filler type I shows the highest l_{fsb} value and the lowest l_{fn} value, while l_{ff} is the highest of the four filler types we are considering here. When we now take the corresponding TEM picture into account, we see that the filler particles are heavily aggregating inside SBR. They avoid the NR phase almost completely. The only connection between the filler particles and NR is given in the outer regions where SBR and NR are also in contact, i.e., the interphase. Therefore, we find more filler particles in the interphase than in NR itself, which is different from the result obtained experimentally. Nevertheless, compared to the experimental results we also observe that the filler particles tend to aggregate more inside SBR than inside NR or the interphase. In [8], the authors used the same technique to measure the filler distribution as in [4]. However, they focused on a 50/50-NR/SBR blend with different types of NR and SBR. They also found that more than half, i.e., 51%, of the carbon blacks were found in the SBR phase, but now only 12% are found inside NR and 37% in the interphase. This result matches the impressions we obtained from the interphase distribution rather than those from [4].

It should be noted that our types of NR and SBR are also different (from both sources). Because we have no information on the surface free energies of the NRs they used, we are not able to draw any conclusions. For the SBR, this is also true for [4]. Fortunately, for the SBR in [8] we have surface free energy data available [20]. Comparing these values with those we use here, we find that the dispersive and polar parts differ only slightly. This indicates that at least the SBR in the blend is mimicked to the same extent in our model system. Exact values for the surface free energies of the NRs and SBRs used in both sources would allow for a better comparison. Up till now, we can claim that we also see the trend of low polarity fillers flocculating inside SBR and the interphase.

Regarding the polymer morphology of the system containing filler type I, we find that SBR shows a more diluted polymer matrix, whereas NR a dense, more continuous one with large domains within SBR. This is supported by the corresponding wetted surface fractions of the polymers: l_{nn} is higher than l_{sbsb}. Additionally, l_{nsb} is quite high, which is an indicator that one polymer is interspersed inside the other. When we look at the cluster mass distribution the less continuous SBR matrix is also supported. When filler particles form a filler network within a certain polymer phase, it is likely to assume that the corresponding polymer phase also forms a continuous phase. However, not building a filler network must not lead to no polymer phase formation. First of all, we find that all particles are bound into clusters and basically no clusters with a mass less than ten, i.e., far below 0.1%. We do find single large clusters in all simulations, which fulfill the definitions of a filler network. They are slightly above the 50% mass threshold with 56%. In two cases, however, we find that the sizes of the networks are with $R_G < 62$ considerably small. Nevertheless, the TEM pictures support the impression of a filler network in all cases.

Increasing the polar part of the surface free energy, we find filler type II. According to the TEM picture, it shows very high dispersion inside NR and seems to avoid SBR. Some of

the filler particles, however, can still be found in the interphase between both polymers. The low flocculation tendency in NR is also displayed by the corresponding wetted surface fractions l_{fn} and l_{ff}, which show their highest and lowest value for all filler types, respectively. l_{fsb} is also quite low and comparable to the l_{fn} value for type I, where we also find more particles in the interphase than in the corresponding elastomer matrix. Regarding the cluster mass distribution, we now observe less particles bound into clusters, i.e., only about 87%. Of those, 30% are found in clusters with a mass less than ten. Clusters with mass more than one thousand appear rarely and do not contribute significantly to the cluster bound particles. Overall, filler type II behaves akin to the single polymer case of NR in Figure 2.25. A major difference, however, is the mean size of the aggregates. We find a fairly high value of about 30 nm, although every aspect gives the impression of filler dispersion. This is explained due to the spatial confinement of the particles inside one elastomer matrix. From the perspective of SAXS, lots of scatterers are found within a narrow region and are therefore considered an aggregate. This is a good example to display the importance of different screening methods. If we relied on the SAXS data alone, a misleading impression would have concluded. The morphology of the polymers also changed under the influence of the higher polar filler type. We now find that SBR forms a continuous elastomer matrix, whereas NR is more 'diluted', albeit to a much lesser extent as SBR for filler type I. Because this filler type does not flocculate, it is no obstacle for the formation of continuous polymer phases. The individual strains appear broader here, although l_{nn} is here less than l_{sbsb} for I. This is justified by the filler particles incorporated inside NR. They claim lots of the available NR surfaces, diminishing the overall value of l_{nn}. Because both of the elastomer matrices have broad strains, the interphase between both is also diminished as indicated by l_{nsb}.

Filler type III shows a high aggregation tendency inside NR in the TEM picture, which is this time correctly supported by the mean size of the aggregates of about 33 nm. The aggregates are more incorporated inside the NR phase and surrounded by the respective NR particles, resulting in an equal value of the wetted surface fractions of l_{ff} and l_{fn}. This distribution leads to a cut-off of the filler particles to the interphase, which is consequently supported by the close to zero value of l_{fsb}. For the elastomer matrix of the blend we find that SBR forms a more dense, network like structure whereas NR is diluted. The NR particles surround the individual strains of the SBR network and build bridges between them, resulting in increasing values for l_{nn} and l_{nsb}. The cluster mass distribution reveals that about 99% of all filler particles are bound into clusters and that we find a single large cluster building a filler network, comprising 98% of all those particles. The individual, large aggregates inside the branches of the network are, albeit to a lesser extent, akin to those build within pure NR (cf. Figure 2.25). Here, however, the spatial confinement allows the filler particles to form a continuous filler network via thin strains, which was formerly not the case.

The last filler type we consider here, i.e., IV, shows more and smaller aggregates. The filler related wetted surface fractions are only slightly different. Those regarding the single polymers show slightly smaller values and that of the polymer interphase, i.e., l_{nsb}, shows an increase. Looking at the phase morphology of the polymers, we see again a more continuous phase for SBR and a more diluted one for NR. The branches of the SBR phase, however, are now less dense. This is due to the fine filler network inside the NR matrix. It binds less NR particles in a certain area and distributes them more inside the whole elastomer. This allows more NR particles to connect with SBR and consequently diminishes the values of l_{nn} and l_{sbsb}. This

is also supported by the cluster mass distribution. While the amount of cluster bound filler particles is unaffected, the single large cluster comprises less filler particles compared to filler type III. Now, it only contains 92% of those particles.

Beside the experimental data for low polarity fillers, also data for the distribution of silica, i.e., high polarity fillers, is available [9]. Therein, the authors investigated the distribution of silanized silica particles inside a tertiary 50/25/25-NR/SBR/BR blend, i.e., with an additional 25% polybutadiene rubber (BR). They focused on using two different mixing procedures, which we cannot mimic in our model. In both procedures, however, SBR and BR were always mixed beforehand and then blended with NR. In method A they used in-situ silanization inside NR with a following blend with SBR/BR and for method B, it is done vice versa. The results they have obtained for the distribution using the same method as in [4] are, however, generally comparable for both methods. The silica particles incorporated inside the blend are Ultrasil VN3 and Coupsil 8113, a pre-silanized version of Ultrasil VN3 with Si 69. We used both in the potential section of chapter 2 and thus know their surface free energies [15]. Unfortunately, it is not specified if the filler particles were used as a granulate or a powder. In the following, we will stick to the former and therefore find: Ultrasil VN3 ($\gamma_f^d = 18.7\,m\mathrm{J/m^2}$ and $\gamma_f^p = 22.7\,m\mathrm{J/m^2}$) and Coupsil 8113 gran. ($\gamma_f^d = 21.1\,m\mathrm{J/m^2}$ and $\gamma_f^p = 15.8\,m\mathrm{J/m^2}$). As a silane, when using Ultrasil VN3 as the filler, Si 75 was used. In some mixtures it was Si 69 to obtain a better comparison to Coupsil 8113. Although we do not know the exact impact on the surface free energy values when those silanes are applied, we do know from chapter 2 that the dispersive part is increased and the polar part is decreased. Consequently, a reasonable comparison can be established for Ultrasil VN3 silanized with Si 69 with filler type IV ($\gamma_f^d = 20\,m\mathrm{J/m^2}$ and $\gamma_f^p = 20\,m\mathrm{J/m^2}$) and for Coupsil 8113 gran. using the filler particle with $\gamma_f^d = 20\,m\mathrm{J/m^2}$ and $\gamma_f^p = 15\,m\mathrm{J/m^2}$. For both filler types in the simulation, we find that the NR phase is favored over the SBR phase. The affinity is higher for filler type IV in comparison. The experimental data agrees with this behavior. Silanized Ultrasil VN3 is found to 77% (65%) inside NR, whereas Coupsil 8113 is found to 71% (52%) inside NR, where the value in the brackets is for method B. Different from those values is the distribution inside the other phase. For both filler types we do not find any particles inside it. A reason might be due to the blend of SBR and BR used in the experiment or the different mixing procedures. Another possibility is the silane distribution, because we are mimicking homogeneously silanized particles here. This is investigated in more detail in chapter 4.

When we now change the dispersive part to $\gamma_f^d = 30\,m\mathrm{J/m^2}$, we find the aggregation phase diagram with TEM pictures and the corresponding wetted surface fractions shown in Figure 3.6.

The overall course of the data is similar to the $\gamma_f^d = 20\,m\mathrm{J/m^2}$ case, with a difference for filler type II. It now shows smaller mean aggregate sizes and the uncertainty for the blue data point, corresponding to 10^7 MC steps, is also less. The trend for aggregate growth for longer flocculation times, i.e., more MC steps, is now only significant for the first three filler types. The overall mean size of the aggregates is also very similar to the $\gamma_f^d = 20\,m\mathrm{J/m^2}$ case. The formerly impression of superposition of the aggregation phase diagrams of the single polymers is supported here, with the exception of filler type II. The overall ordering deduced in the context of Figure 3.4 is, however, correct.

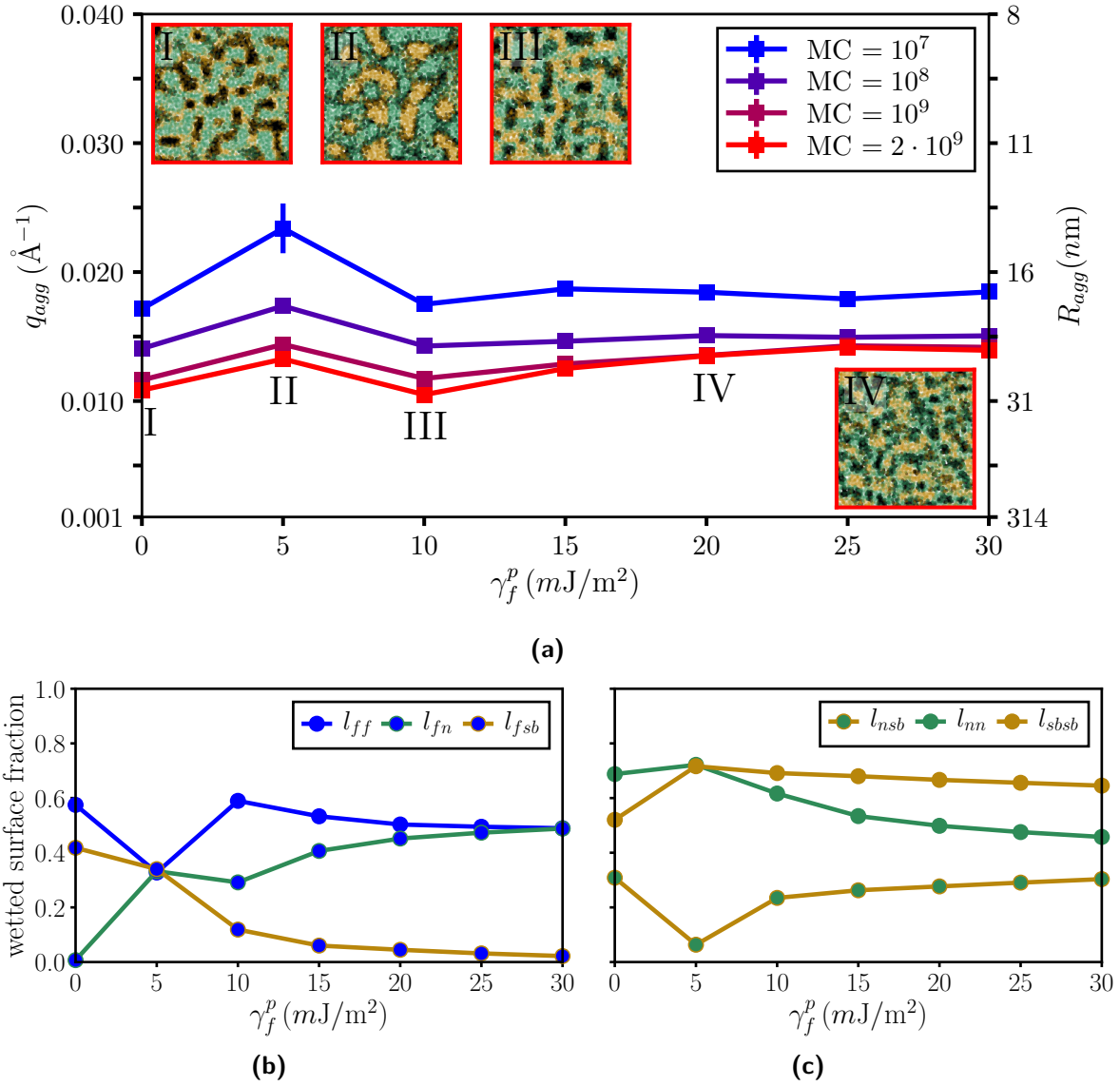

Figure 3.6.: **(a)**: Aggregation phase diagram for filler types with $\gamma_f^d = 30\,mJ/m^2$ incorporated inside a 50/50-NR/SBR blend with $\phi = 0.20$ at $T = 413$ K including embedded TEM pictures for systems indicated by roman numerals. The colored border of each TEM corresponds to the according number of MC steps given in the legend. **(b)**: Wetted surface fractions with the filler in focus. **(c)**: Wetted surface fractions with different polymers in focus. Both wetted surface fractions are corresponding to the TEM pictures in **(a)**.

The TEM picture of filler type I still shows the distinct trend of the filler particles to flocculate inside SBR and to avoid NR as much as possible. Here, however, it is even more pronounced. The filler particles are incorporated inside SBR and it shields them from NR. Consequently, the wetted surface fraction l_{fn} is zero, while l_{fsb} and l_{ff} is very high. As a consequence, we now find no particles in the interphase and have a complete transfer to the SBR matrix. Compared to $\gamma_f^d = 20\,mJ/m^2$, the aggregates look more compact and elongated. Less individ-

ual aggregates can be recognized. Indeed, the cluster mass distribution reveals that we have a percolating filler network. A single large cluster comprising 96% of all filler particles. The polymer morphology shows a very fine and continuous phase built by SBR and one containing thick branches by NR. It appears that SBR is aggregating along the NR branches. In the case of the single SBR polymer, depicted in Figure 2.26, we saw no filler network. Now, due to the fact that a filler network developed, we find a fine and more continuous polymer phase compared to the $\gamma_f^d = 20\,m\mathrm{J/m^2}$ case.

Filler type II shows a very different TEM picture. The filler particles align along the NR/SBR interphase and are partially dispersed in both single elastomer matrices. The filler particles form bridges between both, creating a filler network with small aggregates along its branches. Compared to the structural development of the filler particles inside the single polymers, i.e., Figures 2.25 and 2.26, this is not surprising. In both of the figures the high flocculation tendency leads to a structural development with comparable mean aggregate sizes. In the context of the wetting-envelope - work of adhesion plots in Figure 3.4, we already stated that the similar tendency inside both polymers must lead to an aggregation along the interphase, because none is favored over the other. Indeed, when we take the wetted surface fractions into account, we see that those regarding filler particles are equal. This results in fewer l_{ff} and l_{fsb} and more l_{fn} values compared to filler type I. The cluster mass distribution supports our impression of the filler network. Overall, we find slightly less particles bound into clusters compared to I, i.e., 97%. But still, the single large cluster comprises 93% of all filler particles. The other 7% consist mainly of clusters with a mass less than ten. Those are the dispersed looking particles in the individual polymer phases. The morphology of the polymers shows two almost identical elastomer matrices. Both are forming a continuous phase with dense and wide branches. This is again no surprise, as the basic conditions are very similar to the case of $\gamma_f^d = 20\,m\mathrm{J/m^2}$. In this context, we already stated that the filler particles are the main obstacle for the structural development of the polymers. Here, we again find that they do not form big aggregates and therefore behave as they are 'dispersed'. This does not hinder the structural development of the elastomer matrices, which are in turn able to fully develop a network like structure and permeate each other. The similar values of l_{nn} and l_{sbsb} and the, at the same time, low value of l_{nsb} also support this argumentation.

By further increasing the surface polarity, we are looking at filler type III. We find an increase in the mean size of the aggregates, which is supported by the corresponding TEM picture, since it shows more and bigger structures mostly inside NR. Different from the $\gamma_f^d = 20\,m\mathrm{J/m^2}$ case, the aggregates look more compact and less frayed. A filler network is not recognized. The increase in the filler specific wetted surface fraction, l_{ff}, is in accordance with the larger structures. It is even higher than for $\gamma_f^d = 20\,m\mathrm{J/m^2}$, supporting the impression of more dense structures. As those structures are inside NR, the lower value of l_{fsb} is also as expected. The same is true for the lower value of l_{fn}. The latter can be reasoned by the fact that compact aggregates have a smaller interface than a continuous filler network, like it is in the case of filler type II. Looking at the cluster mass distribution, we indeed find no single large cluster although all particles are bound into clusters. We also find almost no particles in clusters with mass less than ten, i.e., below 1%. More than half of the filler particles are in clusters with a mass greater than one thousand, i.e., about 52%. We even find clusters with masses greater than ten thousand and more. The morphology of the polymers shows a continuous

SBR matrix and a diluted NR matrix. Comparable to the $\gamma_f^d = 20\,mJ/m^2$ case, the NR particles surround the individual SBR strains.

Filler type IV appears to be very similar to the $\gamma_f^d = 20\,mJ/m^2$ case, if we compare the TEM pictures alone. A continuous filler network with small individual aggregates within its branches, is incorporated inside the NR matrix and shielded by it from SBR. Although even the wetted surface fractions of the filler particles look the same, we do find slight differences here. The value of l_{fsb} is higher. The NR particles are therefore not able to shield the filler network completely from the SBR matrix, which appears to be more continuous. The cluster mass distribution reveals a system, where all filler particles are bound into clusters and the single large cluster, which we identify as a filler network, comprises over 80% of those. This is less than in the $\gamma_f^d = 20\,mJ/m^2$ case with 92%. Apart from the more continuous SBR matrix, the blend morphology shows no difference to the other case. The wetted surface fractions of the polymers are supporting this, as they are very similar.

To finish the discussion, we want to look at the mass fractal dimensions of the aggregates of all filler particles. They are conclusively shown in Figure 3.7.

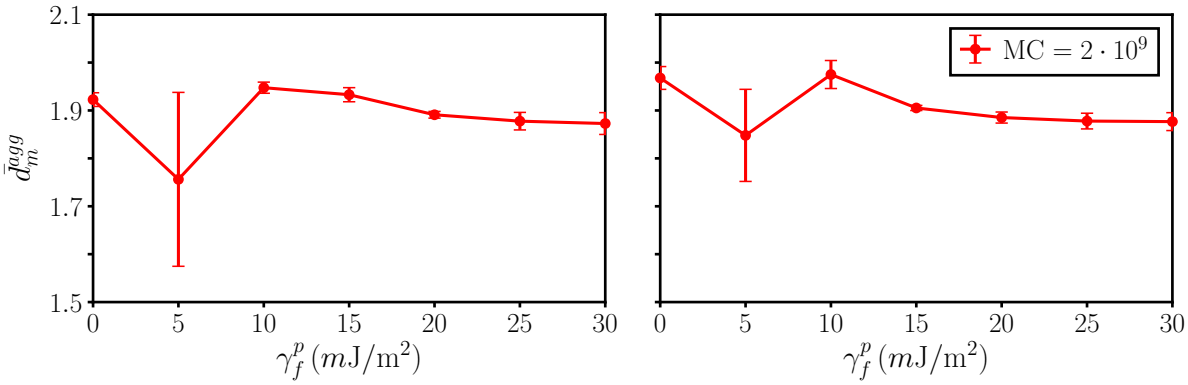

(a) $\gamma_f^d = 20\,mJ/m^2$. **(b)** $\gamma_f^d = 30\,mJ/m^2$.

Figure 3.7.: Comparison of the mean mass fractal dimension of the aggregates, $\bar{d}_m^{agg}$, for filler types with $\gamma_f^d = 20\,mJ/m^2$ and $\gamma_f^d = 30\,mJ/m^2$ inside a 50/50-NR/SBR blend for $\phi = 0.2$ after $2 \cdot 10^9$ MC steps at $T = 413$ K. Note that the filler type with $\gamma_f^p = 5\,mJ/m^2$ show a high uncertainty. In **(a)** the filler types showed no structural development at all and in **(b)** they aggregated along the interphase of both polymers. Note also that the uncertainties are the corresponding mean uncertainties.

Compared to the single polymers, we find that the overall value of $\bar{d}_m^{agg}$ is generally higher for both values of γ_f^d. The variation for the different γ_f^p values is also more distinct. The certainly most pronounced variance is found for $\gamma_f^p = 5\,mJ/m^2$. With $\gamma_f^d = 20\,mJ/m^2$ it showed no structural development at all (cf. Figure 3.5a) and with $\gamma_f^d = 30\,mJ/m^2$, the filler particles aggregated along the polymer interphase (cf. Figure 3.6a). In both cases a sudden increase in the number of occupied boxes is detected by the box-counting algorithm. This consequently yields high uncertainties. The filler types with the three highest surface polarities behave, similar to the single polymers, identical. This is again supported by the same mean size of the aggregates as well as the similar cluster mass distribution. For the non-polar filler type

with $\gamma_f^p = 0\,m\mathrm{J/m^2}$, we noticed in the discussion of the aggregation phase diagrams that the aggregates looked more compact and elongated for $\gamma_f^d = 30\,m\mathrm{J/m^2}$ than for $\gamma_f^d = 20\,m\mathrm{J/m^2}$. We indeed find that the mass fractal dimension is higher for the former dispersive part than for the latter, which supports the more compact impression. With values between 1.7 and 2.1 the aggregates produced here are still in the region of those obtained by kinetic growth processes [21–23] .

Table 3.2 lists all filler types, which were able to form a filler network. For each network, its mean mass, $\bar{m}_n$, and size, $\bar{R}_n$, are listed. Note that the size is calculated from the mean radius of gyration via $\bar{R}_n = \bar{R}_G \cdot R_{si}$ (cf. Equation (2.14)). Note also that all mean values are subject to the uncertainties introductory mentioned. The mean size of the aggregates, $\bar{R}_{agg}$, is obtained from the formerly considered aggregation phase diagrams. Their mean mass fractal dimension, $\bar{d}_m^{agg}$, from Figure 3.7.

Table 3.2.: Filler networks developed by different filler types inside a 50/50-NR/SBR blend for $\phi = 0.20$, $T = 413$ K, and after $2 \cdot 10^9$ MC steps. Listed are their mean mass, $\bar{m}_n$, and size, $\bar{R}_n$, as well as the mean size of their aggregates, $\bar{R}_{agg}$, together with the corresponding mean mass fractal dimension, $\bar{d}_m^{agg}$. Note that the mean size of the filler networks is calculated from the mean radius of gyration via $\bar{R}_n = \bar{R}_G \cdot R_{si}$ (cf. Equation (2.14)). Note also that the mean values are taken over ten simulations and are subject to the uncertainties introductory mentioned. They are listed again for the sake of completeness.

polymer	γ_f^d $[m\mathrm{J/m^2}]$	γ_f^p $[m\mathrm{J/m^2}]$	$\bar{m}_n$ $\pm 5\%$	$\bar{R}_n$ $[n\mathrm{m}]$ $\pm 1\%$	$\bar{R}_{agg}$ $[n\mathrm{m}]$ $\pm 0.5\,n\mathrm{m}$	$\bar{d}_m^{agg}$
50/50-NR/SBR	20	0	234450	505.9	26.3	1.92 ± 0.01
		10	405742	512.1	32.8	1.95 ± 0.01
		15	394569	511.9	26.5	1.93 ± 0.02
		20	382047	512.0	23.9	1.89 ± 0.01
		25	370814	511.3	22.8	1.88 ± 0.02
		30	367468	512.0	22.5	1.87 ± 0.02
	30	0	396763	511.8	29.2	1.97 ± 0.02
		5	380379	511.8	23.0	1.85 ± 0.10
		15	301059	512.3	24.8	1.91 ± 0.01
		20	340549	511.9	23.1	1.89 ± 0.01
		25	351097	512.4	22.8	1.88 ± 0.02
		30	358683	511.7	22.5	1.88 ± 0.02

In the case of $\gamma_f^d = 20\,m\mathrm{J/m^2}$, we find beside the $\gamma_f^p = 0\,m\mathrm{J/m^2}$ filler type that the filler networks become less massive, while their size shows no salience. The size of the aggregates as well as the mass fractal dimension decreases accordingly. While the latter was also observed in both single polymers (cf. Table 2.8), the decrease in mass was not. We even observed a contrary trend, as they became more massive for higher surface polarity. For $\gamma_f^d = 30\,m\mathrm{J/m^2}$,

on the other hand, we do find more massive filler networks for higher surface polarities, although in the beginning a decrease is also observed. For both dispersive parts, however, the filler networks appeared more continuous for higher surface polarity. Similar to the single polymer case, filler networks comparable in mass are more continuous, if they contain smaller aggregates. The corresponding mass fractal dimension of the aggregates is, as well as their size, almost identical to the $\gamma_f^d = 20\,m\mathrm{J/m^2}$ case. The special filler particle, which aggregated along the polymer interphase, i.e., $\gamma_f^p = 5\,m\mathrm{J/m^2}$, shows rather small aggregates with a low mass fractal dimension.

A major difference to the single polymers is found in the number of filler types able to form a network. For both γ_f^d values we formerly only found four networks inside NR and three inside SBR. Here, we find six networks. The blend therefore doubled the possibilities for the formation of filler networks. Filler types with low to intermediate surface polarity, i.e., $\gamma_f^p < 20\,m\mathrm{J/m^2}$, are now able to form networks. Thus, the polymer blend leads to an enhancement of the filler network building properties.

Altogether, we see that filler particles inside 50/50-NR/SBR blends usually show a distinct affinity towards one of the two polymers. This is also seen in various experiments in terms of filler distribution [4, 8, 9]. Low polarity fillers such as carbon black, favor SBR and high polarity fillers such as silica, favor NR. It is assumed that the reason for the affinity of carbon black towards SBR is found in the interaction between itself and the polymer [7, 24]. Because we focus on this interaction in our model and also find this affinity, we can agree with this assumption. Additionally, we can partially agree, i.e., in the $\gamma_f^d = 20\,m\mathrm{J/m^2}$ case, with the affinity of carbon black for the interphase, which was found in the aforementioned sources. Regarding silica, experimental values considering the interphase were not obtainable. We do, however, find that their affinity for the interphase can be very high, i.e., filler type II in the $\gamma_f^d = 30\,m\mathrm{J/m^2}$ case. Overall, we find that in our simulation the extent of filler-polymer affinity is mostly much higher than in experiments. As we saw in the respective discussions of filler distribution, the mixing procedure shows to have a high impact. This impact seems to be heavily depending on the polymers in use [12]. This might be a reason for the discrepancies we find in our model. Another possibility is the usage of additional ingredients, which we are not able to mimic.

The favoring of a distinct polymer phase, subsequently leads to an increase of the corresponding relative filler volume fraction. This in turn enables the filler particles to form networks more likely, which supports the impression we obtained in the context of the variation of the filler content in single polymers. This also explains the higher mass fractal dimensions of the aggregates. We already noticed that for single polymers higher filler volume content generally leads to higher mass fractal dimension of the aggregates. However, for filler network formation a certain threshold must be surpassed, which was not reached for every filler type. An example is filler type II in the $\gamma_f^d = 20\,m\mathrm{J/m^2}$ case. Therefore, the investigation of higher relative filler volume fractions is reasonable. This is achieved in two ways: By alternating the blend ratio, which we do in the next section, and by increasing the overall filler volume content, which we do thereafter.

The polymer morphology is affected by the filler flocculation. For instance, a lower filler flocculation, like for filler type II in the $\gamma_f^d = 20\,m\mathrm{J/m^2}$ case, results in a good individual elastomer development, where both form continuous phases permeating each other. A higher

flocculation tendency, on the other hand, seems to deteriorate the building of the corresponding continuous polymer phase (e.g., filler type I in the $\gamma_f^d = 20\,m\mathrm{J/m^2}$ case or III in the $\gamma_f^d = 30\,m\mathrm{J/m^2}$ case). A special case is certainly filler type II in the $\gamma_f^d = 30\,m\mathrm{J/m^2}$ case, which aggregated along the interphase. The polymer morphology was similar to the $\gamma_f^d = 20\,m\mathrm{J/m^2}$ case, i.e., we find continuous polymer phases permeating each other, although we deal with high flocculation tendency. The main obstacle for continuous polymer phases seems to be found for heavily aggregating filler particles, not forming a continuous network.

3.2.4. 70/30-NR/SBR Blend

Now we change the blend ratio to 70/30-NR/SBR and investigate again the impact of flocculation time, i.e., number of MC steps, as well as the variation of the surface free energies. Beside the impact on the formation of filler networks and the mass fractal dimension of the aggregates, it is of high interest, if the blend ratio will affect the ordering we derived for the wetted surface fractions in the context of Figures 3.3 and 3.4. The overall procedure is the same as for the 50/50-NR/SBR blend. We start with $\gamma_f^d = 20\,m\mathrm{J/m^2}$, which is depicted in Figure 3.8.

The overall course of the data resembles the course of single NR (cf. Figure 2.25) more than a superposition of NR and SBR, as we observed it for the other blend ratio. An eminent difference is therefore found for filler type II. The mean size of its aggregates is only $R_{agg} \approx 12\,n\mathrm{m}$, which accounts for a dispersed state. We know from the other ratio that filler type II indeed shows very high dispersion inside NR. There, the mean size of the aggregate was, however, misleading. Due to the now bigger NR phase it seems that the dispersion is also correctly displayed by the mean aggregate size. Filler type III develops bigger aggregates in comparison, i.e., $R_{agg} \approx 38\,n\mathrm{m}$ versus $R_{agg} \approx 33\,n\mathrm{m}$. This is still below the value obtained in single NR with $R_{agg} \approx 53\,n\mathrm{m}$, but the trend for the formation of bigger aggregates is discernible. The other two filler types, i.e., I and IV, show no difference in their mean aggregate sizes compared to the other blend.

Taking the wetted surface fractions into account, i.e., Figures 3.8b and 3.8c, we find that the ordering is unaffected by the change of the blend ratio. As expected, all wetted surface fractions regarding NR are elevated, whereas those regarding SBR are diminished. This becomes less pronounced for higher filler surface polarity.

Looking at the TEM picture of filler type I, we find that we still have the tendency of the filler particle to flocculate inside SBR. Less from this elastomer matrix can be seen in the TEM, because the same amount of filler occupies a smaller phase. This leads to more l_{fn} contacts, mainly found in the outer regions where both polymers connect, i.e., the interphase. Consequently, the value of l_{fsb} is diminished, albeit only slightly. l_{ff}, on the other hand, is basically unaffected. The polymer related surface fractions show a more significant change. l_{sbsb} is greatly reduced and l_{nn} is increased. l_{nsb} is only merely reduced. Looking at the polymer morphology, we find that the SBR particles aggregate along the outside of the NR branches, where they form a very fine continuous phase. This allows the filler particles to form a network within the SBR matrix. They comprise 72% of all filler particles, because they are all cluster bound. The others are almost completely found in clusters with a mass

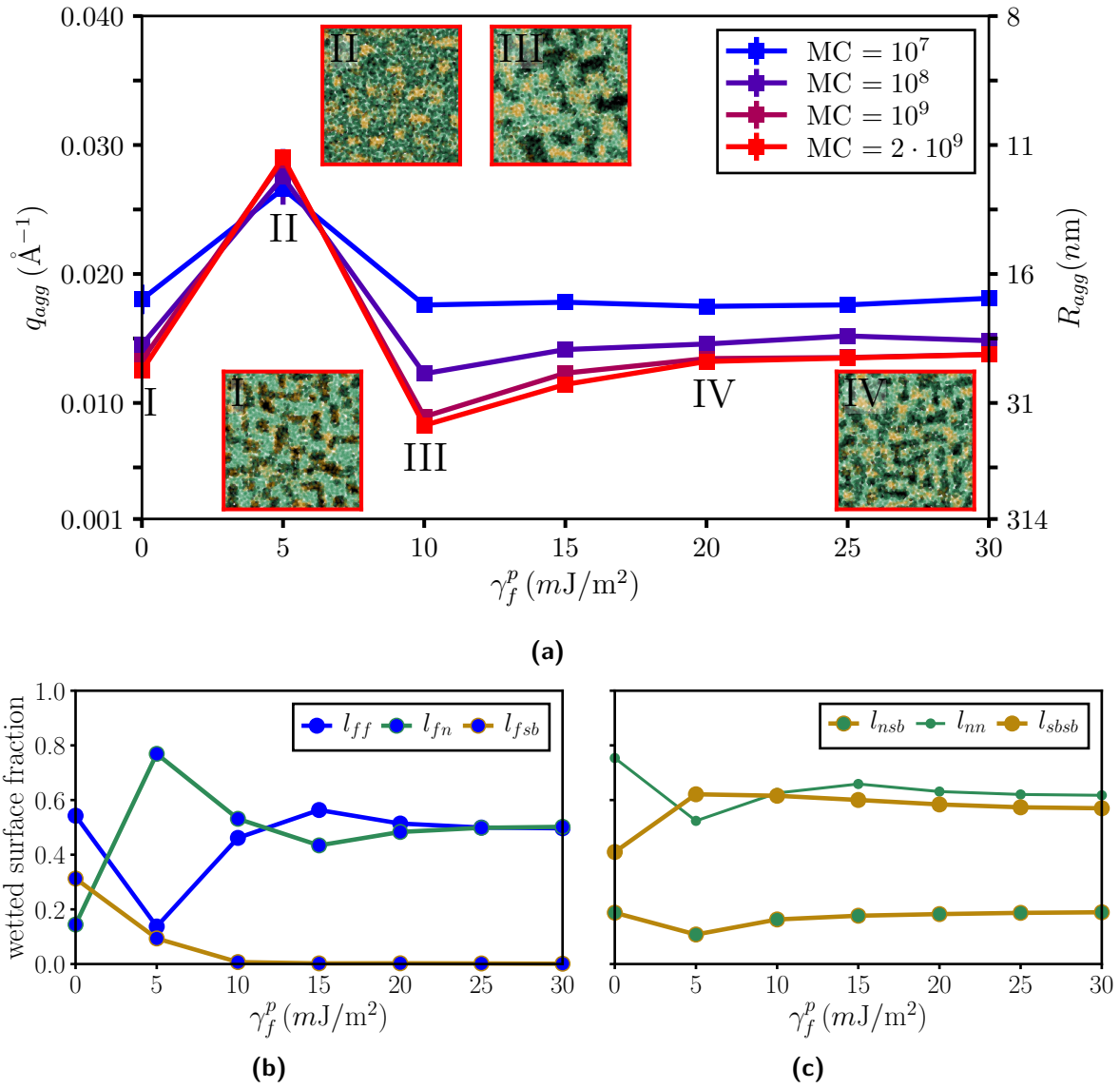

Figure 3.8.: (a): Aggregation phase diagram for filler particles with $\gamma_f^d = 20\,mJ/m^2$ incorporated inside a 70/30-NR/SBR blend with $\phi = 0.20$ at $T = 413$ K including embedded TEM pictures for systems indicated by roman numerals. The colored border of each TEM corresponds to the according number of MC steps given in the legend. **(b)**: Wetted surface fractions with the filler in focus. **(c)**: Wetted surface fractions with different polymers in focus. Both wetted surface fractions are corresponding to the TEM pictures in **(a)**.

greater than ten. The reduction of the filler favored polymer phase consequently leads to a higher relative filler volume fraction. This, in turn, allows for a more likely formation of a filler network.

The TEM picture of filler type II shows the same behavior as in the 50/50 case. We see dispersion inside NR and avoidance of the SBR phase. Consequently, l_{fn} is very high, whereas

l_{ff} and l_{fsb} are quite low. The polymer morphology reveals that NR builds a continuous polymer phase. No dilution or phase building is found for SBR. We instead find several big domains, basically SBR aggregates, inside NR. This reduces the available interface for both the filler and NR, which consequently leads to a low l_{nsb} value. The low value of l_{nn} issues from the high l_{fn} value. The cluster mass distribution supports the impression of dispersion. More than 50000 small clusters, each with a mass below one hundred, are found. As a comparison: filler type I had only about 1000 clusters. Only 80% of all particles are bound into clusters and of those, 50% have a mass less than ten.

For filler type III, we see big structures connected via small strains – identical to the 50/50 case. The aggregation of filler particles inside NR consequently leads to a decrease of l_{fn} and an increase of l_{ff}. The polymer morphology shows again SBR aggregates embedded inside the continuous NR matrix. Different from filler type II, however, the NR matrix completely surrounds the SBR aggregates. This leads to an increase of l_{nsb}. Because of this, the filler particles are shielded from SBR, resulting in a close to zero value of l_{fsb}. The decrease of l_{fn} leads to an increase of l_{nn}. The value of l_{sbsb} is only merely affected. The cluster mass distribution shows again a single large cluster, permeating the NR matrix. It comprises 90% of all cluster bound particles, which make out 97% of all available particles. We still find several smaller clusters with a mass less than ten, holding 4% of the cluster bound particles. The number of clusters is, compared to the 50/50 case, about three times higher, i.e., about 1500 vs. 5000 clusters. For the single NR case we did not find a network at all and the number of clusters was again about three times higher compared to the 70/30 ratio, i.e., about 15000. Altogether, we find that increasing the NR phase for this filler particle leads to a breakdown of the filler network. The relative filler volume fraction is here, however, still high enough for filler network creation.

Looking at the TEM picture of filler type IV, we still find a filler network. However, it looks less acute compared to the 50/50 blend ratio. The filler particles seem to be more dispersed inside the NR matrix. The wetted surface fractions regarding the filler surface show, however, no significant difference. The same is true for the polymer related ones, if we regard the higher NR content of the blend. The polymer morphology shows that NR is now more diluted. SBR aggregates again inside NR, but this time the NR particles can additionally be found inside the SBR aggregates. This leads to an increase of l_{nsb} and to a decrease of l_{nn} and l_{sbsb}. Regarding the cluster mass distribution the number of cluster bound particles is at the same level as for filler type I, i.e., we find no free roaming particles. The impression of a less acute filler network is confirmed. The single large cluster comprises only 70% of the filler particles compared to the 92% for the 50/50 ratio. The other 30% are, however, not found in clusters with a mass less than ten. They are rather found in intermediate clusters with a mass up to one thousand. This supports the presumption that aggregation without filler network formation directly affects the continuity of the polymer phase.

The variation of the blend ratio for the $\gamma_f^d = 20\,m\mathrm{J/m^2}$ case shows that increasing the relative filler volume content in a specific polymer phase increases the possibility to form a network. Decreasing, on the other hand, lowers it. An interesting case is still filler type I. Inside the single SBR it showed no tendency to form a filler network whatsoever, but inside single NR it was able to form one. Blending both polymers, the filler particles do not stay inside NR, where a network formation is easily possible. Instead, they immerse inside SBR and form a

network therein. In order to do so, the relative volume fraction inside SBR only has to be high enough.

Changing the dispersive part to $\gamma_f^d = 30\,mJ/m^2$, we find the aggregation phase diagram in Figure 3.9a and the corresponding wetted surface fractions in Figures 3.9b and 3.9c.

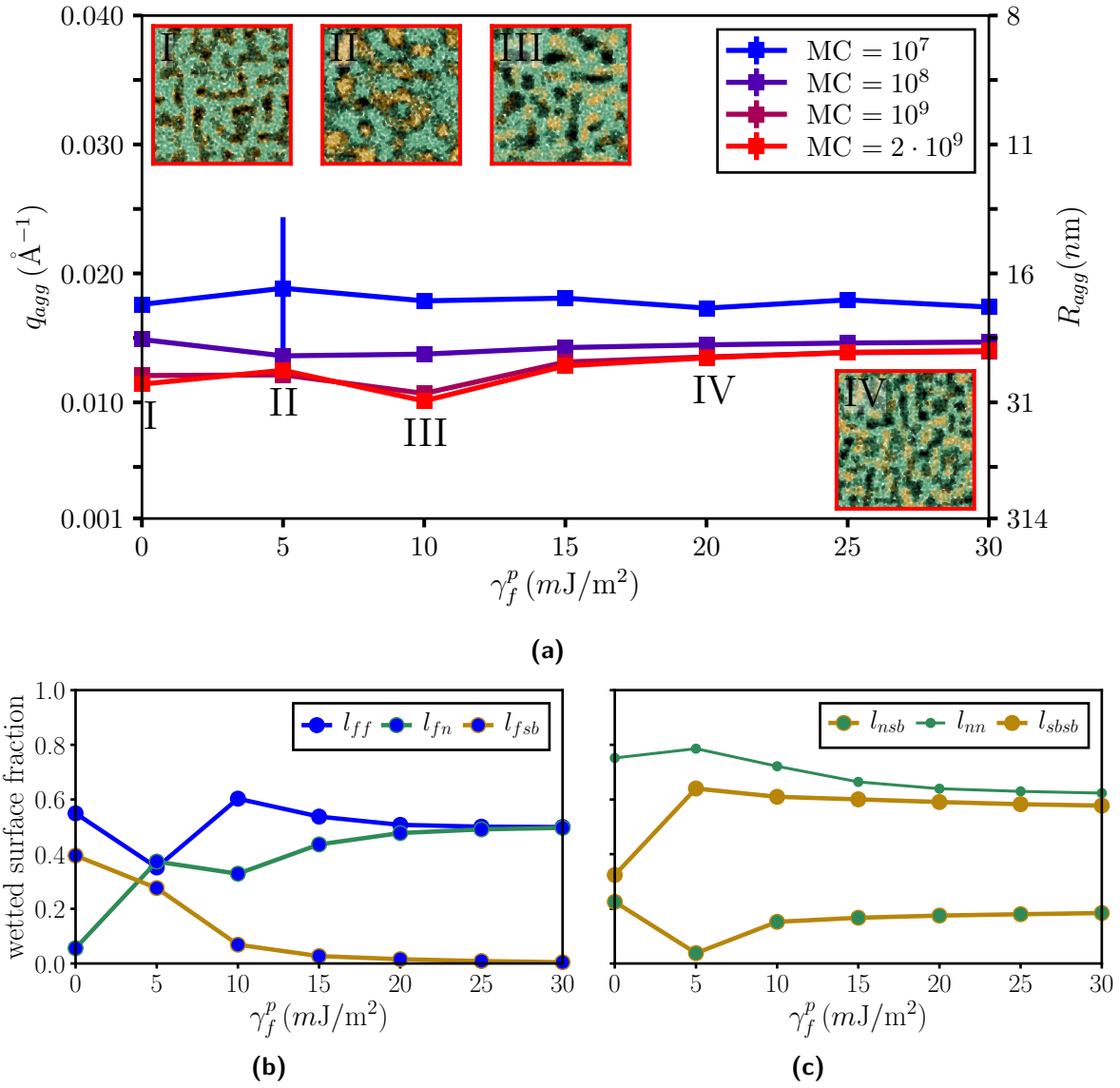

Figure 3.9.: (a): Aggregation phase diagram for filler types with $\gamma_f^d = 30\,mJ/m^2$ incorporated inside a 70/30-NR/SBR blend with $\phi = 0.20$ at $T = 413$ K including embedded TEM pictures for systems indicated by roman numerals. The colored border of each TEM corresponds to the according number of MC steps given in the legend. **(b)**: Wetted surface fractions with the filler in focus. **(c)**: Wetted surface fractions with different polymers in focus. Both wetted surface fractions are corresponding to the TEM pictures in **(a)**.

Compared to the 50/50 blend, we detect only minor differences for the mean aggregate sizes. The size for filler type II is slightly increased and the uncertainty for the lowest number of MC steps considered here is higher. The ongoing growth for higher MC steps for the filler types with the three lowest surface polarities, is less pronounced. The impression of a superposition of single NR and SBR is supported again. The ordering of the wetted surface fractions is not affected, although, due to the higher NR content, the overall values are different.

Filler type I shows a continuous filler network, which is incorporated inside SBR. We see even less of the SBR compared to $\gamma_f^d = 20\,m\mathrm{J/m^2}$, which is supported by the corresponding higher wetted surface fraction l_{fsb} and lower l_{fn}. The value of l_{ff} is unaffected. This behavior can be justified by looking at the polymer morphology and the corresponding wetted surface fractions. l_{sbsb} is lower and, although not displayed here, the value of l_{sbn} is now even higher, i.e., the surfaces of SBR are mostly wetted by NR. Indeed, SBR forms in the same fashion as the $\gamma_f^d = 20\,m\mathrm{J/m^2}$ case a fine continuous phase along the branches of NR, but here it is even finer and only a few particle layers thick. This shields the NR from the filler particles more, resulting in the lower l_{fn} value and higher l_{fsb} value. Consequently, we find less particles in the interphase and a very fine filler network embedded inside the SBR matrix, comprising 99% of all filler particles. This is even higher than the 50/50 case with 96%.

The tendency for filler type II to aggregate along the interphase of the polymers is still discernible, albeit we find the layers to be broader than for the 50/50 case. This is in accordance with the slightly higher mean size of the aggregates, i.e., $R_{agg} \approx 25$ compared to $R_{agg} \approx 23$. A broader filler layer in the interphase displaces the polymer particles, leading to a very low value of l_{nsb} and consequently high values of l_{sbsb} and l_{nn}. Because the filler particles form bridges between the SBR domains, their contact with respect to NR is unaffected, i.e., l_{fn} shows to be similar to the 50/50 case. The morphology of SBR shows several large aggregates embedded inside a distinct NR phase, not able to form a continuous phase on its own. The filler network formed along the interphase comprises more cluster bound particles than the 50/50 blend, i.e., 96% versus 93%, while their amount is equally high with 97% of all filler particles.

The aggregation of filler type III is comparable to the 50/50 blend ratio. We find several big aggregates with no connection via small strains like in the $\gamma_f^d = 20\,m\mathrm{J/m^2}$ case and therefore, no filler network. Even the wetted surface fractions of the filler related surfaces are very similar. A real difference is only found for the polymer morphology, as the continuous SBR phase is now broken down into several aggregates. Also, the cluster mass distribution is basically identical.

Filler type IV appears to behave similarly to the $\gamma_f^d = 20\,m\mathrm{J/m^2}$ case. A network is still discernible, albeit less acute and with more filler particles dispersed inside NR. Comparing the wetted surface fractions to that case, we find no difference. This also holds for a comparison to the 50/50 blend. A change in the polymer morphology is not found compared to the $\gamma_f^d = 20\,m\mathrm{J/m^2}$ case. The cluster mass distribution, however, reveals some differences. We find even less filler particles comprised inside the single large cluster, i.e., only about 63%. For $\gamma_f^d = 20\,m\mathrm{J/m^2}$, we still found 70% and for the 50/50 blend with $\gamma_f^d = 30\,m\mathrm{J/m^2}$ 82%. The biggest network was found for 50/50 and $\gamma_f^d = 20\,m\mathrm{J/m^2}$ with over 90%. Thus, for this surface polarity, the breakdown of the filler network can be achieved by altering the blend ratio, as well as the dispersive part of the surface free energy of the filler particles.

The change of the dispersive part showed the same impact as for the other blend ratio. Comparing systems with equal dispersive part but different blend ratio showed that the trends in the 50/50 case are enhanced. The same source we used in the discussion of the 50/50 blend ratio for filler type I, i.e., [4], also contains values for a 70/30-NR/SBR blend ratio. For that case, the authors found a filler distribution, which is more or less evenly distributed inside the three phases: NR with 36%, SBR with 32%, and the interphase with 32%. This means less particles inside SBR and more inside NR and the interphase, compared to the 50/50 blend. In the discussion of this blend, we already found a discrepancy to their values. For $\gamma_f^d = 20\,mJ/m^2$, the amount of particles in the interphase was higher in our simulation, whereas for $\gamma_f^d = 30\,mJ/m^2$ it was zero, and every filler particle was found inside SBR. While we still not find a significant amount of filler inside NR for the 70/30 blend, we do find that the interphase value is higher. We therefore have a comparable trend, which is also seen in the experiment (at least for the $\gamma_f^d = 20\,mJ/m^2$ case).

We finish the discussion of the 70/30 blend with the investigation of the mass fractal dimension of the aggregates depicted in Figure 3.10.

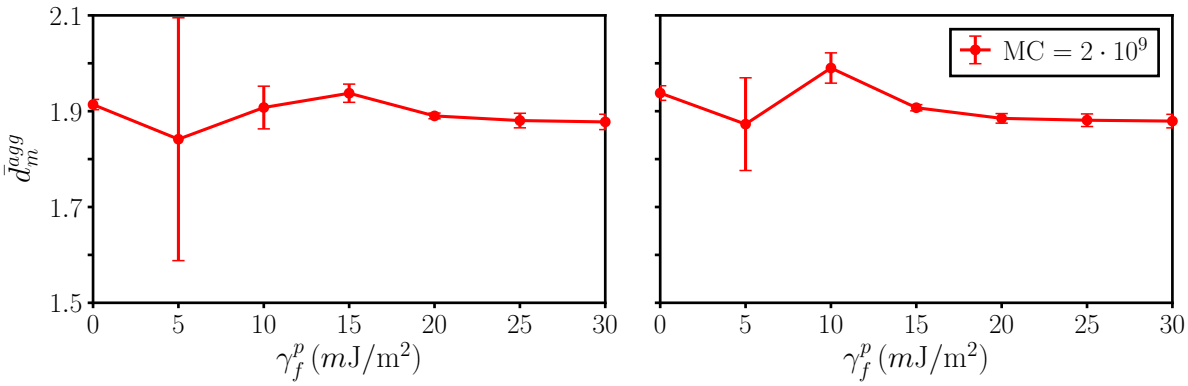

(a) $\gamma_f^d = 20\,mJ/m^2$. **(b)** $\gamma_f^d = 30\,mJ/m^2$.

Figure 3.10.: Comparison of the mean mass fractal dimension of the aggregates, $\bar{d}_m^{agg}$, for filler types with $\gamma_f^d = 20\,mJ/m^2$ and $\gamma_f^d = 30\,mJ/m^2$ inside a 70/30-NR/SBR blend for $\phi = 0.2$ after $2 \cdot 10^9$ MC steps at $T = 413$ K. Note that the filler type with $\gamma_f^p = 5\,mJ/m^2$ show a high uncertainty. In **(a)** the filler types showed no structural development at all and in **(b)** they showed a tendency to aggregate along the interphase of both polymers. Note also that the uncertainties are the corresponding mean uncertainties.

Compared to the single polymers, we find that the overall value of $\bar{d}_m^{agg}$ is again generally higher for both values of γ_f^d. Compared to the 50/50 blend ratio, we find that the case with $\gamma_f^d = 20\,mJ/m^2$ is different. Now, $\gamma_f^p = 15\,mJ/m^2$ has the highest mass fractal dimension instead of $\gamma_f^p = 10\,mJ/m^2$. For $\gamma_f^d = 30\,mJ/m^2$, on the other hand, we find it to be very similar. Only the non-polar filler type has a slightly lower value in comparison. The uncertainty of the values is again most pronounced for $\gamma_f^p = 5\,mJ/m^2$. Due to the higher dispersion for $\gamma_f^d = 20\,mJ/m^2$ in comparison to the 50/50 blend ratio it is even more pronounced. The filler types with the three highest surface polarities behave, in the same way as the single polymers

and the 50/50 blend ratio, very similar. This is again supported by the similar mean size of the aggregates, as well as the cluster mass distribution.

For systems developing a filler network, Table 3.3 lists their mean values of mass and size as well as the mean aggregate size values and the corresponding mass fractal dimension. Note that the size is calculated from the radius of gyration via $\bar{R}_n = \bar{R}_G \cdot R_{si}$ (cf. Equation (2.14)). Note also that all mean values are subject to the uncertainties introductory mentioned. The size of the aggregates is taken from the formerly considered aggregation phase diagrams, their mean mass fractal dimension from Figure 3.10.

Table 3.3.: Filler networks developed by different filler types inside a 70/30-NR/SBR blend for $\phi = 0.20$, $T = 413$ K, and after $2 \cdot 10^9$ MC steps. Listed are their mean mass, $\bar{m}_n$, and size, $\bar{R}_n$, as well as the mean size of their aggregates, $\bar{R}_{agg}$, together with the corresponding mean mass fractal dimension, $\bar{d}_m^{agg}$. Note that the mean size of the filler networks is calculated from the mean radius of gyration via $\bar{R}_n = \bar{R}_G \cdot R_{si}$ (cf. Equation (2.14)). Note also that the mean values are taken over ten simulations and are subject to the uncertainties introductory mentioned. They are listed again for the sake of completeness. A special case is marked with *. Here, not for every simulation a filler network developed. The values are thus means for the cases when it happened.

polymer	γ_f^d [mJ/m^2]	γ_f^p [mJ/m^2]	$\bar{m}_n$ ±5%	$\bar{R}_n$ [nm] ±1%	$\bar{R}_{agg}$ [nm] ±0.5 nm	$\bar{d}_m^{agg}$
70/30-NR/SBR	20	0	302144	512.5	25.5	1.91 ± 0.01
		10	371990	511.3	37.8	1.91 ± 0.05
		15	280557	514.3	27.1	1.94 ± 0.02
		20	293809	510.2	23.5	1.89 ± 0.01
		25	287080	511.5	22.6	1.88 ± 0.02
		30	284653	511.9	22.5	1.88 ± 0.02
	30	0	415316	512.0	29.2	1.94 ± 0.02
		5	388553	512.0	23.0	1.87 ± 0.10
		15*	213690	515.3	24.7	1.91 ± 0.01
		20	267163	513.6	23.2	1.89 ± 0.01
		25	277236	512.8	22.6	1.88 ± 0.01
		30	276857	512.0	22.2	1.88 ± 0.01

A conspicuous difference to the 50/50 blend ratio in Table 3.2 is given for the mass of the filler networks. Almost all networks inside the NR matrix contain considerably less filler particles. The one along the NR/SBR interphase, i.e., $\gamma_f^d = 30\,m\mathrm{J/m^2}$ and $\gamma_f^p = 5\,m\mathrm{J/m^2}$ behaves similarly. Those built inside SBR by filler type I, i.e., $\gamma_f^p = 0\,m\mathrm{J/m^2}$, contain more filler particles than in the 50/50 blend ratio. For both dispersive parts, the biggest clusters with respect to size are found for $\gamma_f^p = 15\,m\mathrm{J/m^2}$, while at the same time they are least massive. A possible explanation for this is that at a certain mass the individual branches of the filler

network connect with one another, which consequently reduces the size of the network. The apparent continuity of the filler networks is again linked to the smaller size of the aggregates, which is achieved for higher surface polarity.

We conclusively find that the presumption of filler network creation being linked to a certain relative filler volume fraction inside the polymer phase where the filler particles flocculate, is correct so far. To investigate this further, we increase the overall amount of filler to $\phi = 25\%$ and compare both blend ratios with one another in the next part. Because we find that the impact on the wetted surface fractions is rather minor (the extent is comparable to the single polymer case) we omit their consideration in the following. It is noted that their ordering is unaffected by altering the filler volume content.

3.2.5. Impact of Higher Filler Volume Content

For a better comparison of the blends, we plot the aggregation phase diagrams obtained by the same value of γ_f^d. Afterwards, we compare the mass fractal dimension of the aggregates. We start with filler types with $\gamma_f^d = 20\,m\mathrm{J/m}^2$, depicted in Figure 3.11. The plot in the top shows the 50/50-NR/SBR blend ratio and the bottom the 70/30-NR/SBR case. For the 50/50 case, the course of the data is comparable to the lower filler volume content.

While this is also mainly the case for 70/30, we find a distinctive dependency on the number of MC steps for filler type II. For the lowest number considered here, i.e., 10^7 MC steps, the value indicates a dispersed system. After 10^8 steps, the value for the mean size of the aggregates gets even lower, which indicates further dispersion of the filler particles. Then, after 10^9 steps, the value suddenly increases and displays aggregates with almost three times the size as before. More steps increase this value only slightly. Taking the corresponding TEM picture into account, no aggregates, structures, or networks are, however, discernible. The system looks dispersed and, beside the polymer morphology, identical to the 50/50 case in the top of Figure 3.11. The argumentation about the spatial confinement and relative filler volume fraction is therefore confirmed here. This is also true for the 50/50 ratio. For that, we find that the relative filler volume fraction of filler type II inside NR has finally reached the threshold for filler network formation. The cluster mass distribution reveals that now 93% of all filler particles are cluster bound. This is higher than for the 70/30 case with about 88% and definitely higher than for the lower filler content, $\phi = 0.2$, with 80%. Of those 93%, 65% are found inside the single large cluster. The rest is found in clusters with a mass less than one thousand. Under the condition that (almost) all filler particles are incorporated inside a single polymer phase we can easily calculate the respective relative filler volume fraction via

$$\tilde{\phi}_f^i = \phi/\eta_i, \tag{3.12}$$

where ϕ is the absolute filler volume fraction and η_i the fraction of polymer i, with i being NR or SBR. The combination resulting in the filler network for filler type II has a value of $\tilde{\phi}_f^{NR} = 0.5$. This is quite high and well above the percolation threshold for a cubic lattice with $p_c = 0.31160768(15)$ [25] . However, this comparison is a little keen. Although we are

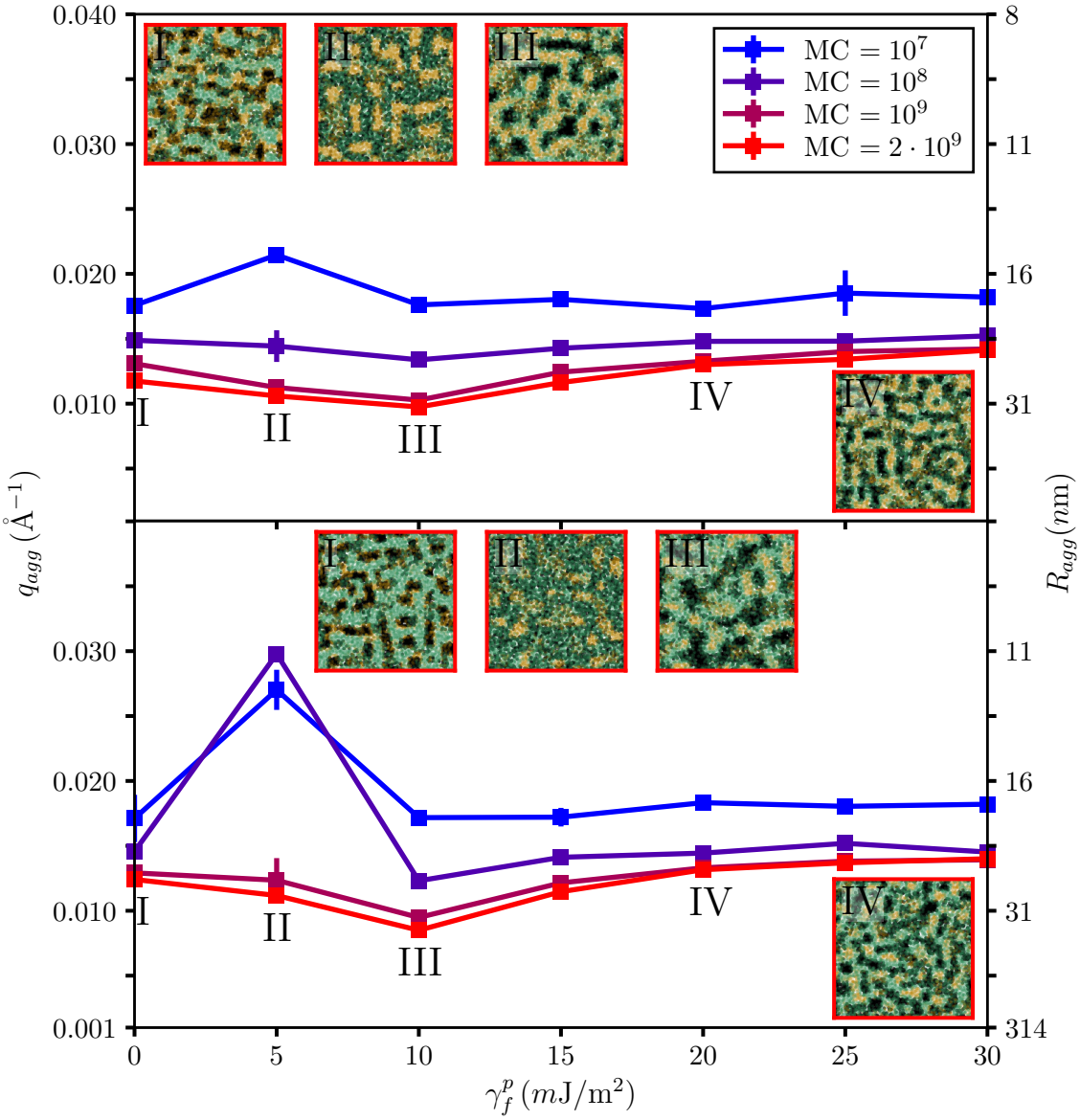

Figure 3.11.: Aggregation phase diagrams for filler types with $\gamma_f^d = 20\,mJ/m^2$ incorporated in 50/50-NR/SBR (top) and 70/30-NR/SBR (bottom) with $\phi = 0.25$ and $T = 413$ K. Embedded TEM pictures are taken for systems indicated by roman numerals. The colored border of each TEM corresponds to the according number of MC steps given in the legend.

dealing with a cubic lattice, the NR phase forms a complete different subsystem inside that lattice. In turn, the filler particles cannot arrange freely inside the original lattice.

The TEM pictures of filler type I, III, and IV are comparable to the case of lower ϕ. We see no difference in structural development. However, the density of the structures appears to be higher, because the areas are darker. Their corresponding cluster mass distributions reveal

that we still find smaller filler networks in the 70/30 blend, which is, after the discussion of the relative filler volume fraction, as expected. This impact, however, becomes less pronounced for higher surface polarity and therefore follows the impression we obtained from the case of $\phi = 0.2$. An interesting case is again found for filler type I, which forms aggregates completely inside SBR. We saw before that in the 50/50 blend no filler network developed. In that case we had a relative filler volume fraction of $\tilde{\phi}_f^{SBR} = 0.4$. For the 70/30 blend this is increased to $\tilde{\phi}_f^{SBR} = 0.67$ and the threshold is surpassed. It turns out that, akin to the case of filler type II inside NR, a value of $\tilde{\phi}_f^{SBR} = 0.5$ is necessary for filler network formation, because we find a filler network for the 50/50 blend with $\phi = 0.25$.

Regarding the amount of clusters for all values of γ_f^p, we always find more clusters for the 70/30 blend than for the 50/50 blend. The most pronounced case is again found for filler type II and that for all of the four combinations considered so far. We find for $\phi = 0.2$ the most clusters: more than 55000 in 70/30 and less than 40000 in 50/50. For $\phi = 0.25$: more than 40000 in 70/30 and about 20000 in 50/50. The increasing relative filler volume fraction in NR therefore merges the smaller clusters into a filler network.

Figure 3.12 depicts the case, when the dispersive part is increased to $\gamma_f^d = 30\,m\mathrm{J/m^2}$. The course of the mean size of the aggregates is again very similar for both blend ratios. The biggest difference can be found again for filler type II in the 70/30 case. Its structures now contain the biggest aggregates of all filler particles considered here.

The corresponding TEM picture of filler type I shows the same structural behavior as for the $\phi = 0.2$ case, only with a higher filler loading in the SBR phase. Filler type II also follows the trends we saw in the lower ϕ case, i.e., the aggregation along the NR/SBR interphase. The only difference we find is for the 'bridges' between the SBR domains. They are now thicker when compared within the same blend ratio. This is a result of limited space of the available polymer interphase. During the simulation, the filler particles quickly assemble inside the interphase. When this space is depleted, the remaining particles aggregate with those in the interphase. This leads to particles inside both polymer domains. The effect is stronger for the 70/30 ratio due to the smaller interphase. The aggregation leads to a more compact filler distribution and consequently to an increased mean size of the aggregates. The increase in the filler volume content leads, for the first time, to the formation of a filler network for filler type III. While it is no surprise for the 50/50 blend ratio, because the relative filler volume fraction is now $\tilde{\phi}_f^{NR} = 0.5$ and therefore higher than for both blend ratios with $\phi = 0.2$, it is one for the 70/30 blend ratio. Therein, the relative filler volume fraction is only $\tilde{\phi}_f^{NR} \approx 0.36$, while for the 50/50 blend with $\phi = 0.2$ we already had $\tilde{\phi}_f^{NR} = 0.4$. The only possible explanation for the formation of a filler network at lower relative filler volume fraction, must be the polymer morphology. Changing the blend ratio from 50/50 to 70/30 leads to a breakdown of the continuous SBR phase. Consequently, the NR matrix is more continuous and the formation of a filler network is less hampered. Filler type IV does not change under higher filler loading. The filler network is still discernible in the TEM picture and the mean size of the aggregates is also unaffected.

The observation we made for the $\gamma_f^d = 20\,m\mathrm{J/m^2}$ case regarding the amount of clusters, also holds for $\gamma_f^d = 30\,m\mathrm{J/m^2}$, albeit only for the filler types with higher surface polarity. For γ_f^p up to $10\,m\mathrm{J/m^2}$ it is the other way around and most pronounced for filler type II.

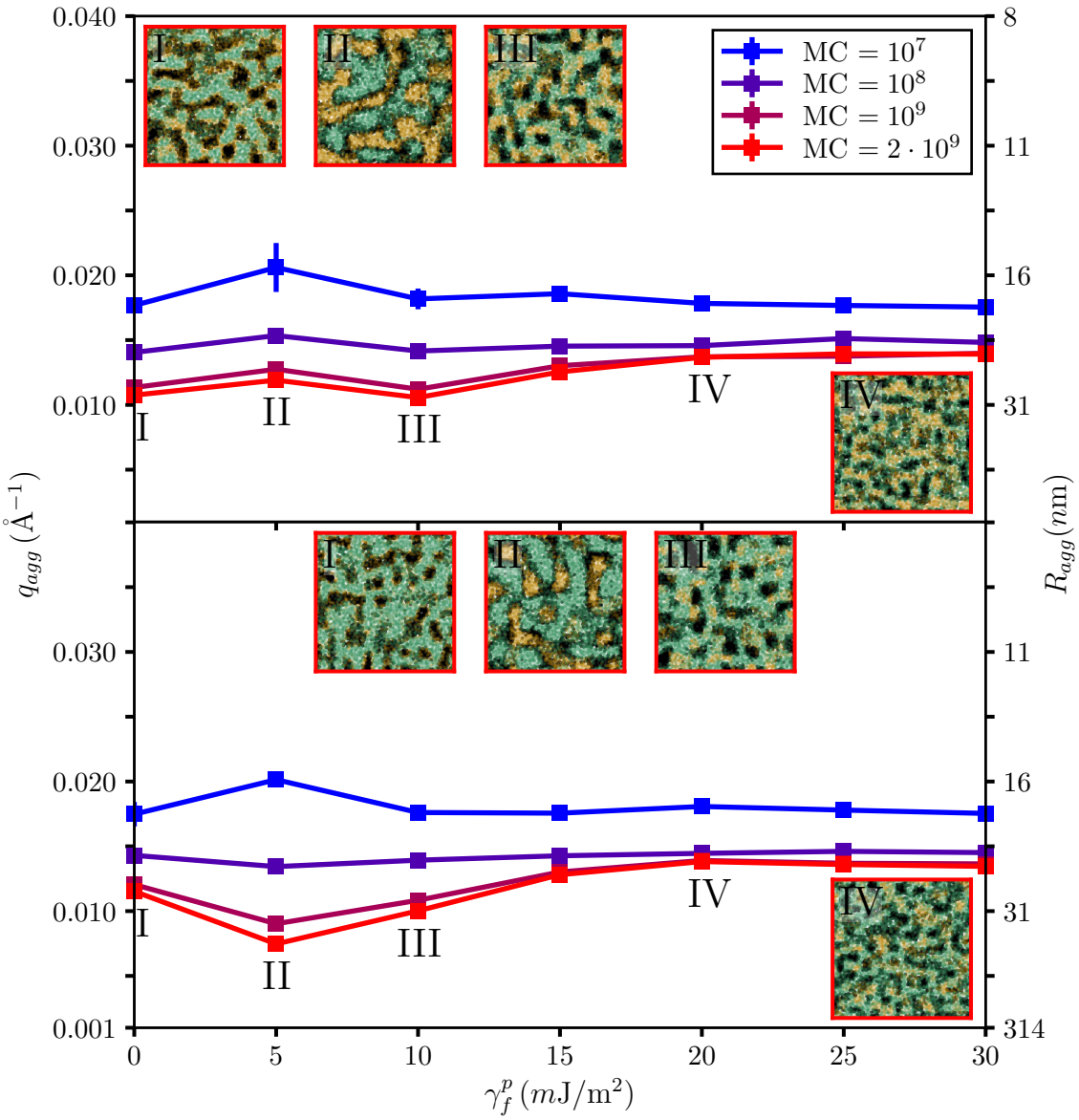

Figure 3.12.: Aggregation phase diagrams for filler types with $\gamma_f^d = 30\,mJ/m^2$ incorporated in 50/50-NR/SBR (top) and 70/30-NR/SBR (bottom) with $\phi = 0.25$ and $T = 413$ K. Embedded TEM pictures are taken for systems indicated by roman numerals. The colored border of each TEM corresponds to the according number of MC steps given in the legend.

At the end of this part, we want to discuss the mass fractal dimension of the aggregates inside systems, in which the filler types are able to develop a network. Due to the high filler volume fraction, this is the case for every particle. For a better comparison, the values are plotted in Figure 3.13. The left column depicts the 50/50 and the right column the 70/30 blend ratio. The top Figures depict the case of $\gamma_f^d = 20\,mJ/m^2$ and the bottom ones $\gamma_f^d = 30\,mJ/m^2$.

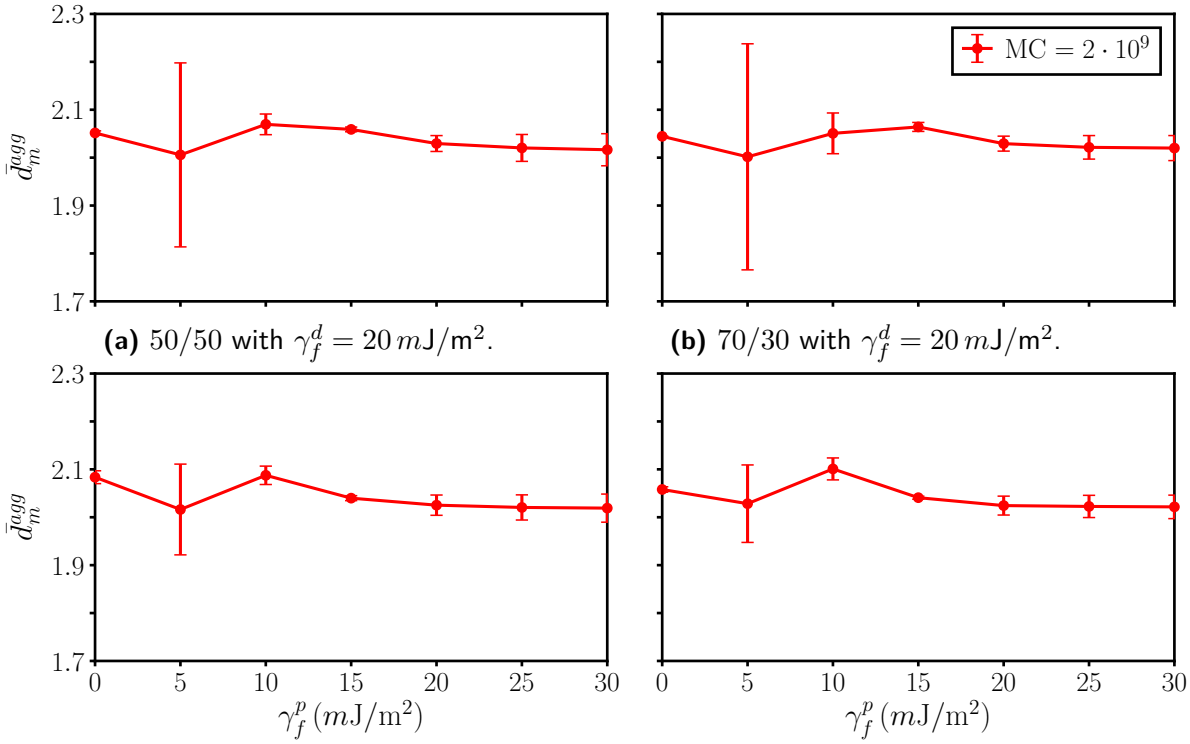

(a) 50/50 with $\gamma_f^d = 20\,mJ/m^2$. **(b)** 70/30 with $\gamma_f^d = 20\,mJ/m^2$.

(c) 50/50 with $\gamma_f^d = 30\,mJ/m^2$. **(d)** 70/30 with $\gamma_f^d = 30\,mJ/m^2$.

Figure 3.13.: Mean mass fractal dimension of the aggregates, $\bar{d}_m^{agg}$, produced by different filler types inside different NR/SBR blends with $\phi = 0.25$ for $\gamma_f^d = 20\,mJ/m^2$ and $\gamma_f^d = 30\,mJ/m^2$ at $T = 413$ K after $2 \cdot 10^9$ MC steps. Note that the corresponding uncertainties are also means.

Due to the higher filler volume content, the value of $\bar{d}_m^{agg}$ is overall increased. This was already discussed in the former chapter regarding the single polymers and is due to the algorithm itself. Nevertheless, the apparently more dense aggregates inside the filler networks agree with the higher mass fractal dimension. The direct comparison of both blend ratios shows that the values do not alter significantly and the course of the data itself is very similar. The uncertainties for the 70/30 blend ratio are generally higher than for the 50/50 ratio. Filler type II, i.e., $\gamma_f^p = 5\,mJ/m^2$ shows due to the poor structural development or the special interphase aggregation behavior the highest uncertainties.

It can be summarized that increased filler volume content affects the development of filler networks. To be more precise, the relative filler volume content inside the polymer phases is the main reason. It leads to a higher filler density, which is in agreement to experimental results [26]. In the discussion of the single polymers, we already argued that systems, which show no tendency to form a filler network at all, need to surpass a certain threshold of filler loading. Our assumption was that this loading is the percolation threshold of the underlying lattice, which is certainly true for single polymers. In blends, however, we are able to circumvent this threshold by using distinct filler types. They must prefer one of the two polymer phases. Then it is possible to use an overall lower filler loading and still obtain a filler network. In the 70/30-NR/SBR blend, for instance, even a value of $\phi = 0.15$ was enough for filler type I. This

is impossible to achieve in single polymers – at least from the results we obtained with our model. However, simply reducing the polymer phase where the filler type show the highest affinity to, is also no possibility. This polymer still needs to be able to form a continuous phase on its own. A special case is certainly the aggregation along the interphase. There, we are not able to argue with relative filler volume content at all.

We therefore conclude that a main contributor for the enhancing properties of blends is the affinity of filler types towards a certain polymer phase, the subsequent increment of their relative volume fraction within that phase, and, as a consequence, the formation of a filler network therein. The right blend ratio therefore allows to minimize the amount of necessary filler particles. Beside that, the flocculation time is of high importance. We already saw in chapter 2 that a certain number of MC steps has to be performed in order to observe structural development. But the results we obtained for our final system configurations showed that the distribution in the different phases was overestimated when compared to experiments. Because we know that our MC steps should be a rough measure of time (cf. discussion in Appendix D), we might have been looking at states where the structural development due to flocculation was too well advanced or simply not advanced enough. In order to investigate this in more detail, we consider the long term structural evolution in the next section, where the focus on different MC steps is taken more into account.

3.3. Long Term Structural Evolution

In this part, we change the maximum number of MC steps from $10^3 \cdot L^3 \approx 2 \cdot 10^9$ to 10^{11}. This allows us to investigate the long term evolution of the system. Due to the high computational effort in this case, we only do it for the 50/50-NR/SBR blend, concentrate on a single filler volume fraction, i.e., $\phi = 0.2$, and conduct only one simulation per system. Beside the longer MC simulation, we change the program in such a way that we are able to extract the interfacial lengths at distinct MC step values. This allows us to investigate the evolution of the wetted surface fractions with flocculation time. While this information is computationally cheap to obtain, the extraction of the cluster mass distribution is, unfortunately, not[3]. The plot of a certain wetted surface fraction vs. the number of MC steps is considered a 'wetting kinetic' plot . This concept is adopted from Le, who investigated intensively the effect of filler wetting in different elastomer blends in correlation with mixing time over several years [5, 16, 24, 27, 28]. Instead of mixing time, however, we consider the flocculation time and extent this view to the wetting of the polymers, i.e., we investigate the structural development of the polymer morphology in addition to that of the filler particles.

Beside the wetting kinetics, we compare results of the former part in the 50/50-NR/SBR case after $10^3 \cdot L^3 \approx 2 \cdot 10^9$ steps with those obtained after 10^{11} steps. This is done with respect to the cluster mass distribution and the evolution of the mean size of the aggregates. Although this is a comparison between two 'different' systems, i.e., not obtained in a single run, the results obtained for systems with the same set of input parameters generally yield very similar results, as seen before. Regarding the information from the cluster mass distribution, we consider the change in the amount of clusters as well as the change in the mass of the biggest cluster

[3]For a detailed discussion regarding the runtime and the computational effort the reader is encouraged to look into Appendix D.

in the system, i.e., the filler network. The former is categorized into regions with distinct mass, i.e., below and above a mass of ten. This allows us to obtain information about the development of the clusters themselves. For instance, less smaller clusters and more bigger clusters imply that they merged during the longer simulation time. The change in mass of the biggest cluster, on the other hand, allows us to obtain direct information on the filler network development. If for longer run times the mass of the biggest cluster decreases significantly, it is almost certain that the network vanished. The mean size of the aggregates obtained after a fixed number of MC steps gives information on how the structures change in detail. Their discussion is done in the same manner as before, i.e., the aggregation phase diagrams are evaluated together with embedded TEM pictures. Those are again corresponding to the maximum number of MC steps, i.e., 10^{11}. The mass fractal dimension of the aggregates is consequently investigated during the MC simulation.

3.3.1. Interphase Aggregation – A Special Case

As an introduction, we want to consider an example system and investigate its structural development with more focus on the TEM pictures. The aggregation phase diagram is therefore neglected for the moment. This example system depicts a special case, because it shows a unique behavior, which is not seen for any other surface energy combination. It contains filler particles with $\gamma_f^p = 5\,m\mathrm{J/m^2}$ and $\gamma_f^d = 30\,m\mathrm{J/m^2}$, i.e., of type II. Figure 3.14 shows the TEM pictures obtained after distinct numbers of MC steps. The top left TEM shows the system after 10^7 steps. Following the arrows, we find representations a decade later, up to 10^{11} steps in the last TEM picture in the middle of the bottom row. The last picture is a 3D representation of the whole cubic lattice. Every TEM picture shows a five layer thick portion of the system with a size of 128×128. Therefore, these TEM pictures show a larger portion of the system compared to those in the aggregation phase diagrams in the former section.

For this example system, it is clearly visible that the filler particles quickly attach to the interphase of the polymers. They, in turn, form continuous phases with growing domains. Due to the merging process the interphase gets smaller. Consequently, the same amount of filler particles need to find space in a smaller spatial region. This is only possible to a certain degree. The leftover particles therefore aggregate with those in the interphase, akin to the case of higher filler volume content. When the distance between the polymer domains is small enough, the clusters are able to bridge between those domains. As can be seen in the 3D representation, this happens throughout the system. The filler particles are therefore no obstacle in the formation process of a continuous polymer phase morphology. It is more the contrary: they are 'gluing' the individual branches together. During this process, the polymer particles in the interphase are completely displaced by the filler particles. This means that the dark filler areas we see in the last TEM picture have no underlying polymer particles at all.

The respective wetting kinetics plot is depicted in Figure 3.15. It is split into a consideration of the wetted surface fractions with the filler particles (left) and those with the polymers in focus (right). Starting with the left plot, we see that the filler-filler related value, l_{ff}, is at about 10%. This indicates a good dispersed start configuration. At 10^7 we find the beginning of an ongoing increase that becomes more pronounced for larger MC steps. For the entire simulation, the filler particles are always wetted evenly by both polymers. This agrees with

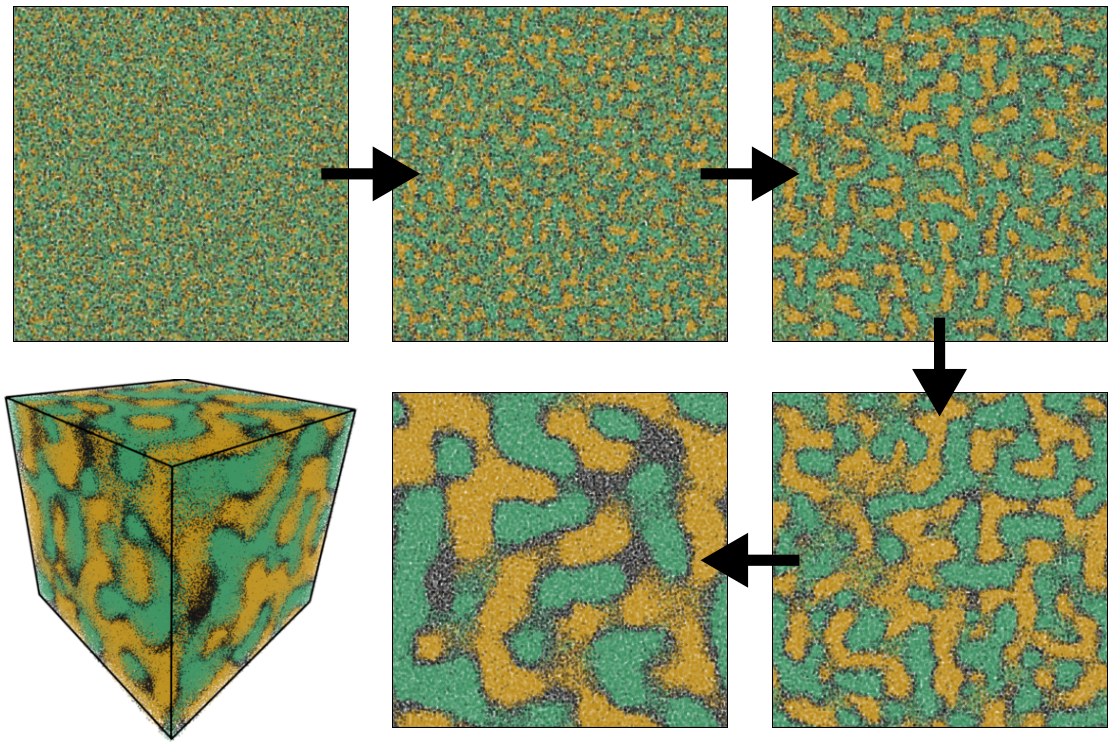

Figure 3.14.: Visualized evolution of an example system after up to 10^{11} MC steps. The example system contains 50/50-NR/SBR and 20% of filler particles with $\gamma_f^p = 5\,m\text{J/m}^2$ and $\gamma_f^d = 30\,m\text{J/m}^2$, i.e., type II. The top left corner shows the system after 10^7 MC steps. Following the arrows, the TEM pictures show the system a decade (in number of MC steps) later. The last picture is a 3D representation of the entire cubic lattice. In the beginning, a structural development of the filler particles or the polymer morphology isn't discernible. The onset is seen in the second picture, i.e., after 10^8 steps. The polymers start to form permeating networks and the filler particles align at their interphase. The more MC steps are performed, the bigger the polymer domains become. The filler particles, still in the interphase, start to form bridges between the individual branches of the polymers. A deeper analysis of the last TEM picture reveals that the areas containing lots of filler particles replaced both polymers completely. The aggregation along the interphase is nicely seen in the 3D representation. Each TEM picture is a five layer thick cut at the same position and line of sight. Different from those in the aggregation phase diagrams, however, their size is 128×128, i.e., about $1\mu\text{m} \times 1\mu\text{m}$.

the evolution of the system we saw in Figure 3.14. With increasing number of MC steps, the polymers wet the filler surface less. Their individual decrease equals half the increase rate of the filler-filler related value l_{ff}. The right plot shows that in the beginning of the flocculation process the interphase between the polymers, l_{nsb}, is at 50%. Ongoing flocculation results in a minimization of the interphase between the polymers. This is a consequence of the filler particles displacing all polymer particles in the interphase. The biggest decrease is found at 10^7 steps, where the filler particles start their structural development. Similar to the wetting

of the filler surfaces, the wetted surface fractions regarding the same polymer, i.e., l_{nn} and l_{sbsb}, increase equally. Overall the system wants to separate all three phases. However, because after 10^{11} steps there is no polymer interphase left and the filler particles are 'trapped' inside the interphase, it is unlikely that this separation will succeed after all.

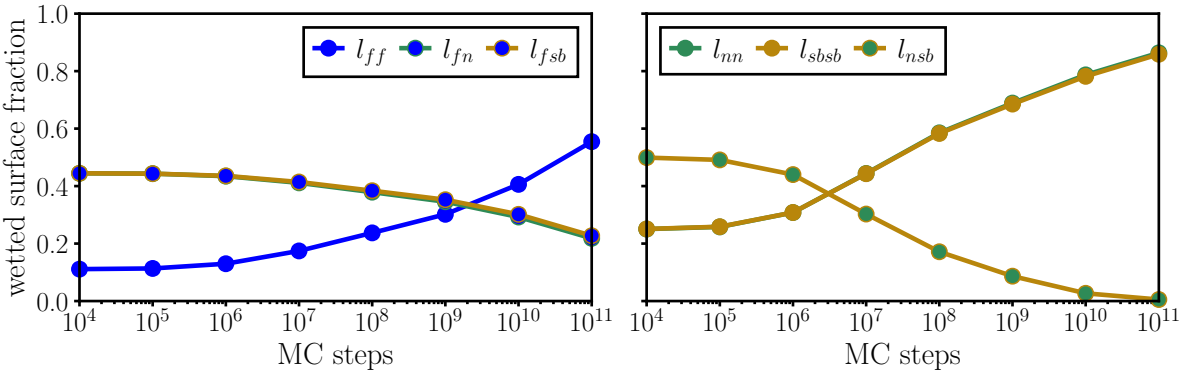

Figure 3.15.: Wetting kinetics of the example system, containing 50/50-NR/SBR together with 20% of filler particles with $\gamma_f^p = 5\,m\mathrm{J/m^2}$ and $\gamma_f^d = 30\,m\mathrm{J/m^2}$, i.e., type II. Left: Wetting kinetics with the filler particle in focus. Right: Wetting kinetics with different polymers in focus. The encoding is the same as for the wetted surface fraction plots used before. The marker face color is indicating the particle to be wetted, whereas the marker edge and line color indicate the wetting partner.

If we compare the cluster mass distribution of this system with its counterpart obtained after $2 \cdot 10^9$ steps, we find that the same amount of filler particles is bound into clusters, i.e., 98%. This is quite surprising, as one would expect after a very long simulation time that no filler particles are freely roaming inside the system. The amount of clusters, however, shows that due to the longer simulation time more clusters merged with one another. We found after $2{\cdot}10^9$ more than 5000 and now only slightly more than 1000 clusters. Those with mass less then ten are reduced to about one fourth, i.e., 4900 vs. 1200. Those with a mass between ten and one thousand got completely erased (before 550). In both cases we find a filler network, which is slightly bigger for the longer simulation time (380000 vs. 410000). Smaller and intermediate clusters are therefore merged with the existing filler network. Looking at the TEM pictures in Figure 3.14 once more, it is reasonable to assume that they got absorbed into the large bridges in between the polymers.

If we take a look at the mean size of the aggregates, we find that their value is more than doubled with $R_{agg} = 57\,n\mathrm{m}$ compared to $R_{agg} = 24\,n\mathrm{m}$. The mass fractal dimension of the aggregates yields $d_m^{agg} = 2.04 \pm 0.01$. This has to be compared to $d_m^{agg} = 1.85 \pm 0.10$, which matches our impression of the TEM pictures and the increasing mean size of the aggregates. The filler network itself becomes less fine and branched due to the formation of bigger bridges. Consequently, the aggregates itself behave uniformly. While their mass fractal dimension is relatively constant for the lower MC steps up to 10^9, we find a sudden increase at 10^{10} and another (bigger) one at 10^{11}. The corresponding uncertainties decrease to almost zero for the highest MC steps.

Another interesting aspect is the necessary filler content to produce a filler network in the interphase. We argued before that a certain threshold in the relative filler volume fraction must be surpassed in order to create filler networks. This concept, however, only applies for the case where the filler particles are to be found inside a distinct polymer phase. This does not apply here. For shorter simulation times, a value of $\phi = 0.2$ was still mandatory to achieve the formation of a filler network in the interphase. For the longer simulation time, however, even $\phi = 0.1$ is enough. Several possible questions may now arise, such as "does longer simulation time always lead to the formation of a filler network?" and as a consequence "is less filler content for network formation needed?". Answers to those questions are provided in the next section, where we discuss all systems conclusively.

3.3.2. 50/50-NR/SBR Blend

In this section, we now consider the aggregation phase diagrams and compare the results of our four filler types after the longer simulation time with that of the state obtained after $2 \cdot 10^9$ steps. The consideration of the mass of the biggest cluster and the amount of clusters is done conclusively for all filler types. Different from the example system, we split the wetting kinetics into single wetted surface fractions, i.e., one for l_{ff}, one for l_{fn}, and so on. This is done to aim for a better overview, because we have four data sets for each wetted surface fraction. We start with $\gamma_f^d = 20\,m\mathrm{J/m^2}$ depicted in Figure 3.16.

Figure 3.16a shows the aggregation phase diagram with embedded TEM pictures. Note that the colors used are the same as before, but the respective encoding changed as indicated by the legend. The colored border of the TEM still corresponds to the number of MC steps indicated in the legend. Figures 3.16b and 3.16c show the relative change in the mass of the filler network, m_n, and the amount of clusters, N_C, for each filler type. The latter is split into two categories, i.e., amount of clusters with mass less than ten, $N_C^{<10}$, and with mass greater than ten, $N_C^{\geq 10}$. The relative change compares the values obtained after $2 \cdot 10^9$ steps with those after 10^{11} steps. Everything in the green shaded area increased and that in the red shaded area decreased after longer run times. Note that the break in the y-axis for m_n is due to the strong increase for $\gamma_f^p = 5\,m\mathrm{J/m^2}$.

Regarding the aggregation phase diagram, we see an increase of the mean size of the aggregates for all γ_f^p values up to a value of $20\,m\mathrm{J/m^2}$. For higher surface polarity, longer run times show no influence on this quantity. The biggest aggregates are found, as before, for filler type III. They almost doubled in size and now have a value of $R_{agg} \approx 60\,n\mathrm{m}$, which is to be compared to $R_{agg} \approx 31\,n\mathrm{m}$.

Looking at the TEM pictures we see strong changes. In some cases for both filler and polymer morphology and in other cases only for the polymer morphology. Filler types I is an example of the former case. We see that the formerly diluted SBR matrix formed big, dense domains which are clearly separated. The filler particles are found as big dense clusters inside these SBR domains which are also separated. If we take a look at the relative change of the mass of the filler network, i.e., Figure 3.16b, we see that it is almost vanished. The ongoing flocculation process destroys the filler network, which is built during the early stages, presumably after around 10^9 MC steps. Along the ongoing process it is consequently broken down. The amount of clusters, depicted in Figure 3.16c, also decreases, albeit to a much lesser extent. However,

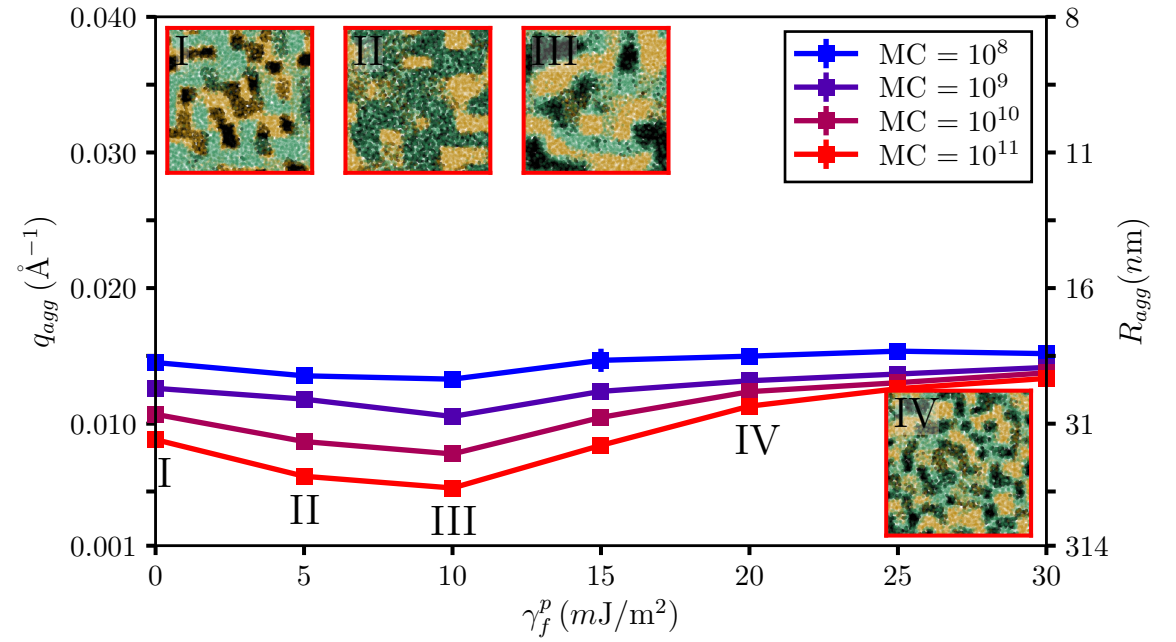

(a) Aggregation phase diagram with TEMs.

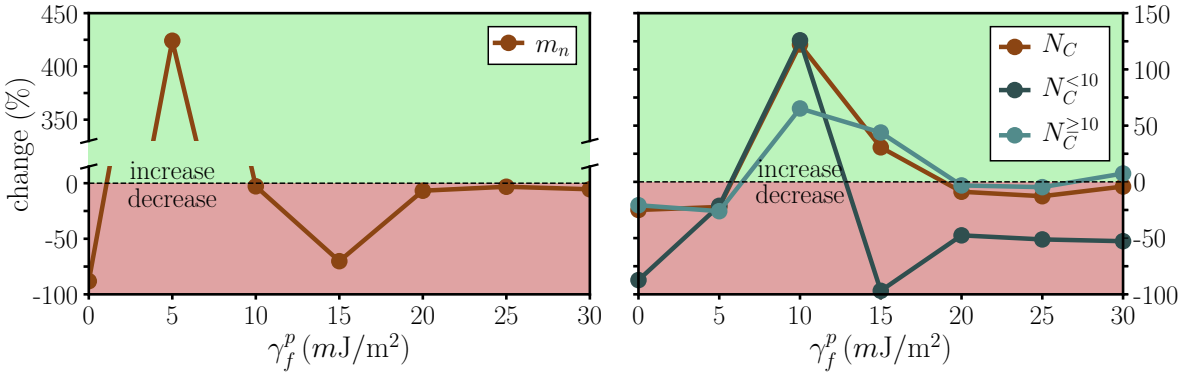

(b) Change in filler network mass.

(c) Change in amount of clusters.

Figure 3.16.: (a): Aggregation phase diagram for filler types with $\gamma_f^d = 20\,mJ/m^2$ incorporated inside a 50/50-NR/SBR blend with $\phi = 0.20$ at $T = 413$ K. Embedded TEM pictures show the systems indicated by roman numerals. The colored border of each TEM corresponds to the according number of MC steps given in the legend. Note that those changed compared to the shorter simulation time. **(b)**: Relative change of the filler network mass, m_n. Although very high, we still find no filler network for $\gamma_f^p = 5\,mJ/m^2$. **(c)**: Relative change of the total amount of clusters N_C, clusters with mass less than ten $N_C^{<10}$, and cluster with mass greater than ten $N_C^{\geq 10}$. All relative changes compare the values after 10^{11} steps with those after $2 \cdot 10^9$ steps.

the clusters with a mass less than ten is also almost vanished. From this follows that the individual mass of clusters overall increased. Smaller clusters are merged together and create bigger ones. Those with a mass over ten are also merged together, but are mainly absorbed

by the remnants of the broken down filler network. For this specific system we already see that the time at which we compare our results to those of the experiment is crucial. From the TEM pictures alone it is obvious that we find almost no particles inside NR or the interphase. Basically all particles are incorporated inside SBR. Thus, the structural development is to well advanced here and we differ more significantly from the experiment than after $2 \cdot 10^9$ steps.

As before, we find for filler type II a strong favoring of NR. The TEM picture shows that they are still pretty good dispersed and some are found in the interphase of both polymers. Their morphology, however, changed completely. Both polymers form extensively bigger domains. Consequently, we find a higher local filler density, which is detected by SAXS as an increase in the mean size of the aggregates, i.e., $R_{agg} \approx 51\,n\text{m}$ compared to $R_{agg} \approx 30\,n\text{m}$. We find the most significant increase in the mass of the biggest cluster for filler type II with more than 400%. Although this is very strikingly, the cluster, which is obtained after the longer simulation time, is still far from being considered a filler network. With a mass of around 4000 it is considered small for other filler particle types. The amount of clusters is generally slightly decreased and that evenly for all categories. Due to the merging of the NR domains, filler particles are brought closer together and consequently form bigger clusters. The amount of cluster bound particles is also only changed slightly, from 87% to 89%. It is therefore reasonable to assume that even longer simulation times will not show big differences for the filler particles. The polymer morphology, however, will most likely form even bigger domains.

The probably most pronounced change is found for filler type III. Here, the increase in the mean size of the aggregates is completely supported by the impression we obtain from the TEM picture. We find that the polymer morphology is changed drastically. Big, elongated SBR domains are discernible. This is different than for the former two filler particles. The strong NR affinity is still given. In the flocculation process the NR and SBR domains are merged. Consequently, the filler aggregates inside NR are also merged. Although the TEM does not support the impression of a filler network, we find that the mass of the biggest cluster shows only a slight decrease. Regarding the amount of clusters we find a pronounced increase for either category. As a result, parts of the filler network must have broken down into smaller and bigger clusters.

Although we have no TEM picture, it is worth to discuss the situation for the filler type with $\gamma_f^p = 15\,m\text{J/m}^2$. The mass of the filler network is decreased drastically compared to the shorter simulation time. The overall amount of clusters is increased, but those with a mass less than ten are completely vanished. In this case we therefore find a complete breakdown of the filler network into several bigger agglomerates, similar to filler type I.

The impact of the longer simulation time for filler type IV is very minor. The mean size of the aggregates is slightly increased. From the TEM picture we obtain the impression that the filler network is still discernible. The affection towards NR is unaltered. The polymer morphology shows slightly bigger domains of each polymer. The change in the mass of the filler network is accordingly very minor. The amount of clusters is also only insignificantly affected. We do, however, find less clusters with a mass less then ten. Consequently, they must have merged into bigger clusters.

We now take a look at the wetting kinetics of the filler types depicted in Figure 3.17. Each of the subplots depicts a certain wetted surface fraction, indicated by the label of the y-axis. The color encoding is similar to that of the wetted surface fractions we used before. The marker face color indicates the particle in focus, while the marker edge color the wetting partner. Roman numerals in the legend indicate the four filler types we focus on.

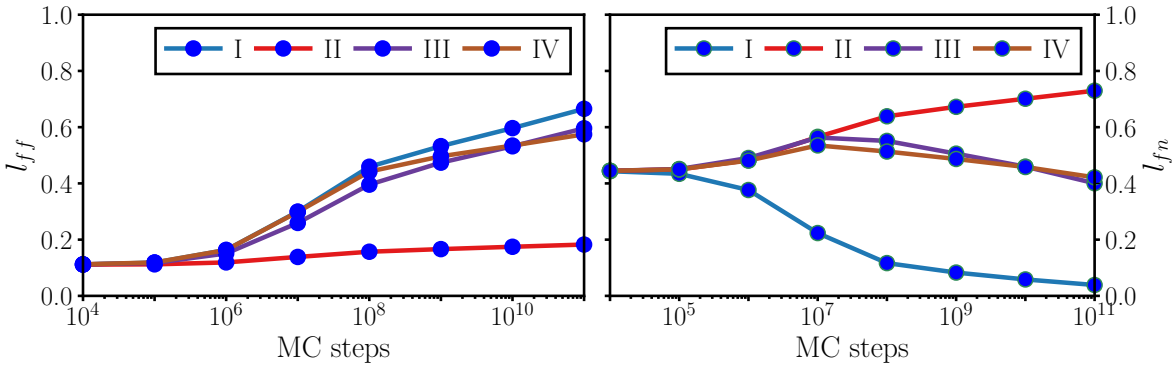

(a) Wetting kinetics for filler-filler.

(b) Wetting kinetics for filler-NR.

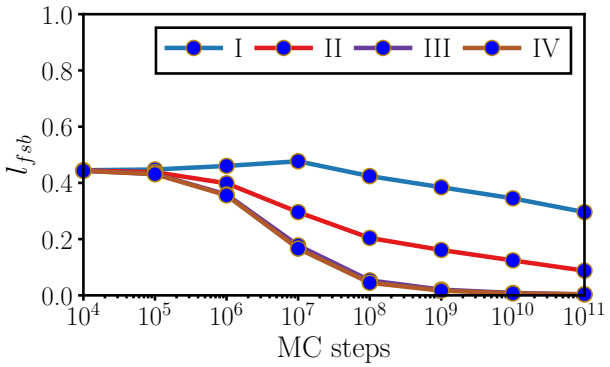

(c) Wetting kinetics for filler-SBR.

Figure 3.17.: Wetting kinetics of filler related surfaces in the case of $\gamma_f^d = 20\,mJ/m^2$ incorporated inside a 50/50-NR/SBR blend with $\phi = 0.20$ at $T = 413$ K. **(a)**: Wetting kinetics for l_{ff}. We find an increase for every filler type. The lowest is found for filler type II. A kink in the slope for all other particles is found at 10^8 MC steps. While the slope for filler types I and III is similar that of filler type IV is getting less. **(b)**: Wetting kinetics for l_{fn}. Low polarity filler type I avoids NR over the course of the simulation. The other filler types favor NR in the beginning. After 10^7 MC steps we find a turning point. Only filler type II increases its wetting towards NR. Both other filler types decrease. It is higher for III than for IV. **(c)**: Wetting kinetics for l_{fsb}. Only filler type I shows initially an increase which starts to turn into a decrease at 10^7 MC steps. Other filler types continuously decrease strongly up to 10^8 MC steps and less thereafter.

Figure 3.17a shows the wetting kinetics of the filler-filler surface fractions, l_{ff}. While filler type II shows only a slight increase, all other filler types increase strongly with the onset of structural development at 10^7 steps. Their individual increase, however, shows a turning

point at 10^8 steps. Thereafter, filler types I and III have the same slope, while that of IV is slightly less. Between 10^{10} and 10^{11} steps we find a higher l_{ff} value for filler type III than for filler type IV.

The filler-NR related wetted surface fractions, l_{fn}, are depicted in Figure 3.17b. At the beginning of the simulation, all particles are evenly wetted by NR. At 10^6 steps we start to see a first separation. Filler type I avoids NR very fast and continues to do so until the end of the simulation. The biggest decrease is found at 10^7. Until that point, all other filler types favor NR. After that point, however, only filler type II continues to increase its value of l_{fn}. Filler types III and IV start from thereon to decrease l_{fn}, whereas it is higher for III than for IV. This is directly correlated with the increase of l_{ff}. The filler particles form big, dense structures and consequently reduce the contact towards NR, although they are still found therein.

In Figure 3.17c, we find the wetting kinetics for filler-SBR related surfaces, l_{fsb}. Only filler type I shows a slight increase, which turns into a decrease at 10^7 steps. All other filler types start to avoid SBR as soon as possible, while their strongest decrease is found at the onset of structural development, i.e., at 10^7 steps. The course for filler types III and IV are identical and show that no filler-SBR contacts are found at the end of the simulation.

The values we find for the individual wetted surface fractions are all well displaying the changes we discussed in the context of the aggregation phase diagram and the cluster development in Figure 3.16. Regarding the carbon black distribution in the polymer phases, i.e., the values of filler type I, a good agreement to experimental values is most likely found somewhere around 10^8 steps. There, we find a high value of l_{fsb}, but still a reasonable high value of l_{fn}. Together with the relatively low value of l_{ff}, the formation of big individual structures at this point is not very likely. The filler particles could therefore have formed a filler network at this point, which is consequently broken down into smaller agglomerates. For the silica distribution, i.e., filler type IV, experimentally reasonable values are only found at 10^7 steps. At this value, however, we are just considering the onset of structural development. Thus, we will not find a filler network which is partially found in SBR for silica particles, regardless of the flocculation time we consider.

In Figure 3.18, we find the wetting kinetics depicting the polymer morphology. The color encoding is unaltered to the case of the filler types. In both of the upper plots, we see the development of the individual polymer matrices. Longer simulation time favors their development. In both plots, we see for all filler types an increase throughout. The strongest increase of l_{nn} is found for filler type I. This is because it solely favors SBR. The flocculation of the filler particles only takes place inside this matrix. The development of NR is therefore only affected by the SBR particles. The lowest increase is found for filler type II, because it shows the best dispersion inside NR. This interferes with the development of the NR matrix. For SBR it is the other way around. Filler type I shows the lowest increase, while II shows the highest. The reasoning is unaltered in this case.

Regarding the interphase of the polymer in Figure 3.18c, we find that it is continuously decreasing. Due to the development of the individual matrices, this is no surprise. While the overall value for filler type II is the lowest, due to its good dispersion inside NR, the decrease is almost equal for all particles. Only filler types I and III, which developed significant big

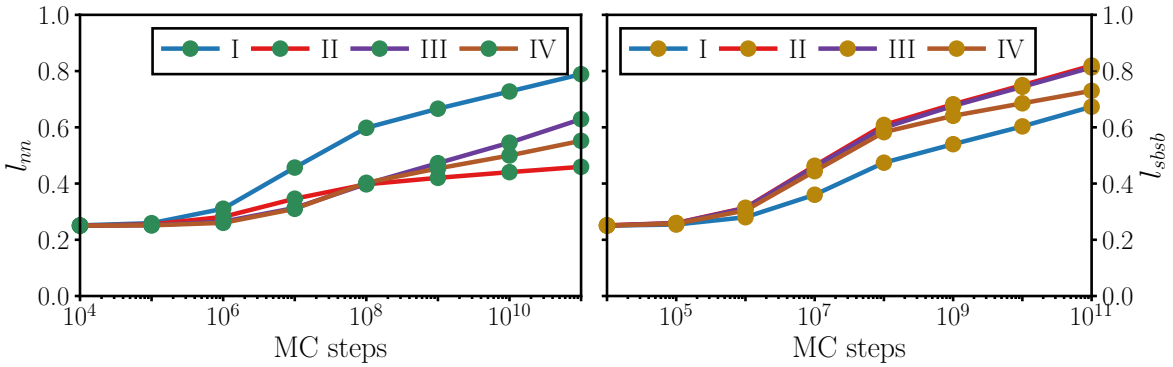

(a) Wetting kinetics for NR-NR. **(b)** Wetting kinetics for SBR-SBR.

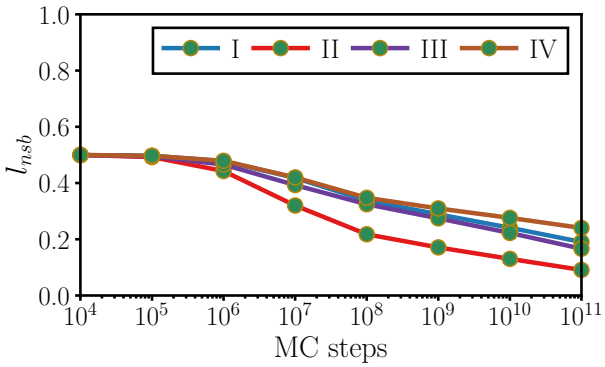

(c) Wetting kinetics for NR-SBR (interphase).

Figure 3.18.: Wetting kinetics of polymer related surfaces in the case of $\gamma_f^d = 20\,mJ/m^2$ incorporated inside a 50/50-NR/SBR blend with $\phi = 0.20$ at $T = 413$ K. **(a)**: Wetting kinetics for l_{nn}. The formation of NR domains is distinct. For filler type I we find the highest increase. This is because SBR is strongly favored by this filler type. Consequently, the development of NR is unaffected. All other filler types favor NR and therefore hamper its development. At 10^8 we find that the slope decreases for all filler type expect III. The strongest decrease is found for filler type II, because it shows the best dispersion inside NR. **(b)**: Wetting kinetics for l_{sbsb}. The development of SBR domains is discernible. Due to the strong affection of filler type I, it is hampered the most. Other filler types show an identical behavior. At 10^8 we find a slight decrease in the slope, which is again highest for filler type IV. **(c)**: Wetting kinetics for l_{nsb}. The increase of the polymer domains is accompanied with the decrease of the polymer interphase.

structures, show a lower decrease. This is because the bigger structures retard the development of the corresponding polymer matrices.

We now look at the case where the filler types dispersive part of the surface free energy is set to $30\,mJ/m^2$ as depicted in Figure 3.19. In the same way as the former case, we find that the impact on the mean size of the aggregates is only minor for higher surface polarities. For the shorter simulation time, we saw that filler type III develops the aggregates with the biggest sizes. Longer simulation time, however, changed this, as we now find that filler type II develops the biggest aggregates according to the SAXS data with $R_{agg} \approx 57\,nm$. Filler

types I and III have, however, almost the same size, i.e., $R_{agg} \approx 48\,nm$ and $R_{agg} \approx 50\,nm$, respectively.

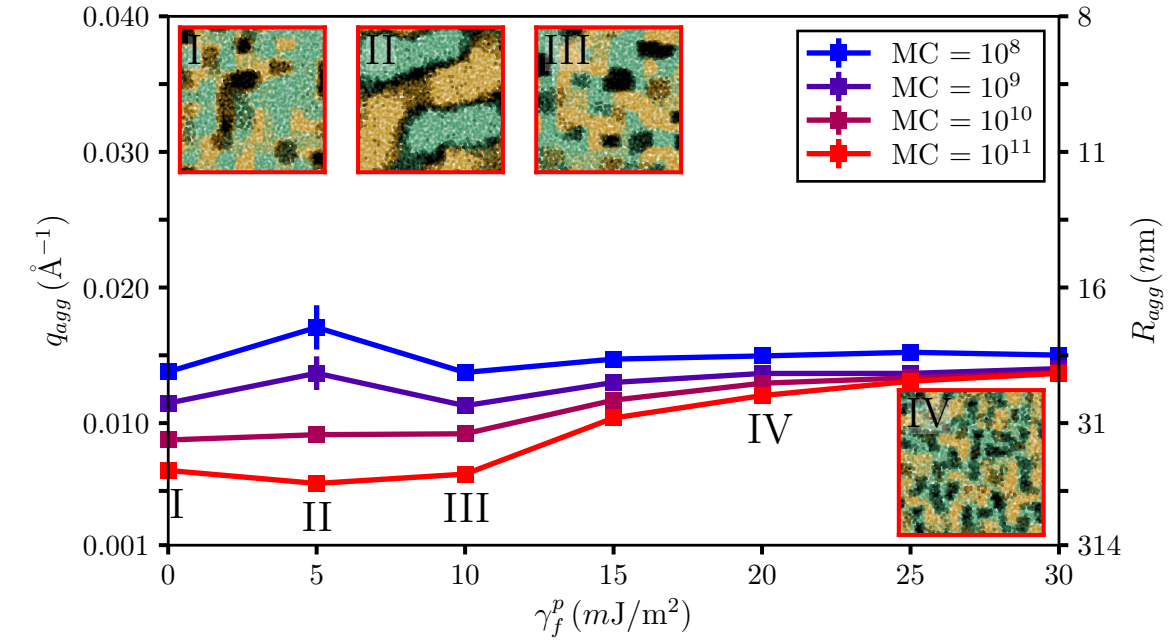

(a) Aggregation phase diagram with TEMs.

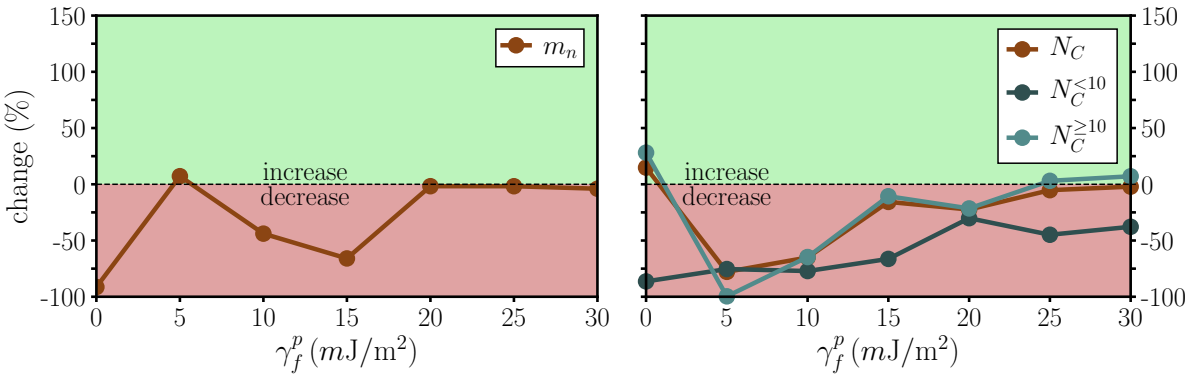

(b) Change in biggest cluster mass.

(c) Change in amount of clusters.

Figure 3.19.: (a): Aggregation phase diagram for filler types with $\gamma_f^d = 30\,mJ/m^2$ incorporated inside a 50/50-NR/SBR blend with $\phi = 0.20$ at $T = 413$ K including embedded TEM pictures for systems indicated by roman numerals. The colored border of each TEM corresponds to the according number of MC steps given in the legend. **(b)**: Relative change of the filler network mass, m_n. **(c)**: Relative change of the total amount of clusters N_C, clusters with mass less than ten $N_C^{\leq 10}$, and cluster with mass greater than ten $N_C^{\geq 10}$. All relative changes compare the values after 10^{11} steps with those after $2 \cdot 10^9$ steps.

Taking the TEM pictures into account, we find that the polymer morphology for filler type I is identical to the case with $\gamma_f^d = 20\,mJ/m^2$. Big SBR and NR domains are found throughout.

Here, however, the filler particles form bigger clusters within the SBR domains, which is also supported by the higher mean aggregate size. The filler network we find after the shorter simulation time is here, however, destroyed. The change in its mass in Figure 3.19b shows, also similar to $\gamma_f^d = 20\,m\mathrm{J/m}^2$, that it is even completely vanished. The same argumentation applies here. Different from this case, however, is the change in the amount of clusters, which is depicted in Figure 3.19c. We find overall a slight increase. This is unique compared to all other filler types. The amount of clusters with a mass greater than ten take a major part in that increase. Those with a mass less than ten are almost vanished. Because we find a breakdown of a filler network, it is reasonable to assume that this is the cause for the increase in the amount of the bigger clusters. In addition, the smaller clusters are merged with the remnants of the filler network or are simply merged with one another, leading to the vanishing value of the amount of clusters with a mass less than ten.

Filler type II is our introductory example case which was already explained in detail.

The TEM picture of filler type III shows very dense, quadratic clusters which are well separated. They show a high NR affinity. The polymer morphology is identical to the $\gamma_f^d = 20\,m\mathrm{J/m}^2$ case. For the shorter simulation time, no filler network is established. Instead, we find several bigger clusters, which are more elongated in comparison. Although the decrease of the mass of the biggest cluster in Figure 3.19b is quite high, comparing their values shows no change in the magnitude, i.e., 22000 vs. 12000 in the longer run. The amount of clusters on the other hand, is decreased and that significantly in both categories. Those with a mass less than ten are even completely vanished. This is in accordance with the impression of the TEM. No small clusters can be found. The decrease in the amount of the bigger clusters also agrees when comparing the TEM pictures after both simulation times. While in Figure 3.6a several bigger structures are identified, we find in Figure 3.19a that due to the change in the morphology of the polymers more filler structures are merged. Consequently, we find less clusters with a mass greater than ten, but they are bigger on average (1300 compared to 800).

The last filler type we want to consider here is IV. It is indistinguishable to the case of $\gamma_f^d = 20\,m\mathrm{J/m}^2$ in almost every aspect. We find a slightly more continuous SBR matrix, which is also avoided by the filler particles. The filler network is slightly smaller and we find a greater amount of clusters. In comparison to the shorter simulation time, however, we find no change in the mass of the filler network. But the amount of clusters decreases equally in both categories. Thus, we find bigger clusters inside the category of $N_C^{\geq 10}$, but not more of them.

We now consider the corresponding wetting kinetics shown in Figure 3.20 and start with the discussion of the filler-filler related wetted surface fraction, l_{ff}, in Figure 3.20a. The lowest increase is given for filler type II. A detailed discussion was already done in our introductory example. The other filler types show a strong initial increase, which continues equally after 10^8 steps for filler types I and III. Their increase is stronger than in the $\gamma_f^d = 20\,m\mathrm{J/m}^2$ case. This is reasonable due to the increased mean aggregate size we saw in the discussion of the aggregation phase diagram. Filler type IV only shows a slight increase, which is comparable to the former $\gamma_f^d = 20\,m\mathrm{J/m}^2$ case.

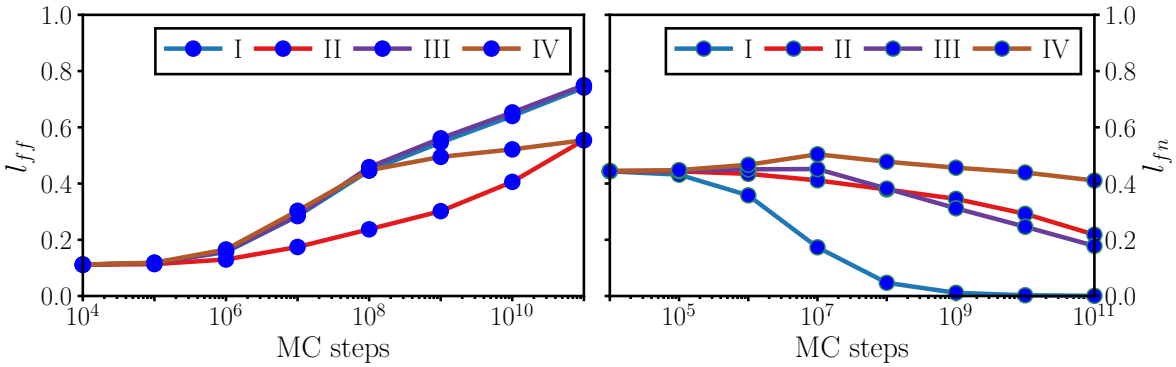

(a) Wetting kinetics for filler-filler.

(b) Wetting kinetics for filler-NR.

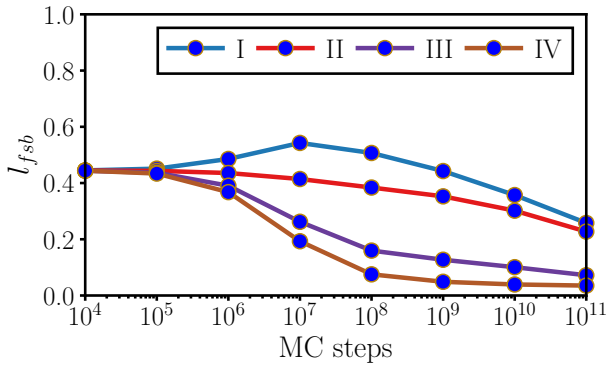

(c) Wetting kinetics for filler-SBR.

Figure 3.20.: Wetting kinetics of filler related surfaces in the case of $\gamma_f^d = 30\,m\mathrm{J/m}^2$ incorporated inside a 50/50-NR/SBR blend with $\phi = 0.20$ at $T = 413$ K. **(a)**: Wetting kinetics for l_{ff}. We find an increase for every filler type. The lowest is found for filler type II. A kink in the slope for all other particles is found at 10^8 MC steps. While the slope for filler types I and III is similar that of filler type IV is getting less. **(b)**: Wetting kinetics for l_{fn}. Low polarity filler type I avoids NR over the course of the simulation. The other filler types favor NR in the beginning. After 10^7 MC steps we find a turning point. From then on, all filler types show a decrease. The strongest is found for filler type III, which has the highest increase regarding l_{ff}. **(c)**: Wetting kinetics for l_{fsb}. Only filler type I shows initially an increase which starts to turn into a decrease at 10^7 MC steps. Filler type II shows the same decrease as for l_{fn}. Other filler types continuously decrease strongly up to 10^8 MC steps and less thereafter. Filler type IV shows even no further decrease at 10^{10} MC steps.

The flocculation behavior towards NR, depicted in Figure 3.20b, is very different from the $\gamma_f^d = 20\,m\mathrm{J/m}^2$ case. We find no continuously favoring of NR. The decrease of filler type I is way stronger and after 10^{10} steps, no contact to NR is found at all. Filler type II, being in the interphase, decreases with half the value of the increase for l_{ff}. The big, dense aggregates, which are formed by filler type III result in a fast minimization of the available surface towards any polymer. Consequently, it is higher than for $\gamma_f^d = 20\,m\mathrm{J/m}^2$. Filler type IV, however, shows the same behavior.

The wetting kinetics for filler-SBR, l_{fsb}, given in Figure 3.20c show an overall trend, which is comparable to NR. The individual behavior of the filler types is, however, different. In the beginning of the simulation, filler type I is moved into the SBR matrix, leading to an initial increase. Along the flocculation process the individual SBR domains, containing the filler particles, merge together. They consequently merge and form bigger clusters. This reduces the surface towards SBR. Filler type II in the interphase shows the same decrease as for NR. The contact towards SBR for filler type III is only given on the outside of the big, dense clusters. They are found mostly inside NR, but also in between the SBR domains. There, the clusters are more dense, which subsequently leads to a lowering of l_{fsb}. The filler network we find for filler type IV is shifted more into NR for longer simulation time. As a consequence, the wetting by SBR is reduced. Different to the $\gamma_f^d = 20\,m\mathrm{J/m^2}$ case, however, the more continuous SBR matrix still maintains some contact to the filler.

The wetting kinetics describing the polymer morphology development are given in Figure 3.21. The increase of the individual polymer domains is discernible. Figures 3.21a and 3.21b show both an increase for every filler type, while at the same time Figure 3.21c, depicting the behavior of the interphase, decreases. The filler type with the least flocculation tendency towards both polymers also affects their morphology development the least. This is II, which is found in the interphase. The most continuous filler structure inside a single polymer is found for filler type IV. Its filler network permeates through the NR matrix. Consequently, its development is hampered and the increase of l_{nn} is found to be the lowest after the onset of structural development at 10^8 MC steps. The development of the polymer morphology under filler types I and III is comparable to the $\gamma_f^d = 20\,m\mathrm{J/m^2}$ case.

By taking the aggregation phase diagrams, change in the mass of the biggest cluster, change in the amount of clusters, and the wetting kinetics into account, we saw that the impact of flocculation time heavily depends on the surface free energies of the filler types. In some cases, the filler types built a network which was destroyed for longer times. A prominent example is given for the filler type with $\gamma_f^p = 15\,m\mathrm{J/m^2}$. Regardless of the dispersive part of the surface free energy we found after the shorter simulation time a filler network and none after the longer simulation time. In other cases, represented by the high surface polarity filler types, the impact of the flocculation time was negligible. For instance, filler type IV. It showed only minor impacts, whether it is for the filler or polymer morphology, mean size of the aggregates, or the amount of clusters. The wetting kinetics revealed that the formation of the filler network most likely happened after 10^8 MC steps. The polymer related surface fractions changed their rates as well as that for the filler particles itself. Filler types not listed here, who also maintained the filler network, i.e., those with $\gamma_f^p \geq 20\,m\mathrm{J/m^2}$ behave similarly. Consequently, the formation and maintaining of a filler network can be identified using the wetting kinetics. The strongest indicator is the slight increase after the onset of structural development of l_{ff}. Other indicators are the low decrease of the wetted surface fraction towards the corresponding polymer where the network develops, here, l_{fn}, and the strong decrease towards the other polymer, which is l_{fsb} in our case. Although filler type III, for instance, showed also a strong decrease of l_{fsb} and a relatively low decrease of l_{fn}, it lacked the low increase of l_{ff} after the onset of structural development. Filler types, which basically show no change in slope for l_{ff}, are therefore identified to form big clusters instead of networks. This also applied for filler type I. Low decrease for l_{fsb}, strong decrease for l_{fn}, but strong increase of l_{ff} and therefore no filler network. For shorter simulation times, however,

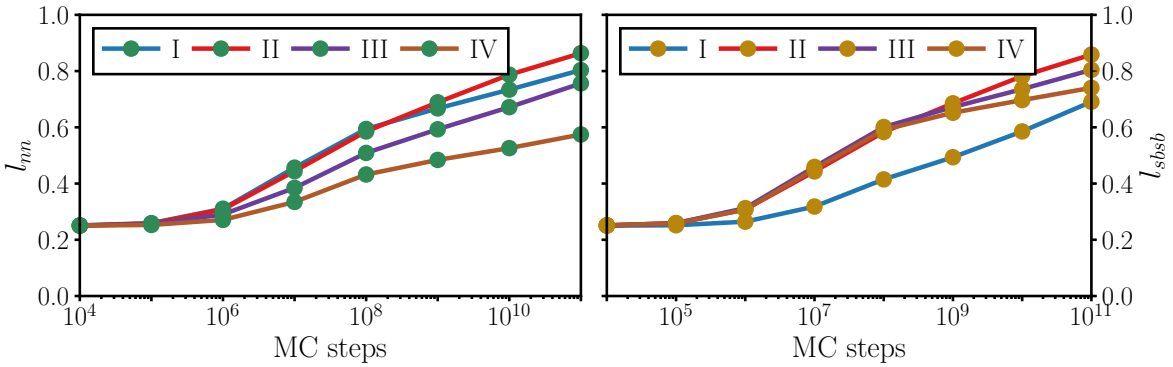

(a) Wetting kinetics for NR-NR.

(b) Wetting kinetics for SBR-SBR.

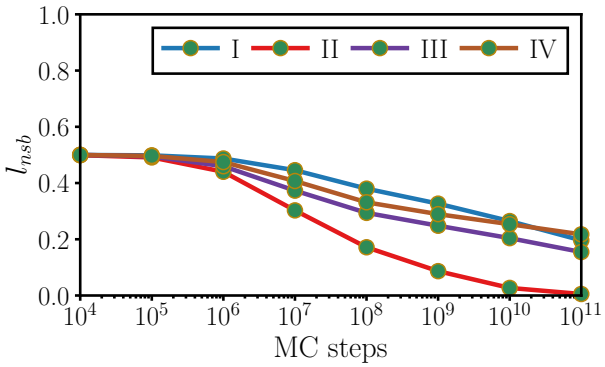

(c) Wetting kinetics for filler-SBR.

Figure 3.21.: Wetting kinetics of polymer related surfaces in the case of $\gamma_f^d = 30\,mJ/m^2$ incorporated inside a 50/50-NR/SBR blend with $\phi = 0.20$ at $T = 413$ K. **(a)**: Wetting kinetics for l_{nn}. Filler types II and III show the highest increase, directly followed by I. Filler type I is found solely in SBR and therefore does not affect the NR development. Filler type II is in the interphase between both polymers and consequently behaves similarly. For filler type III it appears that the big, dense clusters are also no obstacle. At 10^8, the slope decreases for all filler types. **(b)**: Wetting kinetics for l_{sbsb}. Due to the strong affection for SBR of filler type I, we find the lowest initial increase. At 10^8, we find a decrease in the slope for all filler types. The highest is found for filler type IV. **(c)**: Wetting kinetics for l_{nsb}. The increase of the polymer domains is accompanied with the decrease of the polymer interphase, regardless of the filler type. The strongest effect is, however, given for filler type II, which displaces the polymer particles in the interphase completely.

it developed a filler network. There, the increase of l_{ff} was not enough. A more difficult case for identifying a filler network was found for filler type II. Here, the onset of the network formation was simply not accessible by using the wetting kinetics. For an experimentally comparable filler distribution in the polymer phases, it might be reasonable to take TEM pictures, wetted surface fractions, and the cluster mass distribution after shorter simulation times into account.

An open question is, if longer simulation times allow the formation of networks for lower filler volume contents. It turns out that our special case is unique in this behavior. No other system

was able to do so. Another question, which now arises, is how the mass fractal dimension of the aggregates is affected due to the longer simulation time. Do they become more compact and consequently show a higher value? Or are they more loose and show lower values? To answer these questions we take a look at Figure 3.22.

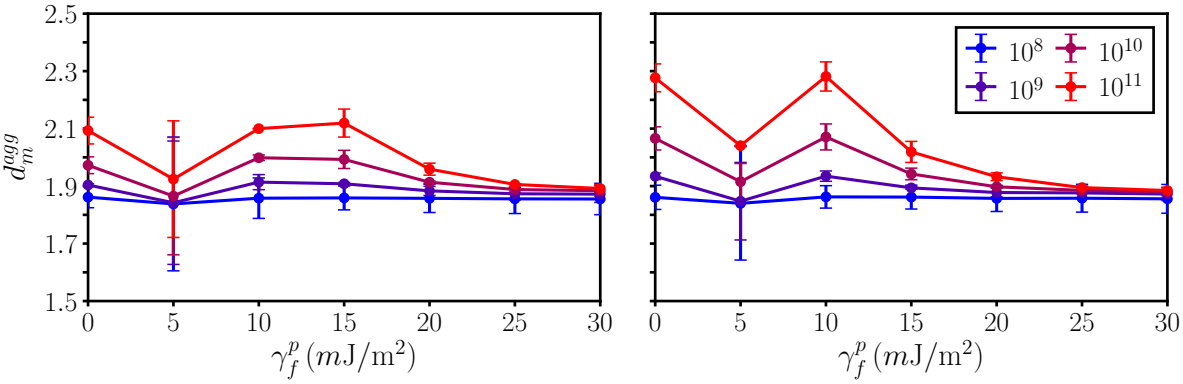

(a) $\gamma_f^d = 20\,mJ/m^2$. **(b)** $\gamma_f^d = 30\,mJ/m^2$.

Figure 3.22.: Comparison of the mass fractal dimension of the aggregates for filler types with $\gamma_f^d = 20\,mJ/m^2$ and $\gamma_f^d = 30\,mJ/m^2$ inside a 50/50-NR/SBR blend for $\phi = 0.2$ after different MC steps at $T = 413$ K. Note that the filler type with $\gamma_f^p = 5\,mJ/m^2$ shows a high uncertainty. In **(a)** the filler types showed no structural development at all and in **(b)** they showed a tendency to aggregate along the interphase of both polymers. For longer simulation times this structure becomes more distinct, leading to lower uncertainties.

Overall, longer simulation times lead to a higher mass fractal dimension of the aggregates. For filler types with high surface polarity, i.e., $\gamma_f^p \geq 20\,mJ/m^2$, the impact becomes strikingly less. The intermediate filler types with $\gamma_f^p \geq 10\,mJ/m^2$ show the highest impact on longer flocculation time. This agrees with the discussion of the aggregation phase diagrams and the wetting kinetics. The aggregates appeared more dense and generally became bigger. With values around 2.1, they show a similar mass fractal dimension as pure silica particles [29]. Filler type II, i.e., $\gamma_f^p = 5\,mJ/m^2$, shows again high uncertainties. For $\gamma_f^d = 30\,mJ/m^2$, however, they become less for longer simulation times. This is due to the distinct development of the structure in the interphase of both polymers. For $\gamma_f^d = 20\,mJ/m^2$, it stays dispersed throughout the simulation and consequently the algorithm yields relatively high uncertainties. The non-polar filler types show the same trend as those found in the intermediate surface polar region, but to a lesser extent.

3.4. Conclusion

In this chapter, we have applied the morphology generator, previously introduced in chapter 2, to binary polymer blends including homogeneous filler particles. This leads to a simplification of the corresponding MC-based algorithm, i.e., only the diagonal particle exchange is necessary. The formerly derived screening methods were adjusted to the conceptual changes of the model. A change in the TEM pictures was necessary to identify the different polymer phases

and the filler distribution therein. In the same manner as in chapter 2, we mimicked the filler particles by varying their dispersive and polar parts of the surface free energies. This enabled us to analyze different (homogeneous) surface modifications or different untreated filler types. The temperature T was fixed to 413 K, while the filler volume fraction ϕ was investigated for two values, i.e., 0.20 and 0.25. We focused on two different NR/SBR blend ratios, i.e., 50/50 and 70/30. Each component, i.e., the two polymers and the filler, are characterized by their surface free energies, each possessing a dispersive and a polar part, respectively. For both ratios and filler volume fractions ten independent simulations were performed. For the 50/50 blend ratio, the maximum number of MC steps was, additionally, elevated to investigate the long term structural development. This was, however, done for one simulation per surface free energy combination.

The systems were analyzed by the methods elucidated in the screening methods section of chapter 2. Wetting-envelope - work of adhesion plots were generated for the respective polymers to predict the filler distribution inside the polymer blend. Simulated systems were straightforwardly analyzed by simulated SAXS to obtain information about the mean size of the aggregates and their mass fractal dimension. Plotting the former versus the polar part of the surface free energy creates aggregation phase diagrams. They are accompanied by simulated TEM pictures. The mean size of the aggregates showed to deviate insignificantly for the same set of simulation parameters. The same was true for all other basic quantities and the mass fractal dimension of the aggregates, regardless of the blend ratio or filler volume fraction in use. Together with the wetted surface fractions, we were able to analyze the distribution of filler particles qualitatively and to compare them to experimental results [4, 7–9, 12, 24]. Additionally, the comparison to the results of single polymers in chapter 2 yielded an overall conclusive picture.

We found a distinct affinity to the SBR component, if the filler possesses low surface polarity, which is, for instance, the case for carbon black. A higher affinity of carbon black to SBR compared to NR is also found experimentally [4, 8]. If, on the other hand, the filler possesses high polarity, which is the case for most precipitated silica types, then we found a higher affinity to NR. This is also found experimentally [9]. An interesting case was found, when the wetting behavior and flocculation tendency of the filler is equally good for both polymers. Then the filler particles are trapped in the polymer interphase and displace the polymer particles therein.

The formation of filler networks in the favored polymer phase is heavily depending on the relative filler volume fraction within that phase. Additionally, the flocculation time and the polymer network formation are crucial. A simple change in the blend ratio for a fixed filler volume content is generally not possible due to the lack of polymer network formation. Longer simulation times may lead to the breakdown of filler networks or enhance their building probability for lower filler contents. The latter was, however, only observable for filler type II with $\gamma_f^d = 30\,m\mathrm{J/m^2}$. It turns out that if the relative filler volume fraction reaches a value of 0.50, the formation of a filler network is always possible. Lower values may, however, also yield filler networks but it depends on the polymer network whether this is the case. The group of high polarity filler types turns out to fulfill this. This might be explained due to the strong binding to NR and themselves. But also other filler types, such as III with $\gamma_f^d = 20\,m\mathrm{J/m^2}$, are able to do so.

Although we find lots of recent studies on filled and unfilled polymer blends (e.g., [6, 28, 30–32]), most of them focus on the dynamic-mechanical behavior or the distribution of the filler particles within the blend. Scattering experiments performed on blends are very rare [33]. An obvious question is therefore, if the information of the morphologies we obtained here is useful with respect to the dynamic moduli, e.g., their dependence on strain amplitude. In recent works, the aggregate-to-aggregate contacts within filler network strands and their contribution to energy dissipation has been studied [34, 35]. An application to the calculation of storage and loss moduli based on this model and its simulation is presented in [36]. An essential information, which in principle can be contributed by this morphology generator, is the number of aggregate-to-aggregate contacts along a load bearing path. A good approximation to a load bearing path is the shortest path between two filler network nodes. An analysis with regards to these paths, in principle, can be applied to the morphologies obtained on the basis of the present lattice model. This analysis should not only yield the distribution of shortest paths but also an estimate of the number of aggregate-to-aggregate contacts along a path. In addition, the magnitude of the dynamic moduli scales with a factor $\propto \phi^y$, where $y \approx 4/(3 - d_m)$ and d_m is the mass fractal dimension of the filler network [36], which is obtainable for bigger systems.

In the next chapter we combine the methods of the first and second chapter, i.e., we mimic heterogeneously treated filler particles inside polymer blends. The polymers are not altered. Consequently, the screening methods and the model itself need to be changed. Similar to the change between the first and second chapter, however, the changes are very minor and basically consist of adjustments.

3.5. References

[1] Hess, W. M., Herd, C. R., Vegvari, P. C., Characterization of Immiscible Elastomer Blends. *Rubber Chem. Technol.* **1992**, 66 (4), 330–375, DOI: 10.5254/1.3538316.

[2] Lin, H., Jiang, Z., Study on the effect of rubber sole on pressure change of foot movement. *Leather Footwear J.* **2018**, 18 (1), 33–38, DOI: 10.24264/lfj.18.1.4.

[3] Röthemeyer, F., Sommer, F., Kautschuk Technologie: Werkstoffe - Verarbeitung - Produkte. München: Carl Hanser Verlag, **2001**, ISBN: 978-3-446-43760-9.

[4] Wunde, M., Klüppel, M., Impact of mixing procedure on phase morphology and fracture mechanical properties of carbon black-filled NR/SBR blends. *Contin. Mech. Thermodyn.* **2017**, 29 (5), 1135–1148, DOI: 10.1007/s00161-017-0562-1.

[5] Le, H. H. et al., Master curve of filler localization in rubber blends at an equilibrium state. *J. Mater. Sci.* **2012**, 47 (10), 4270–4281, DOI: 10.1007/s10853-012-6277-6.

[6] Klat, D., Karimi-Varzaneh, H. A., Lacayo-Pineda, J., Phase morphology of NR/SBR blends: Effect of curing temperature and curing time. *Polymers (Basel).* **2018**, 10 (5), 1–15, DOI: 10.3390/polym10050510.

[7] Cotten, G. R., Murphy, L. J., Mixing of Carbon Black with Rubber. VI. Analysis of NR/SBR Blends. *Rubber Chem. Technol.* **1988**, 61 (4), 609–618, DOI: 10.5254/1.3536207.

[8] Lorenz, H., Steinhauser, D., Klüppel, M., Morphology and Micro-mechanics of Filled Elastomer Blends: Impact on Dynamic Crack Propagation. *Lect. Notes Appl. Comput. Mech.* Edited by Grellmann, W. et al., Berlin, Heidelberg: Springer-Verlag Berlin Heidelberg, **2013**, chapter 3, 81–128, DOI: 10.1007/978-3-642-37910-9_3.

[9] Meier, J. G. et al., Kieselsäuregefüllte Elastomerblends durch Masterbatchtechnologie - Steuerung des Mischungszustandes und der Materialeigenschaften. *Kautschuk Gummi Kunststoffe* **2005**, 58, 587–594, URL: https://www.researchgate.net/publication/235673707.

[10] Gundlach, N., Hentschke, R., Karimi-Varzaneh, H. A., Filler flocculation in elastomer blends - an approach based on measured surface tensions and monte carlo simulation. *Soft Mater.* **2019**, 00 (00), 1–14, DOI: 10.1080/1539445X.2019.1568261.

[11] Vilmin, F. et al., Reactivity of bis[3-(triethoxysilyl)propyl] tetrasulfide (TESPT) silane coupling agent over hydrated silica: Operando IR spectroscopy and chemometrics study. *J. Phys. Chem. C* **2014**, 118 (8), 4056–4071, DOI: 10.1021/jp408600h.

[12] Tsou, A. H., Waddell, W. H., Morphology of elastomer blends by dynamic AFM. **2002**, URL: http://www.all-electronics.de/ai/resources/d1f8ed31d4d.pdf (visited on 08/30/2019).

[13] Slomkowski, S. et al., Terminology of polymers and polymerization processes in dispersed systems (IUPAC recommendations 2011). *Pure Appl. Chem.* **2011**, 83 (12), 2229–2259, DOI: 10.1351/PAC-REC-10-06-03.

[14] Mihara, S., Reactive processing of silica-reinforced tire rubber: new insight into the time- and temperature-dependence of silica rubber interaction. Dissertation, University of Twente, **2009**, DOI: 10.3990/1.9789036528399.

[15] Stöckelhuber, K. W. et al., Contribution of physico-chemical properties of interfaces on dispersibility, adhesion and flocculation of filler particles in rubber. *Polymer (Guildf).* **2010**, 51 (9), 1954–1963, DOI: 10.1016/j.polymer.2010.03.013.

[16] Le, H. H. et al., Location of dispersing agent in rubber nanocomposites during mixing process. *Polym. (United Kingdom)* **2013**, 54 (26), 7009–7021, DOI: 10.1016/j.polymer.2013.10.038.

[17] Qu, L. et al., Contribution of silica-rubber interactions on the viscoelastic behaviors of modified solution polymerized styrene butadiene rubbers (M-S-SBRs) filled with silica. *RSC Adv.* **2014**, 4 (109), 64354–64363, DOI: 10.1039/c4ra09492a.

[18] Kaewsakul, W. et al., Factors influencing the flocculation process in silica-reinforced natural rubber compounds. *J. Elastomers Plast.* **2016**, 48 (5), 426–441, DOI: 10.1177/0095244315580456.

[19] Hentschke, R., The Payne effect revisited. *Express Polym. Lett.* **2017**, 11 (4), 278–292, DOI: 10.3144/expresspolymlett.2017.28.

[20] Stöckelhuber, K. W. et al., Impact of filler surface modification on large scale mechanics of styrene butadiene/silica rubber composites. *Macromolecules* **2011**, 44 (11), 4366–4381, DOI: 10.1021/ma1026077.

[21] Fry, D. et al., Structural crossover in dense irreversibly aggregating particulate systems. *Phys. Rev. E - Stat. Physics, Plasmas, Fluids, Relat. Interdiscip. Top.* **2004**, 69 (6), 10, DOI: 10.1103/PhysRevE.69.061401.

[22] Schaefer, D. W., Justice, R. S., How nano are nanocomposites?. *Macromolecules* **2007**, 40 (24), 8501–8517, DOI: 10.1021/ma070356w.

[23] Takenaka, M., Analysis of structures of rubber-filler systems with combined scattering methods. *Polym. J.* **2013**, 45 (1), 10–19, DOI: 10.1038/pj.2012.187.

[24] Le, H. H. et al., Filler Phase Distribution in Rubber Blends Characterized by Thermogravimetric Analysis of the Rubber-Filler Gel. *Rubber Chem. Technol.* **2008**, 81 (5), 767–781, DOI: 10.5254/1.3548231.

[25] Xu, X. et al., Simultaneous analysis of three-dimensional percolation models. *Front. Phys.* **2014**, 9 (1), 113–119, DOI: 10.1007/s11467-013-0403-z.

[26] Baeza, G. P. et al., Multiscale filler structure in simplified industrial nanocomposite silica/SBR systems studied by SAXS and TEM. *Macromolecules* **2013**, 46 (1), 317–329, DOI: 10.1021/ma302248p.

[27] Le, H. H. et al., Kinetics of the phase selective localization of silica in rubber blends. *Polym. Compos.* **2010**, 31 (10), 1701–1711, DOI: 10.1002/pc.20960.

[28] Le, H. H. et al., Filler Wetting in Miscible ESBR/SSBR Blends and Its Effect on Mechanical Properties. *Macromol. Mater. Eng.* **2016**, 301 (4), 414–422, DOI: 10.1002/mame.201500325.

[29] Kohls, D. J. et al., Silica Fillers for Elastomer Reinforcement. *Curr. Top. Elastomers Res.* Edited by Bhowmick, A. K., Boca Raton: CRC Press, **2008**, 505–517, DOI: 10.1201/9781420007183.ch17.

[30] Thomas, S. et al., editors, Natural Rubber Materials - Volume 1: Blends and IPNs. Volume 1, Cambridge: The Royal Society of Chemistry, **2013**, DOI: 10.1039/9781849737647.

[31] Robertson, C. G., Flocculation in Elastomeric Polymers Containing Nanoparticles: Jamming and the New Concept of Fictive Dynamic Strain. *Rubber Chem. Technol.* **2015**, 88 (3), 463–474, DOI: 10.5254/rct.15.85950.

[32] Legters, G., Kuppa, V., Beaucage, G., Coarse-Grained Simulation of Polymer-Filler Blends. *APS March Meet. Abstr.* **2017**, URL: http://meetings.aps.org/link/BAPS.2017.MAR.M1.83 (visited on 08/30/2019).

[33] Mihara, S. et al., Ultra Small-Angle X-Ray Scattering Study of Flocculation in Silica-Filled Rubber. *Rubber Chem. Technol.* **2014**, 87 (2), 348–359, DOI: 10.5254/rct.13.88958.

[34] Meyer, J. et al., A nano-mechanical instability as primary contribution to rolling resistance. *Sci. Rep.* **2017**, 7 (1), 11275, DOI: 10.1038/s41598-017-11728-6.

[35] Meyer, J. et al., Molecular Simulation of Viscous Dissipation due to Cyclic Deformation of a Silica-Silica Contact in Filled Rubber. *Macromolecules* **2017**, 50 (17), 6679–6689, DOI: 10.1021/acs.macromol.7b00947.

[36] Hentschke, R., Macroscopic mechanical properties of elastomer nano-composites via molecular and analytical modelling. *Soft Mater.* **2018**, 16 (4), 315–326, DOI: https://doi.org/10.1080/1539445X.2018.1518243.

4. Binary Polymer Blends – Impact of Heterogeneity

Filler particles which can be considered homogeneous with respect to their surface free energy are generally untreated. An example for this is carbon black or pure silica. To obtain reasonable reinforcing properties, a good interaction with the filler particles themselves (creation of higher order structures, such as agglomerates and filler networks) and with the surrounding elastomer matrix is necessary. Carbon black fulfills both demands without surface treatments and is investigated as unpolar particle types in chapter 3, i.e., filler types I therein. Silica as an inorganic material, on the other hand, shows a very high tendency to form bare silica-silica contacts due to hydrogen bonding [1]. The adherence to the elastomer matrix is minor [2]. Both effects can be controlled by silanization. To obtain a completely homogeneous silanized silica particle is, however, very unlikely. The surface roughness of the silica particle, for instance due to cavities or pores, leads to regions with a higher available surface area. They are consequently more likely to be covered by silanes. Additionally, it is reasonable to assume that areas already containing silanes are (dis-)favored by other silanes. Further reasons are the breakdown of higher order silica structures during the mixing process. When silanes adhere to silica particles arranged in, for instance, agglomerates, not every part of the silica particle is accessible by the silanes. Consequently, it is reasonable to assume that the silanes are distributed heterogeneously on the silica surface. Another indicator is the fact that after silanization the formation of filler networks is still possible [3]. This can happen during mixing or in the post mixing stages, i.e., due to flocculation [1], on which we focus in this work. More detail on this topic is found in Appendix A.3.

In the beginning of chapter 2, we introduced the parameter θ. It modifies the faces of the cubic filler particles independently. In the case of silica particles – on which we focus in this chapter – this modification is equal to silanization. Thus, θ steers the silane density, amount, and, most importantly, its distribution. It narrows the available surfaces down by which the silica particles can form networks. For $0 < \theta < 1$ the silane distribution is considered to be heterogeneous. We narrowed this regime even further down and concluded that values below 0.25 are not reasonable to consider (cf. chapter 2). Consequently, we will investigate three different θ values in this chapter, namely, 0.25, 0.50, and 0.75. Different from chapter 2, we alter the surface free energy of the silanized silica and not those of the bare silica surfaces. This is closer to the industry, because generally the silane and not the silica is altered, although this is also feasible. Altering the silane includes changing the type of silane, but also varying its amount. Because the same amount of silane distributed on a smaller area increases its surface density, the surface free energy must change. The precise extent of this change is, unfortunately, not known. Varying numerous values, however, sweeps a broad possible spectrum.

Similar to the former chapter 3, we can analyze the distribution of the silanized silica particles inside the blend and compare them to experimental results [4]. Here, however, we consider only one blend ratio, i.e., 50/50-NR/SBR. Based on that source and the fact that it is a widely used silica (e.g., [5, 6]), we mimic our bare silica surfaces with the surface free energy

of Ultrasil VN3 taken from [7]. Specifically, we choose the granulated form. From that source and others (e.g., [8]) it is known that silanization reduces the surface polarity and increases the dispersive part of the bare silica surface. Consequently, the surface free energies will be varied differently than those in chapters 2 and 3. The resulting differently silanized silica particles are again termed as filler types named with roman numerals – in accordance to the nomenclature of the former chapters.

We start with the changes due to the introduction of heterogeneous filler particles inside polymer blends. Thereafter, we elucidate the recipe in detail. Then we create the corresponding wetting-envelope - work of adhesion plots for the different filler types. Different from the former chapters, we are not able to deduce an overall exact ordering. The reason is the variation of θ which we consider here. Thus, we describe the behavior of the different filler types in general. A consistency check is again provided by the aggregation phase diagrams with embedded TEM pictures together with the wetted surface fractions. This is done for one fixed value of θ. To investigate the impact of variable silane distribution, we consider aggregation phase diagrams with θ as the variable parameter. The mass fractal dimension of the aggregates is always considered. The impact of a higher filler content is not explicitly considered due to the similar behavior compared to the former chapters, but it is discussed in the conclusion of this chapter.

4.1. Changes due to Heterogeneity

The heterogeneity of the filler particles leads to the reinstatement of the rotation step for the MC simulation introduced in chapter 2. Additionally, the wetted surface fractions need to be updated. We start with the changes of the morphology generator and then discuss those regarding the screening methods.

4.1.1. The Morphology Generator

The basic model is not changed here. It still is a cubic lattice of size L^3, consisting of cubic cells, which mimic different primary particles, i.e., filler and polymer. The probability with which a cell is considered a filler particle is called ϕ, i.e., the filler volume fraction. Each face of the cubic filler cell can be modified with probability θ. The MC simulation consists now again of a rotation and an exchange step. A picture of the model together with the MC steps is depicted in Figure 4.1. Note that the rotation step only affects the filler particles and that the diagonal particle exchange is not limited to the combinations depicted therein.

Here, we consider three distinct values, i.e., $\theta = 0.25$, $\theta = 0.50$, and $\theta = 0.75$. In the context of silane density for a fixed silane type – here TESPT – this leads to values of $\sigma_{silane} \approx 3.00\,n\mathrm{m}^{-2}$, $\sigma_{silane} \approx 1.50\,n\mathrm{m}^{-2}$, and $\sigma_{silane} \approx 1.0\,n\mathrm{m}^{-2}$, respectively[1]. While the value for $\theta = 0.25$ is on the theoretically possible boundary, the other two values coincide with values obtained by MD simulations (cf. Appendix A.3). Altogether, we find in our model three distinct particles (or cube types) of which one cube has two different surfaces. In this chapter, we explicitly identify them as silanized and bare silica surfaces.

[1] Using the same values as in Equation (2.4), i.e., $\rho_{silica} = 2\,\mathrm{g/cm}^3$, $R_{silica} = 8\,n\mathrm{m}$, $\Gamma_{silane/silica} = 0.125$, and $m_{TESPT} = 8.95 \cdot 10^{-22}\mathrm{g}$

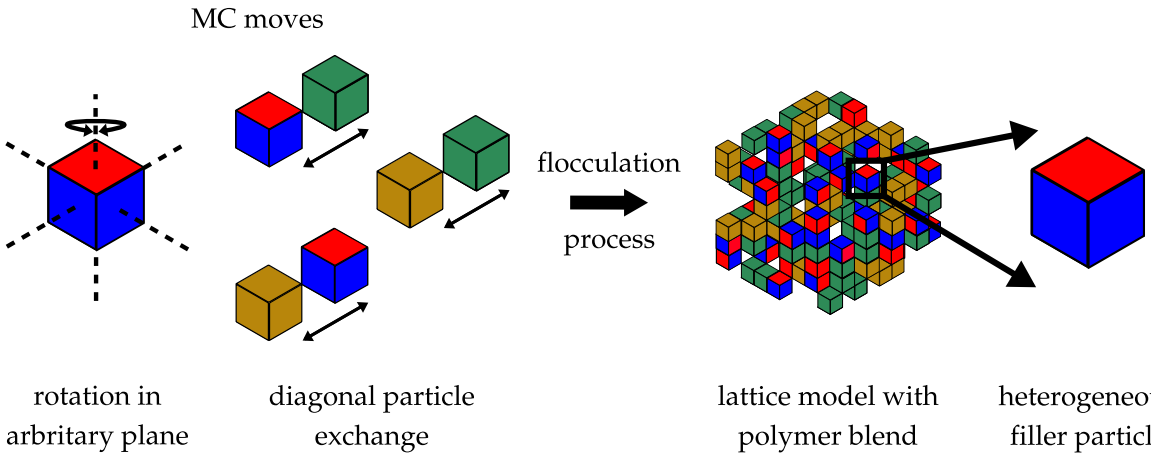

Figure 4.1.: Illustration of MC moves within binary polymer blends containing heterogeneous filler particles. The MC step consists of a rotational step and and diagonal exchange of neighboring particles. **Green** and **golden** cells: polymer of NR and SBR, respectively. **Blue** sides: unmodified filler. **Red** sides: modified filler.

All other aspects regarding the model are not altered. The Metropolis criterion is given as

$$\exp[\beta \Delta W] \geq \xi \; . \tag{4.1}$$

It is, including the necessary quantities, just stated and briefly elucidated once more for the sake of completeness. The quantity ΔW is given by $\Delta W = -\gamma_j \Delta A_j = -\gamma_j a \Delta n_j$, where γ_j denotes the interface tension of a face-to-face pairing of type j and $A_j = n_j\, a$ denotes the attendant total area of j-type interfaces in the system. The constant a is the effective contact area per face, which we assume to be the same for all j. The interface tension is dependent on the surface free energies of the attendant particles. Corresponding values are stated in the beginning of the results part. The theory behind MC in general is found in Appendix D, whereas that for the surface free energies in Appendix B.

4.1.2. Screening Methods

All screening methods are unaffected by the introduction of heterogeneity with exception of the wetted surface fractions. They need to be updated in their nomenclature. As for the change in chapter 3, the procedure to obtain them is unaltered. We need again the number of corresponding contacts, n_{ij}, between cells of types i and j. Here, the different sides of the cells are abbreviated as f (bare silica, i.e., equal to the filler in former chapters), s (silanized silica, i.e., surface modified filler), n (NR), and sb (SBR). The wetted surface fractions l_{ij} are now calculated in the same manner as before. The normalization depends on the first letter, i.e., the cell type i. For instance, the information to what extent the silanized silica surfaces, s, adhere to SBR, sb, is given by the corresponding wetted surface fraction, l_{ssb}, as

$$l_{ssb} = \frac{n_{ssb}}{\sum_j n_{sj}} = \frac{n_{ssb}}{n_{ss} + n_{ssb} + n_{sn} + n_{sf}}. \tag{4.2}$$

Analogously, we compute the other combinations. Bare silica-silica surface fractions are the main indicator for the formation of filler networks. Others are those between silanized silica and polymer and bare silica and polymer. Both give us information about to what extent the different filler types are incorporated inside the respective polymer matrix. High values between silanized silica and polymer are favorable here, as a strong interaction with the elastomer matrix is desirable. Naturally, lower θ values will also show high values for bare silica-polymer related surface fractions. Silanized-bare silica and silanized-silanized silica surface fractions can give us information about the composition of the filler structures. From the perspective of experiments, the latter should be relatively low as the silica particles do not aggregate via silanized surfaces. Both are, however, governed by the extent of the bare silica-silica fractions due to the spatial confinement of the cubes. The polymer-polymer related ones are tools to investigate the polymer morphology.

Note that, as before, changing the positioning of i and j leads to different wetted surface fractions due to the normalization, i.e., considering our example $l_{ssb} \neq l_{sbs}$. The information obtained from one combination, however, is mostly sufficient. Thus, three plots of wetted surface fractions are needed to fully understand the behavior of a system. A bare silica related one, containing l_{ff}, l_{fs}, l_{fn}, and l_{fsb}, a silanized silica related one, containing l_{ss}, l_{sf}, l_{sn}, and l_{ssb}, and a polymer related one, containing l_{sbsb}, l_{nn}, and l_{nsb}.

4.2. Mimicking Heterogeneous Filler Particles in Polymer Blends

Here, we present the results obtained from the simulated systems of a 50/50-NR/SBR blend containing heterogeneous filler particles. We start with the recipe and thereafter create the wetting-envelope - work of adhesion plots. Note that we want to focus on the variation of the silanized silica surfaces. Consequently, the plots will be depicted in the γ_s^p-γ_s-plane instead of the γ_f^p-γ_f-plane. Nevertheless, the positioning of the bare silica surfaces is also crucial – especially in the case of low θ values. It should also be noted that both surface free energies, i.e., γ_s and γ_f, represent a solid. However, in the context of bare and silanized silica surfaces alone, γ_s is considered to be a liquid. We then discuss the behavior of the individual filler types. We focus on the impact of variable surface free energies by fixing θ, i.e., the surface distribution. For this specific case, we make a consistency check whether the general behavior of the wetted surface fractions is correct. Additionally, we create aggregation phase diagrams with embedded TEM pictures. To investigate the impact of variable grades of heterogeneity, aggregation phase diagrams for variable values of θ are created. The accompanied TEM pictures consequently depict a distinct surface free energy pairing at a fixed value of θ. Other pairings are displayed and discussed by their TEM pictures alone. In this context, the mass fractal dimension of the aggregates is discussed.

4.2.1. The Recipe

The recipe for this chapter is given in Table 4.1. Both polymers are identical to the former chapter and therefore taken from [9]. The filler particle is Ultrasil VN3 gran., a widely used silica particle throughout industry and academic research [5, 10–12]. The corresponding surface free energies are taken from [7]. Those of the silanized silica surfaces, denoted with

the subscript s in the following, are variable. Different from the former chapters their variation is adapted. The reason for this is that silanization generally leads to higher dispersive and lower polar surface free energies [7, 8]. The reference is the silica particle Ultrasil VN3 gran. Consequently, the silanized surfaces must have higher dispersive and lower polar surface free energies in comparison. For a more detailed analysis an intermediate value in the dispersive surface free energy is added, i.e., $\gamma_s^d = 25.00$ mJ/m^2. This allows us to mimic different types of silanized silica particles such as Coupsil 8113 gran. (TESPT surface modified Ultrasil VN3 gran., $\gamma_s^d = 21.10$ mJ/m^2 and $\gamma_s^p = 15.80$ mJ/m^2 [7], bifunctional), octyl-mod-silica ($\gamma_s^d = 28.00$ mJ/m^2 and $\gamma_s^p = 3.00$ mJ/m^2, monofunctional), and chloro-mod-silica ($\gamma_s^d = 30.45$ mJ/m^2 and $\gamma_s^p = 5.76$ mJ/m^2, monofunctional) both taken from [13]. Due to the additional variation of θ, it is also possible to mimic the same silanized silica particle but with a different silane surface density. This is investigated in detail in the last subsection.

Table 4.1.: Surface free energies of the components used in the binary polymer blend with heterogeneous fillers. The polymer values as well as the filler values are fixed and those of the silanized silica surfaces, abbrevated as 'mod. sil.', are varied. This mimics different silanized silica particles as well as different silane surface densities on those silica particles. Note that the dispersive part is kept fixed, while the polar part is varied in steps of $5\,m$J/m^2. Note also that silanization increases the dispersive part and lowers the polar part of the silica particle. Thus, all dispersive values are above and all polar values are below that of Ultrasil VN3 gran. Its values are taken from [7]. NR and SBR values were measured via the sessile drop technique and are taken from [9]. The SBR is called SBR-LV in the named reference.

type	name	γ^d [mJ/m^2]	γ^p [mJ/m^2]	γ - total [mJ/m^2]
mod. sil.	-	20/25/30	5,. . . ,20	25,30,. . . ,50
filler	Ultrasil VN3 gran.	18.7	22.7	41.4
polymer	NR	20.24	5.46	25.70
polymer	SBR	29.91	1.64	31.55

Other system parameters are chosen as follows:

- system size L: 128
- filler volume content ϕ (in vol. %): 20
- heterogeneous silanization θ: 0.25, 0.50, and 0.75
- temperature T in K: 413
- maximum number of MC steps: $10^3 \cdot L^3$

With the exception of θ, all values are identical to those in chapter 3. For the upcoming section with the fixed θ value, the impact of different flocculation times is taken into account. Note that different from the last chapter only one simulation per system is conducted. In total 36 recipes are screened in this chapter – not including the different flocculation times.

For a better understanding of the different θ values, it is useful to consider the scheme in Figure 4.2. In the top row, we find the primary filler particles with different silane distributions depicted as red areas on the blue silica particles. Due to flocculation, filler particles merge together and form aggregates. Note that this mainly happens via the bare silica surfaces due to their ability to form hydrogen bonds. For higher silane distributions, i.e., going from left to right, silanized-silanized silica and bare-silanized silica contacts become more likely. This is a result of the spatial confinement. As a result, the ability of the silica particles to form networks is reduced, but their connection with the elastomer matrix is enhanced [8]. The balance between network formation and elastomer affection is key for good mechanical properties.

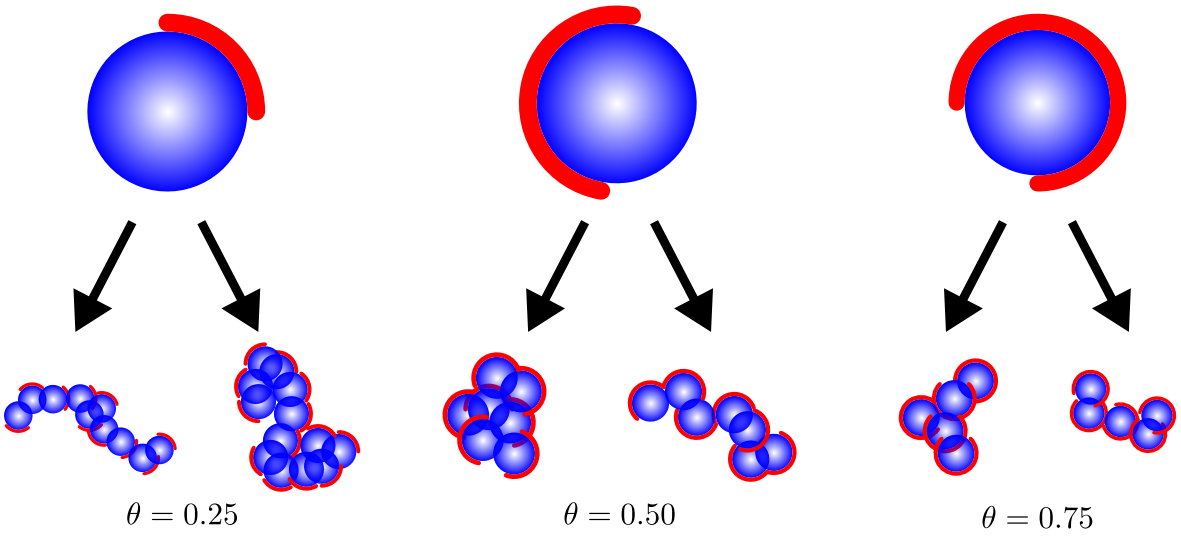

Figure 4.2.: Schematic depiction of different heterogeneous silanizations θ. From left to right: $\theta = 0.25$, $\theta = 0.50$, and $\theta = 0.75$. In the top row we find the primary particles. In the row below exemplarily different aggregates are depicted. Note that the aggregation mainly happens due to bare silica-silica contacts, i.e., via the blue surfaces. Higher values of θ diminish those surfaces. Consequently, more silanized-silanized silica and bare-silanized silica contacts emerge and hence, the aggregates become smaller.

In the next section, we discuss the wetting-envelope - work of adhesion plots. On the pure relation of surface free energies, we can discuss the overall behavior of the different filler types within the different polymers and between the different silanized surfaces and the bare silica surface. Statements about the polymer morphology are also feasible. This yields an overall conclusive picture of the morphology of the systems.

4.2.2. Wetting-Envelope - Work of Adhesion Plots

To discuss the overall behavior, we must again take the flocculation tendencies and the wetting behavior of the different constituents into account. Basically, this is not different from the former chapters. Here, however, the parameter θ leads to difficulties on deriving an ordering as we did in the former chapters. Nevertheless, we keep the order of the discussion

identical. We start with the case where the silanized silica surfaces have a dispersive part of $\gamma_s^d = 20\,mJ/m^2$. This is shown in Figure 4.3.

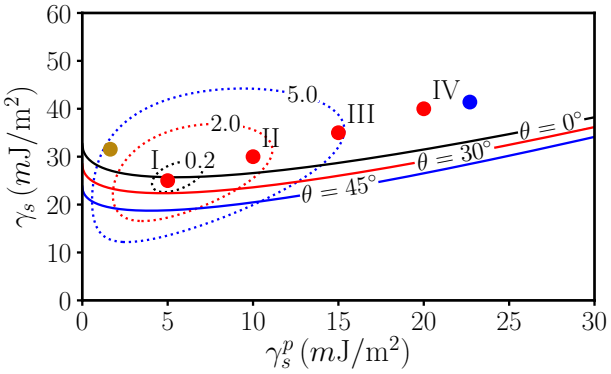

(a) NR as the liquid.

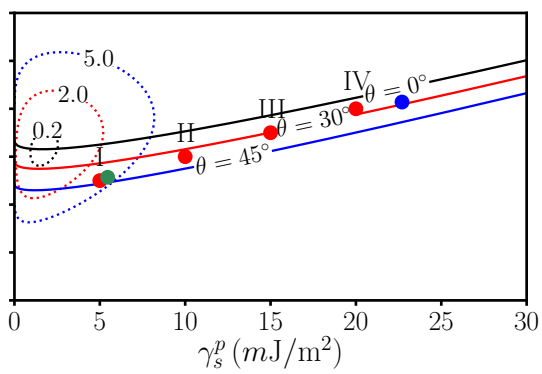

(b) SBR as the liquid.

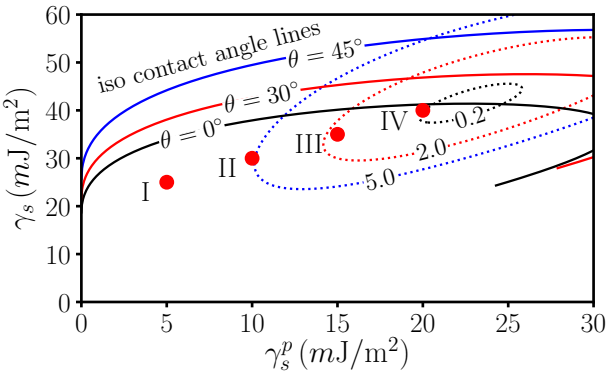

(c) Ultrasil VN3 gran. as the solid.

Figure 4.3.: Wetting-envelope - work of adhesion plots for NR **(a)**, SBR **(b)**, and Ultrasil VN3 gran. **(c)** with different filler types with $\gamma_s^d = 20\,mJ/m^2$. The red dots labeled with roman numerals in each plot display the filler types due to the different silanized silica surfaces. The blue dot in **(a)** and **(b)** shows the position of the bare silica, i.e., Ultrasil VN3 gran. The golden dot in **(a)** and the green dot in **(b)** shows the interaction between the respective other polymer. Filler type I shows the best dispersion inside NR and SBR, but the worst with respect to silanized-bare silica. Here, filler type IV shows the best dispersion.

Both plots in the top, i.e., Figures 4.3a and 4.3b show the compatibility and flocculation tendency with respect to the polymers. They contain information about the behavior of the mimicked silanized silica particles, i.e., the filler types (labeled red dots), the bare silica, i.e., Ultrasil VN3 gran. (blue dot), and the respective other polymer (golden or green dot). The shape of the wetting-envelope plot in Figure 4.3c is different from the other two. The reason for this is that the surface free energy of the solid, which is in this case Ultrasil VN3 gran., was fixed when the wetting-envelope Equation (2.9) was solved. This is done, because we want to focus on the interplay between the silanized and bare silica surfaces. Thus, we vary the silanized surface, i.e., the liquid, on the solid silica. A plot in the style of Figures 4.3a and

4.3b is certainly possible. But it would have to been done for every filler type. This would result in four plots in total. The information content is, however, the same in both cases. Thus, this plot style is merely a more compact depiction. With respect to the iso contact angle lines, everything below the black solid line is considered to be perfectly wetted by the bare silica. The interpretation with respect to flocculation is unaltered, i.e., the closer a filler type is positioned to the black dotted loop, the lower is its tendency to flocculate. Note that the filler types in this chapter are different compared to those in the other chapters. Note also that this description applies to all other wetting-envelope - work of adhesion plots.

Before we start with the labeled filler types, we want to take a look at the behavior of the bare silica, i.e., the location of the blue dot in both polymers. For NR we find perfect wetting and a very high flocculation tendency. For SBR the wetting is mediocre and the flocculation tendency is even higher than for NR. Thus, Ultrasil VN3 gran. has a high tendency to form structures within both polymers. But due to the lower tendency it is more likely to form them within NR than SBR, regardless of the θ value. This is reasoned by the fact that Ultrasil VN3 gran. has almost the same properties as filler type IV with $\gamma_f^d = 20\,m\mathrm{J/m}^2$ in chapter 3. The variation of θ will, however, alter the absolute value of l_{ff} and l_{fn}: The highest should be found for $\theta = 0.25$ and the lowest for $\theta = 0.75$. l_{fsb}, on the other hand, should be very low throughout. Both applies for each value of γ_s^p. Overall, however, an impact of γ_s^p variation on all bare silica related wetted surface fractions should be noticeable. This is reasoned by the impact on the silanized silica surfaces together with their spatial confinement.

We now start with filler type I. It shows perfect dispersion inside NR and a mediocre one inside SBR. The wetting behavior towards NR is almost perfect, whereas that against SBR is bad. Consequently, l_{sn} and l_{ssb}, i.e., the connection between the silanized silica surfaces and both polymers should be very high. The silanized silica surfaces show a very high flocculation tendency when surrounded by bare silica surfaces, together with a perfect wetting behavior. The latter is true for all filler types to come. Thus, that towards the bare silica surfaces, l_{sf} (l_{fs}), should be very low and that towards silanized silica surfaces, i.e., l_{ss} also low. This is justified by the fact that almost all silanized silica surfaces will be found in contact with the polymers. However, for higher values of θ it is reasonable to assume that l_{ss} is increased.

Starting from filler type II, all other types show perfect wetting towards NR. The dispersion of this filler type inside NR is considered good. Regarding the behavior inside SBR we find that the dispersion and the wetting is bad. Thus, SBR is now more avoided than for filler type I, which leads to a decrease for l_{ssb}. Because the dispersion of the silanized silica surfaces when surrounded by bare silica surfaces is now slightly better, we expect a slight increase of l_{sf} (l_{fs}). However, the dispersion is still bad and thus most of the l_{ssb} surface fraction will be transformed into l_{ss} and l_{sn}. The increase of the former is again higher for higher θ values, whereas the impact on the latter should behave vice versa.

Filler type III shows mediocre dispersion inside NR and a poor one inside SBR. The trend of the reduction of l_{ssb} should therefore continue. The positioning in Figure 4.3c indicates that due to the good dispersion between the silanized and the bare silica surfaces, l_{sf} (l_{fs}) should continue to increase. Depending on the θ value we now expect different behavior. For lower θ values, the structure formation due to l_{ff} contacts is dominant throughout. Thus, the silanized silica surfaces can be turned outwards and maintain the contact to the favored polymer, i.e., NR. This means that l_{sn} should be more or less unaffected. The same

is consequently true for l_{ss}. For higher θ values the increase of l_{sf} (l_{fs}) is presumably higher. Because of that and the fact that naturally less bare silica-silica contacts are available, l_{ff} must consequently decrease. Another consequence is then that due to the spatial confinement more l_{ss} contacts appear (cf. the scheme in Figure 4.2). Hence, l_{sn} must decrease.

Finally, we consider the filler type IV. It is very close to the bare silica, i.e., the blue dot in both polymer related Figures 4.3a and 4.3b. This means very high flocculation tendency. However, the dispersion of the silanized silica surfaces surrounded by bare silica surfaces is perfect. Thus, l_{sf} (l_{fs}) must be very high and is presumably the highest of all other filler types. Consequently, other silanized and bare silica related surface fractions should decrease. An exception is again l_{ss} due to the spatial confinement.

Because the SBR phase is avoided for all filler types except I, it is reasonable to assume that the pure polymer related wetted surface fractions l_{nn}, l_{sbsb}, and l_{nsb} should only show a minor impact due to the different filler types. Generally, an overall higher value of l_{sbsb} compared to l_{nn} is very likely. A decrease on the wetted surface fraction of the interphase, l_{nsb}, is most likely to be found for type I, because of its adherence to both polymers. Hence, the value for the interphase increases for increasing surface polarity.

In Figure 4.4, we find the case where the dispersive part of the silanized silica surfaces of all filler types is increased to $\gamma_s^d = 25\,m\mathrm{J/m^2}$.

The higher dispersive part leads to a vertical shift of all – now dark red – dots in all three plots. Consequently, the wetting behavior of the filler types is increased for the polymers. Their flocculation tendency is mostly higher or unaltered. For the silanized-bare silica interplay we find that wetting as well as dispersion becomes poor for all filler types. Due to the higher flocculation tendency inside NR and the better wetting for SBR it is reasonable to assume that contacts between silanized silica surfaces and SBR, l_{ssb}, are increased. Consequently, l_{sn} is decreased. This is additionally reasoned by the poor dispersion inside NR. Both effects should be most discernible for filler type I. Both intermediate types, i.e., II and III, show only minor differences in their flocculation tendencies, regardless of the surrounding environment, i.e., polymer or bare silica. Therefore, it is very likely that they will behave similarly to the $\gamma_s^d = 20\,m\mathrm{J/m^2}$ case. When surrounded by bare silica, filler type IV shows no more perfect dispersion. Thus, the increase of l_{sf} (l_{fs}) is presumably less than in the former case.

The change in the polymer morphology is also similar compared to the former case. A more discernible difference should, however, be found for filler type I due to its affinity to both polymers. Consequently, the wetted surface fraction of the polymer interphase, l_{nsb}, should be decreased and those of l_{nn} and l_{sbsb} should be more similar. This effect is more pronounced for higher θ values.

The last case is depicted in Figure 4.5. Here, the silanized silica surfaces of all filler types have a dispersive part of $\gamma_s^d = 30\,m\mathrm{J/m^2}$. The further increase leads to a higher vertical shift of the – now purple – dots in each plot. The filler types show poor dispersion inside NR in consequence. For those inside SBR we find slightly better dispersion due to the shape of the dotted loops. Additionally, the wetting behavior is now perfect inside each polymer. Thus, the overall value of l_{sn} should be lower and that of l_{ssb} should be higher compared to both other γ_s^d values. The silanized-bare silica interplay shows poor dispersion throughout. Here, also the wetting behavior becomes poor and no silanized silica surface is considered to be

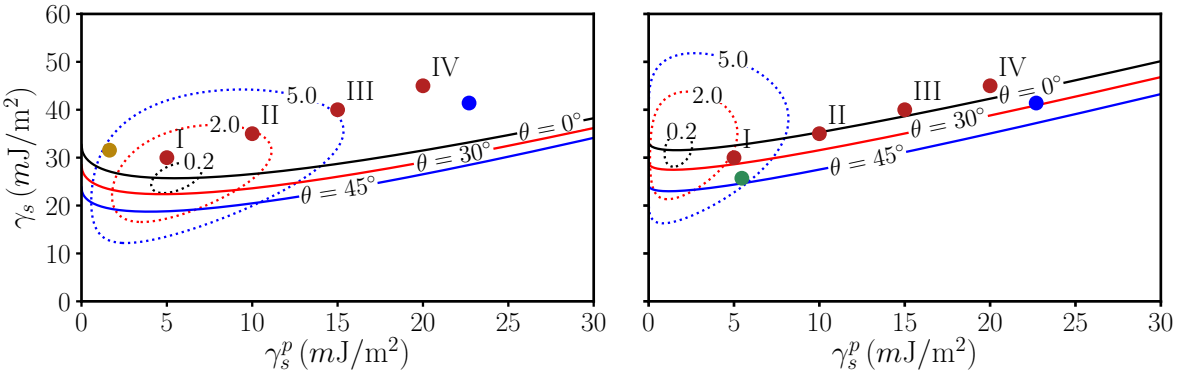

(a) NR as the liquid.

(b) SBR as the liquid.

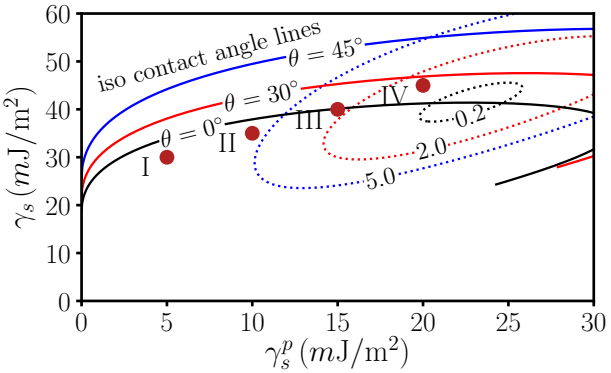

(c) Ultrasil VN3 gran. as the solid.

Figure 4.4.: Wetting-envelope - work of adhesion plots for NR **(a)**, SBR **(b)**, and Ultrasil VN3 gran. **(c)** with different filler types with $\gamma_s^d = 25\,mJ/m^2$. The dark red dots labeled with roman numerals in each plot display the filler types due to the different silanized silica surfaces. The blue dot in **(a)** and **(b)** shows the position of the bare silica, i.e., Ultrasil VN3 gran. The golden dot in **(a)** and the green dot in **(b)** shows the interaction between the respective other polymer. The higher dispersive surface free energy increases the flocculation tendency for most filler types regardless of their surroundings or leaves it unaltered. An exception is found for I inside SBR where it is decreased. The wetting behavior for the polymers is increased, whereas that for the bare-silanized silica interplay is decreased. Here, no filler type shows perfect dispersion anymore.

perfectly wetting the silica anymore. Hence, the values of l_{sf} (l_{fs}) should be lower throughout, but more pronounced for filler types III and IV. Those of l_{ss}, on the other hand, should be higher.

A worthwhile type to discuss in more detail is I. For that, we now find evenly good dispersion and wetting inside both polymers. Consequently, both silanized silica-polymer related surface fractions, l_{sn} and l_{ssb}, should be equal. This fits the initial assumption of their decrease and increase. The flocculation tendency with respect to the bare silica is, however, still very high

and even slightly higher than for the other cases. Because we identified that l_{sf} (l_{fs}) is already very low, it is reasonable to assume that this is here also the case.

For the polymer morphology we find that for filler type I, the values of l_{nn} and l_{sbsb} should be equal, while that of l_{nsb} should be low. For increasing values of γ_s^p the wetted surface fraction of SBR, l_{sbsb} should increase, because the filler types adhere less to SBR. Subsequently, the interphase value l_{nsb} increases too. That for NR, i.e., l_{nn}, on the other hand, should decrease. This is reasoned by the fact that l_{ss} increases. Due to the spatial confinement, less l_{ff} is found. Hence, the open filler surfaces attach to their favored polymer, which is NR.

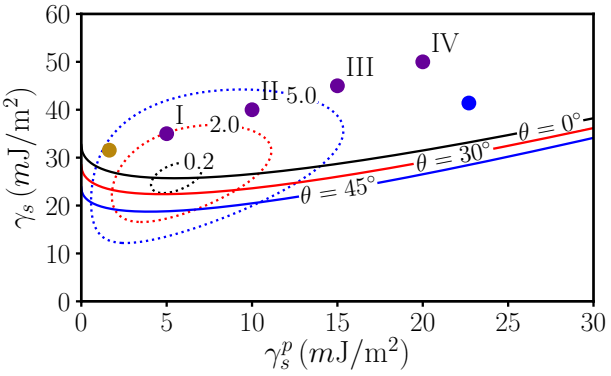

(a) NR as the liquid.

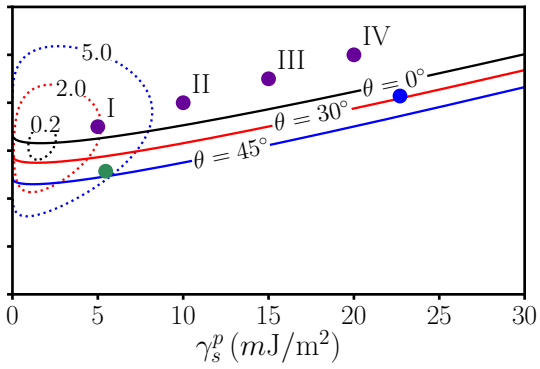

(b) SBR as the liquid.

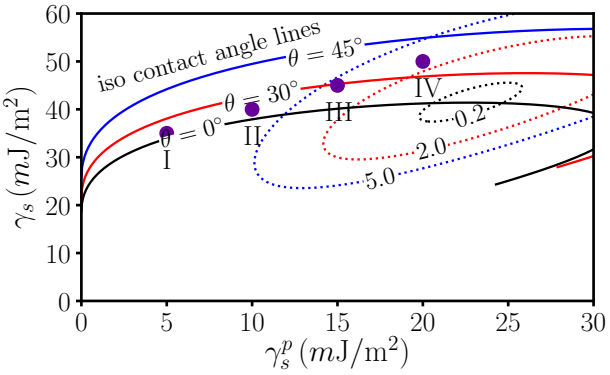

(c) Ultrasil VN3 gran. as the solid.

Figure 4.5.: Wetting-envelope - work of adhesion plots for NR **(a)**, SBR **(b)**, and Ultrasil VN3 gran. **(c)** with different filler types with $\gamma_s^d = 30\,mJ/m^2$. The purple dots labeled with roman numerals in each plot display the filler types due to the different silanized silica surfaces. The blue dot in **(a)** and **(b)** shows the position of the bare silica, i.e., Ultrasil VN3 gran. The golden dot in **(a)** and the green dot in **(b)** shows the interaction between the respective other polymer. The higher dispersive surface free energy increases the flocculation tendency for all filler types in NR and for the silanized silica surfaces with respect to bare silica. For SBR the flocculation tendency slightly decreases. The wetting behavior for polymers is now perfect for every filler type, whereas that for the bare-silanized silica interplay is decreased such that no silanized silica surface perfectly wets bare silica anymore.

Overall we can state that increasing the dispersive part of the silanized silica surfaces decreases the value of l_{fs} (l_{sf}) and increases the value of l_{ss}. Regarding the contact to the polymers, we find more particles in contact to NR the lesser the dispersive part is. For SBR it is vice versa. Here, varying θ leads to less silanized silica-polymer and silanized-bare silica contacts and more silanized-silanized silica contacts. To diminish the bare silica-silica contacts, l_{ff}, higher surface polarity of the silanized silica surfaces is crucial. This also increases the contact of the bare silica surface to NR, l_{fn}. Both effects may be increased by higher values of θ. Steering their contact to SBR is not achievable by altering any surface free energies of the silanized silica surfaces.

In the next section, we consider systems, which have evenly distributed silanized and bare silica surfaces on average, i.e., we set $\theta = 0.50$. For this special case, we take the wetted surface fractions into account and check, whether the behavior we derived is correct.

4.2.3. 50/50-NR/SBR Blend with $\theta = 0.50$

In chapter 3, we investigated the impact of homogeneous filler particles inside NR/SBR blends with different ratios. We found that mostly a distinct favoring for one of the two elastomer matrices is discernible, which is also observed experimentally (cf. references in chapter 3). Additionally, we observed that the formation of filler networks depends on the relative filler volume fraction inside the favored elastomer matrix. But it is not the only requirement. The formation of a continuous polymer phase on its own is also crucial. However, the former chapter described a case where all particles with any surface polarity can be considered pure silica particles or homogeneously silanized ones. The former interpretation explains why the filler particles are able to form networks. It is because this process depends on the hydrogen bonding between the silica surfaces [1]. The adherence to the elastomer matrices, on the other hand, is in this context rather minor [2]. For the latter it is the other way around. Silanized silica particles adhere well to the elastomer matrix, but the filler network formation cannot take place to this extent due to the missing bare silica surfaces. With heterogeneously silanized silica particles both processes can be controlled. It is assumed that the silanized silica surfaces adhere to the elastomer matrix and the bare silica surfaces are used for filler network formation. This is reasoned by the fact that formation of filler networks for silanized silica particles is still found experimentally [5].

In this section, we consider a specific example where $\theta = 0.50$, i.e., on average we have the same amount of silanized and bare silica surfaces on each particle. The top plot in the following figures depicts the aggregation phase diagram. It shows the dependency of the mean size of the aggregates, q_{agg}, on the polar part of the surface free energy of the silanized silica surfaces, γ_s^p. Smaller values of q_{agg} represent larger real space values, R_{agg}, as they are calculated via $R_{agg} = \pi/q_{agg}$. The uncertainties result from the procedure explained in detail in the screening methods section of chapter 2 and are given for the q_{agg} values. The embedded TEM pictures are taken in the same manner as in the former chapters, i.e., they represent a 50×50 portion of the system, five particle layers thick. This is equal to a $0.4\mu\text{m} \times 0.4\mu\text{m}$ sample with a thickness of $40\,n\text{m}$. All TEM pictures are taken at the same position and in the same line of sight. Their colored border corresponds to the number of MC steps indicated in the legend. The two plots at the bottom depict the corresponding wetted surface fractions for the bare and the silanized silica particle, respectively. Those of the polymers are shown

conclusively at the end of the discussion for better comparison. All plots of the wetted surface fractions correspond to the TEM pictures given in the aggregation phase diagram and thus with the red data points therein.

Note that the bare silica surfaces of the filler particles we consider here are approximately comparable to those of filler type IV in the $\gamma_f^d = 20\,m\mathrm{J/m^2}$ case in chapter 3. Thus, it is reasonable to take this filler type as a reference for changes due to silanization. It showed the formation of a filler network inside NR and close to zero contact to SBR. Its aggregates had a size of $R_{agg} \approx 23\,n\mathrm{m}$. In the following, we refer to this as the 'reference type'. We start with the case of $\gamma_s^d = 20\,m\mathrm{J/m^2}$, i.e., Figure 4.6. Regardless of the number of MC steps we always find bigger aggregates at higher surfer polarities γ_s^p. The increase on aggregate size due to longer simulation times is rather minor, but still discernible. At the onset of structural development, i.e., the blue data points obtained after 10^7 MC steps, we find aggregates with a mean size between approx. $15\,n\mathrm{m}$ for the lowest and approx. $17\,n\mathrm{m}$ for the highest surface polarity. At the end of the simulation, i.e., the red data points obtained after $2 \cdot 10^9$ MC steps, we find values between approx. $19\,n\mathrm{m}$ and approx. $23\,n\mathrm{m}$, for the lowest and highest surface polarity, respectively. Thus, the filler types with lower surface polarity create structures with smaller aggregates compared to the reference type. Those with higher surface polarity, on the other hand, are nearly the same in size. This is reasonable, because the silanized silica surfaces have in this case the same surface free energy as the reference type.

If we now take the TEM pictures together with the wetted surface fractions in Figures 4.6b and 4.6c into account, we find that the overall behavior we derived in the context of the wetting-envelope - work of adhesion plots is confirmed here. We discuss it particle-wise in the following and include the TEM pictures in the discussion.

The filler types with low surface polarity, i.e., those labeled with I, show high values of l_{sn} and l_{ssb} and therefore a connectivity to both polymers. The low value of l_{fs} (l_{sf}) agrees with the small aggregate sizes. In chapter 2, we saw that the higher those values are, the more likely it is to find bigger aggregates. Taking the scheme in Figure 4.2 into account, this is reasonable. The probability to find contacts of this specific type is higher, the closer the particles are. The TEM picture gives the impression of dispersed particles inside the NR matrix. The corresponding wetted surface fractions, i.e., l_{ff} and l_{fn}, however, indicate a filler network. Taking the cluster mass distribution into account, we indeed find a single large cluster, which comprises 67% of all particles. We find overall 98% of all particles bound into clusters. Compared to the reference type, the amount of cluster bound particles is similar. The filler network, however, comprised with 92% significantly more particles. Those not found within the filler network have mostly aggregated in clusters with mass greater than ten. Those below only make up 4% of all particles. Thus, the bare silica surfaces form a filler network inside NR whereas the silanized silica surfaces want to be dispersed in both matrices. This turns them outwards, which results in good connectivity.

Increasing the surface polarity and looking at filler type II, we find an increase for l_{sn} and the predicted decrease of l_{ssb}. Due to the lower flocculation between the bare and silanized silica surfaces, we find a slight increase in l_{fs} (l_{sf}), which consequently increases the size of the aggregates and yields a TEM picture with an overall more discernible filler network. The corresponding wetted surface fractions, l_{ff} and l_{fn}, show a slight increase and decrease, respectively. This is in accordance with the impression obtained from the TEM picture. The

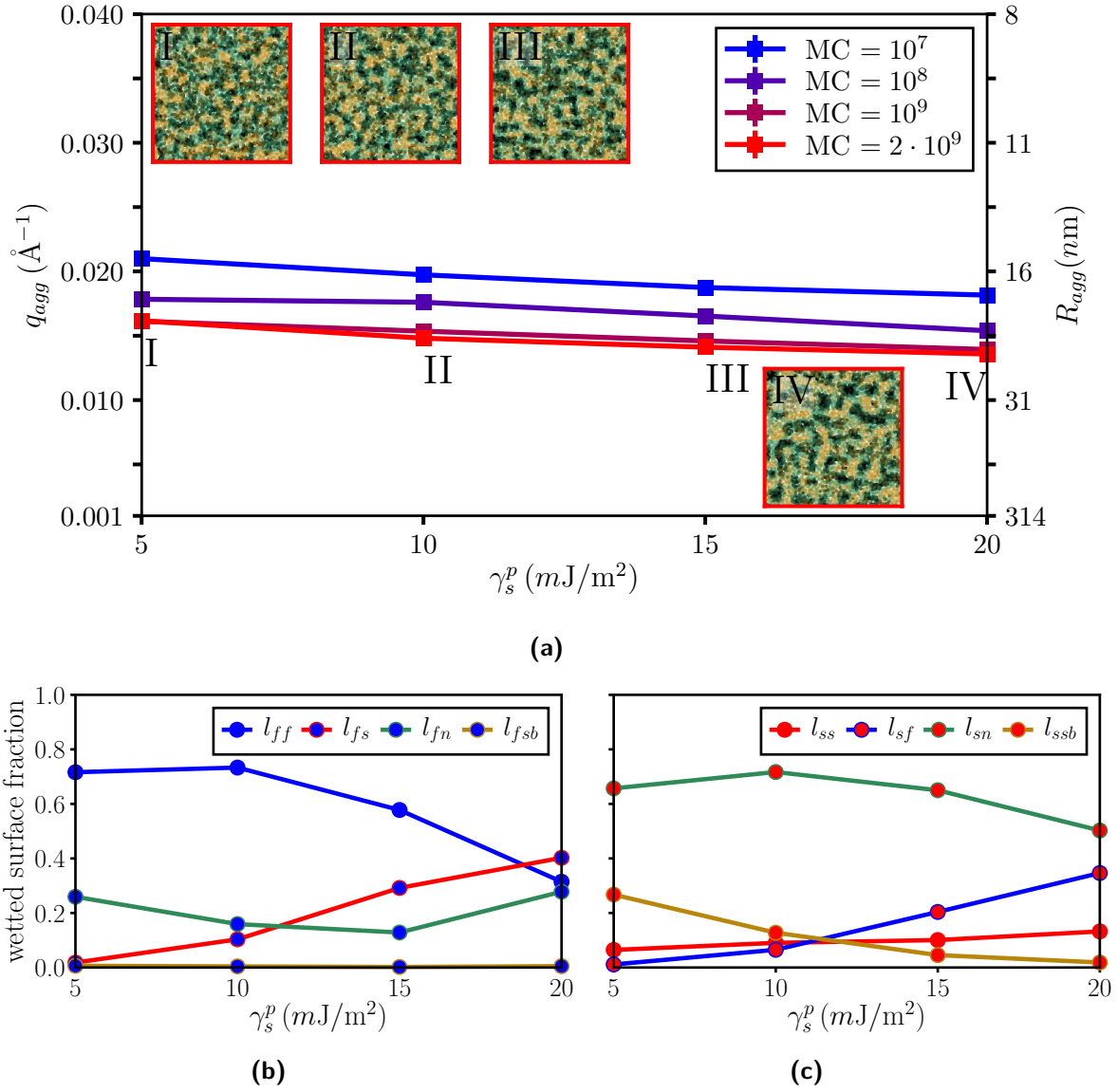

Figure 4.6.: (a): Aggregation phase diagram for silanized silica particles, $\theta = 0.50$, with $\gamma_s^d = 20\,mJ/m^2$ incorporated inside a 50/50-NR/SBR blend with $\phi = 0.20$ at $T = 413$ K. For higher surface polarity the size of the aggregates increases slightly, which is supported by the TEM pictures. In I, the particles look dispersed inside NR with small aggregates in between the SBR domains. In II, the formation of structures becomes more pronounced. This trend continues in III and IV. Wetted surface fractions of bare **(b)** and silanized surfaces **(c)**: The decreasing value of l_{ff} and increasing value of l_{fs} (l_{sf}) indicate a breakdown of the filler network into to bigger aggregates. Filler types with higher surface polarity show lower l_{ssb} values, indicating a shift away from this elastomer matrix. The favoring of NR is discernible due to the high value of l_{sn}. This is additionally supported by the only non-zero bare silica-polymer fraction, l_{fn}.

cluster mass distribution also supports this. We find a more massive network, comprising 77% of all particles. The amount of cluster bound particles is not different from filler type I. We find overall less clusters and the portion of particles not found in the filler network with a mass less than ten is with only 2% even less. Thus, the filler network within NR becomes more massive, if the surface polarity of the silanized silica surfaces is increased. The drawback is that the connectivity to the SBR elastomer matrix is slightly hampered. That towards NR, on the other hand, is enhanced.

For filler type III the TEM picture shows even bigger structures. The appearance of a filler network is still given. However, considering the wetted surface fractions we find that l_{ff} is considerably decreased. A slight decrease is found for l_{fn}, l_{sn}, l_{ssb}. Together with the strong increase of l_{fs} (l_{sf}), we have all indicators for the breakdown of the filler network, although the TEM conveys a different impression. The cluster mass distribution confirms the impression obtained from the wetted surface fractions. We find no filler network at all. The amount of cluster bound particles slightly decreased to 94%. The number of clusters, on the other hand, increased three times to over 12000. Of those, about two third have a mass less than ten. This consequently increases the corresponding amount of particles to 6%. The rest of the particles are mostly found in bigger structures with a mass greater than one thousand. They can be considered the remnants of the filler network found for filler type II. The appearance of the filler network is therefore mostly given due to l_{fs} (l_{sf}) and l_{ss} contacts.

The last filler type we consider here, i.e., IV, now possesses the same surface polarity on its silanized surfaces as our reference type. As expected, the TEM pictures resemble each other. However, the trends we saw coming from type II to III partially continue here. We find a strong decrease in l_{ff} and slight decreases in l_{sn} and l_{ssb}. The increase of l_{fs} (l_{sf}) is also discernible. A difference, however, is given for l_{fn} as it shows a strong increase and even the highest value of all four filler types. This is reasoned by the fact that the filler particles now primarily aggregate via bare-silanized silica interfaces. As a consequence, the structures are limited in their mass and form more, but with less mass. This enhances the connectivity to NR. The cluster mass distribution supports this reasoning. The mass of the clusters is now generally reduced to a few hundred particles. Less particles are cluster bound, i.e., only 80%. The number of clusters increased more than four times compared to III and thus about ten times compared to I and II, i.e., to over 50000. About 90% of them have mass smaller than ten. Subsequently, about 43% of all cluster bound particles are found therein.

Summarized we can state that the strongest adherence of a filler network to both polymers is found for filler type I. The most massive network with a strong adherence to NR and a still reasonable adherence to SBR is found for II. Both other filler types are not able to form a filler network at all and also show poorer adherence to both polymers via their silanized surfaces.

The next case we consider is $\gamma_s^d = 25\,m\mathrm{J/m^2}$, i.e., Figure 4.7. The overall trend for bigger aggregates at higher surface polarity of the silanized surfaces is again discernible. The impact of different flocculation times is different then for the former case. While the impact is generally minor, we find that filler type II now takes longer to form bigger aggregates. The size range of the individual aggregates is equal to the former case.

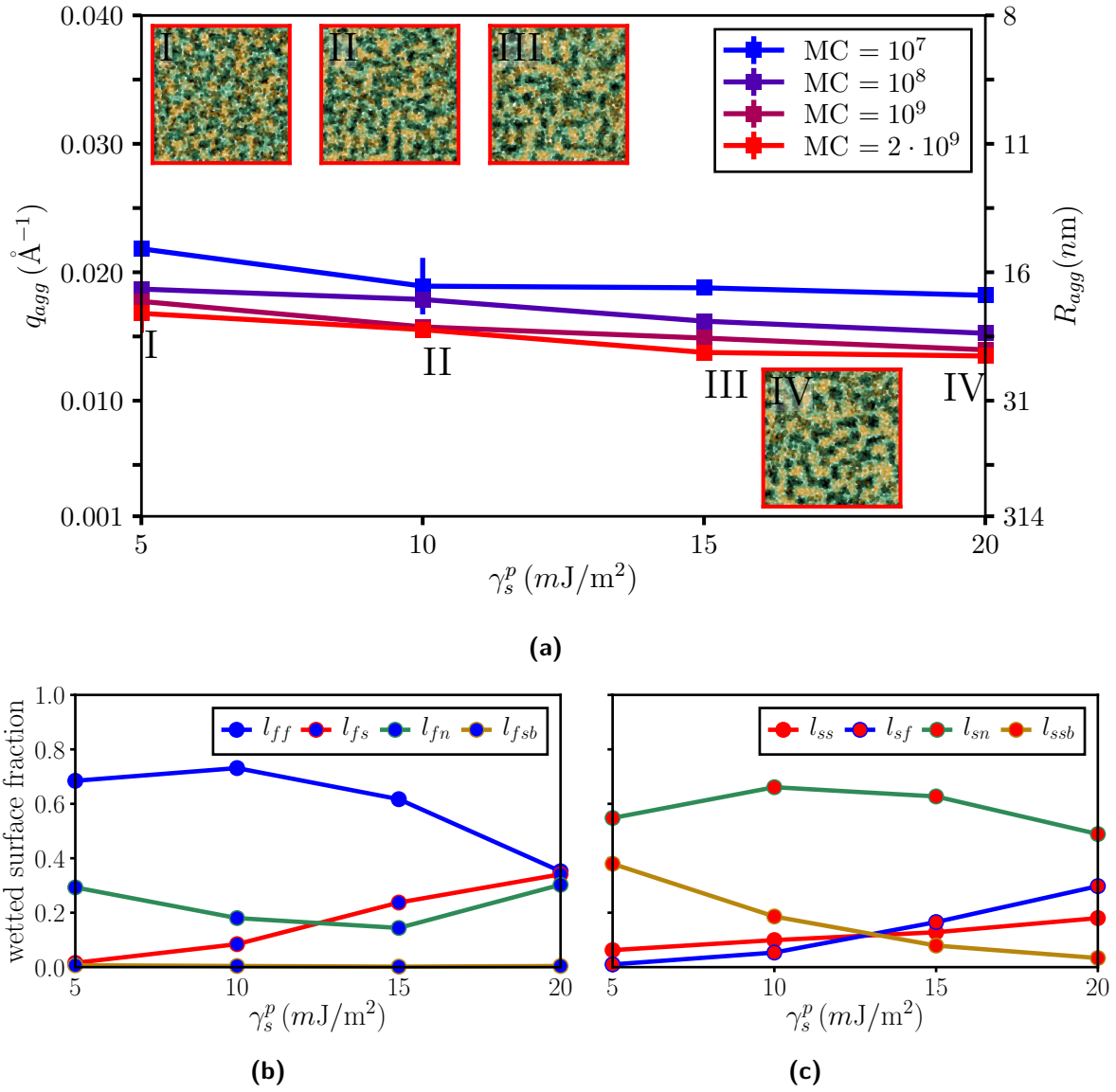

Figure 4.7.: (a): Aggregation phase diagram for silanized silica particles, $\theta = 0.50$, with $\gamma_s^d = 25\,mJ/m^2$ incorporated inside a 50/50-NR/SBR blend with $\phi = 0.20$ at $T = 413$ K. For higher surface polarity the size of the aggregates increases slightly, which is supported by the TEM pictures. In I, the particles look mostly dispersed inside NR but also show adherence to SBR by aggregating more in the interphase. This is reduced in II. Here, a continuous filler network is discernible. For III and IV we find more and bigger structures - similar to the $\gamma_s^d = 20\,mJ/m^2$ case. Wetted surface fractions of bare **(b)** and silanized surfaces **(c)**: The stronger adherence to SBR is discernible by the elevated values of l_{ssb}. The breakdown of the filler network is supported by the overall decrease of l_{ff} and increase of l_{fn}. The formation of bigger structures is again supported by the increase of l_{fs} (l_{sf}) and here also l_{ss}.

.

Due to the increase in the dispersive part of the surface free energy of the silanized silica surfaces, we derived in the context of the wetting-envelope - work of adhesion plots that the overall dispersion inside NR should get poor. That of SBR should be more or less unaltered. Additionally, the dispersion between silanized and bare silica should be poor. While the former is supported by the TEM pictures, the latter is not accessible and must be discussed together with the wetted surface fractions.

Filler type I still looks dispersed inside NR. The improved adherence to SBR is, however, noticeable. The filler particles aggregate more in the interphase between NR and SBR. In some areas, the particles are even found in the SBR matrix itself. The wetted surface fractions support this. The values of l_{sn} and l_{ssb} are closer together. This means a distinct increase in l_{ssb} and a decrease in l_{sn}. We also find less l_{ff} and more l_{fn} contacts, which indicates a less massive filler network. It is presumably found in the interphase of both polymers. Taking the cluster mass distribution into account, we indeed find a single large cluster. But it does not match the requirements of a filler network. It comprises only 38% of all particles. The amount of cluster bound particles is equal to the former case. Most of the particles are found in clusters with a mass greater than ten. Clusters below this threshold only account for 5% of the cluster bound particles. Although the adherence via the silanized surfaces to SBR is improved, we do not find any increase in the connectivity between the bare surfaces. This is explained by the energetically more favored NR matrix over the SBR matrix or the bare surfaces themselves. The surface fractions we accounted for the formation of individual aggregates, i.e., l_{fs} (l_{sf}) and l_{ss}, are equal to those of the former case. This agrees with the impression of the TEM picture as well as with the mean aggregate size. Thus, increasing the dispersive part of the silanized silica surfaces enhances the connectivity to the elastomer matrices with the cost of a hampered network building property.

Increasing the surface polarity renders the TEM picture again more acute. A filler network is now discernible. The increase in l_{ff} together with the slight decrease in l_{fn} supports this reasoning. The same is true for the cluster mass distribution. Although the filler network is with 70% less massive compared to the former case, it still fulfills the requirements. The amount of particles inside clusters with a mass less than ten is reduced to 3%. The number of clusters is also decreased, although it is slightly higher compared to the former case, i.e., 5000 vs. 4000. The amount of cluster bound particles is unaltered. The connectivity to both polymers is still discernible, although the decrease in l_{ssb} is rather pronounced. The increase in l_{fs} (l_{sf}) and l_{ss} is still moderate, which overall fits the impression of the TEM and the mean size of the aggregates. This filler type shows a 'better' version of filler type I in the former case, in the sense that the network is more massive while the connectivity to both polymers is basically the same.

The increase of l_{fs} (l_{sf}) and l_{ss} and decrease of all other surface fractions is for filler type III similar to the former case. The same is true for the impression we obtain from the TEM picture. Consequently, it is no surprise that also the cluster mass distribution coincides. No filler network is found and the amount of cluster bound particles is the same. A minor difference is found for the amount of clusters, which is with about 10000 slightly smaller than the 12000 in the former case. This consequently afflicts the amount of particles found in clusters with a mass smaller than ten, although very slightly, i.e., 5% vs. 6%.

For filler type IV, we find no difference when comparing the TEM picture with the former case. Several large aggregates and agglomerates are observable inside the NR phase. The cluster mass distribution confirms the absence of a filler network. We, however, find that more particles are bound into clusters in comparison, i.e., 84% vs. 81%. Subsequently, we find about 20% less clusters. Their contributions come from every mass category. The particles within clusters of mass less than ten comprise 34% of all cluster bound particles. Other particles are found in clusters with a mass greater than ten and less than one hundred. The decrease in l_{ff} and increase in l_{fs} (l_{sf}) and l_{ss} agree with this. The bare silica surfaces are evenly distributed towards other bare silica surfaces, silanized silica surfaces, and the NR phase.

Summarized, the increase in the dispersive part of the silanized silica surfaces decreases the building properties of filler networks. But it increases the connectivity towards both elastomer matrices. The most balanced result is found for filler type II. The particles not building networks at all, show less, but more massive clusters. They are primarily built via bare-silanized silica and silanized-silanized silica interfaces.

The last case we want to consider, with $\gamma_s^d = 30\,m\mathrm{J/m^2}$, is depicted in Figure 4.8. In the aggregation phase diagram in Figure 4.8a, we find the same behavior as for the former two cases with respect to the mean size of the aggregates. They increase in size for higher surface polarity of the silanized surfaces. For the onset of structural development, i.e., the blue data points obtained after 10^7 MC steps, we find for the lower surface polarity with approx. $14\,n$m slightly smaller and with $18\,n$m for the higher surface polarity, slightly bigger aggregates. At the end of the simulation, i.e., the red data points obtained after $2 \cdot 10^9$ MC steps, we find values of approx. $18\,n$m and approx. $23\,n$m, for low and high surface polarity, respectively. They are also slightly smaller compared to the $\gamma_s^d = 20\,m\mathrm{J/m^2}$ case, at least for the low surface polarity.

For filler type I, we find for the first time a higher value of l_{ssb} than of l_{sn}. The connectivity between the bare silica surfaces, l_{ff}, continues its decreasing trend we saw from $\gamma_s^d = 20\,m\mathrm{J/m^2}$ to $\gamma_s^d = 25\,m\mathrm{J/m^2}$. The same is true for l_{fn} with the difference of an ongoing increase. The value of l_{fs} (l_{sf}) is slightly lower in comparison, while that of l_{ss} is slightly higher. This means that the clusters are now primarily built via silanized surfaces. Because of the dispersed impression inside the entire elastomer matrix we obtain for the TEM and the behavior of the wetted surface fractions, a filler network is unlikely. This is confirmed by the cluster mass distribution. The amount of cluster bound particles is, however, unchanged. We now find considerably more clusters, i.e., twice as many compared to $\gamma_s^d = 20\,m\mathrm{J/m^2}$ and about one third more than $\gamma_s^d = 25\,m\mathrm{J/m^2}$. The same is true for the particles inside clusters with a mass less than ten, i.e., we now find 7%. The further increasing dispersive part consequently leads to a breakdown of the filler network into to several big agglomerates, which show good connectivity towards both polymers.

Increasing the surface polarity further we find filler type II. Similar to the former cases, a filler network is discernible. The slight increase in the mean size of the aggregates is explained by the increase in l_{fs} (l_{sf}) and l_{ss}. The filler network itself is supported by the increasing value of l_{ff} and decreasing value of l_{fn}. The cluster mass distribution confirms this impression. The filler network is, however, with 52% of all particles comprised on the lower threshold. The reduction of the filler network we saw for filler type I is thus also found here. It is likely to assume that an even further increase of the dispersive part will lead to a breakdown.

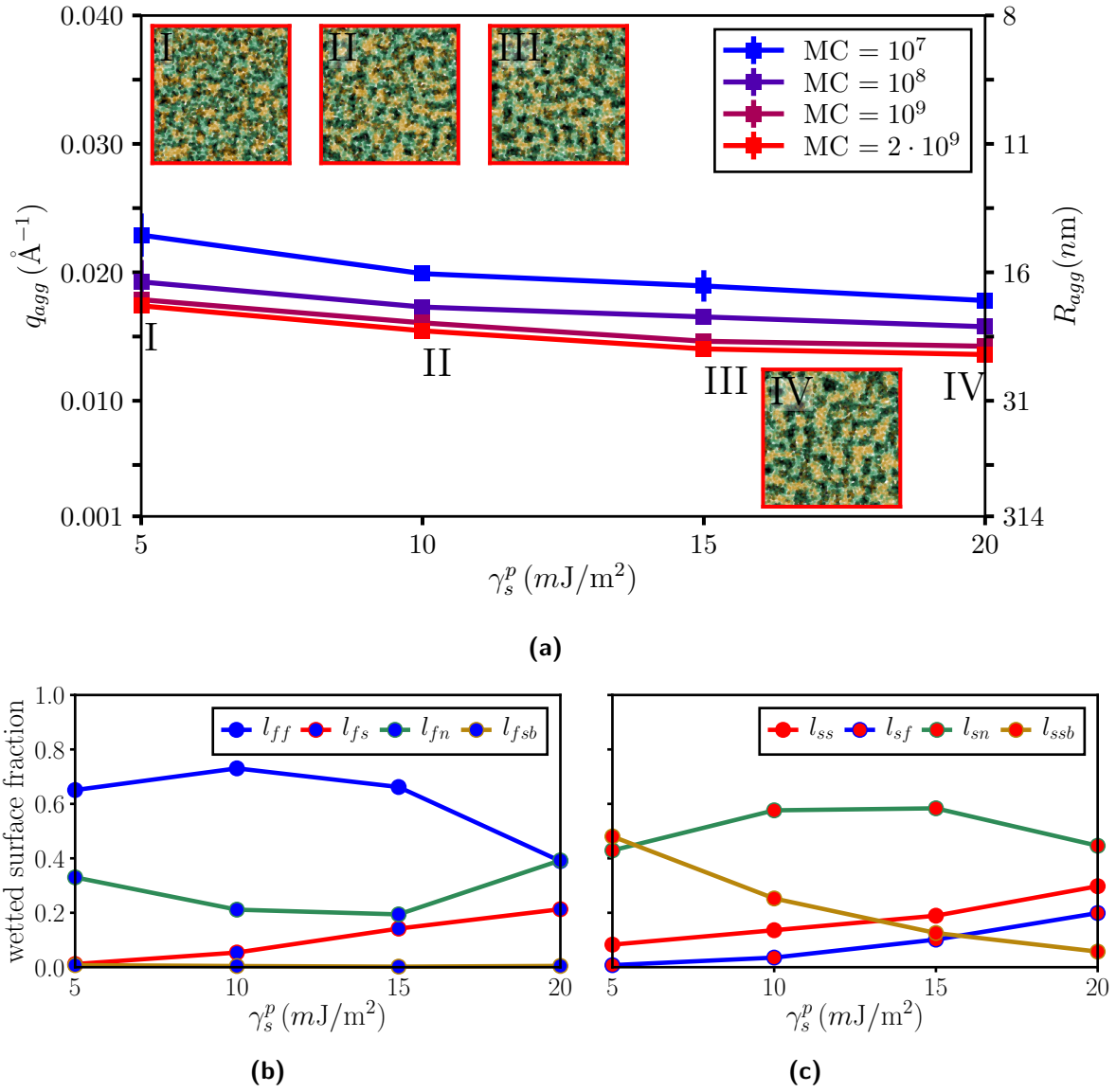

Figure 4.8.: (a): Aggregation phase diagram for silanized silica particles, $\theta = 0.50$, with $\gamma_s^d = 30\,m\mathrm{J/m}^2$ incorporated inside a 50/50-NR/SBR blend with $\phi = 0.20$ at $T = 413$ K. For higher surface polarity the size of the aggregates increases slightly, which is supported by the TEM pictures. In I, the particles look dispersed throughout the whole elastomer matrix. This is reduced in II. Here, a filler network is discernible inside NR with rather good contact to SBR. For III and IV we find more and bigger structures inside NR. Wetted surface fractions of bare **(b)** and silanized surfaces **(c)**: The stronger adherence to SBR is discernible by the elevated values of l_{ssb}. The breakdown of the filler network is supported by the overall decrease of l_{ff} and increase of l_{fn}. The formation of bigger structures is again supported by the increase of l_{fs} (l_{sf}) and here even more pronounced by l_{ss}.

.

Although slightly more clusters can be found in comparison, other values of the cluster mass distribution are comparable.

The TEM picture of filler type III looks similar to both former cases. Most of the trends regarding the wetted surface fractions continue here. The decrease of l_{ff}, l_{fn}, and l_{fs} (l_{sf}), however, becomes less, while the increase in l_{ss} is more pronounced. For the first time we observe no decrease in l_{sn} coming from filler type II. Instead we find a very slight increase. This means that the agglomerates are generally more massive and less smaller clusters are found, which is confirmed by the cluster mass distribution. Even the amount of cluster bound particles is slightly increased to 96% (95% in both other cases).

The last filler type we consider is IV. The TEM picture is in comparison indistinguishable to the former two cases. The wetted surface fractions of the bare silica surfaces are less for l_{fs} (l_{sf}) and more for l_{fn}. This is reasoned by the high value of l_{ss}. Inside the clusters, the particles primarily aggregate via the silanized surfaces. This reduces on the one side the values towards both polymers, i.e., l_{sn} and l_{ssb}, and on the other side, those of l_{fs} (l_{sf}). The now free bare surfaces adhere to the polymer in which the clusters are most prominently found, i.e., in this case NR. The cluster mass distribution supports again this argumentation. We find slightly more cluster bound particles compared to the other γ_s^d values (87%), less clusters in total (38000), and less particles inside clusters with a mass less than ten (23%).

With this last discussion, we can thus conclude that improved polymer connectivity only comes with the cost of filler network reduction. Finding the right balance between both can, for instance, be steered by the surface free energies of the silanized silica surfaces. The impact on the variation of the dispersive part seems to be more pronounced than the polar part. Higher dispersive parts lead to the aggregation via silanized surfaces. The TEM pictures alone oftentimes conveyed a different impression than the cluster mass distribution or the wetted surface fractions. The best balance between the reinforcing properties of a filler network and a good adherence to the elastomer matrix is found for filler type II in the $\gamma_s^d = 25\,m\mathrm{J/m^2}$ case.

So far we considered the wetted surface fractions with respect to the filler particles alone. At last, we want to consider the impact of their surface free energy variation on the polymer morphology. The three plots for each dispersive part are depicted in Figure 4.9.

For the lowest dispersive part, i.e., Figure 4.9a, we find almost no impact on the variation of the polar part of the surface free energy. Only for the lowest value we find a slight depression for the interphase value, l_{nsb}, and a slightly higher value of l_{nn}. Further increasing the dispersive part supports the impression we obtained in the discussion of the filler particles before. For $\gamma_s^p = 5\,m\mathrm{J/m^2}$, the filler particles aggregate in the interphase of both polymers. This results in a decreased value of l_{nsb}. The polymer particles of NR consequently build a more continuous phase, which is displayed by an increase value of l_{nn}. The SBR particles are primarily found in the connection towards the silanized filler surfaces as we have already discussed. This effect is more pronounced for higher dispersive parts, which can be seen in Figure 4.9c. Thus, identical to the homogeneous particles inside polymer blends in chapter 3, we find that the particles found in the interphase make the most pronounced contribution to the variation of the polymer morphology.

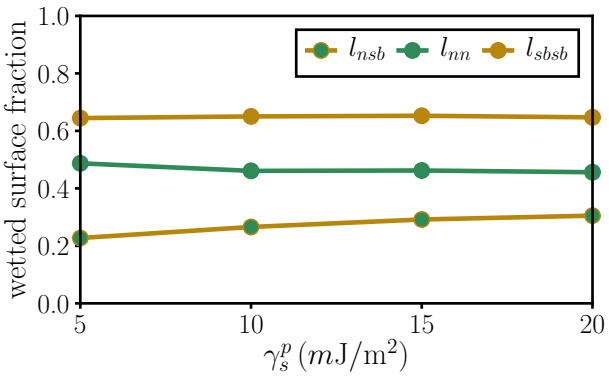

(a) $\gamma_s^d = 20\,mJ/m^2$.

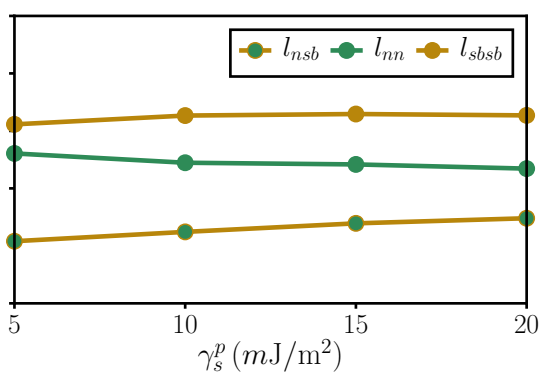

(b) $\gamma_s^d = 25\,mJ/m^2$.

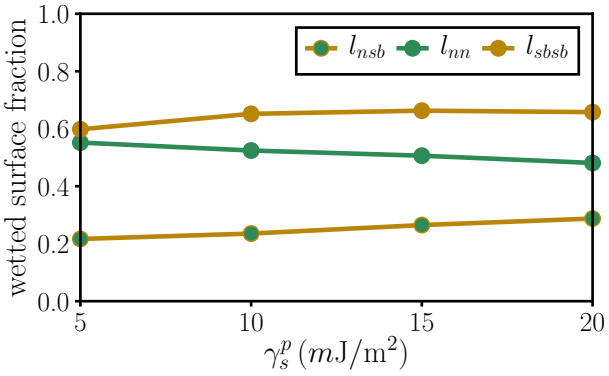

(c) $\gamma_s^d = 30\,mJ/m^2$.

Figure 4.9.: Wetted surface fractions of the polymers for silanized silica particles, $\theta = 0.50$, incorporated inside a 50/50-NR/SBR blend with $\phi = 0.20$ at $T = 413$ K for different dispersive parts of the surface free energy. **(a)**: $\gamma_s^d = 20\,mJ/m^2$. The impact is rather minor. A slight increase in the polymer interphase l_{nsb} and a slight decrease in l_{nn} can be found for higher surface polarity. **(b)**: $\gamma_s^d = 25\,mJ/m^2$. For $\gamma_s^p = 5\,mJ/m^2$ the interphase is considerably lower and the values of both pure polymers is nearly equal. l_{nn} is overall increased and the interphase l_{nsb} is decreased. However, the increase for higher surface polarity is still discernible. **(c)**: $\gamma_s^d = 30\,mJ/m^2$. Most pronounced effect is found for $\gamma_s^p = 5\,mJ/m^2$. A very low interphase value is found, while both pure polymers are equal. The trends in **(b)** continue here.

The last parameter we want to discuss is the mass fractal dimension of the aggregates. Together with a comment about the ability to build a filler network and the mean size, they are listed for each filler type considered so far in Table 4.2. Although the uncertainties for the mass fractal dimensions are in some cases rather big, it is perceptible that bigger aggregates have bigger mass fractal dimensions. Those cases are given for the filler particles able to build a filler network or were able to build one for lower dispersive parts. Because higher surface polarity leads to bigger aggregates, as we already discussed, we find here the correlation of more compact aggregates for higher surface polarity, i.e., higher values of d_m^{agg}. The reference type from chapter 3 has a value of $d_m^{agg} = 1.89 \pm 0.01$. Silanization resulting in low polarity

Table 4.2.: Mass fractal dimension of the aggregates developed by different filler types, $\theta = 0.50$, inside a 50/50-NR/SBR blend for $\phi = 0.20$, $T = 413$ K, and after $2 \cdot 10^9$ MC steps. Additionally, their size is listed and if a filler network was developed. Generally, higher surface polarity produces bigger and more compact aggregates, i.e., their corresponding mass fractal dimension has higher values.

polymer	γ_s^d $[m\mathrm{J/m^2}]$	γ_s^p $[m\mathrm{J/m^2}]$	filler network	R_{agg} $[n\mathrm{m}]$	d_m^{agg}
50/50-NR/SBR	20	5	yes	19.4 ± 0.2	1.84 ± 0.13
		10	yes	21.2 ± 0.1	1.85 ± 0.08
		15	no	22.3 ± 0.1	1.88 ± 0.03
		20	no	23.1 ± 0.1	1.88 ± 0.02
	25	5	no	18.7 ± 1.7	1.84 ± 0.14
		10	yes	20.2 ± 0.2	1.85 ± 0.08
		15	no	22.8 ± 0.3	1.87 ± 0.03
		20	no	23.3 ± 0.1	1.89 ± 0.01
	30	5	no	18.1 ± 0.3	1.85 ± 0.08
		10	yes	20.3 ± 0.2	1.86 ± 0.05
		15	no	22.4 ± 0.2	1.87 ± 0.03
		20	no	23.1 ± 0.4	1.88 ± 0.02

therefore leads to more fractal aggregates, while high polarity show no impact. This effect is stronger for filler types with the same dispersive part and becomes less in the case of higher dispersive surface free energies. Compared to the single polymer case in chapter 2, we find that the aggregates have almost the same mass fractal dimension. A difference is found in the dependency of the polar part. While for the single polymer case the mass fractal dimension became less, we find here a contrary behavior.

4.2.4. 50/50-NR/SBR Blend – Impact of Variable θ

In this section, we want to investigate the impact of variable silane distribution, i.e., vary the parameter θ. For lower θ values we find more bare silica surfaces, which become less for higher θ values. As a result, the ability to form higher order structures via bare silica surfaces is more and more hampered. Nevertheless, particles can, and most presumably will, build aggregates, agglomerates, and networks. Either via their bare or their silanized silica surfaces, which are then not considered as such due to our cluster definition in chapter 2. As a comparison, the results of the former chapter 3 are added for two of the three γ_s^d cases. This needs some clarification. As mentioned before, the particles in chapter 3 can be considered completely bare, i.e., $\theta = 0.0$, or completely silanized, i.e., $\theta = 1.0$. In either case we have a completely homogeneous particle. Here, we vary the surface free energy of the silanized surfaces and mimic, in certain cases, the same energies as we did for the homogeneous surfaces in chapter 3. Thus, it is reasonable to identify the results from this chapter as the same results we would have obtained for $\theta = 1.0$.

We start again with the aggregation phase diagrams with embedded TEM pictures. The basic description of the plot regarding the size of the aggregates is equal to that in the former section. The variable parameter is, however, not the number of MC steps, as they are fixed to $2 \cdot 10^9$, i.e., to the end of the simulation. It is θ which we vary from low to high. Consequently, we find the corresponding TEM pictures from left to right, with a matching color encoding between their borders and the legend. They are taken for a distinct surface free energy combination. Because filler type II was able to form filler networks regardless of the dispersive part for $\theta = 0.50$, it is reasonable to consider it for different θ values. The consideration of the wetted surface fractions is omitted here. The results we obtained in the former section for $\theta = 0.50$ are simply less pronounced for $\theta = 0.25$ and more pronounced for $\theta = 0.75$. The overall behavior we derived in the context of the wetting-envelope - work of adhesion plots is unaffected. In the discussion of the aggregation phase diagrams, the cluster mass distribution is taken into account. Thereafter, we consider for a distinct γ_s^d value the TEM pictures of all other, formerly not considered, polar parts in dependency of θ. In this context, the mass fractal dimension of the aggregates is discussed conclusively. At this point the experimental results obtained in [4] are also reasonable to discuss.

The first case we want to consider is for filler types with $\gamma_s^d = 20\,m\mathrm{J/m^2}$ as depicted in Figure 4.10. The mean size of the aggregates is for $\theta = 0.25$ and $\theta = 0.50$ basically the same, regardless of the polar part of the surface free energy. A minor difference, where the particles are slightly smaller for $\theta = 0.50$, is found for the filler type with $\gamma_s^p = 5\,m\mathrm{J/m^2}$. Further increasing the amount of silanized surfaces, i.e., considering $\theta = 0.75$, we find bigger aggregates for the intermediate polar values. For $\gamma_s^p = 5\,m\mathrm{J/m^2}$, the aggregates have a size in between those of $\theta = 0.25$ and $\theta = 0.50$. For the highest surface polarity we find equally sized aggregates, regardless of θ. For the case of a homogeneously coated particle, i.e., $\theta = 1.0$, we find the biggest aggregates throughout. For filler type II, we even find the overall biggest aggregates with $R_{agg} \approx 33\,n\mathrm{m}$. In the case of this particle, we therefore observe growing aggregates for increasing values of θ.

When we now take the TEM pictures into account and start with the most left one with the blue border, which represents $\theta = 0.25$, we find several structures incorporated inside NR. The appearance of a filler network is discernible. The SBR phase is avoided by the filler particles and only in the interphase of both polymers we find contact between the silanized surfaces of the particles and SBR. The cluster mass distribution reveals a massive filler network comprising 96% of all particles. The number of all particles and those which are cluster bound are equal. There are far less than 1% of the particles inside clusters with a mass less than ten. Subsequently, those not inside the filler network are found within clusters with a mass greater than ten.

For $\theta = 0.50$, i.e., the purple bordered TEM picture, we find a very similar picture. In some areas, the structures look slightly more frayed compared to $\theta = 0.25$. The favoring of NR is still discernible as well as the aforementioned adherence to SBR in the interphase of both polymers. The filler network comprises with 77% considerably less filler particles than for $\theta = 0.25$. Additionally, the amount of clusters increased by a factor of five and subsequently we now find more particles in clusters with a mass less than ten, i.e., 2%, and more than ten, i.e., 21%. The amount of cluster bound particles is slightly decreased to 98%.

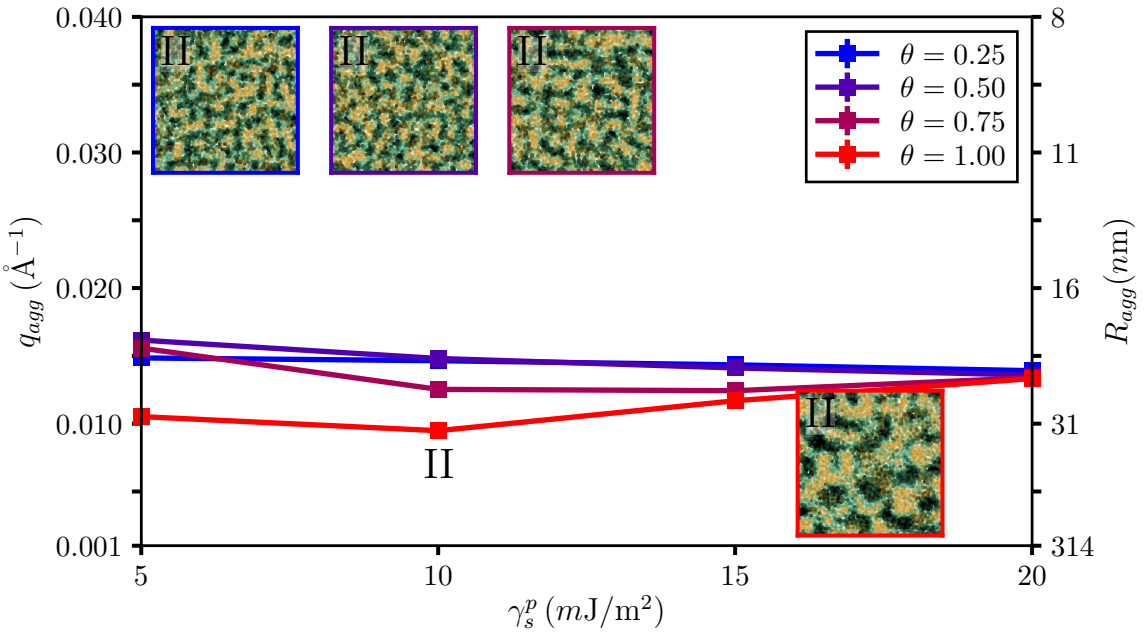

Figure 4.10.: Aggregation phase diagram for silanized silica particles with $\gamma_s^d = 20\,m\mathrm{J/m}^2$ incorporated inside a 50/50-NR/SBR blend with $\phi = 0.2$ at $T = 413$ K under variable silane distribution, θ. The TEM pictures show from left to right more silanized surfaces. They correspond to filler type II and their colored border matches the legend. For the blue bordered TEM, i.e., $\theta = 0.25$, we find small aggregates and a discernible filler network. The purple TEM, i.e., $\theta = 0.50$, still shows a noticeable network, which overall looks more frayed. In the dark red TEM, i.e., $\theta = 0.75$, we find again more and bigger structures. The red bordered TEM, i.e., $\theta = 1.0$, shows very massive structures comprising a considerable amount of filler particles. For all TEM pictures, NR is the favored elastomer matrix.

Further increasing θ to 0.75, i.e., considering the dark red bordered TEM, we find that the structures become visibly more dense. This is supported by the increase in the mean size of the aggregates. The particles are still completely incorporated inside NR. The cluster mass distribution shows no filler network and only clusters with a mass less than one hundred. 44% are found within clusters with a mass less than ten. With 77%, less particles are overall cluster bound. The number of clusters increased by a factor of fifteen compared to $\theta = 0.50$. The hampered structural development agrees with the introductory mentioned expectation. The appearing darker areas must therefore result from the coupling of silanized with bare or other silanized silica surfaces.

The last case is given for the red bordered TEM representing $\theta = 1.0$, i.e., the case of homogeneously coated particles from chapter 3. Here, the filler particles formed big dense structures inside NR. SBR is now completely avoided. The visual increase of size is also supported by the bigger mean aggregate size. For the cluster mass distribution we find that a filler network developed, but now via the silanized surfaces, of course. Its mass is with 98% of all filler particles slightly bigger than the case with $\theta = 0.25$. The number of clusters is more

than twice as much in comparison. While for the former three cases the polymer matrices looked very similar, here we find that the individual domains of each polymer grew.

Altogether, the impact of θ for this filler type is given by the increase of the mean size of the aggregates with increasing values of θ. Although silanized, the surfaces of the silica particles are energetically most favorable for each other leading to the formation of networks, which are less massive for higher θ values. In the individual branches, the structures become more massive for higher values of θ. The most balanced case with a filler network and reasonable adherence to both polymer networks is found for $\theta = 0.50$, which was discussed in the former section.

For the next case with $\gamma_s^d = 25\,m\mathrm{J/m^2}$, i.e., Figure 4.11, we have no comparable data from the former chapter 3, i.e., for $\theta = 1.0$. But, since we saw in the former case that trends in the filler morphology are already observable in the changes from $\theta = 0.25$ to $\theta = 0.75$, we are able to predict the behavior for $\theta = 1.0$.

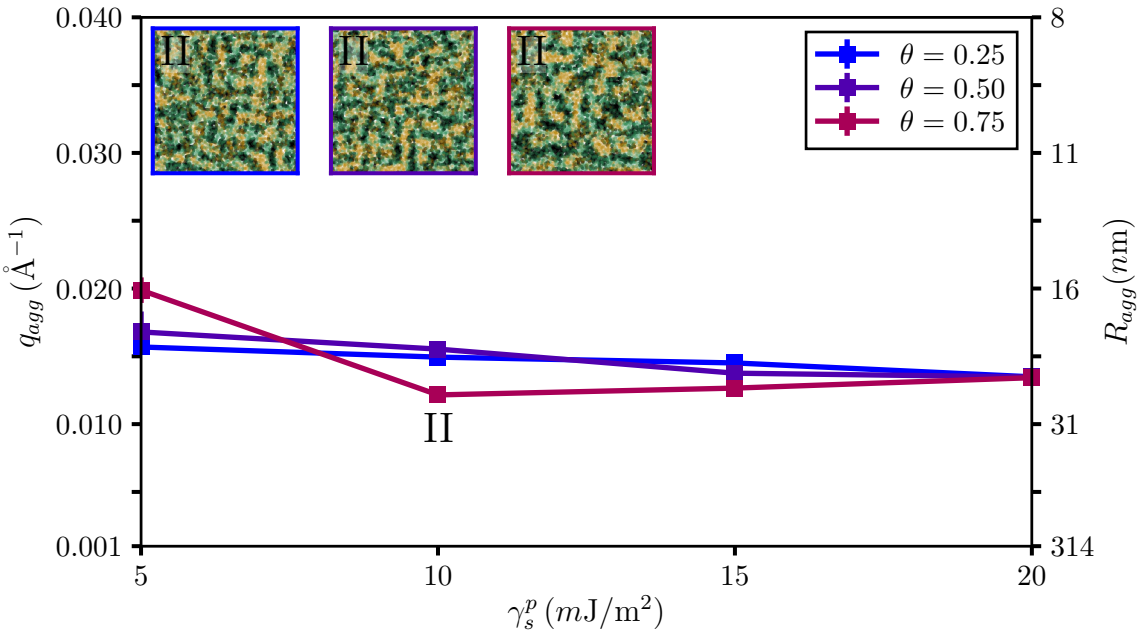

Figure 4.11.: Aggregation phase diagram for silanized silica particles with $\gamma_s^d = 25\,m\mathrm{J/m^2}$ incorporated inside a 50/50-NR/SBR blend with $\phi = 0.2$ at $T = 413$ K under variable silane distribution θ. The TEM pictures show, from left to right, more silanized surfaces. They correspond to filler type II and their colored border matches the legend. Note that for this case no data for $\theta = 1.0$ of the former chapter is available. The blue bordered TEM, i.e., $\theta = 0.25$, shows several aggregates connected into a filler network inside NR. The same is true for the purple bordered TEM, i.e., $\theta = 0.50$. No visible difference is discernible. For the dark red bordered TEM, i.e., $\theta = 0.75$, we find more and denser regions, which is quantitatively supported by the increased mean aggregate size.

The mean size of the aggregates for $\theta = 0.25$ and $\theta = 0.50$ is unaltered in comparison to the case of $\gamma_s^d = 20\,m\mathrm{J/m^2}$. Although we find similar behavior for $\theta = 0.75$, the extent is elevated. For $\gamma_s^p = 5\,m\mathrm{J/m^2}$ the aggregates are with $R_{agg} \approx 16\,n\mathrm{m}$ notably smaller ($R_{agg} \approx 20\,n\mathrm{m}$ before). For the intermediate polarities they are slightly bigger. For $\gamma_s^p = 20\,m\mathrm{J/m^2}$ they again coincide, regardless of the θ parameter. Because the trends are similar to the former case, it is reasonable to assume that for $\theta = 1.0$ we will also find the biggest aggregates overall.

For the blue and purple bordered TEM pictures, i.e., $\theta = 0.25$ and $\theta = 0.50$, no visible differences can be estimated. In both cases a filler network is discernible and the structures within the branches are indistinguishable. The cluster mass distribution, however, shows a significant decrease in the mass of the filler network for the higher θ value, i.e., 70% vs. 95%. While the value for the lower θ value is comparable to the former case, we find a lower value for $\theta = 0.50$. The increase in the dispersive part thus additionally decreases the mass of the filler networks. Other quantities, such as the number of cluster bound particles, the amount of clusters, and the amount of particles in clusters of either mass category are slightly increased. This is most likely a consequence of the mass reduction of the filler network.

The dark red bordered TEM shows no continuous filler network anymore. Instead, several elongated and bigger structures are discernible. The areas of the SBR matrix also appear bigger. The cluster mass distribution reveals that this system is almost equal to that of the former case for the same θ value in every aspect. A slight difference is, however, found for the cluster bound particles, i.e., 79% vs. 77% for the former case. Also the amount of clusters is slightly decreased, which results in slightly less smaller and more bigger clusters, albeit the maximum mass of the clusters does again not exceed one hundred.

It is thus reasonable to assume that for $\gamma_s^d = 25\,m\mathrm{J/m^2}$ and $\theta = 1.0$ the TEM picture is comparable to the red bordered one in Figure 4.10. The structures are, however, most likely bigger. Because the network formation in the former case was achieved via very thin strains connecting the individual structures, it is also feasible that no network via silanized surfaces will be found. Instead, the structures should be more separated and compact.

The last case we want to consider is $\gamma_s^d = 30\,m\mathrm{J/m^2}$ depicted in Figure 4.12. The mean size of the aggregates is very similar to those in Figure 4.10. A difference is found for $\gamma_s^p = 5\,m\mathrm{J/m^2}$ in the $\theta = 1.00$ case. Here, the aggregates are slightly smaller. For the filler type in focus, i.e., II, the trend for increasing aggregate size with increasing θ values is still discernible.

Considering the TEM pictures, we find again very similar behavior for the blue and purple bordered ones, depicting the cases of $\theta = 0.25$ and $\theta = 0.50$. A slight difference might be the overall more frayed impression of the filler networks inside the NR matrix. The corresponding cluster mass distributions reveal that the networks are indeed less massive, i.e., 92% and 52%, respectively. Thus, the decrease we saw from $\gamma_s^d = 20\,m\mathrm{J/m^2}$ to $\gamma_s^d = 25\,m\mathrm{J/m^2}$ is continued here. In addition, we find considerably more clusters in each of the mass categories due to the less particles comprised in the networks. This explains the more frayed impression of the TEM.

For the dark red bordered TEM, i.e., $\theta = 0.75$, the appearance is similar to the former case. No network is discernible and several larger clusters are found within NR. The SBR domains

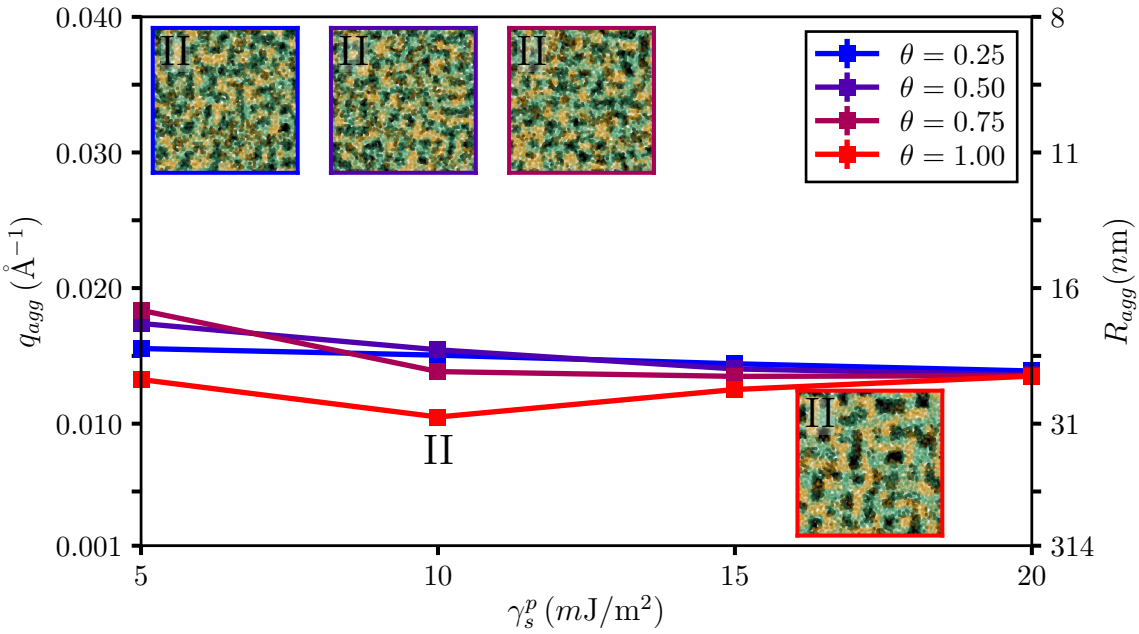

Figure 4.12.: Aggregation phase diagram for silanized silica particles with $\gamma_s^d = 30\,m\mathrm{J/m^2}$ incorporated inside a 50/50-NR/SBR blend with $\phi = 0.2$ at $T = 413$ K under variable silane distribution θ. The TEM pictures show, from left to right, more silanized surfaces. They correspond to filler type II and their colored border matches the legend. The filler networks in the blue and purple bordered TEMs are still discernible, although they look overall more frayed in comparison to the other cases. For the dark red bordered TEM, the SBR domains appear bigger and the network is more broken down into several structures solely found inside NR. The red bordered TEM shows very dense, compact and rectangular structures inside NR.

appear once more slightly bigger. The cluster mass distribution shows a further decrease in the amount of clusters, which is again found in either mass category.

For the homogeneously coated particles, depicted in the red bordered TEM, the trends from the change of $\theta = 0.50$ to $\theta = 0.75$ are continued. The filler particles are found within big, dense structures inside NR. Both elastomer matrices appear more continuous. The cluster mass distribution matches with the visual feedback from the TEM, as we find several more than ten thousand particles massive clusters.

To check whether the same impact of θ is found for the other filler types I, III, and IV, we consider their TEM pictures in direct comparison. Not every filler type was able to form a filler network for $\theta = 0.50$. It is therefore of interest, if they form one for lower values of θ, where the possibilities are elevated. Figure 4.13 depicts a table of TEM pictures for filler types with $\gamma_s^d = 20\,m\mathrm{J/m^2}$. They are bordered according to the color encoding used throughout this section. Thus, θ is increased by 0.25 from top to bottom in each column. The names of the columns match the names of the filler types. Subsequently, γ_s^p is increased in each row from left to right. The corresponding aggregate sizes for each TEM picture can be taken

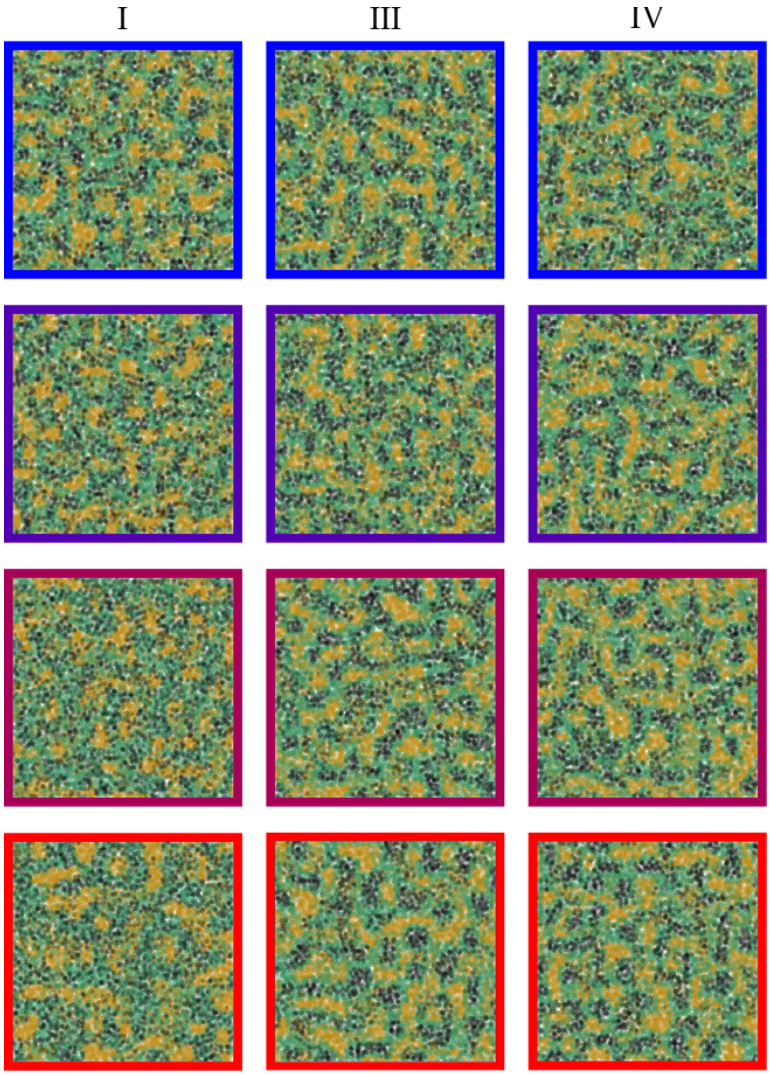

Figure 4.13.: Comparison of TEM pictures for silanized silica particles with $\gamma_s^d = 20\,m\mathrm{J/m}^2$ incorporated inside a 50/50-NR/SBR blend with $\phi = 0.2$ at $T = 413$ K under variable θ and γ_s^p values after $2 \cdot 10^9$ MC steps. Note that the colored borders matches the color encoding used throughout this section, i.e., from top to bottom θ increases in steps of 0.25. The roman numerals indicate the particle in focus, i.e., from left to right the polar part increases. **I**: $\gamma_s^p = 5\,m\mathrm{J/m}^2$. Increasing the number of silanized surfaces leads to better dispersion and a growing SBR phase. **III**: $\gamma_s^p = 15\,m\mathrm{J/m}^2$. The aggregates inside the filler network, which is discernible for $\theta = 0.25$, become bigger and more dense for increasing values of θ. **IV**: $\gamma_s^p = 20\,m\mathrm{J/m}^2$. No difference in the TEMs is visible. This matches the data on the size of the aggregates in Figure 4.10.

from the aggregation phase diagram in Figure 4.10. To investigate the effect on variable θ, Figure 4.13 is discussed column-wise.

We start with filler type I, i.e., the first column. For the lowest θ value we observe a filler network within the NR matrix. Within SBR, non of the filler particles are incorporated. A connection between them and the SBR matrix is, however, found in the polymer interphase.

Because we saw in the former section that the wetted surface fractions between the bare silica and SBR is zero, this is reasonable. The cluster mass distribution shows a filler network comprising 96% of all particles, which are all cluster bound. Beside the filler network, we find few particles within clusters with a mass less than ten, i.e., below 1%. Other filler particles are consequently found in the other mass category. For increased θ, a filler network is still perceptible. The overall impression of the TEM indicates that it is, however, less continuous. The polymer morphology looks similar to the blue bordered TEM. Due to the increased silanized silica surfaces, we find some particles incorporated inside SBR, but still most of the connectivity is given due to aggregation in the polymer interphase. The filler network is with 67% less massive and the number of cluster bound particles also decreased to 98%. Overall, the amount of clusters increased by factor of seven. Those with a mass less than ten, however, increased more. Consequently, we find 4% of all particles within this category. Further increasing θ, the particles look overall dispersed inside NR with some of them found within SBR. Thus, the trend we described before continues here. The polymer morphology is unaltered. No filler network is found and even less particles are cluster bound, i.e., 82%. The number of clusters increased by a factor of ten and most of them are found within the mass category of less than ten, i.e., 82%. Thus, we find 51% of all particles within this category. For the homogeneous silica particles in the red TEM, we find that they look even more dispersed and SBR is now more avoided than before. The connectivity in the polymer interphase is, however, still noticeable. No filler network is built via the silanized sides. With 87% more particles are, however, found in clusters. In addition, we find less clusters, but with 79% most of them still have a mass less than ten. They do, however, only comprise 26% of all particles. This means that the overall mass of the individual clusters formed via silanized sides increased. This behavior matches with the fact that this filler type is similar to silica particles silanized with a monofunctional silane such as octyl-mod-silica or chloro-mod-silica [13].

For the filler type III, i.e., the second column, the effect on the variation of θ is, in comparison to I and II, discussed in the aggregation diagram in Figure 4.10, greatly reduced. In each of the TEM pictures, the particles are primarily found within NR. A connection to SBR is only merely found for the first two TEM pictures. Over the course of increasing θ, the structures within the NR matrix appear more dense. A continuous network is discernible for all TEM pictures. From the last section we already know, however, that for $\theta = 0.50$, i.e., the purple bordered TEM, no filler network exists. The same is true for $\theta = 0.75$. The filler network for $\theta = 0.25$ comprises 92% of all filler particles. Thus, the increase in the surface polarity lead to a less massive filler network. The amount of cluster bound particles and the number of clusters are unaltered. We find, however, less clusters with a mass less than ten and consequently less particles within this mass category. Increasing θ we observe, beside the filler network, the same behavior as for filler type I, but more pronounced. This means less cluster bound particles (94%), more clusters (increased by a factor of fourteen), which are mostly increased in the category of mass less than ten, and consequently more particles within that category (6%). This continues partially for $\theta = 0.75$. The cluster bound particles are down to 58%. The amount of clusters increased by a factor six. But we find 30% more clusters compared to I. Almost all clusters fall in the mass category less than ten (98%). With 52% they do, however, comprise only slightly more particles. In the red bordered TEM, i.e., for $\theta = 1.00$, the filler network is built via silanized sides and comprises 94% of all filler particles. This is more than for $\theta = 0.25$. The amount of clusters is about half in comparison and almost no

clusters with a mass less than ten are found. The amount of cluster bound particles, on the other hand, is unchanged and thus all particles are found within clusters.

For filler type IV, i.e., the last column, an effect due to the variation of θ is not discernible. The only different TEM picture is found for $\theta = 0.25$. Here, the structures look less dense and the overall impression is a more frayed TEM. This also agrees with the cluster mass distribution. We find for $\theta = 0.25$ a very large cluster, which comprises 43% of all filler particles. This means, however, that it does not match the definition of a filler network. Less cluster bound particles are found (98%) and considerably more clusters compared to all other silanized silica particles (factor five more). They are increased in the mass category of less than ten and decreased in that of more than ten. For $\theta = 0.50$, less particles are cluster bound (81%) and we find with an increase by a factor of more than twenty the biggest increase for all filler types. 83% of all clusters account for the mass category less than ten. Subsequently, they comprise 35% of all particles. For $\theta = 0.75$, we find now less than half of all particles bound into clusters (35%). The amount of clusters is only slightly higher than for $\theta = 0.50$ (15%). Now, every cluster has a mass less than ten. For the case of homogeneously coated particles, a filler network via the silanized sides is built. It comprises 92% of all particles, which are all cluster bound. We find the lowest number of clusters for all θ values of filler type IV. It is only 10% of those in the $\theta = 0.25$ case. Almost no particles are found in clusters falling into the mass category less than ten.

We can thus summarize that the variation of the parameter θ leads, beside to less massive filler networks, to more compact structures. Both effects are enhanced, if the dispersive part is increased. For an increased polar part we find a similar effect, i.e., it might hamper the building abilities of filler networks. Although the network building probabilities are decreased due to higher θ, γ_s^d, and γ_s^p values, the ability to form clusters, i.e., the amount of cluster bound particles, is increased due to the increase of each surface free energy. Accordingly, the amount of clusters itself is generally increased. It is, however, noted that an exception is found for filler type IV. It increases the amount of particles comprised into the single large cluster for increasing values of γ_s^d instead. Experimentally, this means that if a filler network is desired, which also shows good adherence to the elastomer matrix, heterogeneously silanized particles with low surface free energies are the best option for this specific NR/SBR combination. For a system with good dispersed particles, homogeneously silanized particles with low surface free energies are most reasonable. It is overall shown that the morphology generator is a useful tool to find filler types with desired properties such as filler network formation, elastomer adherence or dispersion.

Before we start with the comparison to experimental values in the sense of filler distribution, we take a look at the mass fractal dimension of the aggregates in each combination considered so far. Table 4.3 lists all filler types with different θ values and surface free energies. Beside the mass fractal dimension, the size of the aggregates is listed for the sake of completeness. Additionally, the ability to form a filler network is stated.

The low polarity filler types have the highest uncertainties for each θ value. For increasing θ, the mass fractal dimension decreases. The size of the aggregates only decreases initially and starts to increase again for $\theta > 0.5$. For higher surface polarity we find that for increasing θ the mass fractal dimension increases, leading to more compact aggregates. The size of the aggregates behaves similarly. For this filler type we find filler networks in three out of four

Table 4.3.: Mass fractal dimension of the aggregates developed by differently silanized silica particles, i.e., variable θ, with $\gamma_s^d = 20\,m\mathrm{J/m^2}$ inside a 50/50-NR/SBR blend for $\phi = 0.20$, $T = 413$ K, and after $2 \cdot 10^9$ MC steps. Additionally, their size is listed and if a filler network was developed. For θ up to 0.5, higher surface polarity produces bigger aggregates with higher mass fractal dimensions, which indicates more compact ones. For $\theta \geq 0.75$, the particles with intermediate surface polarity produce the biggest aggregates with the highest mass fractal dimensions. Increasing values of θ hinders the ability of the particles to build filler networks. Note that for $\theta = 1.00$ the silanized particles with * built a filler network via their silanized surfaces.

polymer	θ	γ_s^p $[m\mathrm{J/m^2}]$	filler network	R_{agg} $[n\mathrm{m}]$	d_m^{agg}
50/50-NR/SBR	0.25	5	yes	21.2 ± 0.1	1.86 ± 0.06
		10	yes	21.5 ± 0.1	1.86 ± 0.05
		15	yes	21.9 ± 0.1	1.87 ± 0.03
		20	no	22.6 ± 0.2	1.88 ± 0.02
	0.50	5	yes	19.4 ± 0.2	1.84 ± 0.13
		10	yes	21.2 ± 0.1	1.85 ± 0.08
		15	no	22.3 ± 0.1	1.88 ± 0.03
		20	no	23.1 ± 0.1	1.88 ± 0.02
	0.75	5	no	20.2 ± 0.0	1.84 ± 0.19
		10	no	25.1 ± 0.0	1.88 ± 0.05
		15	no	25.3 ± 0.4	1.90 ± 0.01
		20	no	23.5 ± 0.5	1.89 ± 0.01
	1.00	5	no	29.1 ± 0.3	1.76 ± 0.18
		10	yes*	32.8 ± 0.1	1.95 ± 0.01
		15	yes*	26.5 ± 0.3	1.93 ± 0.02
		20	yes*	23.9 ± 0.4	1.89 ± 0.01

cases, although it is again stressed that the network build with $\theta = 1.0$ utilizes silanized surfaces. For $\gamma_s^p = 10\,m\mathrm{J/m^2}$ we find the same trend, but less pronounced. This filler type is only able to form a filler network for the two extreme cases of $\theta = 0.25$ and $\theta = 1.00$. The filler types with the highest surface polarity show a slight increase in the size of their aggregates with increasing θ, while the corresponding mass fractal dimension is unaltered. For this filler type we only find a filler network for homogeneously silanized particles. This shows that even if only one fourth, i.e., $\theta = 0.25$, of a particle has a different surface free energy, it is able to control the filler network building properties. For other dispersive parts, which we do not want to explicitly state here, the same trends are discernible. They are, however, more pronounced for higher dispersive parts.

At last, we want to compare our results to those obtained by the experiment [4]. In order to achieve a most faithful comparison, we have to identify the right silanized silica particles obtained by our simulation. As mentioned before, the parameter θ steers not only the distri-

bution of the silane, but also the silane density, if the amount of silane is fixed. A higher silane density most presumably leads to a stronger effect on the variation of the surface free energy, i.e., a higher dispersive part and a lower polar part. Unfortunately, a tangible correlation is not available. But we do know that lower θ values result in higher silane densities (cf. (2.4) in chapter 2). Thus, it is reasonable to correlate the highest density with the particle with the biggest difference in surface free energy compared to the bare reference surface. This is found for filler type I in the $\gamma_s^d = 30\,m\mathrm{J/m^2}$ case. The lowest density is identified with filler type IV in the $\gamma_s^d = 20\,m\mathrm{J/m^2}$ case, i.e., the lowest difference between the bare and silanized silica surfaces. Together with the amounts and densities of the constituents of the (simplified) recipe of the experiment[2], we can then calculate the silane densities for the different θ values using the aforementioned equation and correlate them to the simulated particles as follows

$$\begin{aligned}
\sigma_{silane}(\theta = 0.25) &\approx 1.80\,n\mathrm{m}^{-2} \rightarrow I \quad @\ \gamma_s^d = 30\,m\mathrm{J/m^2} \\
\sigma_{silane}(\theta = 0.50) &\approx 0.90\,n\mathrm{m}^{-2} \rightarrow II \quad @\ \gamma_s^d = 25\,m\mathrm{J/m^2} \\
\sigma_{silane}(\theta = 0.75) &\approx 0.60\,n\mathrm{m}^{-2} \rightarrow III\ @\ \gamma_s^d = 20\,m\mathrm{J/m^2} \\
\sigma_{silane}(\theta = 1.00) &\approx 0.45\,n\mathrm{m}^{-2} \rightarrow IV \ @\ \gamma_s^d = 20\,m\mathrm{J/m^2}.
\end{aligned} \tag{4.3}$$

With this identification, we mimic particles with the same type of silane, but different silane densities and distributions. This means that a comparison to the experimental results is done only on the basis of the variation of θ. In order to do this, we consider the aggregation phase diagram of the aforementioned particles at the end of the simulation together with the wetted surface fractions of the bare and silanized silica surfaces. This is depicted in Figure 4.14. Note that for filler type IV, which represents our homogeneously silanized particle, no bare silica wetted surface fractions exist, i.e., l_{fj}, with $j \in \{f, s, n, sb\}$ is not available. The same is true for l_{sf}. In the legend of the aggregation phase diagram, the corresponding dispersive parts are listed. The borders of the TEM pictures are again color encoded according to the legend, i.e., from left to right we find lower dispersive surface free energies.

The mean size of the aggregates is increased for the higher θ values. This means that a higher silane density and a more narrow silane distribution leads to the formation of smaller aggregates, compared to a broad distribution with less silane density. The affinity towards the NR phase is discernible in the TEM pictures of each filler type. It does, however, become more pronounced for a more even silane distribution, i.e., for higher θ values. For a homogeneously silanized particle, i.e., $\theta = 1.00$, we find no particles within SBR at all. In the experiment silanized Ultrasil VN3 is found to 77% (65%) inside NR [4]. The value in the bracket describes a different mixing procedure elucidated in detail in the discussion of Figure 3.5. Other particles are consequently found within the other elastomer matrix consisting of SBR/BR. Although the wetted surface fractions do not replace or allow an exact statement about the distribution of the filler particles, we can distinguish them in this quantity and use the TEM pictures as further guidance. We then find that filler type III with $\theta = 0.75$, shows a comparable adherence to NR as filler type IV with $\theta = 1.00$. The l_{fn} and l_{sn} as well as the l_{fsb} and

[2]The silane is fixed to 3 phr (TESPT, $\rho \approx 1.10\,\mathrm{g/cm^3}$ [14]), the filler content is 40 phr (Ultrasil VN3 gran., $\rho \approx 2.00\,\mathrm{g/cm^3}$ [15]), the rubber content is 50 phr NR (SMR 20, $\rho \approx 0.93\,\mathrm{g/cm^3}$ [16]), 25 phr SBR (VSL 5025-0, $\rho \approx 0.94\,\mathrm{g/cm^3}$ [17]), and 25 phr BR (Buna CB 25, $\rho \approx 0.91\,\mathrm{g/cm^3}$ [18]). Note that the last two polymers are always blended beforehand and are considered as one elastomer matrix. The 40 phr filler result in approx. 15% vol., which is less than the 20% we used here.

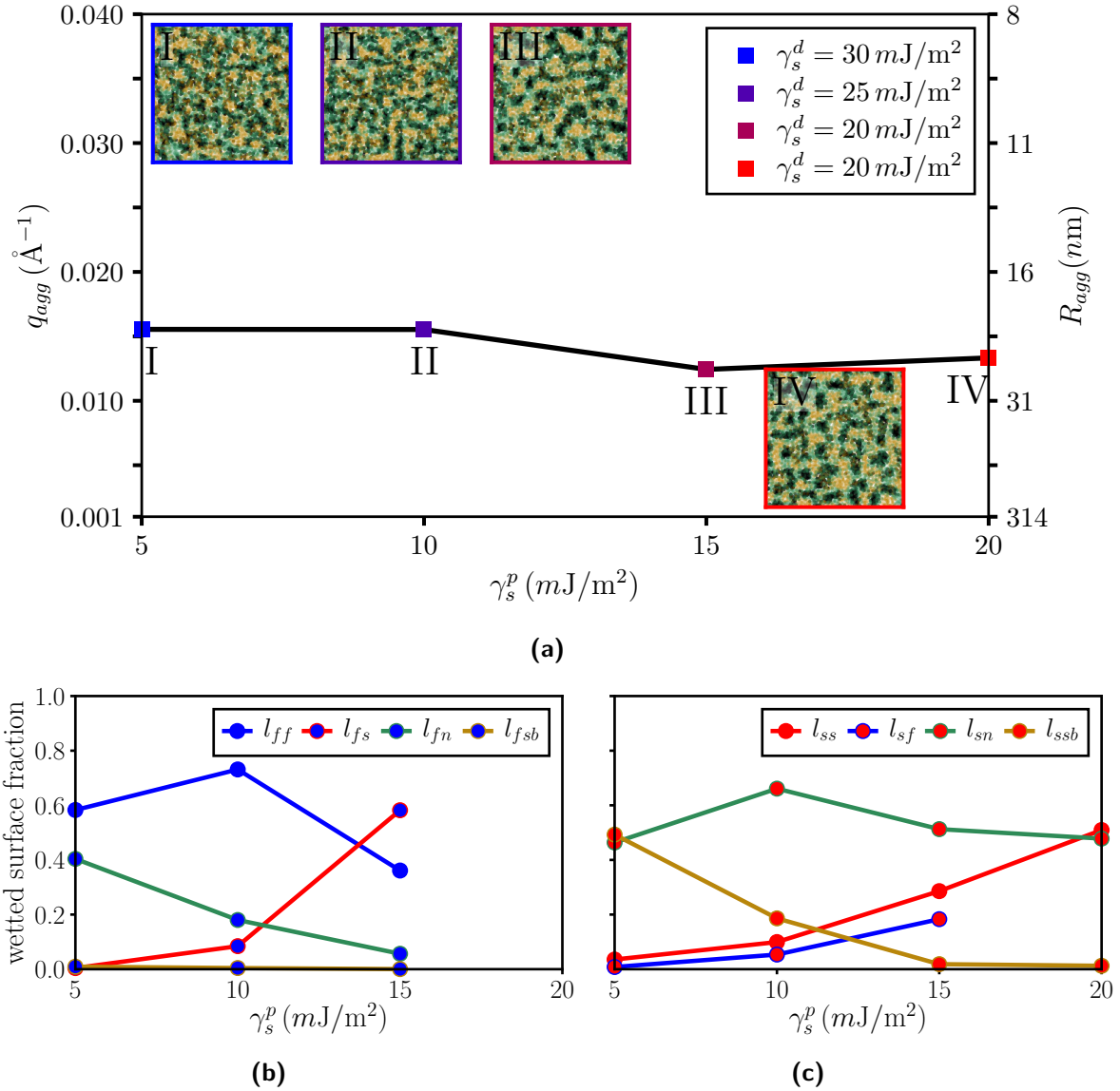

Figure 4.14.: Aggregation phase diagram for variably silanized silica particles with different dispersive surface free energies incorporated inside a 50/50-NR/SBR blend with $\phi = 0.20$ at $T = 413$ K together with wetted surface fractions after $2 \cdot 10^9$ MC steps. **(a)**: Particle **I** is $\theta = 0.25$ with $\gamma_s^d = 30\,m\mathrm{J/m}^2$, particle **II** is $\theta = 0.50$ with $\gamma_s^d = 25\,m\mathrm{J/m}^2$, particle **III** is $\theta = 0.75$ with $\gamma_s^d = 20\,m\mathrm{J/m}^2$, and particle **IV** is $\theta = 1.00$ with $\gamma_s^d = 20\,m\mathrm{J/m}^2$. For higher θ values the affinity to NR becomes more discernible. Wetted surface fractions of bare **(b)** and silanized silica surfaces **(c)**: Note that for homogeneously silanized particles no bare silica surfaces exist. The affinity for the bare silica surfaces towards NR decreases, while that towards the silanized surfaces increases. No affinity towards SBR is discernible. For the silanized surfaces, the affinity towards SBR diminishes for increasing θ, while that towards the particles themselves increases.

l_{ssb} surface fractions indicate this. For II things are different. First of all, the TEM picture shows again that most particles are found within NR, but the structures formed therein find adherence to SBR in their outer regions. Subsequently, more particles are found inside the polymer interphase. This is supported by the wetted surface fractions, which are elevated for all but l_{fsb}. For filler type I, the TEM picture looks overall more frayed and some particles are even completely incorporated within SBR. The increased l_{ssb} and decreased l_{sn} value support this impression. Consequently, even more particles are found within the polymer interphase and, in addition, some now in SBR. Thus, this result matches most with the experimental values. For most of the discussed particles, filler networks are found within the elastomer matrix. The only exception is filler type III. Because only 25% of all surfaces allow to form a filler network according to our definition, this is as expected. It is, however, noted that the most massive filler network, while at the same time showing the best adherence to both polymers, is found for filler type I. Thus, this particle is also reasonable to consider for strong mechanical reinforcement.

We can conclude that the differences we found in the discussion of Figure 3.5 are – at least to some extent – caused by the homogeneity of the silanized silica particles. It is thus most likely to assume that the filler particles in the experiment are heterogeneously silanized. If the silane density or the distribution matches the $\theta = 0.25$ case is impossible to say. It is, however, of high interest to analyze the silane density on silica particles in experiments, characterizing the mechanical properties of rubber compounds. It can be achieved using time-resolved operando FTIR spectroscopy and chemometrics [19] or, in the perspective of simulations, using molecular dynamics [20].

4.3. Conclusion

The methods in Chapters 2 and 3 were combined and analyzed in this chapter. This means that heterogeneously silanized silica particles were investigated with respect to flocculation inside elastomer blends. Specifically, a widely used silica (Ultrasil VN3 gran.) was differently silanized and incorporated inside a 50/50-NR/SBR blend. The different silanization was achieved by altering the surface free energies of the silanized surfaces together with their distribution controlled by the parameter θ. Beside the distribution, θ also steers the silane density, if the amount is fixed in a given recipe. Because of the different impact of silanization on the surface free energies of the silica surface, the values were altered differently compared to the former chapters. Due to the combination of the methods, the corresponding MC-based algorithm was changed. The rotational step, first introduced in chapter 2, was reinstated. The temperature T was fixed to 413 K, the filler volume fraction was set to $\phi = 0.20$, and the maximum number of MC steps was again $10^3 \cdot L^3 \approx 2 \cdot 10^9$.

The systems were analyzed by the methods elucidated in the screening methods section of chapter 2 and thus with the same as those used in chapter 3. Due to the increase of available surfaces, the wetted surface fractions increased significantly in number. This rendered the prediction of their ordering in the context of wetting-envelope - work of adhesion plots difficult. In addition, the variable silane distribution, controlled by the parameter θ, did not allow to establish it. Nevertheless, at least the overall behavior of the filler types within the compound could be predicted. Fixing the value of θ, an explicit focus on the variation of the

surface free energies was possible. It revealed that increasing the dispersive part hampers the network building properties of the different filler types, but increases their adherence to the elastomer matrix. A variation of the polar part showed similar, but less pronounced results. Thus, a good balance between both properties can be steered by fixing θ and varying the surface free energies. To investigate the impact of different silane distribution, θ was varied. It showed that higher θ values led to less massive filler networks and more compact structures. Altering the surface free energies along with θ, increased this effect. Altogether, it was thus found that fillers with a heterogeneously silanized surface of low polarity are best suited to achieve filler network formation with reasonable adherence to the elastomer matrix.

The consistent comparison to the case of homogeneously silanized particles, i.e., the results of chapter 3, allowed to classify the results for the comparison with the experiment [4]. The distinct affinity towards NR was observed throughout and agrees well with the experiment (e.g. [21, 22]). But a better adherence to SBR and the interphase was observed for filler types with a rather low silane distribution and high silane density, represented by a high dispersive and low polar surface free energy.

4.4. References

[1] Lin, C. J. et al., On the Filler Flocculation in Silica-Filled Rubbers Part I. Quantifying and Tracking the Filler Flocculation and Polymer-Filler Interactions in the Unvulcanized Rubber Compounds. *Rubber Chem. Technol.* **2002**, 75 (5), 865–890, DOI: 10.5254/1.3547689.

[2] Wang, M.-J., Effect of Polymer-Filler and Filler-Filler Interactions on Dynamic Properties of Filled Vulcanizates. *Rubber Chem. Technol.* **1998**, 71 (3), 520–589, DOI: 10.5254/1.3538492.

[3] Mihara, S., Datta, R. N., Noordermeer, J. W. M., Flocculation in Silica Reinforced Rubber Compounds. *Rubber Chem. Technol.* **2009**, 82 (5), 524–540, DOI: 10.5254/1.3548262.

[4] Meier, J. G. et al., Kieselsäuregefüllte Elastomerblends durch Masterbatchtechnologie - Steuerung des Mischungszustandes und der Materialeigenschaften. *Kautschuk Gummi Kunststoffe* **2005**, 58, 587–594, URL: https://www.researchgate.net/publication/235673707.

[5] Mihara, S., Reactive processing of silica-reinforced tire rubber: new insight into the time- and temperature-dependence of silica rubber interaction. Dissertation, University of Twente, **2009**, DOI: 10.3990/1.9789036528399.

[6] Stöckelhuber, K. W. et al., Impact of filler surface modification on large scale mechanics of styrene butadiene/silica rubber composites. *Macromolecules* **2011**, 44 (11), 4366–4381, DOI: 10.1021/ma1026077.

[7] Stöckelhuber, K. W. et al., Contribution of physico-chemical properties of interfaces on dispersibility, adhesion and flocculation of filler particles in rubber. *Polymer (Guildf).* **2010**, 51 (9), 1954–1963, DOI: 10.1016/j.polymer.2010.03.013.

[8] Röthemeyer, F., Sommer, F., Kautschuk Technologie: Werkstoffe - Verarbeitung - Produkte. München: Carl Hanser Verlag, **2001**, ISBN: 978-3-446-43760-9.

[9] Klat, D., Karimi-Varzaneh, H. A., Lacayo-Pineda, J., Phase morphology of NR/SBR blends: Effect of curing temperature and curing time. *Polymers (Basel).* **2018**, 10 (5), 1–15, DOI: 10.3390/polym10050510.

[10] Le, H. H. et al., Location of dispersing agent in rubber nanocomposites during mixing process. *Polym. (United Kingdom)* **2013**, 54 (26), 7009–7021, DOI: 10.1016/j.polymer.2013.10.038.

[11] Kaewsakul, W. et al., Factors influencing the flocculation process in silica-reinforced natural rubber compounds. *J. Elastomers Plast.* **2016**, 48 (5), 426–441, DOI: 10.1177/0095244315580456.

[12] Hentschke, R., The Payne effect revisited. *Express Polym. Lett.* **2017**, 11 (4), 278–292, DOI: 10.3144/expresspolymlett.2017.28.

[13] Natarajan, B. et al., Effect of interfacial energetics on dispersion and glass transition temperature in polymer nanocomposites. *Macromolecules* **2013**, 46 (7), 2833–2841, DOI: 10.1021/ma302281b.

[14] Evonik Industries AG, Product Information Si69. **2014**, URL: http://hbchemical.com/wp-content/uploads/2016/03/Si-69-Silane-Product-Information-Sheet.pdf (visited on 08/30/2019).

[15] Evonik Industries AG, Safety Data Sheet Ultrasil VN3 GR. **2015**, URL: http://hbchemical.com/wp-content/uploads/2016/03/SDS-GHS-ULTRASIL-VN3-GR.pdf (visited on 08/30/2019).

[16] Ward, A., El-Sabbagh, S. H., El-Gaffar, M. A., Studies on the dielectric and physical properties of phosphate pigment/rubber composites. **2013**, URL: https://www.kgk-rubberpoint.de/wp-content/uploads/migrated/paid_content/artikel/2539.pdf (visited on 08/30/2019).

[17] Arlanxeo, Product Data Sheet - Buna VSL 5025-2 HM. **2016**, URL: http://www.symtake.com/en/modules/filelist/index.php/download/get/696 (visited on 08/30/2019).

[18] Arlanxeo, Product Data Sheet - Buna CB 25. **2015**, URL: http://www.symtake.com/en/modules/filelist/index.php/download/get/630 (visited on 08/30/2019).

[19] Vilmin, F. et al., Reactivity of bis[3-(triethoxysilyl)propyl] tetrasulfide (TESPT) silane coupling agent over hydrated silica: Operando IR spectroscopy and chemometrics study. *J. Phys. Chem. C* **2014**, 118 (8), 4056–4071, DOI: 10.1021/jp408600h.

[20] Deetz, J. D., Ngo, Q., Faller, R., Reactive Molecular Dynamics Simulations of the Silanization of Silica Substrates by Methoxysilanes and Hydroxysilanes. *Langmuir* **2016**, 32 (28), 7045–7055, DOI: 10.1021/acs.langmuir.6b00934.

[21] Lorenz, H., Steinhauser, D., Klüppel, M., Morphology and Micro-mechanics of Filled Elastomer Blends: Impact on Dynamic Crack Propagation. *Lect. Notes Appl. Comput. Mech.* Edited by Grellmann, W. et al., Berlin, Heidelberg: Springer-Verlag Berlin Heidelberg, **2013**, chapter 3, 81–128, DOI: 10.1007/978-3-642-37910-9_3.

[22] Wunde, M., Klüppel, M., Impact of mixing procedure on phase morphology and fracture mechanical properties of carbon black-filled NR/SBR blends. *Contin. Mech. Thermodyn.* **2017**, 29 (5), 1135–1148, DOI: 10.1007/s00161-017-0562-1.

5. Conclusion

The objective of the research described in this thesis was to develop a model that mimics the flocculation process within filled rubber compounds. Flocculation, also known as re-agglomeration, is a process where the filler particles build larger structures within the elastomer matrix in the post-mixing stages like storage, extrusion or vulcanization [1–6]. The micro structure – or morphology – of the rubber compound is a key parameter to the mechanical properties of tires like rolling resistance, grip or wear (e.g. [3, 7]). In this work, we focused on structures in the size region of up to 1 μm. This includes primary particles, aggregates, agglomerates, and filler networks. The developed model is the morphology generator – a coarse grained simulation approach utilizing a Metropolis Monte Carlo nearest neighbor site-exchange algorithm. The key parameters for the algorithm are surface free energies and the resulting interfacial free energies. They are used to describe the interactions between the individual components, which subsequently control the flocculation process. The resulting morphologies were investigated by means of different screening methods. They include small angle (X-ray) scattering (SAXS) and transmission electron microscopy (TEM).

In chapter 2, the morphology generator was introduced together with the aforementioned screening methods. Additionally, the concept of wetting-envelope - work of adhesion from [8] was introduced. It allowed to analyze the compatibility between fillers and polymers as well as fillers and silanes on the basis of surface free energies. Hence, it is suited to predict the general behavior of the considered compounds. It was used throughout this work to check the simulated morphologies against the underlying theory. A main question of this chapter was, if the morphology generator is capable of creating morphologies similar to the experiment. Further questions were how different ingredients interact with one another, which filler particles create what kind of structures within natural rubber (NR) and styrene-butadiene rubber (SBR), and what impact the simulation parameters have. Throughout this chapter, heterogeneously treated filler particles inside single polymers were considered. If the generator is able to create systems similar to experiments, was analyzed by creating morphologies on the basis of surface free energies exclusively taken from the experiment. The flocculation process of silica particles covered with different silanes inside chloroprene rubber (CR) was considered. Due to the hydrophobizing effect of the silanes on the silica surface a different behavior was expected. It was shown that the morphologies were created according to this expected behavior, i.e., silica covered with monofunctional silanes showed more dispersed morphologies than those covered with bifunctional silanes. Additionally, the accordance to the theory of the wetting-envelope - work of adhesion plots was demonstrated. Thereafter, the surface free energy values from different literature sources [8–11] were taken and, by utilizing a scheme derived from the wetting-envelope - work of adhesion plots, categorized. To answer the question of structural development of different filler particles within NR and SBR, their surface free energies were mimicked in close proximity to real experimental values. This allowed for a broad spectrum of filler particles such as carbon black and different types of silica like methylated, fumed, and precipitated. The simulation parameters, i.e., flocculation time (number of MC steps), filler volume content ϕ, and temperature T were then tested with the mimicked filler particles. It was shown that the flocculation time is crucial. Too long and too short times lead to deviations between simulations and experimental results.

Those include the size of the aggregates and their mass fractal dimension. Furthermore, it is crucial for filler network formation. In NR fillers with no and high surface polarity are able to build those regardless of the dispersive part. These filler particles resemble carbon black and precipitated silica, respectively. For SBR only the high surface polarity fillers, i.e., precipitated silica, build a filler network. Investigation of the filler volume content showed that a certain minimum value is necessary for filler networks. The size of the aggregates, however, is almost unaffected. Their mass fractal dimension, on the other hand, is increased. The last parameter was the temperature. It shows for both polymers only a minor impact. However, it turned out that it needs to be treated cautiously. Unexpected behavior can appear at low temperatures for the filler particles inside NR – in the sense of flocculation simulations. This may be due to the fact that the variation of the surface free energy with temperature is not considered so far. Throughout the testing of the parameters, distinct systems were successfully compared to experimental values. These include the size of the aggregates and their mass fractal dimensions.

In chapter 3, homogeneous filler particles inside polymer blends were considered. The blends always consisted of NR and SBR, but with variable proportion. The main question of this chapter was, if the filler particles preferentially aggregate inside a specific polymer phase when incorporated inside a blend. An additional question was, how the filler network building properties are effected by the introduction of a polymer blend and the usage of homogeneously surface treated filler particles. Independent of the blend ratio, fillers with no surface polarity showed a distinct affection for SBR over NR, which is also found experimentally [12, 13]. For higher surface polarities, the fillers show different structural developments, but always an affinity for NR. The higher the surface polarity is, the better the network building properties within NR are. A special case was, however, found. In that case, the filler particles aggregated along the interface between both polymers. The usage of a 50/50-NR/SBR blend allowed more filler particles to form a filler network inside the elastomer matrix compared to each of the individual single polymer cases. It was argued that this is a direct consequence of the affinity for a distinct polymer phase of the filler particles. Due to the spatial confinement, less filler particles are needed to surpass the threshold of filler network formation. This was investigated further by considering a 70/30-NR/SBR blend. Therein, the preferences for the filler particles did not change. The network building property for the filler particles inside NR was decreased due to the lower spatial confinement. That inside SBR increased. Furthermore, the filler volume content was increased inside both polymer blend ratios to investigate whether the argumentation of spatial confinement is reasonable. The relative filler volume content was then introduced. It was shown that a value of 50% needs to be surpassed in order to always find filler networks – independent of the type of polymer. For lower values the formation is also possible. It is then depending on the polymer morphology developing during the flocculation process. A last question was how longer simulation times affect the morphologies. It turned out that it heavily depends on the type filler. For some the filler networks were enhanced. For others they were destroyed in the longer run. Here, the mass fractal dimension of the aggregates was also affected majorly. It was increased in most of the cases – except for the high polarity fillers.

In chapter 4, heterogeneously surface treated filler particles inside polymer blends were considered. A focus was hereby on silanized silica particles. It was a combination of the approaches found in chapters 2 and 3. But only the 50/50-NR/SBR blend was considered. The main

question was how silanization impacts the filler morphology inside elastomer blends. At first the silane distribution was fixed. In the following it was varied. Because silanization increases the dispersive and decreases the polar part of the surface free energy of the silica particle [9], the corresponding values were altered differently compared to the other chapters. The surface free energy of the 'bare' silica surfaces was fixed with those of Ultrasil VN3. The silanized surfaces were then altered in their dispersive and polar parts. For the fixed silane distribution the building properties for filler networks are decreased for an increasing dispersive part of the surface free energy of the silanized surface. The effect in the variation of the polar part follows the same trend but to a lesser extend. However, at the same time the adherence to both polymers is increased. Thus, for a strong filler network with good adherence to the surrounding elastomer matrix the surface free energies of the silanized surfaces can be used as steering parameters. For variable silanization it was found that a broader distribution of silanized surfaces leads to less pronounced filler networks and more compact structures. Filler networks with good adherence to the elastomer matrix were found for the case of silica particles with silanized surfaces of low polar and high dispersive surface free energies.

Overall it was shown that the morphology generator is suited for screening studies. Additional components can be implemented fairly easy. Throughout this work, about 560 recipes were investigated in total. This does not include the different flocculation times. The resulting simulated morphologies matched with those obtained by experiments in quantities such as size of the aggregates and their corresponding mass fractal dimension.

5.1. Outlook

In future work, the morphology generator can be used for different types of polymers and filler particles. Due to its modular concept, additional cubic cells – mimicking other ingredients – can be implemented with low effort. This, however, renders the analysis of the results more difficult. This could already be seen in chapter 4. The temperature dependence is certainly a crucial issue, which needs to be solved. In Appendix B, it is discussed that a consistent theory does not exist to this day. A possible solution could thus be provided by measured surface free energies at different temperatures and the subsequent extrapolation for very high temperatures. To obtain the mass fractal dimension of the networks, larger systems need to be investigated. This was shown on a example system inside chapter 2. The resulting mass fractal dimension matched with experimental values in good accordance. Due to the long runtime, it is reasonable to overthink the MC algorithm itself. As it is implemented at the moment, it contributes most significantly to the overall runtime (cf. discussion in Appendix D). Dividing the complete system into subsystems and performing the MC within those subsystems could allow to parallel the algorithm, increasing the runtime by several orders of magnitude.

Another question, already mentioned in the conclusion of chapter 3, is, if the information of the morphologies we obtained here is useful with respect to the dynamic moduli, i.e., loss and storage modulus. For instance, their dependency on strain amplitude can be considered. The ratio between loss and storage modulus is a crucial quantity for the elastomer industry and termed $\tan\delta$. An adaptation of the here introduced morphology generator was created by Mariia Viktorova. It utilizes a randomized FCC-lattice instead of a simple cubic one. The flocculation process is again mimicked via a Metropolis Monte Carlo algorithm, which

is adjusted to the new structure. It also uses the surface free energies as parameters. The resulting morphologies in the case of NR/SBR polymer blends are comparable to the results obtained throughout this work in the sense of TEM pictures. This, subsequently, includes the preference of the filler particles for a distinct polymer phase inside the elastomer blend. An analysis of the size of the aggregates and their mass fractal dimension has not been performed so far. Those morphologies are then subject to dynamic-mechanical analysis (DMA). In preparation, the resulting interfacial tensions are replaced by viscous springs with different spring constants, depending on the type of interaction. Then the system is sheared – either with constant frequency and variable strain amplitude or vice versa.

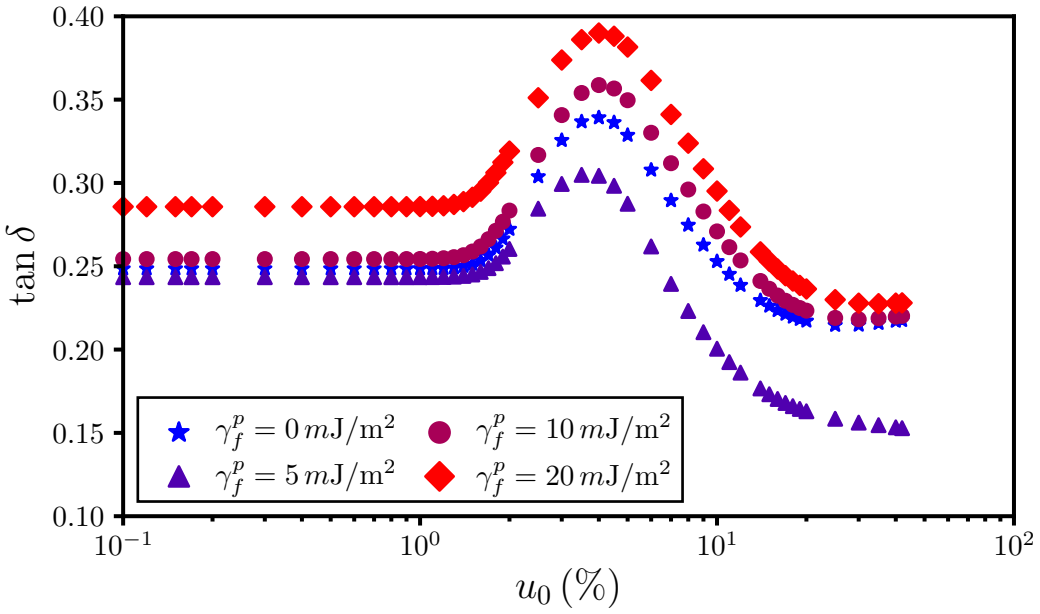

Figure 5.1.: Ratio between loss and storage modulus, $\tan\delta$, vs. amplitude of deformation, u_0, for different filler particles inside a 50/50-NR/SBR blend. These results were obtained by Mariia Viktorova. The blue stars resemble carbon black. They are preferentially found inside SBR and build a continuous network inside it with considerably big aggregates. The purple triangles resemble silica treated with monofunctional silanes. They show no structural development at all and are completely dispersed. The dark red circles resemble precipitated silica treated with bifunctional silanes. They are preferentially found inside NR and build big aggregates connected via thin strains to a filler network. The red diamonds resemble pure precipitated silica. It is preferentially found inside NR and shows a strong tendency to build filler networks. Although the mass of the filler network is slightly smaller than for the dark red circles, the size of the aggregates is considerably smaller. Hence, we find the highest $\tan\delta$ peak.

In Figure 5.1, $\tan\delta$ vs. u_0, i.e., the ratio between loss and storage modulus versus the strain amplitude at a fixed shear frequency is shown for a 50/50-NR/SBR blend. The frequency, in terms of simulation parameters, is fixed at $\omega = 0.2$. The mapping to real values has not

been established yet and will be done in future work. Different symbols represent systems containing different filler particles fixed by their surface free energies. For all filler particles the dispersive part is fixed to $\gamma_f^d = 20\,m\mathrm{J/m^2}$. Note that all particles are homogeneous. Hence, the analysis of the morphology for those systems was done in chapter 3 and we apply the same nomenclature for the filler particles. Because this is ongoing work, the following statements are possible interpretations and should not be taken as a detailed analysis.

The blue stars mimic filler particles with $\gamma_f^p = 0\,m\mathrm{J/m^2}$, i.e., filler particle I. It resembles in its values carbon black. It was shown that it preferentially aggregates inside the SBR phase of the blend and builds a continuous network therein. However, due to the rather big aggregates and comparably small mass, the number of filler-filer bonds that break under shearing is also rather low. The bonds between the filler and the corresponding polymer, on the other hand, break in large proportion. The loss produced due to the different breakages yields a peak in $\tan\delta$. Note that beside the breakage between the filler particles and the filler particles with the elastomer matrix, also the elastomer matrix itself can break. This also contributes to the loss and subsequently yields a peak in $\tan\delta$. Thus, not only filled systems produce a peak in $\tan\delta$.

The purple triangles mimic filler particles with $\gamma_f^p = 5\,m\mathrm{J/m^2}$, i.e., filler particle II. These may be identified as silica particles treated with monofunctional silanes such as octeo or APDMES. They are mostly found inside the NR phase of the blend and are completely dispersed therein – as expected by silica treated with monofunctional silanes (cf. Appendix A.3). From the perspective of the filler particles, only the bonds towards the elastomer matrix can break. The lack of a filler network is correspondingly displayed by less loss under shearing and thus a lower peak.

The dark red circles mimic filler particles with $\gamma_f^p = 10\,m\mathrm{J/m^2}$, i.e., filler particle III. These may be identified as precipitated silica treated with bifunctional silanes such as TESPT. They are again mostly found inside NR but create big aggregates therein. They are connected with one another via thin strains to a filler network. Overall, we find more particles in this network compared to filler particle I, i.e., the blue stars. Subsequently, the loss under shearing is greater and we find a higher peak. Note, however, that the filler particles inside the rather big aggregates contribute less than those inside the branches of the network. This is reasoned by the fact that under shearing the filler particles are less separated inside the aggregates than inside the branches. Consequently, we find bond breakage of filler particles, but not to such an extent as for the last particle we consider, i.e., the red diamonds.

They mimic filler particles with $\gamma_f^p = 20\,m\mathrm{J/m^2}$, i.e., filler particle IV. These may be identified as untreated precipitated silica, which has a very high tendency to build filler networks. They build the most continuous filler network of the particles considered so far. This means that the individual branches are equally thick, which is displayed by rather small size of the aggregates. Under shearing, more filler-filler contacts can consequently break. This leads to a higher loss and thus to a higher peak for $\tan\delta$.

The static quantities obtained by the morphology generator, such as the mass of the filler network, can thus be related to the dynamic moduli. Although an early work, this example shows that if more continuous filler networks are produced, larger peaks of $\tan\delta$ are obtained. If no structural development is observed, the peak is accordingly very low.

5.2. References

[1] Böhm, G. G., Nguyen, M. N., Flocculation of carbon black in filled rubber compounds. I. Flocculation occurring in unvulcanized compounds during annealing at elevated temperatures. *J. Appl. Polym. Sci.* **1995**, 55 (7), 1041–1050, DOI: 10.1002/app.1995.070550707.

[2] Lin, C. J. et al., On the Filler Flocculation in Silica-Filled Rubbers Part I. Quantifying and Tracking the Filler Flocculation and Polymer-Filler Interactions in the Unvulcanized Rubber Compounds. *Rubber Chem. Technol.* **2002**, 75 (5), 865–890, DOI: 10.5254/1.3547689.

[3] Vilgis, T. A., Heinrich, G., Klüppel, M., Reinforcement of Polymer Nano-Composites: Theory, Experiments and Applications. New York: Cambridge University Press, **2009**, ISBN: 9780521874809, DOI: 10.1017/CBO9780511605314.

[4] Mihara, S., Datta, R. N., Noordermeer, J. W. M., Flocculation in Silica Reinforced Rubber Compounds. *Rubber Chem. Technol.* **2009**, 82 (5), 524–540, DOI: 10.5254/1.3548262.

[5] Tunnicliffe, L. B. et al., Flocculation and viscoelastic behaviour in carbon black-filled natural rubber. *Macromol. Mater. Eng.* **2014**, 299 (12), 1474–1483, DOI: 10.1002/mame.201400117.

[6] Robertson, C. G., Flocculation in Elastomeric Polymers Containing Nanoparticles: Jamming and the New Concept of Fictive Dynamic Strain. *Rubber Chem. Technol.* **2015**, 88 (3), 463–474, DOI: 10.5254/rct.15.85950.

[7] Gerspacher, M. et al., Flocculation in carbon black filled rubber compounds. **2002**, URL: http://www.all-electronics.de/ai/resources/72d8ab665f3.pdf (visited on 08/30/2019).

[8] Stöckelhuber, K. W. et al., Impact of filler surface modification on large scale mechanics of styrene butadiene/silica rubber composites. *Macromolecules* **2011**, 44 (11), 4366–4381, DOI: 10.1021/ma1026077.

[9] Stöckelhuber, K. W. et al., Contribution of physico-chemical properties of interfaces on dispersibility, adhesion and flocculation of filler particles in rubber. *Polymer (Guildf).* **2010**, 51 (9), 1954–1963, DOI: 10.1016/j.polymer.2010.03.013.

[10] Natarajan, B. et al., Effect of interfacial energetics on dispersion and glass transition temperature in polymer nanocomposites. *Macromolecules* **2013**, 46 (7), 2833–2841, DOI: 10.1021/ma302281b.

[11] Klat, D., Karimi-Varzaneh, H. A., Lacayo-Pineda, J., Phase morphology of NR/SBR blends: Effect of curing temperature and curing time. *Polymers (Basel).* **2018**, 10 (5), 1–15, DOI: 10.3390/polym10050510.

[12] Lorenz, H., Steinhauser, D., Klüppel, M., Morphology and Micro-mechanics of Filled Elastomer Blends: Impact on Dynamic Crack Propagation. *Lect. Notes Appl. Comput. Mech.* Edited by Grellmann, W. et al., Berlin, Heidelberg: Springer-Verlag Berlin Heidelberg, **2013**, chapter 3, 81–128, DOI: 10.1007/978-3-642-37910-9_3.

[13] Wunde, M., Klüppel, M., Impact of mixing procedure on phase morphology and fracture mechanical properties of carbon black-filled NR/SBR blends. *Contin. Mech. Thermodyn.* **2017**, 29 (5), 1135–1148, DOI: 10.1007/s00161-017-0562-1.

Appendices

A. Filler, Rubber, and Silanization – The Nomenclature

In this part, we elucidate the nomenclature of the work. The physical and chemical context as well as the production methods are described in detail. Subsequently, we make a distinct connection to our model and identify the cubic volume elements therein. We start with elastomers, which are the rubber elements in our model and continue with the filler particles. We describe the main contributors to their reinforcing properties, i.e., structure, surface area, and surface activity. Additionally, we explain the importance of mixing and dispersion. The dynamic properties of reinforcement originate from the development of filler morphologies within the elastomer matrix. In order to understand this connection we discuss it briefly. Due to the fact that carbon black and silica are until today the main fillers used in the rubber industry, we describe their production and properties in detail. Finally, we explain the term silanization, i.e., surface treatment of silica particles.

A.1. Elastomers

An elastomer is defined by the IUPAC[1] as any "Polymer that displays rubber-like elasticity" [1], i.e., polymers with viscoelasticity and very weak intermolecular forces. A polymer is a macromolecule, with a chain-like, branched or network like structure, consisting of repeating subunits known as monomers. Monomers are compounds of several elements like carbon, hydrogen, oxygen and silicon. They are linked to form a polymer by covalent bonds in a process called polymerization. It can be subdivided into several cases and is the main reason for the individual conformations of polymers (cf. page 28ff. [2]). Covalent bonds in combination with the length of the polymer chains limit the mobility of the monomers resulting in high viscosity. Figure A.1 shows an example of a polymer(-chain), which is of importance for this work: cis-1,4-polyisoprene. It is the main part of natural rubber (NR). At this point we want to stress that the nomenclature is not consistent throughout literature. The term rubber is often interchangeably used with elastomer. This can be most prominently seen when we look at natural or synthetic rubbers: Both are classified as elastomers.

Straining an elastomer leads to stress within its molecular chains. The result is significant elongation, which upon removal of the stress leads to considerable molecular reconformation. This property, known as rubber-like elasticity, is the combined result of cross-links between the polymer chains and entropy changes.

Cross-links are bonds that link different polymer chains to another in a small region from which at least four chains emanate [4]. They can be roughly divided into two categories: physical and chemical bonds. Physical bonds are entanglements between polymer chains where two or more chains cross each other in one point. Compared to chemical bonds physical bonds are weaker. Especially, if the elastomer is kept over its glass transition temperature T_g. Then it can disentangle due to contour length fluctuations or reptation, a concept derived by de

[1] International Union of Pure and Applied Chemistry

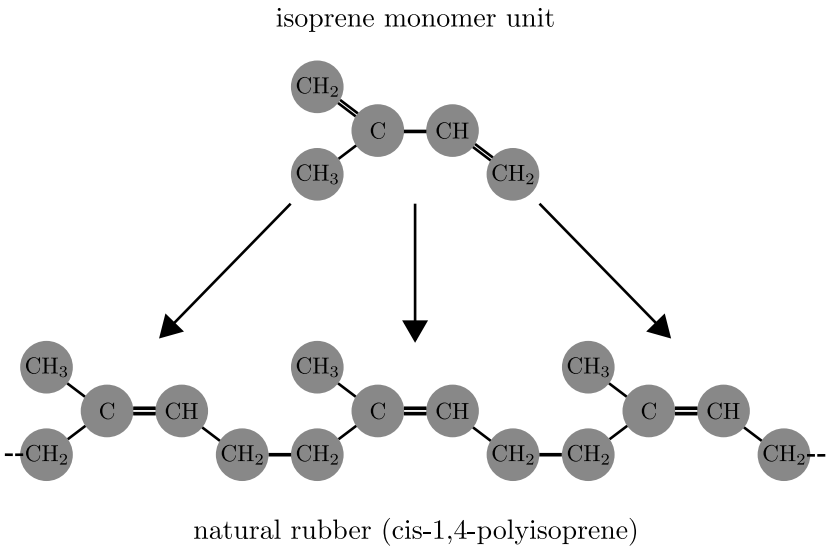

Figure A.1.: Schematic depiction of natural rubber (cis-1,4-polyisoprene) consisting of isoprene monomers. Figure in style of [3].

Gennes [5] – as long as no permanent (trapped) entanglements are produced. Glass transition is defined as the "Process in which a polymer melt changes on cooling to a polymer glass or a polymer glass changes on heating to a polymer melt" [6]. Depending on the application area, elastomers are maintained either above, for instance in tire applications, or below this point, as for hard plastics like polystyrene. The elastomers used throughout this work have a T_g way below 0 °C and are therefore commonly used in the rubber industry[2]. Chemical bonds are due to covalent or ionic bonds. The former emerge from sharing of electron pairs between the atoms whereas the latter from the electrostatic attraction between oppositely charged ions. For the rubber industry, a special type of cross-linking procedure, or curing – by introducing covalent bonds – is of importance: vulcanization. It was discovered in 1839 by Charles Goodyear by adding a small amount of sulfur into natural rubber and then heating it up. The result was a highly elastic material with low hysteresis after deformation and good tear resistance. In the vulcanization process the sulfur atoms form covalent bonds between the different polymer chains resulting in a three dimensional network, i.e., a matrix. Another type of vulcanization by adding peroxides is also possible for certain elastomers [7]. Since the usage of sulfur alone leads to a slow reaction, accelerators are added to increase the cure rate, cross-link structure and final properties.

The entropy changes that lead to the elasticity of elastomers can be explained by looking at the equilibrated, or natural, configuration of an elastomer. It has lots of cross-links, either due to entanglements or to covalent bonds between the different polymer chains. This configuration looks like a random coil which allows for a high number of available microstates and thus a state of maximum entropy. When tension is applied those entanglements straighten, reducing the number of possible microstates and subsequently decreasing the entropy. When the tension is removed the cross-links ensure that the elastomer returns to its original configuration and therefore increases its entropy. Those entropy changes result in a force whose direction is opposed to the applied strain - the reason for the reconformation. In theory we can

[2]Natural rubber for instance: $T_g = -72$ °C ([2] page 37).

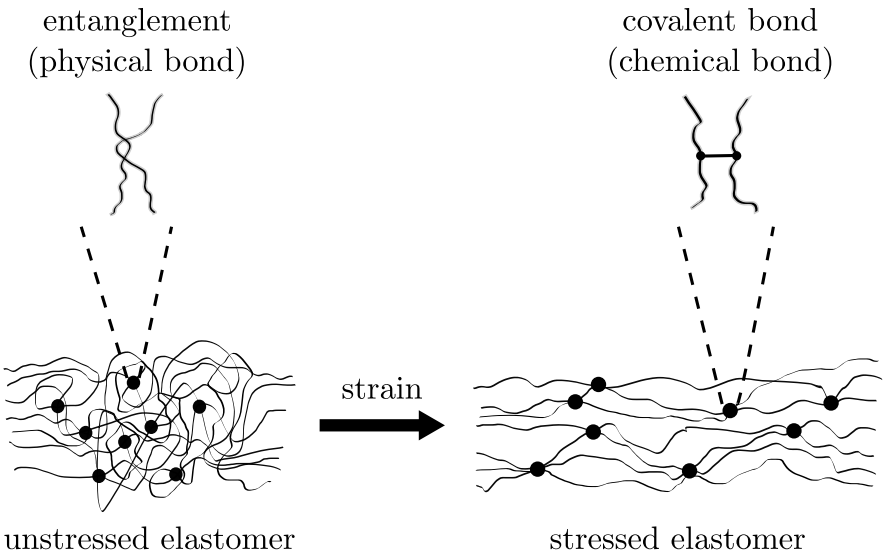

Figure A.2.: Schematic depiction of a unstressed and stressed elastomer. The strings are polymer chains and the dots are cross-links. Left: In its natural state the elastomer has a random coil like configuration with several cross-links, either physical (top-left) or chemical (top-right). Right: After the elastomer is strained, the polymer chains straighten and the cross-links ensure that it will return to its natural state after the strain disappears. On both sides both types of cross-links may occur.

describe this procedure thermodynamically or statistically. Both ways are described detailly in [2] on page 14ff. Figure A.2 shows a schematic representation of an unstressed and stressed elastomer and its configurational changes. We want to stress here that the elongation is not due to the stretching of chemical bonds or molecules at all. Particularly there is no storage of potential energy. All work done on or by the elastomer immediately appears as thermal energy[3].

At this point we can identify the rubber particles in our model: They represent randomly coiled elastomers which attach through six bonds, i.e., the six sides of the cubic cell, with other particles (filler or other elastomer particles). Due to the assignment of different surface free energies we mimic different types of polymers. Depending on the preparation process of the elastomers in the experiment, the rubber particles either represent cured or uncured elastomers, i.e., with or without vulcanization.

Although NR is still of high importance to the industry[4], synthetic rubbers such as butadiene rubber (BR), styrene-butadiene rubber (SBR), chloroprene rubber (CR) and ethylene propylene diene rubber (EPDM), to name just a few, are essential. They are made by polymerization of petroleum-based products and are a result of the high demand of natural rubber due to bicycle tires in the early 1900s. Ongoing research led to a variety of synthetic rubbers

[3]We can take a rubber band as an example: Stretching the rubber band releases heat. We can easily confirm this by pressing it against our lips after stretching. The absorption of heat is noticeable in a similar manner: Starting with a highly stretched rubber band, we release it and immediately push it against our lips. The rubber band feels cool.

[4]The distribution of natural rubber in the industry is about 40% and didn't change over the past years (cf. table 1 in chapter 4 of [8]).

mostly due to shortage of natural rubber during both world wars. Nowadays, 80% of synthetic rubbers are used in the automobile industry (cf. chapter 4.3 in [8]).

The importance of NR for the industry lies in the broad application area. It can be used in a wide temperature range between −50 °C to 40 °C [2] and inhibits good mechanical properties without adding filler particles. This is because NR crystallizes due to its stereoregular structure, i.e., having small regularly oriented units in a single sequential arrangement, for temperatures between −50 °C to 0 °C. The crystallites act like additional cross-links inside the elastomer matrix and raise the Young's modulus, E, tear strength, and tear resistance. When NR is strained the melting temperature T_m is shifted to higher values as described by the Clausius-Clapeyron equation

$$\frac{1}{T_m} - \frac{1}{T_{m,0}} = -\frac{R}{\Delta H_0} f(\lambda), \tag{A.1}$$

allowing for crystallization over 0 °C. Here $T_{m,0}$ is the melting point of the equilibrated system, ΔH_0 the molar melting enthalpy, R the gas constant and $f(\lambda)$ a function of the stretch ratio. Higher strains lead to faster crystallization which in turn leads to a higher E-modulus. This self-reinforcing process is called strain-induced crystallization. Stereoregular synthetic rubbers such as BR and CR also exhibit this behavior, but on another temperature range. The melting temperature of BR for instance is at around 2 °C and thus strain-induced crystallization is no option for applications at room temperature. Other synthetic rubbers such as SBR and EPDM do not even show strain-induced crystallization. They need to be incorporated with filler particles in order to achieve sufficient mechanical properties.

A.2. Filler Particles

The vulcanization process led to a product, which satisfied the needs of proper viscoelasticity and made rubber usable as we know it today. But still, different application areas demand different properties. As stated above, synthetic rubbers do not fulfill the required mechanical properties of the industry even if they are vulcanized and NR is still not solely suitable for all purposes. The rubber industry demands a certain amount of durability, tensile strength, hardness, and resistance to tear, wear, solvents, weather, ozone, oxidation, and heat[5]. To fulfill those demands, filler particles, or shortly fillers, are incorporated inside the compound during the mixing process, which itself is subdivided into many steps. They are oftentimes classified by their properties in the product whether they are either inert or (semi-)reinforcing (for example cf. to [2, 10–12] on which we mainly relate on in the following). Although this kind of classification is not very accurate, it is a widely used convention which we also follow here. In fact, no filler is completely inert. The properties of the rubber always change due to the addition filler. It depends on the point of view from which the change is judged. For instance, by influencing the compounding process by using processing aids, which are considered inert, we may in turn deteriorate other properties such as hardness or tensile strength. For the sake of completeness, we briefly state the properties of inert fillers, although the filler particles in our model solely represent reinforcing ones.

[5]This list is oriented on table 33.2 in [9], which is most likely not complete due to the huge amount of individual demands but gives a quite good overview.

A.2.1. Inert Fillers

Inert – or non-active/inactive – fillers are used to influence the compounding process by making the rubbers easier to process, adding specific resistance to certain chemicals and environmental influences or simply – and mostly – to reduce the cost. Accelerators, activators, anti-oxidants, anti-ozonants, coloring agents, plasticizers, process oils, retarders, softeners, vulcanizing agents and so on and so forth – to give a complete list on all inert fillers is a voluminous task. Still, to give some insight on what the properties of inert fillers inside the rubber compound are: They can reduce the stickiness, adjust the hardness, change the viscosity, protect against ozone, UV radiation and aging or even influence the vulcanization process by accelerating or retarding it. Plasticizers and softeners for instance, are low viscosity substances with good solubility. They increase the mobility of the polymer chains and thus reduce the viscosity and glass transition temperature. Tensile strength and hardness of the vulcanizate decrease as their amount increases. Processing aids on the other hand have a low solubility and help the polymer chains to glide. They also influence the compatibility between different substances in the compound. The size of inert fillers is between 500 and 1000 nm.

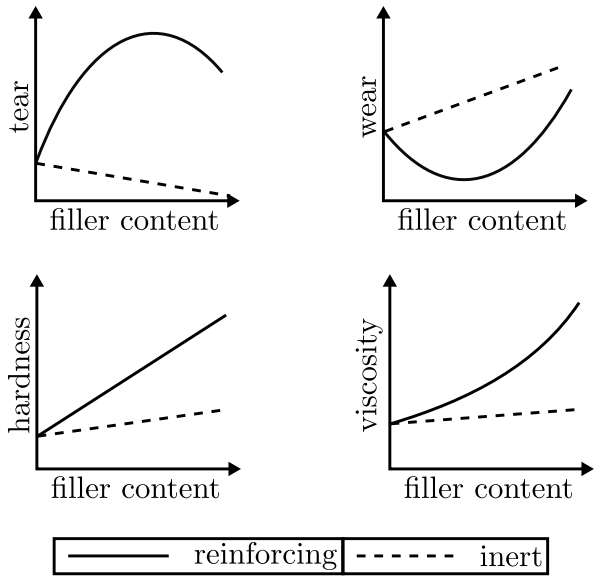

Figure A.3.: Schematic depiction of the influence of filler particles on exemplary properties of rubber compounds. Dotted lines are due to inert and solid lines due to reinforcing fillers. Picture in style of [2].

A.2.2. Reinforcing Fillers and Properties

The most widely used reinforcing – or active – fillers in the tire industry are carbon black and silica. Reinforcing fillers in general influence the physical properties of the rubber compound by interacting with the elastomer matrix in a variety of ways. They can change mechanical properties, such as tensile strength, tear and wear resistance, and hardness. Some fillers, i.e., carbon black, are even responsible for the appearance of the final product. According to Wiegand ([2]), the reinforcing properties depend on the structure, specific surface area,

and surface activity of the filler particles. Other important parameters are the filler volume content, which in turn influences the structures that the filler particles build, and the degree of dispersion during the mixing process. The key area of research when dealing with reinforcing fillers is to tailor the interfacial interactions. Figure A.3 depicts schematically the influence of inert and reinforcing fillers on a selection of different physical properties of the rubber compound. It is produced in style of [2]. The typical size of reinforcing fillers is in the nanometer range between 5 nm to 500 nm. Larger filler particles show lower reinforcement than smaller ones and are therefore sometimes referred to as semi-reinforcing (between 100 nm and 500 nm). In the following, we want to elucidate the reinforcing properties in more detail.

Structure

With structures of filler particles, we describe their morphologies, i.e., their size, form, and size distribution in aggregates (primary structures), agglomerates/clusters (secondary structures), and networks. The smallest units are the primary particles. Their composition is defined by the individual microstructure depending on the filler type. Aggregates are the smallest stable structures consisting of several primary particles which can not be broken down by shear forces during the mixing process. Aggregates can form agglomerates due to weak interactions such as van der Waals forces and hydrogen bonds, again depending on the type of filler. They are not as stable as aggregates and can thus be broken down. The size of aggregates and agglomerates is, as for the primary particles, highly depending on the filler type. Roughly it is up to several hundred nm for aggregates and up to several μm for agglomerates. Figure A.4 shows the respective classifications.

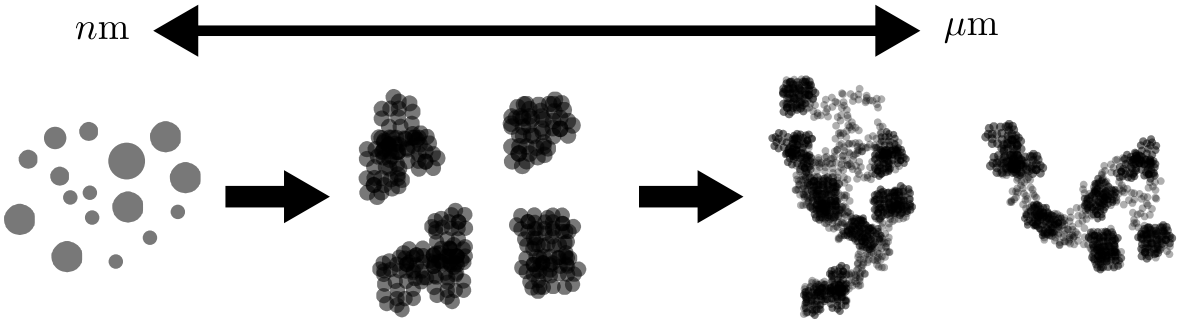

Figure A.4.: Schematic depiction of the size terminology of filler particles. From left to right: Primary particles in the range of 5 to 100 nm - represented by cubic cells in our model. Aggregates of sizes up to several hundred nm and agglomerates of sizes up to microns. The darker areas in the agglomerates represent the aggregates. The size between the sketches is not to scale.

Aggregates may also form a continuous network inside the elastomer matrix, leading to high reinforcement. One way to assess the structure of the aggregates and the characteristics of the network is by using small angle scattering. It is independent on the type of filler and can be used to analyze carbon black as well as silica. The combined use of small angle X-ray scattering (SAXS) and transmission electron microscopy (TEM) to investigate the structures within the elastomer compound is used throughout this work and explained in detail in Appendix C.

There are other techniques to obtain information about the structure of the aggregates, but they are dependent on the type of filler and discussed in detail in their respective sections.

Mixing and Dispersion

In practice, single primary particles are not used by the industry. As most fillers are forming higher order structures such as aggregates due to their production process, the low bulk density and dust development while handling is another problem. Thus, they are normally pelletized. During the mixing process the pelletized fillers are subdivided and then incorporated inside the elastomer matrix. Subsequently, they are dispersed inside the elastomer compound and then distributed. The process is illustrated in Figure A.5.

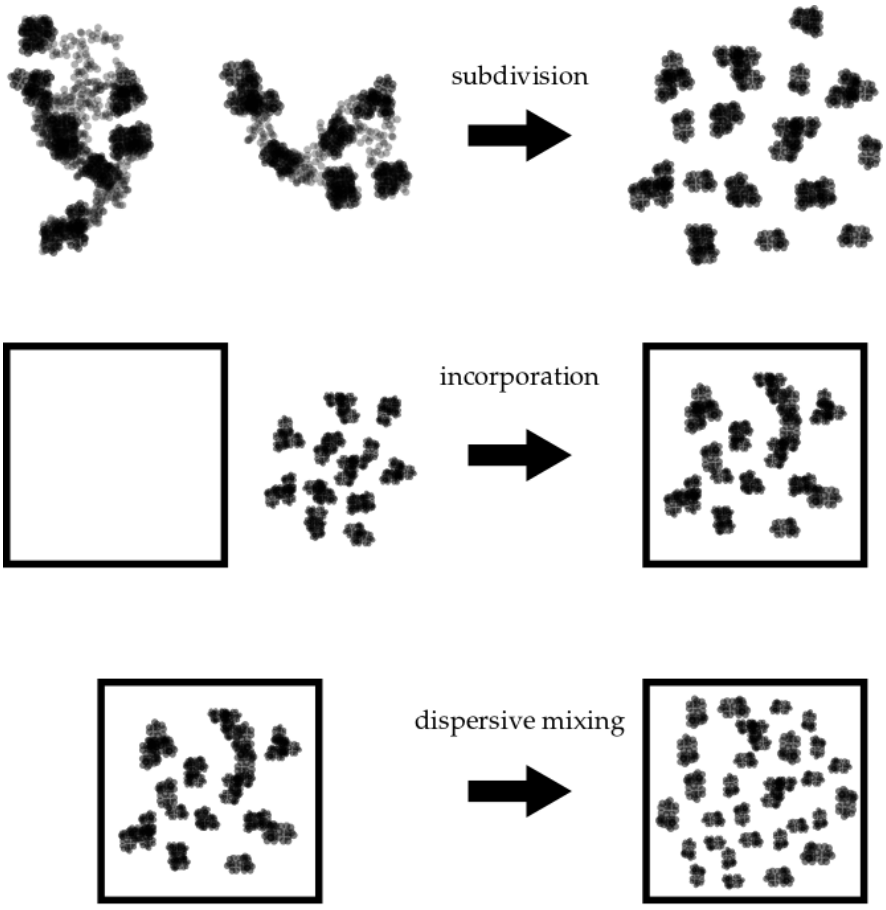

Figure A.5.: Illustration of the different mixing stages for filled rubber. Subdivision: Larger lumps of filler or agglomerates are subdivided into smaller structures, suitable for incorporation into the elastomer matrix. Incorporation: The smaller structures are incorporated into the elastomer matrix. Without incorporation the ingredients would be simply tumbled around in the mixer and no mixing would take place. Dispersive mixing: Further reduction of the smaller structures into their final size of aggregates. This figure is done in style of Figure 2.22 in [13].

Depending on the length scales for the evaluation of the degree of incorporation and dispersion, we distinguish between visual, macro-, and micro dispersion [14]. In a process called

flocculation – or re-agglomeration – the dispersed primary filler structures are able to form higher order structures such as agglomerates or networks [15]. Because the cubic cells in our model represent filler particles and not aggregates, we start with a highly micro-dispersed configuration, which is to this extent not accessible in experimental work. Nevertheless, we mimic the same procedure, i.e., flocculation. In both situations, experimentally and simulation-wise, the systems are capable of producing higher order structures to any degree.

Specific Surface Area

The specific surface area of monodisperse particles can be directly calculated from their mean size. Real particles, however, are polydisperse and form anisotropic aggregates. Gas adsorption techniques are used to measure the available specific surface area of polydisperse particles. For silica and carbon black the most common techniques are BET, after Brunauer, Emmett, and Teller [16], and CTAB . The latter technique is named after the molecule used for adsorption, i.e., cetyl-trimethyl-ammonium-bromide. It is too large to enter the micropores of the filler particles and thus determines the available contact area to the elastomer matrix and for the coupling agents. The BET method uses nitrogen as the adsorbate. It is much smaller than CTAB and can penetrate into the micropores, providing an accurate value for the specific surface area. Additionally, the pore size distribution is obtained. Thus, the BET value is generally larger than the CTAB value. For silica the BET and CTAB values vary between 30 to 800 m^2/g [17] and 100 to 400 m^2/g [18] depending on the production process. For carbon blacks in the tire industry we find values between 10 to 250 m^2/g and 10 to 150 m^2/g [19] which are again highly depending on the production process.

Surface Activity

The surface activity describes the interaction between filler and elastomer or filler and filler. Functional groups and free radicals on the surface of the filler particles influence its surface activity. Polymer molecules may adsorb on the surface of the filler particles physically or chemically. The interactions between fillers as well as filler and elastomer originate from two main sources: dispersive and polar interactions. The former arise in all type of molecules and are termed London dispersion forces [20]. They make up a majority of the van der Waals force of polymers. The latter are all contributions due to other components of the van der Waals force, i.e., the Keesom [21] and Debye [22] force , hydrogen bonding and chemical bonds. This manifestation of attractive forces between all molecules is called adhesion and can be thermodynamically described by surface free energies [23–32]. The usage of surface free energies is essential for the morphology generator as they are the foundation to calculate the transition probabilities in the MC. Therefore, they are discussed in detail in the Appendix B.

Rubber Reinforcement

Depending on all of the above parameters and the volume content of the filler particles we find different types of interactions which contribute to reinforcement. At low volume content, we solely find interactions between filler particles and the elastomer matrix. At higher concentrations, the formation of filler networks is feasible. This is of high importance for the reinforcement [33, 34]. They can either form due to direct interactions (silica) or due to a rubber shell surrounding the filler particles (carbon black). During the formation of the filler network, rubber is constrained to different degrees which contribute differently to

the reinforcement. Figure A.6 depicts a model of the formation of a filler structure and the different types of constrained rubbers.

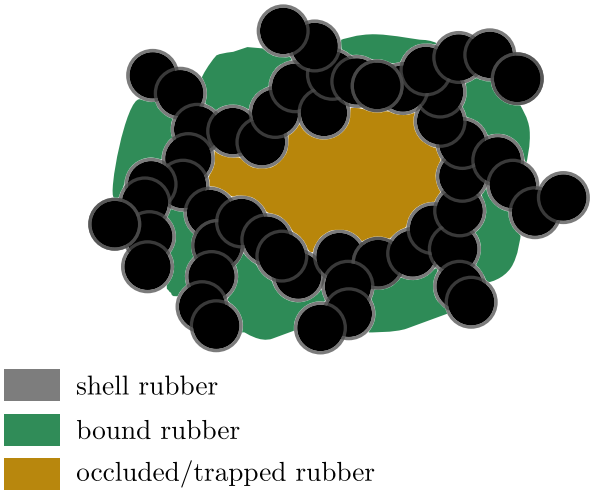

Figure A.6.: Schematic depiction of different degrees of constrained rubbers within a filler structure. The central, goldish rubber is the occluded rubber trapped inside the void of the filler structure. The greenish surrounding rubber is the bound rubber. The encircling grey area around each particle is the shell rubber.

Here, occluded rubber is the immobilized part of the rubber which is trapped in the voids of the filler aggregates. It is shielded against deformation and acts as additional filler. When the polymers adsorb on the surface of the filler particles they can form an immobilized rubber shell around them, i.e., shell rubber. Bound rubber is defined as the rubber portion that has strong interactions with the filler surface and cannot be extracted by a good solvent of the polymer. It is often taken as a measure of the filler surface activity [12].

Depending on the extent and type of deformation, we find different types of contribution to reinforcement. They can originate either due to low or high filler content or to the different constrained rubbers. Storage and loss modulus are used to describe the behavior of the rubber compound due to the dynamic deformation. The former measures the stored energy in viscoelastic materials, representing the elastic portion. The latter measures the energy dissipated as heat, representing the viscous portion. According to Payne [35–38], we find four contributions to reinforcement. Three of them, i.e., polymer network, hydrodynamic effect, and filler-rubber interaction, are strain-independent and one, the filler-filler interaction or specifically the filler network, is strain dependent. The pure polymer network contributes to the storage modulus in every rubber whether it is due to physical or chemical cross-links. At low filler volume content, the change in the moduli can be described by hydrodynamic reinforcement [39–41]. While those two contributions are accepted to be strain-independent, it is argued that the third interaction, i.e., filler-rubber is not. The reason for this is the so-called Payne effect. At low strain amplitudes (above 0.1%) and high filler volume content the elastomer compound shows a rapid decrease in the storage modulus under cyclic loading conditions. The loss modulus, on the other hand, is low and starts to show a maximum at slightly higher strain amplitudes (between 1 and 10%). Both effects are highly temperature dependent. It is essential for frequency and amplitude-dependent dynamic stiffness and

damping behavior of rubber materials. Payne originally thought that it is only due to the breakdown of the filler network and consequently claimed that the filler-filler interaction is the only strain-dependent contribution. But since it only appears in filled elastomers, the contribution due to the filler-rubber interaction is also feasible. Today, several attempts are made to describe this effect[6]. Some of them account for the breakdown and reformation of the filler network and the release of the constrained rubbers, mainly following the argumentation of Payne. Others state it is due to polymer debonding from filler surfaces, i.e., it originates from the filler-rubber interactions. Until today, there exists no model to describe this effect faithfully. At high filler volume content and high strain amplitudes we find another effect, the so-called Mullins effect: In tensile stress-strain tests considerable softening is only present at elongations less than the previous stretch. At higher elongations the stress-strain curve is relatively unaffected by previous stretching [43].

A.2.3. Types of Reinforcing Filler

In recent years different layered silicates such as organophilic modified clay minerals or carbon nanotubes and others got more and more attention. Several patents submitted by big tire companies such as Continental and Pirelli [44–49] show the motivation to find new filler materials. They have shown great potential to yield enhanced properties under laboratory conditions. However, the high surface areas and large surface free energies lead to agglomeration and the dispersion methods used in the laboratory are not economically applicable on a large scale. The main issue of utilization of nano-particles is dispersion and controlling the surface activities [12, 14, 50]. Filler particles in our model are assigned different surface free energies and mimic such reinforcing fillers. Although we are only limited by sufficient experimental data on surface free energies to mimic any kind of filler, we focus on silica and carbon black in the following.

Carbon Black

Carbon black is a product of incomplete combustion of organic compounds or thermal decomposition of hydrocarbon fuel such as gas or oil. Over the last 150 years a variety of production processes have been established. They differ in the yield and the morphology of the produced carbon blacks as well as in their physical and chemical properties. Nowadays, most carbon blacks used in the rubber industry are produced by thermal-oxidative decomposition of oil using the furnace process [12]. It is depicted as a process diagram in Figure A.7. A preheated feedstock of an aromatic liquid hydrocarbon is injected continuously into the combustion zone, which is heated up between 1300 °C to 1900 °C by a precombustion chamber. The mixture of hot gases with the feedstock leads to decomposition of carbon black. Primary quench water cools the gases down to 500 °C and interrupts the decomposition process. The dwell time inside the combustion zone is between a couple of milliseconds to a few seconds. The exhaust gases entraining the carbon black particles are further cooled to about 230 °C by passage through heat exchangers and direct water sprays. A fabric filter separates the carbon blacks from the gas stream. At this stage the carbon blacks are called fluffy due to their very low bulk density of about 50 g/l. By pulverizing and wet pelletizing the bulk density is increased to about 350 g/l. The wet pelletizing process is performed by treating the carbon black with water and molasses and drying it afterwards. Subsequently, the carbon black is

[6] [42] gives a broad spectrum in his introduction and also proposes a new approach.

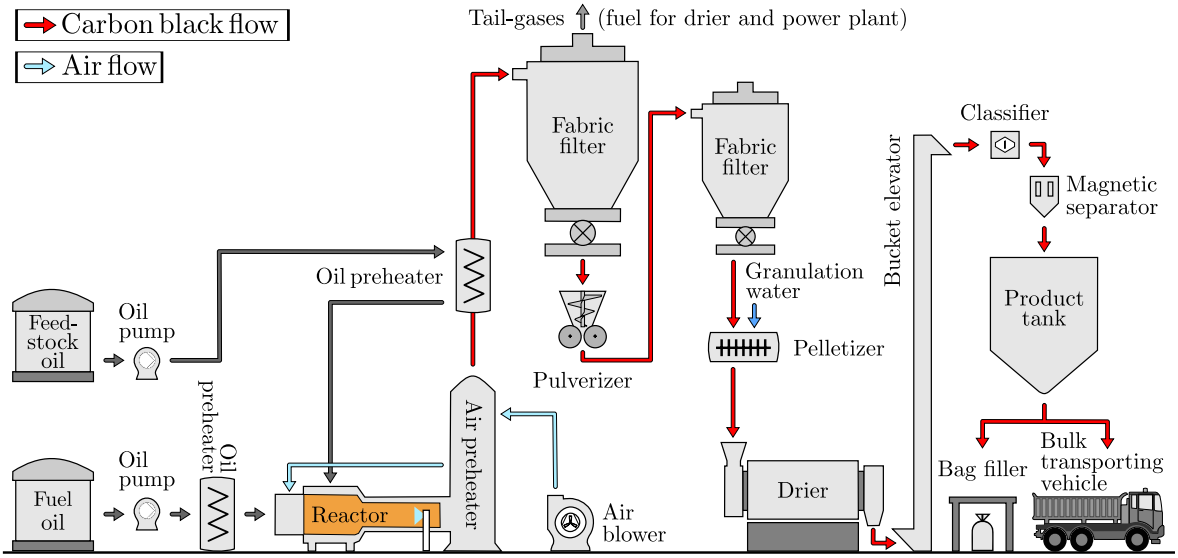

Figure A.7.: Process of carbon black production as described in the text. Translated and edited from `https://de.wikipedia.org/wiki/Ru%C3%9F`.

classified and separated, stored into a product tank and filled into bags. The exhaust fumes, or tail-gases, of the process are used to dry the carbon black and, due to its high heating value, also to produce electricity. The size of the primary particles and other physical and chemical properties are determined by the furnace designs and operating conditions. High temperature and low dwell time result in small particles. The yield of the process is between 30% to 70% and is generally higher for larger particles.

The primary particles, the so-called colloidal black, are spherical and form higher order structures such as aggregates and agglomerates. The particles contain 10^5 to 10^9 carbon atoms in an amorphous molecular structure. This structure is made of a microcrystalline array of condensed rings, similar to those formed by graphite, with the difference that the distance between the rings is higher. The orientation of the arrays appears to be random which results in a large percentage of arrays with open edges at the surface of the particle. At those open edges we find a large number of unsatisfied carbon bonds providing sites for hydrogen atoms or oxygen groups, predominantly phenolic. Rubber grade carbon blacks show a low surface coverage by oxygen groups and therefore the effect of surface chemistry is generally minor [51]. Depending on the production process and the size of the primary particles, the size distribution differs. Usually larger particles have a broader distribution than smaller particles. Inside the aggregates their size distribution is quite narrow. Typically, carbon blacks are classified after ASTM[7] using a code of a letter (N or S whether the grade is normal or slow curing) and three digits.

The first digit gives information about the size of the primary particles, the last two are freely chosen by the manufacturer. Generally, lower numbers correspond to lower structure blacks and higher numbers to higher structure blacks. A zero as the last digit indicates normal structure blacks. Table A.1 shows the correspondence between first digit and particle size, as well as the CTAB value for the surface area.

[7] American Society for Testing and Materials

Table A.1.: First digit assignment by ASTM in carbon black nomenclature system after [19].

first digit	average particle size [nm]	CTAB [m^2/g]
0	1-10	> 150
1	11-19	121-150
2	20-25	100-120
3	26-30	70-99
4	31-39	50-69
5	40-48	40-49
6	49-60	33-39
7	61-100	21-32
8	101-200	11-20
9	201-500	0-10

Just as the size distribution of the primary particles differs, it does for the aggregates. One way to categorize the aggregates is by their shape: spheroidal, ellipsoidal, linear, and branched. Smaller primary particles tend to form more branched aggregates. They become more linear with increasing size of the primary particles. Big particles, i.e., above 200 nm, form more spheroidal and ellipsoidal ones. The categories issue from the length/width ratio and the perimeter-area fractal of the aggregates and were first introduced in [52]. Therein, the structures are measured by using TEM and automatic image recognition software.

Table A.2.: Classification of various carbon black grades in the four shape categories in weight percent according to [52].

carbon black	spheroidal (%)	ellipsoidal (%)	linear (%)	branched (%)
N 234	0.3	7.9	28.6	63.2
N 330	0.2	10.2	44.1	45.5
N 550	0.6	13.8	45.3	40.3
N 762	2.5	22.4	47.7	27.5
N 990	44.9	34.8	14.4	5.9

In style of this source, Figure A.8 depicts the morphological categories of carbon black aggregates and Table A.2 lists some typical carbon blacks and their weight percent in the four shape categories. Spheroidal shapes origin usually from single particles and are only found in significant quantities in thermal blacks. This type of classification is not limited to carbon black. It is also used for silica and easily applicable for other types of filler.

Beside this method and the aforementioned small angle scattering, the structures can experimentally also be assessed by the measurement of the void volume from dynamic compression [53] or mean pressure measurements as suggested as a standard by the ASTM [54]. According to that source, the compressed void volumes are obtained by measuring the compressed volume of a weighed sample in a cylindrical chamber as a function of pressure exerted by a

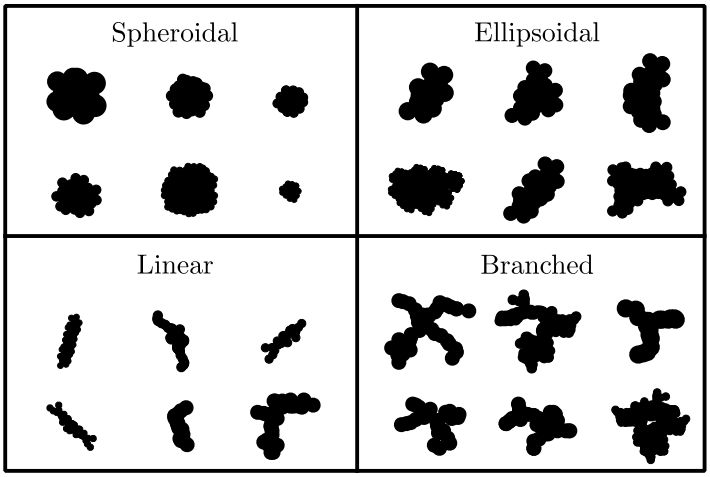

Figure A.8.: Schematic depiction of the shape categories of carbon black according to [52]. A pattern recognition program automatically identified the aggregates from the TEM pictures. Subsequently, a best fit determined the appropriate category for each identified aggregate.

movable piston. A profile of void volume as a function of pressure provides a means to assess carbon black structure at varying levels of density and aggregate reduction.

Silica

Silicates are oxides of silicon with a chemical formula of SiO_2. In nature, they are by far most occurring as quartz – a major constituent of sand. The most common components of the earths surface are silicates[8]. They are also present in living organisms such as certain algae [17]. Beside its pure form it can come in conjunction with other elements such as in talc ($Mg_3[Si_4O_{10}(OH)_2]$). Pure silica comes in two forms: amorphous and crystalline. Representatives for the crystalline forms in nature are the aforementioned quartz and cristobalite, a high-temperature polymorph of silica. Amorphous forms in nature are rare and mostly come with impurities such as in opals or flints. Natural silicates are used in their crystalline form for technical products such as cement, glass, porcelain and bricks. For reinforcement, colloidal spherical silicates are used with sizes of 5 to 100 nm, similar to the sizes of carbon black. Although it is widespread in nature, the crystalline form is generally not used for reinforcement in rubber. It has a low surface area, is highly contaminated with various metal ions, and is potentially health damaging [57]. Due to the lack and hard to control properties of natural amorphous silicates, the industry uses synthetic ones. Categorized by the phase of the silica feedstock, the production methods can be divided into two synthesis routes, i.e., gaseous and liquid. Although in both routes several methods were developed, we focus here on two of them, fumed and precipitated synthesis. For an overview over the other methods the reader may look at [57]. Beside this source, we follow here on [2, 12, 17, 50].

The process of fumed silica synthesis, also known as the Aerosil process or flame hydrolysis method, is shown in the process diagram in Figure A.9. In this process, vaporized silicon tetrachloride ($SiCl_4$) is mixed with oxygen and hydrogen and fed into a combustion chamber at 1100 to 1800 °C. Inside the chamber, the oxyhydrogen process forms water and a hydrolysis of $SiCl_4$ with this water takes place as a spontaneous, quantitative reaction inside the flame.

[8] 60.6% continental and 48.6% oceanic [55, 56].

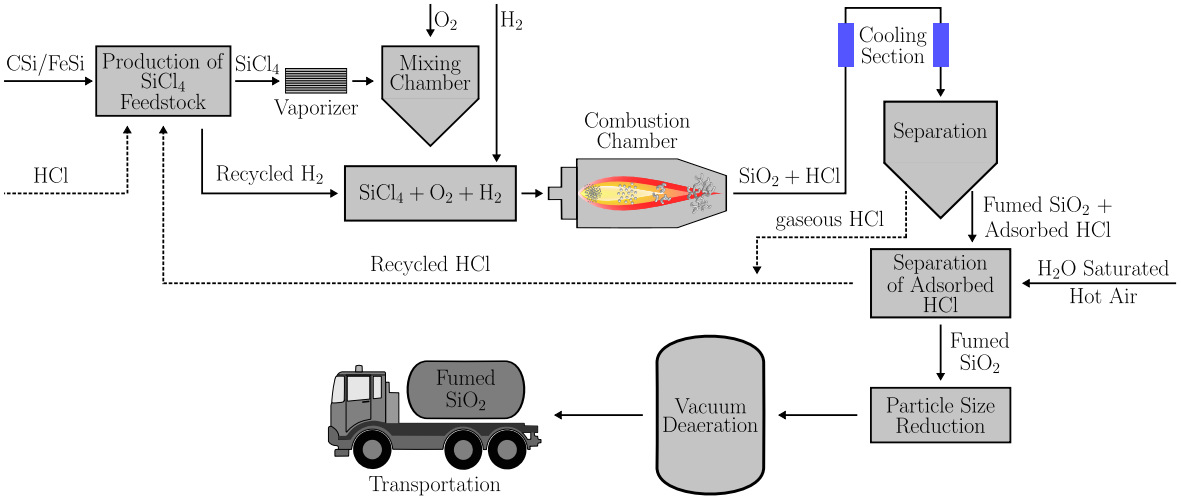

Figure A.9.: Process of fumed silica production as described in the text. The formation process of the silica particles inside the combustion chamber is more detailed in Figure A.10.

The products of this process are gaseous hydrochloric acid and silicon dioxide. It is described by an exothermic reaction via

$$SiCl_4 + 2\,H_2 + O_2 \longrightarrow SiO_2 + 4\,HCl \tag{A.2}$$

and takes place in a fraction of seconds. The formation process of the silica product is described by the simplified droplet model shown in Figure A.10. It assumes that the gases start their reaction at the base of the flame at the highest temperature. Molten silica nuclei are formed within this region and collide stochastically with one another. They merge and form larger molten, spherical, and nonporous primary particles with sizes between 5 to 50 nm and a density of roughly 2.2 g/cm^3. The more the size of the particles grows, the lesser their number becomes. This continues as long as the flame is hot enough to keep the particles in a liquid state. This area of the flame is also known as the zone of coalescence. As the particles move through the flame into a colder area they start to partially solidify. The primary particles collide further and now coalesce only partially. The results are mesoporous silica aggregates with a higher specific surface area of 50 to 500 m^2/g (BET) and wider size distribution. The aggregates solidify completely in colder parts of the flame. When they collide they do not merge at all and are instead held together by weak interactions, such as van der Waals and hydrogen bonding, to form agglomerates. The concentration of the reactants, the temperature of the flame and the dwell time of the gas inside the combustion chamber controls the particle size, its distribution, the specific surface area, the structure and the surface activity of the silica (similar to the furnace process of carbon black).

Once formed, the aerosol is cooled down and subsequently separated into solid and gas, i.e., fumed silica and gaseous HCl. The fumed silica still contains large quantities of HCl adsorbed to its surface. They are furthermore removed by water-saturated hot air. Depending on the costumer needs, it can be milled to break the aggregates down into primary particles or the additives can be introduced to alter the surface properties. The final product has a rather low bulk density of 40 g/l comparable to furnace blacks. For ease of transportation a vacuum

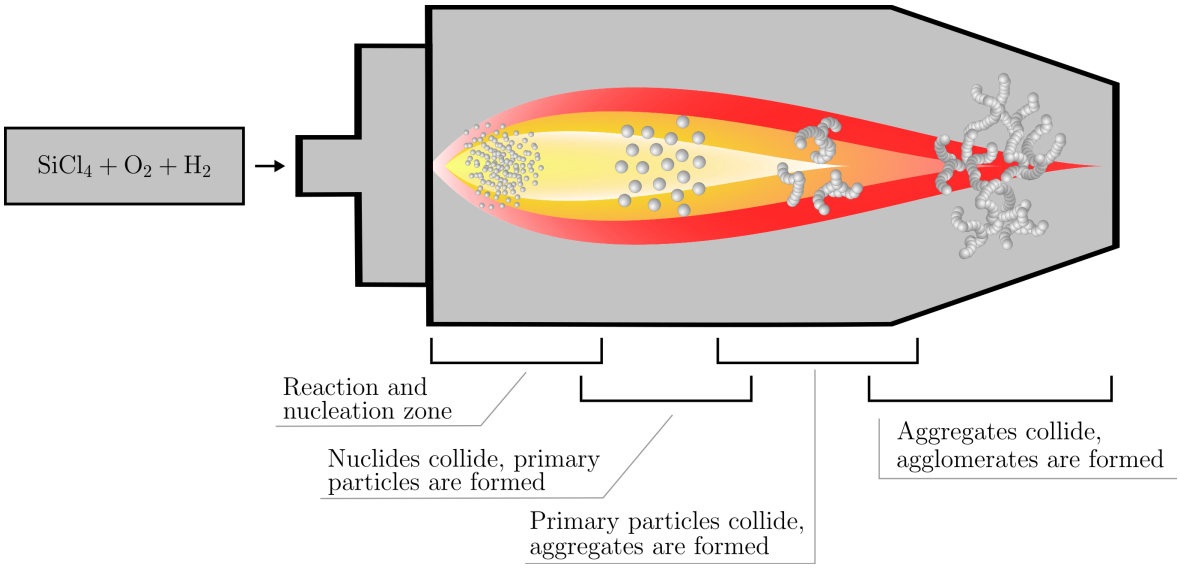

Figure A.10.: Formation of fumed silica according to the droplet model as described in the text. The particles collide from left to right and form higher ordering structures with growing sizes.

deaeration step generally follows, increasing the density up to 150 g/l. The purity of silica produced this way is very high with $> 99.8\%$ SiO_2. It displays very good thixotropic, i.e., shear thinning, properties once dispersed in the elastomer matrix due to the relatively low surface activity, compared to silica produced out of a solution. The separated byproduct of the process, i.e., the HCl, is recycled to manufacture $SiCl_4$ as described by

$$Si + 4\,HCl \longrightarrow SiCl_4 + 2\,H_2. \tag{A.3}$$

The silicon in this process can be ferro-silicon (FeSi), a byproduct in the production of steel or silicon carbide (CSi). The hydrogen produced within this process is fed back into the combustion chamber, making the whole process quite ecological. It is the only one with a sufficient yield to be viable for the industry using a gaseous feedstock. Although fumed silica has a lot of positive properties for reinforcement in tires, it is scarcely used, due to its high production costs compared to other methods.

One of those cost effective methods is the precipitated synthesis. In this process amorphous silica is produced by acidification of (preheated) solutions of sodium silicate (water glass) as described by the process diagram in Figure A.11. The acid, most commonly sulfuric acid, generates a silicic acid concentration greater than the solubility limit of silica. This leads to its polymerization and precipitation out of the solution. The idealized chemical equation for this process is

$$Na_2SiO_3 + H_2SO_4 \longrightarrow SiO_2 + Na_2SO_4 + H_2O. \tag{A.4}$$

The suspension of precipitated silica derived during the synthesis, contains salt impurities which are removed by washing and filtering. The so-called wet cake, containing approximately

20% of the solid silica, is then dried. The huge evaporated amounts of water (up to 400 l per 100 kg) account for a large proportion of the production cost. Milling after drying is mandatory due to the traces of water in the dried silica (3 to 7%). The mean size of the primary particles is between 5 to 100 nm with a mean BET surface area of 30 to 800 m^2/g and density of 1.9 to 2.1 g/cm^3. The final product is offered as powder or granulate with a tamped density of 50 to 500 g/l similar to furnace carbon black. The purity of the silica is with 98−99% slightly less compared to the fumed process. Due to its cost effectiveness, precipitated silica accounts for the largest share of amorphous silica production. The temperature, pH, and concentration of the reactants as well as the stirring rate and duration of precipitation influences the final properties of the product, like primary particle size, porosity, and surface activity. Most of these operating conditions are confidential. The temperature range is thus quite broad in its values, i.e., between 60 to more than 170 °C. The same is true for the residence time with 60 to 240 min and the pH, which is usually at 8 to 10. More operating conditions were not publicly available. The influence of these parameters can, nevertheless, be discussed. The polymerization rate, for instance, is heavily depending on the pH, although the process itself occurs at neutral pH. Thus, more basic conditions increase it. Stirring is required to prevent the formation of silica gel and to obtain the desired discrete colloidal silica particles.

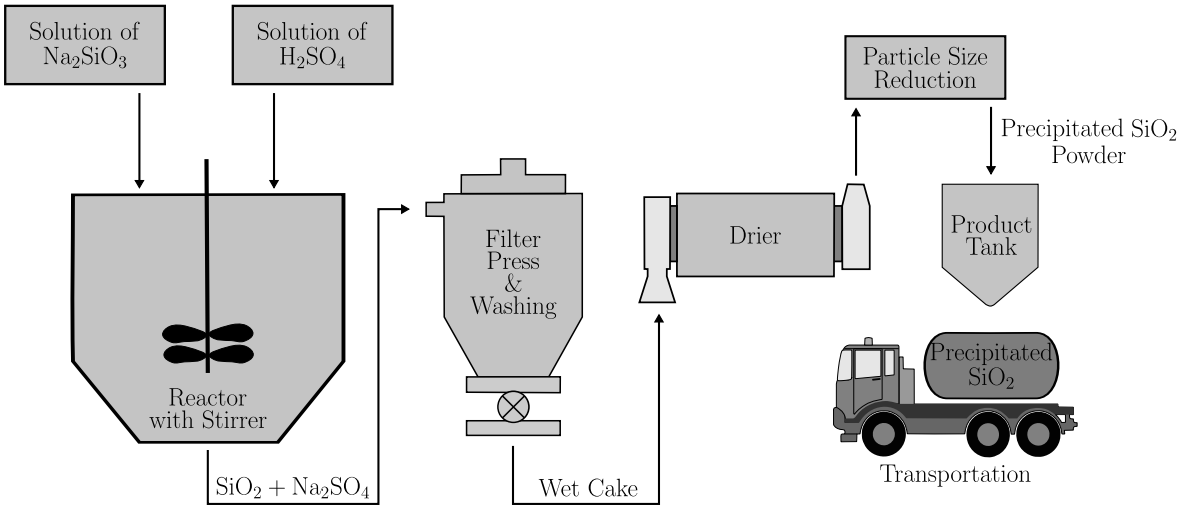

Figure A.11.: Process of precipitated silica production as described in the text. Inside the reactor the properties of the final product are determined.

The silica particles produced in either way are very reactive and hydrophilic due to their surface chemistry. The higher order structures they form differ in their morphology and size depending on the production process between several nm up to 40 μm for aggregates and 1 to 100 μm for agglomerates. Fumed silica forms more chain-like and branched structures similar to carbon blacks in the same size region. Precipitated silica aggregates are larger and more porous, leading to a large inner surface. There is no universal nomenclature like for carbon blacks. The usage of SAXS and TEM for classification of structures is quite common and thus similar to carbon black. At same BET surface values, carbon black and silica have different structures. The reason are the additional hydrogen bonds supporting the formation of higher order structures. This tendency is higher compared to carbon black

filled elastomers. The formation of continuous networks within the elastomer matrix due to re-agglomeration/flocculation is more developed for pure silica than for carbon black. This explains the high reinforcing character of silica at relatively low filler content. Unfortunately, this leads to other difficulties during the mixing process. The dispersion of silica particles inside the elastomer matrix is hindered and they influence the vulcanization with sulfur. Additionally, they do not link to the elastomer matrix since they are inorganic. To overcome these issues, the surface of the silica particles is generally treated with silanes.

A.3. Surface Treatment of Filler Particles

The surface of every filler particle can be treated in order to alter its physical and chemical properties. The treatment itself can be done chemically or physically. Chemical treatment, for instance, can be esterification with monofunctional alcohols [58]. An example for physical surface treatment of carbon blacks is their graphitization. At very high temperatures, i.e., around 2700 °C the functional groups are decomposed [23]. Due to the poor reinforcing properties it is generally not used by the tire industry [59]. An example for silica particles is the adsorption of chemicals on the surface, such as silanes. This process is also known as silanization. Because it is the most common way of surface treatment in the elastomer industry, we will focus on it in this section. We mainly follow [2, 3, 23, 60].

Non-silanized silica particles have a strong tendency to aggregate and consequently form agglomerates or networks. Their interactions with the elastomer matrix, however, are very weak. The interaction between the silica particles as well as with the elastomer matrix are necessary to obtain a product with good mechanical properties. This can be achieved by using silanes. In order to understand the mechanisms of silane coupling – or silanization – a closer look on the surface of the silica particles is necessary. It is covered with silanol groups of different types and siloxan groups as shown in Figure A.12.

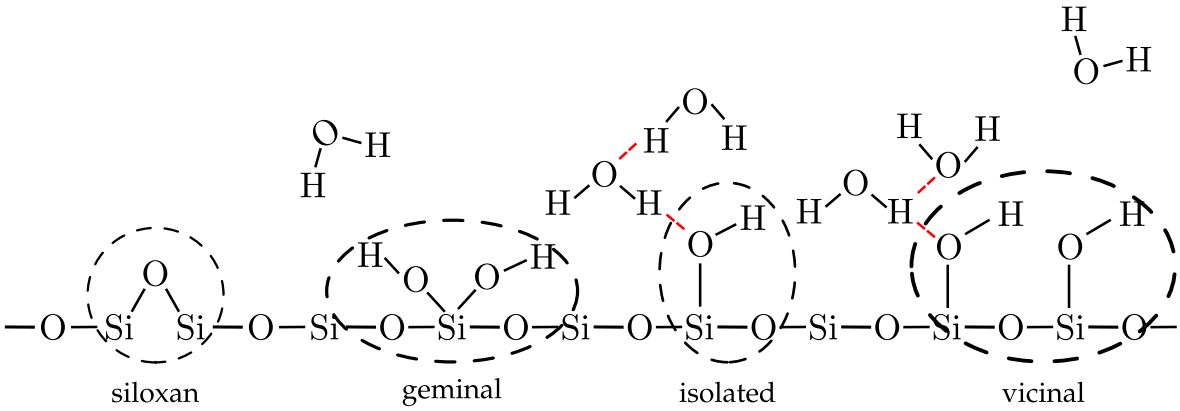

Figure A.12.: Illustration of the different possible chemical configurations on the silica surface. Form left to right: siloxan group, geminal, isolated, and vicinal silanol group. The illustration is done in style of Figure 2.11 in [13].

The OH-groups are the reason for the hydrophilic nature of silica particles. They are also the docking stations for the silanes. During vulcanization the sulfur atoms bind to the, mostly

isolated, OH-groups and thus hinder the vulcanization process. Their concentration is determined via infrared (IR) or nuclear magnetic resonance (NMR) spectroscopy. It differs for fumed and precipitated silica between 2.5 to 3.5 and 5 to 6 per $n\text{m}^2$ respectively.

There are generally two types of silanes: bifunctional and monofunctional. Bifunctional silanes have the ability to link between the elastomer matrix and the silica particles. They are often referred to as a coupling agent. One of the most commonly used representative in industry and science for precipitated silica is TESPT (Bis[3-(triethoxysilyl)propyl] Tetrasulfide), which is also known as Si69 [58, 61–63]. The chemical structure consists of two functional groups (triethoxysilyl propyl) which are linked with a polysulfide (tetrasulfide), making the molecule resemble a horseshoe. This organofunctional group, i.e., the tetrasulfide of the silane, forms covalent bonds with the methyl groups of the polymer strains inside the elastomer matrix. The vulcanization process now steers the connection between silane and polymer, as well as between the individual polymer strains. The functional groups are hydrolyzable and form reactive silanol groups, which can condense with the silanol groups on the filler surface to form siloxan linkages. Due to its form, both functional groups bind to the surface of the silica particle. The concentration of TESPT molecules is therefore (theoretically) between 1 and 3 per $n\text{m}^2$. Using MD simulations with other silanes, values of 1 to 1.5 are found [64], whereas experimentally far lower values with approximately 0.5 per $n\text{m}^2$ are found [65]. Monofunctional silanes react only with the surface of the silica particles and alter their hydrophilic nature into hydrophobic. This makes the silica particles easier to disperse. Common brands are are octeo and APDMES.

Silanization can be performed before or during the mixing process (in situ). Most commonly used are in situ methods due to the low effort. The silanes are added to the mixture after the silica particles are incorporated. To accelerate the chemical reaction between silica and silane, typically the mixing chamber is heated up to 130 to 175 °C [61, 62, 66, 67]. The addition of silanes influence the surface energy of the silica particles, making them less polar and more dispersive. For instance, this can be seen when comparing Ultrasil VN3, a typical precipitated silica used in the tire industry, with its in situ silanized counterpart Coupsil 8113 [68].

A.4. References

[1] Alemán, J. V. et al., Definitions of terms relating to the structure and processing of sols, gels, networks, and inorganic-organic hybrid materials (IUPAC Recommendations 2007). *Pure Appl. Chem.* **2007**, 79 (10), 1801–1829, DOI: 10.1351/pac200779101801.

[2] Röthemeyer, F., Sommer, F., Kautschuk Technologie: Werkstoffe - Verarbeitung - Produkte. München: Carl Hanser Verlag, **2001**, ISBN: 978-3-446-43760-9.

[3] Meyer, J., Molekulare Modellierung der mechanischen Eigenschaften von elastomeren Nano-Kompositen. Dissertation, University of Wuppertal, **2018**.

[4] Jenkins, A. D. et al., Glossary of basic terms in polymer science (IUPAC Recommendations 1996). *Pure Appl. Chem.* **1996**, 68 (12), DOI: 10.1351/pac199668122287.

[5] De Gennes, P. G., Reptation of a polymer chain in the presence of fixed obstacles. *J. Chem. Phys.* **1971**, 55 (2), 572–579, DOI: 10.1063/1.1675789.

[6] Meille, S. V. et al., Definitions of terms relating to crystalline polymers (IUPAC Recommendations 2011). *Pure Appl. Chem.* **2011**, 83 (10), 1831–1871, DOI: 10.1351/PAC-REC-10-11-13.

[7] Simpson, R. B., Rubber Basics. Edited by Simpson, R. B., Shawbury: Rapra Technology Limited, **2002**, ISBN: 1-85957-307-X.

[8] Thomas, S. et al., editors, Natural Rubber Materials - Volume 1: Blends and IPNs. Volume 1, Cambridge: The Royal Society of Chemistry, **2013**, DOI: 10.1039/9781849737647.

[9] Schaefer, R. J., Mechanical Properties of Rubber. *Harris' Shock Vib. Handb.* Edited by Harris, C. M., Piersol, A. G., 5th ed., McGraw-Hill, **2009**, chapter 33, 1456, ISBN: 0-07-137081-1.

[10] Chandrasekaran, C., Essential Rubber Formulary: Formulas for Practitioners. **2007**, URL: https://books.google.de/books?id=KLN5Dqn8HI4C (visited on 08/30/2019).

[11] Mostafa, A. et al., Rubber-Filler Interactions and Its Effect in Rheological and Mechanical Properties of Filled Compounds. *J. Test. Eval.* **2010**, 38 (3), 101942, DOI: 10.1520/JTE101942.

[12] Abraham, J. et al., Progress in Rubber Nanocomposites. Edited by Thomas, S., Maria, H. J., 1st ed., Duxford: Woodhead Publishing, **2017**, ISBN: 9780081004289.

[13] Mihara, S., Reactive processing of silica-reinforced tire rubber: new insight into the time- and temperature-dependence of silica rubber interaction. Dissertation, University of Twente, **2009**, DOI: 10.3990/1.9789036528399.

[14] Lacayo-Pineda, J., Filler Dispersion and Filler Networks. *Encycl. Polym. Nanomater.* Edited by Kobayashi, S., Müllen, K., Berlin, Heidelberg: Springer Berlin Heidelberg, **2015**, chapter F, 771–776, DOI: 10.1007/978-3-642-29648-2_291.

[15] Mihara, S., Datta, R. N., Noordermeer, J. W. M., Flocculation in Silica Reinforced Rubber Compounds. *Rubber Chem. Technol.* **2009**, 82 (5), 524–540, DOI: 10.5254/1.3548262.

[16] Brunauer, S., Emmett, P. H., Teller, E., Adsorption of Gases in Multimolecular Layers. *J. Am. Chem. Soc.* **1938**, 60 (2), 309–319, DOI: 10.1021/ja01269a023.

[17] Evonik Industries AG, Aerosil - Fumed Silica: Technical Overview. **2015**, URL: http://www.aerosil.com/sites/lists/IM/Documents/Technical-Overview-AEROSIL-Fumed-Silica-EN.pdf (visited on 08/30/2019).

[18] ASTM D6845 - 18, Standard Test Method for Silica, Precipitated, Hydrated—CTAB (Cetyltrimethylammonium Bromide) Surface Area. (West Conshohocken, PA), **2018**, DOI: 10.1520/D6845-18.

[19] ASTM D1765-17, Standard Classification System for Carbon Blacks Used in Rubber Products. (West Conshohocken, PA), **2017**, DOI: 10.1520/D1765-17.

[20] London, F., The general theory of molecular forces. *Trans. Fara. Soc.* **1937**, 33, 8–26, DOI: 10.1039/TF937330008B.

[21] Keesom, W. H., On Waal's cohesion forces. *Phys. Zeitschrift* **1921**, 22, 129–141.

[22] Debye, P., The van der Waals cohesion forces. *Phys. Zeitschrift* **1921**, 21, 178–187.

[23] Wang, M.-J., Effect of Polymer-Filler and Filler-Filler Interactions on Dynamic Properties of Filled Vulcanizates. *Rubber Chem. Technol.* **1998**, 71 (3), 520–589, DOI: 10.5254/1.3538492.

[24] Wu, S., Calculation of interfacial tension in polymer systems. *J. Polym. Sci. Part C Polym. Symp.* **1971**, 34 (1), 19–30, DOI: 10.1002/polc.5070340105.

[25] Girifalco, L. A., Good, R. J., A theory for the estimation of surface and interfacial energies. I. Derivation and application to interfacial tension. *J. Phys. Chem.* **1957**, 61 (7), 904–909, DOI: 10.1021/j150553a013.

[26] Fowler, R., Guggenheim, E. A., Statistical Thermodynamics. Edited by Fowler, R., Guggenheim, E. A., 4th ed., Cambridge: Cambridge University Press, **1956**, ISBN: 978-1114712706.

[27] Good, R. J., Girifalco, L. A., A theory for estimation of surface and interfacial energies. III. Estimation of surface energies of solids from contact angle data. *J. Phys. Chem.* **1960**, 64 (5), 561–565, DOI: 10.1021/j100834a012.

[28] Fowkes, F. M., Attractive Forces At Interfaces. *Ind. Eng. Chem.* **1964**, 56 (12), 40–52, DOI: 10.1021/ie50660a008.

[29] Good, R. J., Girifalco, L. A., Kraus, G., A theory for estimation of interfacial energies. II. Application to surface thermodynamics of Teflon and graphite. *J. Phys. Chem.* **1958**, 62 (11), 1418–1421, DOI: 10.1021/j150569a016.

[30] Owens, D. K., Wendt, R. C., Estimation of the surface free energy of polymers. *J. Appl. Polym. Sci.* **1969**, 13 (8), 1741–1747, DOI: 10.1002/app.1969.070130815.

[31] Wu, S., Interfacial And Surface Tensions of Polymers. *J. Macromol. Sci. Part C* **1974**, 10 (1), 1–73, DOI: 10.1080/15321797408080004.

[32] Cherry, B. W., Polymer surfaces. Edited by Clarke, D. R., Suresh, S., 1st ed., Cambridge: Cambridge University Press, **1981**, ISBN: 0521230829.

[33] Vilgis, T. A., Heinrich, G., Cross-Linked Polymer Blends - Theoretical Problems From Rubber Physics To Technology. *Kautschuk Gummi Kunststoffe* **1995**, 48 (5), 323–335.

[34] Vilgis, T. A., Heinrich, G., Klüppel, M., Reinforcement of Polymer Nano-Composites: Theory, Experiments and Applications. New York: Cambridge University Press, **2009**, ISBN: 9780521874809, DOI: 10.1017/CBO9780511605314.

[35] Payne, A. R., The dynamic properties of carbon black loaded natural rubber vulcanizates. Part I. *J. Appl. Polym. Sci.* **1962**, 6 (21), 368–372, DOI: 10.1002/app.1962.070062115.

[36] Payne, A. R., The Dynamic Properties of Carbon Black Loaded Natural Rubber Vulcanizates. Part II. *J. Appl. Polym. Sci.* **1962**, VI (21), 368–372, DOI: 10.1002/app.1962.070062115.

[37] Payne, A. R., Dynamic Properties of Heat-Treated Butyl Vulcanizates. *J. Appl. Polym. Sci.* **1963**, 7, 873–885, DOI: 10.1002/app.1963.070070307.

[38] Payne, A. R., Strainwork Dependence of Filler-Loaded Vulcanizates. *J. Appl. Polym. Sci.* **1964**, 8 (6), 2661–2686, DOI: 10.1002/app.1964.070080614.

[39] Einstein, A., Eine neue Bestimmung der Moleküldimensionen. *Ann. Phys.* **1906**, 19, 289–307, DOI: 10.1002/andp.200590008.

[40] Einstein, A., Berichtigung zu meiner Arbeit: "Eine neue Bestimmung der Moleküldimension". *Ann. Phys.* **1911**, (34), 591–592, DOI: 10.1002/andp.200590031.

[41] Smallwood, H. M., Limiting law of the reinforcement of rubber. *J. Appl. Phys.* **1944**, 15 (11), 758–766, DOI: 10.1063/1.1707385.

[42] Hentschke, R., The Payne effect revisited. *Express Polym. Lett.* **2017**, 11 (4), 278–292, DOI: 10.3144/expresspolymlett.2017.28.

[43] Mullins, L., Softening of Rubber by Deformation. *Rubber Chem. Technol.* **1969**, 42 (1), 339–362, DOI: 10.5254/1.3539210.

[44] Elspass, C. W., Peiffer, D. G., Nanocomposite materials formed from inorganic layered materials dispersed in a polymer matrix. US6034164A, Research, E., Company, E., **2000**.

[45] Giannini, L., Fino, L., High-performance tyre for vehicle wheels. WO 2005/049340 A1, S.p.A., P. T., **2003**.

[46] Romani, F., De Cancellis, P., Studded Tire. WO 2006/002672 A1, S.p.A., P. T., **2004**.

[47] Heinrich, G. et al., Rubber compound for tire tread rubber. US6818693B2, GmbH, C. R. D., **2004**.

[48] Zanzig, D. J., Yang, X., Cohen, M. P., Tire with component comprised of a blend of polybutadiene rubber and composite of styrene/butadiene elastomer which contains exfoliated clay platelets. US7714055B2, Company, G. T. &. R., **2010**.

[49] Hojdis, N. W., Recker, C., Schwefelvernetzte Kautschukmischung für Fahrzeugreifen enthaltend carbon nanotubes (CNT), Fahrzeugreifen, der die schwefelvernetzte Kautschukmischung aufweist, sowie Verfahren zur Herstellung der schwefelvernetzten Kautschukmischung enthaltend CNT. DE102017208137A1, GmbH, C. R. D., **2018**.

[50] Roland, C. M., Reinforcement of elastomers. *Ref. Modul. Mater. Sci. Mater. Eng.* Elsevier, **2016**, 1–9, DOI: 10.1016/B978-0-12-803581-8.02163-9.

[51] Medalia, A. I., Elastomers , Reinforcement of. *Encycl. Mater. Sci. Technol.* Edited by Buschow, K. H. J. et al., 2nd ed., Elsevier Ltd, **2001**, 2475–2480, ISBN: 978-0-08-043152-9, DOI: 10.1016/B0-08-043152-6/00447-2.

[52] Herd, C. R., McDonald, G. C., Hess, W. M., Morphology of Carbon-Black Aggregates: Fractal versus Euclidean Geometry. *Rubber Chem. Technol.* **1992**, 65 (1), 107–129, DOI: https://doi.org/10.5254/1.3538594.

[53] Joyce, G. A. et al., Carbon black intra-aggregate void volume from dynamic compression measurements. *Rubber World* **2011**, 244 (6), 21–28.

[54] ASTM D7854 - 18c, Standard Test Method for Carbon Black-Void Volume at Mean Pressure. (West Conshohocken, PA), **2018**, DOI: 10.1520/D7854-18C.

[55] Rudnick, R. L., Gao, S., Composition of the Continental Crust. *Treatise on Geochemistry*, edited by Holland, H. D., Turekian, K. K., 3rd ed., New York: Elsevier Science, **2003**, 1–64, DOI: 10.1016/B0-08-043751-6/03016-4.

[56] White, W. M., Klein, E. M., Composition of the Oceanic Crust. *Treatise on Geochemistry*, edited by Holland, H. D., Turekian, K. K., 4th ed., New York: Elsevier Science, **2014**, 457–496, DOI: 10.1016/B978-0-08-095975-7.00315-6.

[57] Hyde, E. D. et al., Colloidal Silica Particle Synthesis and Future Industrial Manufacturing Pathways: A Review. *Ind. Eng. Chem. Res.* **2016**, 55 (33), 8891–8913, DOI: 10.1021/acs.iecr.6b01839.

[58] Lin, C. J. et al., On the Filler Flocculation in Silica-Filled Rubbers Part I. Quantifying and Tracking the Filler Flocculation and Polymer-Filler Interactions in the Unvulcanized Rubber Compounds. *Rubber Chem. Technol.* **2002**, 75 (5), 865–890, DOI: 10.5254/1.3547689.

[59] Tunnicliffe, L. B. et al., Flocculation and viscoelastic behaviour in carbon black-filled natural rubber. *Macromol. Mater. Eng.* **2014**, 299 (12), 1474–1483, DOI: 10.1002/mame.201400117.

[60] Hager, J., Modellierung dynamischer Module von Silica gefüllten Elastomeren auf der Basis molekularer Simulationen. Dissertation, University of Wuppertal, **2015**.

[61] Le, H. H. et al., Kinetics of the phase selective localization of silica in rubber blends. *Polym. Compos.* **2010**, 31 (10), 1701–1711, DOI: 10.1002/pc.20960.

[62] Qu, L. et al., Contribution of silica-rubber interactions on the viscoelastic behaviors of modified solution polymerized styrene butadiene rubbers (M-S-SBRs) filled with silica. *RSC Adv.* **2014**, 4 (109), 64354–64363, DOI: 10.1039/c4ra09492a.

[63] Meyer, J. et al., A nano-mechanical instability as primary contribution to rolling resistance. *Sci. Rep.* **2017**, 7 (1), 11275, DOI: 10.1038/s41598-017-11728-6.

[64] Deetz, J. D., Ngo, Q., Faller, R., Reactive Molecular Dynamics Simulations of the Silanization of Silica Substrates by Methoxysilanes and Hydroxysilanes. *Langmuir* **2016**, 32 (28), 7045–7055, DOI: 10.1021/acs.langmuir.6b00934.

[65] Vilmin, F. et al., Reactivity of bis[3-(triethoxysilyl)propyl] tetrasulfide (TESPT) silane coupling agent over hydrated silica: Operando IR spectroscopy and chemometrics study. *J. Phys. Chem. C* **2014**, 118 (8), 4056–4071, DOI: 10.1021/jp408600h.

[66] Bouty, A. et al., Nanofiller structure and reinforcement in model silica/rubber composites: A quantitative correlation driven by interfacial agents. *Macromolecules* **2014**, 47 (15), 5365–5378, DOI: 10.1021/ma500582p.

[67] Kaewsakul, W. et al., Factors influencing the flocculation process in silica-reinforced natural rubber compounds. *J. Elastomers Plast.* **2016**, 48 (5), 426–441, DOI: 10.1177/0095244315580456.

[68] Stöckelhuber, K. W. et al., Contribution of physico-chemical properties of interfaces on dispersibility, adhesion and flocculation of filler particles in rubber. *Polymer (Guildf).* **2010**, 51 (9), 1954–1963, DOI: 10.1016/j.polymer.2010.03.013.

B. Surface and Interfacial Free Energies

Rubber compounds contain many different ingredients, such as polymers, fillers, and additives (cf. Appendix A). Due to the interactions between the ingredients, a coherent mass is formed, which can be technologically used. Those interactions take place at the molecular level and via the surfaces of the materials. In order to control their behavior, it is thus essential to understand the very nature of those interactions and hence the surfaces themselves. An example is given for the mechanical stress. It is put into the material by nothing other than the stress transfer through the surface of a material [1].

When considering interactions of surfaces, we encounter two terms, i.e., surfaces and interfaces. The term interface is used whenever the results from an interaction between substances is found on each side of the interface. The term surface, on the other hand, is used when the resulting interactions of a material on one side of the interface are considered. It is certainly true that exposed surfaces will always have an interaction with the surrounding vapor. However, its concentration is generally low and can be neglected. Depending on the material, several contributors may account for the interactions. For instance, when dealing with metals or inorganic semiconductors, covalent or metallic bonding mostly govern the interactions [2]. In the case of inorganic filler particles, such as silica, hydrogen bonding plays a prominent role (Appendix A). However, for all materials a class of interactions is always present, i.e., the van der Waals (vdW) interactions. In the case of soft materials, such as polymers, they even play a prominent role and are a host of phenomena such as adhesion, cohesion, surface energies, and wetting [2]. The concepts of adhesion and cohesion are directly related to surface energies, interfacial energies, and wetting. All of these are considered in this chapter.

The goal of this chapter is to achieve a conclusive picture of the formerly mentioned terms. All of them are connected with one another and oftentimes terms are used interchangeably. For instance, the terms surface energy, surface free energy, and surface tension. Because vdW interactions are accounted for the most important mechanism of adhesion [3], and are also a prominent contributor for the surface energy, we start with its elucidation. Thereafter, we discuss the surface energies, followed by the interfacial energies. The latter may be considered between like or unlike surfaces, such as liquid-solid ones, which we consider in this work throughout. Both energy types are considered theoretically by using thermodynamics and statistical mechanics. Subsequently, the concept of wetting is explained. It connects the theory with the experiment. Finally, some state-of-the-art experiments to measure surface free energies, surface tensions, and interfacial tensions are explained.

B.1. Van der Waals Forces

Van der Waals forces[1] are a certain class of intermolecular forces, i.e., the forces which are present between molecules. It is a distance-dependent interaction between atoms and molecules and should not be confused with the intramolecular forces, i.e., the forces that

[1] After Johannes Diderik van der Waals developed theory of capillarity to explain the behavior of liquids in 1893.

bind the atoms together forming a molecule or compound. In general, intermolecular forces consist of many contributors, which are divided into attractive and repulsive forces. Attractive forces contain, for instance, hydrogen bonding, ionic bonding, ion-induced dipole forces, ion-dipole forces, and, depending on the literature source, vdW forces. The repulsive forces originate from the Pauli exclusion principle, preventing the collapse of the molecules, or due to electrostatic interactions between permanent charges and multipoles. Here, we want to follow the constituion used in [2]. This means that we consider the set of forces characterized by the same power dependence on distance, i.e., $1/r^6$ with r being the distance between the atoms or molecules. In addition, they have the dipole moment and the atomic polarizability as important parameters. This results in three anisotropic forces, i.e., the Keesom force [4], the Debye force [5], and the London dispersion force [6].

The Keesom force is due to electrostatic interactions between charges (in molecular ions), dipoles (for polar molecules), quadrupoles (all molecules with symmetry lower than cubic), and permanent multipoles. Oftentimes, it occurs between two molecules with permanent dipoles and is thus referred to as dipol-dipol-interaction instead. Those molecules are called polar. It is the only contributing force, which can be attractive or repulsive, because due to the rotation of the molecules the electrostatic interaction can change its sign. It is also heavily temperature dependent. It arises, if the electronegativity between two atoms inside the molecule differs significantly. This contribution is generally zero, because only few atoms carry a permanent dipole. For atoms in the spherically symmetric state, like for H-atoms or noble gas atoms, which do not carry any multipole, this force is completely absent. If, however, this force contributes it is the major part of the vdW force.

The second force is the Debye or also induction (or polarization) force, which arises from the interactions between rotating permanent dipoles and the polarization of atoms and molecules. It consequently accounts, similar to the Keesom force, towards the polar interactions. The electrical field of a permanently rotating dipole induces a dipole moment inside another molecule, which results in the mutual attraction of both. The occurrence is not possible between atoms. Different from the Keesom force is the temperature dependency, which is not as high due to the fact that the induced dipole can move and rotate freely.

Beside the polar interactions, the third one occurs between all molecules and atoms. It is termed London (dispersion) force and describes the interaction between a fluctuating dipole and an induced dipole. The term dispersion is used because of the similarity to the quantum mechanical description of light dispersion. It is caused by the random fluctuations in electron density in an electron cloud. Due to the fluctuation of the electrical field, the electron cloud is shifted with respect to the nucleus, which in turn leads to fluctuating dipole moments, even in non-polar atoms or molecules. Consequently, neighboring atoms and molecules are induced polarity. Because every atom or molecule is polarizable, the London (dispersion) force is a fundamental contributor towards the vdW force. Although the mean value of the entire dipol moment is zero, the quadratic contribution is non-zero. Overall, the contribution of the London force is bigger for atoms with a large number of electrons.

In total, the attractive vdW interaction between two molecules, a and b, can consequently be described by the sum of the three contributions, i.e.,

$$U_{vdW}(r) = -\frac{C_{ab}}{r^6} = \frac{C_{orient} + C_{ind} + C_{disp}}{r^6} = -\frac{C_{vdW}}{r^6}. \tag{B.1}$$

Here, C_{orient}, C_{ind}, and C_{disp} are the coefficients for the Keesom (orientation), Debye (induction), and London force (dispersion).

The constant C_{vdW} is given by [2]

$$C_{vdW} = -\left[\frac{\mu_1^2\mu_2^2}{3(4\pi\epsilon_0\epsilon_r)^2 k_B T} + \frac{\mu_1^2\alpha_2 + \mu_2^2\alpha_1}{(4\pi\epsilon_0\epsilon_r)^2}\right]_{\nu=0} + \left[\frac{3\alpha_2\alpha_1}{2(4\pi\epsilon_0\epsilon_r)^2}\frac{h\nu_1\nu_2}{\nu_1+\nu_2}\right]_{\nu>0} \tag{B.2}$$

where α_1 and α_2 are the polarizabilities of the molecules, μ_1 and μ_2 the dipole moments, ϵ_0 the vacuum permittivity, ϵ_r the relative permittivity, k_B Boltzmann's constant, T the temperature, $h\nu_1$ and $h\nu_2$ the first ionization potentials of the molecules with the ionization frequencies ν_1 and ν_2, and Planck's constant h. The first term with $\nu = 0$ contains the Keesom and Debye contributions, i.e., they depict the polar or entropic contribution [4, 5]. Subsequently, the second term with $\nu > 0$ is the dispersion part acting between all molecules [6].

For an outright description of the forces acting between two molecules, the repulsive part originating from the Pauli exclusion principle needs to be considered. It is empirically described by the following potential

$$U_{rep}(r) = \frac{A}{r^{12}}, \tag{B.3}$$

where A characterizes its strength. This description is not unique. Several other equations exist to describe the repulsive part, for instance using exponential functions (Buckingham potential [7]). The given potential is used in the Lennard-Jones potential [8], a very common potential to describe the interaction between a pair of neutral atoms of molecules, frequently used throughout the simulation community

$$U_{LJ}(r) = \frac{A}{r^{12}} - \frac{B}{r^6} = 4\epsilon_{ij}\left(\left(\frac{\sigma_{ij}}{r}\right)^{12} - \left(\frac{\sigma_{ij}}{r}\right)^{6}\right). \tag{B.4}$$

Here, the simplified form using A and B is the original description of the potential [9]. The form thereafter, is today's most common form, where ϵ_{ij} is the depth of the potential well and σ_{ij} is the finite distance at which the inter-particle potential is zero. Both are specific for the materials i and j.

The attractive, r^{-6}, term used in the potential originates from the London dispersion forces alone. Due to the necessary calculation of this power law, the choice of r^{-12} for the repulsive part is most clever, because its calculation is reduced to the square of the other part.

In the following, this potential is used to derive a formula to calculate the surface energies of liquids and solids. Note that when considering surface energies, one always has to keep

in mind that these energies are generally interfacial energies of the liquid-vapor or solid-vapor interface. This is reasoned by the fact that only surfaces in vacuum are not subject to interactions with the surrounding vapor. Nevertheless, the concentration inside the vapor is generally very low and thus the interaction with it is neglected in the following section.

B.2. Surface Free Energies and Surface Tensions

In this section we want to elucidate the difference between the terms surface free energy and surface tension. For a purely phenomenological explanation the reader is encouraged to consider the next subsection only. For a deeper understanding and the derivation using thermodynamics and statistical mechanics, another section is provided.

B.2.1. Motivation

The terms surface free energy and surface tension are strongly correlated with each other. The former is more general, as it also applies to solids. The latter is used for liquids only. Because several occurrences of surface tension, such as soap bubbles and water striders, are more common for the reader, we motivate this topic on this basis.

Surface tension is the tendency of fluid surfaces to shrink into the minimum surface area possible. It originates from the difference of intermolecular forces acting on the molecules in the bulk and the surface. Molecules in the bulk are surrounded in each direction by another molecule. Consequently, the attractive and repulsive force, described by Equation (B.4), act equally on each molecule. The short ranged repulsive force due to the hard core of the molecules can be thought of as a 'contact force'. Thus, it is not very sensitive to changes in the structure of the liquid and therefore isotropic in nature. The attractive force, on the other hand, is strongly anisotropic, as mentioned in the former section. For molecules near the surface[2], we have a break in up-down symmetry as depicted in Figure B.1.

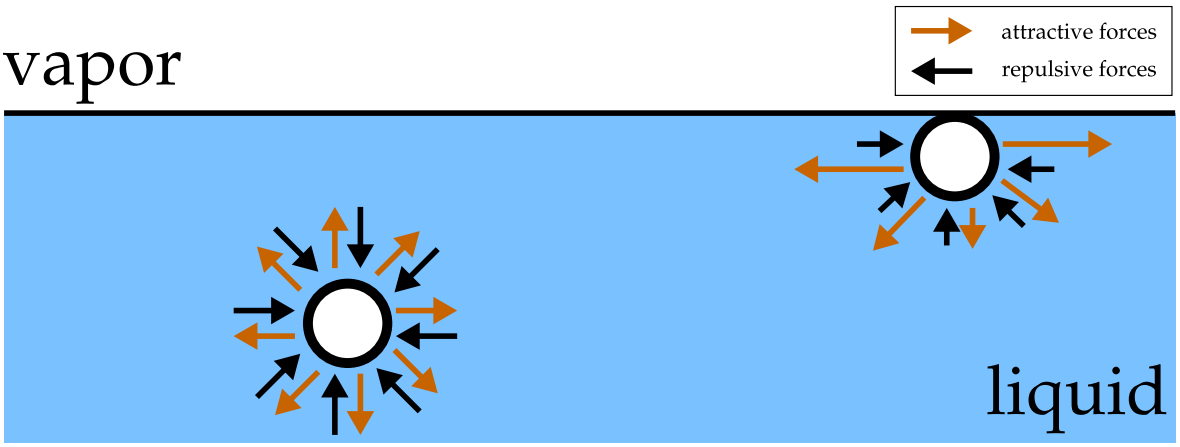

Figure B.1.: Schematic depiction of the repulsive (black arrows) and attractive (orange arrows) forces in the bulk and at the surface. Figure in style of [10].

[2]Or the liquid-vapor interface. The surface is nearly always exposed to the surrounding vapor.

Therefore, repulsive forces act only from the bottom of the molecules in vertical direction (black arrow). To restore the force balance they have to be equal in magnitude. For the direction parallel to the interface, on the other hand, the symmetry is unbroken, which automatically ensures the force balance. Consequently, there is no reason why the attractive forces should have the same magnitude as the repulsive forces. In practice, the attractive forces are stronger, which results in a positive surface tension force [10]. This allows water striders, although denser than water, to float and slide on a water surface. Another common effect is the capillary action, which is also used to measure surface tensions (in detail discussed in cf. section B.5). In either way, surface tension can be thought of a force per unit length. This is, however, equivalent to energy per surface area, which is the commonly used unit when considering solids. In this case, the term surface free energy is used.

Hence, the similarity between both terms and their oftentimes interchanged usage is apparent. However, in order to distinguish both terms more accurately, another viewpoint for the surface free energy is used. It is certainly true that also the molecules at the surface of a solid have excess energy due to the same reasons as a liquid. But let us assume that we cut a solid material into two pieces. This disrupts the intermolecular bonds, which consequently increases the free energy. When we consider this process as reversible, then due to conservation of energy the energy needed for the cut must be equal to the energy inherent in the two new surfaces created. This energy must then equal half of the energy of cohesion, i.e., the energy between like molecules. Thus, as an alternative viewpoint, the surface energy can be defined as the work required to cut a bulk sample and creating two surfaces.

B.2.2. Thermodynamics and Statistical Mechanics

From a thermodynamic point of view, we must first chose an ensemble to derive the corresponding quantities. The free energies, associated with the excess energies on the surface of liquids or solids, may be the Helmholtz free energy, F, or the free enthalpy, G. The former is the characteristic state function in the canonical ensemble, also known as the NVT-ensemble, where temperature T, number of particles N, and the system's volume V are the dependent variables. The latter is a constant in the isothermal-isobaric ensemble, also known as the NPT-ensemble, where instead of the volume the pressure P is kept constant. Although surfaces have per definition a location and an area but no volume and consequently the choice of the canonical ensemble is reasonable, we chose the isothermal-isobaric ensemble for the derivation of the surface energy, as it is more commonly used [1]. Either way, both thermodynamic potentials are related by $G = F + PV$ and can thus be easily converted.

In the next step, we must define the thermodynamic variables for the surfaces. As briefly described in the former section, a system containing a surface behaves differently from one in absence of a surface. It is thus reasonable to define a surface variable as the difference of the total state and the unpertubated bulk state, B. Therefore, we find for the free enthalpy of the surface

$$G^a = G - G^B. \tag{B.5}$$

When dealing with surfaces, oftentimes 'specific' thermodynamic quantities are used. They are defined as the surface variables per unit area and denoted with a lower case symbol. Thus, we find for the specific internal energy, $e^a = E^a/A$, for the entropy, $s^a = S^a/A$, and for the free enthalpy, $g^a = G^a/A$, where A is the corresponding surface. The last quantity, g^a, is the (loose) thermodynamic definition of the surface free energy [1, 11], which suits our needs in this context.

The relation between the tension and the surface free energy is now derived in the following. Let us first consider a system without a surface and N_i number of moles of the ith component which are present in the system. The corresponding chemical potential is then written as $\mu_i = \partial G/\partial N_i|_{N_{j\neq i},P,T}$. If we now consider the first law of thermodynamics, where $\mathrm{d}q$ is a small heat input into the system, then we find for the internal energy of the complete system

$$\mathrm{d}E = \mathrm{d}q - \mathrm{d}w + \sum_i \mu_i \mathrm{d}N_i, \tag{B.6}$$

with $\mathrm{d}w$ is the work done by the system. If a surface is now present in the system, then the work can be done by extending the surface against the surface tension forces

$$\mathrm{d}w = P\mathrm{d}V - \gamma \mathrm{d}A. \tag{B.7}$$

Here, γ is the corresponding force per unit length needed to extend the surface, i.e., the surface tension. Using the definition of the free enthalpy, i.e., $G = H - TS$, and the enthalpy, i.e., $H = E + PV$, we find for the total differential of the free enthalpy

$$\mathrm{d}G = \mathrm{d}E + P\mathrm{d}V + V\mathrm{d}P - T\mathrm{d}S - S\mathrm{d}T, \tag{B.8}$$

and thus by substituting $T\mathrm{d}S$ for $\mathrm{d}q$ in Equation (B.6) and inserting Equation (B.8)

$$\mathrm{d}G = V\mathrm{d}P - S\mathrm{d}T + \gamma \mathrm{d}A + \sum_i \mu_i \mathrm{d}N_i, \tag{B.9}$$

or

$$\gamma = \left.\frac{\partial G}{\partial A}\right|_{N_{j\neq i},P,T}. \tag{B.10}$$

The surface tension is therefore equal to the change in the free enthalpy of the whole system associated with the unit increase of surface area (an energy per unit area). This is not necessarily the same as the surface free energy, which is the change of free enthalpy of the surface associated with unit increase of surface area. The difference is rationalized by considering the extension of a surface of an isotropic solid. This is only achieved if work is performed, which is displayed by $\gamma \mathrm{d}A$. This must be equal to the increase in total surface free energy $\mathrm{d}G^a$ in Equation (B.5) and thus

$$\gamma \mathrm{d}A = \mathrm{d}G^a = \mathrm{d}(Ag^a). \tag{B.11}$$

From this follows for the surface tension

$$\gamma = g^a + A(\frac{\mathrm{d}g^a}{\mathrm{d}A}), \tag{B.12}$$

which for a liquid, as any attempt on extending the surface results in more molecules flowing into it and thus leaves the composition unchanged, is equal to the surface free energy, i.e., $(\mathrm{d}g^a/\mathrm{d}A) = 0$. For a solid, on the other hand, the surface composition generally changes due to stretching and therefore $(\mathrm{d}g^a/\mathrm{d}A) \neq 0$. This conclusively shows that for a solid, surface tension and surface free energy are not necessarily equal.

With the thermodynamic description in one hand and the knowledge of the intermolecular forces acting between the particles, described by the Lennard-Jones potential in Equation (B.4), in the other, we can calculate the surface free energy of liquids and solids using statistical mechanics. We mainly follow [1, 11] here. Note that a couple of assumption are made here and thus only a rough estimation can be obtained. A first one is that we consider a material of unit cross-sectional area, liquid or solid, to be separated into two plane surfaces, or semi-infinite volumes A and B, facing each other as depicted in Figure B.2.

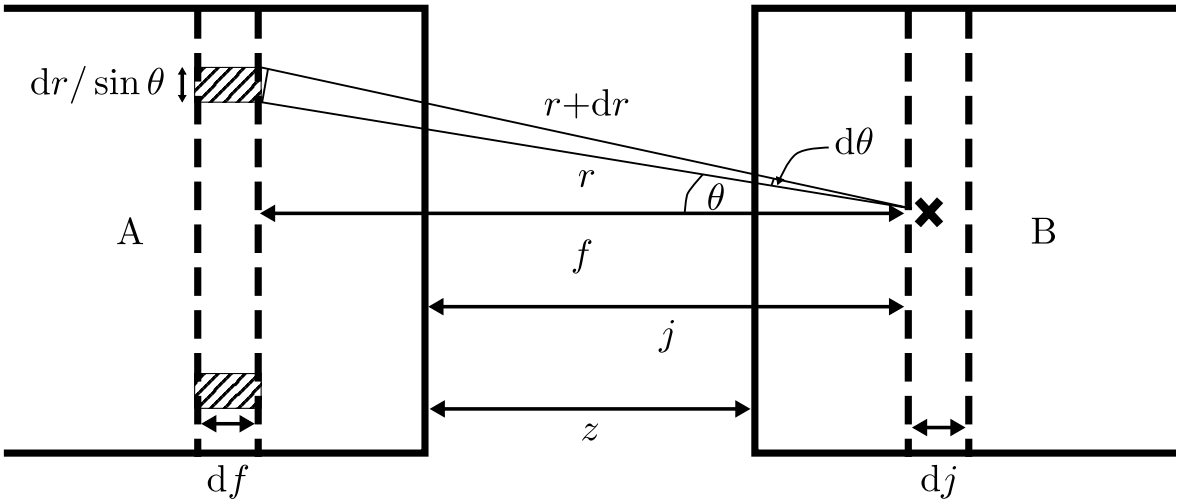

Figure B.2.: Schematic depiction of the intermolecular forces acting across an interface of a material separated by a plane into two pieces. Figure in style of [1, 11, 12].

Additionally, we only consider the force acting between the two molecules, which is given by the derivative of interaction potential acting between them, i.e., the Lennard-Jones potential

$$F = \frac{\partial U_L J(r)}{\partial r} = \frac{6A}{r^7} - \frac{12B}{r^{13}}. \tag{B.13}$$

This assumes that the molecules are in an average position of minimal potential energy, thus omitting the contributions of the translations and internal degrees of freedom[3].

The density of molecules in the shaded annulus of width $\mathrm{d}f$ in the dashed column inside A shall be denoted by the variable n. It is assumed to equal everywhere. Hence, inside A and B. The width of the annulus is $dr/\sin\theta$ and its radius is $r\sin\theta$. Consequently, its volume is $2\pi r\mathrm{d}r\mathrm{d}f$ and hence the number of molecules is given by

$$N = 2\pi r\sin\theta(\mathrm{d}r/\sin\theta)n\mathrm{d}f. \tag{B.14}$$

Now we can calculate the force exerted on a molecule located at the spot marked with X in z direction due to all molecules inside the annulus via $F_a = NF\cos\theta = NF(f/r)$. Consequently, we find for the force of all molecules inside the dashed column

$$F_c = 2\pi nf\mathrm{d}f\int_{r=f}^{r=\infty}\left(\frac{6A}{r^7} - \frac{12B}{r^{13}}\right)\mathrm{d}r. \tag{B.15}$$

The force of all molecules inside A acting on the molecule at X is thus given by $F_A = \int_{f=j}^{f=\infty} F_c\,\mathrm{d}f$. Finally, for the force between the semi-infinite volumes A and B is given by

$$F_t = \int_{j=z}^{j=\infty} F_A n_b\mathrm{d}j = \frac{2\pi n^2}{z^3}\left(\frac{A}{12} - \frac{B}{90z^6}\right), \tag{B.16}$$

with the distance z between both volumes as shown in Figure B.2. As mentioned in the former section, the surface energy is defined as the work needed to cut a bulk sample and creating two surfaces. Because we now calculated the force acting between both surfaces, we can conclude that the work needed to create both should be equal to twice the surface energy, i.e., the energy of cohesion

$$2\gamma = \int_{z=r_{11}}^{z=\infty} F_t\mathrm{d}z. \tag{B.17}$$

Here, r_{11} is the minimum distance between the planes. The index '11' is introduced to indicate that the planes under consideration are of the same type. We then find for the surface free energy

$$\gamma = \frac{\pi n^2}{24r_{11}^2}\left(A - \frac{B}{30r_{11}^6}\right). \tag{B.18}$$

Since r_{11} is the equilibrium distance between the two semi-infinite volumes, the net force between them must be zero. Using Equation (B.16), evaluating it at $z = r_{11}$, and substituting this into Equation (B.17), we finally find

[3] Alternatively, we assume that the internal degrees of freedom and translational motion are the same for molecules in the surface and the bulk.

$$\gamma = \frac{\pi n^2 A}{32 r_{11}^2}. \tag{B.19}$$

As introductory mentioned this equation is not strictly accurate, but it shows that the force needed to separate two planes is initially just the force required to stretch the material. This can be related to Young's modulus, since $E = \partial F_t(r)/\partial r|_{r_{11}}$, such that we find

$$\gamma = \frac{E r_{11}}{32}. \tag{B.20}$$

Young's modulus, also known as the elastic modulus, is a very common quantity measured for lots of materials, especially in the industry. It is defined as the quotient of stress to strain. This equation is therefore quite convenient for the application in the industry, because only the equilibrium distance between the molecules inside a material needs to be known. This can be obtained directly from the Lennard-Jones potential, because it is simply the minimum of the interaction potential. As pointed out in [1], the agreement between measured surface free energies and those obtained via Equation (B.20) are quite reasonable. Beside this method to calculate the surface free energies of material, several other theories were developed, which are out of scope for this work. For further information the reader is encouraged to look into the works of Hamaker [13], who was the first to consider the vdW-interactions between macroscopic bodies and used pairwise addition of the forces, and Lifshitz [14], who generalized the principle and used a continuous approach for the interactions between two macroscopic bodies.

B.2.3. Temperature Dependency

As seen in the thermodynamic derivation of the surface tension, it is depending on temperature. Unfortunately, only empirical formulae for the temperature dependency are known. The general trend is, however, that the surface tension decreases with increasing temperature and that a value of 0 is reached at the critical temperature.

One formula is known as the Eötvös equation [15]

$$\gamma V_m^{2/3} = k(T_c - T), \tag{B.21}$$

where V_m is the molar volume, T_c the critical temperature of the liquid, and k is a universal constant, known as the Eötvös constant, with $k = 2.1 \cdot 10^{-7}$ J/(K$\cdot$ mol$^{2/3}$). According to [16], this rule is not applicable to polymers, because when taking the derivative one finds that the constant diverges when the molecular volume approaches infinity.

Another formula is the Guggenheim-Katayama equation [17]

$$\gamma = \gamma_0 (1 - \frac{T}{T_c})^n, \tag{B.22}$$

where γ_0 is a constant for each liquid and n is an empirical factor, which is 11/9 for organic liquids. The temperature coefficient for organic liquids is subsequently given by

$$-\frac{\partial\gamma}{\partial T} = \frac{11}{9}\frac{\gamma_0}{T_c}(1-\frac{T}{T_c})^{2/9}, \tag{B.23}$$

which results in almost linear γ vs T plots for temperatures far below T_c (cf. those in [16]). Typical values for polymers are in the region of 0.04 to 0.10 mJ/m^2/°C [18].

B.3. Interfacial Tension and the Work of Adhesion

In our model, solids and liquids are put together and we are therefore dealing with three different types of interfaces. The solids are identified as the filler particles and the liquids are identified as the polymers. Hence, the solid-solid interface is represented by the filler-filler contacts, independent of the surface treatment. The liquid-liquid interface is given by the polymer-polymer interactions, regardless of the polymer combination in focus. The last one is the solid-liquid interface, which is found in the filler-polymer contacts. The interaction between similar surfaces, for instance non-silanized filler surfaces – a solid-solid interface, is considered a cohesive joint. This means that to move their surfaces apart during the flocculation process mimicked by the MC, work has to be exerted, which is equal to the work of cohesion. We encountered this already in the former section and thus know its definition, as it is twice the surface free energy of the created surface. But so far, only similar surfaces have been considered.

When interfaces between dissimilar surfaces are considered, the intermolecular interactions on both surfaces need to be taken into account. To create a liquid-solid interface, we can use the same approach as for the solid-solid and liquid-liquid case. A bulk liquid and a bulk solid are each cut into two separate parts and then these parts are joined together. The work necessary to cut both bulk materials are consequently their works of cohesion. For a more general approach, let the solid be component 1 and the liquid component 2. We then find for the works of cohesion $W_c^1 = 2\gamma_1$ and $W_c^2 = 2\gamma_2$. If both surfaces are now put together, the attractive solid-liquid interaction reduces the interfacial tension by the solid-liquid work of adhesion and hence we find

$$W_a^{12} = \gamma_1 + \gamma_2 - \gamma_{12}. \tag{B.24}$$

This equation is also know as the Dupré-Equation after Athanase Dupré [19].

Adopting the same procedure used to obtain Equation (B.20) but for dissimilar materials, we consequently find for the work of cohesion and adhesion

$$\begin{aligned} W_c^1 &= \pi n_1^2 A_{11}/16r_{11}^2 \\ W_c^2 &= \pi n_2^2 A_{22}/16r_{22}^2 \\ W_a^{12} &= \pi n_1 n_2 A_{12}/16r_{12}^2. \end{aligned} \tag{B.25}$$

In a series of papers, Girifalco and Good [12, 20, 21] related the work of cohesion to the work of adhesion, applying the Berthelot relation [22], i.e.,

$$A_{ab} = (A_{aa}A_{bb})^{1/2}. \tag{B.26}$$

Where A_{aa} and A_{bb} are the attractive constants between similar and A_{ab} that between dissimilar molecules. In a more general way they related the works of cohesion and adhesion to a constant ϕ. Applied to the nomenclature we use here we find

$$\phi = \frac{W_a^{12}}{(W_c^1 W_c^2)^{1/2}} \overset{\text{(B.25)}}{=} \frac{A_{12}}{(A_{11}A_{22})^{1/2}} \frac{r_{11}r_{22}}{r_{12}} \overset{\text{(B.26)}}{=} \frac{r_{11}r_{22}}{r_{12}}. \tag{B.27}$$

A more applicable and frequently used equation is obtained when the definitions of the work of cohesion and adhesion are inserted. We then find

$$\gamma_{12} = \gamma_1 + \gamma_2 - 2\phi(\gamma_1\gamma_2)^{1/2}. \tag{B.28}$$

With this equation it is possible to obtain the interfacial tension between a liquid and a solid on the pure basis of their specific surface free energies, which can measured or calculated. For the constant ϕ, Girifalco and Good analyzed dozens of materials and showed that it is very close to unity in most cases. Consequently, it has been set to unity in almost all of the works drawing on their results. Some of those works added useful aspects to the entire concept of surface free energies and interfacial tensions and are therefore briefly discussed. Most prominent are the works of Fowkes [23], Owens and Wendt [24], and Wu [16, 25], who especially considered polymers. Wu was also the only one to take the constant ϕ into account.

Starting with the latter, Equation (B.28) is rewritten as

$$\gamma_{12} = \gamma_1 + \gamma_2 - 2(\phi^d + \phi^p), \tag{B.29}$$

where ϕ^d and ϕ^p are the interaction terms for dispersion and polar energies, respectively [25]. The dispersive interaction arises from the London dispersion forces whereas the polar one from Keesom, Debye, and others. Depending on the theory in focus, the interaction terms are different. All works, however, split the surface free energies in two parts[4] – similar to the interaction terms into a polar and a dispersive one, i.e.,

$$\gamma_i = \gamma_i^d + \gamma_i^p. \tag{B.30}$$

In the work of Fowkes, no polar interactions are considered and hence $\phi^p = 0$. For the dispersive interactions he followed the approach of Girifalco and Good and assumed a geometric

[4] Those considered in this work are two component theories. There are, however, also more component theories, such as the van Oss theory [26].

mean as given by the Berthelot relation in Equation B.23, i.e., $\phi^d = \sqrt{\gamma_1^d \gamma_2^d}$. Owens and Wendt extended the work of Fowkes and also considered a geometric mean for the polar interaction term. Wu, on the other hand, stated that the use of a harmonic mean for both interaction terms yields better results. The following Table B.1 summarizes the different interaction terms.

Table B.1.: Interaction terms for the calculation of interfacial tensions according to Equation (B.26) for different theories given in the table. Note that for Girifalco and Good, the concept of interaction terms does not apply, because no difference in the dispersive and polar part of the surface free energy is made.

method	ϕ^d	ϕ^p	γ_{12}
Girifalco & Good [12]	-	-	$\gamma_1 + \gamma_2 - 2\phi\sqrt{\gamma_1\gamma_2}$
Fowkes [23]	$\sqrt{\gamma_1^d \gamma_2^d}$	-	$\gamma_1 + \gamma_2 - 2\sqrt{\gamma_1^d \gamma_2^d}$
Owens & Wendt [24]	$\sqrt{\gamma_1^d \gamma_2^d}$	$\sqrt{\gamma_1^p \gamma_2^p}$	$\gamma_1 + \gamma_2 - 2\left(\sqrt{\gamma_1^d \gamma_2^d} + \sqrt{\gamma_1^p \gamma_2^p}\right)$
Wu [25]	$\frac{2\gamma_1^d \gamma_2^d}{\gamma_1^d + \gamma_2^d}$	$\frac{2\gamma_1^p \gamma_2^p}{\gamma_1^p + \gamma_2^p}$	$\gamma_1 + \gamma_2 - 4\left(\frac{\gamma_1^d \gamma_2^d}{\gamma_1^d + \gamma_2^d} + \frac{\gamma_1^p \gamma_2^p}{\gamma_1^p + \gamma_2^p}\right)$

Although it is claimed that better results for polymers are obtained when the theory of Wu is applied, recent works on surface free energies rely on the calculation of the interfacial tension using the relation of Owens and Wendt (e.g. [27–33]). Therefore, this relation is used throughout this work.

B.3.1. Temperature Dependency

The temperature dependency on the interfacial tension can directly be calculated using the temperature dependency of the surface tensions, i.e., we differentiate the Owens and Wendt equation in Table B.1 and find

$$\frac{\partial \gamma_{12}}{\partial T} = \frac{\partial \gamma_1}{\partial T} + \frac{\partial \gamma_2}{\partial T} - \left[\left(\frac{\gamma_2^d}{\gamma_1^d}\right)\frac{\partial \gamma_1^d}{\partial T} + \left(\frac{\gamma_1^d}{\gamma_2^d}\right)\frac{\partial \gamma_2^d}{\partial T} + \left(\frac{\gamma_2^p}{\gamma_1^p}\right)\frac{\partial \gamma_1^p}{\partial T} + \left(\frac{\gamma_1^p}{\gamma_2^p}\right)\frac{\partial \gamma_2^p}{\partial T}\right]. \tag{B.31}$$

Typical values are around 0.03 $\mathrm{mJ/m^2/°C}$ [16].

B.4. Wettability and the Contact Angle

Wetting is the ability of a liquid to spread over a solid surface. It is a result of the force balance between adhesion and cohesion. If the adhesion between the liquid and the solid is stronger than the individual cohesive forces than the liquid spreads over the solid, which

consequently leads to a smaller contact angle θ . If the cohesive forces, on the other hand, are stronger then the liquid minimizes the contact to the solid and forms droplets. Hence, we find a larger contact angle θ. The most common effect is certainly the 'Lotus effect'. The degree of wetting, i.e., the value of the contact angle θ, is called the wettability and is an interplay between the interfacial tensions of all three phases, i.e., liquid (L), solid (S), and vapor (V). For $\theta = 0°$, the liquid is considered to be perfectly wetting the solid. For $0° < \theta < 90°$ the wettability is high. For $90° \leq \theta < 180°$ the wettability is low. A value of $\theta = 180°$ is considered non-wetting, but this value is never actually reached as some interactions between the liquid and the solid always occur. In our model we already consider contact angles above 15° as bad wetting in accordance with the concept of flocculation of filler particles in polymers [34]. The overall concept is depicted in Figure B.3.

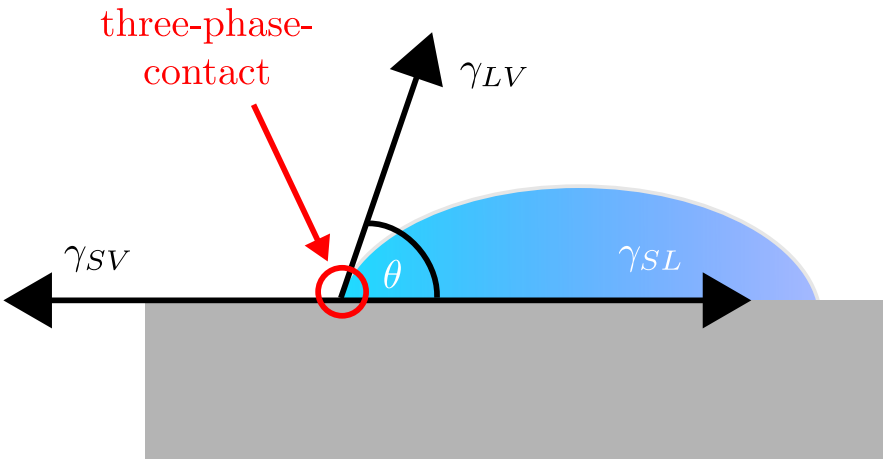

Figure B.3.: Schematic depiction of the force balance at the three-phase-contact point for a liquid drop on a solid substrate. The resulting equation is the so-called Young-Equation (B.32). Note that the surrounding "vapor" can be exchanged with other liquids as long as they are immiscible with the first liquid phase. The angle θ is the contact angle between the liquid and solid substrate.

In the three-phase-contact point we find a force balance, which is described by the so-called Young equation [19]

$$\gamma_{SL} + \gamma_{LV} \cos\theta = \gamma_{SV}. \tag{B.32}$$

Note that although this depiction is common to illustrate the Young-Equation there is a force missing in the normal direction of the solid-liquid interface for a complete picture. This force is equal to $\gamma_{LV} \sin\theta$. It is balanced by the vertical force on the liquid, caused by the attraction of the solid. For a very detailed discussion on this topic refer to [10]. Note also that this equation is only applicable for smooth, plane, and rigid surfaces and that the situation depicted above is the equilibrium state. Real surfaces underlie irregularities due to roughness and are generally not plane. In those cases, the contact angle is split into an advancing and a receding contact angle [35] and subsequently contact angle hysteresis must be taken into

account. Several models are developed for those situations such as Wenzel's model or the Cassie-Baxter model [36].

Its importance lies in the fact that the surface free energy of solids is difficult to be measured directly in experiments. Disrupting the bonds of a solid, which is the definition of the surface free energy, is always accompanied with other deformations of the solid. Using different liquids with known surface tensions and measuring the contact angle with the solid, yields the unknown surface free energy of the solid. This is rationalized by combining the equation for the interfacial tension of Owens and Wendt in Table B.1 with the Young-Equation (B.32) and can furthermore be expanded to the Young-Dupré equation [19] using Equation (B.24)

$$\cos\theta = -1 + \frac{2\sqrt{\gamma_S^d \gamma_L^d}}{\gamma_L} + \frac{2\sqrt{\gamma_S^p \gamma_L^p}}{\gamma_L} \overset{\text{(B.24)}}{=} -1 + \frac{W_a^{SL}}{W_c^L}. \tag{B.33}$$

Note that in this approach the interfacial tensions between the liquid-vapor as well as the solid-vapor interface are considered to be the pure surface free energies of the liquid and the solid, respectively.

Dividing this equation by $2\sqrt{\gamma_L^d}$ yields

$$\frac{\gamma_L(1+\cos\theta)}{2\sqrt{\gamma_L^d}} = \sqrt{\gamma_S^d} + \sqrt{\frac{\gamma_L^p}{\gamma_L^d}}\sqrt{\gamma_S^p}. \tag{B.34}$$

Consequently, a plot of $(\gamma_L(1+\cos\theta))/(2\sqrt{\gamma_L^d})$ versus $\sqrt{\gamma_L^p/\gamma_L^d}$ gives a straight line with intercept $\sqrt{\gamma_S^d}$ and angular coefficient equal to $\sqrt{\gamma_S^p}$ and hence, the surface free energy of the solid. It should be noted that liquids with different polarities have to be used.

In Figure B.4, such a plot is depicted for poly(methyl methacrylate), taken and adjusted to our nomenclature from [37]. The probe liquids with their respective contact angle are given in the figure. The liquids are, due to the abscissa, sorted from left to right with increasing surface polarity. The surface tension values of the probe liquids are given in the caption of Figure B.4.

The concepts of wetting and work of adhesion are crucial for our model interpretation. They are the basis of the wetting-envelope - work of adhesion plots introduced in chapter 2 and thus crucial for flocculation of filler particles inside elastomer matrices [27, 34, 38]. In the case of our systems, the filler particles are identified as the solid and the polymers as the liquid. The difference in work of adhesion is also the foundation of our Metropolis criterion and thus the core of our morphology generator (cf. Appendix D). With the theory of surface free energies, interfacial tensions, work of adhesion, and contact angles we have all the necessary information to understand the concepts of the morphology generator introduced in this work. For conclusive picture, however, some experimental methods need to be explained, which is done in the next section.

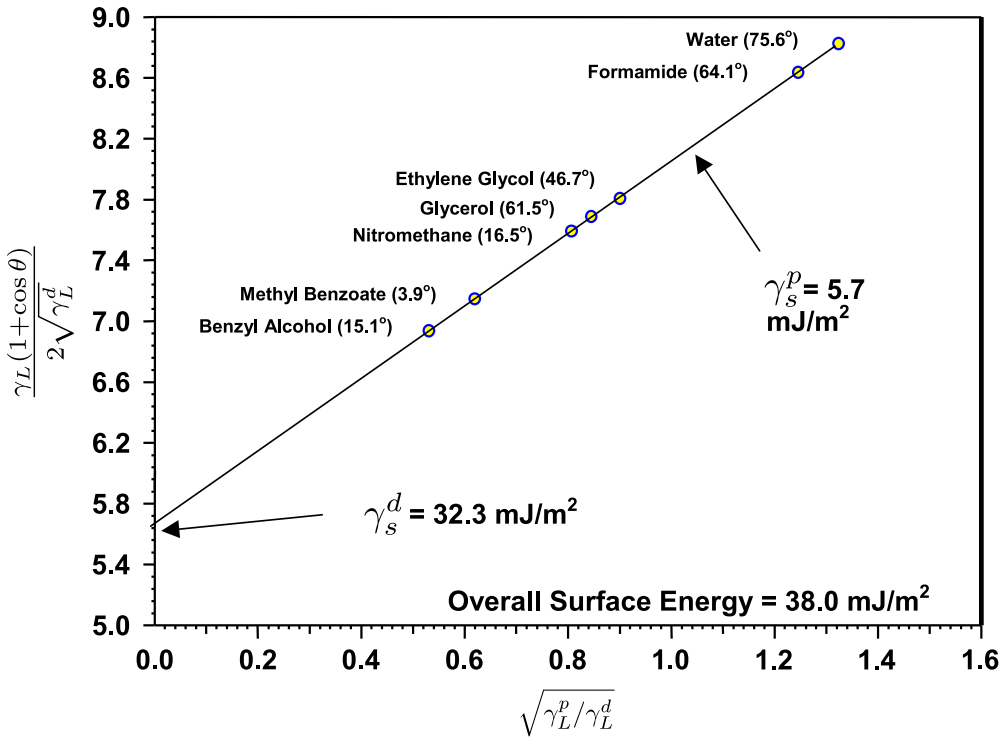

Figure B.4.: Example of an Owens/Wendt plot for poly(methyl methacrylate) taken and adjusted to our nomenclature from [37]. Different probe liquids with different surface polarities are used to obtain the surface free energy components of the solid. Their surface tensions are: Benzyl alcohol ($\gamma_l^d = 30.3\,mJ/m^2$, $\gamma_l^p = 8.7 mJ^2/m^2$), methyl benzoate ($\gamma_l^d = 27.0\,mJ/m^2$, $\gamma_l^p = 10.2 mJ^2/m^2$), nitromethane ($\gamma_l^d = 22.0\,mJ/m^2$, $\gamma_l^p = 14.5 mJ^2/m^2$), glycerol ($\gamma_l^d = 37.0\,mJ/m^2$, $\gamma_l^p = 26.4 mJ^2/m^2$), ethylene glycol ($\gamma_l^d = 26.4\,mJ/m^2$, $\gamma_l^p = 21.3 mJ^2/m^2$), formamide ($\gamma_l^d = 22.4\,mJ/m^2$, $\gamma_l^p = 34.6 mJ^2/m^2$), and water ($\gamma_l^d = 26.4\,mJ/m^2$, $\gamma_l^p = 46.4 mJ^2/m^2$).

B.5. Experimental Methods

The measurement of surface free energies, surface tensions, and interfacial tensions can be conducted using several methods. The precision of the values depends on the combination of the material and the method in use. In [16], the author evaluates several techniques in the aspect of their suitability for performing measurements on polymers. Because we are dealing beside polymers also with filler particles, we need to consider some additional methods. As stated in the named reference, suitable to determine the surface and interfacial tensions of polymers are the Pendant Drop and the Sessile Bubble method. Both utilize the shape of the liquid in conjunction with Laplace's capillary equation. Due to their similarity we will only discuss the Pendant Drop method. Although only suitable for surface tensions in the case of polymers, the Wilhelmy Plate method is used to obtain the surface free energies of

the filler particles [38]. Another method is the Sessile Drop method, in which the contact angle between a drop of liquid on a solid substrate is measured. Those three methods are consequently explained in this chapter. Because it utilizes the concept of contact angles and thus Equation (B.34) can be applied, we start with the Sessile Drop method. This is followed by the Pendant Drop method, as it also utilizes the concept of the shape of the drop. At last we consider the Wilhelmy Plate method.

B.5.1. Sessile Drop

In the Sessile Drop method, a liquid with known surface tension is deposited on a solid substrate using a tube. The contact angle is then measured using a contact angle goniometer. It takes an image from the profile of the drop on the surface, which is subsequently analyzed either by eye or, more commonly, using a drop shape analysis software. An example picture of such an experiment is given in Figure B.5.

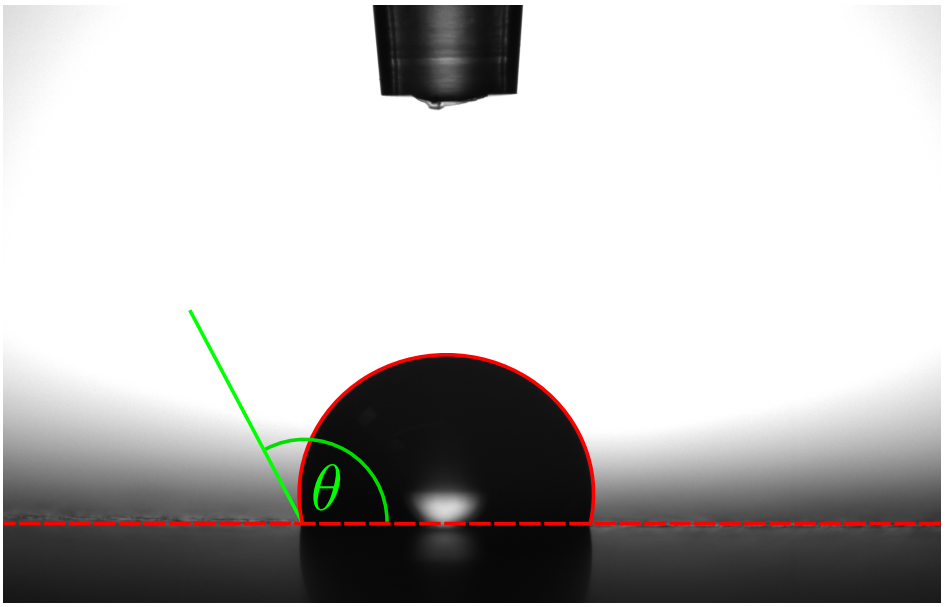

Figure B.5.: Example of a Sessile Drop experiment and subsequent contact angle measurement. The picture is taken from `https://en.wikipedia.org/wiki/Sessile_drop_technique#/media/File:Attension_Theta_CA.png` (last access October 29, 2019). It shows the contact angle measurement of an unknown liquid on an unknown solid. In the top of the picture, the tube, depositing the liquid onto the solid, is seen. The solid red line frames the shape of the liquid. The red dotted line depicts the solid. The measurement of the contact angle (green) has been conducted using Inkscape. Due to the high contact angle of $\theta = 118.24°$, the wettability is low.

It shows a drop of an unknown liquid, deposited by a tube (top) onto an unknown solid. The shape of the liquid is framed with a solid red line, whereas the red dotted line is the border of the underlying solid. The contact angle, depicted with the green θ, is measured using the vector graphics editor Inkscape. Note that, generally, a geometric model is fitted onto the

contour of the sessile drop. With a value of $\theta = 118.24°$, the wettability is in this case low. Under the assumption that the liquid is water, the solid is considered to be hydrophobic.

The repetition of the process with several liquids yields a plot like the one in Figure B.4 and consequently the surface free energy of the solid.

The surface tensions for the polymers in this work are obtained using this method. For this, the polymers are formed into plates with a hot press at 160 °C and a press force of $100k$N. Then different probe liquids are deposited on the plates. The reason for this is that uncured rubber polymers, such as NR and SBR, can not be melted. Consequently, drop shape analysis is no option [38].

B.5.2. Pendant Drop

In the pendant drop method, the drop stays attached to the tube. The surface, or interfacial, tension seeks to minimize the surface area of the drop and thus bringing it into a spherical shape. The gravitation, on the other hand, stretches the drop from its spherical shape. The result is a pear-like shape as seen in Figure B.6. Unlike the Sessile Drop technique, it is independent of the contact angle. Only the shape of the drop itself is considered.

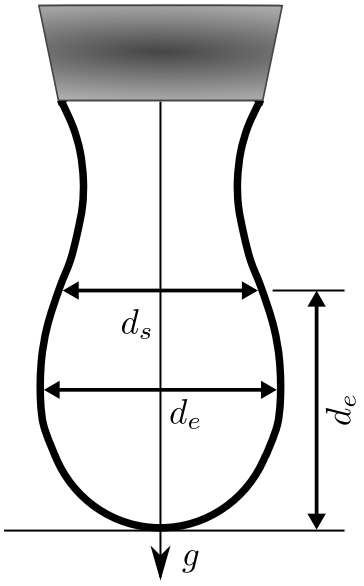

Figure B.6.: Schematic depiction of a Pendant Drop experiment with drop shape analysis. In downwards direction acts the gravitational force. d_e is the equatorial diameter and d_s is the horizontal diameter at height d_e from the vertex of the drop.

The curvature of any liquid surface is governed by the Laplace's capillary equation [1]

$$\Delta P = \gamma \left(\frac{1}{R_1} + \frac{1}{R_2} \right), \tag{B.35}$$

where ΔP is the pressure difference across the curved surface and R_1 and R_2 are the principal radii of curvature. It can be shown (cf. Chapter 6 in [39]) that this equation can be brought into a different form, called the Bashforth-Adams equation, by introducing a set of coordinates. This equation is differential equation and has been solved numerically. As a final result a simple connection between the geometrical form of the drop and the pressure difference, as well the gravitational acceleration g can be found as

$$\gamma = \Delta\rho g d_e^2 / H. \tag{B.36}$$

Here, $\Delta\rho$ is the difference in the densities of the two phases (the drop and the surrounding medium) and d_e is, as defined in Figure B.6, the equatorial diameter. The constant H is a correction factor which varies with the shape of the drop. Values for this parameter for a variety of drop shapes have been tabulated (for instance in chapter 6 in [39]) and derived on the basis of the defined shape parameter S, which is defined as $S = d_s/d_e$. As seen in Figure B.6, d_s is the horizontal diameter at height d_e from the vertex of the drop.

It is important for this method that the drop is at its equilibrium shape. For low viscosity liquids this is achieved instantaneously, but for viscous liquids such as polymers, this may take several minutes or even hours [16]. In that source is stated that a change of d_e with not more than 0.5% in reasonable amount of time, for instance 20 min, can be considered a equilibrium state. It is also noted in that source that the density data must be obtained very accurately, due to the proportionality to the surface tension as seen in Equation (B.36). The surface tension of the liquid is obtained by this method when the surrounding medium is an inert gas, because then its density can be neglected.

B.5.3. Wilhemy Plate

The last method we want to consider can be used to obtain the contact angle between liquids and solids using force measurements. This consequently yields the surface free energy of the solid, if different probe liquids are used. It can, however, also be used to obtain the surface tension of a liquid. In Figure B.7a, the method is depicted. A solid plate is suspended inside a liquid. During withdrawal, as well as during lowering, a liquid meniscus is formed around the perimeter, l, of the suspended plate. It is a result of the surface tension of the liquid, γ. If the apparatus is balanced before the liquid surface is raised to contact position, then the force, F, needed to withdraw the plate is proportional to the weight of the meniscus, w. To be precise, this weight must equal the upward force provided by the surface, which in turn equals the vertical component of the surface tension, i.e., $\gamma\cos\theta$, times the perimeter of the plate. Here, θ is the contact angle. This gives at equilibrium

$$F = \gamma\cos\theta l. \tag{B.37}$$

Therefore, is the contact angle is known from another measurement, for instance the sessile drop technique, then the surface tension of the liquid can be estimated. If, on the other hand, known probe liquids are used, their contact angle to the solid can be measured, without an analysis of the shape of a drop.

Taking the height of the meniscus into account, as shown in the cross-sectional view in Figure B.7b, we can find equations, which allow us to obtain both quantities simultaneously. This is briefly shown in the following. A more detailed derivation is given in [39].

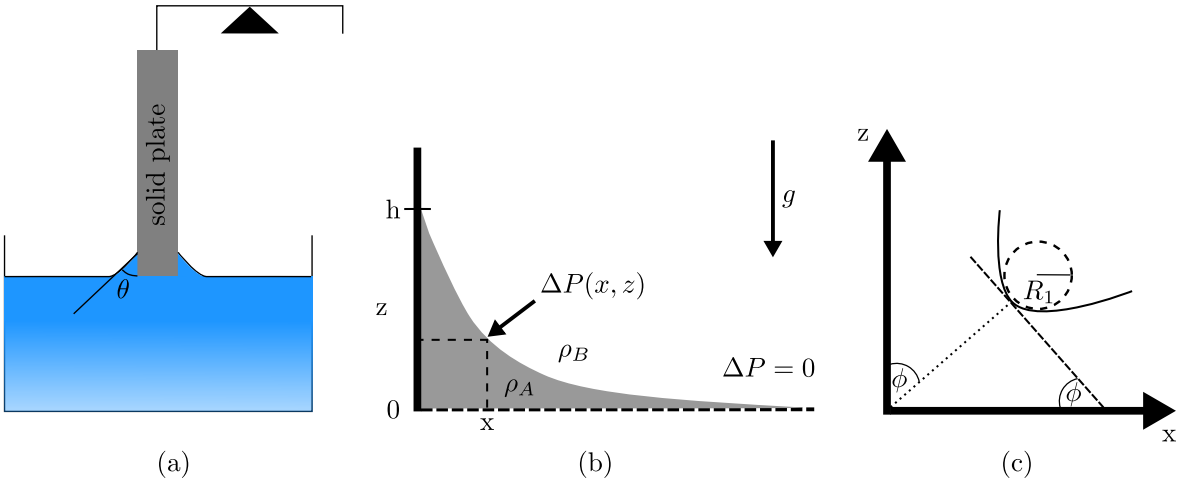

Figure B.7.: (a): Schematic depiction of Wilhelmy Plate method. A solid plate is suspended inside a liquid of known, or unknown surface tension. During withdrawal of the plate the liquid surface is raised and forms a meniscus. If the apparatus is balanced before withdrawal, then the subsequent imbalance is a consequence of the weight of the meniscus. The meniscus is held up by the surface tension of the liquid surface, thus the force measured during withdrawal is proportional to the surface tension, γ, and the contact angle, θ. **(b)**: Cross-sectional view of the meniscus. Rising liquid A displaces the surrounding medium B, exerting a buoyant force on the meniscus. Far from the wall on the left, the pressure difference is zero, which defines the $z = 0$ plane. The contact between meniscus and wall is at $z = h$. At some general point at (x, z), the pressure just beneath the surface is less by $\Delta P(x, z)$ than the reference plane. **(c)**: Local radius of curvature of a general curve. The angle ϕ is the angle made by the extension of the normal with the z axis. This is the same angle as between the tangent and the x axis. R_1 is the radius of the curvature.

The meniscus formed by the liquid A, displaces the surrounding medium B, resulting in a buoyant force acting on the meniscus. Consequently, the difference in the densities must be used. Far from the wall the pressure difference is zero, which we define as the $z = 0$ plane. The contact between the meniscus and the wall is at $z = h$. At some general point (x, z), the pressure just beneath the surface is less by $\Delta P(x, z)$ than the reference plane, where $\Delta P = 0$, i.e., far away from the wall. The liquid is elevated at this point by an amount sufficient to produce a compensating hydrostatic pressure, which is given by $(\rho_A - \rho_B)gz$. Together with Young's capillary equation (B.35) one can find

$$\Delta\rho g z = \gamma / R_1, \tag{B.38}$$

where R_1 is the radius of curvature in the plane of Figure B.7b. It can be shown that

$$R_1^{-1} = \frac{d^2z/dx^2}{[1 + (dz/dx)^2]^{(3/2)}}. \tag{B.39}$$

Using trigonometric relations based on the tangent and the normal to the curve constructed at that point, we find for the local slope of the tangent $dz/dx = -\tan\phi$. This is depicted in Figure B.7c. Inserting this into Equation (B.39) and then into Equation (B.38), a simple differential equation is obtained. Solved, and keeping in mind that $\phi = 0$ at $z = 0$, one finds

$$\cos\phi = 1 - \frac{\delta\rho g}{2\gamma} z^2. \tag{B.40}$$

At $z = h$, i.e., the height of the meniscus, ϕ is the complementary angle to the contact angle θ and hence, $\cos\theta = \sin\theta$. This finally yields

$$\sin\theta = 1 - \frac{\delta\rho g}{2\gamma} h^2. \tag{B.41}$$

This relates the height of the meniscus to the contact angle and the surface tension of the liquid. This is certainly no improvement, since instead of a force, Equation (B.37), the height of the meniscus needs to be measured and we still can't obtain both quantities from a single measurement. However, if we take the square of Equation (B.42) and of Equation (B.37), we can add them together and find

$$\gamma = \frac{\Delta\rho g h^2}{4} + \frac{F^2}{\Delta\rho g h^2 l^2}, \tag{B.42}$$

which can be inserted into Equation (B.37) to obtain

$$\cos\theta = \frac{4\Delta\rho g h^2 l F}{(\Delta\rho)^2 g^2 h^4 l^2 + 4F^2}. \tag{B.43}$$

The last two equations allow to measure the surface tension and the contact angle from conducting a single experiment.

To obtain the surface free energy of colloidal materials, such as the silica or carbon black fillers used in this work, they can be adhered to an adhesive tape, which is then suspended into different probe liquids [38]. Note that the receding contact angle upon withdrawal and the advancing contact angle during immersion is generally measured.

Experimental values for filler particles obtained by the Wilhelmy method in this work are always those obtained by the mean contact angle.

B.6. References

[1] Cherry, B. W., Polymer surfaces. Edited by Clarke, D. R., Suresh, S., 1st ed., Cambridge: Cambridge University Press, **1981**, ISBN: 0521230829.

[2] Leite, F. L. et al., Theoretical models for surface forces and adhesion and their measurement using atomic force microscopy. *Int. J. Mol. Sci.* **2012**, 13 (10), 12773–12856, DOI: 10.3390/ijms131012773.

[3] Lee, L.-H., Adhesive Bonding. Edited by Lee, L.-H., 1st, New York: Springer Science + Business Media, LLC, **1991**, DOI: 10.1007/978-1-4757-9006-1.

[4] Keesom, W. H., On Waal's cohesion forces. *Phys. Zeitschrift* **1921**, 22, 129–141.

[5] Debye, P., The van der Waals cohesion forces. *Phys. Zeitschrift* **1921**, 21, 178–187.

[6] London, F., The general theory of molecular forces. *Trans. Fara. Soc.* **1937**, 33, 8–26, DOI: 10.1039/TF937330008B.

[7] Buckingham, R. A., The Classical Equation of State of Gaseous Helium, Neon and Argon. *Proc. R. Soc. A Math. Phys. Eng. Sci.* **1938**, 168 (933), 264–283, DOI: 10.1098/rspa.1938.0173.

[8] Lennard-Jones, J. E., On the Determination of Molecular Fields. — II. From the Equation of State of a Gas.. *Proc. R. Soc. London A* **1924**, 106 (738), 463–477, DOI: 10.1098/rspa.1924.0082.

[9] Lennard-Jones, J. E., Cohesion. *Proc. Phys. Soc.* **1931**, 43 (5), 461–482, DOI: 10.1088/0959-5309/43/5/301.

[10] Marchand, A. et al., Why is surface tension a force parallel to the interface?. **2012**, 999, DOI: 10.1119/1.3619866.

[11] Fowler, R., Guggenheim, E. A., Statistical Thermodynamics. Edited by Fowler, R., Guggenheim, E. A., 4th ed., Cambridge: Cambridge University Press, **1956**, ISBN: 978-1114712706.

[12] Good, R. J., Girifalco, L. A., Kraus, G., A theory for estimation of interfacial energies. II. Application to surface thermodynamics of Teflon and graphite. *J. Phys. Chem.* **1958**, 62 (11), 1418–1421, DOI: 10.1021/j150569a016.

[13] Hamaker, H. C., The London-van der Waals attraction between spherical particles. *Physica* **1937**, 4 (10), 1058–1072, DOI: 10.1016/S0031-8914(37)80203-7.

[14] Lifshitz, E. M., The theory of molecular attractive forces between solids. **1955**, URL: www.jetp.ac.ru/cgi-bin/dn/e_002_01_0073.pdf (visited on 08/30/2019).

[15] Eötvös, R., Ueber den Zusammenhang der Oberflächenspannung der Flüssigkeiten mit ihrem Molecularvolumen. *Ann. Phys.* **1886**, 263 (3), 448–459, DOI: 10.1002/andp.18862630309.

[16] Wu, S., Interfacial And Surface Tensions of Polymers. *J. Macromol. Sci. Part C* **1974**, 10 (1), 1–73, DOI: 10.1080/15321797408080004.

[17] Guggenheim, E. A., The principle of corresponding states. *J. Chem. Phys.* **1945**, 13 (7), 253–261, DOI: 10.1063/1.1724033.

[18] Donnet, J. B., Qin, R. Y., Empirical estimation of surface energies of polymers and their temperature dependence. *J. Colloid Interface Sci.* **1992**, 154 (2), 434–443, DOI: 10.1016/0021-9797(92)90159-J.

[19] Schrader, M. E., Young-Dupre Revisited. *Langmuir* **1995**, 11 (9), 3585–3589, DOI: 10.1021/la00009a049.

[20] Girifalco, L. A., Good, R. J., A theory for the estimation of surface and interfacial energies. I. Derivation and application to interfacial tension. *J. Phys. Chem.* **1957**, 61 (7), 904–909, DOI: 10.1021/j150553a013.

[21] Good, R. J., Girifalco, L. A., A theory for estimation of surface and interfacial energies. III. Estimation of surface energies of solids from contact angle data. *J. Phys. Chem.* **1960**, 64 (5), 561–565, DOI: 10.1021/j100834a012.

[22] Berthelot, D., Sur le Mélange des Gaz. *Comptes rendus l'Académie des Sci.* **1898**, 126, 1703–1706.

[23] Fowkes, F. M., Attractive Forces At Interfaces. *Ind. Eng. Chem.* **1964**, 56 (12), 40–52, DOI: 10.1021/ie50660a008.

[24] Owens, D. K., Wendt, R. C., Estimation of the surface free energy of polymers. *J. Appl. Polym. Sci.* **1969**, 13 (8), 1741–1747, DOI: 10.1002/app.1969.070130815.

[25] Wu, S., Calculation of interfacial tension in polymer systems. *J. Polym. Sci. Part C Polym. Symp.* **1971**, 34 (1), 19–30, DOI: 10.1002/polc.5070340105.

[26] Good, R. J., Oss, C. J. van, The modern theory of contact angles and the hydrogen bond components of surface energies. *Mod. approaches to wettability*, edited by Schrader, M. E., Loeb, G. I., Springer, Boston, MA, **1992**, 1–27, DOI: 10.1007/978-1-4899-1176-6_1.

[27] Wang, M.-J., Effect of Polymer-Filler and Filler-Filler Interactions on Dynamic Properties of Filled Vulcanizates. *Rubber Chem. Technol.* **1998**, 71 (3), 520–589, DOI: 10.5254/1.3538492.

[28] Landau, D. P., Binder, K., A Guide to Monte Carlo Simulations in Statistical Physics. 3rd ed., New York: Cambridge University Press, **2009**, ISBN: 9780511651762.

[29] Mihara, S., Reactive processing of silica-reinforced tire rubber: new insight into the time- and temperature-dependence of silica rubber interaction. Dissertation, University of Twente, **2009**, DOI: 10.3990/1.9789036528399.

[30] Stöckelhuber, K. W. et al., Impact of filler surface modification on large scale mechanics of styrene butadiene/silica rubber composites. *Macromolecules* **2011**, 44 (11), 4366–4381, DOI: 10.1021/ma1026077.

[31] Tunnicliffe, L. B. et al., Flocculation and viscoelastic behaviour in carbon black-filled natural rubber. *Macromol. Mater. Eng.* **2014**, 299 (12), 1474–1483, DOI: 10.1002/mame.201400117.

[32] Stöckelhuber, K. W. et al., Filler flocculation in polymers-a simplified model derived from thermodynamics and game theory. *Soft Matter* **2017**, 13 (20), 3701–3709, DOI: 10.1039/c6sm02694j.

[33] Klat, D., Karimi-Varzaneh, H. A., Lacayo-Pineda, J., Phase morphology of NR/SBR blends: Effect of curing temperature and curing time. *Polymers (Basel).* **2018**, 10 (5), 1–15, DOI: 10.3390/polym10050510.

[34] Natarajan, B. et al., Effect of interfacial energetics on dispersion and glass transition temperature in polymer nanocomposites. *Macromolecules* **2013**, 46 (7), 2833–2841, DOI: 10.1021/ma302281b.

[35] Tadmor, R., Line energy and the relation between advancing, receding, and Young contact angles. *Langmuir* **2004**, 20 (18), 7659–7664, DOI: 10.1021/la049410h.

[36] Marmur, A., Wetting on hydrophobic rough surfaces: To be heterogeneous or not to be?. *Langmuir* **2003**, 19 (2), 8343–8348, DOI: 10.1021/la0344682.

[37] Rulison, C., So You Want to Measure Surface Energy?. **1999**, URL: https://www.kruss-scientific.com/fileadmin/user_upload/website/literature/kruss-tn306-en.pdf (visited on 06/21/2019).

[38] Stöckelhuber, K. W. et al., Contribution of physico-chemical properties of interfaces on dispersibility, adhesion and flocculation of filler particles in rubber. *Polymer (Guildf).* **2010**, 51 (9), 1954–1963, DOI: 10.1016/j.polymer.2010.03.013.

[39] Hiemenz, P. C., Rajagopalan, R., Principles of Colloid and Surface Chemistry, Third Edition, Revised and Expanded. 3rd, New York: Marcel Dekker, **1997**, ISBN: 0-8247-9397-8.

C. Small Angle Scattering

The rubber compounds we consider in this work contain different constituents, e.g., polymers, fillers, and coupling agents. Each contributes differently to the mechanical properties of the compound. As we know from Appendix A, its morphology is crucial to those properties. A precise knowledge of the structure is therefore inevitable. Scattering, whether it is due to light, neutrons or X-rays, on which we focus in the following, is a non-destructive way to obtain this information. Although light scattering is fast, easy, and inexpensive the longer wavelength in comparison to X-rays or neutrons only enables to probe structures of several microns and larger. The filler particles used in rubber compounds are, however, in the size region of just a few tens of nanometers (cf. Appendix A). Additionally, the strong interaction between light and matter makes it complicated to interpret the intensity pattern [1]. Techniques utilizing small angle X-ray (SAXS) and neutron (SANS) scattering obey the same physical principles and only differ in their resolution and field of application. While SAXS operates on size regions of ten to several thousand Å, SANS operates on slightly higher size regions of hundreds to up to several ten thousand Å. Furthermore, SANS has a higher sensitivity to light elements, can be used to label isotopes, and shows strong scattering by magnetic moments. However, SANS is only available in few facilities world wide [2] and consequently SAXS is more frequently used (e.g. [3–5]). Nevertheless, a combination of several techniques to analyze a broader size spectrum is also very common (e.g. [6, 7]). Both methods have a pendant aiming for higher size regions, namely Ultra-SAXS (USAXS) and -SANS (USANS). They reach up to several tens of microns [8].

The literature behind scattering is vast. Beside the standard books of Guinier and Fournet [9] and Glatter and Kratky [10], several books focusing on colloidal particles inside polymers are available (e.g. [2, 11, 12]). Additionally, a significant amount of research led to several papers [1, 4, 6, 7, 13, 14] and theses [3, 15, 16], to name just a few recent works. A, for this work, special result of research was obtained by Beaucage [17], who developed a theory to combine the results of Porod [18] and Guinier [9]. This resulted in a continuous scattering curve for single particles, which maintained the respective limits of Porod and Guinier. A special focus, since the concept of fractals was developed by Mandelbrot [19], was on the scattering on fractal structures (e.g. [8, 20–22]). In those works, the concepts to obtain the mass and surface fractal dimension of colloidal particles is described. The mass fractal dimension of aggregates, and sometimes the polymer network, is a continuously reviewed quantity of this work.

The purpose of this chapter is to give the reader an overview about the scattering theory tailored to the needs of this work. All of the above cited literature is the foundation. Most sources focus mainly on colloidal particles inside polymers – excluding the standard books, of course. It is stressed that no claim to completeness on the topic of scattering in general is made at any time. Especially, the consideration of experimental processes is out of scope of this work. For a deeper understanding, the reader is thus encouraged to consider the cited books in the former paragraph. The goal is to derive the formula for the intensity stated in chapter 2, which consists of a structure and a form factor. Furthermore, we want to justify the derivation of information about the mass fractal dimensions of aggregates and

larger structures out of the scattering data. In this context, the concept of mass fractals is introduced.

C.1. Basic Theoretical Principles

An incoming coherent monochromatic wave, described by the wave vector $\vec{s}_0$, wave length λ, and intensity I_0 enters the probe and interacts with its atoms, i.e., the scatterers, as shown in Figure C.1.

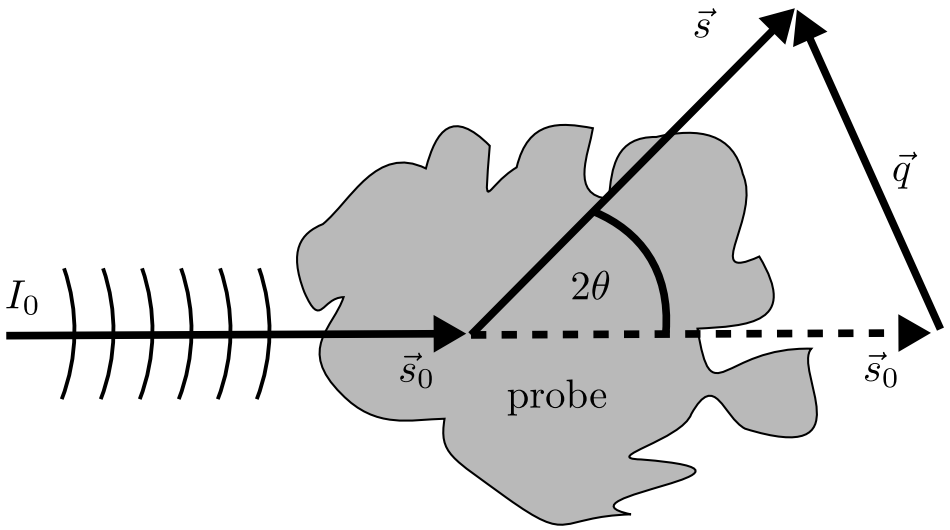

Figure C.1.: Illustration of scattering and definition of the scattering vector. The incoming wave has an intensity of I_0 and is described by the wave vector $\vec{s}_0$. Inside the probe, the wave is scattered under some angle 2θ. The scattered wave is described by the wave vector $\vec{s}$. The scattering vector $\vec{q}$ is then given as the difference between $\vec{s}$ and $\vec{s}_0$.

Depending on the source, i.e., if either X-rays or neutrons are used, the wave is scattered by the electron clouds (X-rays) or by the nuclei of the atoms and by the magnetic moments of the atoms (neutrons). In the case of X-rays, the electrons then resonate with the same frequency as the X-rays passing through the probe. They in turn, according to the Huygens–Fresnel principle[1], emit coherent secondary waves interfering with each other. Now, let the scattered wave be described by the vector $\vec{s}$. Depending on the scattering angle, 2θ, the phase difference between $\vec{s}_0$ and $\vec{s}$ is different. For large angles, the superposition of all waves with all possible phases leads to no scattering at all due to destructive interference. For smaller angles, however, the phase difference becomes smaller and constructive interference leads to an enforcement of the waves. Consequently, the scattering maximum is found in the direction of zero scattering angle. If we now describe the difference between the incoming wave and the scattered wave with $\vec{q}$, i.e.,

$$\vec{q} = (\vec{s} - \vec{s}_0), \tag{C.1}$$

[1]It states that each point on a wavefront acts as a fresh source of distribution of light.

and take into account that X-ray scattering is elastic, i.e., $s = |\vec{s}| = |\vec{s}_0| = 2\pi/\lambda$, then we find for the magnitude of this scattering vector

$$q = |\vec{s} - \vec{s}_0| = \sqrt{(2s^2 - 2s^2 \cos 2\theta)} = \frac{4\pi}{\lambda} \sin\theta. \tag{C.2}$$

Here, 2θ is the scattering angle. This shows that small scattering angles result in small values of q and that it has a unit of inverse length.

The X-rays photons have a very high energy compared to the binding energy of the atom. As a consequence, the electrons behave as they were free. The intensities of the secondary waves emitted due to the scattering process have thus the same intensity, which can be described by Thomson scattering. The difference of these waves is given by the phase, ϕ. Each wave can thus be described by its complex form $e^{i\phi}$, where $\phi = -\vec{q} \cdot \vec{r}$. Here, $\vec{r}$ is the distance between two scatterers in the probe. If both vectors are parallel to each other, we find constructive interference for $q = 2\pi/r$, where $r = |\vec{r}|$. Thus, the scattering length, q, is inversely proportional to the real space distance, r, between the scatterers. Figure C.2 shows the correspondence between r and q in the according context for rubber-filler systems.

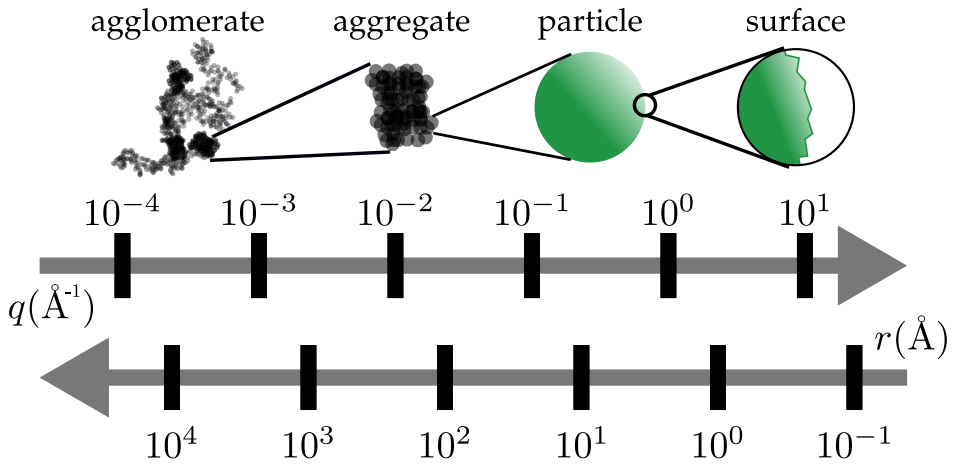

Figure C.2.: Depiction of the scattering lengths in relation to filler structures. Small q values correspond to large r values. In this work, we use throughout $10^{-4}\text{Å}^{-1} < q < 3.3{\cdot}10^{-1}\text{Å}^{-1}$. This probes the complete spectrum, i.e., the simulation box as well as the primary particles.

For the q values we use throughout this work, i.e., $10^{-4}\text{Å}^{-1} < q < 3.3 \cdot 10^{-1}\text{Å}^{-1}$, we consequently find with a typical wavelength used in SAXS (e.g. CuK$_\alpha$-line with 1.54 Å), scattering angles of about $0.001° < 2\theta < 5°$. Note that the lower limit is experimentally only reached by USAXS.

To describe the resulting amplitude of all scatterers, it is now possible to sum up all secondary waves describes by $e^{-i\vec{q}\cdot\vec{r}}$. However, the number of electrons is huge and they cannot be exactly localized. It is therefore convenient to introduce the concept of electron density, i.e., the number of electrons per unit volume (mostly given in cm^3) denoted by $\rho(\vec{r})$. A volume element $\mathrm{d}V$ at position $\vec{r}$ then contains $\rho(\vec{r})\mathrm{d}V$ electrons. Instead of summation, we can thus

integrate over the volume of the probe, V, irradiated by the incident wave to obtain the scattering amplitude, i.e.,

$$A(\vec{q}) = \int_{\mathbb{R}^3} \rho(\vec{r}) e^{-i\vec{q}\cdot\vec{r}} \mathrm{d}V. \tag{C.3}$$

This shows that the scattering amplitude, A, in a certain direction specified by $\vec{q}$ is nothing else than the Fourier transform of the electron density distribution, $\rho(\vec{r})$. Consequently, the intensity, $I(\vec{q})$, is in general given by the absolute square of the scattering amplitude

$$I(\vec{q}) = |A|^2 = \int_{\mathbb{R}^3} \rho(\vec{r}) e^{-i\vec{q}\cdot\vec{r}} \mathrm{d}V \int_{\mathbb{R}^3} \rho(\vec{r}') e^{i\vec{q}\cdot\vec{r}'} \mathrm{d}V'. \tag{C.4}$$

We now introduce the Patterson function which is defined as

$$\tilde{\rho}^2(\vec{r}') = \int_{\mathbb{R}^3} \rho(\vec{r}) \rho(\vec{r} + \vec{r}') \mathrm{d}V. \tag{C.5}$$

The intensity can then be written as

$$I(\vec{q}) = |A|^2 = \int_{\mathbb{R}^3} \tilde{\rho}^2(\vec{r}') e^{-i\vec{q}\cdot\vec{r}'} \mathrm{d}V'. \tag{C.6}$$

Thus, if the electron density distribution is known, Equation (C.6) can be solved and the intensity is obtained. Unfortunately, this can only be achieved for very special cases. Because we are considering small angle scattering, the conditions of those special cases are generally met. The conditions are that the system is statistically isotropic and that there exists no long range order, i.e., it is either consisting of a single particle or is dilute. An explicit example, which fulfills both conditions are spherically symmetric particles like the filler particles we consider throughout this work (cf. Appendix A). In the following, we discuss this case explicitly.

C.2. Single Particles and Dilute Systems

For spherically symmetric particles, the electron density distribution can be considered constant, i.e., it is equal to ρ_0. Subsequently, $\rho(\vec{r})$ is only depending on the shape of the particle. It is convenient to define a form factor, $\sigma(\vec{r})$, with the following property

$$\rho(\vec{r}) = \rho_0 \sigma(\vec{r}) = \begin{cases} \rho_0, & \vec{r} \in V, \\ 0, & \vec{r} \notin V. \end{cases} . \tag{C.7}$$

Similar to Equation (C.5) we can then define the Patterson function as

$$\tilde{\rho}^2(\vec{r}) := \frac{1}{V} \int_{\mathbb{R}^3} \sigma(\vec{r}') \sigma(\vec{r}' + \vec{r}) \mathrm{d}V, \tag{C.8}$$

Hence, for the intensity

$$I(\vec{q}) = V\Delta\rho^2 \int_{\mathbb{R}^3} \tilde{\rho}^2(\vec{r}) e^{-i\vec{q}\cdot\vec{r}} \mathrm{d}V. \tag{C.9}$$

Here, ρ_0 is replaced by the difference in the scattering densities, $\Delta\rho = \rho - \rho_0$, because always systems with more than one component are considered and only the difference between the embedded medium, ρ_0, and the particles, ρ, is of importance.

The assumption of statistically isotropic particles allows us to use the average over all distances r in Equation (C.9). This reduces the calculation to

$$I(q) = \langle I(\vec{q}) \rangle = V\Delta\rho^2 \int_0^\infty \gamma(r) \frac{\sin(qr)}{qr} 4\pi r^2 \mathrm{d}r, \tag{C.10}$$

where $\gamma(r)$ is the characteristic function, which was first introduced by Porod as

$$\gamma(r) = \langle \tilde{\rho}^2(\vec{r}) \rangle. \tag{C.11}$$

This is the averaged Patterson function. The characteristic function represents the probability that a point at a radial distance r from any given point in a particle phase will also be in the particle phase.

The function $\frac{\sin(qr)}{qr}$ in Equation (C.10) weights the product $r^2\gamma(r)$ by a radially symmetric phase factor of q and r. This product is proportional to the so-called distance distribution function, which is given as

$$p(r) = 4\pi r^2 V \gamma(r). \tag{C.12}$$

It has the following the property

$$\int_0^\infty p(r) dr = \int_0^\infty 4\pi r^2 V \gamma(r) \mathrm{d}r = V^2, \tag{C.13}$$

from which directly follows that

$$\int_0^\infty 4\pi r^2 \gamma(r) \mathrm{d}r = V. \tag{C.14}$$

We now investigate the respective limits for the scattered intensity, $I(q)$, in Equation (C.10) of a single particle or a dilute system of particles, at small and large scattering lengths, q. The approximation of Beaucage combines both of those limits and allows to describe the scattering of single particles over several decades in the scattering length.

C.2.1. Limit of Small Scattering Length

We start with the limit for small q and first consider the behavior at $q = 0$. Using Equation (C.14) we immediately find

$$I(0) = V\Delta\rho^2 \lim_{q\to 0} \int_0^\infty \gamma(r) \frac{\sin(qr)}{qr} 4\pi r^2 \mathrm{d}r = V\Delta\rho^2 \int_0^\infty 4\pi r^2 \gamma(r) \mathrm{d}r = V^2\Delta\rho^2. \tag{C.15}$$

This is the square of the total number of electrons in the probe. Note that for $q = 0$ the scattering angle is equal to zero. Consequently, all scattered waves are in phase and the amplitudes are added.

At small values of q, we can expand the weighting factor. This yields

$$\frac{\sin(qr)}{qr} = 1 - \frac{q^2 r^2}{6} + \dots. \tag{C.16}$$

Inserting this expansion into Equation (C.10) and use the result obtained in Equation (C.15) we find

$$I(q) = V^2\Delta\rho^2 \left[1 - \frac{q^2}{6}\frac{1}{V}\int_0^\infty 4\pi r^4 \gamma(r)\mathrm{d}r + \dots\right]. \tag{C.17}$$

Increasing q from zero decreases $I(q)$ following a parabolic curve. The electronic radius of gyration of a particle about its electronic center of mass is defined by the relation

$$R_G^2 = \frac{1}{2}\frac{\int_0^\infty r^4\gamma(r)\mathrm{d}r}{\int_0^\infty r^2\gamma(r)\mathrm{d}r} = \frac{\int_V r^2\rho(\vec{r})\mathrm{d}^3r}{\int_V \rho(\vec{r})\mathrm{d}^3r}, \tag{C.18}$$

where the right hand side is a result of relating the structure of a particle to the radius of gyration in the same manner as in classical mechanics. We then find, for instance, by considering spherical, monodisperse particles with radius R, i.e., the filler particle we use in this work,

$$R_G^2 = \frac{\int_0^R r^4\mathrm{d}r}{\int_0^R r^2\mathrm{d}r} = \frac{3}{5}R^2. \tag{C.19}$$

Using Equations (C.14) and (C.18) and inserting them into Equation (C.17) we obtain

$$I(q) = V^2\Delta\rho^2 \left[1 - \frac{1}{3}R_G^2 q^2 + \dots\right]. \tag{C.20}$$

Guinier found that the right hand side of this equation is equal to the Maclaurin series of

$$I(q) = V^2 \Delta\rho^2 e^{-q^2 R_G^2/3}. \tag{C.21}$$

Consequently, this expression is called the Guinier law. It governs the intensity for statistically isotropic systems with no long range order. Furthermore, it turns out that this is the Fourier transform of the following characteristic function

$$\gamma_{Guinier}(r) = e^{-3r^2/4R_g^2}. \tag{C.22}$$

C.2.2. Limit of Large Scattering Length

In the limit of large q, we can utilize the fact that the Fourier transform of Equation (C.10) yields

$$r\gamma(r) = \frac{2}{\pi} \int_0^\infty \frac{qI(q)}{4\pi\Delta\rho^2 V} \sin(qr)\, \mathrm{d}q. \tag{C.23}$$

Thus, the high q part of $I(q)$ corresponds to the part of the curve of $\gamma(r)$ at small values of r. An approximate expression at small r values is given due to Porod

$$\gamma_{Porod}(r) = 1 - \frac{S}{4V} r + \dots. \tag{C.24}$$

Hence, the characteristic function is governed by the external surface, S, and the volume, V, of the given particle. Substituted into Equation (C.10) we obtain

$$I(q) = \frac{2\pi\Delta\rho^2 S}{q^4} + \dots, \tag{C.25}$$

i.e., Porod's law. The intensity at large q is thus uniquely depending on the external surface, S, of the particle. Note that this behavior only applies for particles with a smooth surface. For surface fractals it can be shown that

$$I(q) \propto q^{-6+d_s}, \tag{C.26}$$

where d_s is the surface fractal dimension of the particle. Because the constant prefactor also depends on d_s, we only state the proportional behavior to the scattering length, q.

C.2.3. Unified Approximation for Small Angle Scattering

Equation (C.27) summarizes the results for low and high q behavior obtained in Equations (C.21) and (C.25), respectively.

$$I(q) \propto \begin{cases} S\,q^{-4}, & q \to \infty, \\ V^2, & q \to 0. \end{cases} \tag{C.27}$$

To approximate the scattering behavior over several decades in q, Beaucage combined both laws of Guinier and Porod by introducing a reduced parameter for q, named q^*, which is given by

$$q^* = q/(\mathrm{erf}(qR_g/6^{1/2}))^3. \tag{C.28}$$

He then found the following approximation for the scattering intensity of a spherical particle

$$I(q) = \Delta\rho^2 \left(V^2 \exp[-q^2R^2/5] + 2\pi S (q^*)^{-4} \right), \tag{C.29}$$

where $q^* = q/(\mathrm{erf}(qR/\sqrt{10}))^3$, $S = 4\pi R^2$, and $V = 4\pi R^3/3$.

To compare whether this approximation is sufficient, we can calculate the intensity of a sphere of uniform density directly. For that, we take the amplitude in Equation (C.3) and make use of the symmetry of a sphere. Then we square the result and obtain for the intensity

$$I(q) = \Delta\rho^2 V^2 \left(3 \frac{\sin(qR) - qR\cos(qR)}{(qR)^3} \right)^2. \tag{C.30}$$

This equation was first derived by Lord Rayleigh and shows in the limit for small and large q the same behavior as given in Equation (C.26).

Figure C.3 shows a plot of the reduced scattering intensity versus the scattering length, q, times the radius of a sphere, R. Note that this representation is chosen, because the factor qR appears in every formula considered so far. The black solid, oscillating line displays the exact behavior as calculated by Rayleigh, i.e., Equation (C.30). The approximation due to Beaucage, i.e., the solid red line obtained by Equation (C.29), shows the same scattering behavior over the complete q range – without oscillations. The green dashed and blue dotted curves are obtained for Equations (C.21) and (C.25), respectively. Those are the limits for small and large q, i.e., the formulae of Guinier and Porod. Compared to the approximation of Beaucage, we find that both limiting behaviors are indeed correctly described.

C.3. Densely Filled Systems

So far we only considered single particles or dilute systems where the particles are separated far enough so that they do not interact with each other. In the latter case, the intensities of the single particles can simply be summed up. The systems we investigate in this work are, however, densely filled. This means that the filler particles interact with each other due to attractive or repulsive forces, such as van der Waals (cf. Appendix B). Consequently, the geometric arrangement of the particles changes and fractal objects, such as aggregates, may

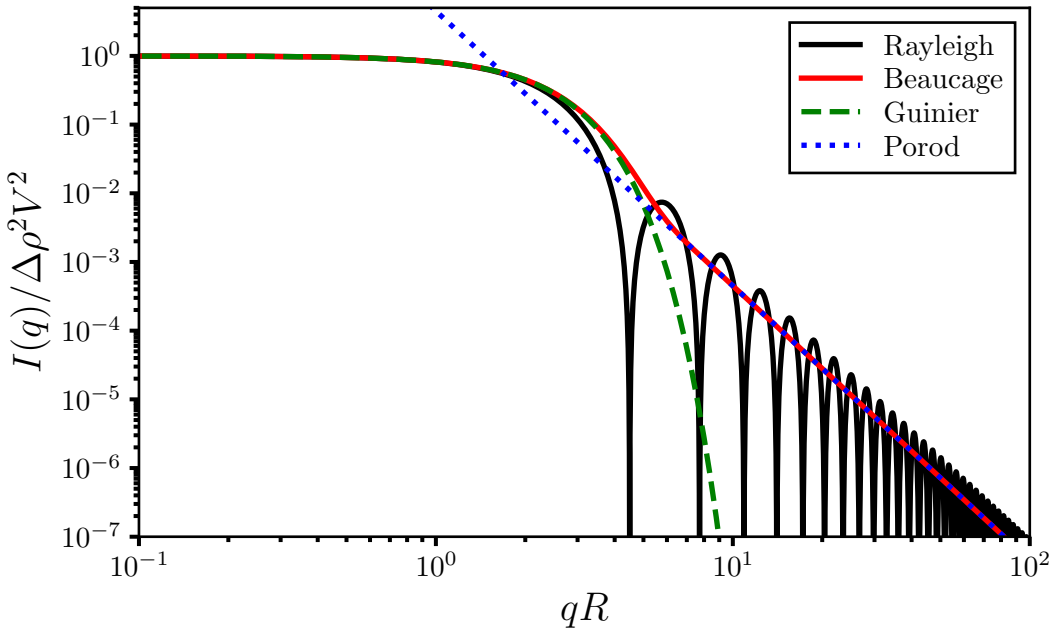

Figure C.3.: Reduced scattering intensity, $I(q)/\Delta\rho^2V^2$ versus scattering length, q, times radius of a sphere, R. The black solid oscillating line shows the intensity after Rayleigh in Equation (C.30). The red solid line is the approximation due to Beaucage after Equation (C.29). The green dashed line is the limit for small q due to Guinier described by Equation (C.21). The blue dotted line is the limit for large q due to Porod described by Equation (C.25). Note that both quantities on each axis have no units.

appear. Because scattering is sensitive to order, we need to account for this effect to produce scattering intensity curves comparable to those obtained in experiments. In the following, we want to focus on the geometry only, i.e., we neglect possible time dependencies occurring in realistic systems. For the case of monodisperse, spherical particles the intensity of a densely filled system can then be decomposed into two factors, i.e.,

$$I(q) = \phi\tilde{S}_{a/n}(q)F_p(q) = S_{a/n}(q)F_p(q), \tag{C.31}$$

where ϕ is the filler concentration, $\tilde{S}_{a/n}(q)$ the so-called structure factor, and $F_p(q)$ the form factor. Note that we define $S_{a/n}(q) \equiv \phi\tilde{S}_{a/n}(q)$.

C.3.1. Mass Fractals

Before we describe the form and structure factor, it is reasonable to consider the concept of fractals, which was introduced by Mandelbrot in 1977. It is best understandable by an example. We take a cube with a side length L. Its volume is then $V(L) = L^3$. Let now the side length be only $L/2$. Then the volume is consequently only $V(L/2) = (1/2)^3L^3 = (1/2)^3V(L)$. This can be generalized, if we consider a cube of side length L/λ, i.e.,

$$V(L/\lambda) = \lambda^{-d} V(L). \tag{C.32}$$

Here, d is the dimension of the object under consideration, i.e., $d = 3$ for our example cube. We thus find that Equation (C.32) leads to $V(L) \propto L^d$. This means that the volume of any given object is dependent of its spatial size L and its dimension d.

For euclidean objects, such as our example cube, the dimension is an integer. The dimension of a length is $d = 1$, that of an area is $d = 2$, and that of a volume is $d = 3$. However, some structures cannot be described by an integer dimension, such as the aggregates produced by our morphology generator. These structures need to be described by a fractal dimension and are consequently named fractals. They are generally divided into two categories: mass fractals and surface fractals. Because we do not model the surface of our particles explicitly, the category of surface fractals will not be discussed. Mass fractals are structures for which we find

$$m(r) \propto V(r) \propto r^{d_m}, \tag{C.33}$$

where $m(r)$ is the mass of the structure with size r and d_m is the so-called mass fractal dimension. It is bounded by the euclidean dimensions, i.e., $1 \leq d_m < 3$. Note that the mass fractal dimension is not sufficient to describe the structure of an object alone. A value of $d_m = 2$, for instance, must not necessarily imply that the structure is an area, it might also be a highly branched structure.

In the case of monodisperse particles with spherical symmetry mass, number of particles, $N(r)$, and volume are equal quantities, if the size of the particles, R, is taken into account. These particles aggregate into larger branched structures, whose size is described by the radius of gyration, R_g. The number of particles within these aggregates is consequently described by

$$N(r) \propto \left(\frac{r}{R}\right)^{d_m}, \tag{C.34}$$

with $r < 2R_g$. Note that R is used to set the size scale of the measurement, i.e., it is the gauge.

The power law behavior of the scattering intensity to describe surface fractal objects given in Equation (C.26) can also be applied for mass fractals. Then we find

$$I(q) \propto q^{-d_m}. \tag{C.35}$$

Note that the q value for which this relation applies is different from that of Equation (C.26). To determine the mass fractal dimension of the aggregates, we need to consider $\pi/R_g < q < \pi/R$ with the corresponding radius of gyration, R_g, and the size of the primary particles, R. In the case of larger structures, the boundaries are shifted accordingly to the size describing the larger structure. This means that, for instance, the aggregates can be considered the building

blocks of the agglomerates. Consequently, the lower boundary is limited by the radius of gyration of the agglomerates and the upper by the that of the aggregates. From Equation (C.35) we immediately find that a log-log plot of $I(q)$ vs. q yields a line with slope d_m in the respective limits of q.

C.3.2. Particle Form Factor

The form factor, $F_p(q)$, describes the scattering of single particles, i.e., the inter-particle interference. Beside the consideration of spherical particles in the last section, other formulae for different shapes, such as ellipsoids or cylinders, can be derived. The exact formula for spherical particles given in Equation (C.30) is thus a possible candidate for the particle form factor we can use. Unfortunately, the oscillations occurring due to this formula lead to several problems in the calculation of the intensity during the simulation. The approximation due to Beaucage in Equation (C.29), however, describes the scattering behavior of spherical particles equally. We consequently use this approximation in the following to describe the form factor for the particles in our work. Hence,

$$F_p(q) = \Delta\rho^2 \left(V^2 \exp[-q^2 R^2/5] + 2\pi S (q^*)^{-4} \right). \tag{C.36}$$

It should be noted that originally an even more general approximation was derived. It covers surface fractals by utilizing Equation (C.26) for the power law behavior described by Porod's law in the case of spherical particles. Because we are interested in the fractal behavior of the bigger structures given by their mass fractal dimension d_m and the surface of silica particles can be considered reasonably smooth (cf. Appendix A), a consideration of surface fractal particles was not followed in this work.

C.3.3. Structure Factor

The structure factor, $\tilde{S}_{a/n}(q)$, for N identical particles of spherical shape inside a system with volume V is defined as

$$\tilde{S}_{a/n}(q) = \frac{1}{N} \left\langle \sum_{k=1}^{N} \sum_{j=1}^{N} e^{i\vec{q}(\vec{r}_k - \vec{r}_j)} \right\rangle = 1 + \frac{1}{N} \sum_{j \neq k} \frac{\sin(q r_{kj})}{q r_{kj}}. \tag{C.37}$$

Here, $\vec{r}_k$ and $\vec{r}_j$ describe the positioning of the centers of mass of particles k and j and $r_{kj} = |\vec{r}_k - \vec{r}_j|$ is the distance between those particles. The last equation is justified, because the double sum contains N terms with $j = k$ for which the phase factor vanishes. Note that this expression is only valid for particles not varying their distances over time. Otherwise a second average over time must be formed to cover all possible arrangements.

Instead of evaluating the sum in Equation (C.37), it is convenient to introduce the pair correlation function, $g_2(r)$, also know as the radial distribution function. It describes how the density varies as a function of distance from a reference particle. Figure C.4 gives a graphical representation. The calculation of $g_2(r)$ is usually performed by binning the distances between

all particle pairs into a histogram and normalize it by the volume of the spherical shell times the number density of the system, ρ. Hence,

$$g_2(r) = \frac{\rho(i)}{\rho} = \frac{n(\mathrm{d}ri, \mathrm{d}r)}{4\pi r^2 \mathrm{d}r\rho}. \tag{C.38}$$

Here, $n(\mathrm{d}ri, \mathrm{d}r)$ is a histogram for the distances. The bin width $\mathrm{d}r$ is chosen appropriately for the system under consideration. The parameter i runs over all particles. Because of the symmetry of the distances, it is convenient to calculate only half of them and then to multiply the result with a factor of two. For the systems we investigate, $\rho(i)$ for large i (with $r = \mathrm{d}ri$) becomes ρ and thus $g_2(r) \to 1$ for large r. We additionally find that for very small values of r the pair correlation function, $g_2(r)$, is zero. This is reasoned by the fact that a minimum distance is found in every system. Below that distance no particles are found. Subsequently, the corresponding bin is empty. For instance, hard spheres of size D have a minimum distance between them due to their size, if they are impenetrable. The first non-empty bin is thus found at $r = D$.

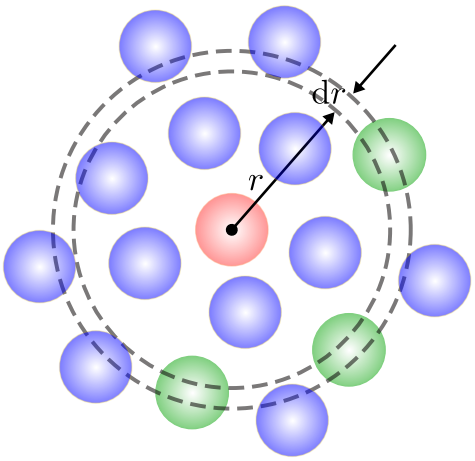

Figure C.4.: Graphical representation of the radial distribution function, $g_2(r)$. It describes the probability of finding a particle (green) within a distance r and $r + \mathrm{d}r$ away from another central particle (red).

Instead of an exact derivation, which can be found in several literature sources (e.g. [23]), we want to motivate the correlation between the structure factor and the pair correlation function. On average, each spherical particle inside the system has statistically the same isotropic surrounding. Thus, it is sufficient to consider only one central particle and to determine the probability that another particle is found in the volume element $\mathrm{d}V$ at a distance r apart. The mean probability is simply $(D)\mathrm{d}V$, where $D = N/V$ is the particle number density. Any deviation from this mean value may be accounted for by a factor $g_2(r)$, which is the pair correlation function defined in Equation (C.38). If we assume that the pair correlation function is unity everywhere, then the interference terms in Equation (C.37) would exactly cancel. Thus, only the difference $(g_2(r) - 1)$ is relevant. We then find for the structure factor

$$S_{a/n}(q) \equiv \phi \tilde{S}_{a/n}(q) = \phi \left[1 + 4\pi D \int_0^\infty r^2 \frac{\sin(qr)}{qr} (g_2(r) - 1) \mathrm{d}r \right]. \tag{C.39}$$

Note that generally $\phi = D$. In our simulation method, however, we may find $\phi \neq D$, because of the cutting procedure described in chapter 2. The factor ϕ is then the overall particle number density of the complete system and D is the particle number density for the cut out box.

The structure factor can also be considered as the form factor of an ensemble of fractal objects distributed at a larger scale in space. This means that the aggregates formed due to primary particles are again form factors of even larger scales, such as agglomerates. Their form factors, however, need to be calculated by means of the here stated structure factor, i.e.,

$$F_{agg}(q) = S_{a/n} F_p(q). \tag{C.40}$$

This procedure may be repeated arbitrarily. For instance, the agglomerates are then building blocks of even larger structures. But since we are interested in the fractal behavior of the aggregates, this is approach is not pursued in this work. Nevertheless, the consideration of the fractal behavior of the large scale network might alternatively be described by using this concept. It is, however, difficult to obtain the coordinates of the aggregates in order to evaluate their radial distribution function.

Note that the structure factor can be calculated directly from the simulated data. This is not possible for experiments, because only the scattered intensity is measured. Thus, the structure factor is generally modeled differently. In the case of fractals, a cut-off function, usually $\exp(-r/\zeta)$, is introduced, which models the behavior of the radial distribution function at large distances. Together with several other assumptions, the following expression for the structure factor can be obtained (a complete derivation is found in [16])

$$S(q) = 1 + \frac{d_m}{R^{d_m}} \int_0^\infty r^{d_m - 1} e^{-r/\zeta} \frac{\sin(qr)}{qr} \mathrm{d}r \tag{C.41}$$

$$= 1 + \frac{\Gamma(d_m + 1)}{(qR)^{d_m}} \left(1 + \frac{1}{(q\zeta)^2} \right)^{\frac{1-d_m}{2}} \frac{\sin\left[(d_m - 1)\arctan(q\zeta)\right]}{d_m - 1}. \tag{C.42}$$

Here, R is the size of the primary particles, d_m is the mass fractal dimension, and ζ is the cut-off distance to describe the behavior of the pair correlation function at large distances. In the case of aggregates this is equal to their radius of gyration. Several other cut-off functions might be used. This expression is only stated for the sake of completeness. As stated in the beginning of the paragraph, determining the radial distribution function from simulated data is straightforward and thus no alternative expression is needed.

C.4. References

[1] Bushell, G. C. et al., On techniques for the measurement of the mass fractal dimension of aggregates. *Adv. Colloid Interface Sci.* **2002**, 95 (1), 1–50, DOI: 10.1016/S0001-8686(00)00078-6.

[2] Teraoka, I., Polymer Solutions. Volume 3, New York: John Wiley & Sons, Inc., **2002**, DOI: 10.1002/0471224510.

[3] Mihara, S., Reactive processing of silica-reinforced tire rubber: new insight into the time- and temperature-dependence of silica rubber interaction. Dissertation, University of Twente, **2009**, DOI: 10.3990/1.9789036528399.

[4] Baeza, G. P. et al., Multiscale filler structure in simplified industrial nanocomposite silica/SBR systems studied by SAXS and TEM. *Macromolecules* **2013**, 46 (1), 317–329, DOI: 10.1021/ma302248p.

[5] Odo, E. A. et al., SAXS Study of Silicon Nanocomposites. *Int. J. Compos. Mater.* **2015**, 5 (3), 65–70, DOI: 10.5923/j.cmaterials.20150503.03.

[6] Schaefer, D. W., Justice, R. S., How nano are nanocomposites?. *Macromolecules* **2007**, 40 (24), 8501–8517, DOI: 10.1021/ma070356w.

[7] Koga, T. et al., New insight into hierarchical structures of carbon black dispersed in polymer matrices: A combined small-angle scattering study. *Macromolecules* **2008**, 41 (2), 453–464, DOI: 10.1021/ma0718671.

[8] Takenaka, M., Analysis of structures of rubber-filler systems with combined scattering methods. *Polym. J.* **2013**, 45 (1), 10–19, DOI: 10.1038/pj.2012.187.

[9] Guinier, A., Fournet, G., Small-angle scattering of X-rays. Edited by Mayer, M. G., Michigan: John Wiley & Sons, Inc., **1955**, DOI: https://doi.org/10.1002/pol.1956.120199326.

[10] Glatter, O., Kratky, O., Small Angle X-ray Scattering. Edited by Glatter, O., Kratky, O., New York: Academic Press, **1982**, DOI: 10.1007/978-3-642-03307-0.

[11] Hiemenz, P. C., Rajagopalan, R., Principles of Colloid and Surface Chemistry, Third Edition, Revised and Expanded. 3rd, New York: Marcel Dekker, **1997**, ISBN: 0-8247-9397-8.

[12] Pedersen, J. S., Modelling of Small-Angle Scattering Date from Colloids and Polymer Systems. *Neutrons, X-rays Light Scatt. Methods Appl. to Soft Condens. Matter*, edited by Lindner, P., Zemb, T., Aarhus: Elsevier Ltd, **2002**, chapter 16, 391–420, ISBN: 978-0-444-51122-5.

[13] Bouty, A. et al., Nanofiller structure and reinforcement in model silica/rubber composites: A quantitative correlation driven by interfacial agents. *Macromolecules* **2014**, 47 (15), 5365–5378, DOI: 10.1021/ma500582p.

[14] Besselink, R. et al., Not just fractal surfaces, but surface fractal aggregates: Derivation of the expression for the structure factor and its applications. *J. Chem. Phys.* **2016**, 145 (21), DOI: 10.1063/1.4960953.

[15] Nusser, K., Modellierung von Füllstoffstrukturen und die Berechnung ihrer Kleinwinkelstreuung. Diplomarbeit, Universität Regensburg, **2006**.

[16] Schneider, G. J., Analyse der Struktur von aktiven Füllstoffen mittels Streumethoden. **2006**, URL: http://epub.uni-regensburg.de/10438/ (visited on 08/30/2019).

[17] Beaucage, G., Approximations Leading to a Unified Exponential/Power-Law Approach to Small-Angle Scattering. *J. Appl. Crystallogr.* **1995**, 28 (6), 717–728, DOI: 10.1107/S0021889895005292.

[18] Porod, G., Die Röntgenkleinwinkelstreuung von dichtgepackten kolloiden Systemen - I. Teil. *Kolloid-Zeitschrift* **1951**, 124 (2), 83–114, DOI: 10.1007/BF01512792.

[19] Mandelbrot, B. B., The fractal geometry of nature. Edited by Freeman, W., Third, San Francisco: Henry Holt and Company, **1982**, ISBN: 9780716711865.

[20] Bale, H. D., Schmidt, P. W., Small-Angle X-Ray-Scattering Investigation of Submicroscopic Porosity with Fractal Properties. *Phys. Rev. Lett.* **1984**, 53 (6), 596–599, DOI: 10.1103/PhysRevLett.53.596.

[21] Teixeira, J., Small-angle scattering by fractal systems. *J. Appl. Crystallogr.* **1988**, 21 (6), 781–785, DOI: 10.1107/S0021889888000263.

[22] Oberdisse, J., Pyckhout-Hintzen, W., Straube, E., Structure Determination of Polymer Nanocomposites by Small Angle Scattering. **2009**, URL: https://hal.archives-ouvertes.fr/hal-00542764 (visited on 08/30/2019).

[23] Hentschke, R. et al., Molekulares Modellieren mit Kraftfeldern: Einführung in die Theorie und Praxis der Computersimulation molekularer Systeme. Edited by Hentschke, R. et al., Mainz, **2004**.

D. Simulation Methodology

In this part, we consider the simulation methodology used in this work. On the one hand we have the morphology generator. It produces the systems we want to analyze by means of the screening methods introduced in chapter 2. It consists in its core of a Metropolis algorithm, which is a Markov chain Monte Carlo (MC) method to obtain a sequence of random samples from a probability distribution. Additionally, other sub-routines are implemented. The filler clusters need to be identified and information about them, such as their mass and size, needs to be obtained. The wetted surface fractions are drawn from the interfacial lengths, which also need to be calculated. On the other hand, we have the simulation of the scattering intensities. Therein, technical aspects such as the box cutting procedure as well as numerical aspects, such as calculating the radial distribution function and calculating the structure factor via an integral (cf. Appendix C), are used. However, these aspects are already elucidated within the introduction of those methods in chapter 2. Hence, here we focus on the morphology generator.

Both programs are written in the language C. Due to its low-level capabilities, it is well suited for performing long time MC simulations involving billions of operations in a reasonable amount of time.

We start with the MC simulations and random numbers, which play a prominent role in our programs. Thereafter, we explain the concepts of periodic boundary conditions and minimum image convention, which are used within the morphology generator and the screening methods. Subsequently, the morphology generator is discussed and the corresponding Metropolis criterion is derived.

D.1. Monte Carlo Simulations

MC methods are a class of computational algorithms to obtain results by utilizing a sequence of random numbers, which is generated during the simulation. Different from other simulation methods, such as molecular dynamics (MD), the 'time dependence' of the particles in focus does not proceed a predefined fashion like, for instance, Newton's equation of motion. The concept of randomness relies on stochastic aspects, most prominently the law of large numbers. Roughly speaking, it states that performing the same experiment a large number of times results in the average of the results obtained from each single experiment. This average is then close to the expected value. A larger number of trials reduces the difference between average and expected value. A simple example is given by rolling a fair, six-sided dice. The expected value is 3.5. Rolling the dice a large number of times, we obtain an average close to the expected value. Transcribed to our simulation of flocculation processes in elastomers, we expect that systems with the same set of simulation parameters, i.e., surface free energies, temperature, and filler content behave similarly after the same 'flocculation time', i.e., number of MC steps. Same systems are only produced, if the starting configurations and the sequence of random numbers are identical. This may be desired for debugging or control purposes, but generally it is avoided by using a robust random number generator.

Although based on randomness, a large number of problems can be solved by this method. We already encountered one possible application: Percolation (cf. subsection 2.5.3). Particles are placed randomly and one by one on a certain lattice. At some point, a percolating cluster appears, i.e., it reaches from one boundary of a system to the opposite one. The determination at which concentration this cluster appears – the percolation threshold – is of particular interest for physical problems such as conductivity of random mixtures or flow through porous rocks. In the case of filled elastomers, percolating clusters are identified as filler networks. They are crucial to the mechanical properties of the final product as described in Appendix A. The percolation threshold is an example of the so-called simple sampling MC methods. Others falling into this category include numerical integration[1], random walks, and creation of a discrete distribution of numbers. In the case of our morphology generator, we draw information out of a probability distribution, i.e., Boltzmann distribution. This class of problems is generally – in statistical mechanics – solved by means of the Metropolis algorithm. It falls in the category of so-called importance sampling MC. To familiarize the reader with both categories, examples are discussed in the following. For a more precise mathematical consideration the reader is encouraged to consider the standard literature (e.g. [1, 2]). Beforehand, however, we discuss random numbers and how we obtain them for all of our programs.

D.1.1. Random Numbers

All MC methods rely on random numbers. Additionally, other processes, such as the initialization of the system in our case, are performed randomly. In order to guarantee that multiple processes with the same set of parameters do not yield the exact same results, a sufficient random number generator – RNG in the following – is mandatory. It must generate a sequence of numbers that cannot be reasonably predicted better than by a random chance. RNGs are generally divided into two categories. They are either true (hardware) or pseudo. True RNGs (TRNGs) utilize physical processes to generate random numbers. Mostly statistically random noise signals are used, such as thermal noise. Pseudo RNGs (PRNGs) generate their numbers according to an algorithm. The resulting sequence of random numbers depends on an initial value, called *seed*. The same seed always leads to the same sequence.

Most programming languages contain libraries for random number generation. Most of those RNGs are PRNGs, but for some languages the determination of true random numbers is possible (for instance in C++). In C, the language used for all programs in this work, i.e., the morphology generator and the scattering simulation, naturally no TRNG exists. Consequently, a robust and reliable PRNG must be chosen. The standard RNG in C is the function $rand()$, which is initialized via a random seed by using the function $srand()$. Mostly, $srand()$ is called with the current time via $srand(time(0))$. Every time a program is started at a different time, the seed is different and thus a different sequence of random numbers is generated by $rand()$. In turn, it is possible to generate the same sequence, if the time of the first program run is known. However, this function has a couple of drawbacks for our use. The range of random numbers is limited by the variable $RAND\_MAX$, which is determined by the largest integer on the operating system. Consequently, the portability of the programs is greatly reduced. It is, however, guaranteed to be at least 32767. This is a fairly small

[1] Can also be solved by means of importance sampling MC.

number as we can immediately rationalize by the fact that the systems we consider in this work mostly contain more than 10^6 particles. Each of those particles is in need of several random numbers, as we will see later on. Additionally, the standard RNGs are almost always linear congruential generators, i.e., they generate integers I_j each between 0 and $m-1$ by a recurrence relation

$$I_{j+1} = aI_j + c \pmod{m}. \tag{D.1}$$

Here, m is the modulus and a and c are positive integers termed 'multiplier' and 'increment', respectively. As we immediately see from Equation (D.1), the random numbers will repeat themselves after a period not longer than m. Furthermore, successive calls of the function are not free of sequential correlation and the low-order bits are much less random than the higher-order bits.

To circumvent all these issues, we instead use the PNRG *ran*2 from [3]. It is implemented as a standalone header file, which is included in the beginning of each program to ensure portability on every operating system. It guarantees a long period of more than 10^{18} random numbers, uniformly distributed between 0.0 and 1.0, which is sufficient for our needs. Additionally, it breaks up the sequential correlation by a shuffling procedure and the randomness of the low- and high-order bits is no issue. According to the named source, it has passed all statistical tests for random numbers to the best of the authors knowledge.

To guarantee that multiple runs of the same program started at the same time do not produce the same sequence of random numbers, a different seed than $time(0)$ is chosen. We use the number of CPU cycles since the last reset of the computer given by

```
1 unsigned long long rdtsc() {
2     unsigned int lo, hi;
3     __asm__ __volatile__ ("rdtsc" : "=a" (lo), "=d" (hi));
4
5     return ((unsigned long)hi << 32) | lo;
6 }
```

Code D.1: Time stamp counter of the number of cycles since last reset.

The returned *unsigned long long* in Code D.1 is then truncated to a *long* and negated to fit the needs of the seed for *ran*2. Code D.2 shows the procedure.

```
1 unsigned long long tsc = rdtsc();
2 long seed = (long)(tsc & 0xFFFFFFFF);
3 idum = -seed;
4 float random_number = ran2(&idum);
```

Code D.2: Setting the seed to generate a random number using the function *ran*2 from [3].

The random numbers produced this way are used throughout all programs. To tailor them to the corresponding needs, such as generating a random number between 0 and $L-1$, where L is the linear dimension of the lattice, *random_number* is simply multiplied by L and then a typecast into an *int* variable is performed.

D.1.2. Introductory Example – Simple Sampling Monte Carlo

Let us consider the following, deterministic problem of integrating a function in – for the sake of simplicity – one dimension, i.e.,

$$y = \int_a^b h(x)\mathrm{d}x. \tag{D.2}$$

A possible MC solution to this problem is the so-called 'hit-or-miss', or acceptance-rejection, method. We produce N random numbers from a uniform distribution and place them inside a box. This box is chosen in such a way that it includes the function $h(x)$ in the given interval from a to b completely. This means that for the height of the box, y_0, we find $y_0 > h(x)$ throughout. Then we simply count the number of random numbers which fall below $h(x)$ for each value of x which we term N_0. An estimate for the integral in Equation (D.2) is then given by the fraction of points which fall below the curve times the area of the box, i.e.,

$$y_{est} = N_0/N \left[y_0(b-a)\right]. \tag{D.3}$$

As a result from the law of large numbers, this estimate converges to the correct answer for $N \to \infty$.

For a more practical example, let us consider the following problem: We want to find an estimate for π using this simple method. This can be achieved by choosing N random numbers in the xy-plane with $0 < x < 1$ and $0 < y < 1$. Then, we calculate the distance from the origin for each point and count only those which are less than a distance 1 from the origin. Because the restriction of x and y covers only one quarter of a circle, the estimate for π is then given by $\pi \approx 4N_0/N$. Figure D.1 depicts the result for this method with $N = 10^5$ random numbers for each coordinate, x and y. The blue dots fall into the region of acceptance, i.e., their distance is less than unity. The red dots are rejected, i.e., their distance is greater than unity. The approximate value obtained this way is $\pi \approx 3.14164$, which is pretty close to the exact result. It is worth to mention that for smaller values of N the value of π is not approximated very accurately. Thus, we always have to keep in mind that a large number of random numbers need to be generated and evaluated to obtain reliable results.

D.1.3. Importance Sampling – The Metropolis Algorithm

The evaluation of integrals is a very prominent example for the usage of MC. It originates from the consideration of ensemble averages of observables. Consider a system containing N particles inside a volume V at a given temperature T, i.e., the canonical ensemble. Each particle i ($i = 1, \ldots, N$) is given a set of parameters, e.g., its momentum or position, denoted

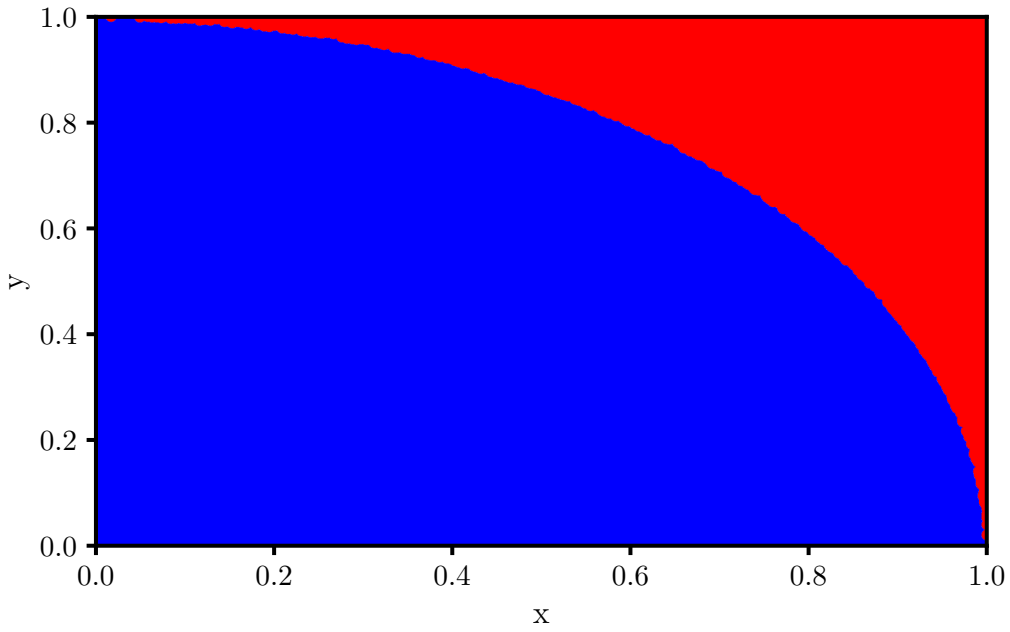

Figure D.1.: Simple MC integration to estimate π. The blue dots are the accepted coordinates and the red dots those which are rejected. $N = 10^5$ random numbers have been drawn for each coordinate x and y. The estimated value is $\pi = 3.14164$.

as π_i. The set $\pi_1, \ldots, \pi_N$ is called a configuration or phase space point X. Then the average for an observable $A(X)$ is defined by

$$\langle A \rangle = \frac{\int A(X) e^{-\beta H(X)} \, \mathrm{d}X}{\int e^{-\beta H(X)} \, \mathrm{d}X}. \tag{D.4}$$

Here, $\beta = 1/k_B T$ is the Boltzmann factor and $H(X)$ is the Hamiltonian. According to the ergodic hypothesis, Equation (D.4) is equal to the time average of A. The chosen average thus depends on the simulation method. While Equation (D.4) is used for MC, the consideration of time averages is used in molecular dynamics. The solution of the integrals in Equation (D.4) is not feasible, because, for instance, for a simple one atomic gas they are already $6N$-dimensional. We must therefore think of another method to solve them, which is elucidated in the following by utilizing the simple example of one dimensional integration of the last section.

Instead of solving Equation (D.2), we expand it with an arbitrary function $f(x)$, i.e.,

$$\int_a^b \left(\frac{h(x)}{f(x)} \right) f(x) \mathrm{d}x. \tag{D.5}$$

If the function $f(x)$ fulfills $\int_a^b f(x)\mathrm{d}x = 1$, i.e., it is a probability density function, then Equation (D.5) can be considered as the mean of the function $h(x)/f(x)$. Note that $f(x) \neq 0$ for all x between a and b needs to be fulfilled additionally, of course. Hence,

$$\int_a^b \left(\frac{h(x)}{f(x)}\right) f(x)\mathrm{d}x = \left\langle \frac{h(x)}{f(x)} \right\rangle . \tag{D.6}$$

Instead of solving the integral in Equation (D.2) directly, it can thus be approximated by creating N random numbers x_i distributed according to the function $f(x)$ and then calculating the mean of $h(x_i)/f(x_i)$ over those numbers, i.e.,

$$\int_a^b h(x)\mathrm{d}x \approx \frac{1}{N}\sum_{i=1}^{N}\left(\frac{h(x_i)}{f(x_i)}\right). \tag{D.7}$$

Although the choice of $f(x)$ is arbitrary, choosing it in such a way that the random numbers are created in the region where $h(x)$ contributes significantly is proficient. This procedure is called importance sampling.

With this knowledge, let us now return to the calculation of the average in Equation (D.4). We then find

$$\langle A \rangle = \frac{\sum_{i=1}^{N} A(X_j)P^{-1}(X_j)e^{-\beta H(X_j)}}{\sum_{i=1}^{N} P^{-1}(X_j)e^{-\beta H(X_j)}}, \tag{D.8}$$

where the N points X_j inside the phase space are chosen randomly according to the distribution function $P(X)$. If we now choose

$$P(X_j) = P_{eq}(X_j) \propto e^{-\beta H(X_j)}, \tag{D.9}$$

then we find for Equation (D.8)

$$\langle A \rangle = \frac{1}{N}\sum_{i=1}^{N} A(X_j), \tag{D.10}$$

i.e., the arithmetic mean. The function $P_{eq}(X_j)$ is not known. According to Metropolis, a random walk of points X_j in the phase space is performed with the property $P(X_j) \to P_{eq}(X_j)$ for $N \to \infty$. This means that for a large number of configurations the stationary state is reached. The distribution of those points is realized by a Markov chain. This means that the state X_j is only depending on its predecessor, which we term $X_{j'}$. The probability of a change for $X_j \to X_{j'}$ is denoted as $W(X_j \to X_{j'})$, which is also known as the transition probability. To find the stationary state as quickly as possible the following property is demanded

$$P_{eq}(X_j)W(X_j \to X_{j'}) = P_{eq}(X_{j'})W(X_{j'} \to X_j). \tag{D.11}$$

It is known as detailed balance. Together with Equation (D.9) then follows

$$\frac{W(X_j \to X_{j'})}{W(X_{j'} \to X_j)} = \frac{P_{eq}(X_{j'})}{P_{eq}(X_j)} = e^{-\beta \Delta H}, \tag{D.12}$$

where $\Delta H = H(X_{j'}) - H(X_j)$. The most frequently used implementation for the transition probabilty was also proposed by Metropolis itself [4]

$$W(X_j \to X_{j'}) = \begin{cases} \exp\left[-\beta \Delta H\right] & \text{if} \quad \Delta H > 0, \\ 1 & \text{if} \quad \Delta H \leq 0. \end{cases} . \tag{D.13}$$

This means that if the new state $X_{j'}$ is energetically more favorable over the old state X_j it is definitely accepted. If, however, the new state is energetically less favorable, then it is only accepted with some probability $\exp\left[-\beta \Delta H\right]$. For very large values of ΔH, the acceptance of the new state goes to zero for a constant temperature T. From this transition probability we can conclude an algorithm, i.e., the Metropolis algorithm.

Metropolis algorithm:

1. set arithmetic mean $s := 0$ and choose temperature T.
2. pick random starting point $X_{current}$ from the phase space.
3. repeat N times:
   (I) pick an additional random point X_{random} from the phase space.
   (II) calculate energy change

$$\Delta H := H(X_{current}) - H(X_{random}).$$

   (III) **if** $\Delta H < 0$:

$$X_{current} := X_{random}.$$

   else:

   (i) create random number $\xi \in [0, 1)$.
   (ii) **if** $\xi < \exp\left[-\beta \Delta H\right]$:

$$X_{current} := X_{random}.$$

   (IV) calculate $A(X_{current})$ and add to sum s.
4. calculate average

$$\langle A \rangle := \tfrac{s}{N}.$$

Code D.3: Pseudo-code for the Metropolis criterion utilizing the transition probability given in Equation (D.13).

D.2. Periodic Boundary Conditions and Minimum Image Convention

The simulation of molecular systems have, compared to experiments, a fundamental drawback: their limited size. This applies to MC as well as to MD simulations. Generally, experiments are conducted with samples large enough to yield the desired results. For instance, when measuring the surface tension of a liquid, a sufficient container of the liquid is used. Its complete simulation is not feasible due to the large number of particles[2] and the finite power of the computers in use. We are thus always modeling a certain region of the container and impose a limited simulation volume, which is magnitudes smaller than that of the experiment. This results in unwanted behavior due to the hard walls of the simulation box. They may be circumvented by introducing periodic boundary conditions as depicted for a two-dimensional case in Figure D.2. The idea behind periodic boundary conditions is to artificially create images of the simulation volume in its direct neighborhood. It is shown as the central, bold boarded square. The virtual images are denoted with A to H in the respective figure. In each of the virtual systems the same processes are performed. This means that if a particle, like the unfilled dot, leaves the simulation volume to the top in direction of B, it re-enters the same volume from the other side, i.e., from the virtual image G in this case. Note that these conditions can be applied either in one direction only or, as it is the case for our simulations, in all directions. The periodic boundary conditions are used within the Metropolis algorithm of the morphology generator, which is explained in the next section.

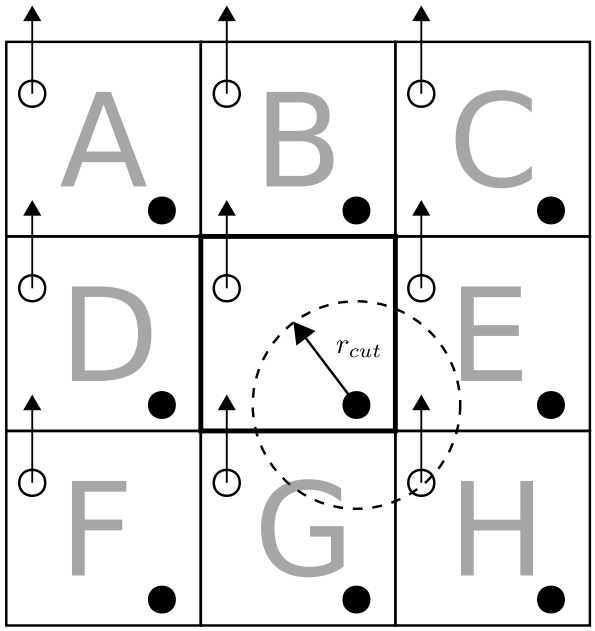

Figure D.2.: Depiction of a two-dimensional simulation volume (bold bordered) embedded inside its virtual images A to H, due to the periodic boundary conditions. Inside the simulation volume are two particles, i.e., filled and unfilled circles. Around the filled particle, the cut-off radius r_{cut} is drawn. It is used for the minimum image convention. This picture is made in style of [5].

[2] in the order of 10^{23} particles

Under periodic boundary conditions, the calculation of distances is altered. Distance calculations appear when small angle scattering is performed[3] or when the radius of gyration of the clusters is calculated, i.e., when the size of the filler networks is determined. The principle calculation of small angle scattering data via simulation is described in subsection 2.3.3 and in Appendix C. The calculation of the squared radius of gyration is given in Equation (2.14). The correct calculation of distances in both cases is achieved by using the so-called minimum image convention. It ensures that the particle only interacts with neighboring particles within a minimum distance, whether it is with the 'real' particle or just with its virtual image due to the periodic boundary conditions. This is illustrated with the filled circle with the radius r_{cut} in Figure D.2. The correct value of r_{cut} depends on the simulation method and the physical description of the system. Here, we use $r_{cut} = L/2$. This is also the largest feasible value, because otherwise the particles could interact with themselves due to their periodic images. If we now wanted to calculate, for instance, the minimum distance between the filled and the unfilled circle, i.e., $d_{\bullet\circ}^{min}$, then it is not done within the original simulation volume. Instead, the distance to the virtual image of the particle in H is calculated. Mathematically, this is achieved by calculating the minimum distances in x and y direction via

$$\begin{aligned} x_{\bullet\circ}^{min} &= x_{\bullet\circ} - L \cdot \text{round}\left(x_{\bullet\circ}/L\right), \\ y_{\bullet\circ}^{min} &= y_{\bullet\circ} - L \cdot \text{round}\left(y_{\bullet\circ}/L\right). \end{aligned} \tag{D.14}$$

Here, $x_{\bullet\circ}$ and $y_{\bullet\circ}$ are the distances along the indicated axes between the filled and unfilled circle inside the same simulation box and L is the linear dimension of the box. Subsequently, the minimum distance is easily calculated via

$$d_{\bullet\circ}^{min} = \sqrt{(x_{\bullet\circ}^{min})^2 + (y_{\bullet\circ}^{min})^2}. \tag{D.15}$$

A generalization for three dimensions is achieved straightforwardly.

D.3. The Morphology Generator

This section is dedicated to the core of our simulation methodology: the morphology generator. Briefly described, it consists of particles, which we model as cubic cells on an attendant cubic lattice. The number of particle types as well as their amounts is variable and changes throughout this work. An initial description is given in the beginning of chapter 2. The changes due to the introduction of other particle types is given in the beginning of the subsequent chapters chapter 3 and chapter 4.

The core of the morphology generator is the Metropolis algorithm and thus the Metropolis criterion. It depends on the surface free energies, which are assigned to each side of each cubic particle type. By employing different MC moves, elucidated in the according chapters, we minimize the free enthalpy, G, of the system. The random path we take through the phase space produces different morphologies, which we analyze by means of our screening methods

[3] To be more precise: It appears in the calculation of the pair correlation function, $g_2(r)$.

(cf. chapter 2). The length of the path is measured in MC steps. Each step may consist of up to two moves, depending on the number of particles types and their individual properties.

The goal of this section is to derive the Metropolis criterion and subsequently the Metropolis algorithm. Thereafter, we show by considering an example that the free enthalpy is minimized by it. Although the core is the Metropolis algorithm, several other functions are implemented into the morphology generator. It is thus reasonable to consider a simplified flow chart of the complete program and to discuss the individual functions – at least in their basic concepts.

D.3.1. Derivation of the Metropolis Criterion

The characteristic state function of the isothermal–isobaric ensemble is the free enthalpy, G. At equilibrium it can be calculated via

$$G = \frac{\sum_i G_i e^{-\beta G_i}}{\sum_i e^{-\beta G_i}}. \tag{D.16}$$

Here, the quantities G_i denote the free enthalpies at fixed configurations, i. This simply follows from $\beta G = -\ln Q_{NPT}$ together with $Q_{NPT} = \sum_i Q_{i,NPT} = \sum_i e^{-\beta G_i}$ in conjunction with $G = N\partial G/\partial N$ and $G_i = N\partial G_i/\partial N$ (extensivity).

In Appendix B, we derived that the surface free energy, γ, is the change of the free enthalpy, G, with respect to the surface area, A, at constant temperature, T, pressure, P, and particle number, N_i

$$\gamma = \left.\frac{\partial G}{\partial A}\right|_{N_i,P,T}. \tag{D.17}$$

For our model it is, however, necessary to consider the interfacial tension, because different particles are brought into contact. It is then reasonable to count the type of face-to-face pairings, j, and to fix the cells of a certain type, k. In addition, we thus find at equilibrium

$$dG|_{T,P,N_k} = \gamma_j dA_j, \tag{D.18}$$

where N_k is number of cells of type k. γ_j denotes the interface tension of a face-to-face pairing of type j and $A_j = n_j\, a$ denotes the attendant total area of j-type interfaces in the system. a is the effective contact area per face, which we assume to be the same for all j. Note that the summation convention applies here. The interface tension between two surfaces α and β is given due to Owens and Wendt (cf. Table B.1), i.e.,

$$\gamma_j \equiv \gamma_{\alpha\beta} = \gamma_\alpha + \gamma_\beta - 2\left(\sqrt{\gamma_\alpha^d \gamma_\beta^d} + \sqrt{\gamma_\alpha^p \gamma_\beta^p}\right). \tag{D.19}$$

Along the random path in phase space the free enthalpy is consequently minimized according to the Metropolis algorithm. The change in the free enthalpy is, however, equivalent to the change in the interfacial tensions, as can be seen from Equation (D.18). This change is given by

the difference in work of adhesion, $\Delta W(\gamma)$, for which we consequently find $\Delta W(\gamma) = -\gamma_j \Delta A_j$ and thus for the transition probability

$$\exp\left[\beta \Delta W(\gamma)\right] = \exp\left[-\gamma_j \Delta A_j\right] = \exp\left[-\beta \gamma_j a \Delta n_j\right]. \tag{D.20}$$

```
1  1. pick random cube.
2  2. rotate by multiple of π/2 in random plane (e.g. x−y plane):
3    (I) calculate change in work of adhesion
4
5          ΔW(γ) := ΔW_new(γ) − ΔW_old(γ).
6
7    (II) create random number ξ ∈ [0, 1).
8
9    (III) accept if:
10
11         exp[βΔW(γ)] ≥ ξ.
12
13 3. pick random diagonal neighbor pair.
14 4. exchange cubes:
15   (I) calculate change in work of adhesion
16
17         ΔW(γ) := ΔW_new(γ) − ΔW_old(γ).
18
19   (II) create random number ξ ∈ [0, 1).
20
21   (III) accept if:
22
23         exp[βΔW(γ)] ≥ ξ.
```

Code D.4: Pseudo-code for the Metropolis algorithm used within the morphology generator. Note that the calculation of the free enthalpy is not explicitly stated. Note also that this code can change depending on the type of cubic cells.

With this criterion, the generated system configurations satisfy Equation (D.16) on average. The pseudo-code for the Metropolis algorithm for the morphology generator is given in Code D.4. Note that this algorithm may change depending on the cubic cells in use. Which MC moves are used is always stated in the beginning of each chapter. Away from equilibrium, this algorithm drives the system towards the lowest possible free enthalpy, G, and the number of MC moves should be a rough measure of time. This may be justified by the local nature of the moves in conjunction with the assumption of a local equilibrium. The latter is commonly invoked during the derivation of transport equations in the framework of non-equilibrium thermodynamics [6]. Nevertheless, it is certainly true that the basic rate constants for the underlying process are input to the MC [2]. Fixing the attendant unit of time of course is a separate problem.

In this work, we circumvent this by comparing the size of the aggregates at different stages of the MC with corresponding small angle scattering results from experimental systems. Furthermore, the mass fractal dimension of the aggregates is taken into account. On a larger

spatial scale, the mass fractal dimension of the filler network may be used for comparison between simulated morphologies, depending on the number of MC steps per cube, and experimental morphologies. It is also important to note that the flocculation starts far from equilibrium, which is never quite reached in our simulations as well as in the experiments. The results we discuss throughout this work are extracted from the simulation when changes are very slow in sense of MC steps. This in particular makes our results, addressing the general dependence of morphology and surface free energy, comparable to attendant experimental studies, which also are conducted on transient, slowly varying material structures. Throughout this work, we investigate the general dependence of morphology and surface free energy. This addresses questions like whether the filler is preferentially dispersed within a certain polymer, accumulates at its interface or produces larger structures inside of it. The general answer to these questions, which the algorithm provides after a large number of MC steps when the 'dynamics' of the system have become very slow, is not expected to depend much on the dynamics at a later stage. This is exemplarily investigated with the long term evolution in chapter 3. Therein, it is shown that the aforementioned preferences of the filler particles do not change for longer simulation times. It is, however, shown that the best comparison with experimental values is not always achieved after a large number of MC steps. This means that, for instance, aggregates are likely to keep growing as the simulation continues or that the interfacial lengths of a specific type increase continuously.

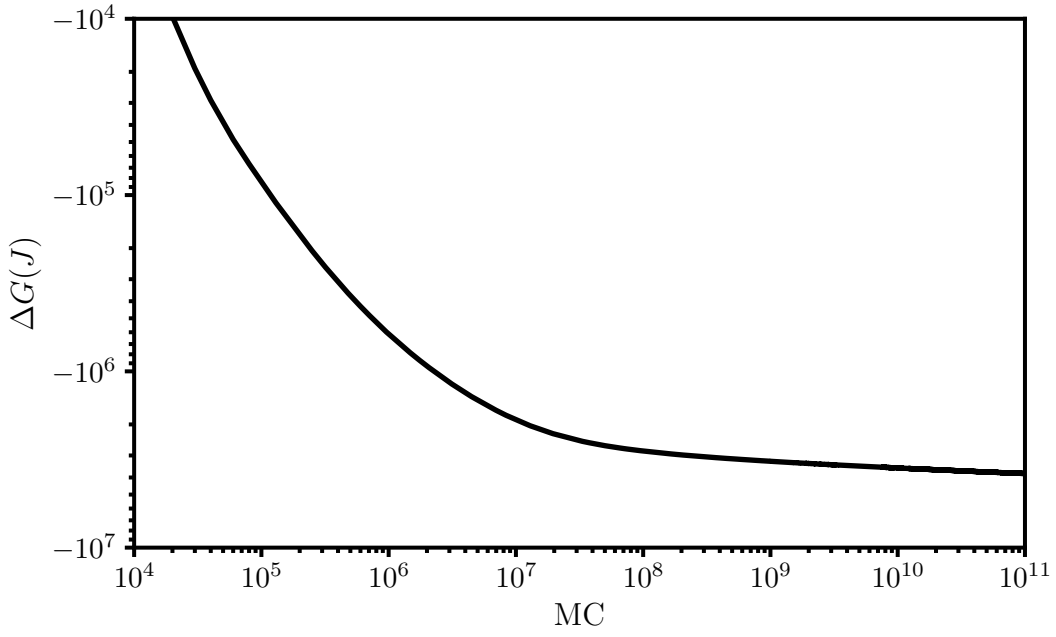

Figure D.3.: Minimization of the free enthalpy by employing the Metropolis criterion of the morphology generator. Although 10^{11} steps are performed, the difference in the free enthalpy from the initial configuration still changes. This indicates that the equilibrium is still not reached.

To show that by employing this Metropolis criterion the free enthalpy of the system is really minimized, we consider Figure D.3. It shows a log-log plot of the difference of the free enthalpy from the initial configuration ΔG vs. the number of MC steps in the case of our morphology generator. The underlying system is a 50/50-NR/SBR, i.e., natural and styrene-butadiene rubber, blend with 20% filler content, $\gamma_f^d = 20\,m\mathrm{J/m^2}$, $\gamma_f^p = 10\,m\mathrm{J/m^2}$, and $T = 413\mathrm{K}$. Note that for this system the initial free enthalpy has roughly a value of $G_{init} = -1.696 \cdot 10^8$ J. The long term structural evolution is considered to show that even after the longest considered simulation time an equilibrium is still not reached. It can, however, be seen that after an initial steep decrease the system continues to minimize the free enthalpy with a considerably lower rate. The discussion of the number of MC steps in chapter 3 showed that good agreement to experimental values is obtained after this region. At 10^{10} steps, systems started to show behavior not seen experimentally. Consequently, systems should be evaluated after 10^8 to 10^{10} MC steps.

D.3.2. Functionality

Figure D.4 shows the flow chart of the morphology generator on the left hand side together with the subsequent evaluation of the morphologies by applying the screening methods shown on the right hand side. In the following, we want to discuss the single steps within the flow chart of the morphology generator.

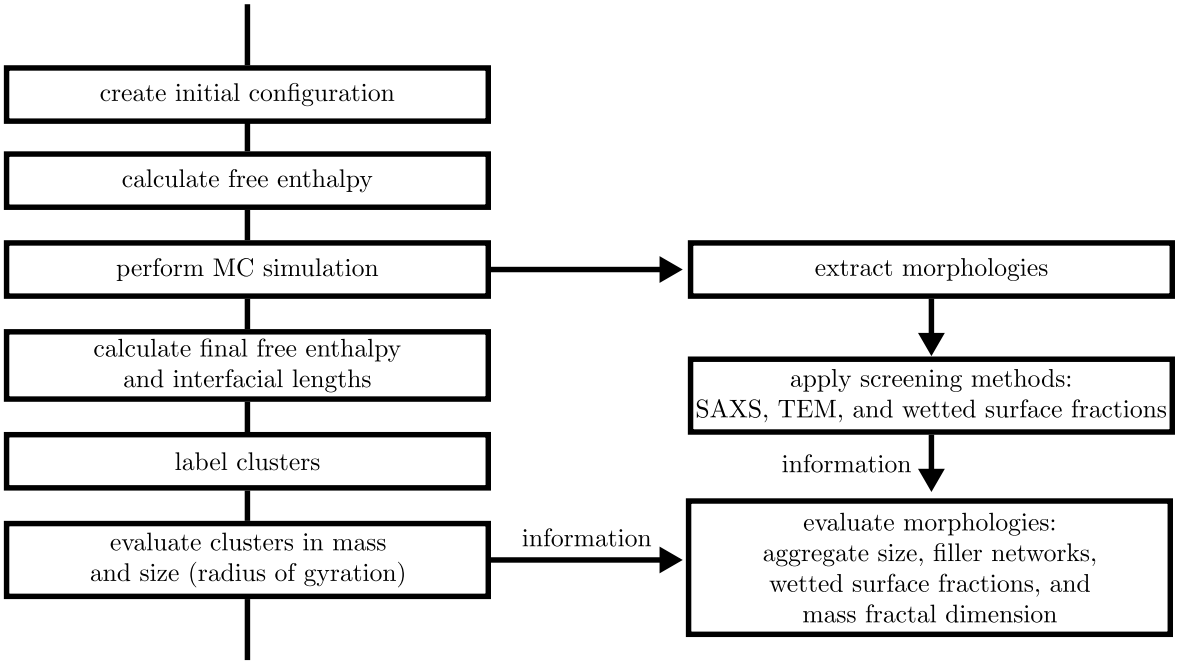

Figure D.4.: Flow chart of the morphology generator and the subsequent evaluation of the morphologies. The left hand side of the flow chart shows the steps performed using the morphology generator. The single steps are described in more detail in the text. The right hand side shows the evaluation of the generated morphologies. After their extraction, they are fed into the screening methods and subsequently analyzed. Note that information from the morphology generator itself is used additionally for a more detailed analysis.

In the first step, the initial configuration of the system is created. This includes assigning the coordinates to each cubic cell as well as its type. The type of the cell is determined by the filler volume content ϕ in the case of single polymer systems (cf. chapter 2), i.e., cells are either polymer or filler. For systems containing polymer blends it is determined by ϕ and the ratio of the individual polymers, i.e., the cells are either filler, polymer A or polymer B. The filler cubes are subsequently assigned the property treated with probability θ to each individual side. When assigning the cell type and the individual surfaces of the filler cubes, the surface free energies of the sides are set accordingly. Thereafter, the free enthalpy of the initial state is calculated, i.e., the work of adhesion, $W(\gamma)$, between all interfaces.

Next, the flocculation process is mimicked by performing the MC simulation. The according pseudo-code for the algorithm is given in Code D.4. Figure D.5 shows the corresponding flow chart of the algorithm. While it is mostly discussed in each of the main chapters of this work, it is worth to note that after a certain number of MC steps information about the system is extracted. This includes the coordinates of all particles, i.e., the morphology, as well as the interfacial lengths and the free enthalpy. We saw in the former section that this is the quantity whose average is calculated and which is minimized along the path through phase space. The first extraction is done after $n = 10^4$ steps. Thereafter, they are extracted an magnitude of steps later until the maximum number of MC steps is reached. This is reasonable when we consider the change in the free enthalpy in Figure D.3. In the first ten million steps, significant changes in the morphology must take place. Thereafter, the changes reduce strikingly and a 'snapshot' of the system after a longer simulation time is sufficient. The coordinates are then used by the screening methods. Just from this information alone, the system can be analyzed in detail. We can obtain the structure of the generated morphology, the size of the aggregates, and their mass fractal dimension, and, if the system is large enough, even the mass fractal dimension of bigger structures. For a deeper understanding, however, additional information must be considered. With the interfacial lengths, from which we calculate the wetted surface fractions (cf. chapter 2), the TEM pictures can be interpreted. For the identification of a possible filler network, we must label the filler clusters inside the elastomer matrix. This is a crucial step to understand the morphologies in full detail.

Before the clusters are identified and labeled, but after the MC simulation is finished, the free enthalpy of the final configuration is calculated and in addition, the interfacial lengths are determined.

Cluster labeling is a common problem encountered in the analysis of lattice models. A very fast and prominent algorithm in two dimensions is given by the Hoshen-Kopelman algorithm. For its detailed functionality we want to refer to the original paper [7]. A three dimensional adaptation of the same algorithm turned out to be a very exhausting task. Thus, a different approach was chosen. At this point it is stressed that the algorithm to identify the clusters was developed and coded by my colleague Sven Engelmann. It utilizes double linked lists. Here we want to briefly discuss how it works.

In the beginning, the complete lattice is searched for filler particles, which are in direct contact with each other and whose sides are both 'untreated'. Those particles follow our cluster definition from chapter 2. Other definitions can be implemented straightforwardly. To find every connection, it is sufficient to perform this search in one direction of each spatial

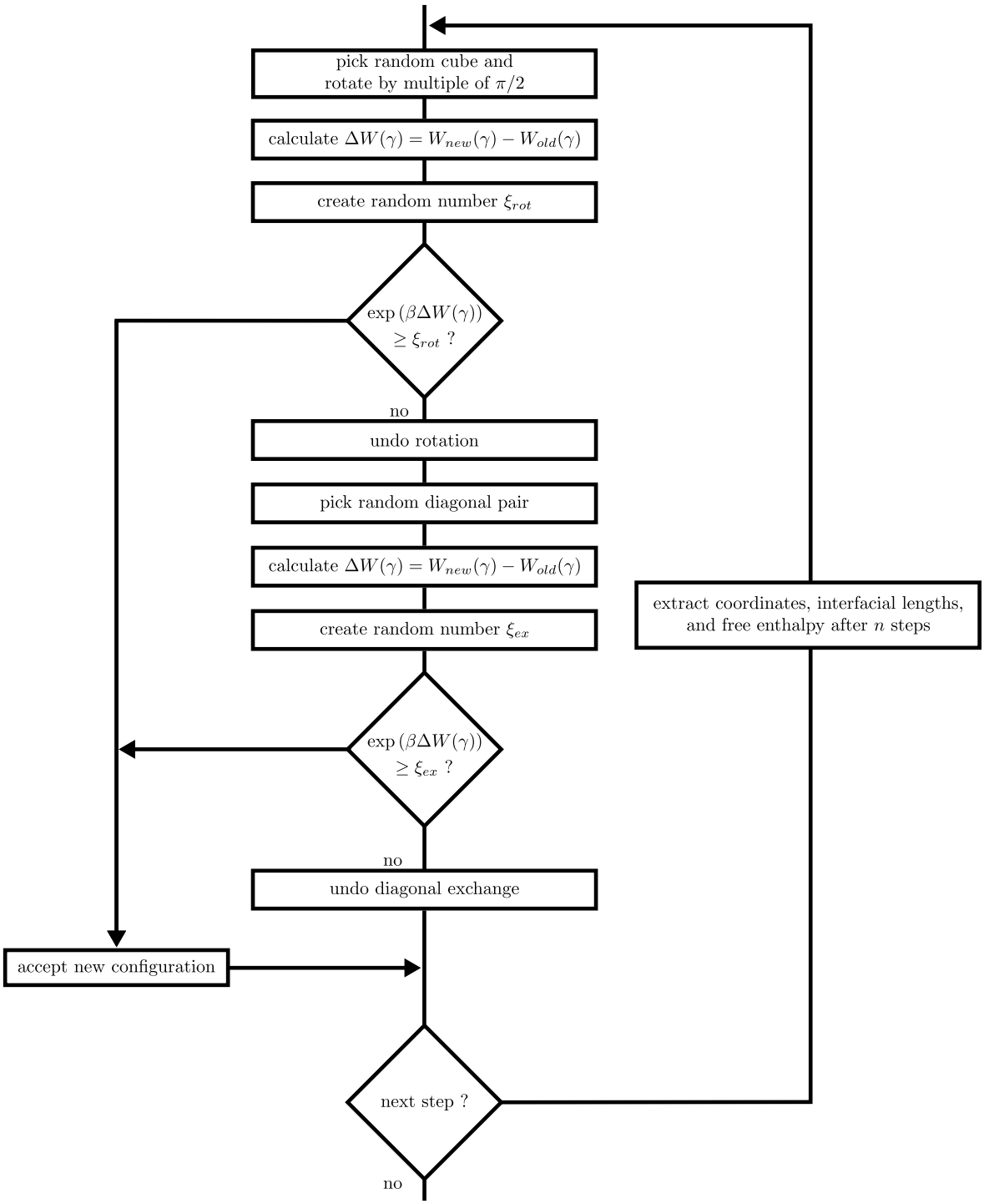

Figure D.5.: Flow chart of the MC algorithm according to Code D.4 used inside the 'perform MC simulation' block in Figure D.4. Note that the random cube rotation is ignored in the case of untreated filler particles (cf. chapter 3). The extraction after n steps is generally performed for the first time after $n = 10^4$ steps. Thereafter, an magnitude of steps later until $n = MC_{max}$, i.e., the maximum number of MC steps is reached.

dimension for each particle. Because we are dealing with cubes, we chose bottom, right, and front. This produces several lists of pairs. For instance, we may find

$$0 \leftrightarrow 1 \qquad \text{and} \qquad 1 \leftrightarrow 2 \qquad \text{and} \qquad 3 \leftrightarrow 4. \tag{D.21}$$

The numbers indicate the position of the particles on the lattice. In a next step, a label counter is set and a new (empty) list is generated. The first pair is then inserted inside this new list and removed from the list of pairs. The new list then looks like this

$$0 \leftrightarrow 1, \tag{D.22}$$

and the list of pairs like this

$$1 \leftrightarrow 2 \qquad \text{and} \qquad 3 \leftrightarrow 4. \tag{D.23}$$

The first entry of the new list is used to search for any coincidental entry in the leftover pairs. For our example this means that the 0 is used and compared to the entries 1 and 2 as well as 3 and 4, which do not coincide. Then the second entry of the new list is used and the process is repeated. For 1, we find an entry in the $1 \leftrightarrow 2$ pair. The 2 is then taken, added to the new list, and the pair is deleted from the list of pairs. Subsequently, we find for the new list

$$0 \leftrightarrow 1 \leftrightarrow 2, \tag{D.24}$$

and for the list of pairs

$$3 \leftrightarrow 4. \tag{D.25}$$

Then the 2 is used to search for any coincidental entries in the list of leftover pairs. We find no match and thus the list with the three entries 0, 1, and 2 is assigned the label set in the beginning of the process. Then, the process starts over with the leftover pair in the list of pairs. A new label counter is set and a new (empty) list is generated. The pair is added to the new empty list and deleted from the list of pairs, which is now empty. Consequently, the process terminates.

In a last step of the morphology generator, the clusters are then evaluated. For instance, we find for our example two clusters. One with mass three, consisting of particles at positions $0 \leftrightarrow 1 \leftrightarrow 2$, and one with mass two, consisting of particles at positions $3 \leftrightarrow 4$. An additional quantity is their size, i.e., their radius of gyration, which can be calculated according to Equation (2.14). All this information is used in addition to that obtained by the screening methods to evaluate the morphologies in detail.

D.3.3. Runtime

The runtime of each of part of the morphology generator varies tremendously. While the initialization, calculation of the free enthalpy and interfacial lengths, and the cluster evaluation is very fast (all algorithms have an order of $\mathcal{O}(N)$, where $N = L^3$ is the number of cubic cells, i.e., the volume of the system), the MC part and the cluster labeling consume most of the runtime.

The MC algorithm also has a linear order, but with $\mathcal{O}(n)$ where n is the number of MC steps. For the most part of this work, we fixed $n = 10^3 \cdot N$. However, we find that for some systems more steps are rejected than for others. This varies for the ingredients in use, i.e., the surface free energies. The result is an additional amount of required time. We roughly find that every one hundred thousand steps take approximately one second. For the systems mostly used throughout this work we consequently find runtimes of $t_{MC} \approx 10^{-2} \cdot N = 10^{-2} \cdot 128^3 = 21000$ s, which is roughly six hours[4]. Nevertheless, this shows why increasing the number of MC steps in chapter 3 by factor of roughly fifty consumes so much time and becomes an issue: Fifty steps per particle more on average results in a runtime of roughly 300 hours, i.e., more than twelve days.

The cluster labeling is of different order. While the identification of pairs is again of order $\mathcal{O}(N)$, the subsequent merging of the lists is of order $\mathcal{O}(P^2)$, where P is the number of pairs. This number is $P_{max} = 3N$ in the worst case, which results in an order of $\mathcal{O}(N^2)$. This worst case, however, never happens. For that, the filler content ϕ has to be 100% and the particles have to have no surface treatment at all. A reasonable upper threshold for the mean number of pairs is approximately given by $P_{mean} = 3N\phi$. This results in roughly one magnitude of operations less for the ϕ values used within this work compared to the worst case scenario.

D.4. References

[1] Chandler, D., Introduction to Modern Statistical Mechanics. New York: Oxford University Press, **1987**, ISBN: 019504276X.

[2] Landau, D. P., Binder, K., A Guide to Monte Carlo Simulations in Statistical Physics. 3rd ed., New York: Cambridge University Press, **2009**, ISBN: 9780511651762.

[3] Press, W. H. et al., Numerical Recipes in C - The Art of Scientific Computing. 2nd ed., Cambridge: Cambridge University Press, **1992**, ISBN: 0521431085.

[4] Metropolis, N. et al., Equation of state calculations by fast computing machines. *J. Chem. Phys.* **1953**, 21 (6), 1087–1092, DOI: 10.1063/1.1699114.

[5] Meyer, J., Molekulare Modellierung der mechanischen Eigenschaften von elastomeren Nano-Kompositen. Dissertation, University of Wuppertal, **2018**.

[6] Glansdorff, P., Prigogine, I., Thermodynamic theory of structure, stability and fluctuations. London: John Wiley & Sons, **1971**, ISBN: 0471302805, DOI: 10.1119/1.1987158.

[7] Hoshen, J., Kopelman, R., Percolation and cluster distribution. I. Cluster multiple labeling technique and critical concentration algorithm. *Phys. Rev. B* **1976**, 14 (8), 3438–3445, DOI: 10.1103/PhysRevB.14.3438.

[4] Those values were established by performing simulations on a AMD Opteron Processor 6344.

List of Tables

Abbreviations

A200 Aerosil 200
AFM atomic force microscopy
APDMES aminopropyldimethylethoxysilane
AR974 Aerosil R974
ASTM American Society for Testing and Materials
BET theory Brunauer–Emmett–Teller theory
BR polybutadiene rubber
CPDMES chloropropyldimethylethoxysilane
CR chloroprene rubber
CTAB cetyl-trimethyl-ammonium-bromide
DMA dynamic mechanical analysis
DPD dissipative particle dynamics
EPDM ethylene-propylene-diene rubber
EPR ethylene-propylene rubber
HD silica highly dispersive silica
HNBR hydrogenated acrylonitrile-butadiene rubber
IR infrared radiation
IUPAC International Union of Pure and Applied Chemistry
MC Monte Carlo
MD molecular dynamics
MEK methyl ethyl ketone
NMR nuclear magnetic resonance
NPT isothermal-isobaric ensemble – constant number of particles (N), pressure (P), and temperature (T)
NR natural rubber
NVT canonical ensemble – constant number of particles (N), volume (V), and temperature (T)
octeo octyl-triethoxysilane
ODMMS octyldimethylmethoxysilane
OWRK theory Owens, Wendt, Rabel, and Kaelble theory
P1846F Perbunan 1846F (acrylonitrile-butadiene rubber)
P3446F Perbunan 3446F (acrylonitrile-butadiene rubber)
P4456F Perbunan 4456F (acrylonitrile-butadiene rubber)
phr parts per hundred rubber
PRNG pseudo random number generator
RNG random number generator
SANS small angle neutron scattering
SAS small angle scattering
SAXS small angle X-ray scattering
SBR styrene-butadiene rubber
silica Silicon Dioxide
S-SBR (solution-)polymerized styrene-butadiene rubber
TEM transmission electron microscopy
TESPT Bis[3-(triethoxysilyl)propyl] Tetrasulfide
TRNG true random number generator
USANS ultra small angle neutron scattering
USAXS ultra small angle X-ray scattering
UV ultraviolet
UVN3 Ultrasil VN3
vdW van der Waals
VN3g Ultrasil VN3 gran.
VN3p Ultrasil VN3 pulv.
wt% percentage by weight
XNBR carboxylated acrylonitrile-butadiene rubber

Table of Variables

variable	description	unit
$[X]$	unit bracket: states unit of variable X	1
a	effective contact area between particles	$n\mathrm{m}^2$
A	general surface area	m^2
A_j	total area of j-type interfaces or amplitude of normal distribution for quantity j (unitless) – described in context	$n\mathrm{m}^2$
β	thermodynamic beta, $\beta = 1/k_B T$. Reciprocal of the thermodynamic temperature T	J^{-1}
C_{vdW}	van der Waals constant in Appendix B	$\mathrm{J{\cdot}m}^6$
D	filler particle number density	1
d_m^i	mass fractal dimension of i	1
d_s^i	surface fractal dimension of i	1
E	internal energy (in J) or Young's modulus (in Pa) (cf. page 213)	$[E]$
η_i	fraction of polymer i. Example: 50/50-NR/SBR $\rightarrow \eta = 0.5$	1
f	abbrevation for filler or filling factor (cf. page 67)	1
F	Helmholtz free energy (in J) or force (in N) – described in context	$[F]$
F_p	form factor of the particles	$c\mathrm{m}^{-1}$
G	free enthalpy	J
g_i	weigth to determine the weighted mean	1
g_2	pair distance correlation function	1
γ, γ_α	surface free energy (of α)	$\mathrm{J/m}^2$
γ_α^d	dispersive part of the surface free energy (of α)	$\mathrm{J/m}^2$
γ_α^p	polar part of the surface free energy (of α)	$\mathrm{J/m}^2$
γ_j, $\gamma_{\alpha\beta}$	interfacial free energy of a j-type interface/between surfaces of type α and β	$\mathrm{J/m}^2$
$\Gamma_{i/j}$	mass ratio of i to j	1
H	enthalpy	J
I	scattering intensity	$c\mathrm{m}^{-1}$
L	linear dimension of the simulation box	1
λ	stretch ratio in Appendix A (unitless) and wavelength in Appendix C (in nm)	$[\lambda]$
$l_{\alpha\beta}$	wetted surface fraction between surfaces of type α and β. Defined in the beginning of each main chapter	1
MC	number of Monte Carlo steps	1
m_i	mass of i. If $i = C$, then mass of a cluster is considered, which is unitless	g
M_i	molar mass of i	g/mol
N	number of particles	1
n_j, $n_{\alpha\beta}$	number of contacts of a j-type interface/between surfaces of type α and β	1
N_i	amount of i. If $i = C$, then amount of clusters is considered	1
ω	simulation frequency	1

variable	description	unit
P	pressure	Pa
ϕ	filler volume fraction	1
$\tilde{\phi}_f^i$	relative filler volume fraction inside polymer i	1
ϕ_c	critical filler volume fraction	1
p_c	percolation threshold	1
ψ, ψ'	angles to parameterize the dispersive and polar part of the surface free energies to create the wetting-envelope plots introduced in chapter 2	1
q	magnitude of the scattering vector $\vec{q}$	$n\mathrm{m}^{-1}$
q^*	reduced magnitude of the scattering vector due to Beaucage (cf. Appendix C)	$n\mathrm{m}^{-1}$
q_i	inverse size of i correlated to real size via $q_i = \pi/R_i$	$n\mathrm{m}^{-1}$
ρ_i	mass density of i	$\mathrm{g}/c\mathrm{m}^3$
ρ, $\Delta\rho$	scattering length density/contrast	$c\mathrm{m}^{-2}$
$\rho(\vec{r})$	electron density	$c\mathrm{m}^3$
R_i	radius of i	$n\mathrm{m}$
R_G	radius of gyration	$n\mathrm{m}$
R	gas constant (only in Appendix B, then in J/K·mol) or radius (in nm) – described in context	$[R]$
S	entropy (only in Appendix B), else surface area (in $n\mathrm{m}^2$)	J/K
σ_i	surface density of i, standard deviation of i (unitless), or width of the normal distribution (unitless) – described in context	m^{-2}
S_i	surface area of i	$n\mathrm{m}^2$
$S_{a/n}$	structure factor of the network/agglomerate	1
θ	heterogeneous silanization or angle – described in context	1
$\tan\delta$	ratio between loss and storage modulus	1
T	thermodynamic temperature	K
T_c	critical temperature	K
T_g	glass transition temperature	K
T_m	melting temperature	K
u_0	amplitude of deformation	1
U_i	potential of type i	J
V	system's volume	$n\mathrm{m}^3$
V_i	volume of i	$n\mathrm{m}^3$
$\vec{r}_i$	arbitrary vector in $\mathbb{R}^3$ of i. For $i = s$: center of mass	1
W, W_a	work of adhesion	J
W_c	work of cohesion	J
ξ	random number between 0 and 1	1
$\bar{x}$	mean of variable x. Unit depending on x	$[\bar{x}]$

Index

P

R

S

T

V

W

Y